Doctoral Dissertations   Graduate School

12-1999

Ziegler-Natta and metallocene catalyzed isotactic polypropylene : a comprehensive investigation and comparison using crystallization kinetics, fiber spinning and thermal spunbonding

Eric Bryan Bond

Follow this and additional works at: https://trace.tennessee.edu/utk_graddiss

To the Graduate Council:

I am submitting herewith a dissertation written by Eric Bryan Bond entitled "Ziegler-Natta and metallocene catalyzed isotactic polypropylene : a comprehensive investigation and comparison using crystallization kinetics, fiber spinning and thermal spunbonding." I have examined the final electronic copy of this dissertation for form and content and recommend that it be accepted in partial fulfillment of the requirements for the degree of Doctor of Philosophy, with a major in Polymer Engineering.

Josoph E. Spruiell, Major Professor

We have read this dissertation and recommend its acceptance:

Roberto Benson, Edward Clark, Paul Phillips, Bernhard Wunderlich

Accepted for the Council:

Carolyn R. Hodges

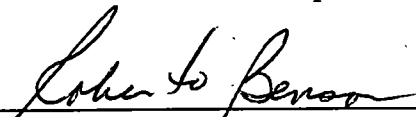Vice Provost and Dean of the Graduate School

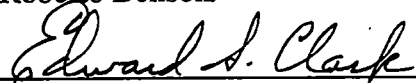(Original signatures are on file with official student records.)

To the Graduate Council:

I am submitting herewith a dissertation written by Eric Bryan Bond entitled "Ziegler-Natta and Metallocene Catalyzed Isotactic Polypropylene: A Comprehensive Investigation and Comparison using Crystallization Kinetics, Fiber Spinning and Thermal Spunbonding." I have examined the final copy of this dissertation for form and content and recommend that it be accepted in partial fulfillment of the requirements for the degree of Doctor of Philosophy, with a major in Polymer Engineering.
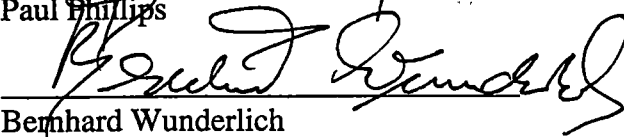
_____
Joseph E. Spruiell, Major Professor

We have read this dissertation
and recommend its acceptance:

_____
Roberto Benson

_____
Edward Clark

_____
Paul Phillips

_____
Bernhard Wunderlich

Accpeted for the Council:

_____
Associate Vice Chancellor and
Dean of the Graduate School

Ziegler-Natta and Metallocene Catalyzed

Isotactic Polypropylene:

A Comprehensive Investigation and Comparison

using

Crystallization Kinetics, Fiber Spinning

and

Thermal Spunbonding.

A Dissertation Presented for the Doctor of Philosophy Degree

The University of Tennessee, Knoxville

Eric Bryan Bond

December 1999

ACKNOWLEDGEMENTS

DEDICATION

To my best friend,

companion,

and future wife, Donna Leigh.

To our wonderful son,

Ethan Alexander. For the

happiness and joy they bring me.

ABSTRACT

Isotactic polypropylene (iPP) can be synthesized using conventional heterogeneous Ziegler-Natta (zniPP) and homogenous metallocene catalysts (miPP). Materials catalyzed using the Ziegler-Natta catalysts typically have broad molecular weight distributions, high peak melting temperatures, a heterogeneous distribution of stereo defects, and significant portions of noncrystallizable (atactic) material. Metallocene resins typically have a narrow molecular weight distribution, lower peak melting temperatures than zniPP resins, a more uniform distribution of stereo and regio defects, and very small amounts of atactic material. The purpose of this work was to investigate and compare and contrast miPP resins to zniPP resins.

The resins in this study were thoroughly characterized by cNMR and solution fractionation to determine the number, type and distribution of defects. The resins were then studied under isothermal and nonisothermal quiescent crystallization conditions to determine the bulk and crystal growth kinetics, crystal structure, crystallinity and thermal properties. The resins were also melt spun into fibers to allow the effects of molecular weight and molecular weight distribution on as-spun filament properties to be determined. The as-spun fibers were then characterized to determine the crystalline and noncrystalline orientation functions, birefringence, density, thermal properties and tensile mechanical properties (elongation-to-break, modulus, tensile strength). In addition, on-line crystallization studies were also conducted using the resins to determine the locations in the spinline where crystallization occurred. Selected resins were then used to study the effects of as-spun fiber properties on nonwoven fabric mechanical properties using a thermal point spunbonding process.

The cNMR and xylene fractionation studies indicated the miPP resins had substantially more total defects in the crystallizable material than either of the zniPP resins in this study. The miPP resins also contained regio type polymerization defects, which were not present in the zniPP resins. The results also found that, in general, the miPP resins contained much smaller portions of atactic material, as determined by xylene fractionation. The totality of the stereoregularity results suggest the miPP resins have a more uniform defect distribution than the zniPP resins.

Combined results from DSC, SAXS and WAXD indicated the miPP and zniPP resins have similar α-monoclinic equilibrium melting temperatures (T_m^0), despite the differences in defect content, type and distribution. The presence of atactic material was found to lower the observed equilibrium melting temperature of a particular resin, whether miPP or zniPP. The γ-crystal structure, observed in the miPP resins using WAXD and DSC, had a lower equilibrium melting temperature than the α-structure. The T_m^0 of the α-monoclinic structure was found to be 186±2°C, while the γ-structure T_m^0 was found to be 178±2°C, when crystallized at atmospheric pressures. The miPP resins were found to melt at lower temperatures than the zniPP resins at similar crystal thicknesses, which is attributed to the miPP resins having significantly higher fold surface free energies when crystallized under isothermal conditions.

The isothermal crystallization studies showed the miPP resins readily produce the γ-crystal structure. The zniPP resins also produced small amounts of the γ-structure, at high crystallization temperatures. Defects were found to be excluded from the crystal under isothermal crystallization conditions. The defects excluded from the crystal core are thought to be rejected into the crystal fold surface region, increasing the fold surface free energy. SAXS studies indicate the lamellae fold surface of isothermally crystallized miPP

v

resins might be rough, possessing a three-dimensional topology instead of a two-dimensional structure. The T_m^0 and fold surface free energy for each resin was determined from the Gibbs-Thompson equation. The Gibbs-Thompson equation normalizes to a two-dimensional crystal fold surface, therefore the apparent fold surface free energy is higher in the miPP resins with a three-dimensional topology. These conclusions are supported by the nonisothermal crystallization studies which showed that defects are incorporated into the crystal core and that the fold surface free energies of the nonisothermally crystallized films using miPP and zniPP resins are similar.

For crystallization under isothermal crystallization conditions, the observed linear growth rates were found to be dependent upon defect content. Under nonisothermal conditions, the growth rate was found to depend mostly on the molecular weight. For resins with similar molecular weights, the number of defects was also found to be important under nonisothermal crystallization conditions. The nucleation density was found to have a strong effect on the overall bulk crystallization kinetics. The relative order of bulk crystallization rates for the resins in this study was found to be strongly determined by the relative nucleation density of a particular resin.

Fiber spinning studies showed that the molecular weight and molecular weight distribution of an iPP resin is largely determined by the point of crystallization in the spinline, the crystallization temperature and as-spun filament properties. Increasing the molecular weight (also increasing the spinning speed) tended to increase the density and crystallization temperature, i.e. crystallization in the spinline occurs closer to the spinneret. Narrowing the molecular weight distribution and decreasing the molecular weight (also with increasing the spinning speed) tended to increase the noncrystalline and crystalline orientation function, birefringence and tensile strength (elongation-to-break was the inverse) for most the resins. The more narrow molecular weight distribution resins also delay crystallization to a distance further away from the spinneret and to lower

crystallization temperatures. The as-spun fiber tensile modulus was found to increase as the spinning speed increased, a result of the birefringence and crystallinity increasing. The observed differences in fiber spinning behavior between the miPP and zniPP resins are mainly attributed to the differences in molecular weight and its distribution.

Studies on the mechanical properties of nonwoven fabrics made using the thermal point spunbonding process were found to be dependent on the fiber properties, when bonded at the optimum bonding temperature. The optimum bonding temperature is the temperature in the bonding curve where the fabric mechanical properties are the best. Increasing the as-spun fiber noncrystalline orientation function and birefringence increased the optimum bonding temperature. Increasing the fabric basis weight also increased the optimum bonding temperature. No significant differences in fabric properties between miPP and zniPP resins could be found that are not explained by differences in the as-spun fiber properties. The as-spun fiber properties were found to be different between the two catalyst systems, a result of differences in their molecular weight and molecular weight distribution.

Table of Contents

Table of Contents

Table of Contents

Table of Contents

Table of Contents

Table of Contents

Table of Contents

Table of Contents

List of Figures

List of Figures

List of Figures

List of Figures

List of Figures

List of Figures

List of Figures

List of Figures

List of Figures

List of Figures

List of Figures

List of Figures

List of Figures

List of Figures

List of Figures

xxx

List of Tables

List of Tables

List of Tables

List of Tables

List of Tables

List of Tables

List of Tables

Chapter 1

Introduction

Isotactic polypropylene (iPP) is a major engineering thermoplastic that has enjoyed widespread use due to its high strength to weight ratio, rheological properties and cost effectiveness. Isotactic polypropylene is used extensively in fiber spinning applications such as spunbonding and staple fiber formation to produce nonwoven fabrics. Polyproylene is also used in many injection molding applications where high temperature dimensional stability is needed near the temperature of boiling water, a region where most polyethylene systems do not have outstanding dimensional stability. Isotactic polypropylene is also important from a scientific standpoint, in that it exhibits several crystal structures, can be copolymerized to yield novel copolymers and is polymerized from the most basic vinyl monomer, propylene.

Until very recently, iPP was produced using Ziegler-Natta catalysts that polymerize through coordination chemistry. Ziegler-Natta isotactic polypropylene (zniPP) resins typically have to be washed after synthesis to remove the large amounts of noncrystallizable material (atactic) produced during the polymerization process. Resins produced using the Ziegler-Natta catalysts also are typically peroxide degraded to narrow the large molecular weight distribution found in as-produced zniPP resins. The large molecular weight distribution and presence of atactic material is due to the heterogeneous catalysts and cocatalysts used in zniPP production that have different numbers and types of catalyst sites. Recently, a new type of homogenous catalyst system was

commercialized for iPP that produces a very narrow molecular weight distribution resin with very small amounts of atactic material, in the as-produced resin. The new catalysts are called metallocene catalysts.

The purpose of this work is to study and compare Ziegler-Natta and metallocene catalyzed isotactic polypropylene resins. The goal is to understand the behavior of each type of resin individually and iPP resins collectively. Each resin will be thoroughly characterized to determine its molecular weight, molecular weight distribution, amount and type of defects, as well as the amount of atactic material. This information is needed before any understanding can be made of the properties of polypropylene resins in general, and more specifically, the iPP resins in this study.

The materials in this work will be studied in a range of ways, from techniques and purposes of purely scientific interest, to methods used in industries that consume billions of pounds of iPP per year worldwide. This investigation can be divided into three different, although intimately related, categories:

(1)   Crystallization kinetics: Studies were conducted under isothermal and nonisothermal conditions to study the behavior of the various resins. SAXS, WAXD and DSC measurements were made on samples produced during the course of the crystallization studies to investigate each sample's properties.

(2)   The same resins were melt spun into fibers to study the effects of molecular weight, molecular weight distribution and defect content on fiber properties. On-line studies using these materials were performed to elucidate the crystallization kinetics in the steady state spinline. The properties of the as-spun filaments were thoroughly characterized to determine and understand the important relationship

that exists between material and processing variables and final filament morphology in the production of melt spun fibers.

(3)   Selected iPP resins were used to study the thermal point spunbonding process. The emphasis in this work was to study the relationship between fiber properties and nonwoven fabric properties.

The various chapters in this work are divided in a manner to reflect the important areas of research involved in this investigation. Chapter 1 is an introduction to this work, giving a brief review of the research and its division. Chapter 2 is a comprehensive literature review of quiescent crystallization behavior under isothermal and nonisothermal conditions, including regime analysis. Chapter 2 also reviews the theory and previous investigations into melt fiber spinning, as well as, the conversion of melt spun fibers into nonwoven fabrics via thermal point bonding. In each case, previous studies on iPP have also been reviewed.

The purpose of Chapter 3 is to present the theory and experimental methods used in conducting the research in this investigation. Detailed instructions are given for why and how the experimental techniques are used in the pursuit of elucidating sample characteristics and properties. The techniques and methods used in this investigation include; small and wide angle x-ray diffraction, optical microscopy, differential scanning calorimetry, tensile mechanical properties, sonic velocity and birefringence.

The results and discussion in Chapter 4 deal with quiescent isothermal and nonisothermal studies performed on the various iPP resins in this investigation. Bulk and crystal growth kinetic studies have been carried out. Films crystallized with the various resins under a variety of conditions were made and characterized to determine their

3

crystallinity, crystal properties, morphology and thermal behavior. The influence of defect type, content, distribution and location in the as-crystallized sample under a variety of crystallization conditions are discussed in relation to the observed film properties.

The results and discussion in Chapter 5 details the small scale monofilament fiber studies performed on several iPP resins. On-line fiber studies were conducted to determine the location of crystallization onset and when crystallization has been completed, under a given set of processing conditions. This on-line data was then used to calculate the on-line crystallization kinetics of the various resins for each processing condition. The as-spun fibers were then fully characterized to determine their mechanical tensile properties, birefringence, crystalline and noncrystalline orientation functions, density and melting points. The underlying fiber morphology is then discussed in terms of the molecular weight and molecular weight distribution of each iPP resin and its influence on structure development during the melt spinning process.

The results and discussion in Chapter 6 concern the studies conducted on thermal point spunbonding of nonwoven fabrics. Chapter 6 develops and explains the relationship between as-spun filament morphlogy as well as properties on determining the optimum bonding temperature and its affect on final fabric mechanical properties.

A summary of results and conclusions from each chapter are in Chapter 7. Chapter 7 also contains recommendations for future research.

Chapter 2

Theoretical Background

2.0 Polypropylene

Polymers are materials composed of many subunits called monomers. Monomers can be composed of almost any type of atoms, but are most frequently composed of carbon, oxygen, hydrogen and nitrogen. Many polymers are constructed with a carbon backbone, although other atoms or groups may constitute the backbone structure, such as: ethers, esters, amides etc. The composition of the backbone , along with any side groups attached to the monomer, are important since the chemical nature of these species will dictate what type of properties the polymer will have. For our definition, we will define a polymer as any molecule having a molecular weight (MW) greater than 10,000 Daltons or composed of 1,000 or more atoms[1].

Polypropylene (PP), is polymerized from the monomer propylene. Prior to 1950, a propylene polymer was a branched low molecular weight oil with no practical interest. Most polymers produced during this time were non-crystalline due to poor stereo arrangement of the monomer units during polymerization. In the 1940s, the first stereoregular polymer from an asymmetric monomer was first discovered, cis-1,4-isoprene, natural rubber. In order to form cis-1,4-isoprene, all monomer units must polymerize in a head to tail manner. At the time, it was impossible for scientists to duplicate this type of polymerization using existing chemical synthesis techniques.

In this era of polymer science, semi-crystalline polymers were in their infancy. A few polymers were known to crystallize. For instance, low density polyethylene (LDPE)

5

was know to have crystalline regions. However, at this time PP was not observed to have any level of crystallinity. Ethylene, as a symmetrical monomer, has no head to tail or R/S insertion stereo configuration needed during the polymerization process. Therefore, ethylene could, in theory, polymerize from any known stereo arrangement of the monomer.

When Ziegler synthesized a linear PE, it was found that branching affected the levels of crystallinity for PE. Shortly after Ziegler formed linear PE, Natta produced a roughly 40% crystalline PP product. Natta and his researchers went on to analyze the crystalline material and found that PP had a helical chain. The researchers also recognized the importance of stereoregular polymerization in achieving the crystalline structure. They defined three different stereo conformations for PP, named after the Greek terms; isotactic, syndiotactic and atactic.

2.1 Stereo Arrangements of Polypropylene

Polypropylene is a vinyl polymer, meaning it has a mono substituted group for a hydrogen on the carbon backbone. In the case of propylene, a methyl group has been substituted in place of a hydrogen. Ethylene and propylene monomers are shown in Figure 2.1. The ethylene monomer is a flat planar molecule having sp^2 hybridized orbitals, in the monomeric form. Propylene is very similar, except the substituted methyl group is considerably larger than the hydrogen. The methyl group also destroys the symmetry found with ethylene molecules. Methyl substitution gives a side group arrangement and handedness to a propylene chain. The methyl groups can be arranged in a head to head, tail to tail or head to tail type organization, as shown in Figure 2.2. The

6
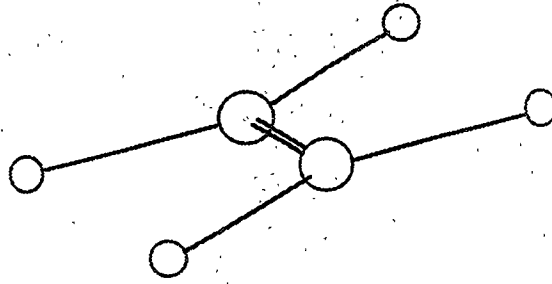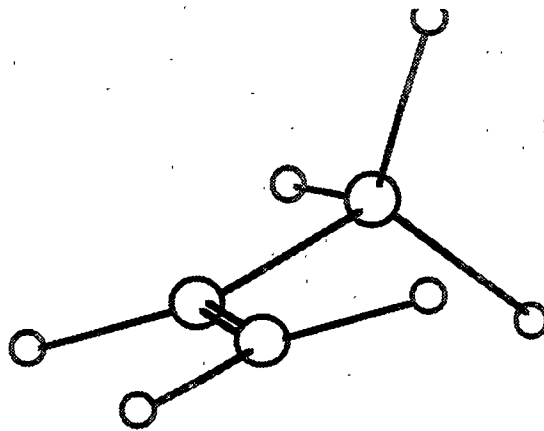
Ethylene Monomer

Propylene Monomer

Figure 2.1 PE and PP Monomers

7

Head-to-Head (regio defect)

Tail-to-Tail (regio defect)

Head-to-Tail or cis addition (meso diad = mm)
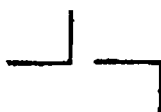
trans addition (racemic diad = mr, stereo defect)

Figure 2.2   iPP insertion and defect types.

8

vertical lines represent the methyl group. The methyl groups can also be arranged in R or S type configuration, inducing a handedness on the chain, meaning there can be a left (R) or right (S) addition of the monomer. Both the side group arrangement and handedness in the polymerization of propylene is important in determining what type of stereo arrangement the synthesized polymer chains will have.

Polypropylene is an α-polyolefin, meaning it is prochiral, having two enantiofaces, R and S. The absolute configuration of the tertiary carbon atoms of the main chain (R and S) is dictated by the enanioface undergoing the insertion. This is shown in Figure 2.3, where the stereochemistry of the metal carbon addition to an olefinic double bond is illustrated. The R and S orientation arises from which enantioface gets inserted, determined by the stereochemistry, being either cis or trans[2]. If the regioselectivity is high and insertion occurs only with cis stereochemistry, multiple insertions of the same enantioface produce a polymer chain with chiral centers of the same configuration; i.e. isotactic chains. The deuterated propylene monomer illustrates the stereochemistry of isotactic polypropylene (iPP) is cis when using an isospecific catalyst. Multiple insertions of alternating enantiofaces produces a polymer chain with carbon chiral centers of alternating configuration; i.e. syndiotactic polymer chains. If there is random enantioface insertion, an atactic polymer chain with no configurational regularity is formed. The types of enantiomeric insertions described above can also occur within the same polymer chain. Therefore, there can exist portions of each stereo arrangement within a single polymer chain. Shown in Figure 2.4, are the three different stereo arrangements that may occur in PP polymerization. The carbon backbones are placed in a plane so that the methyl side groups either fall on the same side (isotactic),

9
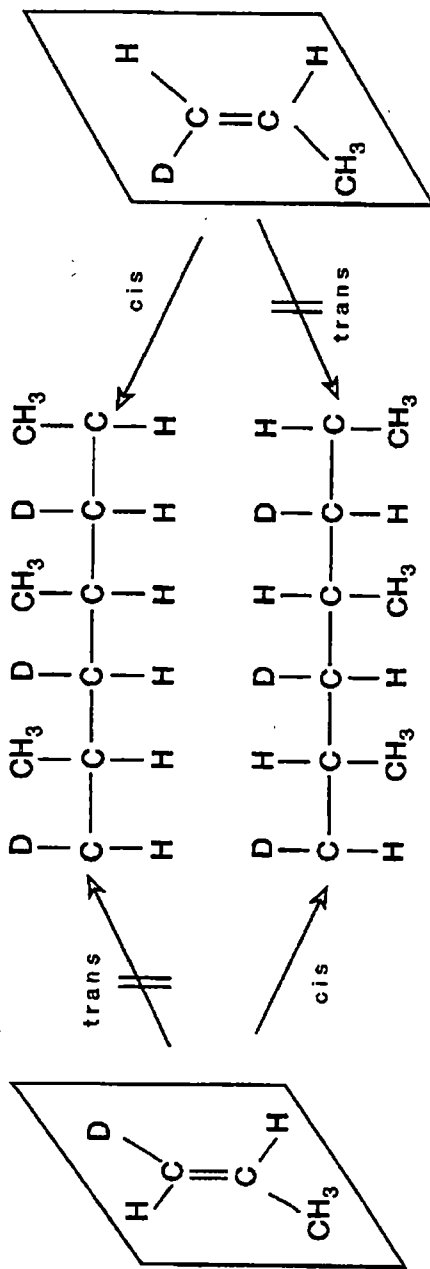
Figure 2.3 Cis/Trans Insertion Mechanism of Deuterated PP Monomer[209].

Isotactic
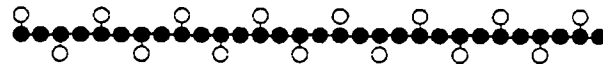
Syndiotactic
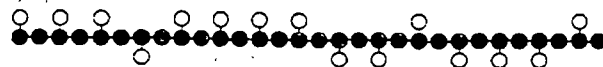
Atactic
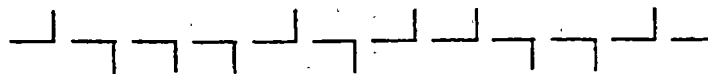
Atactic
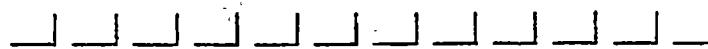
Isotactic
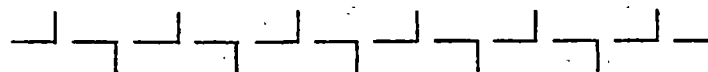
Syndiotactic

Figure 2.4 Stereo Arrangements of PP.

alternate sides (syndiotactic) or some random combination in between (atactic). The remainder of this discussion and work will be centered on isotactic polypropylene (iPP).

Most iPP polymer chains contain some defects. Even highly isotactic chains will contain occasional configurational defects. The two types of configurational defects found in iPP are regio and stereo defects, as shown in Figure 2.2. Regio defects result in a head-to-head methyl group interaction with the adjacent carbon atom and the formation of a ethylene type sequence with the next monomeric unit. Stereo defects result when the enantioface has switched during polymerization so that the methyl groups on adjacent monomer units lie on opposite sides of the carbon backbone. In fact, syndiotactic PP is produced when the frequency of switching the enantioface is very high. If two adjacent monomeric units have the same stereochemistry, a meso diad is formed, abbreviated with an *m*. If two adjacent monomeric units have different stereochemistry, a racemic diad is formed, abbreviated as *r*. The number of monomeric units between configurational defects is called the meso run length.

2.2 Crystallographic Structures of iPP

Isotactic polypropylene forms a 3_1 helix, a result of the steric interaction of the methyl groups. The repulsion of the electron clouds rotates the methyl groups into a minimum energy conformation so there is a methyl group every 120°, with a repeat periodicity of 0.650nm[3-6]. Three propylene units, or three monomers must be added until the unit is repeated, as shown in Figure 2.5. The helix also has a rotational direction, a non-identical "up" and "down" direction that is independent of the handedness. Often

L dw   **R dw**   **L up**   **R up**
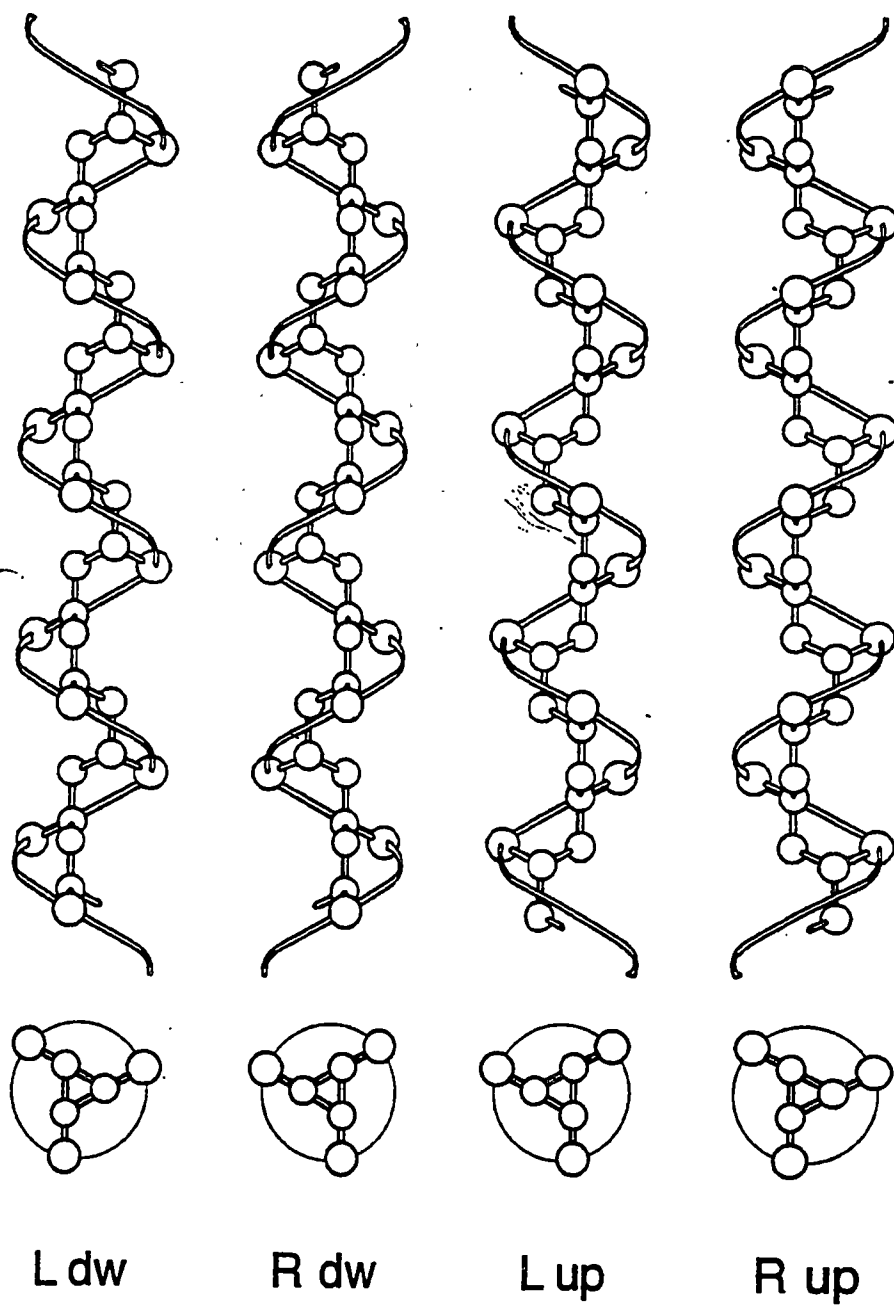
Figure 2.5   Isotactic Polypropylene Helix[210].

13

these are referred to as right and left handed helices. In order for two chains to pack close together, they must be of opposite handedness[3-11].

On a crystallographic level, iPP can assume one (or more) of four different morphological forms, an α, β, γ or condis (smectic) form. These morphologies differ by the arrangement of the polymer chains in the crystal[3-18]. The wide angle x-ray diffraction (WAXD) patterns are shown in Figure 2.6 for the first three crystal structures.

2.2.1 α-Monoclinic Form

The most common crystal phase of iPP, in the absence of nucleating agents and at atmospheric pressure, is the α-monoclinic form (α-iPP). The overall geometry of the unit cell is monoclinic, with parameters a=0.665nm, b=2.096nm, c=0.65nm and β=99.80°. The cell consists of 12 repeat units (four three-fold helical chains) and has a crystal density of 0.938g/cm^3. The space group that has been assigned is C2/c and Cc for the statistically ordered arrangement of the up and down stems in the unit cell. Recent research has supported these values with only slight changes in the c-axis[10,11,17]. These values differ slightly from those proposed by Natta and Corradini in 1960[6].

The chain conformation is a ternary helix based on the tg$^+$ and g$^-$t conformations which minimize the methyl-methyl steric conflicts characteristic of extended isotactic chains and lead to the left and right handed helices, respectively. The packing of the helices is such that any helix interacts mostly with helices of opposite hand. Therefore, α-iPP is based on the alternation, in the b-axis direction, of layers parallel to the ac plane and made only of left-handed, or only of right handed helices. Research has shown[11] that
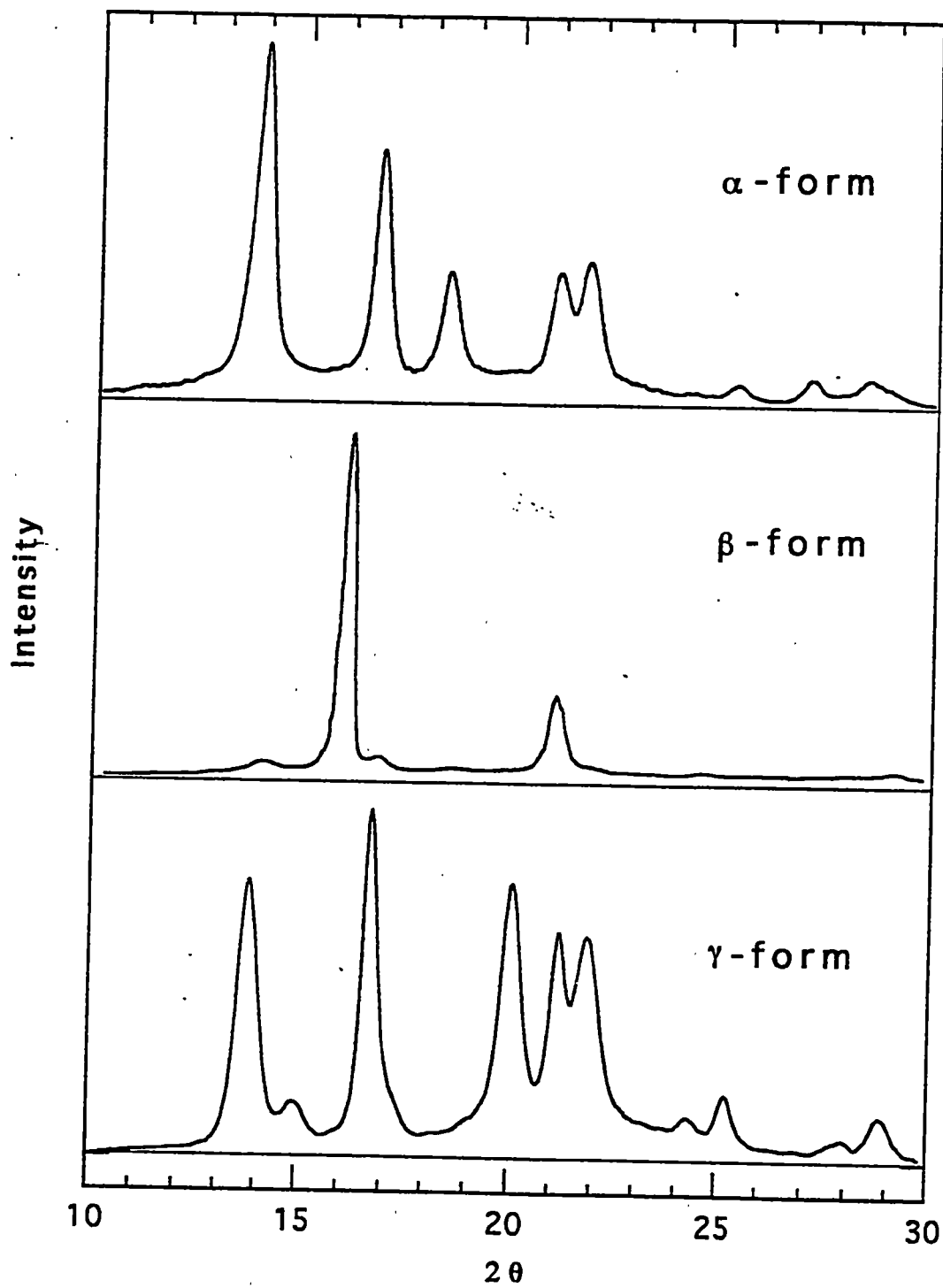
Figure 2.6   Crystal Structures of Isotactic Polypropylene[210].

α-iPP shows various degrees of disorder in the up and down positioning of the chains in the crystal, depending on the thermal and mechanical history of the sample.

2.2.2 β -Pseudohexagonal Form

The structure of β-isotactic polypropylene (β-iPP) is characterized by extensive disorder[11,19]. Formed under special crystallization conditions, using either a temperature gradient method, nucleating agents or at high isothermal crystallization temperatures (typically with a Ziegler-Natta catalyst using crystallization temperatures above 130°C), large amounts of this crystal structure can be formed[11,19-22]. Keith et al.[23] first identified β-iPP but never fully characterized its structure, a result of this crystal structure's thermodynamic and mechanical instability.

The simplest satisfactory model for β-iPP is hexagonal (P$3_1$21 and enantiomorphic P$3_1$21) with a=b=1.103nm and c=0.649nm[19,24-25]. Three monomers form the asymmetric unit, with six chain stems in the unit cell. The crystal density is significantly lower than the other forms of iPP, at 0.92g/cm^3. The lower density, combined with the faster growth rate, indicate that high degrees of disorder exist within β-iPP. Other data exists for this structure[12,13], but the cell is a subcell of the one indicated above. However, the structure presented here is from the most recent research and consists of further investigations done by one of the original investigators who determined the initial β-iPP structure[19].

2.2.3 γ-Orthorhombic Form

The nature of the γ-isotactic polypropylene (γ-iPP) has drawn a considerable amount of attention and work[10,11,13,17,19,22,23,26-30]. The appearance of γ-iPP is favored by molecular features such as short chain length, chain molecular defects or high pressures[10,29,32,33]. Previous studies have shown the formation of γ-iPP with the presence of molecular heterogeneity in the chain, caused be atacticity or by copolymerization[29]. Recent work has demonstrated the production of γ-iPP at elevated pressures from high molecular weight homopolymers with no appreciable defects, confirming an earlier finding[31].

For many years the structure was labeled as triclinic. Recent work has shown the triclinic unit cell is actually a sub-cell of a larger orthorhombic cell[10,11,26]. The triclinic cell has dimensions: a=0.655nm, b=2.140nm, c=0.650, α=97.4°, β=98.8° and γ=97.4°. The cell consists of 12 repeat units having a crystal density of 0.935g/cm^3. These parameters allow the conversion to a larger face-centered orthorhombic unit cell of higher symmetry: a=0.854nm, b=0.993nm and c=4.241nm consisting of 48 repeat units with a crystal density of 0.933g/cm^3. The overall structure is best represented by the statistical copresence of anticlined isochiral helices at each crystallographic position. This is implied by space group Fddd. Local packing modes which cannot retain this feature are satisfactorily described by space groups F2dd or Fd2d.

Much of the early confusion surrounding γ-iPP has originated from the similarity between the α and γ-crystal structures. The WAXD patterns for the α and γ-crystal structures are very similar, except for the shift of one peak to a slightly higher 2θ. As a result, it was assumed that the γ-triclinic cell differed from the α-monoclinic structure.

only slightly in chain conformation. Further confusion arose between whether the γ-triclinic or γ-orthorhombic structure was correct. However, it was shown that the relationship between the γ-triclinic and γ-orthorhombic structures is the c-axis of the smaller triclinic cell is parallel to the diagonals of the ab plane of the larger orthorhombic cell. The orthorhombic γ-iPP is very unusual in that it consists of non-parallel chains packed into a fully ordered array[10,11]. The structures of α-iPP and γ-iPP are shown in Figure 2.7. Notice the similarities between the crystal structures and the very unusual γ-orthorhombic structure composed of sheets of parallel molecules. The molecular orientation between adjacent sheets becomes non-parallel every two sheets with the angle between the non-parallel stems of approximately 81°. The new orthorhombic structure accounts for all observed diffraction peaks in more satisfactory manner than the γ-triclinic[10,11].

The data in Table 2.1 shows the collection of lattice parameters and crystal densities determined for each crystal type, α, β and γ respectively. The values in this table will be used throughout this work.

2.2.4 Conformationally Disordered or Smectic Form

The conformationally disordered (condis) or smectic form is an intermediate metastable crystalline structure[6,34-37]. The smectic form is obtained by quenching thin sheets if iPP from the melt into ice water. The smectic structure can also be found in fibers spun with extremely high cooling rates under small stresses. The smectic structure is thought to be a disordered α-structure, with some experimental evidence to support this claim[38-44]. A comparison of amorphous atactic PP (aPP), the smectic structure
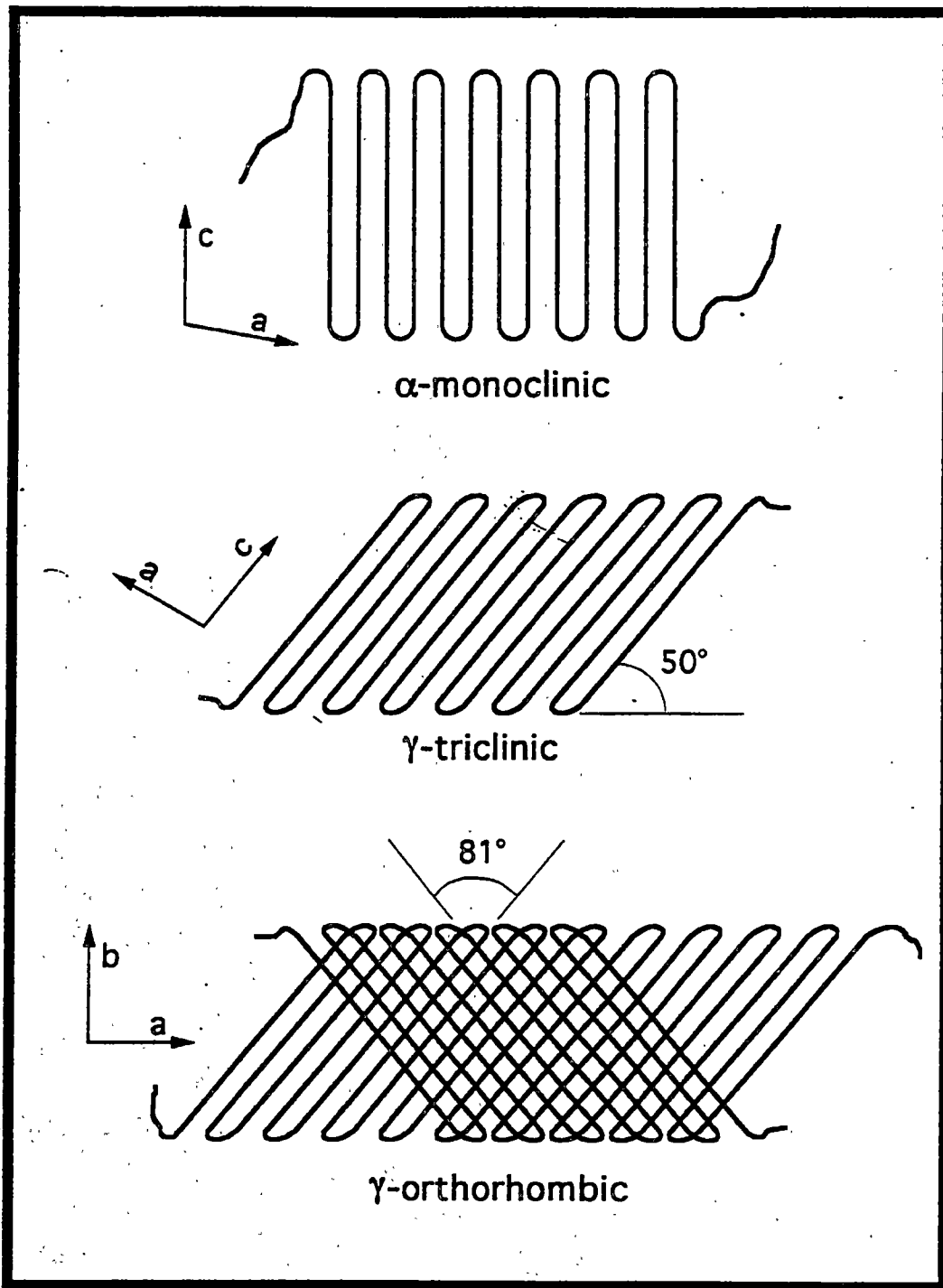
Figure 2.7 Chain stem arrangements in α-monoclinic, γ-triclinic and γ-orthorhombic[210].

Table 2.1 Lattice parameters of iPP structures in this study.

Bravais Lattice	Lattice Parameters (nm)						# of Repeat Units	Space Group	Density (g/cm³)
	a	b	c	α	β	γ			
α-monoclinic	0.665	2.096	0.650	90.0	99.8	90.0	12	C2/c	0.938
β-hexagonal	1.103	1.103	0.649	90.0	90.0	120.0	9	P3$_1$21	0.920
γ-orthorhombic	0.854	0.993	4.241	90.0	90.0	90.0	48	Fddd	0.933

(mesomorphic) and α-form is shown in Figure 2.8. The density of the smectic structure is 0.88g/cm^3. The density of aPP is 0.85g/cm^3, which indicates the smectic structure has a higher molecular order than aPP[6]. An annealed smectic form will gradually transform to the α-form over time or when exposed to elevated temperatures above 70°C.

The morphology that will form is determined by the percent isotacticity of the polymer chains, any monomer defects (such as ethylene instead of propylene) and conditions that the polymer was placed under during the solidification process. The remainder of this work is intended to deepen the understanding of these structure/processing relationships of iPP.

2.3 Polypropylene Synthesis

Isotactic polypropylene is currently synthesized using two different catalyst systems, Ziegler-Natta and metallocene. Ziegler-Natta catalysts produce polymer chains that have a wide range of physical properties, resulting from one or more active polymerization sites. The multiple polymerization sites produce two populations of chains[45-51]. One population consists of high molecular weight (hMW), highly isotactic polymer chains and the other population consist of atactic chains, that are generally non-crystallizable and increase the percent xylene solubles. Metallocene resins typically have very narrow molecular weight distributions (nMWD) with chains of similar molecular structure and properties, a result of only one active catalytic site. Metallocene catalyzed iPP resins have very small amounts of xylene soluble material, while the zniPP resins can have a significant weight percent xylene solubles material[46].

21
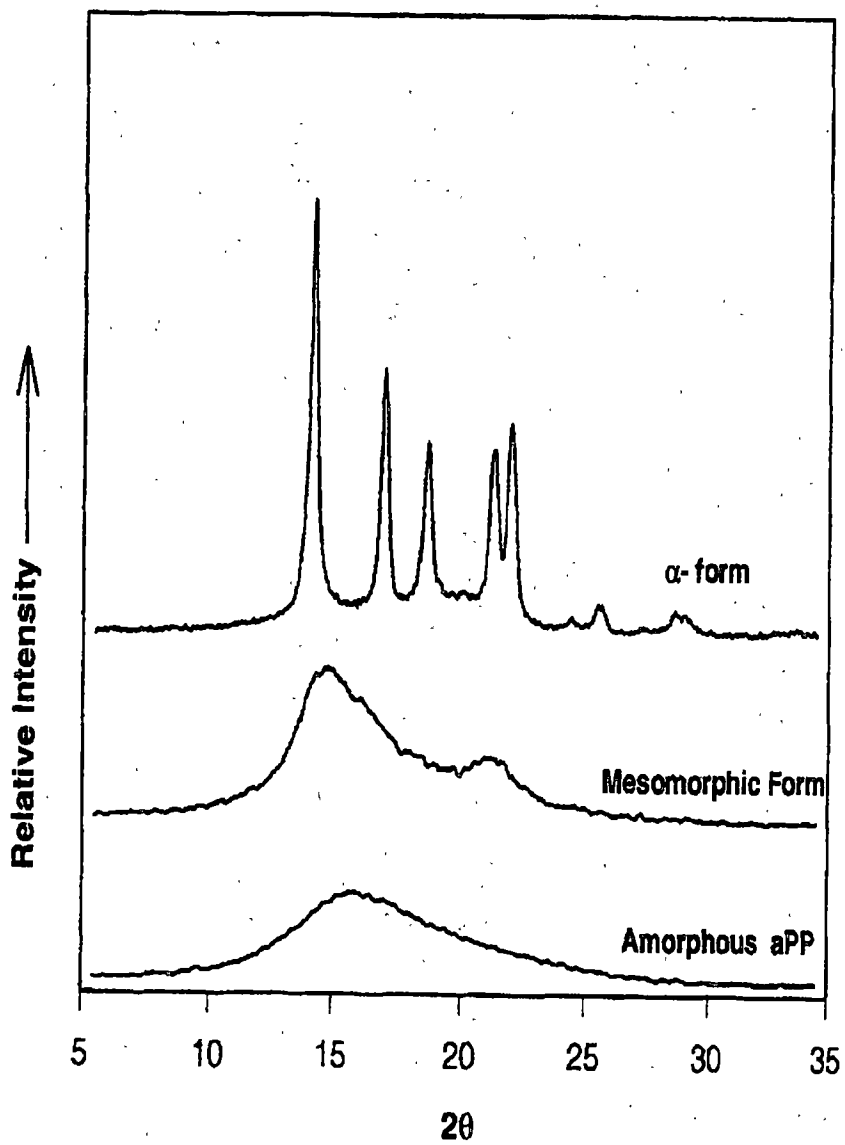
Figure 2.8   Comparison of α-iPP, aPP and the smectic iPP structure[209].

2.3.1 Ziegler-Natta Catalysts

Ziegler-Natta catalysts, often referred to as heterogeneous catalysts, have gone through several generations of development. The original iPP catalysts developed by Natta had only isotactic contents of 30-40%. Current Ziegler-Natta isotactic polypropylene (zniPP) catalysts can produce chains with greater than 99% isotactic content. Due to continuous development, Ziegler-Natta catalysts are in the forth and fifth generations of development. Metallocene catalysts are the sixth generation of iPP catalyst technology, since they are the newest method for polymerization of propylene.

Current Ziegler-Natta polymerization techniques are achieved with supported ($MgCl_2$) catalysts using a cocatalyst to improve catalyst activity and stereospecificity. A current zniPP catalyst/cocatalyst combination is $MgCl_2/TiCl_4/1,3$-diether-$AlEt_3$[52-53]. Since the methods used to produce Ziegler -Natta catalysts are varied, a review would be both time consuming and inaccurate, as many of the methods for Ziegler-Natta catalyst formation are not completely understood. However, a review of the types of polymer chains produced from zniPP polymerization is in order and justified.

Studies since the 1970s have shown that Ziegler-Natta catalysts have multiple active polymerization sites. Multi-site polymerization produces polymer chains that are unique to each site on the catalyst[45-58]. The molecules produced at each catalyst site differ in the number and distribution of stereo defects. Stereo defects strongly influence the crystallinity and thermal properties of the resin produced. In Ziegler-Natta polymerization, one active site, which is called the "primary site", will produce highly isotactic polymer chains that have very few stereo defects and a high molecular weight. Research has revealed[54-58], through MW fractionations and structural analysis (FTIR and

23

cNMR) of xylene fractions, that as the molecular weight of a zniPP molecule increases, the isotacticity of the molecule also increases. The molecular weight/tacticity relationship is explained on the basis that higher molecular weight chains are produced from sites having the highest activity. The high activity sites make very few monomer insertion errors, which allows these sites to have the highest activity. Thus, the primary sites produce the highest MW and isotactic chains. The "secondary" catalyst sites produce atactic chains, that are generally amorphous and do not crystallize. The atactic chains are a significant portion of the total xylene solubles material.

The xylene soluble fraction consists of atactic material, which is composed of short run length isotactic sequences divided by stereo defects, and low molecular weight isotactic chains produced during peroxide degradation. The higher molecular weight, xylene insoluble chains, are composed of highly isotactic sequences. For zniPP resins, as the molecular weight decreases, there is an increase in defect content, producing a non-homogenous distribution of molecules. Therefore, these materials show melting points and breadths that reflect the diversity of molecular architecture among the polymer chains[45-58].

Based on these findings, iPP resins are viewed as being composed of either one or two types of chains: asymmetric chains, where one configuration is dominant, or symmetric chains, where two types of configurations have equal populations[45]. Asymmetric chains are referred to as "enantiomorphic site controlled" and symmetric chains as "chain end controlled"[2]. Enantiomorphic site control inserts a monomer in a preferred configuration every time, regardless of the orientation of the last monomer unit; i.e. it will correct for any irregular insertion in the last step. Chain end control means the

24

catalyst has a precursor from the previous monomer and follows the stereosequence from the previous unit, correct or not. Shown in Figure 2.9 are symmetric and asymmetric chains. Asymmetric chains[45] have almost all the methyl groups located on the same side of the carbon backbone, if a stereo error is made the catalyst will correct the error and continue to polymerize. With symmetric chains, a series of isotactic sequences are made with a switching back and forth (racemic diad) of the methyl group along the backbone. For clarification, a 100% syndiotactic polypropylene chain would be a 100% symmetric chain.

As stated earlier, atactic chains are composed of symmetric sequences, which are often called symmetric chains. Symmetric chains are typically very short, with meso run lengths too short to crystallize, as the meso run length is often much shorter than the crystal thickness. A meso run length or meso diad (denoted by an m), occurs when two monomer units are inserted with the same stereospecificity. The meso run length is typically used to compare how long the monomer sequence is between stereo defects in polymer chains. A racemic diad, would be two monomer units with the same head to tail insertion, but with different enantiomeric faces, i.e. a symmetric sequence. The importance of this work, involves the significance of meso run lengths on crystallization behavior. The longer the meso run length, the fewer the defects and the faster the material should crystallize. In addition, longer meso run lengths will produce thicker crystals that will melt at higher temperatures.

Asymmetric Chains
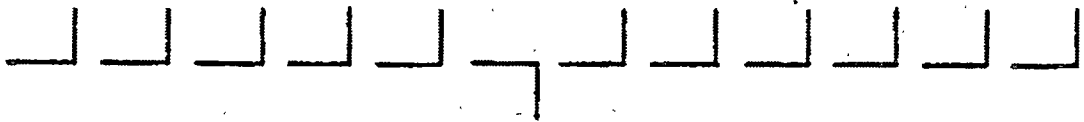
-insertion is preferred
-single stereo defects

Symmetric Chains
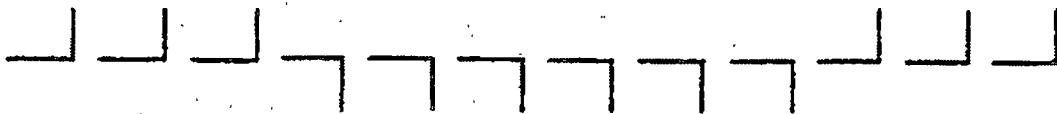
−short isotactic run lengths

Isotactic Chains   80% asymmetric / 20% symmetric

Atactic Chains   20% asymmetric / 80% symmetric

Figure 2.9   Ziegler-Natta polymer chain defects.

2.3.2 Metallocene Catalysts

Metallocene catalysts (homogenous catalysts) are catalysts which enable control of both the molecular weight and defect distribution of polyolefins over a wide range of synthesis conditions. Metallocene catalysts allow for a study and understanding of the catalyst structure/polymer structure relationship. This is due in part to the full understanding of how a metallocene catalyst polymerizes[46].

Metallocene catalysts polymerize from the reaction of metallocenes and a cocatalyst, which is generally an organoaluminum compound. The metallocene atoms generally used for olefin polymerization, are group 4 metals, such as titanium, zirconium or hafnium bent metallocenes. Zirconium produces the most active catalyst followed by hafnium and titanium[46]. These are the same metals used in Ziegler-Natta catalysts. Like Ziegler-Natta catalysts, metallocenes operate by coordination chemistry among the various substituents attached and surrounding the central metal atom. However, metallocenes did not show much productivity until the discovery that the cocatalyst methylaluminoxane (MAO) strongly activated the group 4 metallocenes for polyolefin polymerization[59-61].

Group 4 metallocenes are d^0, pseudotetrahedral organometallic compounds in which the transition metal has two η^5-cyclopentadienyl ligands (Cp ligands) which remain attached during polymerization. The ligands (as with zniPP catalysts) define the catalyst stereoselectivity and activity. The metallocene also has two σ-ligands which are removed when the active site is formed. A general structure of a group 4 metallocene is shown in Figure 2.10. Note that X is the σ-ligand, M is the metal atom, d is the Cp-M distance and α is the Cp-M-Cp angle. The carbon atoms of the Cp ligands can bear

27
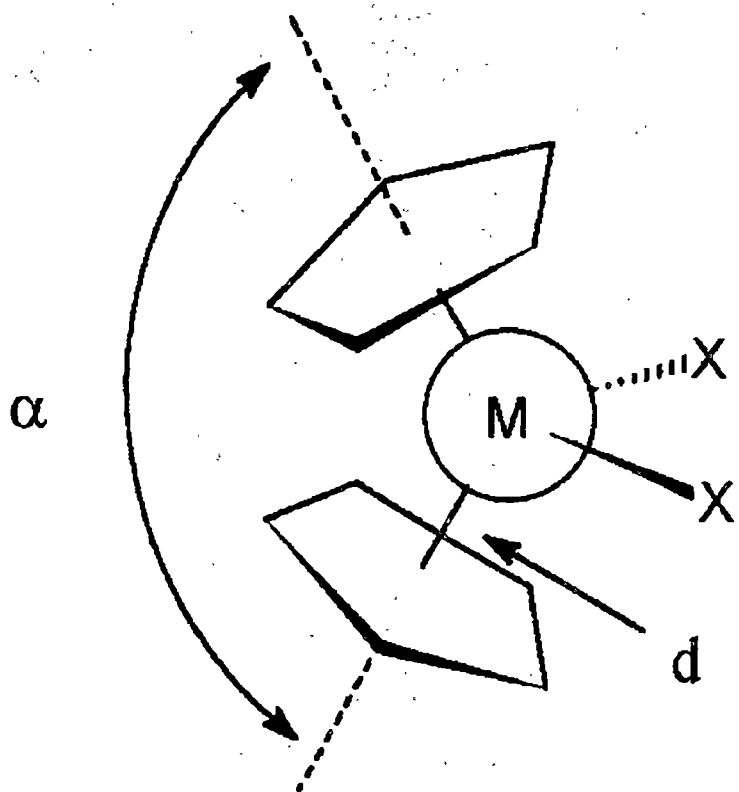
Figure 2.10 General structure of a group 4 metallocene[209].

hydrogen or other groups, such as alkyl, aryl or silane: up to ten different substituents are possible. This structural diversity is the reason for the high steric selectivity and versatility of the miPP catalysts. The different substituents change the size and shape of the Cp ligand and determine the distance between the Cp and metallocene, along with the angle between the bonds of the Cp ligands[62-64]. There is a high degree of freedom on the metallocene atoms, inspite of the bulky rings and the two σ-ligands. However, the structural rigidity of the bulky substituent groups is not sufficient to ensure a constant steric environment at the coordination positions. Without sufficient structural rigidity, the catalyst polymerization site can be compromised, producing polymerization errors.

The structural rigidity problem was solved by linking the η^5 rings through a bridge formed by one or more carbon or silicon atoms[63-64]. The linkage can then control the structural rigidity of the metallocene complex (these are called bridged metallocenes). A general bridged metallocene structure is shown in Figure 2.11, with the "x" representing the bridge. The different classifications of metallocene catalysts are shown in Figure 2.12. The shaded areas are the η^5-ligands. The classifications are broken down and segmented with regard to planes of symmetry.

The key to the high polymerization activity of metallocenes are the cocatalysts. MAO is the most widely used, although some boron cocatalysts are beginning to show promise. Metallocenes are activated by alkylation of the halogens typically found attached to metallocenes from their initial chemical synthesis[65]. For activation of the metallocene catalyst to occur, at least one of the alkyl groups must be substituted. The substitution reaction is shown in Figure 2.13a. Subsequent reactions yield a cationic metallocene, believed to be the active model center in olefin polymerization. The
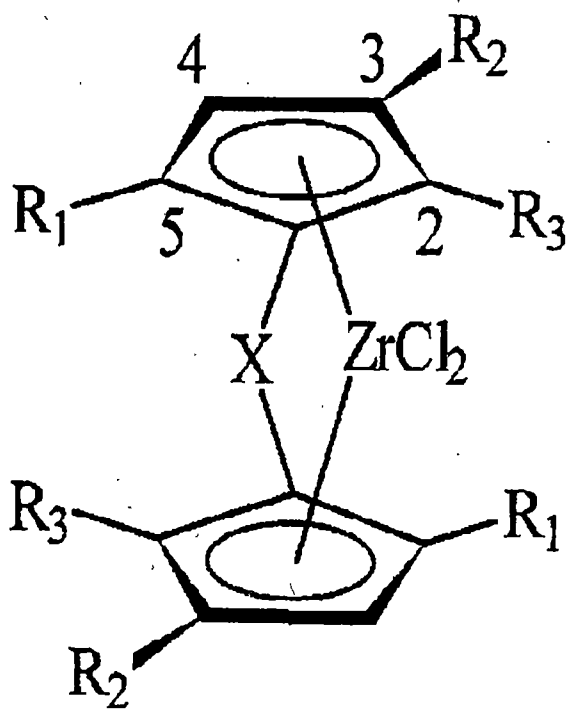
Figure 2.11 Generic formula for a chiral, racemic C_2 -symmetric bridged metallocene[209].
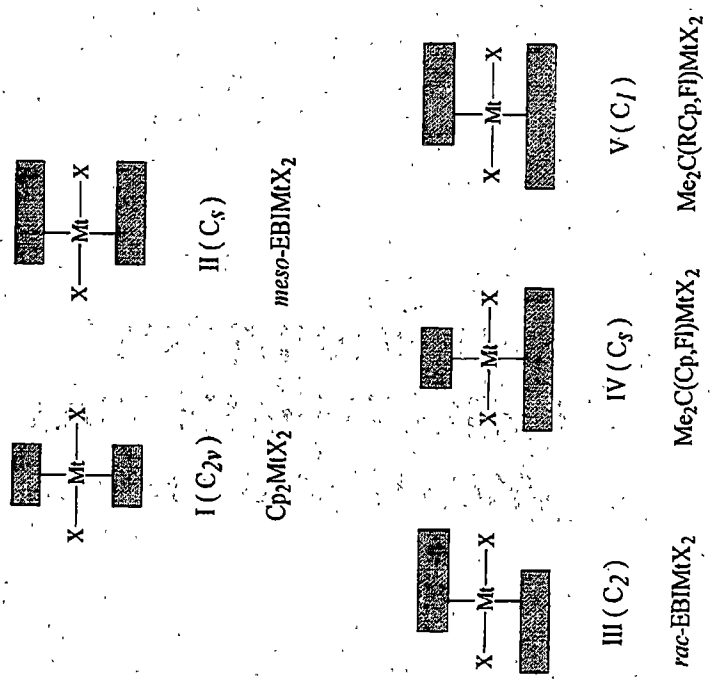
Figure 2.12 Classification of metallocene catalysts according to symmetry[209].
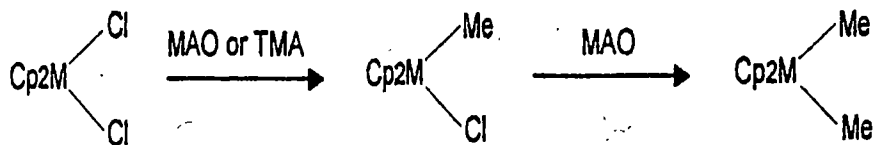
(a) Activation of metallocene, substitution with a alkyl group
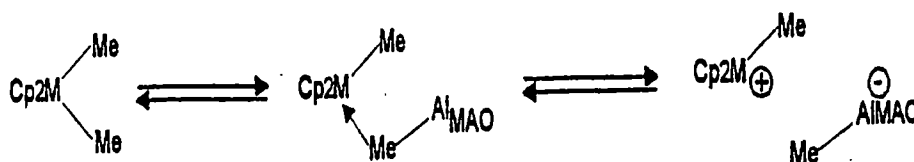
(b) The activated charged system produced by MAO.

Figure 2.13   Acivation of a metaloocene catalyst[46].

cationic species is shown in Figure 2.13b. The activated complex and other catalyst structures are stabilized by Lewis acids and bases[66].

Metallocene activity, as well as stereospecificity, is determined by the η^5-rings, the σ-ligands and the metallocene ring bridge, if any. Through the use of NMR and x-ray diffraction, synthesis and structural characterization has shown the true catalyst site for metallocene polyolefin polymerization is a pseudotetragonal metal cation bearing the η^5-ligands. The growing polymer chain has as a σ-ligand and a new coordination vacancy where the other σ-ligand was present[67-69]. The vacancy allows the coordination of the incoming monomer. For the insertion mechanism (shown in Figure 2.14), a chain migratory mechanism is operating. For metallocene polymerization, pathway A is the rule and pathway B the occasionally skipped step, or it can be made to be the rule if the ligands are symmetric[69]. Therefore, one reason for the high activity in metallocene polyolefin polymerization is that the catalyst can insert a new monomer in two different catalyst conformations.

The relationship between metallocene site symmetry and polymer stereochemistry is fully understood and can be visualized using the lock and key formalism (shown in Figure 2.15). The general mechanism for enantioface selectivity in the chain migratory insertion, with site switching, operating using metallocene (enantiomorphic site control) catalysts is: every metal atom has two available coordination sites, which are the two locks, which can insert the olefin monomer that is different in shape and chirality. For iPP, the two coordination positions available for the incoming monomer and the growing polymer chain are C_2 homotopic and chiral. The configuration of the central metal atom does not change after the shift of the growing
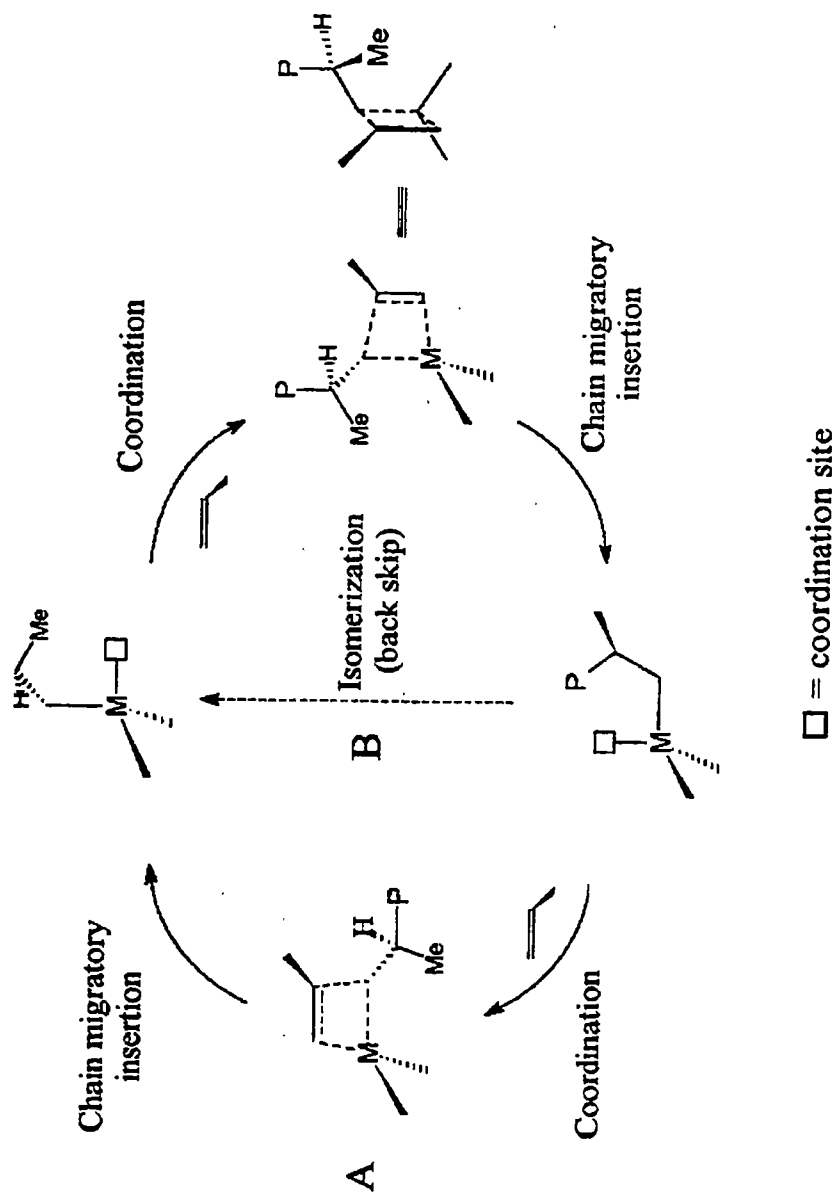
Figure 2.14 Coordination of PP monomer by metallocene catalyst with chain migratory switching mechanism[209].
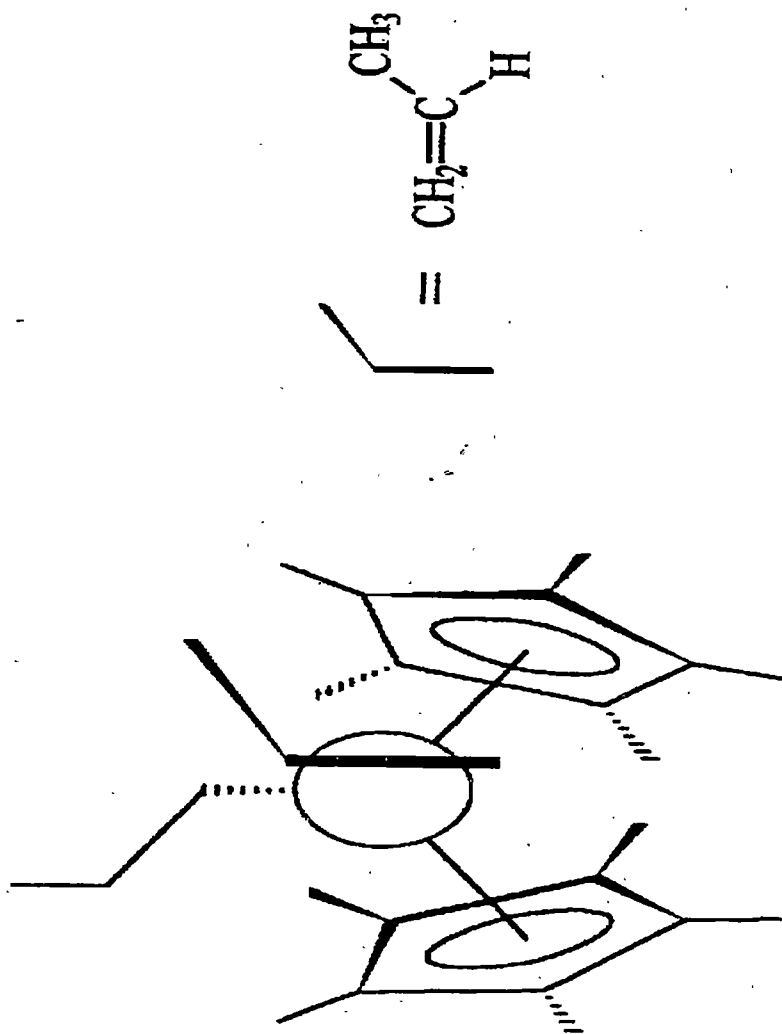
□ = coordination site

Figure 2.15 The lock and key site switching mechanism[209].

35

chain to the position previously occupied by the coordinated monomer[59,69]. A chart of the steric control as a function of metallocene symmetry is shown in Figure 2.16[59].

An aspecific metallocene catalyst is shown in Figure 2.17, while a syndiospecific catalyst is shown in Figure 2.18. Propylene polymerization with a C_2 switching metallocene with isospecificity is shown in Figure 2.19. In all these metallocene catalyst systems, the polymerization site is symmetrical, with the construction of the rings dictating the type of growing polymer chain stereochemistry. These catalysts have a preferred insertion of the next monomer, with the methyl group orientation determined by the ring structure.

2.4 Melting and Crystallization

Current theories of polymer crystallization are both complex and debated. Crystallization is complex from the standpoint of mathematical modeling, where developing models to explain the dynamic process for different materials has been challenging. Crystallization theories are debated by how accurately they describe the actual crystallization process and how well the theories predict future crystallization behavior.

For polymers to crystallize, some basic conditions must be met. Polymers must have a structurally regular, repeating pattern. The polymer main chain must be flexible to allow for chain folding to take place. Polymer chains must be of sufficient length to recover the excess free energy that occurs when a polymer chain folds.

There are three models to describe the way in which polymer chains can be organized to form crystalline domains that diffract x-rays. The earliest was the fringed micelle model[70]. The illustration in Figure 2.20 shows the Wunderlich triangle. Structure
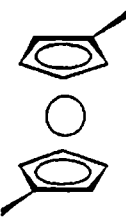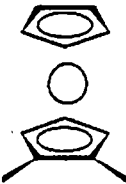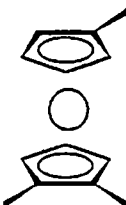
Symmetry		Sites	Polymer
C$_{2v}$ Achiral		A, A Homotopic Homosteric	Atactic
C$_2$ Chiral		I, I Homotopic Homosteric	Isotactic
C$_s$ Prochiral		I, -I Enantiotopic Homosteric	Syndiotactic
C$_i$ Chiral		I, A Diastereotopic Heterosteric	Hemi-isotactic

Figure 2.16 Steric control as a function of metallocene symmetry[209].

Aspecific site

Aspecific site
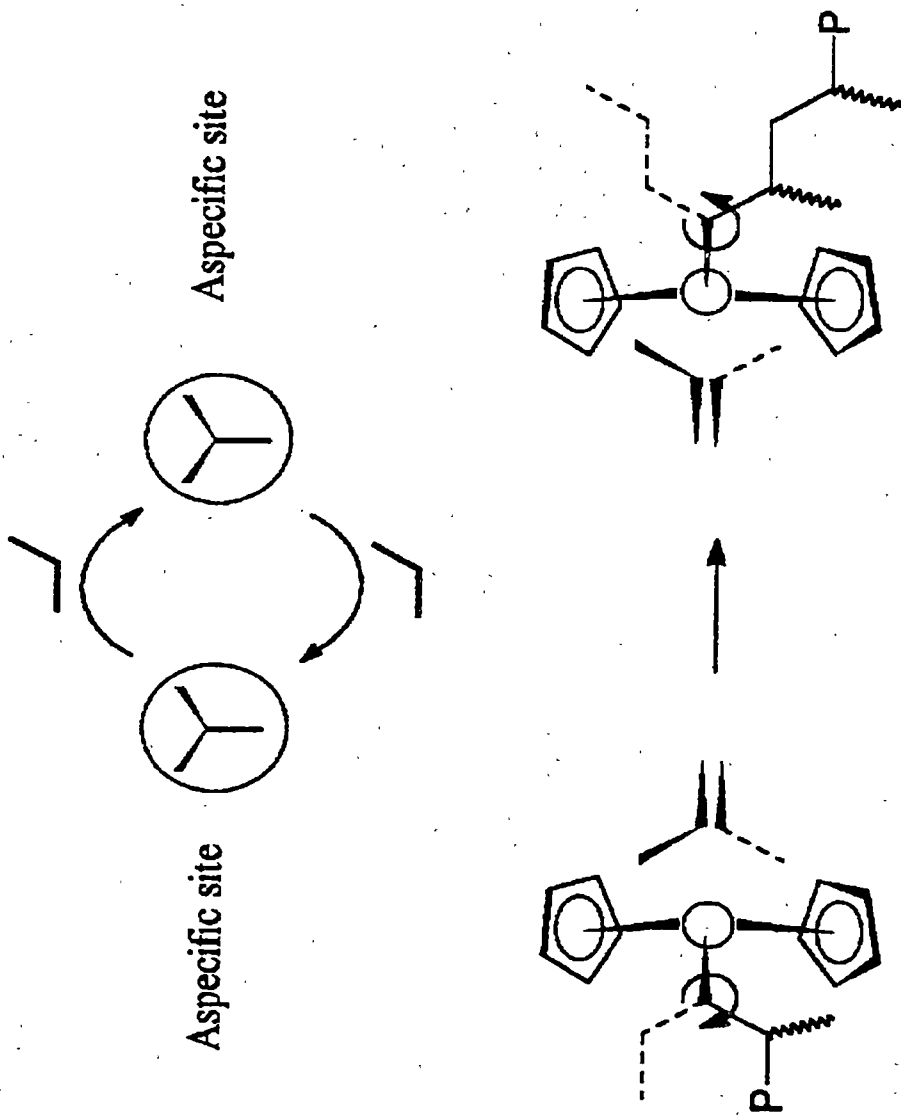
Figure 2.17   Metallocene aspecific catalyst[209].

38
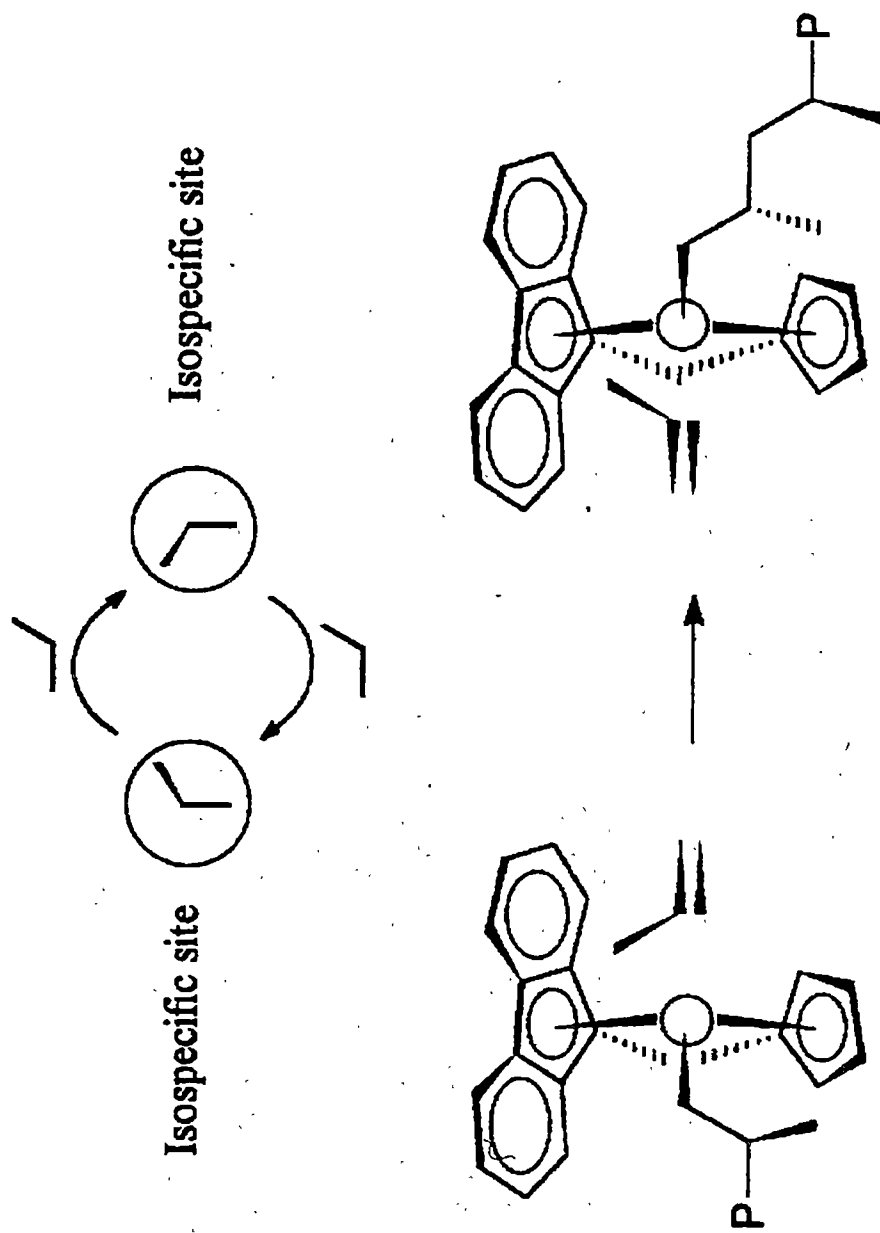
Figure 2.18 Metallocene C_s-symmetric syndiospecific catalyst[209].
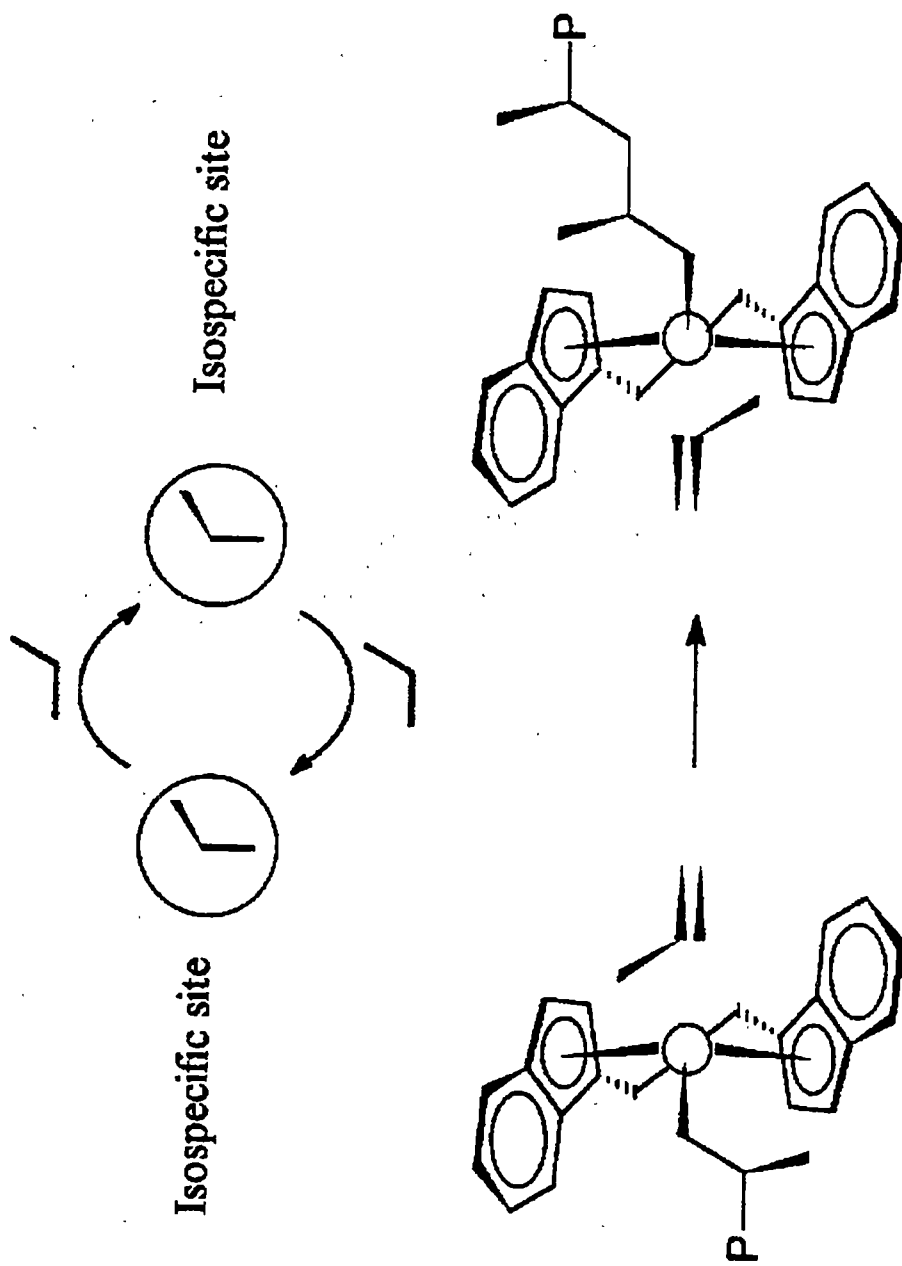
Figure 2.19 Metallocene C_2-symmetric isospecific catalyst[209].
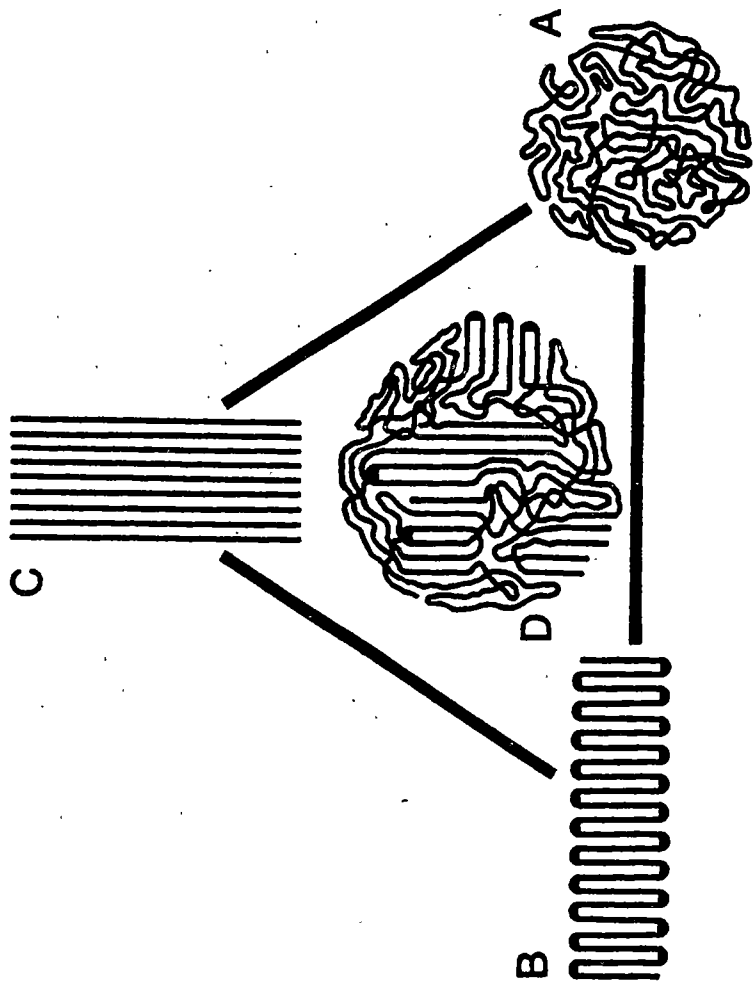
Figure 2.20   Wunderlich Macroconformation Triangle[70].

A is an amorphous random coil polymer. Structure B represents a chain-folding macroconformation with regular folding. Structure C is an extended chain macroconformation. The structure in the middle (D), is the fringed micelle model.

Proposed by Hermann[71] et. al around 1930, the fringe micelle model was based on x-ray diffraction results that showed some crystalline regions in both synthetic and natural polymers. However, there was a problem with the diffraction patterns of polymers. The x-ray diffraction peaks were broader than those found for low molecular weight, non-polymeric materials. The broad x-ray peaks were analyzed and studied, with the results yielding a structure that was approximately 100Å x 400Å. The x-ray structure identified in these studies was a crystal lamellae, as shown in Figure 2.21. The crystal thickness is , and the width W. After this finding, the existence of two domains was suggested for the polymer morphology found. Hermann termed these domains, amorphous and crystalline[72-73]. The crystalline domains are formed by the alignment of the polymer chains along an axis, where the polymer chains align in a parallel fashion to one another. In this model, each molecule travels from one crystallite to another, passing through amorphous domains into other lamellae. The illustration in Figure 2.22 shows the crystalline lamellae stacked on each other with amorphous material in between the crystalline material. Tie molecules are amorphous chains that connect the lamellae together. The crystals formed were though of as physical crosslinks in a polymer solid. Tie molecules were used to explain the physical properties exhibited by bulk polymers. The fringed micelle model was accepted for many years, until the discovery of chain folded lamellae.

On a purely thermodynamic basis, one part of the fringed micelle model that was questionable was the high free energy produced by the arrangement of molecules in the micelle system[74]. From the standpoint of crystallization kinetics, crystal growth with chain folds was found to be more favorable than the micelle model, since the excess free
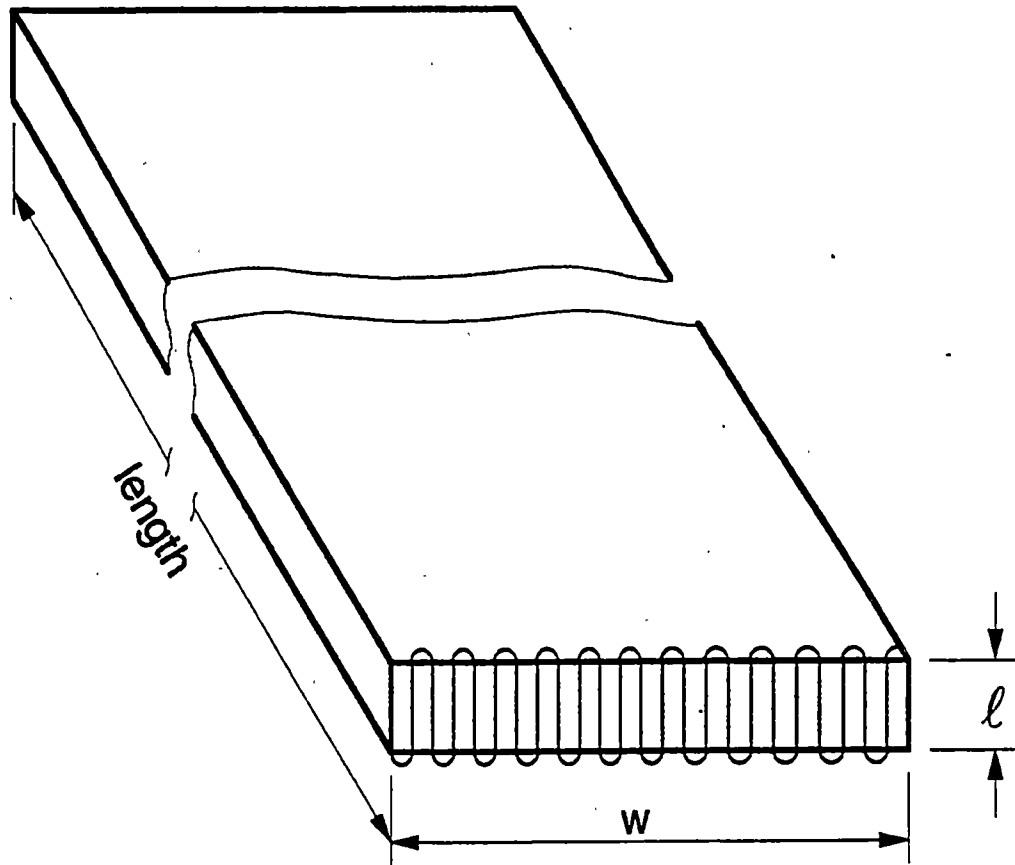
ideally $\ell \ll w \ll$ length

Figure 2.21   Lamellae Structure[210].
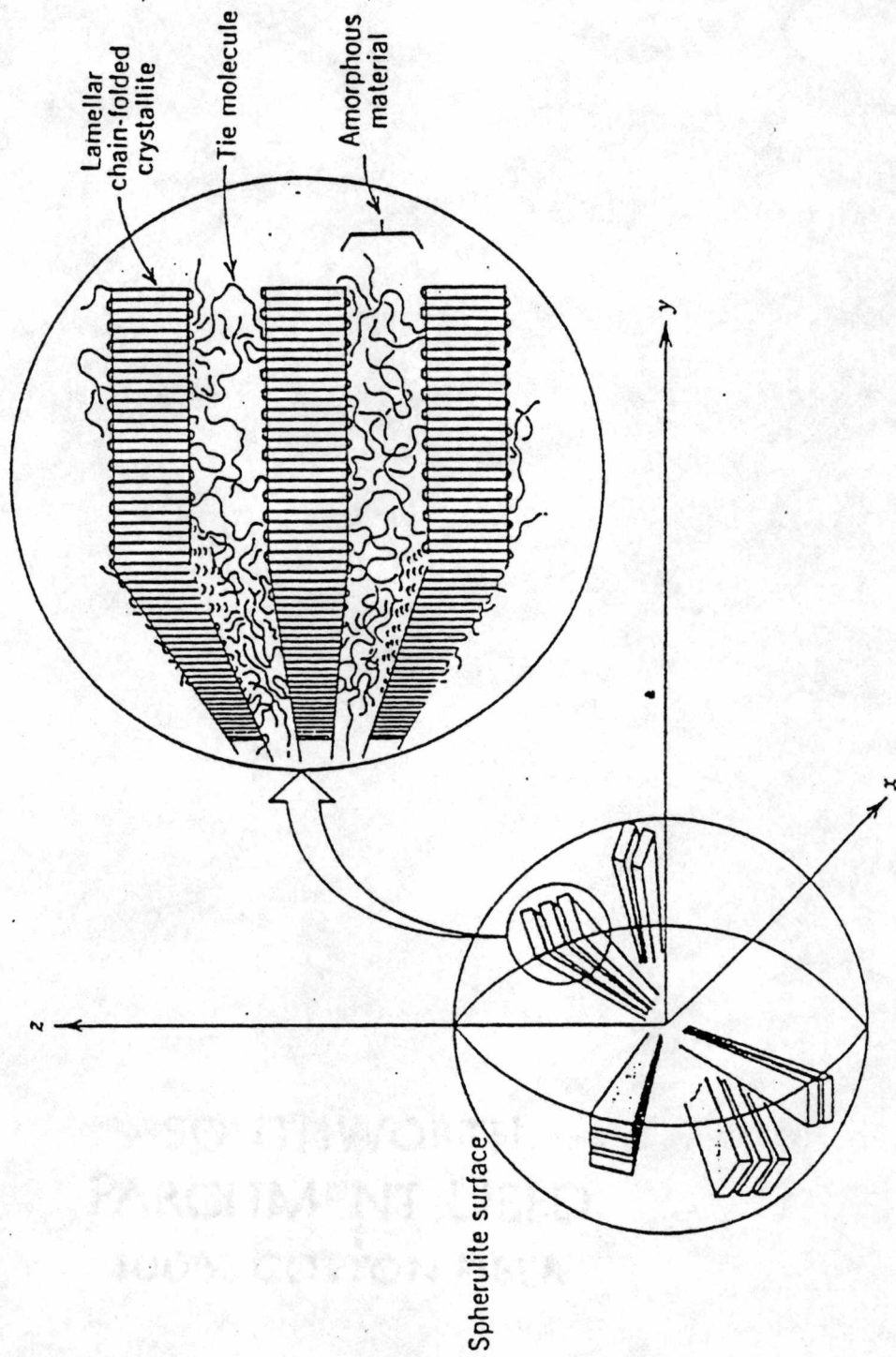
Figure 2.22 Spherulite/Lamellae structure relationship[211].

energy in the micelle is much larger than the energy involved in the fold surface free energies in a chain folded surface. However, until the discovery of lamellae, chain folding was not thought to be possible.

Based upon electron diffraction experiments done using polyethylene single crystals grown in dilute solutions, Bunn[75] proved that the polymer chain axis was approximately orthogonal to the flat planes of the polymer crystal. Keller[76] then suggested that the upper and lower planes of the crystal were composed of polymer chain folds, where the polymer molecules fold back and forth on themselves. Chain folding was proposed since crystal thicknesses were very much smaller than the polymer chain molecule lengths. The illustrations in Figure 2.22 and 2.23 clearly illustrate the relationship of the spherulite, lamellae and crystallographic registry of polymer molecules. Spherulites are composed of lamellae that nucleate and grow from the center of a spherulite. Lamellae are composed of the unit cells produced during the crystallization process. The crystal stem axis to basal plane relationship agreed with a conclusion drawn by Stork[77] in 1938. In addition, the thickness of single polymer crystals seemed to be independent of the polymer species. The crystal thickness for most polymers was almost always near 100Å. The thickness was observed to depend upon the crystallization temperature and pressure, with higher temperatures and pressures producing thicker lamellae.

The discovery of the polymer stem axis laying perpendicular to the crystal surface meant that chain folding had been proven to occur in semi-crystalline polymers. However, another question developed as to whether or not the folds in lamellae formation are adjacent reentry and/or non-adjacent reentry folding. Keller[76] suggested the adjacent reentry model and Flory[78] the non-adjacent model (which is called the switch board model). The idea of adjacent reentry seems reasonable from the relative proximity of the fold and reentry into the crystal structure. The existence of tie-molecules giving
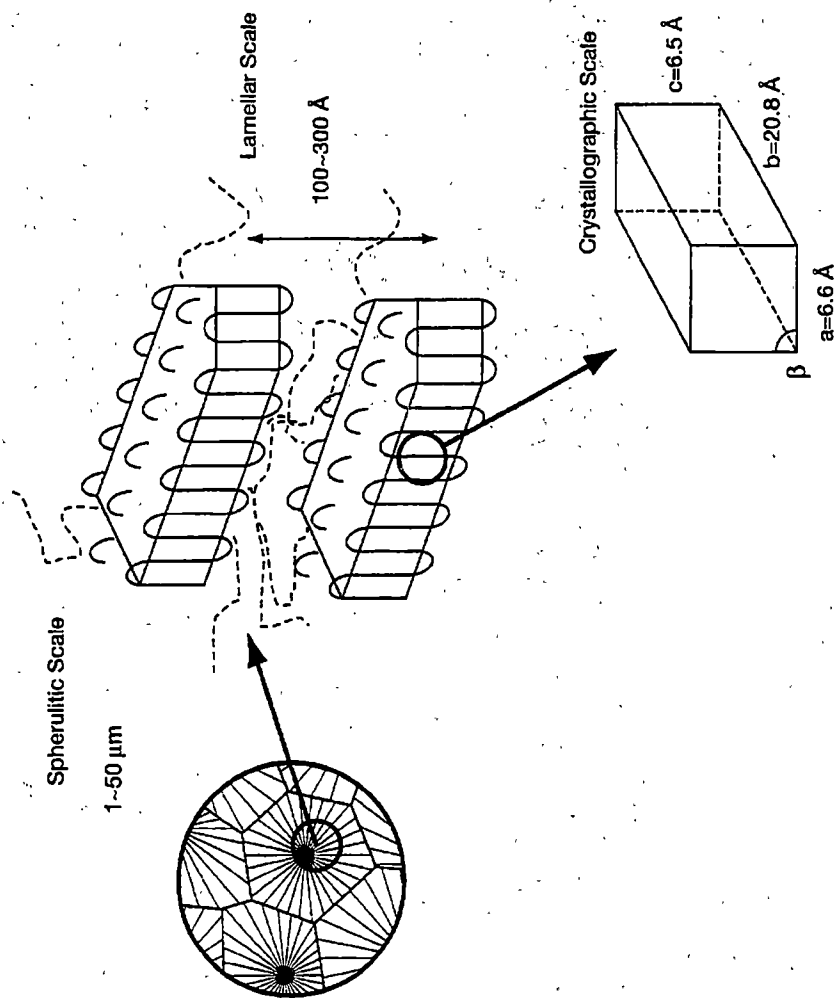
Figure 2.23 Polymer crystal organization for iPP[209].

polymers the observed mechanical properties lead Flory to create and propose the switchboard model.

Research has shown that lamellae crystallized from dilute polymer solution fold according to the adjacent reentry model. Conversely, crystallization from polymer melts produce lamellae that have both the switchboard and adjacent reentry folding. The extent of adjacent reentry is dependent on the cooling rate, molecular weight, flexibility of the main polymer chain and the stress placed on the crystallizing polymer melt[79-84]. The higher the cooling rate, the lower the proportion of adjacent reentry due to a time constraint placed on the crystallizing polymer chain. Chain inflexibility can preclude adjacent folding from occurring, since the entropy and energy barriers are very high in a rigid polymeric material. Stress placed on a polymer melt during crystallization is important, as it occurs in many processing type environments that lead to useful mechanical properties. In bulk polymer crystallization, a combination of the micelle, adjacent reentry and switchboard models is likely to take place, in all but extreme crystallization conditions[73].

2.4.1 Melting

Crystals made up of small molecules generally exhibit a sharp melting point when the temperature is gradually raised. Semi-crystalline polymers do not exhibit a sharp melting point, but melt over a broad range of temperatures. The melting temperature of a polymer depends on ΔS and ΔH of phase transition from the solid to the liquid state. Studies also have shown that the melting point of a polymer crystal depends on the thickness of the crystal. Based on the Gibbs-Thomson[85] equation, for a lamellae crystallite whose length is very much greater than its thickness, the experimental polymer melting temperature, T_m, is:

$$(2.1) \qquad T_m = T_m^0 \left(1 - \frac{2\sigma_e}{\Delta H_u \ell} \right)$$

where σ_e is the fold surface free energy, ΔH_u is the heat of fusion per unit volume of the crystal and ℓ is the lamellae thickness. The equilibrium melting temperature (T_m^0) is defined as the melting temperature of an infinitely thick crystal. The value of T_m^0 can be determined by plotting T_m versus $1/\ell$ and extrapolating to infinite lamellae thickness. The slope of the extrapolation also gives an average value of σ_e.

The T_m^0 can also be determined by a method proposed by Hoffman and Weeks. The Hoffman-Weeks approach[87-88] works by making a plot of T_m versus T_c, then making an extrapolation to $T_m = T_c$. The Hoffman-Weeks method is both fast and convenient, as it can be determined relatively quickly using a DSC.

2.4.1.1 α-iPP Equilibrium Melting Temperature

The equilibrium melting temperature of α-iPP has been quoted in the literature as having two different values, 186°C and 210°C. Krigbaum[89], Miller[90], Campbell and Mezghani[91] report T_m^0 values of 186°C, while Fatou[92], Monnassee[93] and Fujiwara[94] report values near 210°C. Kamide and Yamaguchi[95-96] observed changes in melting temperature with crystallization time. The researchers observed that longer crystallization times lead to increasing melting temperatures. This is now understood to be associated with lamellae thickening. Lamellae thickening increases as the crystallization temperature increases.

Lamellae thickening is the most likely explanation for the two values of T_m^0 for α-iPP. Directly measuring the lamellae thickness and making extrapolations to the T_m^0 will decrease the error found in making extrapolations from the crystallization temperature alone[91].

The thickening ratio can be determined from the slope of a Hoffman-Weeks plot. The crystals produced at high supercoolings are thinner and further away from equilibrium than crystals produced at low supercoolings. Mezghani and Phillips[91] demonstrated the value of $210^{\circ}C$ for T_m° is in error and can be explained due to the lamellae thickening process.

2.4.1.2 γ-iPP Equilibrium Melting Temperature

Until recently, there had been no attempt at accurately measuring the T_m° for γ-iPP. Mezghani[97] determined the T_m° for γ-iPP at elevated pressures and extrapolated the T_m° to atmospheric pressures using the Clapeyron equation. Mezghani obtained a value of $187^{\circ}C$ for the T_m° for γ-iPP, slightly higher ($186^{\circ}C$) than for α-iPP.

2.4.2 Crystallization Theories

There are several methods used for studying the crystallization kinetics of polymers, which fall into two general categories: bulk or volumetric analysis and crystal growth analysis. The simplest method for studying crystallization is to study bulk kinetics. Bulk kinetic analysis describes the overall crystallization behavior of a polymer melt, grouping nucleation and growth events together into an overall numerical description of the crystallization process. Crystal growth analysis involves directly measuring linear growth rates of growing crystals. In principle, the number of nuclei present can be counted, which allows the effects of nucleation and growth to be separated, enabling a more detailed understanding of the crystallization process. However, few investigations have carried out such measurements due to experimental difficulties.

The importance of understanding the crystallization process can not be overstated. The nature of the crystallization process, as determined by molecular microstructure and

constitution (plus other additives, if any) dictate the behavior of a given polymer resin under a set of crystallization conditions.

2.4.2.1 Bulk Crystallization Analysis

Bulk crystallization analysis is broken down into isothermal and nonisothermal kinetic descriptions of the crystallization process. Bulk kinetic processes are usually studied using DSC, dilatometry and light intensity measurements that rely upon the experimentalist to determine the crystallinity as a function of time during the solidification process.

2.4.2.1.1 Isothermal Crystallization

The most widely used approach for analysis of bulk polymer crystallization kinetics was introduced by Melvin Avrami[98-100]. Avrami introduced an equation that is assumed to work under isothermal crystallization conditions, with nucleation occurring throughout the material. The general Avrami equation is:

(2.2) $$\theta(t) = 1 - e^{[-kt^n]}$$

where $\theta(t)$ is the relative crystallinity at time t, k is the isothermal crystallization rate constant, and n the Avrami index. In this equation, at t=0, t begins after an induction time during which no nucleation is observed. This induction time may include the period in which the sample is equilibrated at the crystallization temperature. The Avrami index is used to indicate the nucleation mechanism and growth morphology. A theoretical description of some Avrami exponents are shown in Table 2.2. Two types of nucleation kinetics are assumed in this approach: instantaneous and sporadic. With instantaneous nucleation the nuclei form at the beginning of crystallization and the number of nuclei remain constant throughout crystallization. In the case of sporadic nucleation, the number of nuclei changes with time. It is often assumed that the nucleation rate is

50

Table 2.2 Theoretical values of Avrami n and K for different morphlogies and nucleation mechanisms[212].

Crystal Growth Shape	Nucleation	Avrami Exponent (n)	Avrami Constant (K)
Rod	Instantanous	1	NGA
	Sporadic	2	$\dot{N}G\dfrac{A}{2}$
Disc	Instantanous	2	$\pi NG^2 D$
	Sporadic	3	$\dfrac{\pi}{3}\dot{N}G^2 D$
Sphere	Instantanous	3	$\dfrac{4}{3}\pi NG^3$
	Sporadic	4	$\dfrac{\pi}{3}\dot{N}G^3$
Sheaf	Instantanous	5	-
	Sporadic	6	-

A is constant area of rod
D is the disc thickness
G is the linear growth rate
N is the nucleation density
$\dot{N}$ is the nucleation rate
Instantanous means that number of spherulites is constant.
Sporadic means that the number of nuclei change with time. In the present case it is assumed that the nucleation rate is constant.

constant, but this is just one extreme case of sporadic nucleation. More generally, there may be a combination of both time independent and time dependent nucleation, and the latter may involve variations in nucleation rate.

The method used to analyze and determine the Avrami exponents is by taking the logarithm of both sides of equation (2.2), such that the equation can be linearized on a log-log graph. Taking the log of both sides of equation (2.2) yields:

(2.3) $$\ln\left[\ln\left(\frac{1}{1-\theta(t)}\right)\right] = \ln k + n\ln t$$

where the slope of a plot of the left hand side of this equation versus ln t gives the Avrami index (n) and the y-intercept the crystallization rate constant (k). It can further be shown that the crystallization half-time, $t_{1/2}$, is related to k and n by:

(2.4) $$k = (\ln 2)\left[\frac{1}{t_{1/2}}\right]^n$$

Rarely is the entire Avrami plot straight. The initial and final regions of the graph depart from linear behavior. As shown in Figure 2.24, the initial part of the curve usually has a lower slope than the middle "steady state" region, which typically is linear from 10-80% of the relative crystallinity. Non-linearity of the Avrami plot identifies one of the shortcomings of the Avrami method.

During the growth of polymer spherulites, at least two types of crystallization are occurring, these are referred to as primary and secondary crystallization. Primary crystallization is the process where virgin polymer molecules are reeled into a growing crystal from the melt. Secondary crystallization involves the perfection of existing crystals and the crystallization of any material trapped in the interzonal region between the already formed crystals, often called intercrystalline domains. The Avrami method fails to accurately describe secondary crystallization, and as a result, can give a misleading primary crystallization value, as secondary crystallization (for most polymers) occurs simultaneously with primary crystallization. In addition, Avrami analysis fails to
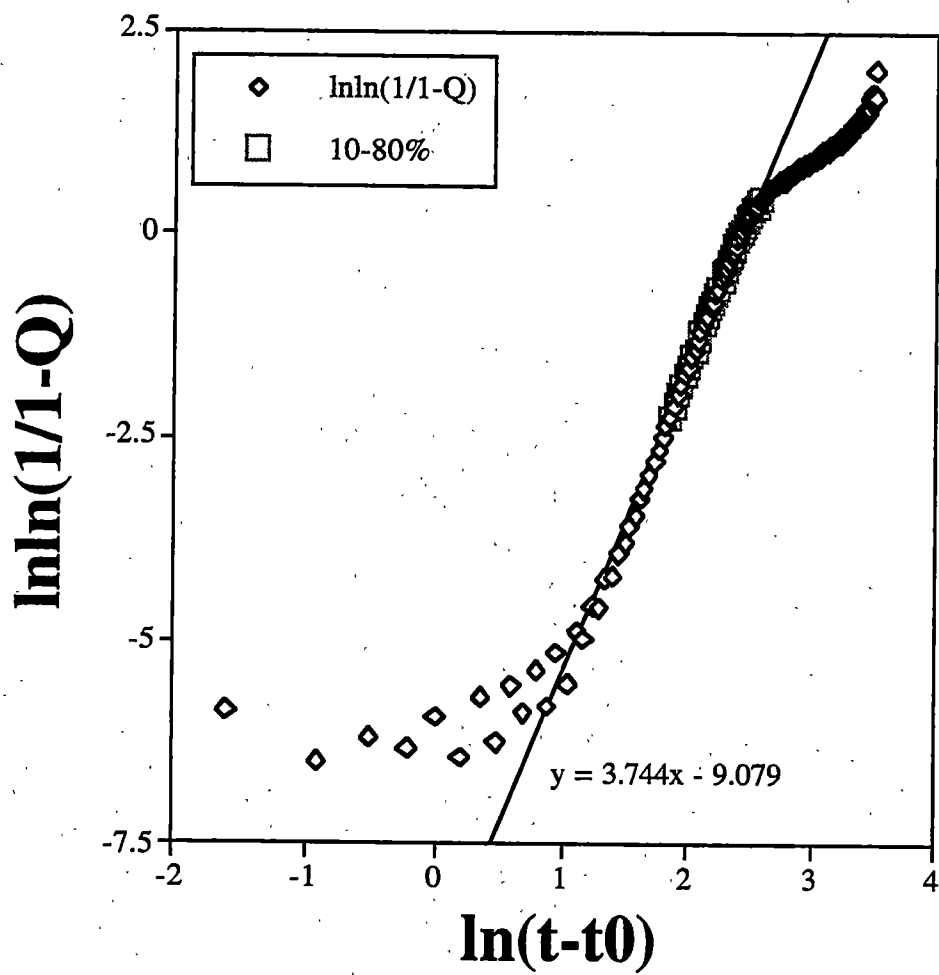
Figure 2.24   Avrami plot of miPP resin.

account for the volume contraction that occurs during crystallization, a result of the change in density from the melt to crystalline solid.

2.4.2.1.2 Non-Isothermal Crystallization

The Avrami analysis was extended by Nakamura et al. to include non-isothermal crystallization kinetics to describe the phase transformation processes with variable nucleation and growth rates. The Nakamura et al. equation[101-102] is:

$$(2.5) \qquad \theta(t) = 1 - e^{\left[-\left(\int_0^t K(T)dt\right)^n\right]}$$

where the variables are the same in the Avrami equation except for K(T), which is the non-isothermal crystallization rate constant. Equation 2.5 is based on the "isokinetic assumption" in which the ratio of N/G is constant. The non-isothermal crystallization rate constant, K(T), is related to the Avrami isothermal crystallization rate constant, k, by the following:

$$(2.6) \qquad K(T) = \left[k(T)\right]^{\frac{1}{n}} = (\ln 2)^{\frac{1}{n}}\left[\frac{1}{t_{1/2}}\right]$$

The Nakamura equation does not address the difficulties with separating primary and secondary crystallization.

Ozawa[103] proposed a nonisothermal crystallization kinetics equation based on the assumption that the sample is cooled at a constant rate. The Ozawa equation is:

$$(2.7) \qquad \theta = 1 - e^{\left[\frac{-K(T')}{\alpha^n}\right]}$$

where K(T') is the cooling function of nonisothermal crystallization at temperature (T), α is the cooling rate and n is the Avrami index. The variables are solved in the same manner as with the Avrami equation.

Another method for analyzing non-isothermal crystallization kinetics was introduced by Ziabicki. The intention was to introduce an equation that would also work for the melt spinning of polymers. Ziabicki[104] introduced the kinetic crystallizability (G_c)

which characterizes the ability of a polymer to crystallize. The assumption is that polymer crystallization follows a first order kinetic equation:

$$(2.8) \qquad \frac{d\theta}{dt} = K(1-\theta)$$

where θ is the relative crystallinity (as above) and K is a crystallization rate constant with the following temperature dependence:

$$(2.9a) \qquad K(T) = K_{max} e^{\left[-4\ln 2 \frac{(T-T_{max})^2}{D^2} \right]}$$

where D is the half width of K vs T, K_{max} is the maximum K value, and T_{max} is the temperature at K_{max}. The kinetic crystallizability is calculated by:

$$(2.9b) \qquad G_c = \int_{T_g}^{T_m} K(T)dT = \left(\frac{\pi}{\ln 2} \right)^{0.5} K_{max} \frac{D}{2}$$

such that K_{max} and D can be determined from non-isothermal crystallization conditions using DSC.

More recently, Ziabicki[204,205] proposed an equation for temperature-dependent crystallization rate derived from nucleation theory:

$$(2.10) \qquad K_{st}(T) = const_1 \left(\frac{T\Delta T}{T_m^2} \right) \exp\left[\frac{-E_a}{kT} \right] \exp\left[\frac{-const_2 T_m^2}{T\Delta T} \right] \exp\left[\frac{-const_2 T_m^3}{(T\Delta T)^2} \right]$$

where the constants are related to physical parameters of nucleation theory. The exact equations depend on whether sporadic or predetermined nuclei are used.

Patel and Spruiell[105] proposed a differential form of the Nakamura model:

$$(2.11a) \qquad \frac{d\theta}{dt} = nK(T)(1-\theta)\left[\ln(\frac{1}{1-\theta}) \right]^{\frac{n-1}{n}}$$

where n is the isothermal Avrami index. This form is useful for application to process modeling in which crystallization is important. Ding and Spruiell[206] recently proposed a power law nucleation rate function using the form of the Avrami equation. The Avrami exponent (n) and crystallization rate constant (k) are then expressed as:

$$(2.11b) \qquad n = n' + m + 1$$

$$(2.11c) \qquad k = N_c n' A_g G^{n'} B(m+2,n')$$

where m is the nucleation index, n' is the geometric index determined by the growth geometry, N_c is the nucleation rate constant that is temperature dependent but time independent, A_g is a constant that depends on the geometric shape of the transformed entities and

$$(2.11d) \quad B(m+2,n') = \int_0^1 q^{m+2-1}(1-q)^{n'-1}dq.$$

These relationships allow bulk transformation kinetics to be analyzed in greater detail with more physical significance than in using the standard Avrami relationship.

Dietz[106] introduced a kinetic equation for nonisothermal crystallization containing an exponential factor to correct for secondary crystallization:

$$(2.12) \quad \theta = \int_0^t nk(1-\theta)t^{n-1}e^{\left[\frac{-a\theta}{1-\theta}\right]}dt'.$$

The formula proposed by Dietz is an extension of Nakamura equation.

Nonisothermal theories have historically been tested with cooling rates determined from DSC and hot-stage light depolarizing microscopy (LDM). DSC and LDM are adequate techniques for determining the bulk Avrami index and crystallization rate constants up to cooling rates of 50-100°C/min. However, obtaining cooling rates above 100°C/min that allow crystallization kinetics to be studied has proven difficult. Recently, Ding and Spruiell introduced a technique for studying bulk and crystal growth crystallization kinetics at high cooling rates. The technique utilizes high cooling rate light depolarizing microscopy (HCR-LDM) and can achieve cooling rates in excess of 5000°C/min. This technique will be introduced and reviewed later.

2.4.2.2 Crystal Growth Kinetics

Crystal growth kinetics entails directly observing and measuring the growth rates of polymeric materials. Experimentally, this usually involves measuring the spherulite radius (R) as a function of time. The slope of the R versus time curve gives the linear

growth rate, dR/dt=G. The most widely accepted approach to linear growth rate analysis is a kinetic description proposed by Lauritzen and Hoffman (LH theory)[49,107-109]. This analysis assumes that polymer crystal growth occurs by a mechanism referred to as "secondary nucleation", in which the rate controlling step is the rate at which a new layer can be nucleated on the surface of a growing crystal. Recently, Hoffman and Miller[108] published an updated version of the original theory that included new developments made since the original LH theory was published nearly 25 years ago. The general expression of crystal growth in the LH theory is:

$$(2.13) \qquad G = G_0 e^{\left(\frac{-U^*}{R(T_c - T_\infty)}\right)} e^{\left(\frac{-K_g}{T_c \Delta T f}\right)}$$

where G is the observed linear growth rate, G_o is the growth rate constant, U^* is the activation energy of the polymer (related to diffusion and reptation), R is the universal gas constant, T_c is the crystallization temperature in Kelvin and T_∞ is T_g -30K. The supercooling is $\Delta T = T_m^0 - T_c$ and the factor f is the correction factor $= \dfrac{2T_c}{T_c + T_m^0}$ which corrects for the change in the heat of fusion as a function of temperature. K_g is the (secondary) nucleation rate constant and is defined as:

$$(2.14) \qquad K_g = \frac{j b_o \sigma \sigma_e T_m^0}{k \Delta H_f}$$

where b_o is the width of the polymer chain (stem), σ is the lateral surface free energy, σ_ε is the fold surface free energy, k is Boltzmann energy constant and j is the operating regime constant. The regime is determined from the relative comparison of the rate of deposition of secondary nuclei (i) and the rate of lateral surface spreading (g). An idealized growth front is pictured in Figure 2.25 (The variables are the same as before). The observed linear growth rate (G) is in the same direction as the secondary nuclei deposition (i). Three scenarios exist when comparing g and i:

1. i<<g, which indicates Regime I, typically found at lower supercoolings (j=4): This regime is characterized by a relatively smooth growth front, one in which most nucleated
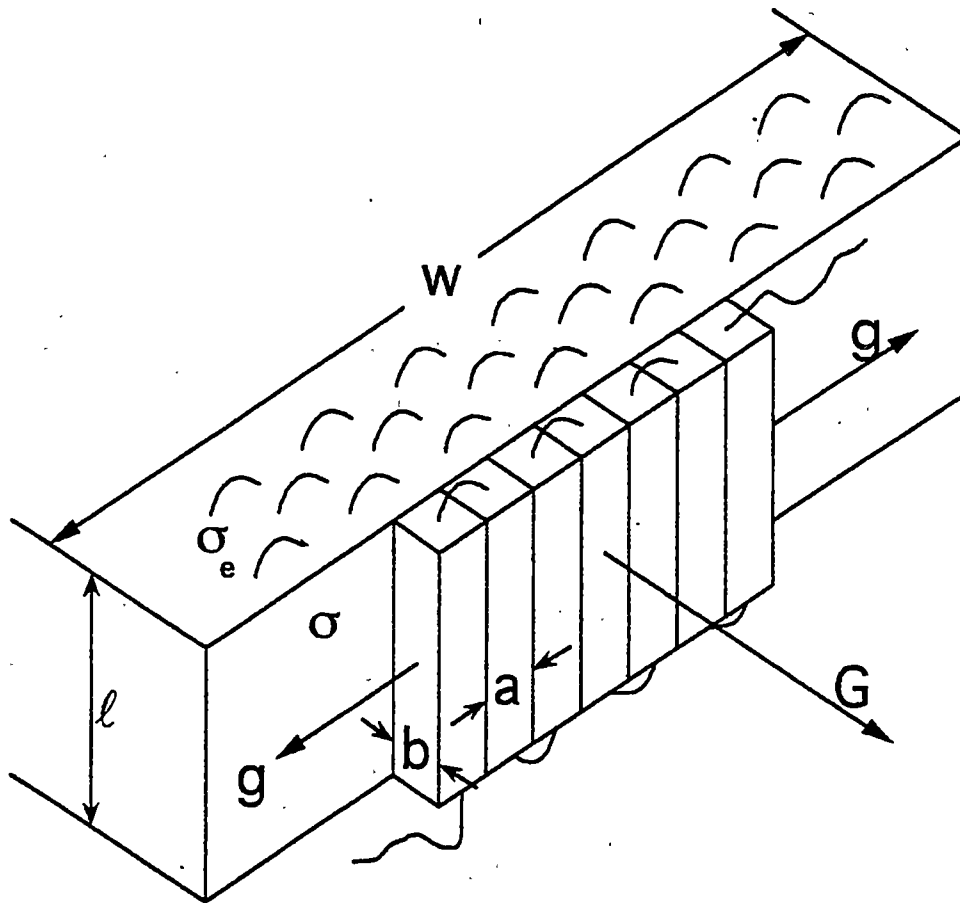
Figure 2.25   Ideal lamellaer growth front[109].

rows are completed before a new row begins. Regime I behavior would most often be found at slow linear growth rates with relatively thick crystals and high degree of crystal perfection.

2. i≈g (same order of magnitude), which indicates Regime II, found at moderate supercoolings (j=2): Regime II is characterized by the rate of surface spreading and nucleation being roughly equivalent, meaning there is spreading from multiple nucleation sites on the same row, with perhaps several rows growing simultaneously. The growth front would appear somewhat rough and jagged.

3. i>g, which indicates Regime III, found at high supercoolings typically found in processing environments (j=4): A regime III growth front would appear very rough as stems nucleate much faster than surface spreading occurs.

An ideal regime plot is shown in Figure 2.26. The slopes in regime I and III are the same and ideally twice the slope found in regime II[108-109].

The overall picture of regime crystallization is best shown by plots of $\log G + U^*/2,303R(T-T_\infty)$ against $1/T(\Delta T)$. The transitions between the regimes are shown by distinct changes in the slopes on this plot. The values for K_g and G_o can be obtained directly from the graph, where the slope in a particular regime is $-K_g/2.303$ and the intercept equal to $\log G_o$. Once K_g is known, the other parameters characteristic of crystal growth can be determined.

If ΔH_f is known, σ can be estimated from:

(2.15) $\qquad \sigma = \alpha \Delta H_f \sqrt{a_o b_o}$

where a_o is the width of the chain stem and b_o the thickness of the chain stem. The factor $\alpha \approx 0.1$ for most polymers. For iPP, a_o=0.549nm and b_o=0.626nm[46]. Together, these factors constitute the cross-sectional area of an iPP stem or chain.

The principle contribution to the fold surface free energy is the work of chain folding required to bend the polymer chain back upon itself so that it may reenter the crystal in a

59
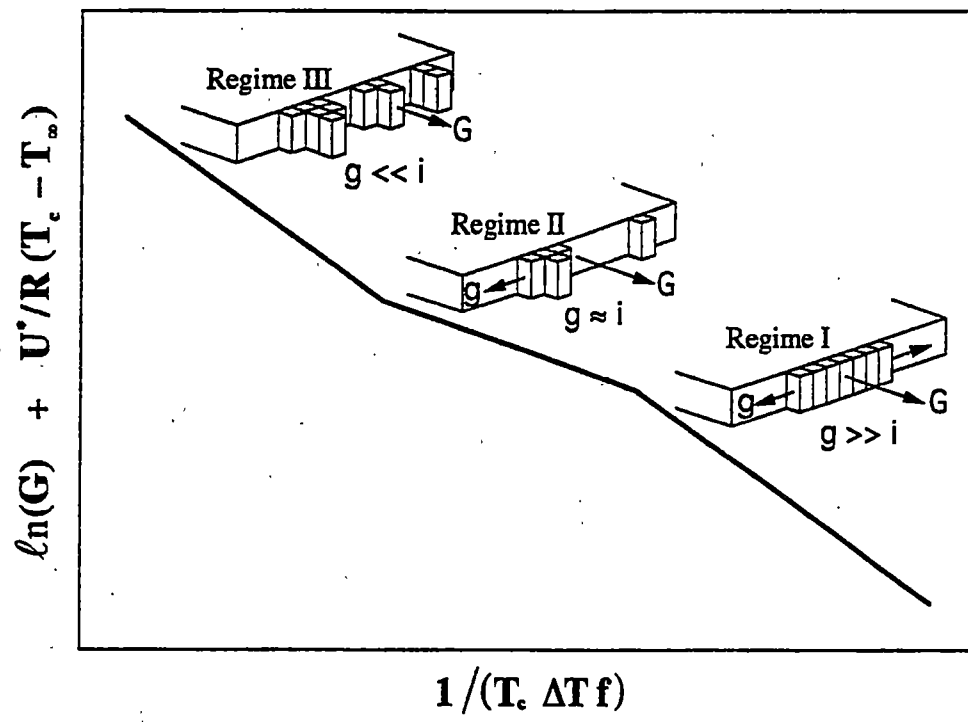
Figure 2.26   Regime Transitions[109].

manner consistent with the crystallographic structure. The work of chain folding (q) is derived from σ_e by:

(2.16) $q=2\sigma_e a_o b_o$

Combining equations 2.13-2.16 allows the various parameters and variables to be evaluated.

Regime behavior varies from polymer to polymer and within a single polymer species. The regimes are affected by the chemical molecular structure of the polymer, molecular weight, molecular weight distribution, pressure, polymer chain chemical homogeneity and its distribution. For instance, cis-polyisoprene[111] and low molecular weight iPP exhibit all three regimes[112], as does PE[113-114,208]. High molecular weight iPP produces only regime II and III behavior[114].

2.4.2.2.1 Regime Behavior of iPP

Most of the regime studies in the past have been done on polyethylene. It is quite surprising how little work has appeared in the scientific journals on regime behavior of iPP. Despite the limited number of publications on iPP regime behavior, some observations have been made.

All three crystallization regimes have been observed in low (15k) molecular weight iPP. Regime III exists above $\Delta T=48K$, regime II exists between $\Delta T=37K$ and 48K, while regime I is observed below $\Delta T=37K$. The $\sigma\sigma_e$ values for low molecular weight iPP were found to be 779 erg^2/cm^4 in regime I, 784 erg^2/cm^4 in regime II and 731erg^2/cm^4 in regime III. For high molecular weight iPP (300k range), only regime II and III have been observed with the regime transition occurring at similar undercoolings as for the low molecular weight case. The high molecular weight $\sigma\sigma_e$ values found were 590erg^2/cm^4 in regime II and 602erg^2/cm^4 in regime III[111].

61

2.4.3 Random Copolymer Crystallization

There are two extreme possibilities that may occur after crystallization of a random copolymer with regard to comonomer locations, the exclusion and inclusion models[79]. The two models are shown in Figure 2.27. In the exclusion model, no comonomer units are incorporated into the crystal. The inclusion model allows comonomer units to be included into the crystal. One of the first researchers to study, in depth, the relationship of comonomer content on crystallization was Flory.

Flory developed his theory of copolymer crystallization in a series of elegant papers that were based on equilibrium thermodynamic relationships[114-118]. Flory's model assumed that a random copolymer consisted of two monomers, A and B. Where monomer A is capable of crystallization, while B is not. Further, B will not be included in the crystal (i.e. the exclusion model) during the crystallization process. The configuration of copolymer chains in the melt is determined by the chemical nature of A and B, where the size and flexibility of the monomers becomes important. Flory made some further assumptions in his model[116]:

1. The ideal mixing law is obeyed ($\Delta H_m = 0$).

2. The chain ends are excluded from the crystal.

3. The crystalline and amorphous regions have a sharp separation at equilibrium, while intermediate situations are non-equilibrium and are not stable.

Flory added some concern about crystallization processes in general, but they are more applicable to copolymers. X-ray studies show the regular repeating structural unit of a polymer plays a role in the crystalline state, which is analogous to that of a monomeric molecule in its crystal lattice. Single molecules protruding from the crystal may pass from one crystallite to another (tie-molecules). The heat of interaction of a
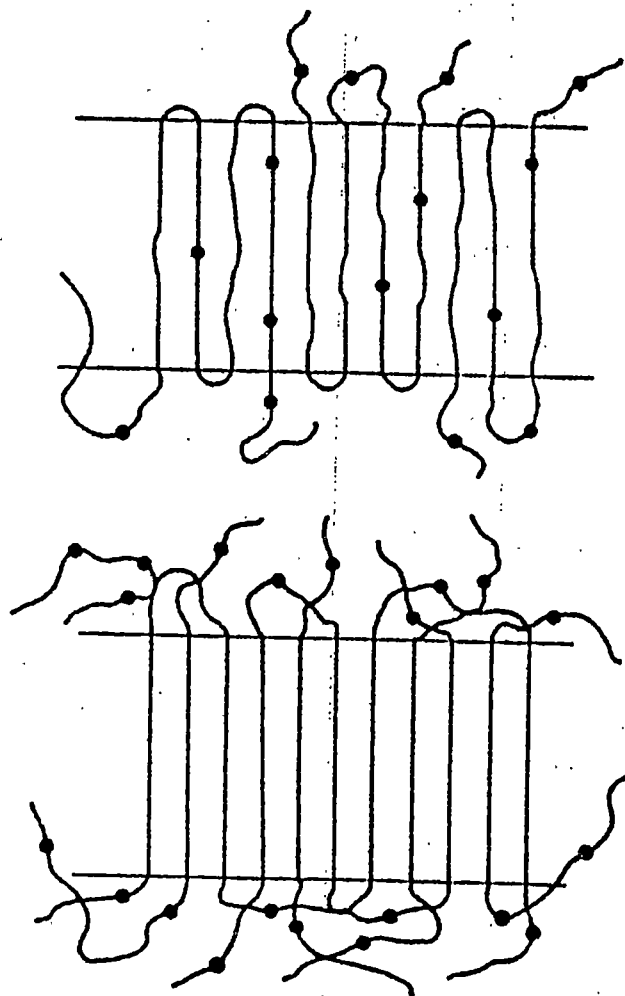
Figure 2.27 Exclusion (left) and Inclusion (right) models[80].

copolymer unit contributes a term equivalent to that found in a polymer diluent mixture[116-118].

Flory showed through experimental work with copolymers of decamethylene and glycol (or dibasic acid radicals) that thermal properties of copolymers depend in a systematic fashion on polymer constitution, and that quantitative relationships can be traced. Flory also found that copolymers with smaller end groups tended to have higher melting temperatures[115].

Copolymers, that are able to crystallize, will be composed of crystallites of various thicknesses, that can be expressed as a thickness (ς), composed of A repeating units in a single chain transversing the crystallite. At equilibrium, crystallites of every length ς containing A units must be at equilibrium with the sequences of A units in the amorphous phase[117]. The equilibrium of the crystallizable A sequences, at a given crystallization temperature, is the ultimate driving force in this theory that determines the lamellae thickness. The equilibruim is produced by the chemical potential difference that manifests as an entropy factor, similar to chemical potential in an osmotic cell. The melting temperature (T_m) for a copolymer is expressed by[117]:

$$(2.17) \qquad \frac{1}{T_m} - \frac{1}{T_m^0} = -\left[\frac{R}{\Delta H_u}\right]\ln X_A$$

where T_m^0 is the equilibrium melting temperature of the homopolymer, R is the universal gas constant, ΔH_u is the heat of fusion per unit and X_A is the mole fraction of A units. The standard free energy of fusion per mole of units (ΔG_u) is:

$$(2.18) \qquad \Delta G_u = \Delta H_u - T\Delta S_u$$

At equilibrium, this allows for the theoretical calculation of the melting temperature. The standard free energy of fusion of a length ς units from a crystallite length ς is defined as:

$$(2.19) \qquad \Delta G\varsigma = \varsigma \Delta G_u - 2\sigma_e$$

where σ_e is the fold surface free energy per mole. Notice that the fold surface contributes to the instability of a crystal as a result of chain folding. An extended chain crystal would not have this term, that is why it is the more stable crystal morphology.

At temperatures slightly below T_m, crystallization is restricted to only very thick crystallites (i.e. large values of ς), therefore only the longest sequences containing A units will be able to crystallize. As the temperature is lowered, ς decreases and progressively thinner crystallites are formed requiring shorter sequences of A units[116-117].

Thus from a thermodynamic point of view, the crystallite thickness is dictated by the crystallization temperature and length of A unit sequences. Ultimately the length of A unit sequences determines the properties. The length of A sequences is determined from the mole content of the uncrystallizable B monomer and its distribution within the chains. Recall that this is an equilibrium thermodynamic theory. The most stable semi-crystalline state is when ΔG assumes a minimum value[79]. So there is a tradeoff among all the thermodynamic factors and non-crystallizable comonomer distribution that determine the crystallite thickness'. Experiments have shown that as the comonomer content is increased, the copolymer melts at successively lower temperatures and the crystallinity decreases[80].

The model presented above was developed by Flory on the grounds that no B units would be incorporated into the crystal (exclusion model) and that the crystallite thickness was determined from thermodynamic considerations. Flory stated his theory is likely more applicable to low average weight molecular chains. The exclusion of B units and chain ends was an assumption in the theory[117]. We now know that in fact chain ends and some commoner units can be and sometimes are included in crystallites[81,119-120].

Structural and morphological evidence has been found that suggests some copolymers consist of lamellae with comonomer units in the crystals. The defects incorporated into crystals result in crystal distortions which increase (or decrease) the

intermolecular distance and effect crystal enthalpy, thereby causing a decrease in the melting temperature. Eby and Colson[81] found the relationship between comonomer concentration (x), melting temperature and lamellae thickness (ℓ) to be:

(2.20)
$$\frac{1}{T_m} = \frac{1}{T_m^0} + \left(\frac{A}{T_m^0}\right) x(1+x) + \frac{B}{T_m^0 \ell}$$

where A is the negative of the ratio of excess Gibbs free energy of melting for each defect to the enthalpy of melting of a unit in a perfect crystal. The quantity B is related to fold surface energy. This is the first modification to incorporate and predict the effects of defects incorporated into crystals.

Colson and Eby[81,119] used tetrafluoroethylene and hexafluoropropylene and found that the variation of melting temperature with lamellae thickness and commoner concentration is consistent with the concept of inclusion of comonomer units in the lamellae crystal as defects.

One of the most important aspects of crystallization, especially copolymer crystallization, was a model presented by Price[121]. Price presented a model that incorporated finite growth rates under equilibrium conditions. Later, an improved model of kinetic growth was presented by Lauritzen[82] et. al that incorporated a polymer chain being able to lay down and then back off of a crystal at the growth front. This was an important step forward in copolymer crystallization, in that this theory built in some of the kinetic factors that figure so prominently in any type of defect/copolymer crystallization.

In 1973, two elegant papers were put forth that proposed an explanation, thermodynamically and kinetically, of copolymer crystallization. Helfand and Lauritzen presented a theory on the crystallization of copolymers of A and B that do not achieve equilibrium composition[83]. The fraction of B (using Flory's terminology) included in the

crystal was determined from kinetic considerations. This theory was based on one developed by Lauritzen, DiMarzio and Passaglia (LDP)[82].

The system is composed of A and B monomer units, as before. As each monomer unit enters the crystal, the free energy of the system is lowered by ΔG_0. However, when a B unit enters the crystal (for whatever reason), the free energy of the system increases by an amount ε that is typically much larger than ΔG_0. The B unit not only changes the thermodynamic properties, but also the kinetic barriers to crystal growth and decay (or removal of a deposited stem). The ε is paid in several parts, ε_1 is paid as soon as the B unit lays down in the niche, ε_2 is paid when the next stem passes beside the incorporated B unit and ε_3 is paid when the next stem lays down on top of the B unit[82-83]. The illustration in Figure 2.28 shows defect inclusion in a chain folded crystal, with defects, in black. The illustration in Figure 2.29 depicts the free energy of the system as stems are deposited. The first section (ε_1, ε_2 and Q_f) represents the large nucleation barrier to initiation of a new growth strip by addition of the first stem onto the surface. The barrier is largely due to the new lateral surface exposed on this stem. As more stems are added, the energy barrier is lowered, on the average, as the initial energy barrier is the highest. The deposition of the first stem is where the free energy penalty is at a maximum. If the polymer crystal contained no B units (i.e. a homopolymer), the energy curve would follow the dotted line. The addition of B units in the crystal, as well as other inclusions, cause the energy well depth to decrease. Therefore, it is easier for the back reaction to occur and the stem to be removed, represented by the solid line in Figure 2.29. Removal occurs as a result of the extra free energy associated with incorporation of a defect. The presence of defects in the growth front will cause the growth rate to decrease, since the probability that a stem will back off at a given crystallization temperature is greater. The increase in the back reaction occurs as a result of the energy barrier decreasing from the presence of the defects in the crystallization front.
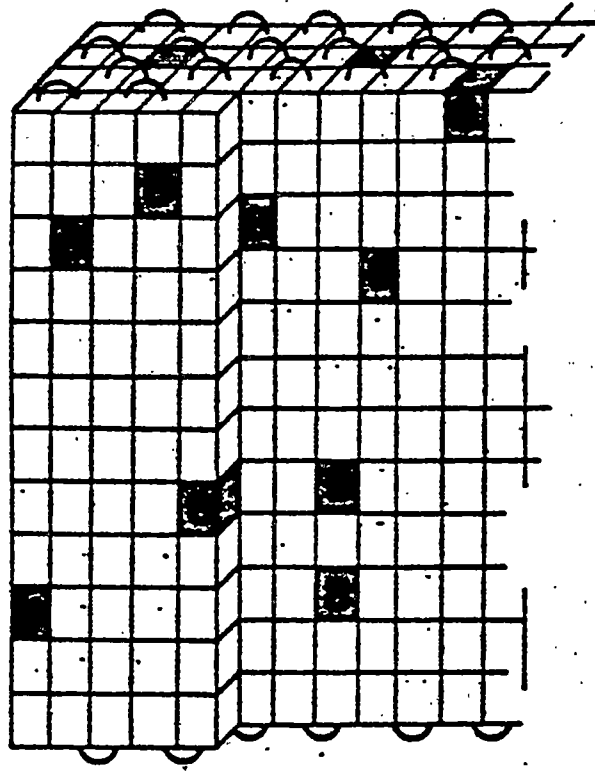
Figure 2.28 Defect incorporation into crystal[83].
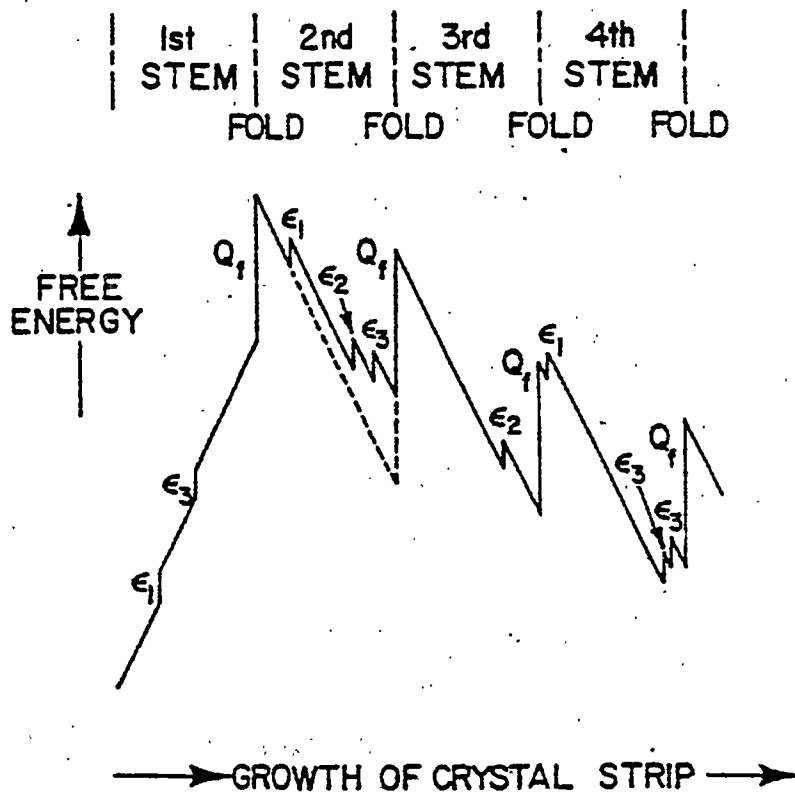
Figure 2.29   Jump rate with and without defects present[80].

Through research done with copolymers, some qualitative features emerge[79-84,114-122].

1. The concentration of B in the crystal is significantly greater than predicted by equilibrium theory. As a result, the crystals will melt at lower temperature relative to the homopolymer from defect inclusion.

2. Increasing the growth rate, or increasing the crystallization kinetics leads to larger inclusions of B. Since the growth rate is faster, the probability that a stem depositing with a B unit increases. The drive toward deposition is higher, regardless of the B unit.

3. The temperature influences kinetic processes in two ways. The energy barriers are divided by kT, which is an energy normalization at a given temperature. Therefore, as the temperature increases the term becomes smaller. The temperature also effects ΔG_0 by the following relationship:

$$(2.21) \qquad \Delta G_0 = \left(\frac{\Delta H_f}{T_m^0} \right) \left(T_m^0 - T_m \right)$$

where ΔH_f is the heat of fusion and T_m^0 is the equilibrium melting temperature of the pure crystal.

4. The copolymer lamellae must be thicker than pure homopolymer lamellae, with the extra thickness being necessary to compensate for the free energy increment associated with the impurities incorporated into the crystal. Another consequence is that the growth rate is reduced. If crystallite thickness increases, there are fewer chain folds, per unit volume, resulting in a lower overall free energy that is needed to compensate for the defect inclusion.

A consequence of this theory is that the concentration of B in the crystal is larger than is predicted by equilibrium theory based on thermodynamics. The equilibrium melting temperature depression will also be higher than the actual observed T_m. As the

70

crystallization temperature decreases, the non-equilibrium inclusion of B increases due to kinetic factors[79,80,83].

In review of the theories presented for random copolymers:

1. Both the inclusion and exclusion models predict depression of the crystalline melting temperature. For the exclusion model, T_m decreases from the preferential ordering of the copolymer chains necessary for crystallization, which increases the entropy of fusion and produces a chemical potential difference. The inclusion model predicts a lowering of T_m due to a lower heat of fusion resulting from the incorporation of defects into the crystal structure.

2. The kinetically determined lamellae thickness is expected to increase while the growth rate decreases, as the concentration of B increases. The equilibrium exclusion model predicts crystal thickness increases with increasing B, to recover the free energy lost in the ordering process.

3. The crystal thickness is predicted to decrease with increasing B concentration, when copolymers are quenched. This is also the case with homopolymer crystallization.

2.4.3.1 iPP Copolymer Crystallization

Most often iPP is copolymerized with ethylene to produce a useful copolymer. Some researchers view metallocene homopolymers with tacticity defects as copolymers. There also are researchers who view zniPP resins as being copolymers to some extent, with the same reasoning as for miPP resins.

Experiments have shown the presence of comonomer significantly reduces linear growth rates and overall crystallization kinetics. The comonomer also decreases melting temperature, while reducing crystallinities. Turner-Jones[13,24,29] showed the melting curves for copolymers were very complicated and were regarded as indicative of fractionation occurring due to major copolymer composition effects. Part of the complexity was

71

attributed to large amounts of atactic material. Therefore, there are two significant findings in copolymer research:

1. The presence of an atactic component that complicates understanding the effects of copolymerization.

2. The distribution of copolymer units is not necessarily random, further complicating the effects of copolymerization.

Mezghani and Phillips[31] have shown that the equilibrium melting temperature of propylene/ethylene copolymer drops as the percent ethylene content increases, as would be expected. Mezghani found that a 0.5mol% copolymer had a T_m^o of 180°C, while a 5.0mol% copolymer had a T_m^o of 151°C.

2.5   Oriented Non-Isothermal Crystallization

The practical aspects of studying crystallization begin when industrial processes are considered. Almost all industrially useful processing methods are non-isothermal in nature and involve orientation of the melt during processing. Injection molding, film blowing and melt fiber extrusion are just some methods in which polymers are commercially processed. Melt fiber extrusion (fiber spinning) will be focused on in this section. Fiber spinning is used in carpet manufacture, the garment industry, tire manufacture and in many other applications. The melt spun filaments can either be used directly or further processed, depending on the application in which they will be used. The fibers can be thermally bonded together to make a non-woven fabric or drawn to produce finer filaments with better mechanical properties, to name just a few possibilities. The first commercial use of melt spinning was by Dupont in 1939 using nylon 6,6 after an invention made by Carothers[123-124] et.al.

Melt spinning of a polymer involves melting and extrusion of a material through a capillary die (usually multihole), followed by a cooling process in which the polymer is drawn and solidified. The solidified filaments are then taken up by a winder or further processed. The basic process is illustrated in Figure 2.30. Polymer is placed into a hopper or fed into the extruder, where the material is melted and delivered to a positive displacement metering pump (spin pump). The spin pump controls the volume of material being processed and provides a steady flow of molten polymer to the spin pack in which the molten polymer is channeled into orifices (spinneret) for extrusion into fibers. The spinneret can consist of a single hole, multiholes and other elaborate constructions (such as bi-component multipolymer systems) depending on the particular process. The extruded filaments are then drawn down into finer filaments and crystallized in the cooling chamber. Cooling is achieved by blowing some type of gas (usually air) across the molten filaments as they are being drawn toward the collector. The collector, in the form of a bobbin or suction device pulls on the molten fibers; this stress produces a finer filament than otherwise would be produced in a gravity pulled system.

2.5.1 Analysis of Spinning Process

An engineering analysis of the melt spinning process is complex, with assumptions, simplifications and approximations to make the math and understanding tractable. An analysis of melt spinning process will include:

1) The dynamics involved in melt spinning.

2) Rheological constitutive equation(s).

73
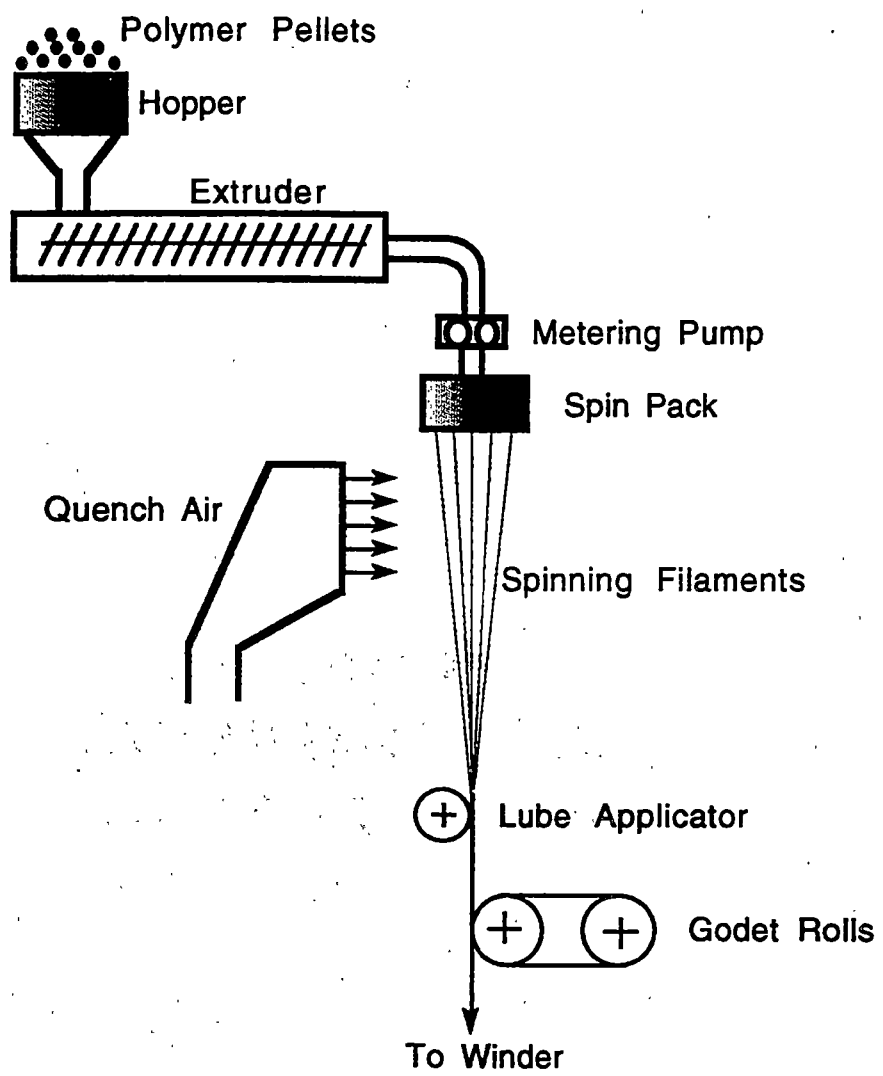
Figure 2.30 Schematic of the melt spinning process.

74

3) Crystallization behavior in a molecularly oriented system.

2.5.1.1 Force and Momentum Balance

An overall force balance on a single filament in a spinline may be written as follows[125], with a total force diagram shown in Figure 2.31:

(2.22) $\qquad F_{rheo} = F_o + F_{inert} + F_{drag} - F_{grav} + F_{surf}$

where F_{rheo} is the rheological force in the fiber at a distance z from the spinneret, F_o is the rheological force at the exit of the spinneret, F_{inert} is the inertial force produced by the acceleration of the polymer mass through the spinline, F_{drag} is the drag force caused by the fiber moving through the cooling medium, F_{grav} is the gravitational force acting on the spinline and F_{surf} is the surface tension force at the fiber/cooling medium interface. The surface tension force is typically neglected for most polymeric materials, since it is only significant for low viscosity materials. The substituent forces are defined as:

(2.23) $\qquad F_{inert} = W(V - V_0)$

(2.24) $\qquad F_{drag} = \int_0^z \pi D \sigma_f dz$

(2.25) $\qquad F_{grav} = \int_0^z \rho g \left(\frac{\pi D^2}{4} \right) dz$

where D is the fiber diameter and V the velocity at a given distance z away from the spinneret. The subscript 0 is at the origin, z=0 of the spinneret. σ_f is the shear stress at the fiber/air interface due to air drag, ρ is the filament density, g is acceleration due to gravity and W is the mass-through-put per hole of the spinneret. A material balance of the mass-through-put requires:

Spinpack

z ———

z ———

$z+dz$ ———

F_{inert}

F_{surf}

F_{drag}

F_{grav}

$F_{rheo} - F_o$

@$Z=L$, $F_{rheo}=F_L$
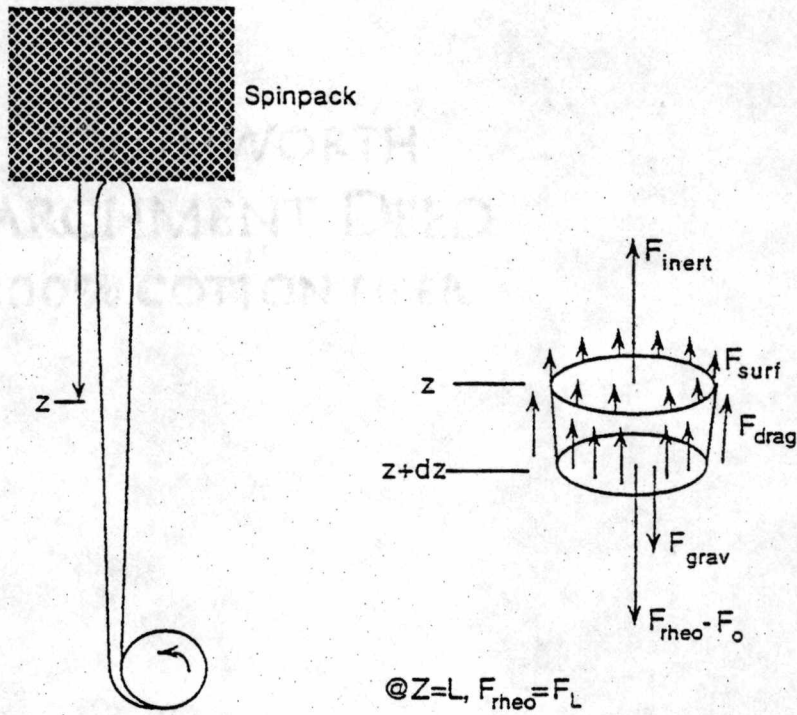
Figure 2.31 Spinline forces acting on a filament.

$$(2.26) \qquad W = \rho A V = \rho \pi \left(\frac{D^2}{4} \right) V$$

Equation 2.26 is called the Continuity equation. It is necessary and true in all steady state spinning processes.

In general, the transition from low spinning speeds to high spinning speeds also changes from a rheology controlled process to one controlled by inertia and air drag. The relationship of the various forces in a spinline as a function of spinning speed is shown in Figure 2.32. Simple boundary layer theory yields air drag controlled shear stress (σ_f) on the surface of the fiber moving with velocity V in a fluid of density (ρ_{air}) as:

$$(2.27) \qquad \sigma_f = \frac{\rho_{air} V_r^2 C_d}{2}$$

where V_r is the relative axial velocity of the filament in air and the cooling medium, C_d is the dimensionless drag coefficient dependent upon the geometry of the moving body and cooling conditions. If there is no parallel air flow to the fiber draw direction, $V_r = V$. The value of C_d has been correlated with the Reynolds number (R_e) through:

$$(2.28) \qquad C_d = K(R_e)^{-n}$$

where K and n are material dependent. Sano and Orii[126] have found the empirical relationship in equation 2.28 to hold true using values of K=0.68 and n=0.8.

Using the above assumptions and simplifications, equation 2.22 can be rewritten, after appropriate substitutions as:

$$(2.29) \qquad \frac{dF_{rheo}}{dz} = W \frac{dv}{dz} + \frac{1}{2} \rho_{air} C_d V^2 \pi D - \frac{Wg}{V}$$

By definition, the rheological force is related to the axial spinline stress (σ_{zz}) by:
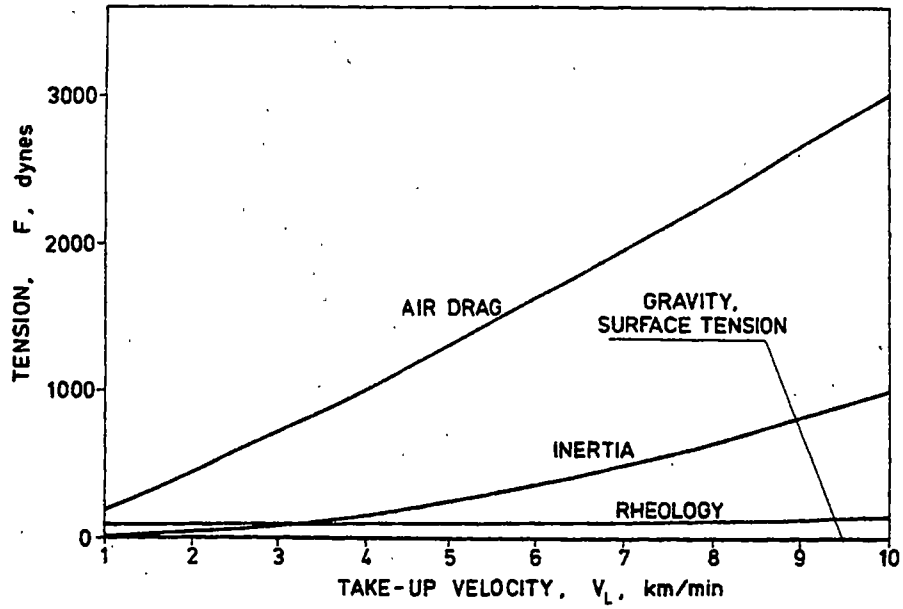
Figure 2.32 Spinline forces as a function of spinning speed[129].

78

$$(2.30) \qquad \sigma_{zz} = \frac{F_{rheo}}{A} = \frac{4F_{rheo}}{\pi D^2}$$

assuming cylindrical fibers. Since the spinline stress is difficult to measure, a directly measurable quantity, F_L, the tension in the spinline at distance L away from the spinneret can be measured using a tensiometer. Thus, equation 2.22 can be rearranged, with appropriate simplification and substitution to yield:

$$(2.31) \qquad F_{rheo}(z) = F_L - F_{drag} - F_{inert} + F_{grav}$$

which expanded is:

$$(2.32) \qquad F_{rheo}(z) = F_L - \int_z^L \rho_{air} C_d V^2 \pi D dz - W[V(L) - V(z)] + \int_z^L \rho g \pi \left(\frac{D^2}{4} \right) dz$$

where the variables are defined as before. From this expression, the rheological force can be calculated at any point along the spinline.

2.5.1.2 Constitutive Equation for Melt Spinning

The rheological behavior of a polymer during melt spinning will govern the deformational nature and structure development that occurs in the spinning process. At low spinning speeds, a Newtonian constitutive equation describing the melt behavior can be used to predict the rheological response. In melt spinning, the shear viscosity is not of primary importance, elongational viscosity becomes the dominate form that limits the effective spinning speed of a polymer, under any given set of conditions. The general Newtonian equation:

$$(2.33) \qquad p_{ij} + p_o \delta_{ij} = 2\eta \dot{e}_{ij}$$

79

where p_0 is the isotropic pressure, p_{ij} is the stress tensor, $\dot{e}_{ij}$ is the deformation rate tensor and η is the shear viscosity. Under steady state spinning, neglecting all forces but take-up tension (F), equation 2.33 becomes:

$$(2.34) \qquad \frac{\rho F}{W}V = \eta^* V'$$

where $\eta^* = 3\eta$ = elongational viscosity and $V' = dV/dx = \dot{e}_{xx}$, the elongation rate. In normal spinning the elongational viscosity is a function of both temperature and deformation rate:

$$(2.35) \qquad \eta^*(x) = \eta^*[T(x), V'(x)]$$

This relationship is also true, by definition, for the shear viscosity. (Also note that the dependence of elongational viscosity and velocity gradient is non-linear). The effect of temperature on viscosity is strong, with the viscosity of polymers very sensitive to changes in temperature. However, it is true for a Newtonian fluid that:

$$(2.36) \qquad \eta = \sigma_{zz}\frac{dV}{dz}$$

if the viscosity is independent of the shear rate (by definition). Some researchers have proposed work that incorporates the viscous elongational behavior of a material whose viscosity decreases with the strain rate. This formula is a generalized power law equation of the Cross and Carreau[127-128] type:

$$(2.37) \qquad \eta(T,\dot{E}) = \frac{\eta_0}{1 + (a\eta_0\dot{E})^b}$$

where η_0 is the zero shear rate viscosity and a and b are constants. The viscosity follows an Arrhenius temperature dependence at higher temperatures and switches to the

Williams-Landell-Ferry (WLF) equation at lower temperatures near the T_g of the polymer.

2.5.1.3 Thermodynamic Energy Balance

Heat can be removed from a spinning fiber via convection, conduction and radiation. In polymer fiber spinning, radiation is negligible, since the temperature differential between the fiber and cooling medium is typically not very large (relative to what is found, for example, in inorganic glass fiber formation where extrusion temperature may be greater than 1000°C). The conductive heat transfer along the fiber axis is also negligible. Thus, convection is the main source for heat transfer away from a filament. As a consequence of convection, the surface area to volume ratio becomes very important in fiber spinning. Convection cooling can cause a radial temperature distribution within the filament, which can be found in thick filaments and filaments cooled under high speed spinning conditions.

Another important aspect that must be considered when constructing an energy balance for a melt spun polymer is the effect a crystallizable polymer (semi-crystalline) has on the spinline when the polymer undergoes crystallization, resulting in a heat of fusion (ΔH_f). If an assumption of no radial temperature variation is made, only a single filament is considered, an energy balance of a crystallizable polymer is[129-132]:

$$(2.38) \qquad \frac{dT}{dz} = \frac{\Delta H_f}{C_p} \frac{dX}{dz} - \frac{\pi D h (T - T_a)}{W C_p}$$

where T is the fiber temperature, T_a is the temperature of the cooling medium (heat sink), X is the percent crystallinity, h the heat transfer coefficient and C_p is the heat capacity of

the molten polymer. The heat transfer coefficient is the difficult term to ascertain. It can either be measured experimentally, which is extremely time consuming and difficult, or calculated from an empirical correlation developed by Kase and Matsuo[132-133]:

$$(2.39) \qquad h = \frac{0.42 k_a \left(\frac{\rho_{air} V_r}{\mu_{air}} \right)^{\frac{1}{3}} \left(1 + \frac{64 \mu_c^2}{V_r^2} \right)^{\frac{1}{6}}}{D}$$

where k_a is the thermal conductivity of air, μ_a is the kinematic viscosity of air and μ_c is the cross component of the air velocity perpendicular to the filament spin direction.

2.5.1.4 Molecular Orientation

One of the industrially important consequences of fiber spinning is the generation of an oriented filament as a final product. Since polymers are macromolecules, and fiber spinning is typically done with undiluted molten polymer, there are many entanglements of polymer chains with one another. These entanglements are what causes polymers to deviate from Newtonian behavior, and fortunately, cause the molecular orientation found in melt spun polymers. Molecular orientation occurs as a result of melt deformation and chain entanglements.

The most common and simplest way to measure molecular orientation is by measuring a material's birefringence. Birefringence (Δn) in a filament is defined as the difference between the index of refraction in the parallel and perpendicular direction to the filament axis:

$$(2.40) \qquad \Delta n = n_z - n_r$$

where n_z is in the parallel direction and n_r the perpendicular direction. It has been observed[134-136] that birefringence, at low stress levels, in an amorphous polymer is proportional to an applied stress such that:

(2.41) $\qquad \Delta n = C_{op}\sigma_{zz}$

where C_{op} is the stress-optical coefficient. From rubber elasticity theory the stress-optical coefficient is defined as:

(2.42) $\qquad C_{op} = \dfrac{2\pi(n^2 + 2)^2(\alpha_1 - \alpha_2)}{45knT}$

where n is the refractive index of the polymer, $(\alpha_1 - \alpha_2)$ is the difference in polarizabilities between the principle directions and k is Boltzman's constant. Birefringence is typically measured using a microscope, by determining the retardation of the wave of light passing through the sample.

Birefringence measurements are composed of both crystalline and noncrystalline portions, where each phase contributes to the total overall level of molecular orientation. Often it is useful to know the amount each phase contributes to the overall amount of observed birefringence.

Research has established that semicrystalline polymers are composed of more than two types of molecularly oriented regions. Originally, a two phase model consisting of crystalline and amorphous regions was used. Research has shown that even isotropic semicrystalline polymers have at least a third domain, referred to as the rigid amorphous phase. This region is amorphous, with a higher level of organization (density) than a true amorphous domain. The molecules are not in crystallographic registry, although their total entropy is lower than that of a true amorphous solid. Therefore, there exists an

entire distribution of states that run between totally amorphous and totally crystalline phases. The methods used to interpret data are most often average results, that fall somewhere between the two morphological extremes.

The level of orientation can be expressed by orientation factors developed by Hermans[137-138] et.al. The average orientation of the crystallites, in a semicrystalline material, can be described on a quantitative numerical basis using the Hermans' orientation function (f). The orientation function f describes the orientation of a phase relative to some reference direction in a sample. The orientation function is defined as:

(2.43) $$f_x \equiv \frac{3\overline{\cos^2 x} - 1}{2}$$

where x is the crystallographic direction and $\overline{\cos^2 x}$ is the average cosine squared value of the angle (x) between the reference direction in the sample and the crystallographic direction. Typically, these measurements are done on crystalline polymers where, a comparison is made between the fiber axis and c-axis of the crystal.

Stein and Norris[139] have shown that the crystalline and amorphous domains of a semicrystalline polymer can be related to birefringence by:

(2.44) $$\Delta n = (1 - X_c)f_{nc}\Delta_{nc}^0 + X_c f_c \Delta_c^0 + \Delta n_{form}$$

where X_c is the crystalline fraction, f_{nc} is the non-crystalline orientation function, f_c is the crystalline orientation function, Δ_{nc}^0 is the non-crystalline intrinsic birefringence, Δ_c^0 the crystalline intrinsic birefringence and Δn_{form} is the form birefringence resulting from light interaction with the two phases. In semicrystalline polymers, form birefringence is small and is typically neglected[139-140]. The intrinsic birefringence values can be theoretically calculated from bond polarizability values as given by Bunn[141] and Denbigh[142], with

Denbigh's method being more accurate for some polymer systems. The theoretical results often are not the same as those found experimentally, so careful consideration and justification must be used in utilizing this procedure. One of the interesting findings from this work, as pointed out be Stein[143] and Vuks[144], is the intrinsic non-crystalline birefringence is higher than the crystalline. This is a result of the ordered lattice arrangement in the crystal of chains experiencing not only the electromagnetic field of the incident light, but also the polarization field of the surrounding molecules. The internal field of the crystal is more anisotropic in the crystal phase, resulting in a difference in polarizabilities between the crystalline and non-crystalline phases. Experimental results with some polymers (e.g. polypropylene) have shown that the theoretical prediction is true.

2.5.2 Crystallization with Forced Molecular Orientation

Crystallization in the spinline is very different than crystallization found under non-isothermal quiescent conditions. In melt spinning, there is molecular orientation of the polymer chains in the melt at the time crystallization occurs. However, many of the same parameters that govern quiescent crystallization, those factors that influence nucleation and growth rates, will be active in the spinline, along with the effects of molecular orientation. Experience has shown[154-155] that crystallization in the spinline occurs at higher temperatures than what has been found under this same cooling rate under quiescent conditions. The higher crystallization temperature has been attributed to the role of molecular orientation in the spinning process. This has led to the phrase "stress induced crystallization", meaning the addition of stress to the melt causes

crystallization to occur, under stress, where it otherwise would not. The illustration in Figure 2.33 shows the transition from an amorphous molten polymer to a more ordered semi-crystalline fiber. Overall molecular orientation increases as the melt is cooled due to an increase in viscosity. Figure 2.34 shows the radial variation of variable across a fiber diameter in the spinline. The velocity gradient of molecules is uniform across the filament radius. The temperature profile shows the fiber surface is slightly cooler than the interior of the fiber. Understanding the temperature profile explains the viscosity, stress and molecular orientation results. The coolest portion of the fiber will have the highest viscosity, therefore more stress, producing more molecular orientation.

The basic crystallization theories were reviewed earlier. The sections on quiescent isothermal and nonisothermal crystallization have developed the theories presented below, only an extension of those theories will be presented.

Ziabicki was the first researcher to attempt to describe the effects of molecular orientation on the melt spinning process. Ziabicki[148-152] proposed that the overall crystallization rate constant, K, was a function of not only the temperature, but of molecular orientation and wrote:

(2.45) $\qquad K(T,f) = K(T,0) + a_1 f + a_2 f^2 + a_3 f^3 + ...$

The series expansion can be simplified by symmetry and under normal orientation levels:

(2.46) $\qquad \ln\left[\dfrac{K(T,f)}{K(T,0)}\right] = A(T) f^2$

where A(T) is an experimental quantity that is sensitive to temperature and molecular orientation. Ziabicki also developed the following relationship for quiescent crystallization:
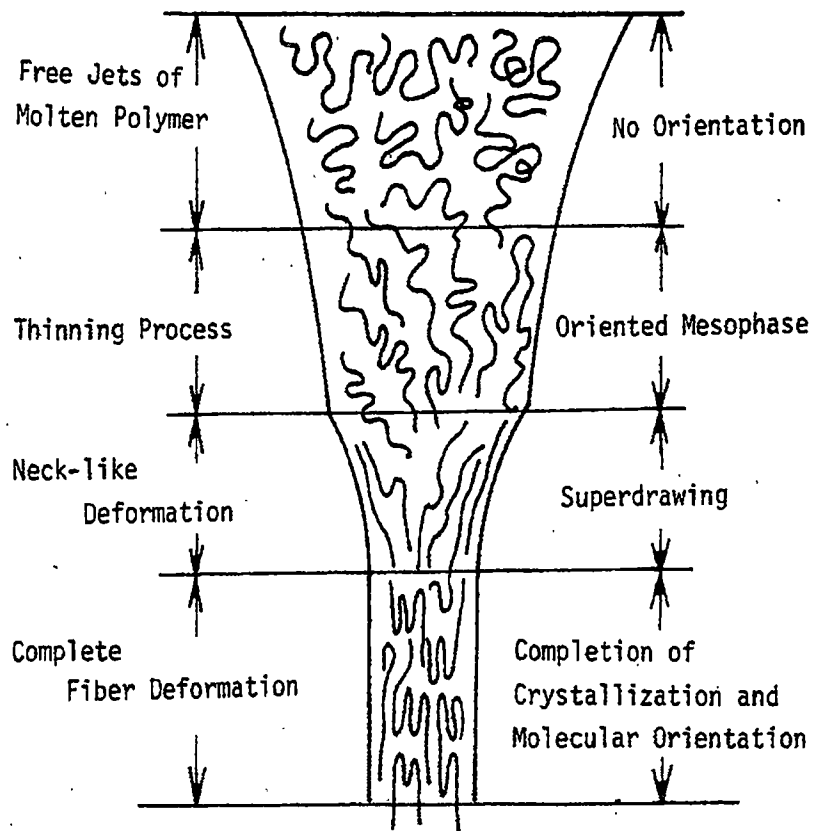
Figure 2.33 Molecular orientation during solidification[129].
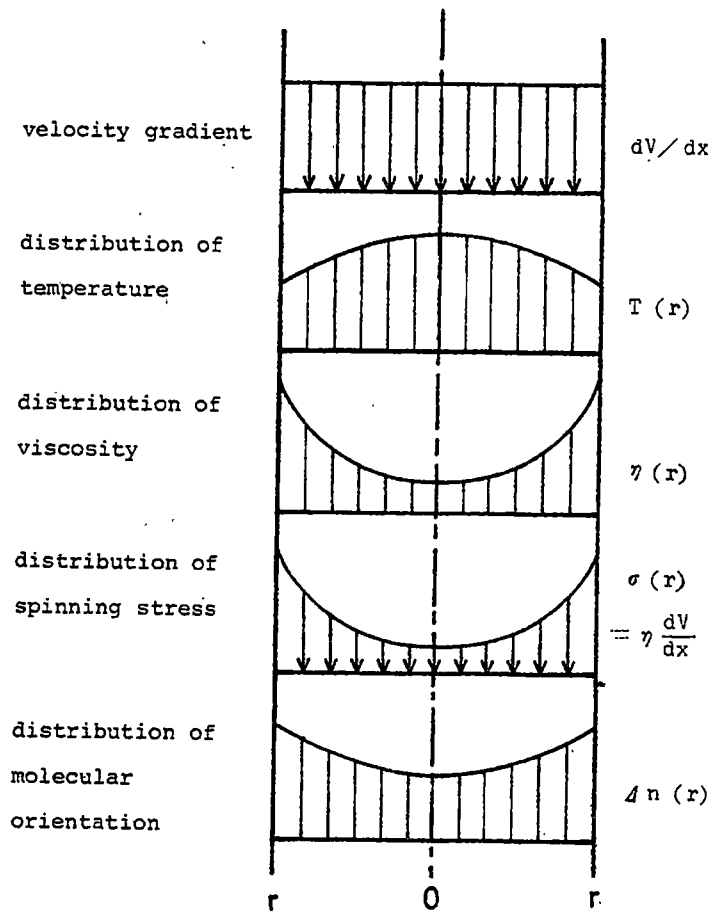
Figure 2.34 Radial variations in filament properties during spinning[129].

$$(2.47) \qquad K(T) = K_{max}e^{\left[\frac{-2.78(T-T_{max})}{D^2}\right]}$$

where K_{max} is the maximum crystallization rate constant at temperature T_{max} and D is half width value on the K vs T graph. By substitution of equation 2.47 into equation 2.46 an expression incorporating molecular orientation on the crystallization rate can be obtained. The problem with this theory is that it does not separate and address nucleation and growth rates as separate steps, that may operate independent of one another.

Utilizing the Hoffman theory of molecular nucleation and growth, as well as rubber elasticity theory, Katayama and Yoon[145] introduced a kinetic equation that included the effects of orientation on crystallization. The authors stated the change in crystallization rates was a result of the thermodynamic effect of deformation on a molecular network. Doi and Edwards[207], while not specifically addressing the issue, came to a similar conclusion. The authors state that a change of free energy in the melt due to deformation and orientation (ΔF_{def}) is the difference in the free energy of the crystal and amorphous melt for an isotropic system (ΔF_{iso}) and with crystallization from an ordered melt (ΔF_{or}) is:

$$(2.48) \qquad \Delta F_{def} = \Delta F_{or} - \Delta F_{iso}$$

Assuming $\Delta H_{iso} \cong \Delta H_{or}$, equation 2.48 can be rewritten as:

$$(2.49) \qquad \Delta F_{def} = -T(\Delta S_{or} - \Delta S_{iso}) = -T\Delta S_{def}$$

by definition. Where ΔS_{def} is the entropy difference between the isotropic and oriented amorphous melt. From rubber elasticity theory, ΔS_{def} is related to molecular extension ratio (λ) and birefringence by:

(2.50) $\Delta S_{def} = k_1\left(\lambda^2 + \dfrac{2}{\lambda} - 3\right)$

and

(2.51) $\Delta n = k_2\left(\lambda^2 - \dfrac{1}{\lambda}\right)$

For small extensions ($\lambda \cong 1$),

(2.52) $\Delta S_{def} = k_3(\Delta n)^2$

Where k_i are material constants. An orientation function can be defined as:

(2.53) $f = \dfrac{\Delta n}{\Delta^0}$

where Δ^0 is the total intrinsic birefringence of the material. Therefore, from orientation arguements[146] we may write:

(2.54) $\Delta F_{or} = \Delta F_{iso} + CTf^2$

These results can then be directly inserted into Hoffman's nucleation and growth rate equations by substituting ΔF_{or} for ΔF_{iso} to yield:

(2.55) $\dot{N}(T,f) = \dot{N}_0 e^{\left[\frac{-U^*}{R(T-T_\infty)}\right]} e^{\left[\frac{-C_1}{T\Delta T + CT^2 f^2}\right]}$

for the heterogeneous nucleation rate in the presence of orientation and

(2.56) $G(T,f) = G_0 e^{\left[\frac{-U^*}{R(T-T_\infty)}\right]} e^{\left[\frac{-C_2}{T\Delta T + CT^2 f^2}\right]}$

for the growth rate in the presence of orientation.

From this work, Katayama and Yoon, as well as Patel and Spruiell assumed that the overall crystallization kinetics rate constant has the same form.

(2.57) $K(T,f) = K_0 e^{\left[\frac{-U^*}{R(T-T_\infty)}\right]} e^{\left[\frac{-C_3}{T\Delta T + CT^2 f^2}\right]}$

where K_0 and C_3 can be obtained from quiescent crystallization data. The value of C can only be obtained from back calculation from experimental data on the spinline.

2.5.3 iPP Fiber Spinning Behavior

One of the first researchers to study the dynamics and structure development of melt spun polymeric fibers was Ziabicki and Kedzierska[148-153]. These authors studied the effects of changing melt spinning variables, both processing and resin variables that led to a more fundamental understanding of the melt spinning process. They were the first to offer quantitative formulations as to what was taking place during the spinning process. The main variables that affect the spinning process were elucidated and studied. The major processing variables that affect the melt spinning process are:

1) Polymer extrusion temperature (T_e)

2) Mass-throughput (Q)

3) Take-up velocity or spinning speed

4) Cooling rate of the filaments (C_r)

5) Spinneret orifice shape, size and relative location to one another

6) Length of the spinline (L_s)

These process variables are not independent of one another and their interdependency is important to understand.

The major materials variables are:

1) Those that effect the rheology of the melt

   a) molecular weight

   b) molecular weight distribution

91

c) chain stiffness

d) other additives and fillers

2) Those that effect the crystallization kinetics

a) chain stereoregularity

b) molecular weight

c) additives such as nucleating agents, antioxidants and pigments etc.

2.5.3.1 Influence of Process Variables

The processing variable effects are considered from the point of view that changes in them are made with all other conditions held constant.

2.5.3.1.1 Take-up Velocity

The take-up velocity is generally the most important process variable. The speed at which the molten resin is drawn down significantly affects the resulting crystallinity, as measured by density, and overall molecular orientation, as measured by birefringence. At a constant mass throughput, the final filament diameter decreases with increasing take-up velocity and the cooling rate along the running spinline is increasing. As the spinning speed increases, the spinline stress increases and both crystallinity and molecular orientation increase in spite of the increase in cooling rate which should suppress the development of crystallinity. This is strong evidence that the stress and molecular orientation lead to stress-enhanced crystallization. On-line measurements of temperature, birefringence and x-ray diffraction patterns show that crystallization begins

at higher temperatures in the spinline than under quiescent conditions with similar cooling rate[154-155]. This is further evidence of stress-enhanced crystallization.

The crystal structure of melt spun iPP is most often the α-monoclinic form[156]. However, if the fiber is quenched rapidly or the stress in the spinline is low, a conformationally disordered (condis) or smectic structure is formed. The smectic structure is not thermally stable and transforms to the monoclinic form when annealed above 70°C.

2.5.3.1.2 Extrusion Temperature

As the extrusion temperature is increased, the elongational viscosity in the upper part of the spinline decreases, thereby lowering the stress in the spinline and reducing the molecular orientation and crystallinity developed at a given spinning speed. However, as the spinline stress is increased (by increasing the spinning speed) the density and birefringence tend to become independent of the extrusion temperature, indicating that the increased stress due to increased spinning speed eventually overrides the decreased stress due to higher extrusion temperature.

2.5.3.1.3 Mass Through-Put

Increasing mass through-put per spinneret hole, while keeping take-up speed constant, produces larger filament diameter (continuity condition) and lowers the stress in the spinline. This in turn leads to lower filament birefringence. Increasing mass throughput also reduces the cooling rate in the spinline due to the greater amount of material that must be cooled. One might expect that the slower cooling rate would

increase crystallinity and density due to more available time for crystallization. However, the lower stress decreases molecular orientation and causes less stress-enhancement of the overall crystallization rate. The final crystallinity results from a balance between these two factors which also depends on the nature of the cooling process and the characteristics of the specific resin.

2.5.3.1.4 Cooling Conditions

As with the take-up velocity, the cooling conditions have a significant influence on the crystallization behavior during the spinning process. As the cooling air temperature decreases or volume of air blown across the filament increases, the cooling rate of the spinning filaments increases. This moves the solidification point in the filament closer to the spinneret. As the freezing point moves closer to the spinneret, the deformation rate increases since the filament must reach its final diameter closer to the spinneret; this produces an increase in the spinline stress. This increase in stress closer to the spinneret results in an increase in molecular orientation which is more readily frozen-in due to the higher cooling rate. There is again a balance between the retardation of crystallinity development due to faster cooling and the enhancement of crystallinity development due to increased stress.

2.5.3.1.5 Length of Spinline

The length of the spinline is important for two reasons. First, the spinline must be long enough to allow the polymer to freeze before being contacted by guides or godet rolls. Because of this, the spinline length is controlled by the efficiency of spinline

cooling; longer spinlines are required for slower cooling. However, longer spinlines also increase the gravitational contribution to F_{rheo} which increases the spinline stress. In most cases, especially for fine filaments, spinline length will have relatively little effect on the structure and properties of the spun filaments due to the low value of F_{grav} relative to other contributions to F_{rheo}.

2.5.3.1.6 Filament Shape

The filament shape and die orifice design affect the heat transfer rate between the filament and surroundings. The larger the surface area for a given volume of material, the faster the polymer will transfer heat away and crystallize. This case is similar to the effect of increasing the cooling rate by other means described above.

2.5.3.2 Material Variables

The material variables effects are considered from the point of view that changes in them are made with all other conditions held constant.

2.5.3.2.1 Molecular Weight

Both molecular weight and its distribution (MWD) strongly affect the spinnability of iPP. Generally, spinnability, as measured by the maximum take-up speed at which spinning can be carried out in the absence of instabilities, increases as molecular weight distribution is narrowed. There tends to be a maximum in the spinnability with increase in molecular weight. At very low molecular weight the spinline exhibits instabilities due to low melt strength. For high molecular weight,

various other instabilities, including melt fracture and spinline breaking arise due to the high stresses in the spinneret capillaries and in the spinline.

Within the range of molecular weight and MWD where spinnability is relatively good, these characteristics also affect the resulting crystallinity and molecular orientation in as spun filaments. This can be understood on the basis that increasing M_w produces higher spinline stress and molecular orientation in the melt which, in turn, causes crystallization rates to increase and crystallization to occur closer to the spinneret and at higher temperatures[156]. There is also an effect of MWD; broader distribution resins with the same MFR develop higher crystallinity at equivalent spinning speeds. This appears to be caused by broader MWD resins being more susceptible to stress-enhanced crystallization as a result of the high molecular weight tails in the distribution providing a source of "row nuclei" which seed the stress-induced crystallization[157].

The higher molecular orientation in the melt state produced by higher molecular weight usually results in higher birefringence in the spun filaments. Lower orientation in the broader distribution samples has been attributed to a bimodal orientation that occurs preferentially in broader distribution resins[157]. This bimodal orientation has one component in which the polymer chains are parallel to the fiber axis and a second component in which the chains are approximately perpendicular to the fiber axis. This latter component lowers the overall molecular orientation with respect to the fiber axis and hence the fiber birefringence. Another possible contribution to the difference between the broad and narrow distribution samples is a difference in the non-crystalline orientation developed by a given spinning condition.

2.5.3.2.2 Percent Isotacticity

As percent isotacticity decreases, both the crystallization rate and ultimate crystallinity of iPP generally decreases. During melt spinning this causes the crystallization to occur farther from the spinneret and at lower crystallization temperature[158]. The resulting as-spun filaments have lower density, but their overall molecular orientation and birefringence are mostly unaffected.

2.5.3.2.3 Propylene/Ethylene Copolymers

The addition of ethylene units to form a random copolymer (RCP) lowers the crystallinity that can be developed by virtue of the lower stereoregularity of the chain. This is analogous to the effect of stereo defects when decreasing the isotacticity of the chain.

2.5.3.2.4 Nucleating Agent Additions

The addition of nucleating agents raises the crystallization temperature and the resulting crystallinity substantially for quiescently crystallized iPPs. These effects also occur during melt spinning of iPP fibers, but they are more pronounced under conditions of low spinline stress (i.e. low spinning speeds)[158]. At high spinning speeds and/or other conditions that produce high stresses in the spinline, the differences due to nucleating agents are smaller, but not eliminated, arising from the influence of stress in raising the rate of crystallization. Nucleating agents tend to lower the molecular orientation in the filaments. This is a result of crystallization occurring at higher temperatures and nearer the spinneret, where the molecular orientation in the melt is lower.

2.5.3.3 Tensile Properties of Melt Spun iPP Filaments

As noted above, increasing the stress in the spinline tends to increase the overall molecular orientation of filaments in the spinning process. Recall that overall molecular orientation is composed of both crystalline and amorphous orientation. Research has shown that the amorphous region most strongly contributes to the tensile strength of iPP fibers. This arises from the fact that tie molecules connect the various crystalline regions, thereby allowing the transfer of stress and the load from one crystallite to another. The crystalline regions are important in providing a medium in which to anchor the various molecules that make up and run throughout the fiber, but the crystallinity alone is a poor indicator of mechanical properties. Under normal spinning conditions, a strong correlation of tensile strength with birefringence is observed. The elongation-to-break obeys a somewhat similar, but inverse dependence on the molecular orientation in the spun filament; it decreases from several hundred percent (~1000%) at low birefringence values to less than 200% at a birefringence of about 0.025.

Although the initial elastic modulus (Young's modulus) increases as molecular orientation increases, it is also a function of crystallinity. Since the higher crystalline modulus contributes roughly according to the rule of mixtures, the overall modulus of the filament increases as the crystallinity increases. For this reason, the modulus does not correlate well with birefringence alone, as do the tensile strength and elongation-to-break. In the case of modulus, both the level of molecular orientation and degree of crystallinity must be considered. For this reason the modulus of ethylene copolymer melt spun filaments is substantially lower than for the homopolymers when prepared under similar

spinning conditions, even though their tensile strengths are equal or slightly higher. On the other hand, nucleating agent additions may lead to lower modulus because of lower molecular orientation, in spite of a higher degree of crystallinity.

2.6 Thermal Spunbonding

Feminine-hygiene, disposable-diaper and medical-products businesses combine for about $6 billion in retail and institutional sales of non-woven fabrics. One component of the non-woven fabric market is thermal spunbonding. Thermal spunbonding offers high production rates because bonding is accomplished at high productivity with heated calender rolls or ovens in a continuous process.

Thermal bonding requires a thermoplastic component, which is typically a fiber, powder or film that are bonded together. There are several options available in thermal bonding: area bond calendering, point bond-calendering, through-air bonding, ultrasonic bonding and radiant bonding. The most widely used method for thermal bonding is point bonding, which will be used in this work.

2.6.1 Point Bonding Process

A typical thermal point spunbonding line will be arranged similar to the set-up illustrated in Figure 2.35. The process consists of polymer fed into an extruder, where the polymer (either pellets or granules) is melted and pumped via a positive displacement pump to the melt spin pack. The spin pack consists of filters and channels that supply molten polymer to the die aperture, where the polymer is extruded into the cooling environment. The cooling environment consists of quenching air that is blown across the filament, or more simply, ambient conditions. However, often elaborate chambers can be constructed so the cooling environment can be strictly controlled, depending on the process. The extruded filaments are then drawn down into finer filaments by the

99

KEY

1. Hopper
2. Extruder
3. Spin pump
4. Die block
5. Cooling & stretching chamber
6. Primary Air
7. Secondary Cooling Air
8. Tertiary Drawing Air Jets
9. Suction blower
10. Spin belt
11. Guide belt
12. Bonding unit
13. Winding unit
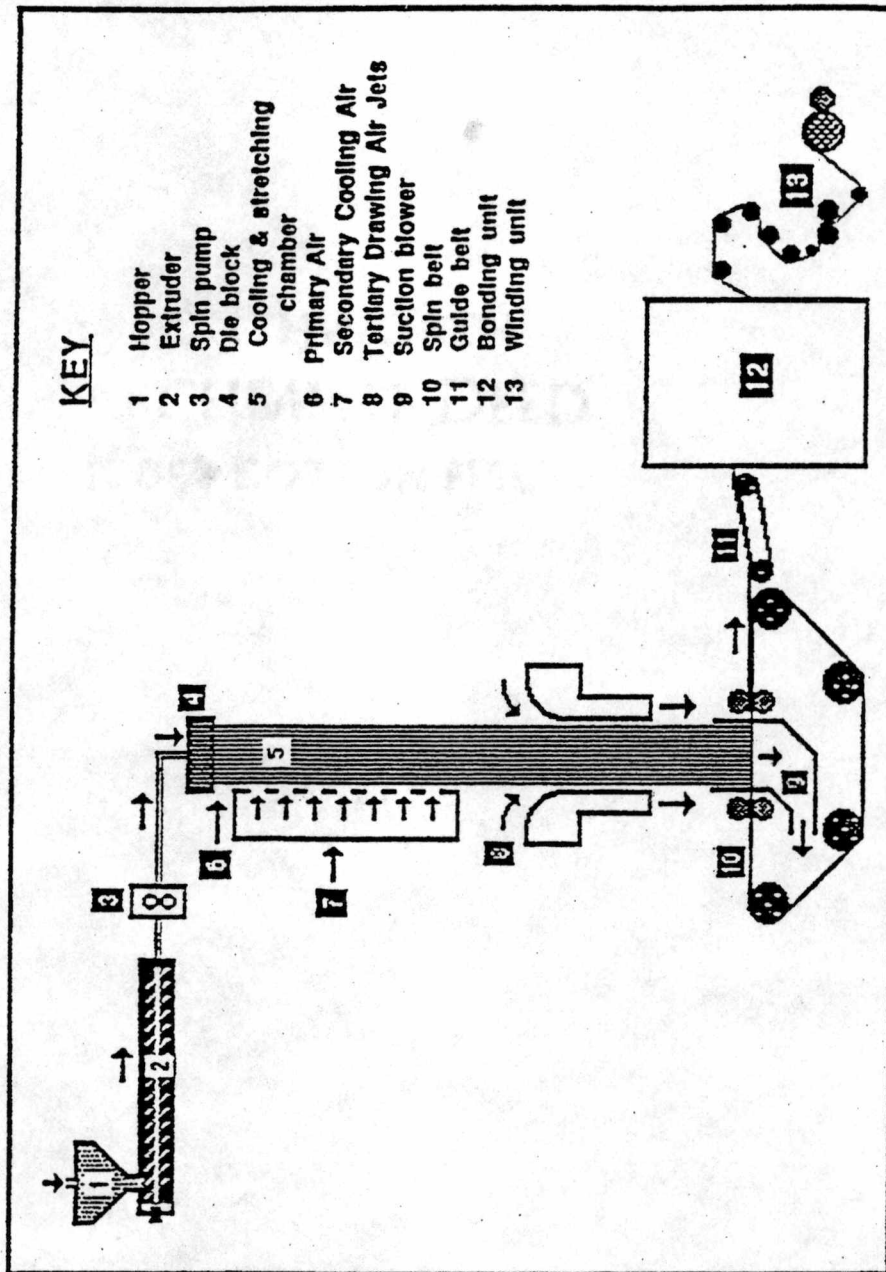
Figure 2.35 Spunbond line.

100

application of force by some type of suction device or wound onto a bobbin. The take-up process is largely dependent upon the end use of the polymer filaments. In thermal spunbonding, the web is fed by an apron leading to a calender nip consisting of one engraved and one smooth roll.

When the web enters the hot calender nip, the fiber temperature is raised to the point at which tackiness and melting cause fiber segments caught between the tips of the engraved points and the smooth roll to adhere together[159-162]. The thermal point bonding process is illustrated in Figure 2.36. The unbonded fabric is melt pressed together under pressure between an upper and lower calender roll and partially melted to bond the fibers together. Filament fusion is desirable on the web surfaces for abrasion resistance, but for maximum tensile properties and toughness, the bonds in the interior of the web need to be just weaker than the filaments. The general idea is when strain is applied to the web, some filaments release from each other at the bond site, permitting more homogenous load-sharing, which increases strength and toughness. Producing release bonds requires a careful balancing of bond pressure, bonding roll temperature, process speed and initial fiber structure.

In the thermal spunbonding process, the main factors that affect the optimization of the bonding process can be broken down into three categories: process related factors, fiber related factors and polymer related factors.

2.6.1.1 Process Related Factors

Process related factors include orientation of fibers in the web, bonding temperature, bonding pressure, contact time, quench rate and calender pattern. The two major process factors influencing thermal point bonding most are the roll temperature and nip-line pressure. Residence time in the nip is determined by the production or line speed
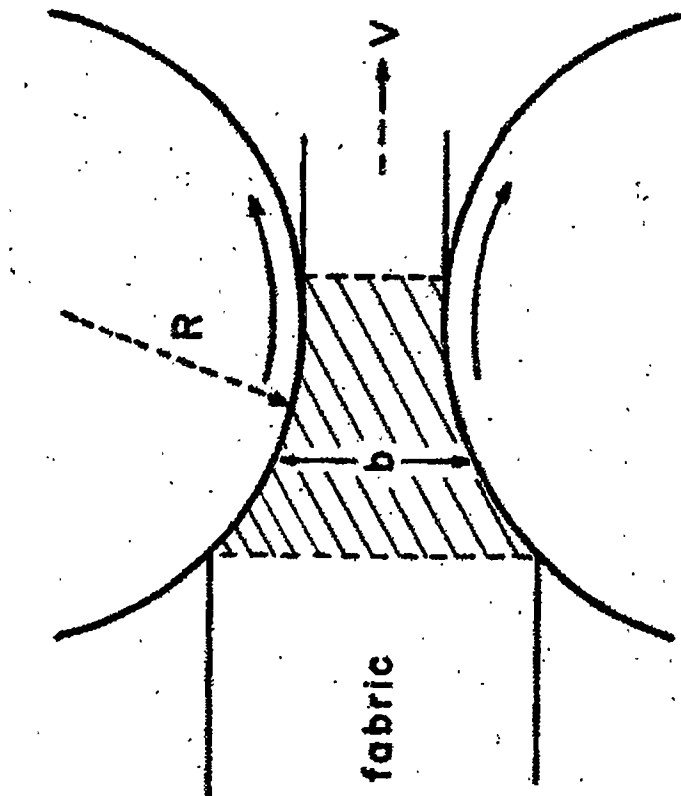
Figure 2.36 Thermal point bonding process[168].

and roll diameters. Once the line speed is set, the temperature and pressure are adjusted to get the desired fabric properties[163].

2.6.1.1.1 Bond Temperature

The bonding temperature refers to the temperature of the heated calender rolls. A temperature profile is established through the web, which is produced by heat transfer from the rolls to the web and governed by the thermal characteristics of the compressed web.

Studies have shown that for a given nip-line pressure and line speed, the breaking strength reaches a maximum at a critical bonding temperature. Below the critical bonding temperature, fabric failure is attributed to poor fiber adhesion at the thermal bond point. The decrease in breaking strength above the critical temperature level is attributed to the loss of fiber integrity and the formation of film-like spots at high temperatures in the fabric[164-167]. In addition, fabric damage due to adhesion to the calender rolls can occur.

The general finding is that each set of fibers has a set of critical bonding temperatures, above and below which, the fabric properties decrease. The critical bonding temperature lies near the melting point of the formed fibers.

2.6.1.1.2 Bonding pressure

Studies have shown the effect of bond pressure is less significant than that of line speed or bonding temperature. The bonding temperature at which the maximum fabric strength occurs is unaffected by bond pressure. However, the ultimate maximum strength of the fabric is influenced by the bond pressure. The influence depends on the melting behavior of the fibers. If the position of the bonding maxima occurs in the softening region of the fibers, a higher pressure will increase fabric strength. If the maxima occurs

in the early melting zone, a low calendering pressure is desirable so that the bonding zone is not disturbed[164-167].

The bond pressure is also important since it influences the heat transfer from the calender to the web. The main mechanism of heat transfer into the fabric is conduction[164-167]. The line speed being so rapid that little convection heating occurs. The application of pressure squeezes the air out of the web, increasing fiber-to-fiber contacts and enhances the heat transfer throughout the material. The application of pressure also forces the fibers together and deforms them to form the point bond.

2.6.1.1.3 Line Speed or Contact Time

Contact time is primarily influenced by the line speed and roll diameters. Contact time in the bonding zone is on the order of milliseconds . Studies have shown that as line speed increases:

1. The calender temperature required for maximum strength increases to compensate for the reduced contact time.

2. The influence of calendering pressure is greater at faster line speeds.

3. The maximum achievable strength increases.

The important parameter when considering the effects of bond temperature, bond pressure and contact time is the temperature of the fibers in the bond zone (nip) [165-167]. The combination of these factors all influence the fabric properties, but they mostly effect the temperature profile of the fibers in the bond zone.

2.6.1.1.4 Quench Rate

The critical quench rate for achieving maximum bond strength results from two competing processes. Increasing the quench rate initially reduces crystal sizes and flaws between the crystals, leading to stronger bonds. As the quench rate further increases, the

stress concentrations are not able to relax after the bonding process, decreasing the fabric strength. Therefore, there exists an optimum quench rate for achieving a maximum fabric strength[164,169-170].

2.6.1.2 Fiber Structure Factors

Fiber spinning in thermal spunbonding is the same as described in the oriented non-isothermal crystallization section.

2.6.1.3 Polymer Related Factors

Fiber spinning in thermal spunbonding is the same as described in the oriented non-isothermal crystallization section.

2.6.2 Thermal Spunbonding of iPP

There are several advantages to using iPP for thermal spunbonding applications. One of the most important factors is cost, PP monomer is much cheaper than other non-woven grade polymers such poly-ethyleneterephthalate (PET). Other advantages of using iPP are:

1. surface smoothness

2. resistance to microorganisms

3. chemical resistance

4. hydrophobicity

5. low density, meaning the fabrics are light

6. low melting point, operating costs are lower

Since the fiber spinning behavior of iPP has already been reviewed, the effects of fiber properties on the actual bonding process will be reviewed. The influence of crystallinity, molecular weight and fiber molecular orientation will be discussed.

2.6.2.1 Crystallinity

Very little research has been published on the effects of crystallinity on the thermal spunbonding process. Most of the information available is on fabric property relationships and how they correlate with crystallinity.

The effects of crystallinity are most often grouped with changes in fabric strength on pre-annealing of non-bonded fibers. The researchers don't directly say crystallinity, but it is implied. Annealing causes a higher order of crystalline perfection ,which smoothes the crystal surface and decreases fabric strength. The basic trend is to keep crystallinity down to improve the bonding properties of the fabric. However, keeping the crystallinity down tends to make fabric shrinkage a problem[171-172].

2.6.2.2 Molecular Weight

The effects of molecular weight have been linked with determining melt spun fiber properties, but not linked directly to the bondability of any given fabric.

Warner[168] calculated diffusion rates of polymer molecules across the contact boundary. The rough calculations showed the diffusion rate was much to slow to have any effect on the bonding process. The molecular weight and tacticity distribution could be very important in any type of diffusion process. Warner may have been too quick in ignoring diffusion parameters in the bonding process.

Experimental studies have shown that increasing the molecular weight distribution produces fabrics that bond better, although the fiber mechanical properties generally decrease. It has been argued that this is a result of higher crystallinity produced

106

by the wider molecular weight distribution resin over a narrow distribution polymer of similar molecular weight with all other factors remaining constant[171-173].

2.6.2.3 Molecular Orientation

The effects of molecular orientation of the fibers on fabric properties have been studied extensively. Most all studies have shown there is an inverse relationship between fiber molecular orientation and fabric mechanical properties.

The studies on molecular orientation effects have indicated that having lower molecular orientation on the surface may help the bonding process. Lower molecular orientation increases the cocrystallization (inter fiber bonding) of fibers, as cited by one author. Experimental[171-173] studies have shown that degrading the outer skin of a fiber during the spinning process increases fabric strength. Degradation of the skin achieves two results, lowers the molecular weight on the surface and produces less orientation, as the stress is transferred more toward the core since the viscosity and stress is higher in that region.

2.6.3 Studies are Needed

It is clear that more studies are needed to understand the complex relationships that exist in the thermal spunbonding process. Much of the work has been done by researchers trained in textiles. Very little work that has appeared in the open literature has been done by polymer physicists, researchers that understand polymer behavior first and foremost.

Chapter 3

Experimental Methods

3.0 Materials

The materials examined in this study were nine isotactic polypropylene resins catalyzed by one of two different methods. Three of the resins were conventional Ziegler-Natta catalyzed iPP resins, while the other six resins are metallocene catalyzed iPP resins. All nine resins were not used in each and every aspect of this investigation, the use of a particular resin was dependent upon the experimental method. The zniPP resins were given the code names ZN35, ZNHT and ZN-5RCP. The miPP resins were named M10, M22, M32, M45, M70 and M100. The numerical number in each case is the nominal melt flow rate of each resin. A more detailed description of the resin characteristics is presented in section 3.8.

3.1 Sample Preparation

The samples in this work were prepared in different ways, depending on each sample's use. Samples were prepared for use in x-ray analysis (both small and wide angle x-ray diffraction), differential scanning calorimetry (DSC) and optical microscopy. In addition, the fibers and fabrics produced by melt spinning and thermal spunbonding were also characterized without further treatment..

3.1.1 X-Ray Analysis

Samples for x-ray analysis were prepared using a calibrated Mettler hot stage as 40mm x 20mm x 1mm films. These samples were prepared in a hollow Al mold that fits the hot stage sample chamber and has glass slides on either side. The samples were prepared under a nitrogen atmosphere to minimize thermal oxidation degradation. The

samples were held in the melt at 230°C for 10 minutes to erase its thermal history. The samples were then isothermally crystallized at the desired temperature. X-ray diffraction patterns of the as-produced films were then made for crystal structure and crystallinity determination.

The high cooling rate samples were produced in a similar manor, except the films were cooled at high cooling rates in the HCR-LDM apparatus. The HCR-LDM samples also had a variety of sample thicknesses, depending on the cooling rate and thermocouple thickness. X-ray patterns of the as-produced films were then made for crystal structure and crystallinity determination.

X-ray patterns of fibers were also obtained. The fiber patterns were obtained on as-spun fibers aligned parallel to one another for crystalline orientation measurements and crystal structure determination using a wide angle diffractometer and flat plate x-ray film techniques.

3.1.2 Differential Scanning Calorimetry (DSC)

The samples used in the DSC study were made from a stock film melt pressed to a nominally 0.2mm film. The DSC samples were then punched from the stock film using a hole punch, with a sample typically weighing 7-9mg.

The heat of fusion(ΔH_f) used in crystallinity calculations was 167J/g for the α-monoclinic crystal structure and 150J/g for the γ-orthorhombic for 100% crystalline samples. The DSC samples were typically scanned from −20°C to 230°C at 20°C/min, unless stated otherwise.

3.1.3 Optical Microscopy

The optical microscopy films were made from the stock film used in the DSC study. Polymer disks were punched out of the stock film and placed on the glass slide until the desired thickness and surface area is achieved.

3.1.3.1 Linear Growth Rate

The samples are prepared under a nitrogen atmosphere to minimize thermal oxidation degradation. The samples were held in the melt at 230°C for 10 minutes to erase the samples thermal history. While melting the sample, the thickness was decreased to approximately 0.1mm. The sample was then rapidly transferred to a calibrated hot stage and isothermally crystallized at the desired temperature. The process of crystallization was recorded using a video camera and VCR. The tapes were then played back to allow the spherulitic diameter to be measured as a function of time.

3.1.3.2 High Cooling Rate Light Depolarizing Microscopy (HCR-LDM)

The samples were made as films between 0.05mm and 0.15mm thick, using the stock DSC film. A thermocouple was embedded in the sample during preparation so the temperature profile of the sample could be recorded. Two types of thermocouples were used; a 0.0762mm and 0.0254mm, depending on the thickness of the sample and the cooling rate to be used. The sample/thermocouple arrangement is illustrated in Figure 3.1. The thermocouple is embedded in the sample which is sandwiched between two glass slides. Further details of the technique are described later in section 3.5.2.

3.1.4 Melt Spun Fibers

Fiber samples were produced using a Fourne extruder. The samples were extruded at 210°C through a single hole die, 0.762mm in diameter with an L/D ratio of 5. The

Top View

Front View (with scale enlargement)
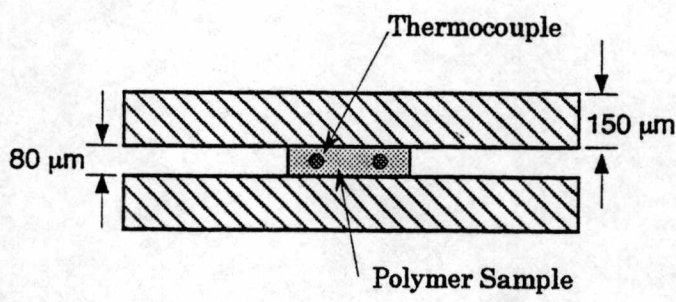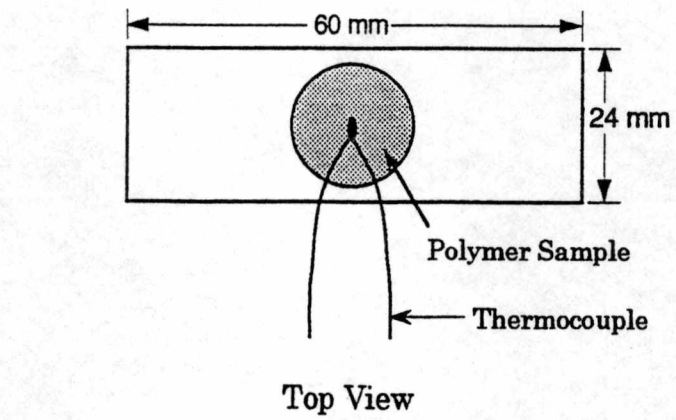
Figure 3.1 Sample thermocouple arrangement for HCR-LDM system.

samples were drawn down using a venturi pneumatic suction device located 260cm below the die orifice. The force drawing the fibers down was controlled by adjusting the air pressure to the venturi. Four to six air pressures were used to collect fiber samples with each polymer.

3.1.5 Thermal Spunbond Fabrics

All thermal spunbond fabrics were produced at the Textiles and Nonwovens Development Center (TANDEC) located on the UTK campus. The spunbond line used was a second generation Reicofil (1m wide) thermal point bonding research line. The die used in fiber production had 4036 holes of 0.60mm with an L/D ratio of 2. Mass-throughput capabilities ranged from 0.15-0.4g/min-hole with the maximum line speed of 60m/min.

The thermal spunbond fabrics were produced under a number of different conditions. The extrusion temperature was varied between 210-250°C for samples to be made. Other factors adjusted during sample preparation were bond pressure, bond temperature, primary air speed (PAS), cooling air speed (CAS), belt speed and mass-through-put.

3.2 Material Characterization Techniques

The materials in this investigation were characterized using cNMR, FTIR, GPC and xylene solubles to ascertain the average molecular properties of the materials. In some cases, the data were determined by Exxon Chemical Company.

3.2.1 Percent Xylene Solubles

The percent xylene solubles was determined according to ASTM standard D5492-94. This test provides a relative measure of the total soluble fraction of propylene and

propylene copolymers. The soluble fraction is approximately correlated with the fraction of atactic material in bulk polymerized iPP.

3.2.2   Carbon-13 Nuclear Magnetic Resonance

3.2.2.1   Theory

One of the most powerful techniques used in polymer characterization, is carbon-13 nuclear magnetic resonance (cNMR).   cNMR allows the measurement of polymer stereochemical configuration.

Like electrons, the nuclei of certain atoms are considered to spin. The spinning of charged particles generates a magnetic moment along the axis of the spin, so that each nuclei acts as a magnet. If a proton is placed in a magnetic field, according to quantum mechanics, the proton will align its field either with or against the external magnetic field. Alignment with the field is more stable, energy must be absorbed by the proton to "flip" it to the less stable alignment against the field[174].

The energy to flip the proton depends on the external field strength: the stronger the field, the greater the tendency of the proton to remain lined up with it and the higher is the frequency of the radiation needed to induce the proton to flip. The frequency at which the proton absorbs energy depends on the magnetic field the proton feels, this effective field strength is not the same as the applied field strength. The effective field strength depends on the environment of that proton; the electron density at the proton and presence of other protons. Each set of equivalent protons will have a slightly different environment from every other set of protons and will require a slightly different applied field strength to produce the same effective field strength. At a given radio frequency, all protons absorb at the same effective field strength, but they absorb at different applied field strengths. cNMR information can be broken into four primary groups[174]:

1. the number of signals tells how many different kinds of protons are present

2. the position of the signals tells the electronic environment of the proton

3. the intensity of the signal tells how many protons of each type are present

4. splitting of a signal into several peaks, which tells about the environment of a proton with respect to each other and nearby protons.

From a practical NMR standpoint, a tactic polymer can be considered a copolymer, with dyad configurations of similar configuration called meso and unlike dyads are called racemic. The magnitude of the chemical shift between distinguishable structures is dependent upon the screening of the nuclei by the electron cloud.

One of the powerful aspects of cNMR is that the range of chemical shift of carbon-13 (c-13) nuclei is about 30 times that of standard proton NMR. Therefore, very small differences in chemical and steric environment are visible using cNMR[175-179].

The illustration in Figure 3.2 shows the cNMR spectra of iPP, aPP and sPP. Each carbon substituent in PP, CH, CH_2 and CH_3 has a characteristic peak. iPP and sPP have well defined peaks that are nonidentical with respect to one another, while aPP has peaks that are intermediate between iPP and sPP. Figure 3.3 shows the full cNMR spectra of a highly isotactic iPP. The region of interest in stereochemical analysis is the methyl region in iPP, between 20-25ppm from tetramethylsilane (TMS). As shown in Figure 3.3, there are three triads, the peaks of interest are mm, mr and rr. As the isotacticity decreases, the mr and rr peaks increase, as shown in Figure 3.4. The illustration in Figure 3.5 shows that each triad is composed of many pentad peaks, with each pentad corresponding to a specific stereochemical sequence, as indicated in the figure[175-179].

3.2.2.2 Experimental Procedure

The carbon-13 data was obtained at 100Mhz at 125°C on a Varian VXR 400 NMR spectrometer. A 90° pulse, acquisition time of 3.0s and a pulse delay time of 20s were

114
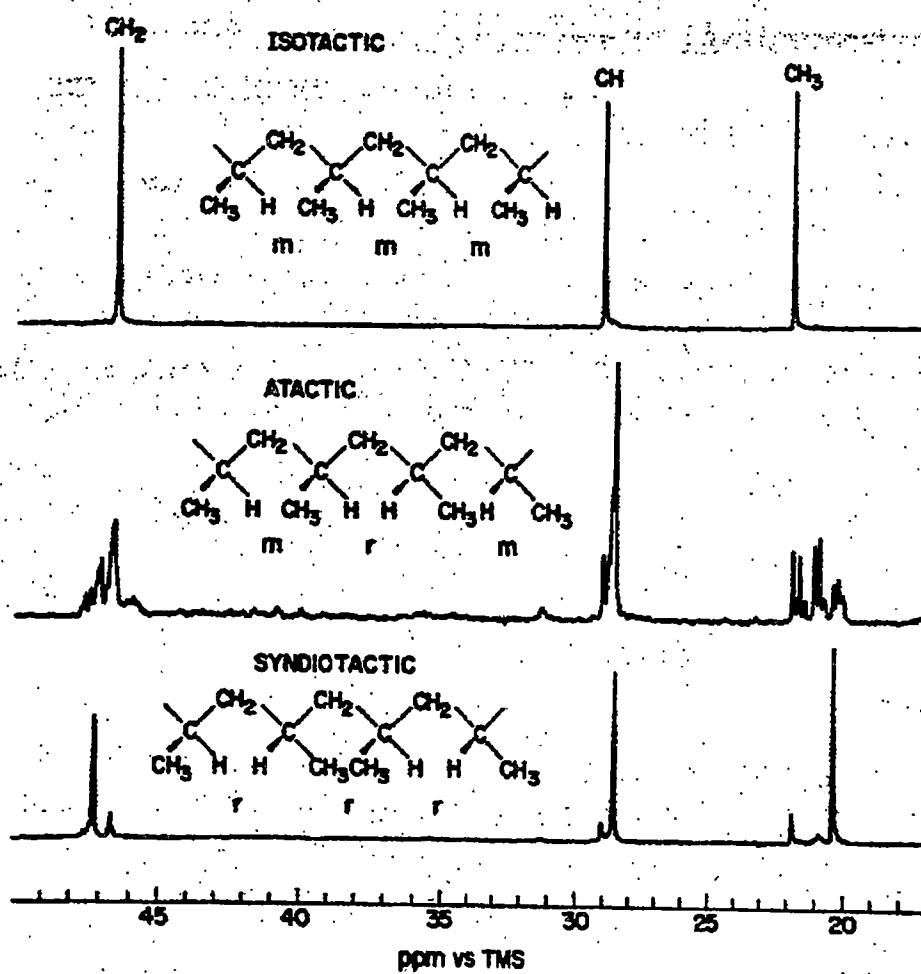
Figure 3.2   cNMR spectra of iPP, aPP and sPP[177].
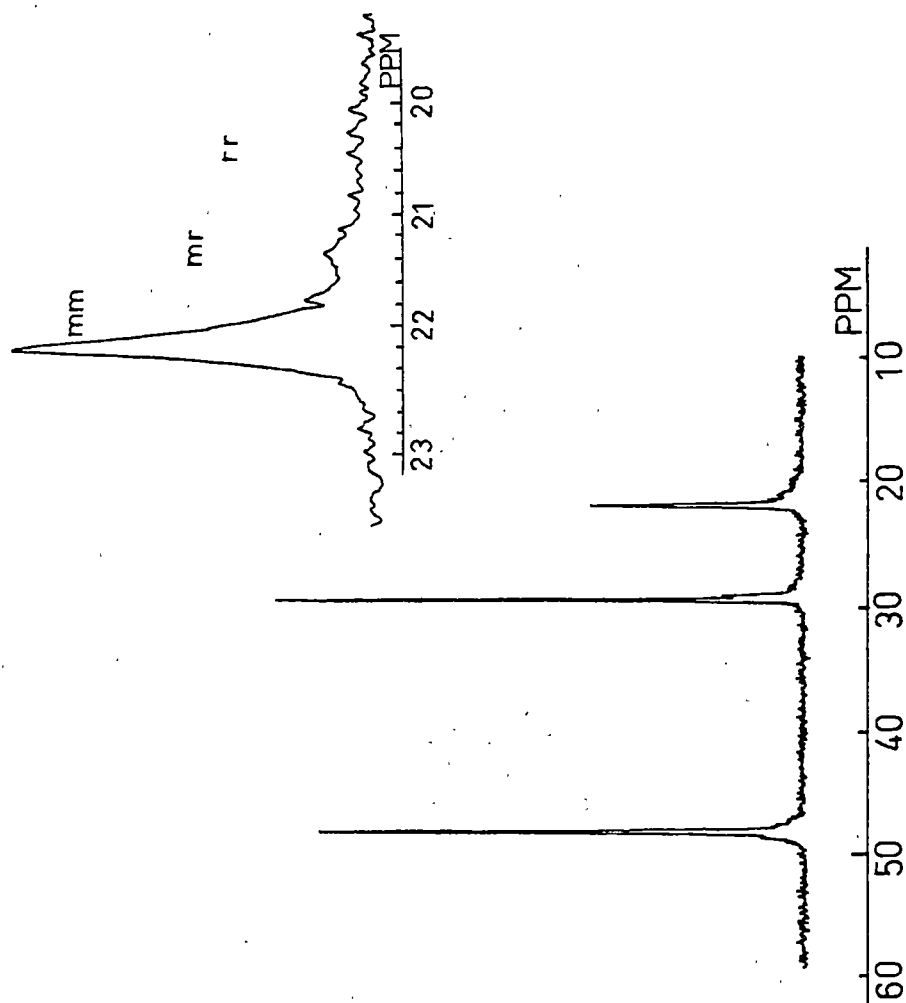
Figure 3.3 cNMR spectra of highly isotactic iPP[178].
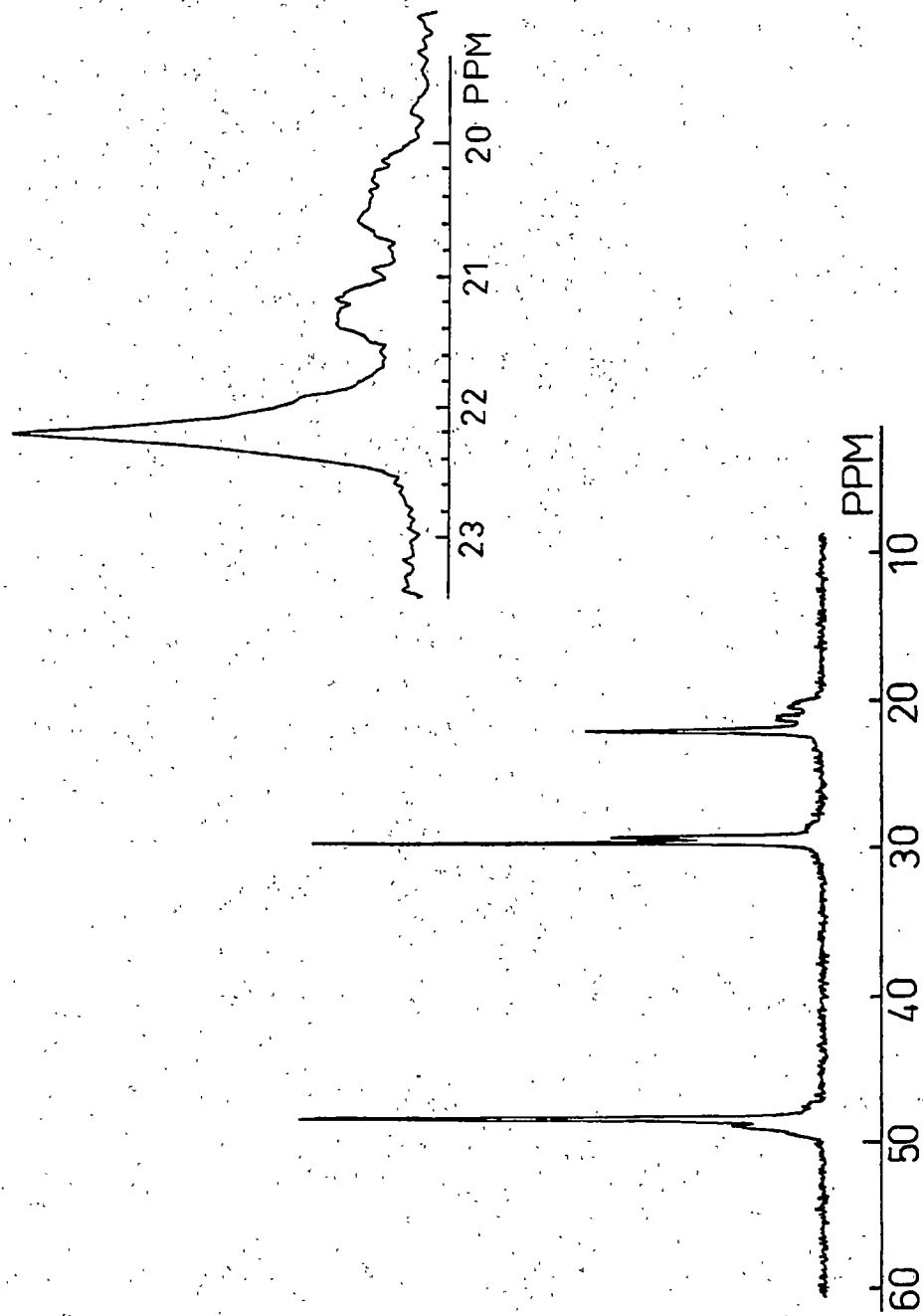
Figure 3.4 cNMR spectrum[178] of isotactic iPP with lower tactcity than the sample whose spectrum is shown in Figure 3.3.
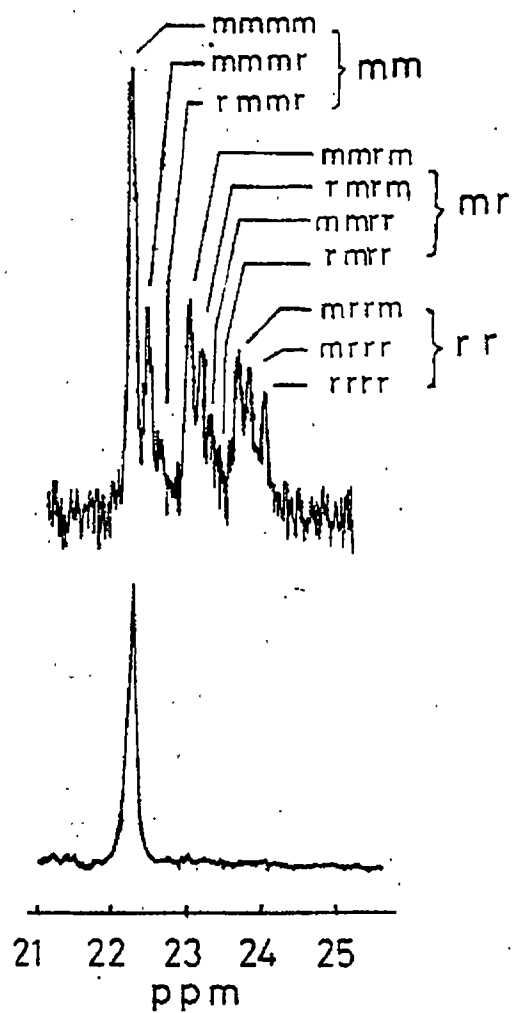
Figure 3.5 cNMR peak composition of methyl region of iPP[179].

used. A typical number of transients collected was 2500. The samples were dissolved in tetrachloroethane-d$_2$ at concentrations between 10 and 15%, by weight. Spectral frequencies were recorded with respect to 21.81ppm for mmmm, which was determined with respect to internal reference TMS and is close to the reported literature value of 21.855ppm[45].

3.2.3 Fourier Transform Infrared Analysis

Infrared analysis is an important tool used in physical characterization of polymers. IR absorption bands are known for iPP and allow determination of configuration and conformation for a particular sample. IR bands can be strongly affected by physical factors of the polymer, such as crystal structure, crystallinity and sample thermal history. As such, sample preparation is critically important if using peak absorption values. Using integrated peak areas allows a somewhat less strict approach, although peak overlap becomes an important factor.

3.2.3.1 Theory

Infrared spectroscopy has proven to be a valuable tool in the analysis of polymer structure (molecular identification, determination of chemical functionality, chain and sequence length, quantitative analysis, stereochemical configuration and chain conformation). Infrared spectroscopy is based on the principle that the total energy of a molecule consists of contributions from the vibrational, rotational, electronic and electromagnetic spin energies (van der Waals forces, the nature of the bonds, masses of the bonded atoms, etc.).

The infrared region of the electromagnetic spectrum covers the range from 13,300 cm^{-1} to about 10 cm^{-1}, with the range used depending on the type of IR being used (near, mid or far IR). Infrared spectra are obtained by passing infrared radiation through a sample

and observing the wavelengths of absorption. The absorption peaks are caused by conversion of the electromagnetic radiation into specific molecular motions. Molecular bonds are constantly stretching, bending, contracting and expanding. When a molecule is exposed to electromagnetic radiation, the vibrating bond will absorb energy from the light if the frequencies of the light and the vibration are the same. Since each light frequency absorbed by the molecule corresponds to a specific bond vibration, one can see what kind of molecular vibrations a sample has by measuring its infrared spectrum. Interpreting the infrared spectrum allows the kind of bonds or functional groups present to be determined. Thus a specific molecular bond can be assigned to a specific electromagnetic radiation frequency[180-182].

3.2.3.2 Experimental Procedure

Some of the films used in the isothermal crystallization study were used for characterization by FTIR. The films were aged at room temperature for a minimum of 30 days before testing. To the extent possible, the crystallinity and sample thicknesses was kept constant from sample to sample. The bands investigated were 809, 841, 941 and 973cm^{-1}. The first three are crystalline bands that characterize the tacticity and the last is an amorphous band that contributes to all known groupings, as such it is treated as a normalization band for relative comparisons between samples.

3.3 X-Ray Analysis

Two x-ray techniques were used to characterize the various samples in this work. WAXD was used to characterize the crystal morphology, calculate the crystallinity and determine the crystalline orientation function. SAXS was used to determine the long period and estimate the interfacial thickness of the samples.

3.3.1   WAXD

3.3.1.1   Theory

WAXD is based on the Bragg equation for determining the crystal properties of any crystalline or semi-crystalline material. The Bragg equation is:

(3.1a) $n\lambda = 2d_{hkl}\sin\theta$

where n is an integer and indicates the order of the reflection, λ is the wavelength of the scattering radiation, d_{hkl} is the spacing between (hkl) planes and θ is the Bragg scattering angle.

WAXD is used on polymers to determine the crystal morphlogy and crystallinity. Utilizing WAXD is the only method for directly measuring the crystalline component of a material. However, WAXD is not an absolute measurement technique since the location of the background and amorphous contribution of the combined pattern lead to uncertainty. The uncertainty arises from two principle sources, crystalline peak overlap and thermal motions of atoms that are in quasi-crystallographic registry i.e. atoms that are vibrating and moving about due to thermal motions. Techniques exist for correcting these problems, but utilizing these methods does little to improve on the experimental accuracy of the technique, which is 2-5% (or more), depending on the technique and researcher[184-187].

Shown in Figure 3.6 is the diffraction pattern of a semi-crystalline iPP sample. The technique for determining the crystallinity involves separating the background, amorphous and crystalline components of this pattern, as illustrated. After subtracting out the background, the amorphous contribution is estimated by the shaded curve. The percent crystallinity is then calculated from the relative area of the two domains.
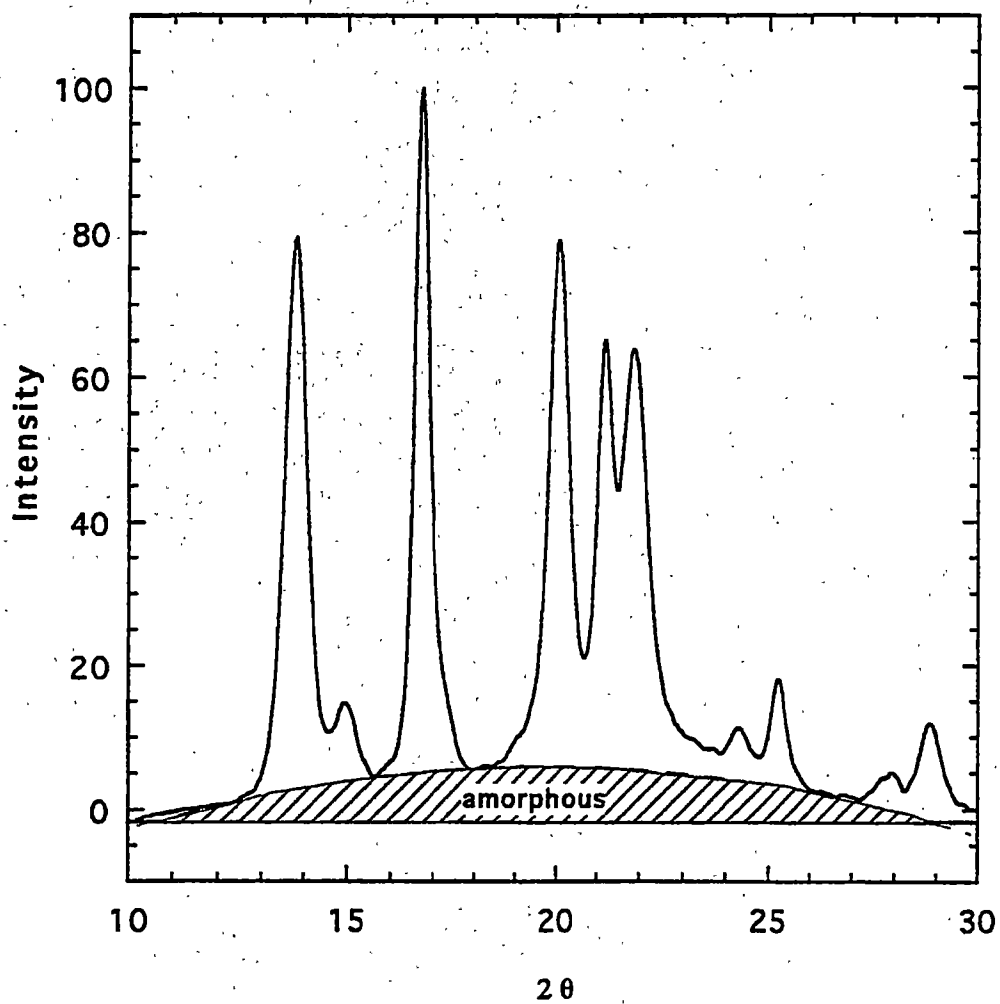
Figure 3.6 Calculation of percent crystallinity using relative area calculations[210].

3.3.1.2 Experimental Procedure

Wide angle x-ray diffraction studies were carried out using a Rigaku Denki diffractometer (λ=0.1542nm) calibrated with a silicon powder standard. The WAXD crystallinity measurements were made by subtracting the background and curve fitting the amorphous contribution to the peak crystalline intensities and using relative integrated areas for calculation. The crystallinity calculations were made using software on a recently upgraded computer system utilizing a software package called JADE 3.0. The technique used was proposed by Hermans and Weidinger[184-185].

The samples were scanned from 2θ values of 5-35°, as the peaks of primary interest fall in that range. The relative crystallinity was calculated by using the volume fraction of crystalline and amorphous material estimated from the area of each phase according to:

$$(3.2) \qquad X_{crystal} = \frac{A_{crystal}}{A_{crystal} + KA_{amorphous}}$$

where K is typically set to unity for comparative purposes. For an absolute crystallinity measurement, K should be determined from another accurate method for determining crystallinity, such as a density gradient column[184-185].

Another method for determining the degree of crystallinity (W) using WAXD was the graphic multipeak resolution technique developed by Mo and Zhang[235]. Each crystalline reflection is indexed and its peak intensity measured. The amorphous peak intensity is also measured. The degree of crystallinity is then determined according to[235]:

$$(3.2b) \qquad W_{c,x} = \frac{\sum_i C_{i,hkl}(\theta) I_{hkl}(\theta)}{\sum_i C_{i,hkl}(\theta) I_{hkl}(\theta) + k_i C_a(\theta) I_a(\theta)} x100\%$$

where I_{hkl} is the relative intensity of the crystalline peaks; I_a is the relative intensity of the amorphous peak; $C_{I,hkl}$ correction factor of the crystalline peaks; C_a is the correction factor for the amorphous peak. Based on x-ray diffraction intensity theory, Kx is defined as

$Kx=C_a(\theta)\bullet k_I$, where Kx is the relative scattering coefficient for the unit weight of crystalline and amorphous polymer i.e. a calibration constant. The correction of lost coherent intensity in this method is very important. $k_I=\Sigma I_{I,cal}/\Sigma I_{I,total}$ ($k_I\leq 1$); k_I is the relative scattering coefficient, which is the ratio of the calculated diffraction intensity ($\Sigma I_{I,cal}$) to total scattering intensity($\Sigma I_{I,total}$) for the crystalline polymer specimen of unit weight. $C_{I,hkl}$ or C_a can be calculated by the following equation:

$$(3.2c) \qquad C_{i,hkl}^{-1}(\theta) \, or \, C_a^{-1}(\theta) = \frac{1+\cos^2 2\theta}{\sin^2\theta\cos\theta}f^2 e^{-2B(\sin\theta/\lambda)^2} = \sum_i N_i f_i \frac{1+\cos^2 2\theta}{\sin^2\theta\cos\theta}$$

where f is the atomic scattering factor of a repeating unit, f_i is the scattering factors of the ith atom, N_I is the number of the ith atom in a repeating unit, 2θ is the Bragg angle, B=5, $\frac{1+\cos^2 2\theta}{\sin^2\theta\cos\theta}$ is the angle factor (LP) and the exponential term ($e^{-2B(\sin\theta/\lambda)^2}$) is the temperature factor. The formula for calculating the degree of crystallinity of iPP at room temperature using the indicated *hkl* reflection is:

$$(3.2d) \qquad W = \frac{I_{100}+1.63I_{040}+2.14I_{130}+3.51I_{111 \atop 040}}{I_{100}+1.63I_{040}+2.14I_{130}+3.51I_{111 \atop 040}+1.25I_a}$$

This technique was also used to calculate crystallinity of our iPP samples.

3.3.2 SAXS

3.3.2.1 Theory

When performed properly, the most accurate method for determining the equilibrium melting temperature (T_m^o) of a material is to directly measure the crystal

124

thickness or lamellae thickness ( ) of the material and the melting temperature of that sample with a specific thermal history.

The lamellae thickness is derived from the SAXS measurements. SAXS is used to determine the long period (L) of semicrystalline materials. The long period is derived from the scattering peak (Q_{max}) by using Bragg's Law (Equation 3.3) and the momentum transfer equation (Equation 3.4):

(3.3) $\qquad n\lambda = 2L\sin\theta$

where n is the order of the reflection, λ is the wavelength of the radiation and 2θ is the scattering angle. Expressed in terms of:

(3.4) $\qquad Q = 4\pi\lambda^{-1}\sin\theta$

Bragg's law becomes:

(3.5a) $\qquad L = \dfrac{2\pi}{Q_{max}}$

where Q_{max} is the value of Q at the scattering maximum, which is determined from the Lorentz corrected data. It also must be noted that the long period consists of the crystal thickness, interfacial thickness and any amorphous material separating the domains; i.e., it is the repeat distance between identical points in the long period, as shown in Figure 3.7. The interfacial thickness is not shown in this figure, it is simply the two phase model.

Stacked lamellae structures produce electron density fluctuations due to the various packing densities of molecules in polymers, meaning the amorphous, crystalline and interfacial regions. The density fluctuations produce x-ray scattering at small angles and allow the measurement of the long period or spacing[188-191]. The long period relates the center-to-center distance of the stacked lamellae averaged over the entire irradiated volume of the sample. The long period will have a maximum where the population of spacings of a given distance occurs most often. This is called the scattering maximum. The scattering maximum is then converted from three dimensional to one dimensional space by using a
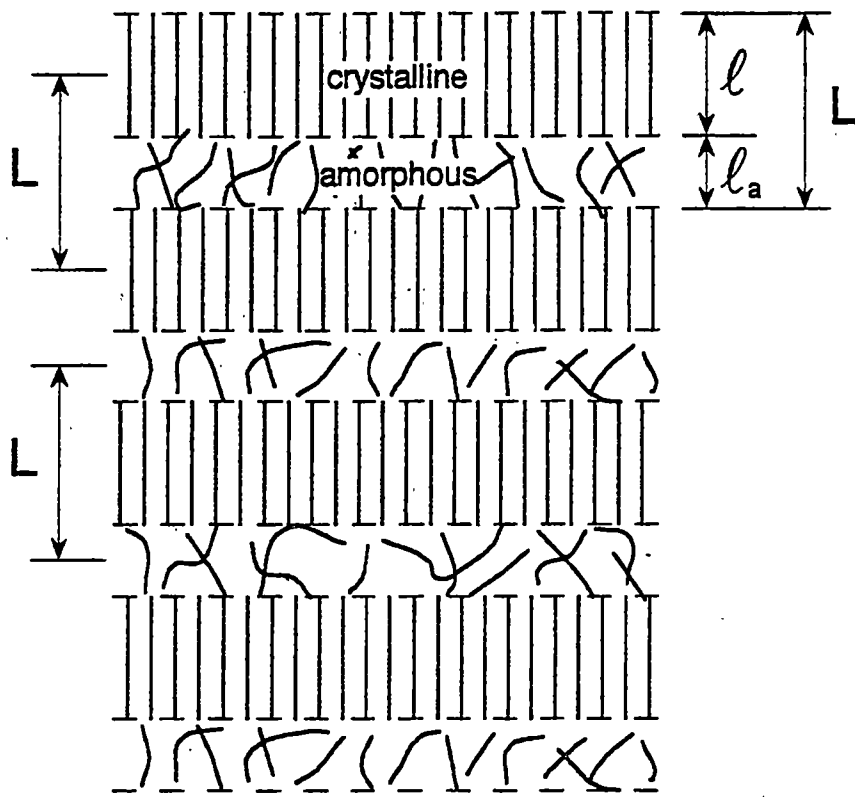
Figure 3.7 Crystalline and amorphous repeat domains in a two-phase stacked lamellae structure[210].

method developed by Lorentz, called the Lorentz correction. This is done by taking the raw data, typically the Intensity (I) and distance function (Q), and plotting Q^2I vs Q. The peak is then the scattering maximum (Q_{max}).

In this study, it was of interest to determine a qualitative value for the interfacial thickness. The interfacial region in a polymer system composed of crystalline lamellae and amorphous domains would be the interface between the two phases, in essence it is a third phase located between the lamellae and the truly amorphous regions. This region is important because it is where the fold surface free energy determined from the Gibbs-Thomson equation and secondary nucleation analysis is located.

The method used to estimate the interfacial thickness in this study was put forward by Ruland; it is a modified version of Porod's law[236,237]. It should also be stated that another method for determining the interfacial thickness is by use of a correlation function[238-240]. However, the modified Porod's law has been recommended for use in polymers[239]. SAXS raw intensity (I_{raw}) data must be corrected for thermal density fluctuation to give a corrected absolute intensity (I_{corr}). Ruland's expression for correcting the intensity is:

(3.5b) $$I_{corr}(q) = C(q) \cdot \exp(b \cdot q^2)$$

where C(q) is the thermal density fluctuation constant and b is the slope of the line on a log-log plot of equation 3.5b. The tail region of the log-log plot is linear curve fit to obtain C(q). This value is then subtracted from I_{raw} to give I_{corr}.

The transition layer thickness (E) can then be determined in a qualitative manner (the treatment is more rigorous for an absolute determination) by plotting $I_{corr}q^4$ versus q^2, which uses the assumption of a sigmodal electron density gradient across the boundary. The tail region again is then linear curve fitted to determine the slope and intercept of the line and used in the following equation to calculate E:

ORNL - DWG 89 - 6368
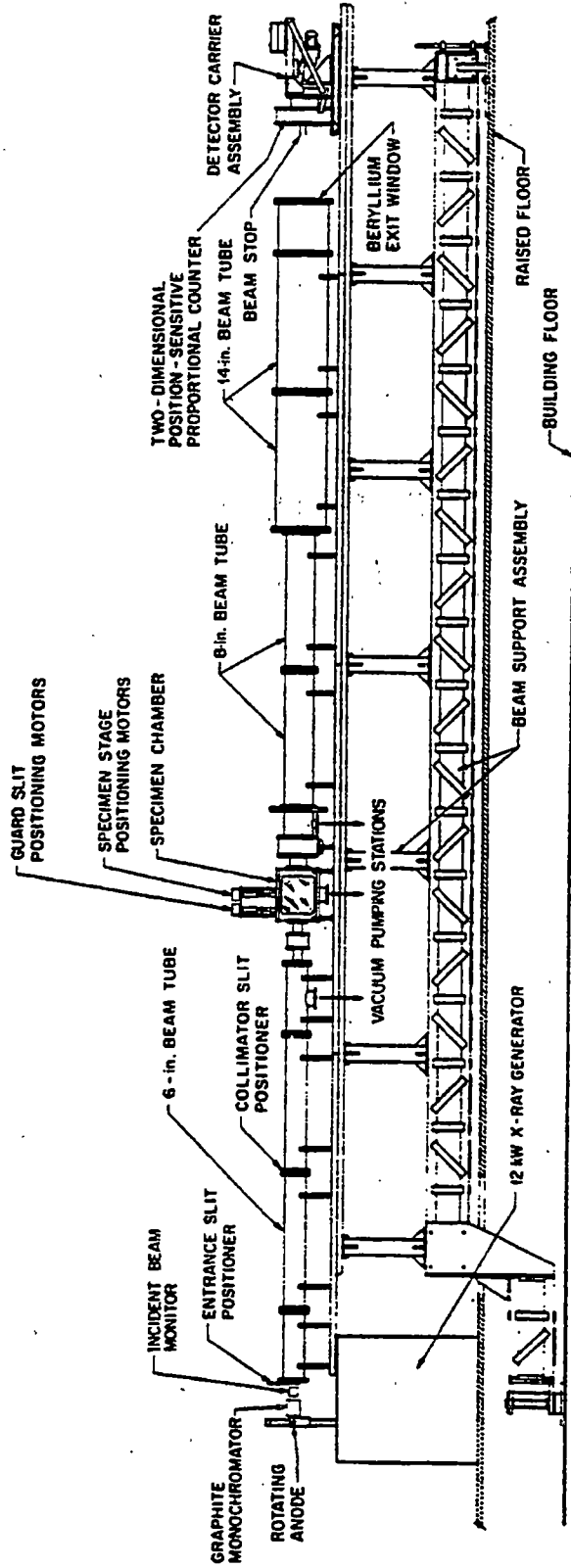
THE ORNL 10-m SAXS CAMERA

Figure 3.8 ORNL SAXS camera set-up.

128

$$(3.5c) \qquad E = \sqrt{\frac{-SLOPE}{INTERCEPT}}$$

The range of applicability for this version of Porod's law is for all interfacial thickness values. However, this method introduces a 5% error in the estimate of E. Note: This method was used since the I vs Q data was obtained from 5m. If data had been obtained from 1m (meaning larger Q values), a correlation function could have been used to determine the long period and interfacial thickness. However, a previous researcher using a similar homogenous and heterogeneous polyethylene samples with different branch contents found that the relative differences were accurate using the method described above[248].

3.3.2.2 Experimental Procedure

The SAXS work was carried out at Oak Ridge National Laboratory's 10m SAXS instrument using a source to sample distance of 3m and sample to detector distance of 5m; the x-ray generator was operated at 100mA and 40kV using CuK_{α} radiation (0.1542nm).

A schematic of the ORNL SAXS system is shown in Figure 3.8. A 20cm x20cm two-dimensional position-sensitive detector was used with each virtual cell element 3mm apart. The scattering intensity was stored in a 64x64 data array. Corrections were made for instrumental background, dark current due to cosmic radiation and electronic noise, and detector non-uniformity and efficiency (via an Fe^{55} radioactive standard which emits γ-rays isotropically) on a cell-by-cell basis. The data were radially averaged and converted to an absolute differential scattering cross section by means of pre-calibrated secondary standards. The Lorentz correction method was used to change the raw data from 3-d to 1-d for long period interpretation.

The intensity data was corrected by subtracting the background and dark current, which are collected in separate runs. The net corrected scattering intensity (I_{corr}) is defined as:

$$(3.6) \quad I_{corr} = \frac{1000}{d Mon_s T_{m,s} s_{i,j} F_{abs}} \left[\left(I_s - \frac{t_s}{t_{DC}} I_{DC} \right) - \frac{T_{m,s}}{T_{m,MT}} \left(\frac{Mon_s}{Mon_{MT}} I_{MT} - \frac{t_s}{t_{MT}} I_{DC} \right) \right]$$

where Mon is the monitor counts of the scattering measurement (s for sample, DC for dark current and MT for empty chamber for all the subscripts), I is the scattering intensity, t is time of sample run, T is the transmission coefficient, d is the sample thickness, $s_{i,j}$ is the detector pixel sensitivity factor and F_{abs} is the absolute intensity conversion factor from derived standards. The sensitivity of the detector was determined by collecting data of a radioactive material, Fe^{55}. The sample transmission coefficient (T_m) was determined from a 40s collection of data with the sample, sample plus glassy carbon, empty beam and dark current. The sample transmission coefficient for each sample was calculated by :

$$(3.7) \quad T_m = \frac{\left(I_{gcs} - I_{DC} \right) - 0.686\left(I_s - I_{DC} \right)}{\left(I_{gc} - I_{DC} \right) - 0.686\left(I_{MT} - I_{DC} \right)}$$

where I is the intensity, gcs is glassy carbon plus sample, DC is dark current, s is the sample, gc is the glassy carbon and MT is the empty beam.

Each sample was mounted onto a sample wheel (shown in Figure 3.9) that allowed many samples to be run in succession. A typical run consisted of ten samples, plus an empty beam and dark current measurement for each set of samples run on a sample wheel.

3.4.0 DSC

DSC is the most common experimental method used in studying and characterizing polymeric materials, and for good reason. DSC is a relatively fast and simple method for determining a material's thermal properties. DSC was used to study the melting and crystallization temperatures of different samples and to obtain the heat of fusion.

Sample Wheel for ORNL SAXS Laboratory

0 . 14"

0 .75"

bore diameter = 0.563"

2.00"

0 .30"

1/8" slot

All centers
should be aligned

diameter 4 .50"
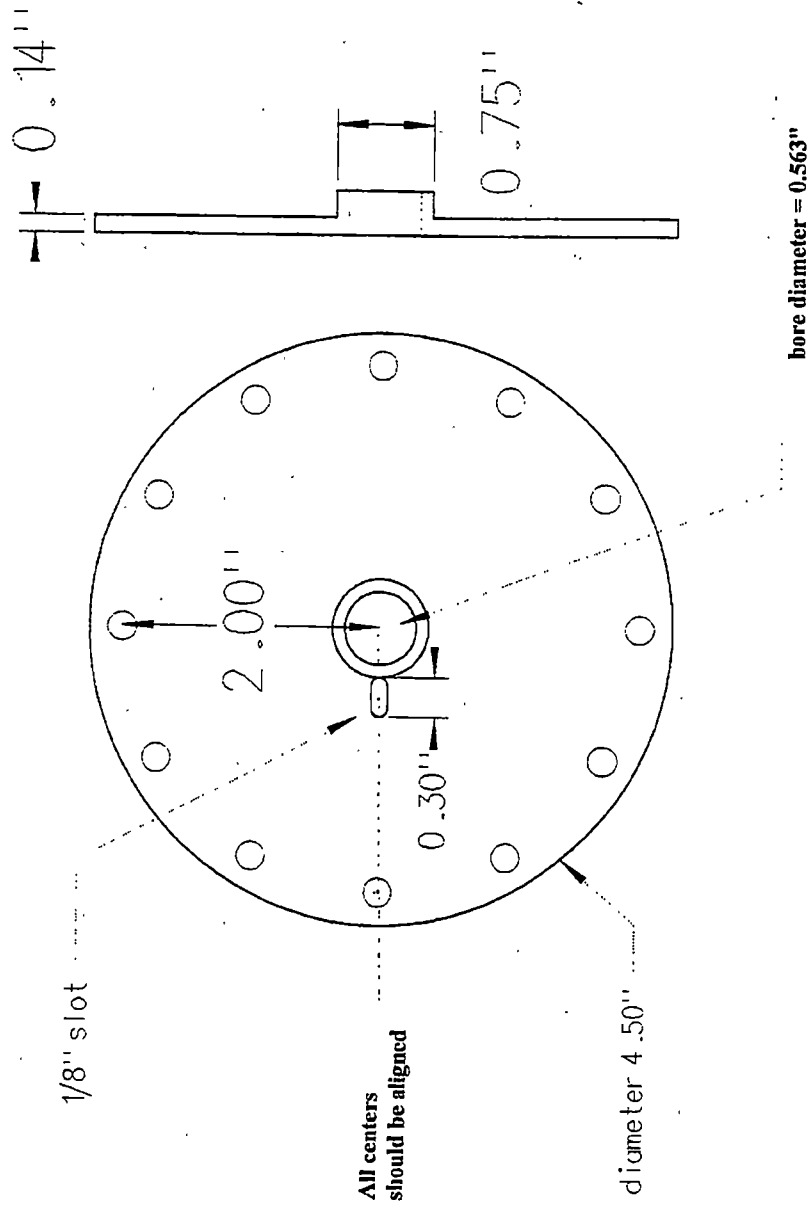
Figure 3.9 ORNL SAXS sample wheel.

131

3.4.1 Theory

A DSC typically consists of a sample and reference arrangement with the chambers made of a Pt/Rb alloy. Each chamber is a separate calorimeter and has a resistance heater and sensor for temperature measurement and control. Instead of relying on a heat reference from a single sample, governed by the temperature difference, reference and sample are heated separately as required by their temperature and temperature difference. The losses from the two calorimeters are equalized as much as possible, and residual differences between the two calorimeters are eliminated through calibration. In reality, this type of calorimeter operates by a difference potential generated by the presence of a sample. The temperature difference is proportional to the differential power applied and gives information on the difference in heat input per second into each calorimeter. The heat input difference is then displayed and used for any sample characterization (i.e. glass transition, heat of fusion, etc.).

3.4.2 Experimental Procedure

DSC scans were carried out using a Perkin-Elmer DSC-7 calibrated with indium standard every 5 hours. The thermal cycle is heating and cooling rates of 20°C/min, with a cycle temperature from 0-230°C and a hold time of five minutes at 230°C. For isothermal crystallization studies, the sample is cooled from 230°C to the desired temperature at 100°C/min. The sample was then heated at 20°C/min from the isothermal crystallization temperature until fully melted.

The heat of fusion(ΔH_f) used in crystallinity calculations is 167J/g for the α-monoclinic crystal structure and 150J/g for the γ-orthorhombic for 100% crystalline samples[97]. The percent crystallinity can then be calculated:

$$(3.8) \qquad X_c = \frac{\Delta H_f}{\Delta H_{fc}} x100$$

where ΔH_f is the heat of fusion of the sample, ΔH_{fc} is the heat of fusion of a 100% crystalline sample.

3.5 Optical Microscopy

An Olympus microscope was used to study linear growth and nucleation rates, as well as, for the high cooling rate light depolarizing microscopy (HCR-LDM) investigation. The samples were typically monitored between crossed polars during the crystallization process. For the linear growth rate and nucleation density measurements, a $1/4\lambda$ waveplate was often used to follow the crystallization process.

3.5.1 Optical Nucleation Study

A microscope stage was used to mount a Mettler hot stage. The microscope and hot stage were then used to perform optical nucleation and linear growth rate measurements. The crystallizing sample was viewed through the eye pieces, while the sample was also recorded for further study using a 35mm film or recording the image using a video camera and VCR. Obviously, for any type of accurate growth and nucleation measurement, the various lens/objective/camera combinations must be calibrated to make absolute length measurements. The calibration was performed using a calibrated microscope slide placed under the microscope using conditions under which the sample was studied.

3.5.2 High Cooling Rate Light Depolarizing Microscopy (LDM-HCR)
3.5.2.1 Theory

Ding and Spruiell[192-194] developed a method to study quiescent non-isothermal kinetics of polymer at very high cooling rates. The technique utilizes a polymer film with a

133

thermocouple embedded. The film is then subjected to a flow of hot air to melt the sample and erase the thermal history. The sample is then cooled by blowing constant temperature nitrogen over the sample. The cooling rate is changed by the volume of air moving across the sample. The technique has been reviewed extensively[192-196].

The main assumption for this technique is to have a uniform temperature distribution across the thickness of the film. A uniform temperature distribution is obtained by balancing sample thickness with the cooling rate. In order to quantitatively analyze the temperature behavior of the system, a heat transfer analysis was performed. The heat transfer equation is:

$$(3.9) \qquad V\frac{\rho C_p dT}{dt} = -AH_{ga}(T - T_s)$$

where ρ is the density, C_p is the specific heat, V the volume of the specimen, A is the area of heat transfer, H_{ga} is the overall heat transfer coefficient and T_s is the temperature of the cooling medium. H_{ga} is defined as:

$$(3.10) \qquad \frac{1}{H_{ga}} = \frac{l_g}{k_g} + \frac{l_a}{k_a}$$

where k_g and l_g are the thermal conductivity and thickness of the cover glass (respectively), while k_a and l_a are the thermal conductivity of air and the thickness of the air boundary. By assuming that k_g, k_a, ρ, and C_p are constant in the cooling process prior to crystallization, equation 3.9 can be solved to give:

$$(3.11) \qquad T - T_s = (T_o - T_s)\exp\left[-t\left(\frac{AH_{ga}}{V\rho C_p}\right)\right]$$

where the term in (brackets) is defined as the cooling rate factor (CRF) and T_o is the initial temperature of the sample.

$$(3.12) \qquad CRF = \left(\frac{AH_{ga}}{V\rho C_p}\right)$$

During HCR-LDM crystallization, significant light scattering occurs from the large number of nuclei that form. To correct for this problem, the measurement of light intensity with and without analyzer are used. The analyzer contains a polarizer so that the total light intensity can be recorded (without analyzer) and light under cross polars (with analyzer) can be recorded.

Under quiescent crystallization conditions, the light intensity transmitted through crossed polars is proportional to the absolute crystallinity (X_t) at any time (t), sample thickness (l) and intensity of incident light (I_o). The intensity of the transmitted light (I) can be expressed as:

$$(3.13) \qquad I = C_1 I_o l X_t + I_z$$

where C_1 is a proportionality constant related to the optical properties and geometry of the sample, I_z is the small amount of light that leaks through the cross polars in the absence of a sample. I_z can be expressed as:

$$(3.14) \qquad I_z = R_o I_o + C_2$$

where C_2 is a polymer related constant that is determined experimentally. Substituting equation 3.14 into equation 3.13 gives:

$$(3.15) \qquad R = C_1 l X_t + R_0$$

where R is the relative light intensity and R_0 is the light intensity at zero crystallinity (i.e. in the melt for a crystallizable polymer). At time $t=\ddot{I}$, the absolute crystallinity is denoted as $X_{\ddot{I}}$ and the relative light intensity as $R_{\ddot{I}}$. Therefore, equation 3.15 can be expressed as:

$$(3.16) \qquad \theta(t) = \frac{X_t}{X_\infty} = \frac{R - R_o}{R_\infty - R_o}$$

This relation provides the relative crystallinity, $\theta(t)$, needed for the measurement of the bulk crystallization kinetics.

The power in this technique arises from the ability of determining the bulk crystallization kinetic component of a crystallizing polymer, while simultaneously knowing the temperature at that given instant, not simply the time frame over which the crystallization occurred. A thermocouple is embedded into the sample in the region where the light intensity data is collected. Therefore, the ability to track the behavior of the polymer as a function of cooling rate is allowed.

Studies from this system[192,194-196] have shown that induction time and plateau crystallization temperature can be determined from this work. It is also possible to collect growth and nucleation rate data by optically recording the process with the microscope. The limitation of the cooling rate range is determined by the mass of the sample and the size of the thermocouple. Thinner samples can be cooled more rapidly while still maintaining an approximately uniform temperature distribution across the sample. For growth rate measurements at high cooling rates, the cooling rate may also be limited by the speed of the recording media.

3.5.2.2   Experimental Procedure

A schematic diagram of the HCR-LDM set-up is shown in Figure 3.10. The set-up consists of an Olympus BH2 optical microscope, IBM PC, a very low noise light source, a cooling unit, heating unit, sample chamber, gas controller board and electronics gear to amplify and relay the light intensity and temperature data to the computer. The sample chamber is placed on the microscope stage and the heating and cooling lines are attached.

The gas control board allows the volume of N_2 to be controlled, upon both heating and cooling. The sample is melted by controlling the temperature of the N_2 that passes over the sample. The temperature of the sample is monitored using the computer. Once the sample is melted to erase its thermal history, the heated N_2 can be turned off and cool N_2 channeled to the sample chamber. There is some amount of control of the volume of N_2
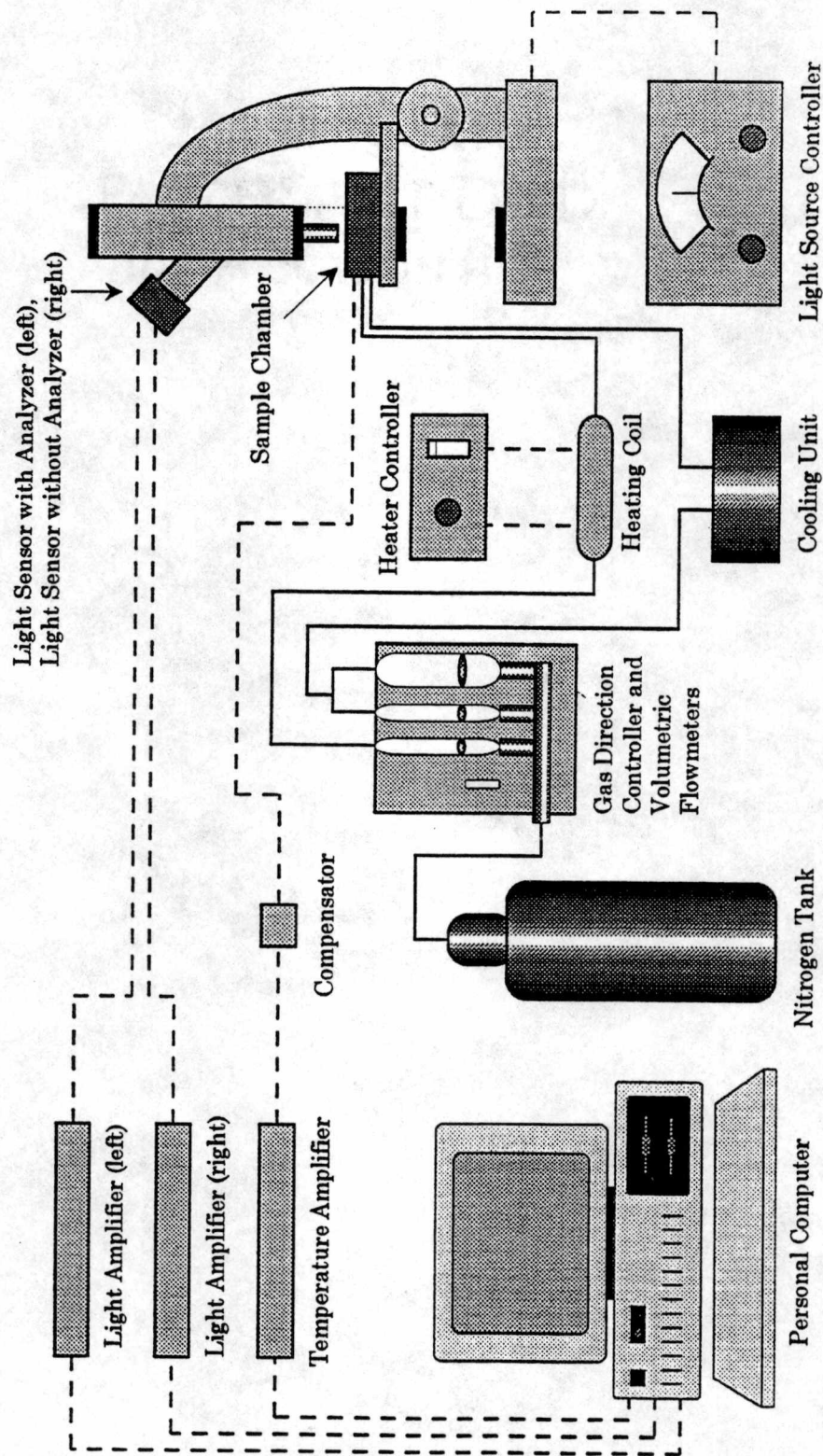
Figure 3.10 Schematic of HCR-LDM system.

Light Sensor with Analyzer (left),
Light Sensor without Analyzer (right)

Sample Chamber

Light Source Controller

Heater Controller

Heating Coil

Cooling Unit

Gas Direction
Controller and
Volumetric
Flowmeters

Compensator

Nitrogen Tank

Light Amplifier (left)

Light Amplifier (right)

Temperature Amplifier

Personal Computer

137

passing through the gas control board, although exact reproducibility is not possible. The light intensity and temperature profiles can be recorded as the sample cools and crystallizes.

Experimental determination of constants and system calibration instructions can be found elsewhere[192-194].

3.6 Melt Fiber Spinning

3.6.1 Melt Spinning Equipment

The melt spinning machine used in this study was designed by Fourne Associates of Germany. The Fourne extruder had a single screw 300mm long by 13mm in diameter. The polymer is fed to the extruder in the form of pellets from a seven liter nitrogen purged hopper. The extruder is heated by two band heaters along the extruder barrel. Molten polymer is then delivered at pressure (1-3000psi) to a Zenith constant volume displacement gear pump (spin pump). The spin pump and extruder pressure control the volumetric flow rate of the polymer. The polymer is then fed to the spinneret, which can consist of one or more holes. The spin pump and spinneret are heated by two large band type heaters similar to the extruder heaters. The extruder and spin block are mounted on a head that can move up and down vertically, to control the length of the spinline. The filament exiting the die can be drawn by either a winder or airjet drawdown device with air pressure.

In this study, a single hole die was used. The die is 0.762mm in diameter with an L/D ratio of 5.0. The mtp in the present study was kept constant at approximately 1.52±0.05g/min.

3.6.2 On-Line Measurements

3.6.2.1 Diameter

The on-line diameter measurements were done using a Zimmer diameter monitor (model 460A/2) and Digital Display Controller (model 466/2) from Zimmer OHG,

138

Germany. The Zimmer works on a non-contact electro-optic principle, which allows measurement of opaque and semi-transparent materials. The Zimmer can accurately measure diameters from 0-2mm with a resolution of 0.5μm and is calibrated using standard wire diameters. The system is mounted on a movable platform that allows data collection at various heights along the spinline.

The Zimmer is connected to an IBM PC that directly collects the data. The data is then transferred to another IBM PC for diameter calculation using a program in Quick Basic that allows for accurate analytical analysis of fiber diameters, including a correction for fiber transparency. At least five measurements were made for each spinning condition with 2000 data points collected for each sample.

3.6.2.2 Birefringence

On-Line birefringence measurements were made using an Olympus polarizing microscope (model 206080). This is the same microscope used in off-line measurements. A six-order compensator was used for retardation measurements. The same stand on which the Zimmer is mounted contains space for the microscope. The only change from off-line measurements is the addition of a V-grooved guide that stabilizes the filament during measurement. The experimental set-up is shown in Figure 3.11.

3.6.2.3 Filament Tension

The tension was measured using a Rothchild Tensiometer (model INTEG R-1198) as a function of fiber diameter and air pressure. The tension was measured at the bottom of the spinline near the draw down device (within 10cm). The Tensiometer was calibrated off-line using fibers of known diameter with calibrated weights attached.

3.6.3 Off-Line Fiber Characterization

139
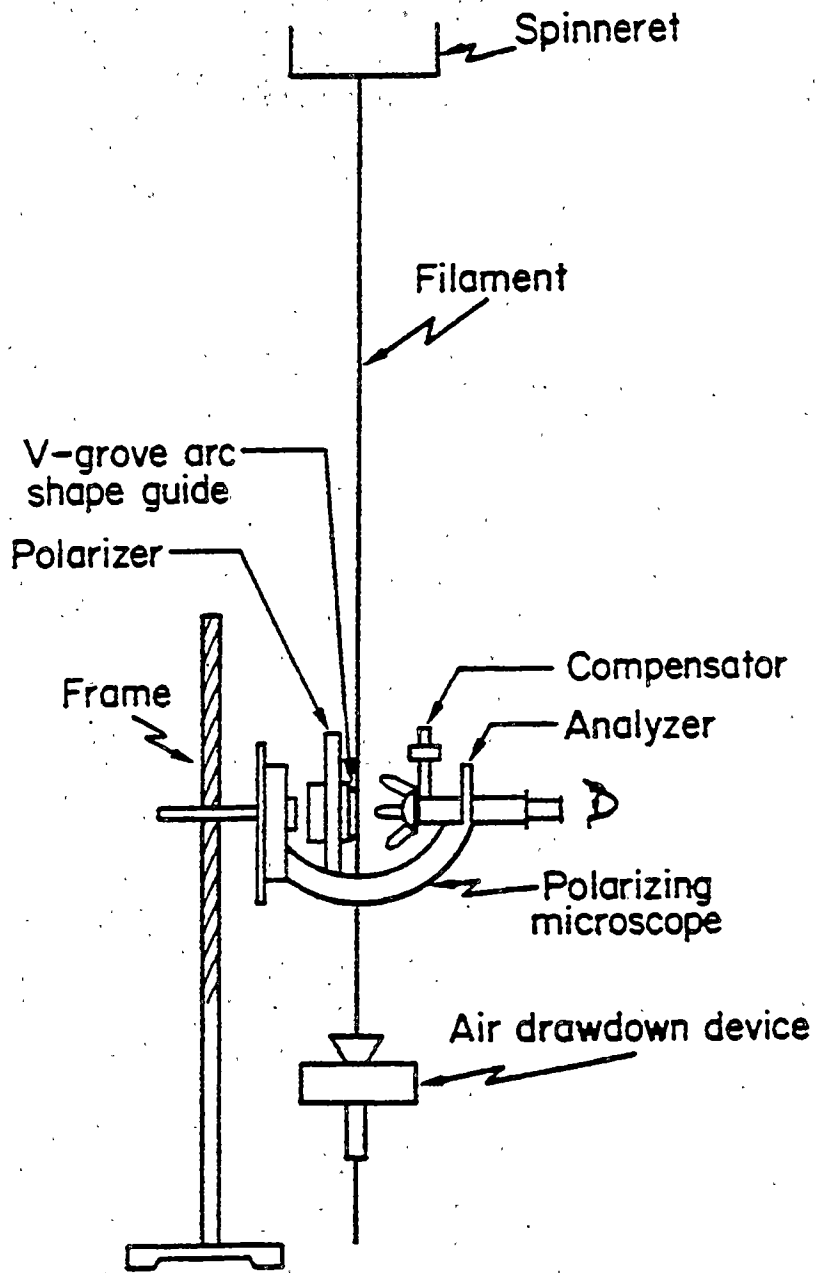
Figure 3.11 On-Line birefringence set-up[155].

140

The melt spun fibers were characterized by determining their density, birefringence, mechanical properties, crystalline orientation and morphlogy and sonic velocity.

3.6.3.1 Density

The density of iPP simply reflects the crystallinity of a sample. Although, molecular orientation of non-crystalline molecules can add some error in density crystallinity measurements, it is the best way to ascertain a fibers crystallinity. Percent crystallinity can be calculated from density according to[181-182,197]:

$$(3.17) \qquad v_c = \frac{\rho - \rho_a}{\rho_c - \rho_a}$$

where v is the volume crystallinity, ρ is the sample density, ρ_a is the density of amorphous material and ρ_c is the density of the unit cell. For iPP[6,10-11,17], ρ_a is 0.85g/cm^3 and ρ_c is 0.936g/cm^3.

The density of the fibers was determined using a density gradient column made of isopropanol and ethylene glycol. The column was calibrated using DGC beads that have a known density. The density range of the columns in this work ranged from 0.870-0.920g/cm³.

3.6.3.2 Birefringence

The significance of birefringence and overall molecular orientation was discussed earlier. Birefringence is determined by measuring a sample's retardation and dividing by the sample's thickness (in the case of fibers, fiber diameter).

Retardation involves measuring the phase difference between two mutually perpendicular, plane polarized waves emerging from a sample. The phase difference was measured using an Olympus microscope with a six order compensator. The diameter was then measured on the same sample in the same region where the orientation measurement

was made. Once the retardation was computed, it was divided by sample thickness to determine the sample's birefringence.

The birefringence measurements are related to the crystalline and non-crystalline orientation functions by:

(3.18) $$\Delta n = \beta \Delta_c^o f_c + (1 - \beta) \Delta_{nc}^o f_{nc}$$

where Δ_c^o is the intrinsic crystalline birefringence (for iPP Δ_c^o=0.0291) and Δ_{nc}^o is the intrinsic non-crystalline birefringence (for iPP Δ_{nc}^o=0.0600) [201-203]. This was discussed in section 2.5.1.4.

Ten measurements were made on each set of fibers. The reported values are the average of these ten measurements.

3.6.3.3 Mechanical Properties

3.6.3.3.1 Theory

When a polymer is deformed above its glass transition temperature, the samples morphlogy will determine its mechanical properties. Research has shown that preferential molecular orientation in the test direction has a substantial impact on the low strain rate tensile mechanical properties of a polymer, both modulus and tensile strength. Absent of any molecular orientation, the crystallinity and detailed morphlogy are the primary factors that determine the mechanical properties.

The deformation of a semi-crystalline polymer occurs in two basic steps under uniaxial extension. The crystalline regions begin to become oriented in the applied stress direction at small deformations, before orientation of the chain axis of the amorphous component. As extension continues, the amorphous component begins to orient in the applied stress direction. If the sample is highly crystalline, these transitions happens very rapidly and is accompanied by necking in the sample.

Stress (σ) is defined as the force per unit cross-sectional area of sample. Stress can be shown mathematically in two different ways, as engineering stress and true stress.

Engineering stress is defined as:

(3.19) $\qquad \sigma_e = F/A_o$

where σ_e is the engineering stress, F is the force and A_o = initial cross section area.

Engineering strain is defined as:

(3.20) $\qquad \gamma_e = \Delta L/L_o$

where γ_e is the engineering strain, ΔL is the change in length and L_o is the initial length.

Engineering values are determined from the initial cross sectional area and length. True stress and true strain are defined in terms of very small deformation increments that take place during the deformation process. Typically, the actual true stress must be calculated and requires more work than the engineering stress to calculate. The true stress is defined as:

(3.21) $\qquad \sigma_t = F/A$

where σ_t is the true stress and A is the actual cross section area of the sample.

The differential of true strain is defined as:

3.8 $\qquad d\gamma_t = \dfrac{dL}{L}$

where γ_t = true strain and L = actual length. Integrating from the initial sample length (L_o) to the final sample length (L), we obtain:

(3.23) $\qquad \gamma_t = \ln\left(L/L_o\right)$

143

At sufficiently small deformations, the deformation is recovered when the load is removed, i.e. the deformation is elastic. In this case, the relation between stress and strain is a linear one and is known as Hooke's law: $\sigma = E\gamma$, where σ is the stress, γ is the strain and E is the Young's elastic modulus. The slope of the stress-strain curve in this initial section is equal to E.

The important material properties determined in this study were the Young's modulus, elongation-to-break (ETB) and ultimate tensile strength (UTS). ETB is simply $\Delta L/L$ at the time of sample fracture or failure and UTS is the maximum load divided by the initial cross-sectional area of the sample.

3.6.3.3.2 Experimental Procedure

A table model Instron tensile testing machine was used to determine the tensile properties of the as-spun fibers. At least ten fibers for each set were tested. The sample gauge length was 25mm with an extension rate of 50mm/min (200%/min). The data was recorded and averaged using the Instron software.

This testing procedure is in accordance with ASTM standard D3218-93.

3.6.3.4 Flat Plate X-Ray Patterns

The morphlogy and orientation of the fiber samples were studied using a flat plate x-ray film technique. The samples were prepared by aligning filaments parallel to one another on an Al frame. This sample was then exposed to a collimated beam of x-rays. The scattered x-rays then strike the film and allow qualitative orientation and crystal morphlogy determinations to be made.

The patterns were produced using a pin-hole technique with CuKα radiation at 35kV and 17mA settings. The sample chamber is not evacuated. Typical exposure time was four hours.

3.6.3.5 Sonic Modulus

3.6.3.5.1 Theory

When a polymeric material is oriented, deformation leads to a change in the crystalline and noncrystalline (sometimes referred to as amorphous) regions of the sample. In order to characterize the final morphlogy, the orientation of the crystalline and noncrystalline regions must be known. Crystalline orientation can be determined from WAXD measurements, utilizing Hermans[138] orientation functions. In principle, the diffuse halo produced by the scattering from the non-crystalline regions can yield the noncrystalline orientation function, but has proven elusive experimentally since the intensity distribution is not known to a high level of accuracy. One technique for estimating the level of non-crystalline orientation is to use sound waves.

Ward[198-199] initially examined sound propagation in uniaxially oriented fibers. Ward demonstrated the relationship between the sonic modulus (E), the intrinsic lateral (transverse) modulus of a perfectly oriented fiber (E_t^o), and the average angle (θ) between the direction of sound propagation and the symmetry axis is:

$$(3.24) \qquad \frac{1}{E} = \frac{1 - \overline{\cos^2 \theta}}{E_t^o}$$

Mosely[200] came to a similar conclusion using a single phase model.

Samuels[201] extended the sonic modulus equation to a two-phase system by use of a mixing equation involving bulk compressibilities. For a homogenous mixture, both the density and bulk compressibility are additive properties and the equation takes the form:

145
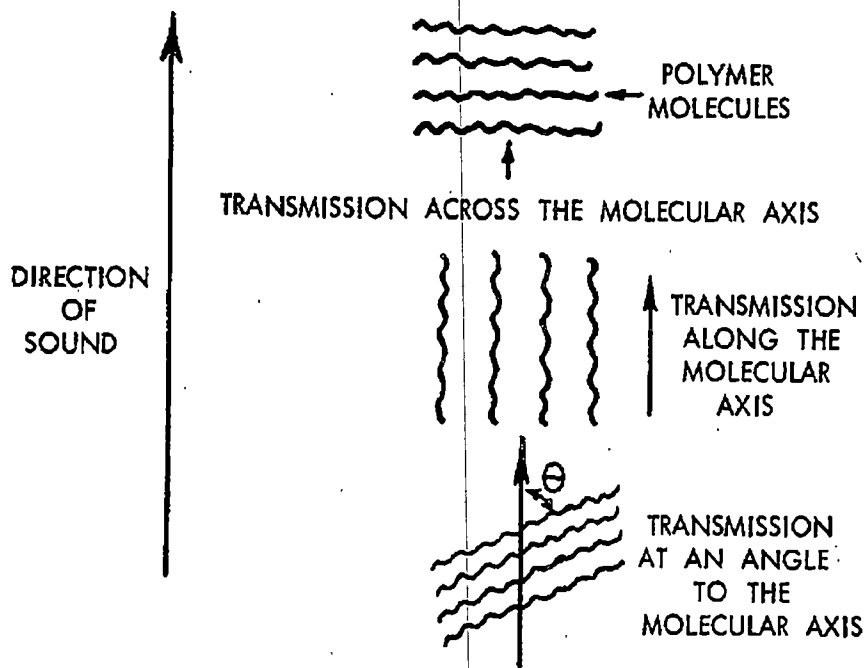
Figure 3.12 Molecular alignment of polymer molecules with sound propagation[213].

(3.25) $K = \beta K_c + (1-\beta)K_{am}$

where K is the bulk compressibility of the mixture (the subscripts c and am stand for crystalline and amorphous)and β is the fraction of crystalline material. The bulk compressibility (K) is related to the bulk modulus (B), Young's Modulus (E) and Poisson's ratio (υ) by:

(3.26) $K = \dfrac{1}{B} = \dfrac{3(1-2v)}{E}$

For iPP at room temperature, $\upsilon=0.33$. Further, for iPP[202]:

(3.27) $E = \rho C^2$

Thus for an oriented sample we obtain the following expression for the measured sonic modulus (E_{or}):

(3.28) $E_{or} = \left(\dfrac{\beta}{E_{t,c}^o}\right)\left(1 - \overline{\cos^2 \theta_c}\right) + \left(\dfrac{1-\beta}{E_{t,am}^o}\right)\left(1 - \overline{\cos^2 \theta_{am}}\right)$

for an unoriented sample $\overline{\cos^2 \theta} = 1/3$ and equation 3.28 reduces to:

(3.29) $\dfrac{3}{2E_u} = \dfrac{\beta}{E_{t,c}^o} + \dfrac{1-\beta}{E_{t,am}^o}$

where E_u is the measured sonic modulus of an unoriented sample. Combining equation 3.27 and 3.28 gives the expression for the sonic modulus of oriented iPP at room temperature:

(3.30) $\dfrac{3}{2}\left(\Delta E^{-1}\right) = \dfrac{\beta f_c}{E_{t,c}^o} + \dfrac{(1-\beta)f_{am}}{E_{t,am}^o}$

where $\left(\Delta E^{-1}\right) = \left(E_u^{-1} - E_{or}^{-1}\right)$. For iPP[201-203], $E_{t,c}^o=3.96\times10^{10}$dyne/cm^2 and $E_{t,am}^o=1.06\times10^{10}$dyne/cm^2.

3.6.3.5.2 Experimental Procedure

The sonic velocity of the fiber samples was determined using a KLH Series Four Pulse Propagation Meter. The sonic velocity reported is the average measurement made on five different samples. The experimental set-up consists of transmitter and receiver transducers that measure the velocity of sound propagation through the material, as illustrated in Figure 3.13. The density was determined using a density gradient column, as indicated in 3.6.3.1.

3.7 Thermal Spunbonding

As previously discussed, there are resin, fiber and process factors that effect fabric properties in the spunbonding process.

3.7.1 Resin Factors

Resins having different molecular weight and molecular weight distributions were studied. Resins M22, M32 and ZN35 (see section 3.8) were used to study the effects of resin characteristics on fiber structure development in the spunbonding process. These resins were used to produce fibers with differing properties under identical processing conditions, so that effects of fiber properties on the bonding process could be investigated. In effect, different resins were used to change the fiber properties since the range of processing variables is somewhat limited with the current spunbond line.

3.7.2 Fiber Properties

Extrusion temperature, mass-throughput, cooling air fan speeds and draw down air fan speeds were adjusted to make changes in the unbonded fiber properties. These fiber spinning process variables were utilized to produce fibers of different diameter, overall molecular orientation and crystallinity.
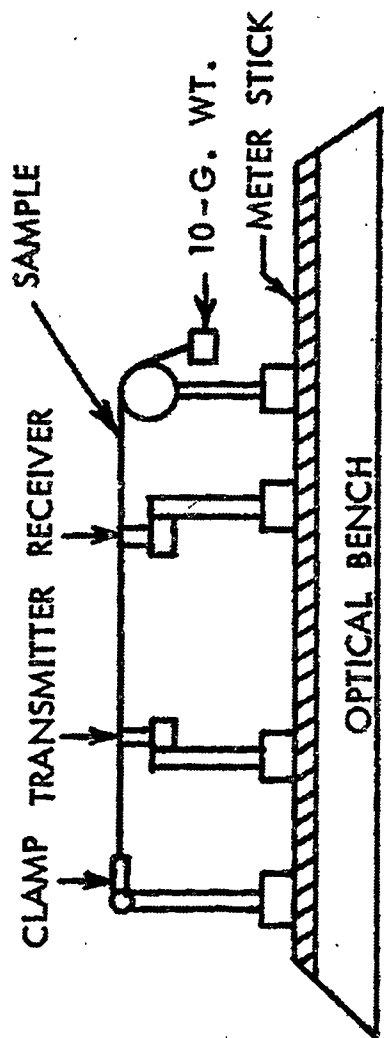
Figure 3.13 Schematic of Sonic velocity apparatus[213].

3.7.3 Bonding Process Conditions

Bonding temperature, bonding pressure, and line speed were the processing conditions changed to study the thermal point spunbonding process. The main emphasis was to evaluate the effects of changing process conditions on fabric mechanical properties as determined by fabric tensile strength and elongation-to-break.

3.7.4 Experimental Procedure

The fabric mechanical properties of interest are elongation-to-break and tensile strength in the machine direction and transverse directions. The testing procedure was in accordance with ASTM standard D1117-80. The sample gauge length is 5" and 1" wide with an extension rate is 5"/min. The results for strength are reported as load per unit width at a certain basis weight. The actual fabric thickness is not used in these measurements since it is difficult to measure. Therefore, the width is standardized and the strength of the fabric is reported for a given width and mass of fabric.

Basis weight is the mass of material per unit area and is determined using ASTM standard D3776-85.

3.8 Characterization of Materials

Seven isotactic polypropylene resins typically used in fiber spinning and two experimental resins were kindly supplied by Exxon Chemical Company. Six of the resins were prepared with a metallocene catalyst system and the other three by a Ziegler-Natta catalyst system. The zniPP resins are viscosity broken with peroxides to lower their average molecular weight and to narrow their molecular weight distribution. The two Ziegler-Natta resins differ substantially in their isotacticity as discussed below. The molecular weights were determined by gel permeation chromatography (GPC) and are

given in Table 3.1. The ZN35 resin has a higher polydispersity than the other resins, but is still quite narrow for a vis-broken zniPP.

Thermal Analysis

DSC scans were carried out using a Perkin-Elmer DSC-7 calibrated with indium standard every 5 hours. Unless stated otherwise, the thermal cycle was heating and cooling rates of 20°C/min, with a cycled temperature from 0-230°C and a hold time of five minutes at 230°C. The heat of fusion(ΔH_f) used in crystallinity calculations is 167J/g for the α-monoclinic crystal structure and 150J/g for the γ-orthorhombic for 100% crystalline samples[22-23]. The basic thermal properties for these resins are shown in Table 3.2. The measured melting temperatures of the metallocene catalyzed resins are approximately 13°C lower than the ZN35 resin and more than 16°C lower than the higher tacticity ZNHT resin. The crystallization temperatures for the miPP resins are about 2-3°C lower than for the ZN35 resin, but they are 14-15°C lower than the ZNHT resin.

The properties of the resins in this work, shown in Tables 3.1 and 3.2, point out some of the difficulties found in studying isotactic polypropylene. The thermal properties data show that the miPP resins have significantly lower melting temperatures than ZN35, while having only slightly lower crystallization temperatures. The difference in melting and crystallization temperatures is also similar when comparing the metallocene resins to the ZNHT resin. In previous research, these differences would be attributed to the resins having different isotacticities, as this has been the classic explanation for explaining differences in quiescent thermal properties[8].

Stereoregularity of the Resins

The stereoregularity of these samples was characterized using both xylene solubles and carbon-13 NMR. Percent xylene solubles was determined according to ASTM standard D5492-94. The carbon-13 data were obtained at 100Mhz at 125°C on a Varian VXR 400 NMR spectrometer. A 90° pulse, acquisition time of 3.0s and a pulse delay time

151

Table 3.1 Resin Molecular Weight Characteristics.

Sample Code	Catalyst	MFR*	Polydispersity	M_z(Daltons)	M_w(Daltons)	M_n(Daltons)
M10	Metallocene	10	2.65	454.7k	256.4k	96.8k
M22	Metallocene	22	2.25	324.9k	192.1k	85.4k
M32	Metallocene	32	2.28	287.4k	172.5k	75.6k
ZN35	Ziegler-Natta	35	3.29	427.9k	189.1k	57.5k
M45	Metallocene	45	2.83	271.3k	164.5k	58.2k
M70	Metallocene	70	2.53	250.0k	141.6k	55.9k
M100	Metallocene	100	2.27	219.0k	123.6k	54.5k
ZNHT	Ziegler-Natta	36	2.22	-	131.1k	59.0k
ZN-5RCP	Ziegler-Natta	31	2.26	-	150.1k	66.5k

*g/10min at 230°C

Table 3.2 Resin Thermal Property Characteristics.

Sample Code	Melting Temperature (°C)		Crystallization Temperature (°C)		Melting Enthalpy
	Peak	Onset	Peak	Onset	(J/g)
M10	149.0	140.8	104.1	109.1	80
M22	150.9	143.4	100.2	105.5	84
M32	150.6	143.2	100.2	105.7	84
ZN35	163.8	152.4	102.6	109.1	91
M45	151.7	144.0	105.4	110.8	87
M70	151.1	143.9	102.4	107.6	88
M100	147.1	140.1	103.6	108.4	81
ZNHT	167.7	160.1	115.0	120.8	98
ZN-5RCP	136.4	129.2	93.1	97.8	43

of 20s were used. A typical number of transients collected was 2500. The samples were dissolved in tetrachloroethane-d_2 at concentrations between 10 and 15%, by weight. Spectral frequencies were recorded with respect to 21.81ppm for mmmm, which has been determined with respect to internal reference tetramethylsilane and is close to the reported literature value of 21.855ppm. This part of the work was carried out by Dr. J. C. Randall at Exxon Chemical Company.

The stereoregularity data for these materials is shown in Table 3.3. The xylene solubles data show that the miPP resins and ZNHT have very little soluble material, while the ZN35 resin has a significant portion of material soluble in xylene. This is in agreement with the non-uniform defect distribution previously found in most zniPP resin research. It is also worth noting that M100 also had significantly more xylene solubles material than any other miPP resin. The cNMR data were obtained with the xylene soluble fraction removed, i.e. a purified polymer. This is particularly important for the ZN35 resin, since it contains a substantial atactic fraction. As discussed in the introduction, the xylene soluble material is composed primarily of atactic chains. The atactic chains have very short isotactic sequences that are not typically capable of crystallization, resulting from defects incorporated into the polymer chain during the polymerization process. The total [meso] diads for the first three materials are very similar, after the removal of the atactic component for each resin. The [meso] content of the ZNHT resin is substantially higher than that of the other homopolymer resins.

The average meso run length is determined by taking the inverse of the total number of defects per 10,000 monomer units.

The total number of defects per 10,000 propylene units is composed of regio (head-to-head and tail-to-tail) and stereo defects. Regio defects occur with metallocene catalysts and depend upon the π-ligands, polymerization temperature and monomer concentration; they are generally 2,1 addition type polymerization errors found in high activity catalysts[25-]

Table 3.3   Stereoregularity Characteristics of Resins.

Sample Code	%Xylene Solubles	%(w/w) Ethylene	[meso]	Meso Run Length (# of Monomers)	defects per 10,000 Units			
					regio	stereo	ethylene	total
M10	0.60	-	0.9781	60	91	76	-	167
M22	0.36	-	0.9776	68	43	103	-	146
M32	0.35	-	0.9752	64	44	113	-	157
ZN35	3.62	-	0.9774	102	0	80	-	80
M45	0.41	-	0.9756	67	42	107	-	149
M70	0.48	-	0.9766	63	38	121	-	159
M100	1.33	-	0.9738	52	88	104	-	192
ZNHT	0.30	-	0.9840	200	0	50	-	50
ZN-5RCP	6.72	5.91	0.9827	13*	0	83	680	763

- ignoring ethylene content would yeild an average MRL of 121

[26]. Regio defects are not typically found in Ziegler-Natta catalyzed materials as these defects terminate the polymerization process, i.e. it is a chain termination step[27]. Stereo defects occur when the cis enantioface changes to trans (propylene is chiral), which can occur at low temperatures or when the active site structure of the catalyst is compromised. Research has indicated that miPP resins are site controlled, therefore stereo errors during polymerization are corrected by the catalyst[25]. Conversely, zniPP resins are chain-end controlled, meaning the stereo error is propagated[26]. The chain-end control mechanism is thought to be responsible for producing the atactic material found in zniPP resins. As Table 3.3 indicates, the miPP resins have almost twice the number of total defects as the ZN35 resin after removal of the xylene soluble fraction. The ZNHT resin has even fewer defects than the ZN35 resin. The M32 resin has 11 more defects per 10,000 units than the M22 resin. If the xylene solubles material were included in these defect calculations, the total defects for the ZN35 resin would be much higher. However, since the atactic chains do not crystallize, they are removed and not considered part of the crystallizable material. On this basis, the average meso run length is slightly longer for ZN35 than for the miPP resins, as it has fewer defects in the crystallizable material. The meso run length for the ZNHT material is almost twice that of the ZN35 resin and approximately three times that of the miPP resins.

Infrared Spectrum

Raman infrared spectrum for M22 and ZN35 are shown in Figures 3.14 and 3.15. Virtually all the peaks are accounted for by crystalline and amorphous absorption assignments. There is not evidence of an ether and/or vinyl methyl ether due to oxygen degradation in any material. However, this can not be ruled out as some of these absorptions may be masked by the much stronger bond absorptions located near these spectral locations.
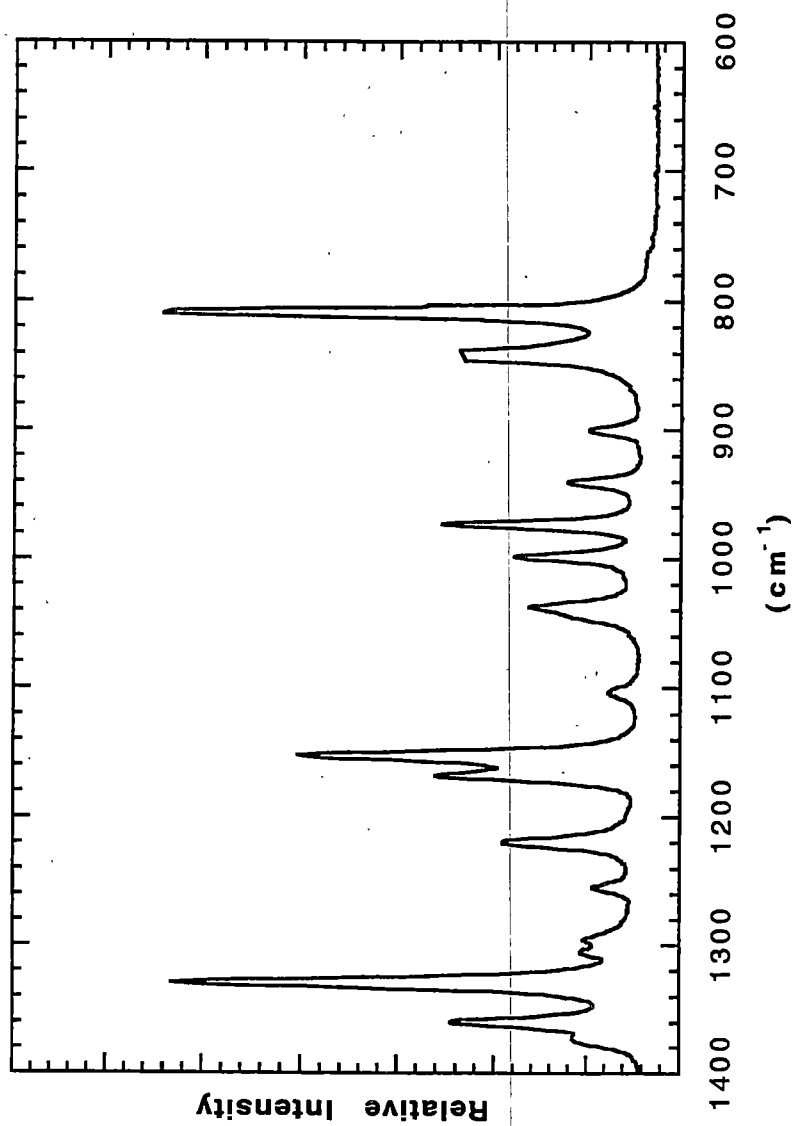
Figure 3.14 Raman infrared spectrum of M22 crystallized at a cooling rate of 0.5K/min.
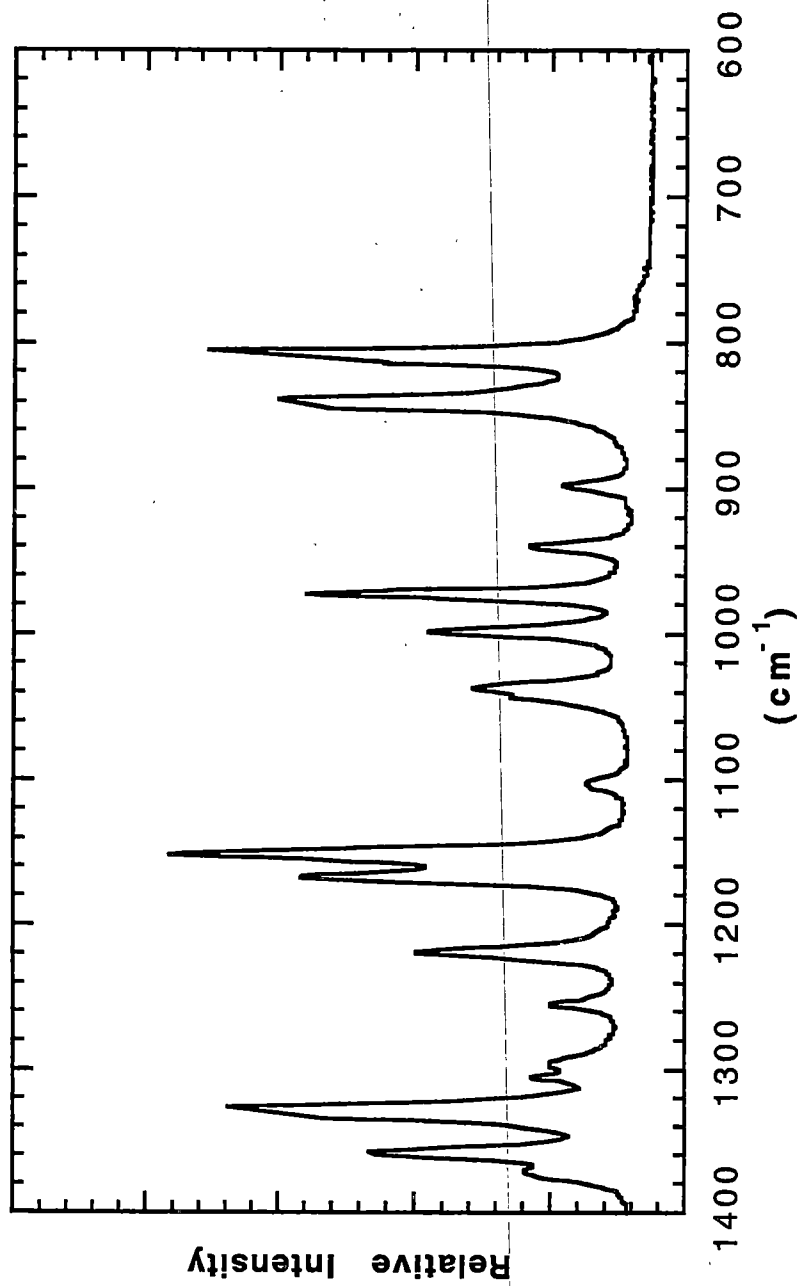
Figure 3.15 Raman infrared spectrum of ZN35 crystallized at a cooling rate of 0.5K/min.

Chapter 4

Results and Discussion of Quiescent Isothermal and Nonisothermal Crystallization Studies

4.0 Introduction

In this chapter the results of quiescent isothermal and nonisothermal studies performed on M10, M22, M32, ZN35, ZNHT and M100 will be presented and discussed. Films made from each resin were crystallized isothermally and nonisothermally and studied to determine each sample's morphology, thermal characteristics and crystallization kinetics. The morphology and properties after crystallization depend on thermal history and the detailed microstructure of the polymer molecules. Emphasis was placed on understanding and relating a particular resin's underlying chain microstructure to final sample properties and characteristics.

The morphology and melting behavior of isothermally crystallized samples using the various iPP resins will be discussed in section 4.1, while the crystallization kinetics during isothermal crystallization are presented in section 4.2. The morphology and melting behavior of nonisothermally crystallized samples using the high cooling rate light depolarizing microscopy (HCRLDM) technique are presented in section 4.3. The crystallization kinetic studies under nonisothermal conditions using HCRLDM are discussed in section 4.4. Studies involving crystallinity and interfacial thickness

measurements made from isothermally and nonisothermally crystallized samples will be presented in section 4.5.

4.1 Morphology and Melting Behavior of Isothermally Crystallized Resins

The morphlogy of films isothermally crystallized in a Mettler hot stage were investigated using WAXD and SAXS. The thermal properties of each sample were characterized using DSC. These results are combined in the present presentation to determine the equilibrium melting temperature and heats of fusion for each resin.

4.1.1 WAXD of iPP Resins

Isotactic polypropylene is known to crystallize in several different crystalline forms. Polypropylene can crystallize into an α-monoclinic, β-pseudohexagonal and γ-orthorhombic form. The most common form of iPP is the α-monoclinic, with β-pseudohexagonal and γ-orthorhombic formed under special conditions. The β-pseudohexagonal can be formed by using special nucleating agents or a temperature gradient crystallization method[46]. The γ-orthorhombic structure can be produced with zniPP resins at elevated pressures or utilizing low molecular weight iPP that has little or no chain folding[38]. The γ-structure has also been observed when PP is copolymerized with ethylene or butene[14,32,33]. Recently, it has been shown that metallocene catalyzed iPP homopolymers can produce the γ-orthorhombic structure at atmospheric pressures[21].

Each of the three crystal forms of iPP has a distinctive reflection in a WAXD scan. These peaks are found between 2θ values of 18-19° for the α-monoclinic structure, 16-17° for the β-pseudohexagonal structure and 19.2-20.5° for the γ-orthorhombic structure. The appearance of these characteristic peaks indicates the presence of that

particular structure. Samples used in x-ray analysis were isothermally crystallized into films. WAXD patterns for several samples used in this study for each resin are shown in Figures 4.1-4.6. The isothermal crystallization temperature is indicated near each WAXD scan.

The WAXD patterns for the miPP resins show the existence of both the α and γ crystal structures, with the γ intensity generally increasing as the isothermal crystallization temperature increases. For the miPP resins, as the total number of defects increases, the percent γ-iPP content also increases. Recall that total defects for these materials decreased in the order M100>M10>M32>M22>ZN35>ZNHT. (Note: The percent γ content for each material is shown in Figure 4.22 as a function of lamellae thickness.) Initially this was a quite surprising result, as the literature had only recently reported a non-copolymer iPP producing the γ structure[27] at atmospheric pressure. Studies by Turner-Jones[13,24,29] showed that the γ structure was produced when propylene is polymerized with ethylene and other copolymers. Additionally, Turner-Jones found that the slower the crystallization process, the greater the amount of γ-crystal structure is formed. More recently[31], work was done on highly isotactic propylene ethylene copolymers that indeed repeated the findings of Turner-Jones.

As the WAXD scans for the zniPP resins (ZN35 and ZNHT) show (Figures 4.4 and 4.5) a small amount of γ structure is also produced at higher isothermal crystallization temperatures in these resins. As there exist no regio defects in the zniPP resin, the appearance of the γ structure in the zniPP material suggests that it is not the type of stereochemical defect that induces the γ structure, but the presence of these defects and their distribution. This is in agreement with earlier speculation proclaiming
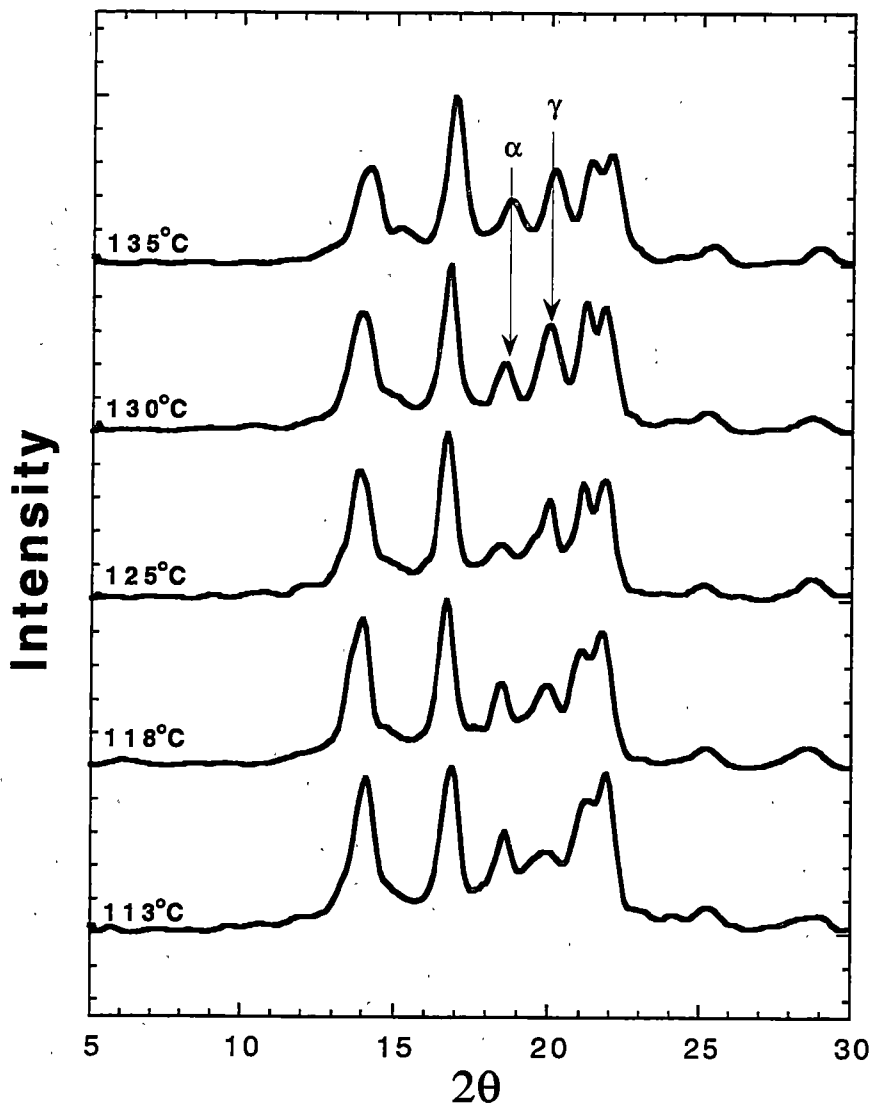
Figure 4.1 Isothermal WAXD of resin M10.
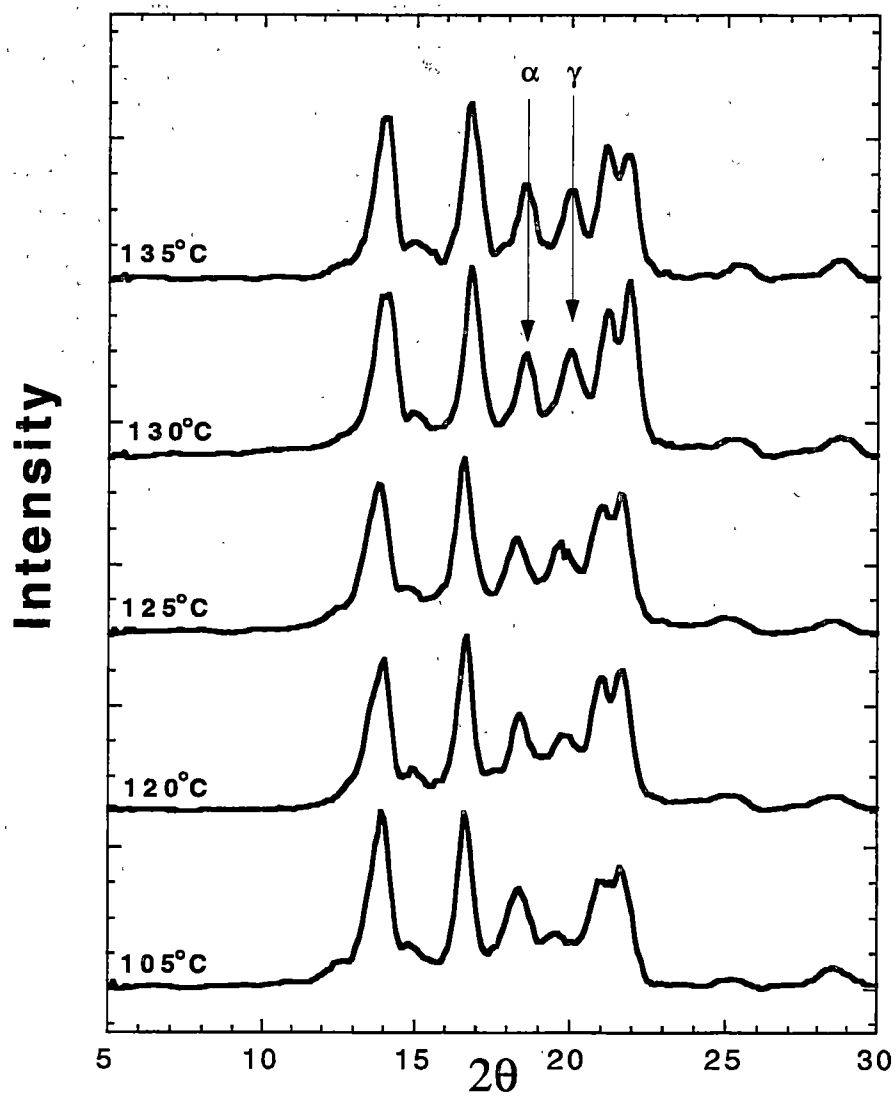
Figure 4.2   Isothermal WAXD of resin M22.
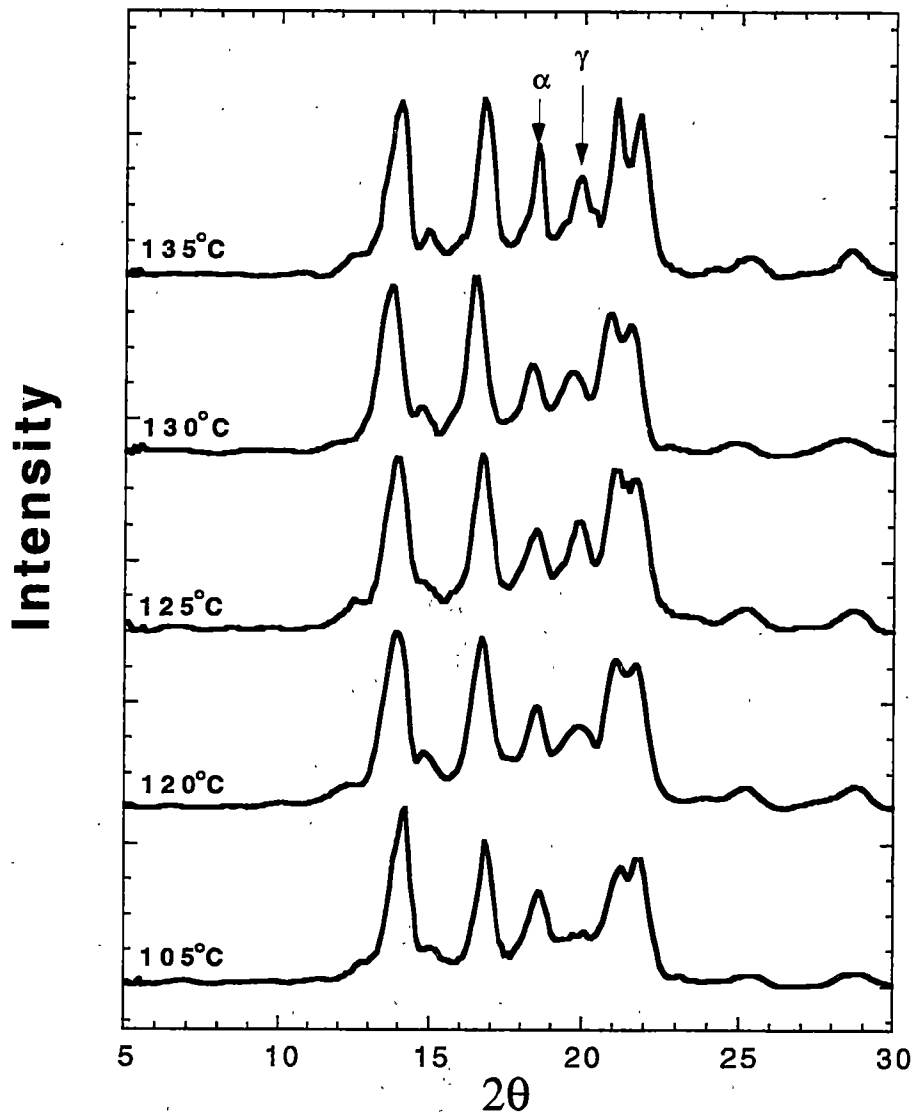
Figure 4.3 Isothermal WAXD of resin M32.

164
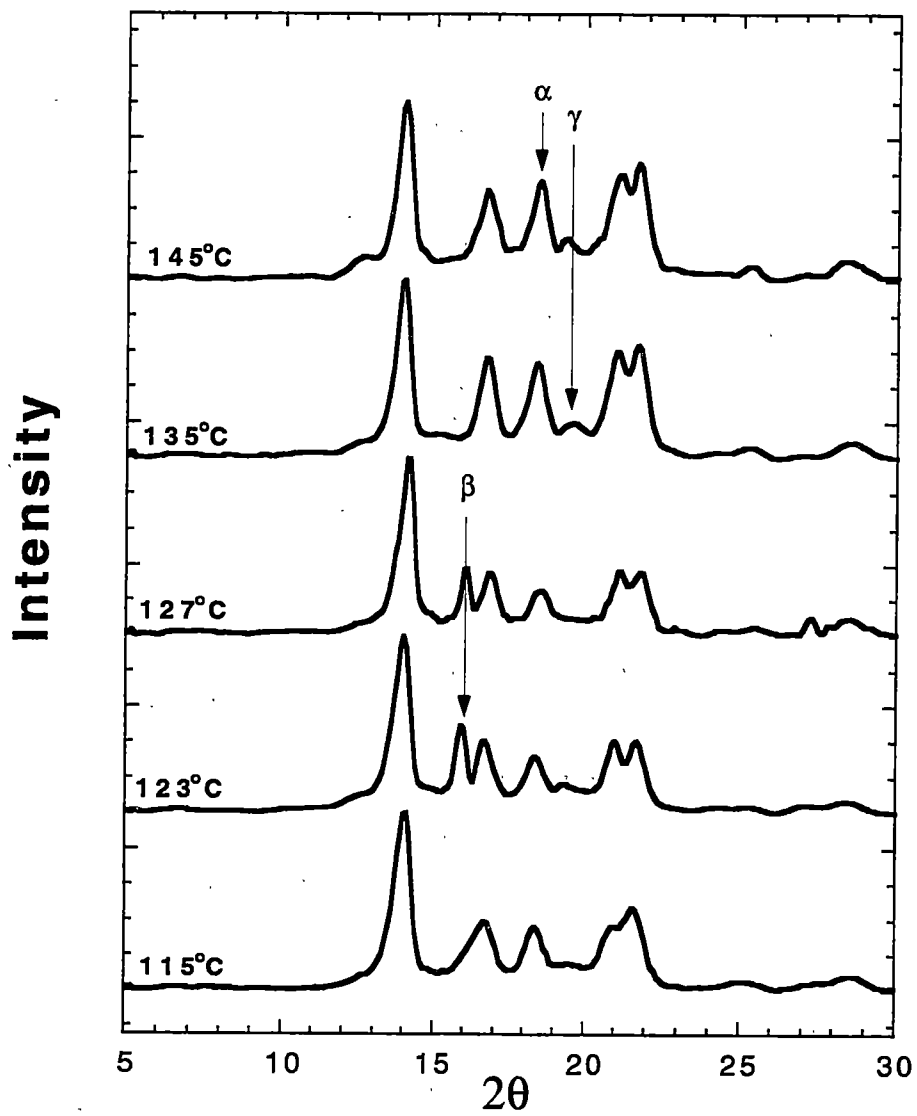
Figure 4.4   Isothermal WAXD of resin ZN35.
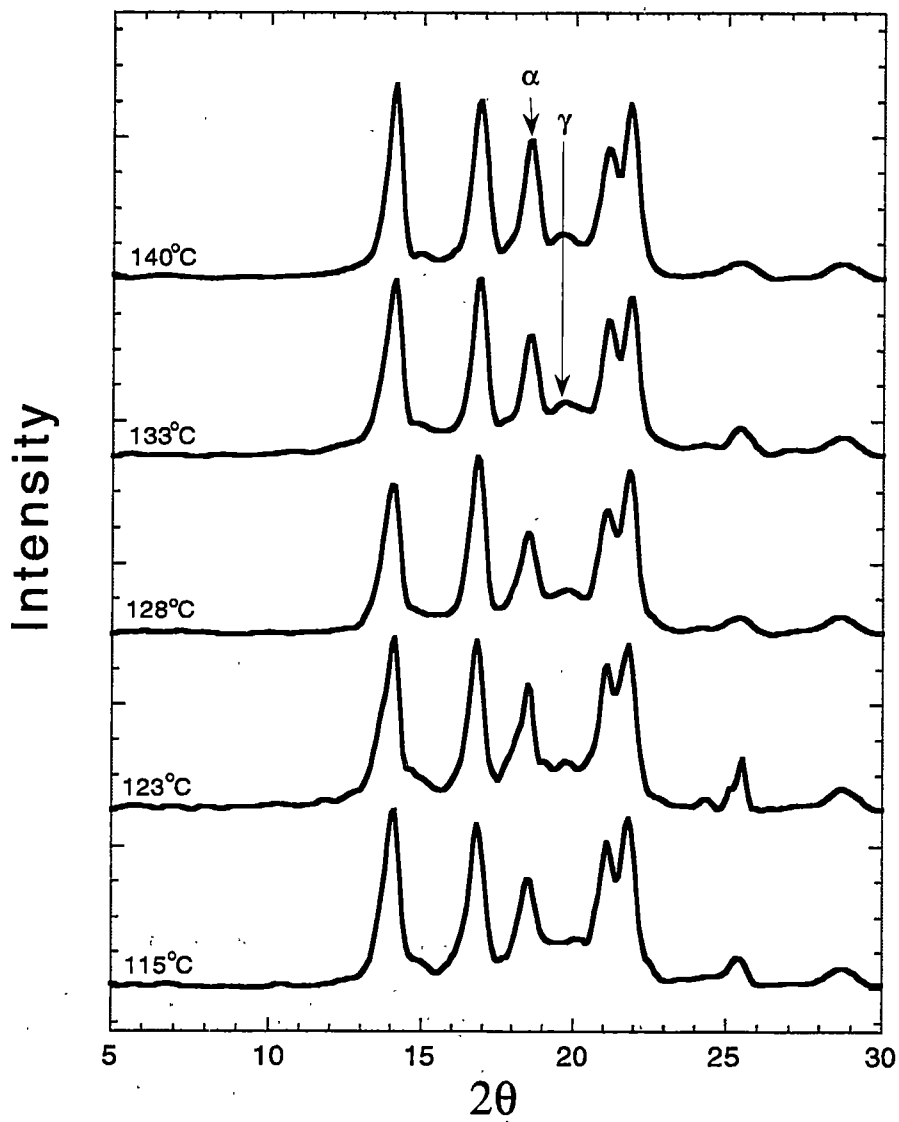
Figure 4.5   Isothermal WAXD of resin ZNHT.
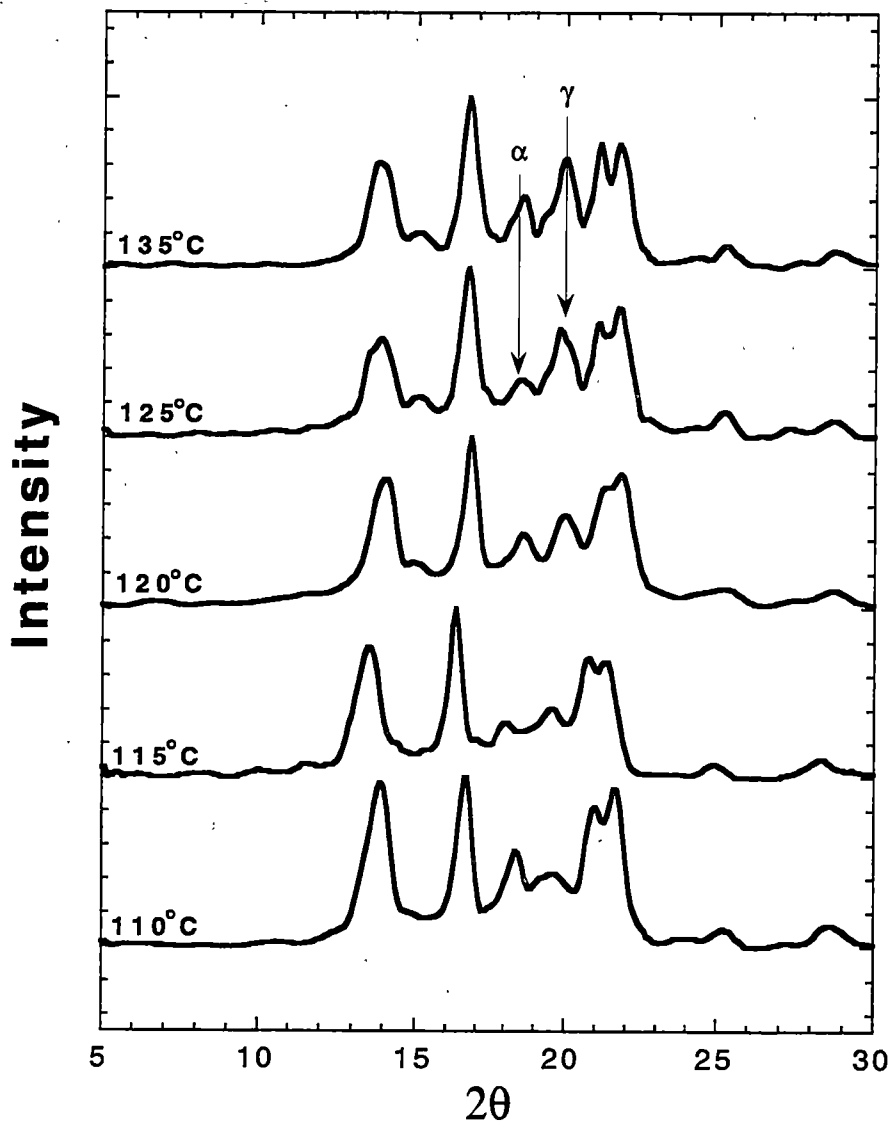
Figure 4.6   Isothermal WAXD of resin M100.

167

the nature of the defect being less important than the mere presence of the defect[13,24,29,31]. The possibility also exists that the γ-crystal structure is formed in the zniPP resins as a result of low molecular weight chains crystallizing. The low molecular weight chains are produced from the peroxide degradation process to narrow the molecular weight distribution of most zniPP resins. It should be noted that some β structure is formed in the ZN35 resin at some intermediate conditions.

4.1.2 Differential Scanning Calorimetry

The results in Figure 4.7, show heating curves for M22 crystallized in the DSC over a range of temperatures, from 120-125°C, as indicated in the figure. Notice in Figure 4.7 that at a crystallization temperature of 120°C there exists one peak with a rather broad low temperature shoulder. As the crystallization temperature is increased a broad, but definite, endotherm develops at a temperature in the neighborhood of 143°C.

In Figure 4.8, the crystallization temperature range has been expanded for M22. There exists no low temperature endotherm when the sample is crystallized non-isothermally at a cooling rate of 20°C/min. As the isothermal crystallization temperature increases from 110°C to 120°C, a shoulder and low temperature endotherm develops. The shoulder becomes a pronounced peak at 130°C. At 140°C, the low temperature endotherm has all but disappeared. This procedure was also conducted on the other miPP resins with similar results.

The low temperature endotherm in Figure 4.7 is indicated as being associated with the melting of the γ-phase and the higher temperature endotherm with the melting of the α-phase. Two experiments were conducted to prove this assertion.
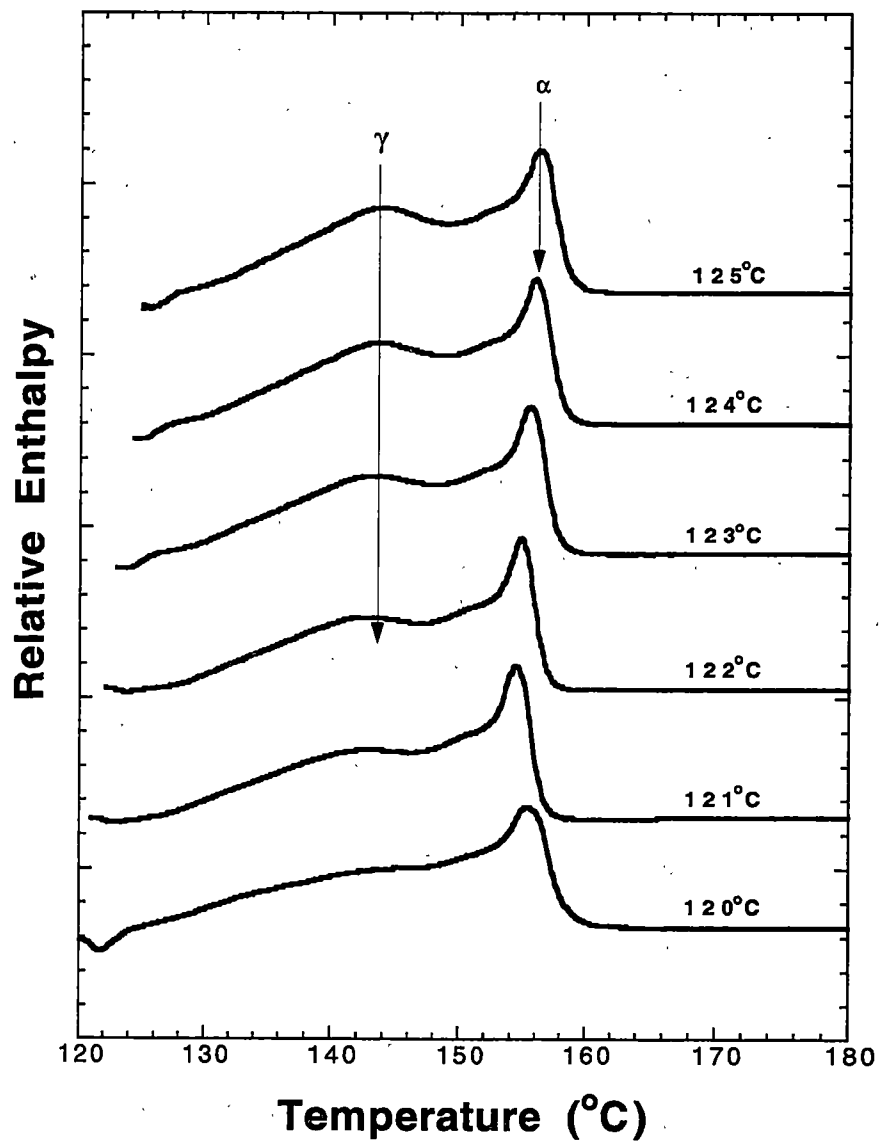
Figure 4.7 Isothermal crystallization of M22 between 120-125°C.
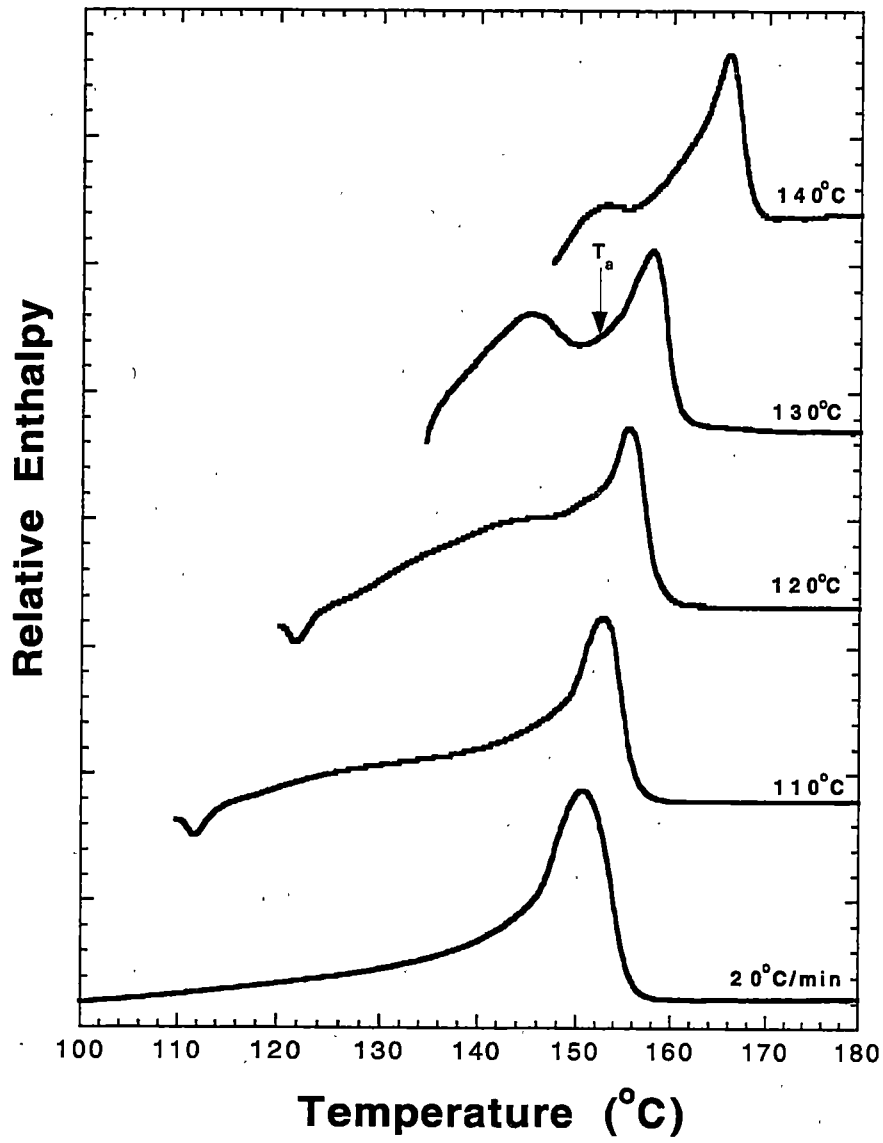
Figure 4.8   Crystallization of M22 over wide temperature range.

The first experiment involved crystallizing a film at 130°C in a Mettler hot stage, to reproduce a sample similar to the one found in Figure 4.8 at 130°C. The sample was then placed in the Rigaku diffractometer to obtain the WAXD pattern. The pattern is shown in Figure 4.9, and is labeled as "virgin". Notice for the virgin WAXD pattern that both the α and γ structures are present in significant amounts. The film was then annealed at 152°C for one minute in the Mettler stage and quenched in ice water. The annealing temperature picked is the saddle point between the two melting peaks of a sample crystallized at 130°C, as indicated by T_a in Figure 4.8. The WAXD pattern labeled "annealed" in Figure 4.9 shows that the γ-structure peak decreased significantly such that only a small amount of the γ-orthorhombic structure remains. A similar WAXD crystal melting procedure was performed on all other resins. As the results in Figures 4.10-4.14 show, the γ peak decreased significantly for all miPP resins and even for ZNHT. In Figures 4.10-4.14, the annealed and virgin WAXD patterns are overlaid so that the change in the diffraction pattern can be seen. Additionally, each pattern is of the same region of the same sample before and after the thermal cycle. According to Pae[214], the γ to α transition occurs very slowly and can not be detected by DSC scanning at 10 °C/min.

The second experiment was to crystallize a film in the DSC at 130°C for six hours, followed by annealing at 152°C to simulate in the DSC the thermal treatment of the annealed film whose x-ray pattern is shown in Figure 4.9. The sample was then cooled at 20°C/min to room temperature before reheating in the DSC. The heating curve following this treatment is shown as the lower curve in Figure 4.15. The higher melting temperature peak associated with the initial α-phase annealed at 152°C remains, but a
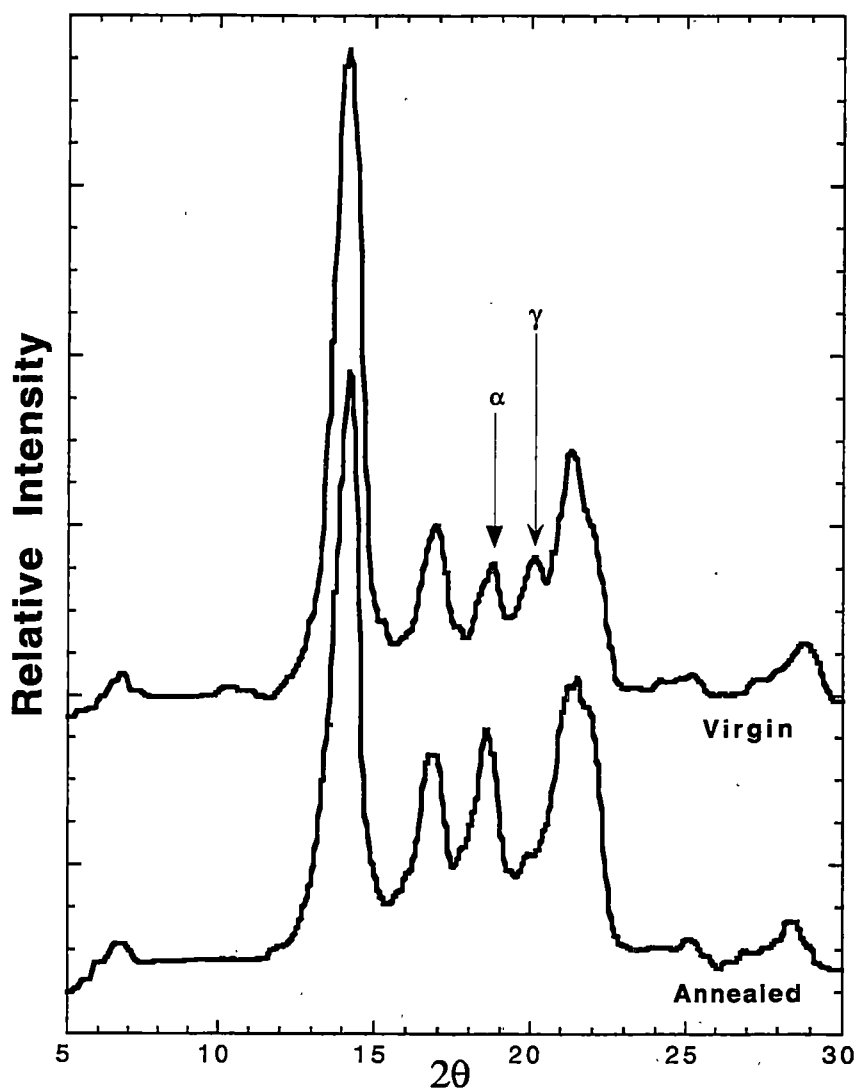
Figure 4.9 WAXD pattern of virgin and annealed M22.
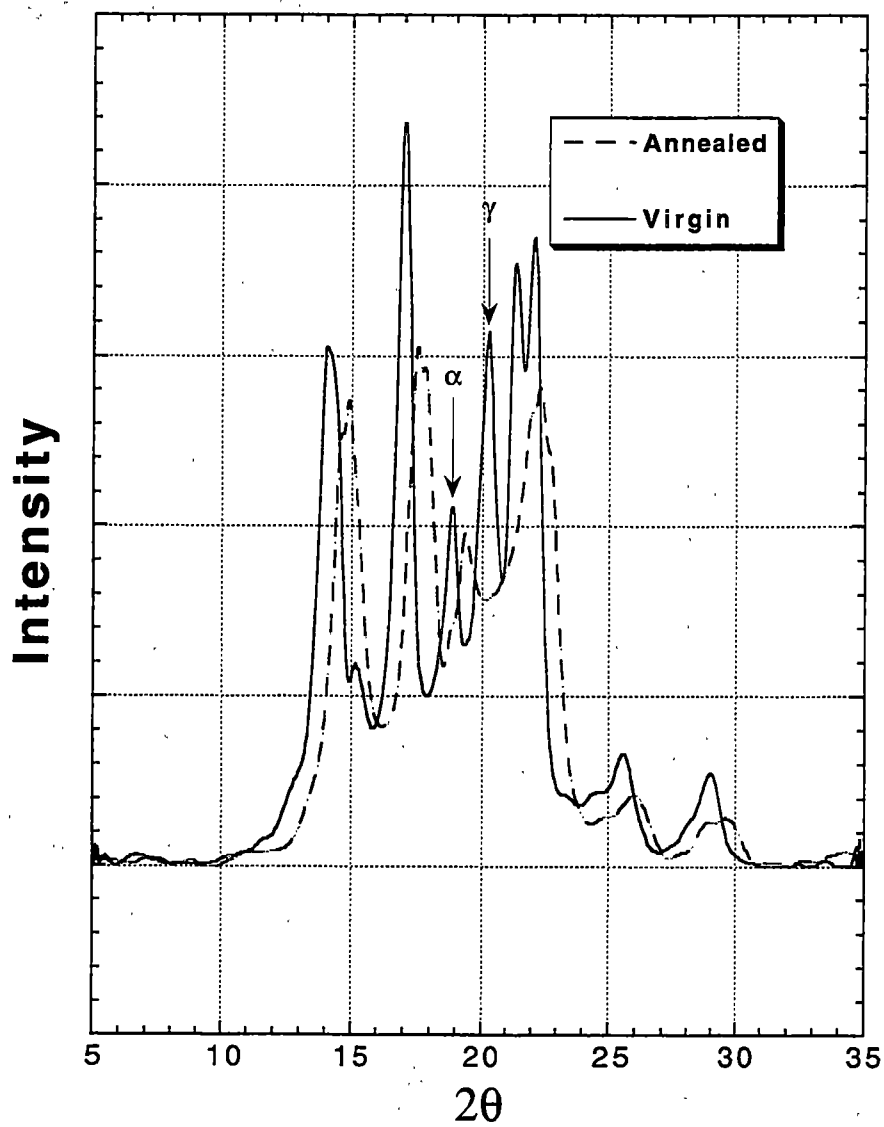
Figure 4.10   WAXD pattern of virgin and annealed M10.
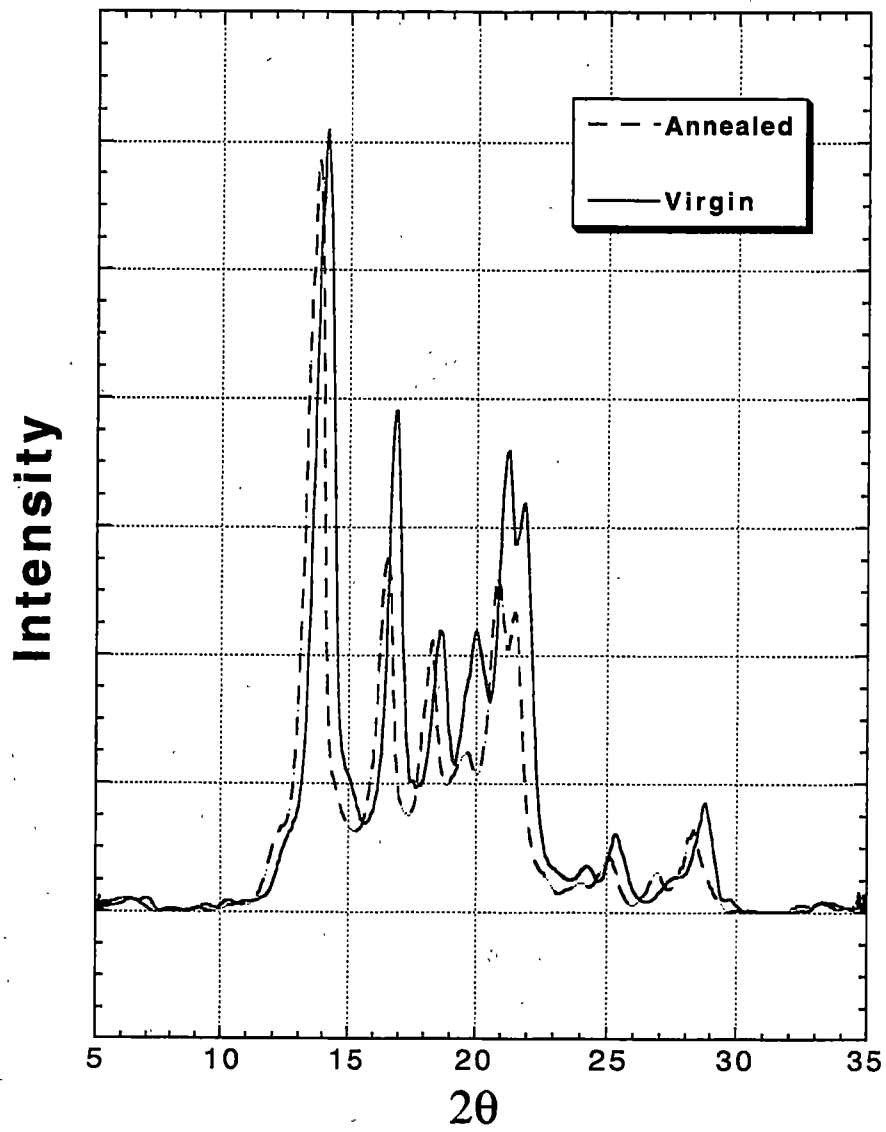
Figure 4.11   WAXD pattern of virgin and annealed M32.
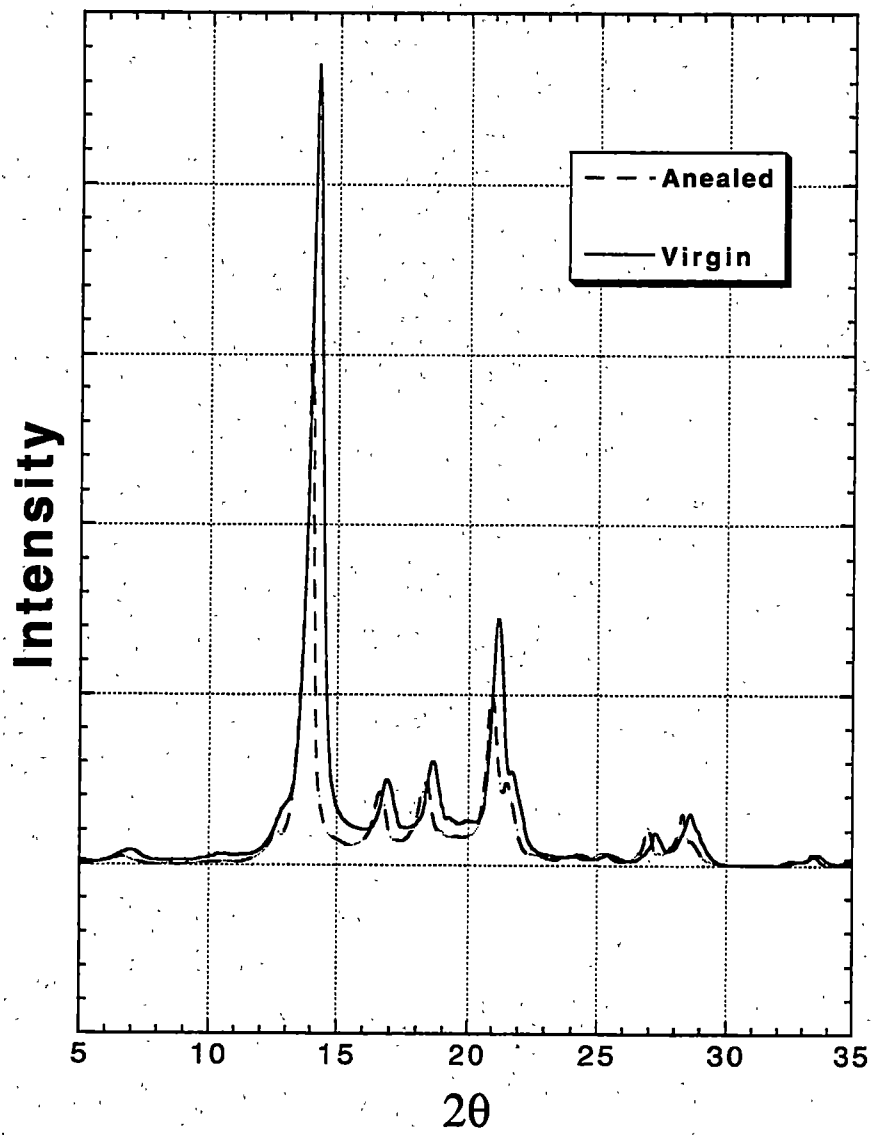
Figure 4.12 WAXD pattern of virgin and annealed ZN35.
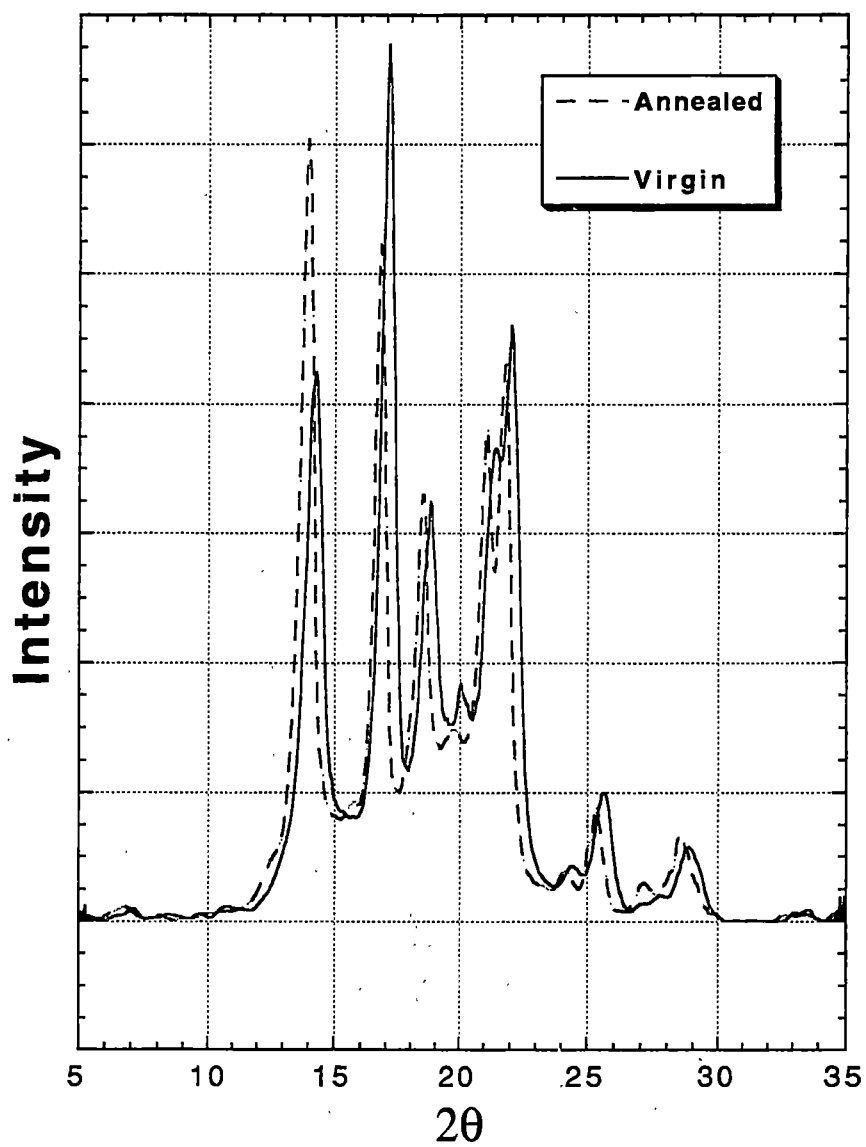
Figure 4.13   WAXD pattern of virgin and annealed ZNHT.
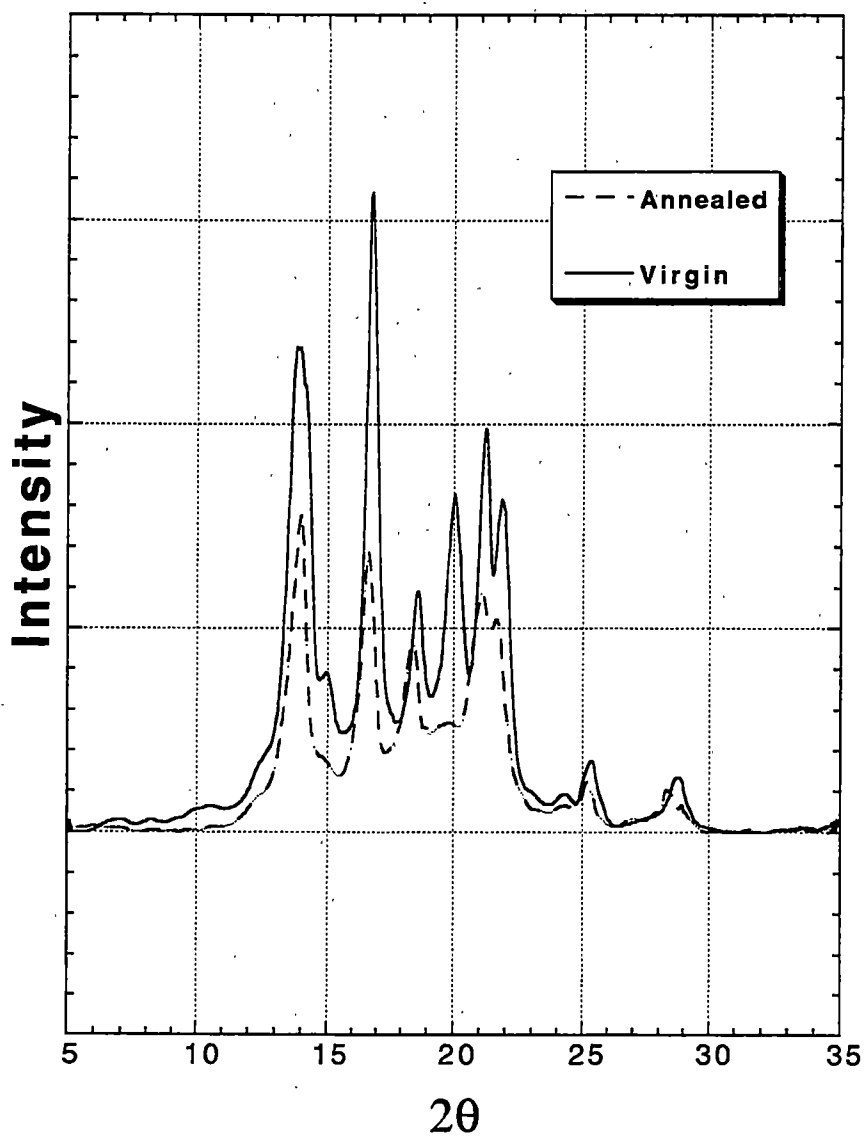
Figure 4.14   WAXD pattern of virgin and annealed M100.

Normal Enthalpy Curve

Crystallize 130°C and annealed at 152°C for 1 minute

Relative Enthalpy

Temperature (°C)
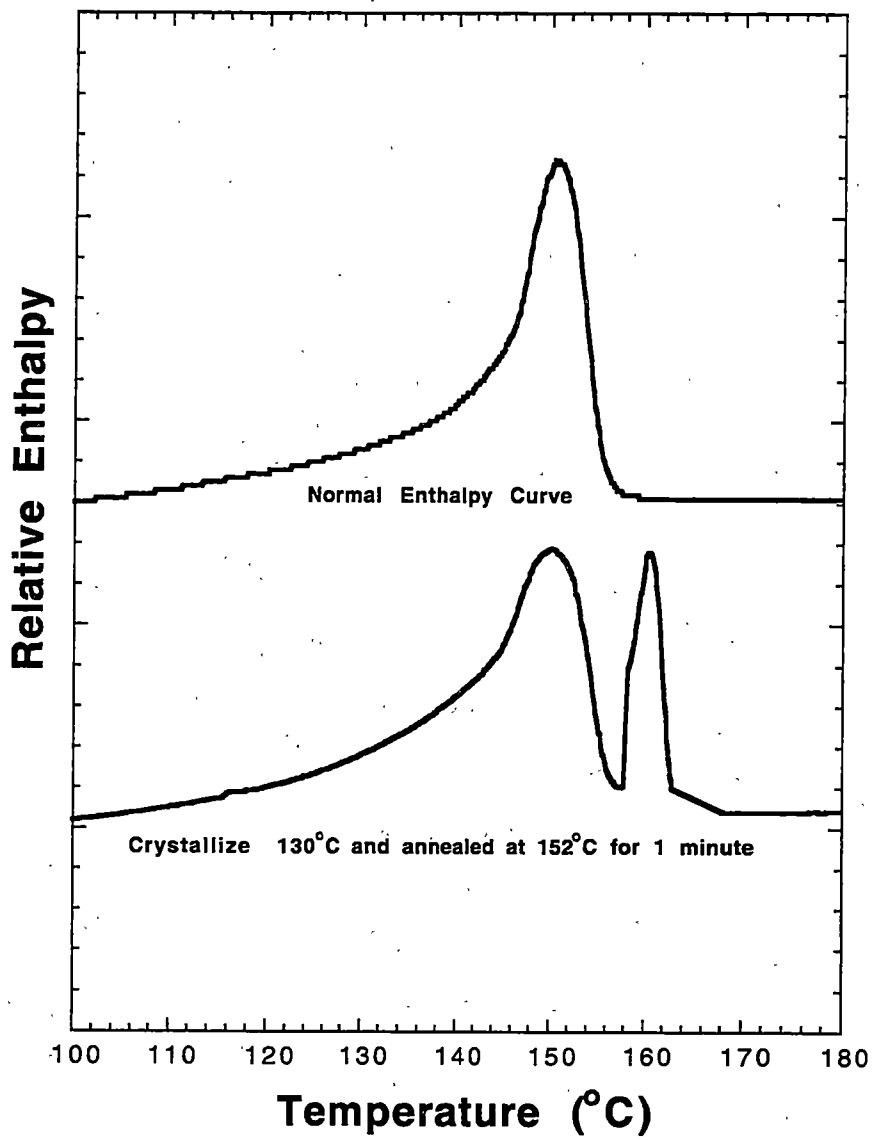
Figure 4.15   M22 results of virgin and anneal DSC scan.

lower melting peak is also observed almost identical to the one found when crystallizing the sample by cooling from the fully melted condition at 20°C/min, as in the upper curve in Figure 4.15. This lower temperature melting peak also represents melting of α-phase, but the lamellar thickness is smaller and the melting point is lower due to the nonisothermal crystallization. These results establish with a high degree of certainty that the lower temperature endotherm found in these miPP samples at higher crystallization temperatures is indeed associated with melting of the γ-crystal structure.

One reason for using a multiple technique analysis of the miPP resins was to rule out the two melting peaks of Figures 4.7 and 4.8 being a result of the melting recrystallization phenomena observed in polymers[215-217]. Careful experimental work could rule out this possibility using DSC alone. However, a check of the crystallographic structure revealed information about the underlying morphology and determined that the melting recrystallization phenomena is not responsible for the observations. The WAXD and DSC work show that each melting peak is associated with a crystal phase.

4.1.3 Lamellae Thickness and Equilibrium Melting Temperature

The results of the SAXS analysis to determine the lamellae thickness for each of the resins is shown in Tables 4.1-4.6. The crystallinity values were determined from WAXD analysis. The total crystallinity values represent the total crystalline fraction; no attempt was made to separate α and γ-phase fractions in the bulk crystallinity analysis. Also included in these tables for reference are the calculated stem length and number of monomer units traversing the crystal lamellae for the α-phase.

Table 4.1 M10 Crystal characteristics determined by SAXS, WAXD and DSC.

Sample	X	(nm)	Tm(α) (°C)	σe(α) (mJ/m²)	α stem length (nm)	# of Monomers (α)	Tm(γ) (°C)	σe(γ) (mJ/m²)	γ stem length (nm)	# of Monomers (γ)
iso105	0.623	8.32	149.6	49.6	8.43	39	-	-	-	-
iso108	0.633	8.48	150.3	49.5	8.59	40	-	-	-	-
iso110	0.623	8.64	150.8	49.7	8.75	40	-	-	-	-
iso113	0.650	8.93	151.8	49.9	9.05	42	-	-	-	-
iso115	0.622	8.93	151.7	50.0	9.04	42	-	-	-	-
iso118	0.629	8.76	151.4	49.5	8.87	41	142.3	46.9	11.4	53
iso120	0.644	9.06	152.9	48.9	9.17	42	143.8	46.4	11.8	55
iso123	0.660	9.39	153.4	49.9	9.51	44	145.6	45.5	12.3	57
iso125	0.681	9.65	154.1	50.1	9.78	45	146.3	45.7	12.6	58
iso130	0.700	10.6	157.4	49.3	10.9	50	148.4	47.0	13.9	64

Table 4.2 M22 Crystal characteristics determined by SAXS, WAXD and DSC.

Sample	X	(nm)	Tm(α) (°C)	σ_e(α) (mJ/m²)	α stem length (nm)	# of Monomers (α)	Tm(γ) (°C)	σ_e(γ) (mJ/m²)	γ stem length (nm)	# of Monomers (γ)
iso105	0.579	7.90	152.6	45.2	8.00	37	-	-	-	-
iso110	0.598	8.32	155.1	44.1	8.43	39	-	-	-	-
iso113	0.540	7.62	152.2	44.1	7.72	36	-	-	-	-
iso115	0.601	8.26	154.9	44.0	8.37	39	-	-	-	-
iso118	0.587	8.65	155.6	45.1	8.77	41	-	-	-	-
iso120	0.629	8.83	156.1	45.2	8.94	41	-	-	-	-
iso123	0.576	8.76	155.9	45.2	8.87	41	146.0	43.1	11.4	53
iso125	0.628	8.50	155.1	45.0	8.61	40	145.6	42.4	11.1	51
iso130	0.669	11.5	162.1	47.1	11.6	54	154.0	42.2	15.0	69
iso135b	0.631	12.3	165.1	44.2	12.4	57	154.8	43.7	16.0	74
iso135c	0.699	13.9	167.1	45.2	14.1	65	157.2	44.2	18.1	84
mpV135	0.688	11.9	165.0	43.1	12.0	56	155.2	41.6	15.5	72
mpA135b	0.728	12.2	165.2	43.7	12.3	57	155.2	42.6	15.9	73

Table 4.3 M32 Crystal characteristics determined by SAXS, WAXD and DSC.

Sample	X	(nm)	Tm(α) (°C)	$\sigma_e(\alpha)$ (mJ/m²)	α stem length (nm)	# of Monomers (α)	Tm(γ) (°C)	$\sigma_e(\gamma)$ (mJ/m²)	γ stem length (nm)	# of Monomers (γ)
iso105	0.559	7.64	151.9	44.6	7.74	36	-	-	-	-
iso108	0.570	7.87	152.6	45.0	7.97	37	-	-	-	-
iso110	0.589	8.09	153.7	44.7	8.19	38	-	-	-	-
iso113	0.571	8.14	154.2	44.4	8.25	38	-	-	-	-
iso115	0.557	7.86	153.8	43.4	7.97	37	-	-	-	-
iso118	0.578	8.53	155.9	44.0	8.64	40	-	-	-	-
iso120	0.595	8.59	155.8	44.5	8.71	40	145.6	42.9	11.2	52
iso123	0.580	8.70	156.4	44.1	8.81	41	146.1	42.7	11.4	52
iso125	0.570	8.53	155.8	44.2	8.64	40	145.7	42.4	11.1	51
iso130a	0.645	9.89	159.9	44.7	10.0	46	150.8	40.5	12.9	60
iso130b	0.616	10.5	161.1	45.1	10.6	49	152.8	43.5	13.7	63
iso135a	0.669	13.8	167.0	44.3	14.0	64	157.4	41.3	18.0	83
iso135b	0.657	9.83	160.5	43.1	9.96	46	151.2	40.5	12.8	59

Table 4.4 ZN35 Crystal characteristics determined by SAXS, WAXD and DSC.

Sample	X	(nm)	Tm(α) (°C)	σₑ(α) (mJ/m²)	α stem length (nm)	# of Monomers (α)
iso115	0.605	9.94	163.1	25.1	10.0	47
iso120	0.619	11.6	165.7	24.0	11.7	54
iso123	0.651	11.9	166.4	23.2	12.0	56
iso125	0.680	12.4	166.7	23.6	12.6	58
iso127	0.632	12.6	166.9	23.4	12.7	59
iso130	0.663	12.7	167.1	23.2	12.8	59
iso133	0.636	13.1	167.5	23.2	13.3	61
iso135	0.717	10.7	164.9	23.8	10.9	50
iso140	0.659	8.47	162.0	23.0	8.58	40
iso145a	0.604	8.79	162.3	23.4	8.90	41
iso145b	0.679	9.63	163.7	23.3	9.75	45

183

Table 4.5 ZNHT Crystal characteristics determined by SAXS, WAXD and DSC.

Sample	X	(nm)	Tm(α) (°C)	$\sigma_e(\alpha)$ (mJ/m²)	α stem length (nm)	# of Monomers (α)
iso110	0.687	11.4	168.6	33.3	11.6	53
iso115	0.695	11.5	168.7	33.3	11.6	54
iso118	0.700	11.8	169.4	33.0	12.0	55
iso120	0.697	12.1	169.7	33.0	12.2	56
iso123	0.730	12.7	170.6	32.9	12.9	60
iso125	0.720	13.0	170.6	33.6	13.2	61
iso128	0.710	13.4	171.2	33.3	13.6	63
iso130	0.715	13.5	171.3	33.3	13.7	63
iso133	0.709	13.8	171.5	33.6	14.0	65
iso135	0.701	14.3	171.9	33.8	14.5	67
iso140	0.709	15.7	173.6	32.6	15.9	74

Table 4.6 M100 Crystal characteristics determined by SAXS, WAXD and DSC.

Sample	X	(nm)	Tm(α) (°C)	σe(α) (mJ/m²)	α stem length (nm)	# of Monomers (α)	Tm(γ) (°C)	σe(γ) (mJ/m²)	γ stem length (nm)	# of Monomers (γ)
iso105	0.580	7.66	148.9	44.2	7.76	36	-	-	-	46
iso110	0.611	8.18	150.4	45.1	8.28	38	-	-	-	49
iso112	0.600	8.22	150.8	44.7	8.33	38	-	-	-	50
iso115	0.620	8.50	151.0	46.0	8.61	40	-	-	-	51
iso118	0.591	8.20	150.8	44.6	8.31	38	143.3	41.1	10.7	49
iso120	0.631	8.95	152.8	45.6	9.06	42	146.0	40.7	11.7	54
iso123	0.630	9.16	153.3	45.9	9.28	43	147.2	40.6	12.0	55
iso125	0.640	9.35	153.9	45.9	9.47	44	147.7	40.7	12.2	56
iso130	0.660	9.90	156.3	44.6	10.0	46	149.5	40.3	12.9	60
iso135	0.710	11.7	161.0	43.4	11.9	55	153.0	41.4	15.3	71

There existed only one maxima on the raw SAXS 1-d azimuthally averaged scan. Based on this and the lack of information to the contrary, we assumed a similar crystal thickness for both the α and γ-crystal structure when two phases were present. For the samples that have a significant fraction of γ-phase, stem length in the γ-phase and the number of monomer units traversing the γ-crystal is also given. The difference between these values for the α and γ phases is due to the inclination of the chains to the lamellae surface in the γ-phase.

The assumption of similar crystal thickness for both α and γ-crystal structure is supported by the uncorrected and Lorentz corrected SAXS data for the miPP resins, as shown in Figures 4.16-4.21. M10 raw and Lorentz corrected data are shown in Figures 4.16-4.17, M22-Figures 4.18-4.19 and M100-Figures 4.20-4.21. M22 had the fewest number of configurational defects of the metallocene resins, and in general had the lowest percent γ-content as shown in Figure 4.22, which shows γ content as a function of lamellae thickness for all the metallocene resins. The largest percent γ-content for M22 was roughly 42%. However, M10 and M100 had more configurational defects that produced percent γ-content values greater than 70% for some samples. Therefore, if a bimodal population of crystal thicknesses exists, it should show up for M10 and M100 in the SAXS data. Clearly it does not. The peak value of Q for M10, M22 and M100 (Figure 4.17, 4.19 and 4.21 respectively) all have similar long period values, which further indicates our assumption of similar crystal thickness for each crystal structure is most likely correct.

An additional high temperature in situ experiment was performed on isothermally crystallized films using SAXS to further support the assertion of a single maxima or long

186
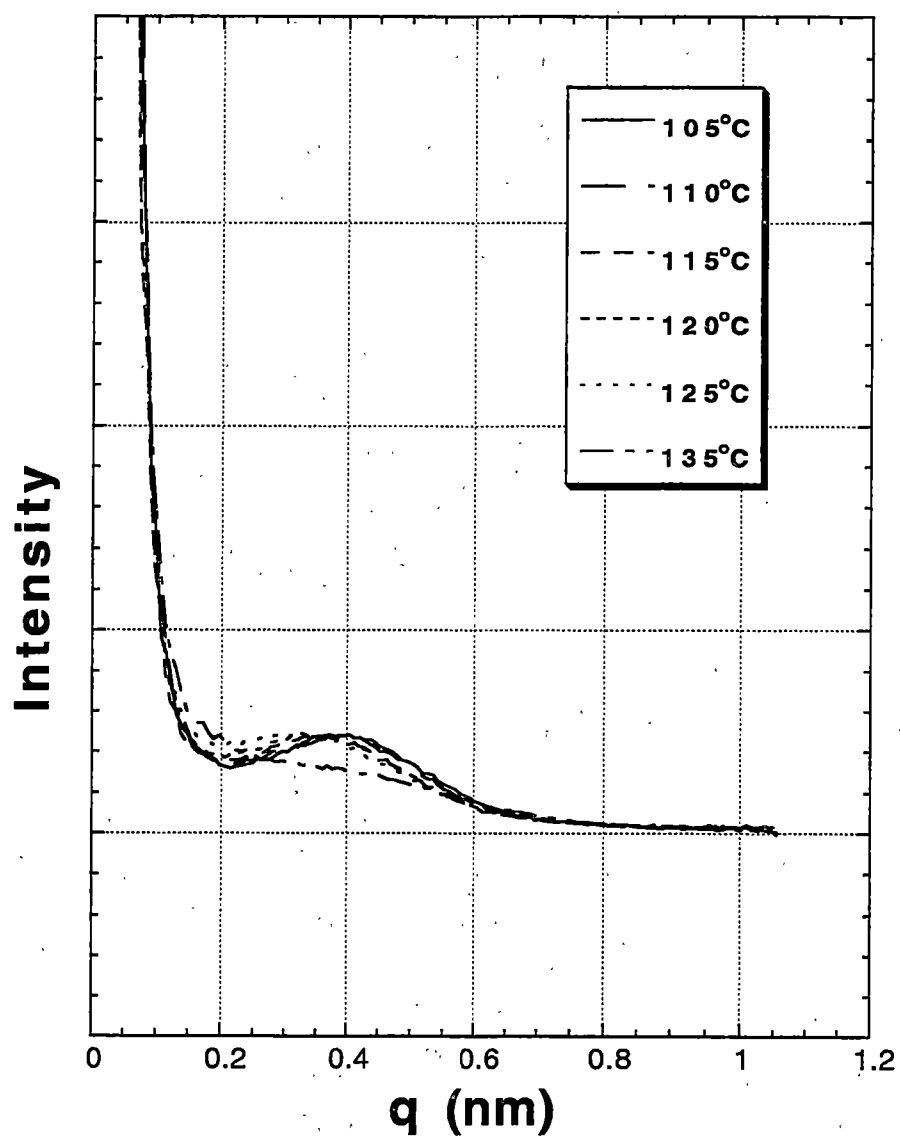
Figure 4.16   M10 raw SAXS data.
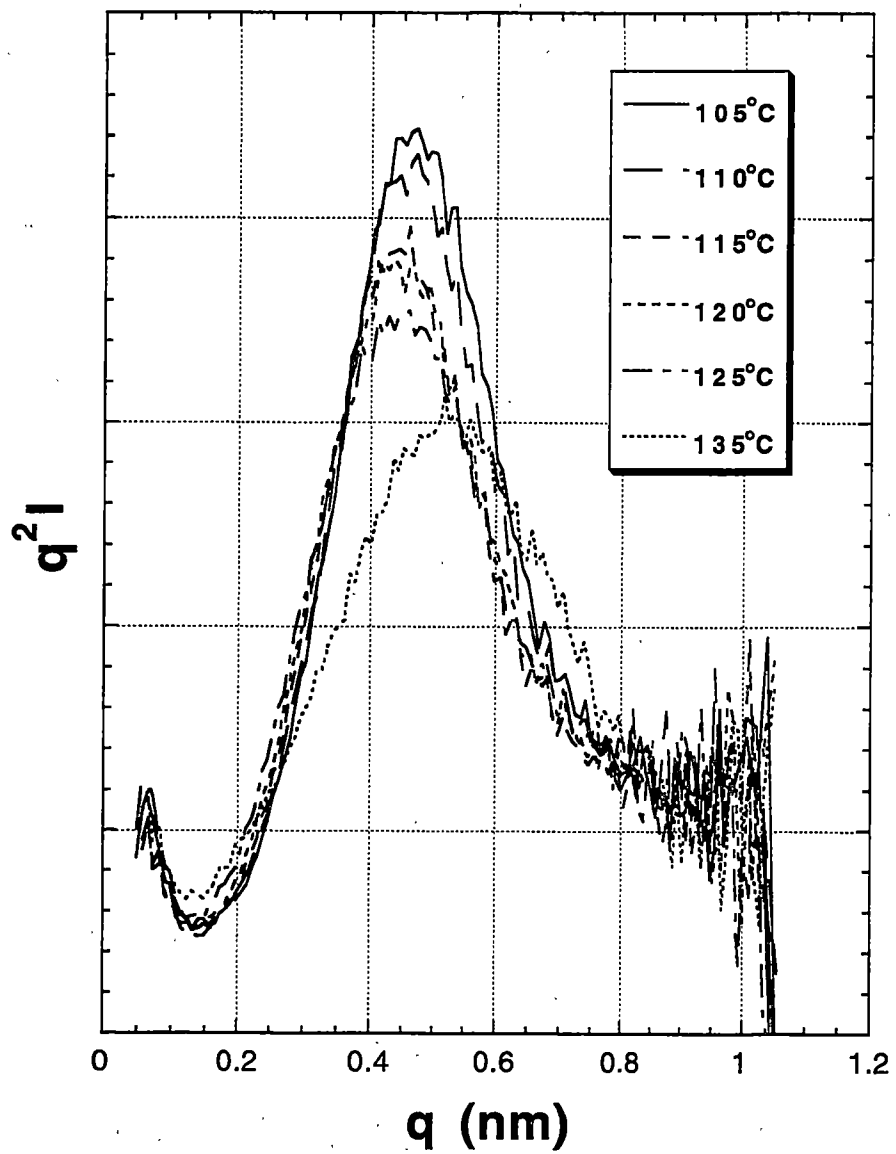
Figure 4.17 M10 Lorentz corrected SAXS data.
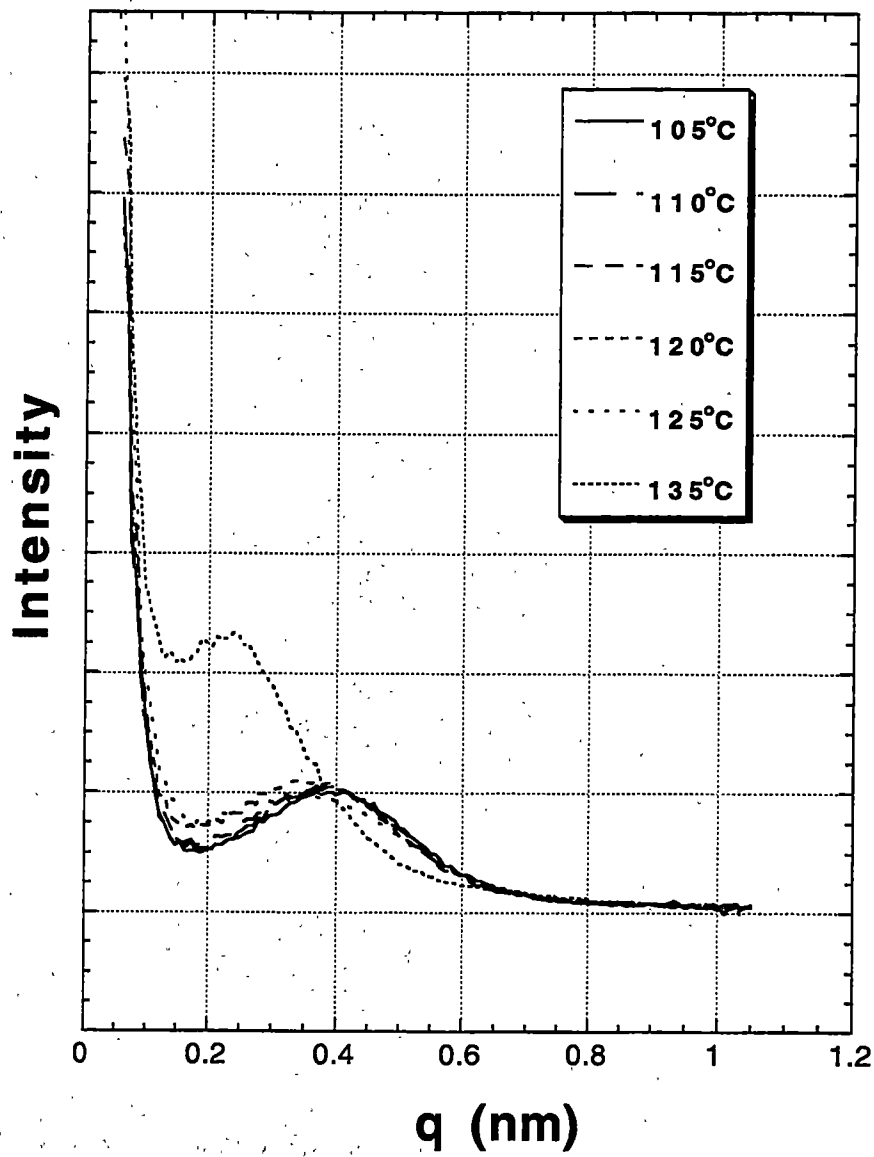
Figure 4.18   M22 raw SAXS data.
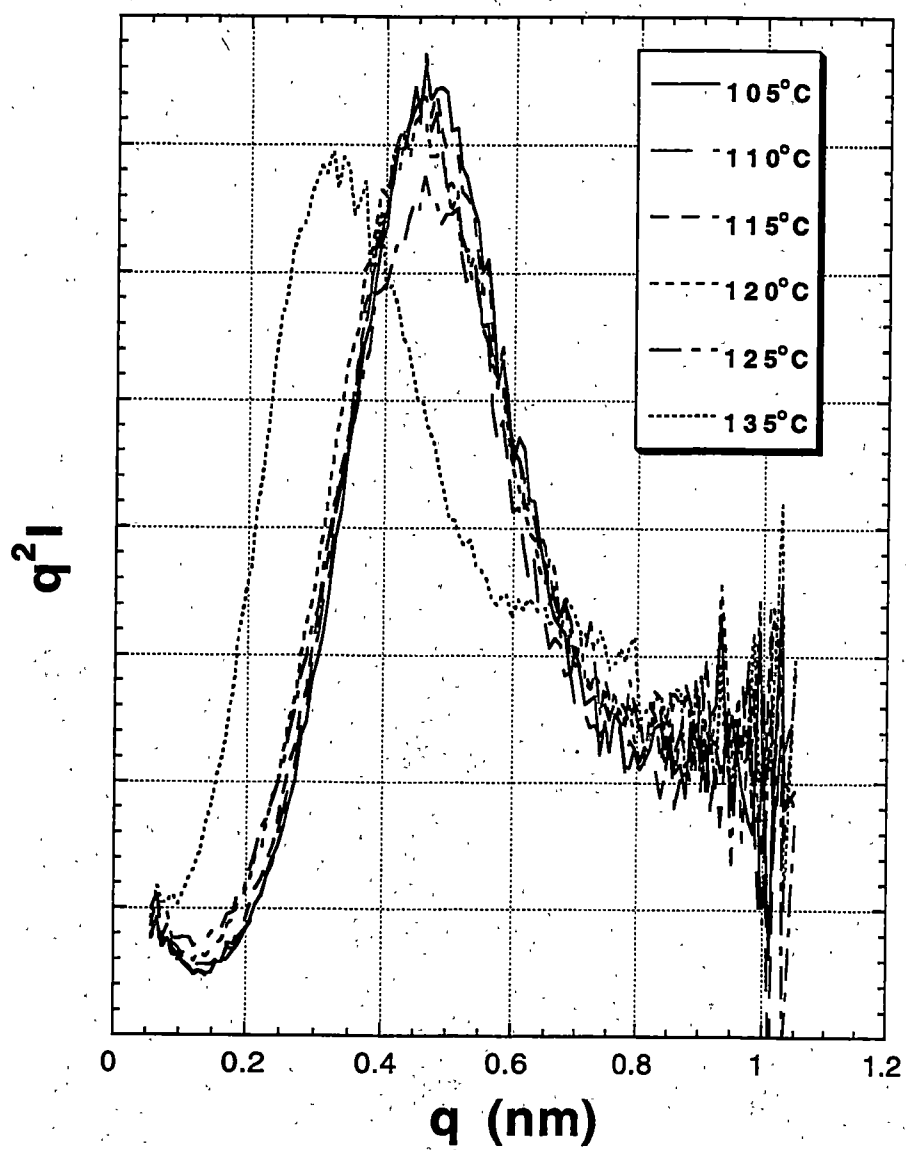
Figure 4.19 M22 Lorentz corrected SAXS data.
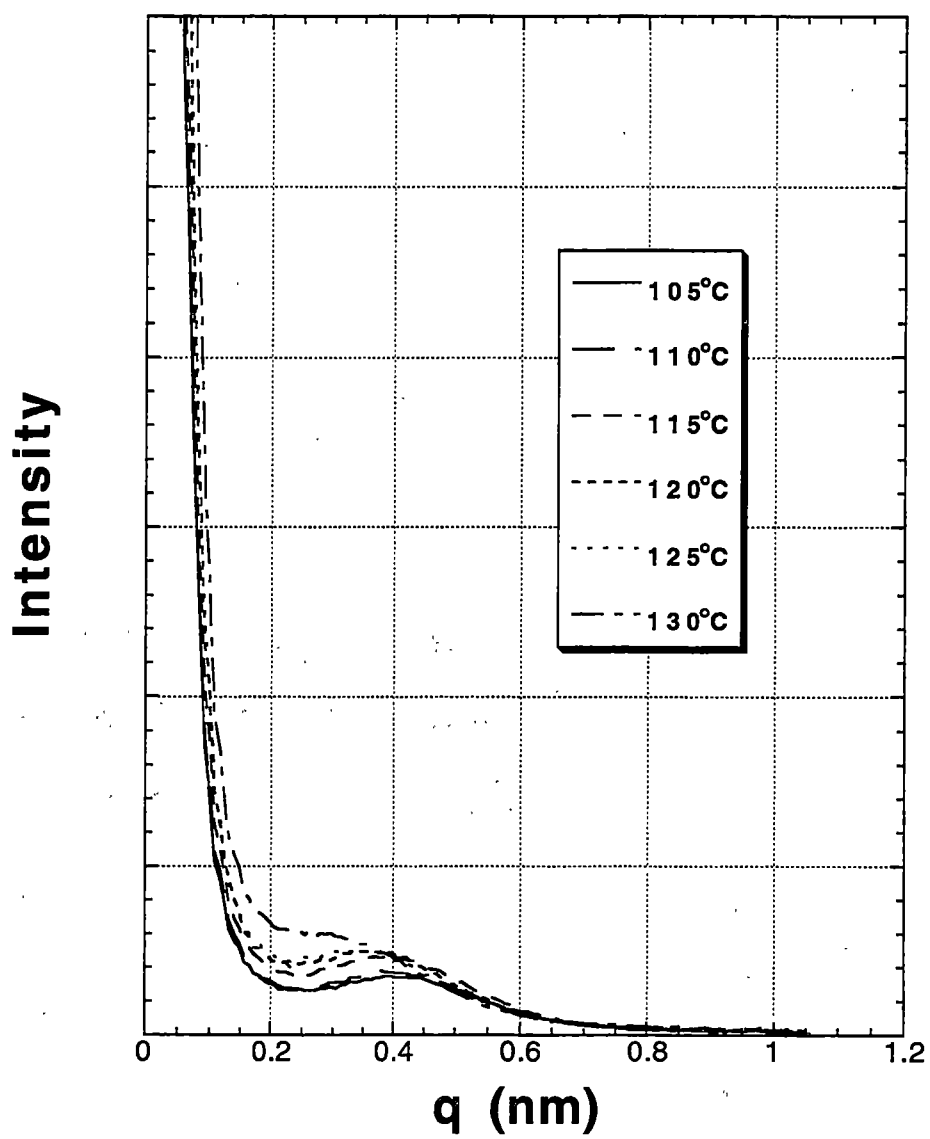
Figure 4.20 M100 raw SAXS data.
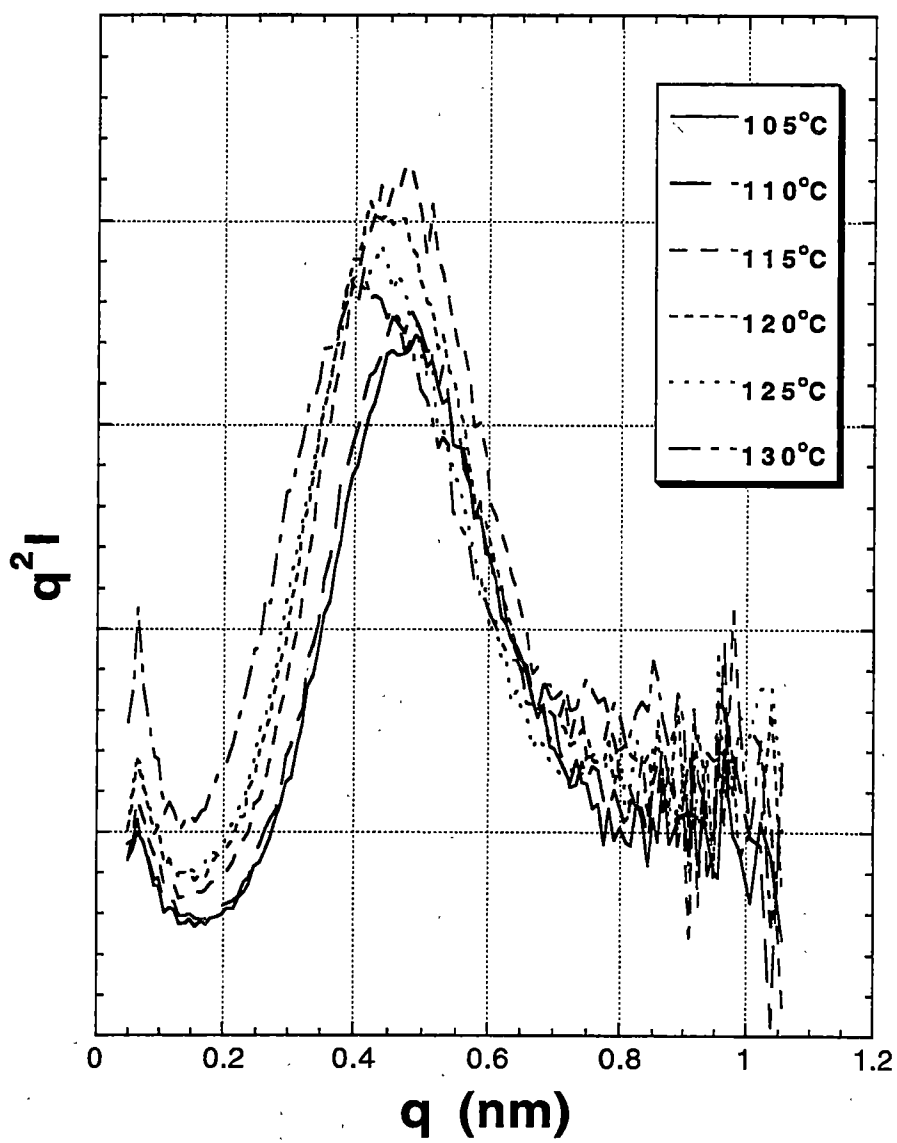
Figure 4.21 M100 Lorentz corrected SAXS data.
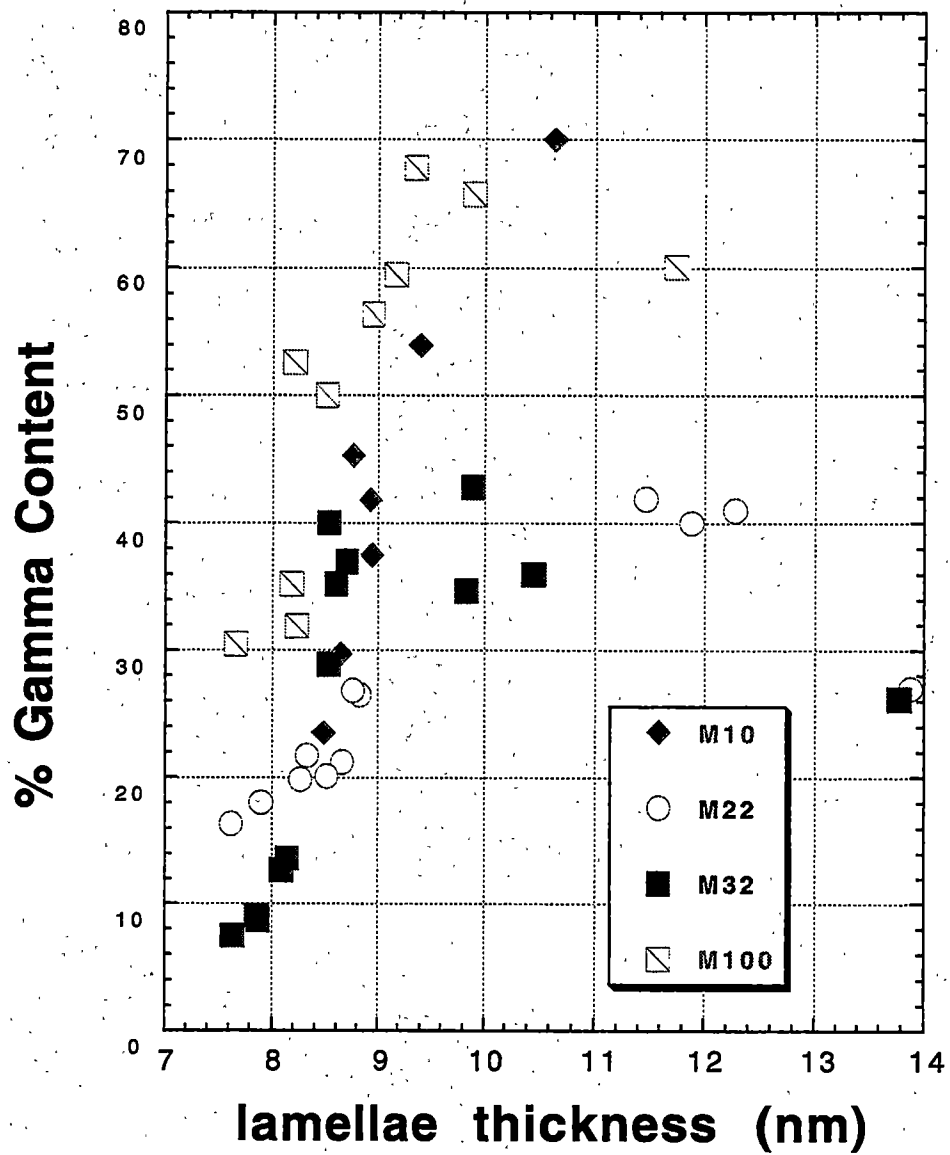
Figure 4.22 Percent γ-iPP content versus lamellae thickness.

period for both the α and γ crystal structures. The sample chamber was heated to 154°C, a temperature sufficient to melt the γ-phase present in samples of M10 and M22, along with ZNHT isothermally crystallized at 130°C. The results showed that the long period increased for all the samples over the long period at room temperature with the miPP resins long period increasing more than ZNHT. However, when the lamellae thickness was calculated using the room temperature crystallinity values adjusted for the removal of the γ-phase, the lamellae thicknesses changed by roughly similar amounts for M10, M22 and ZNHT.

The results in Figure 4.23 show the observed melting temperature of the α-iPP as a function of lamellae thickness. Figure 4.23 illustrates quite clearly that the miPP resins have lower melting temperatures than the zniPP resins with similar lamellae thickness values.

The Gibbs-Thomson extrapolation for the resins in this study are shown in Figures 4.24-4.28. In Figures 4.24-4.26 and 4.28, two extrapolations are shown -- one for the α-phase and one for the γ-phase. The extrapolation for the α-phase is based on the measured lamellae thickness values and the high temperature endotherms from DSC data. Since we have established that the lower temperature endotherm is associated with the γ-phase, we can determine the $T_m°$ value for the γ-phase with the assumption described above, that the lamellae thickness is the same as that of the α-phase. This was done for the lower curves in Figures 4.24-4.26 and 4.28.

The extrapolation for the α-phase of the M22 resin gives a $T_m°$ of 186±2°C, as does the M32 resin. The Ziegler-Natta resins give a value of 186±2°C for the ZNHT
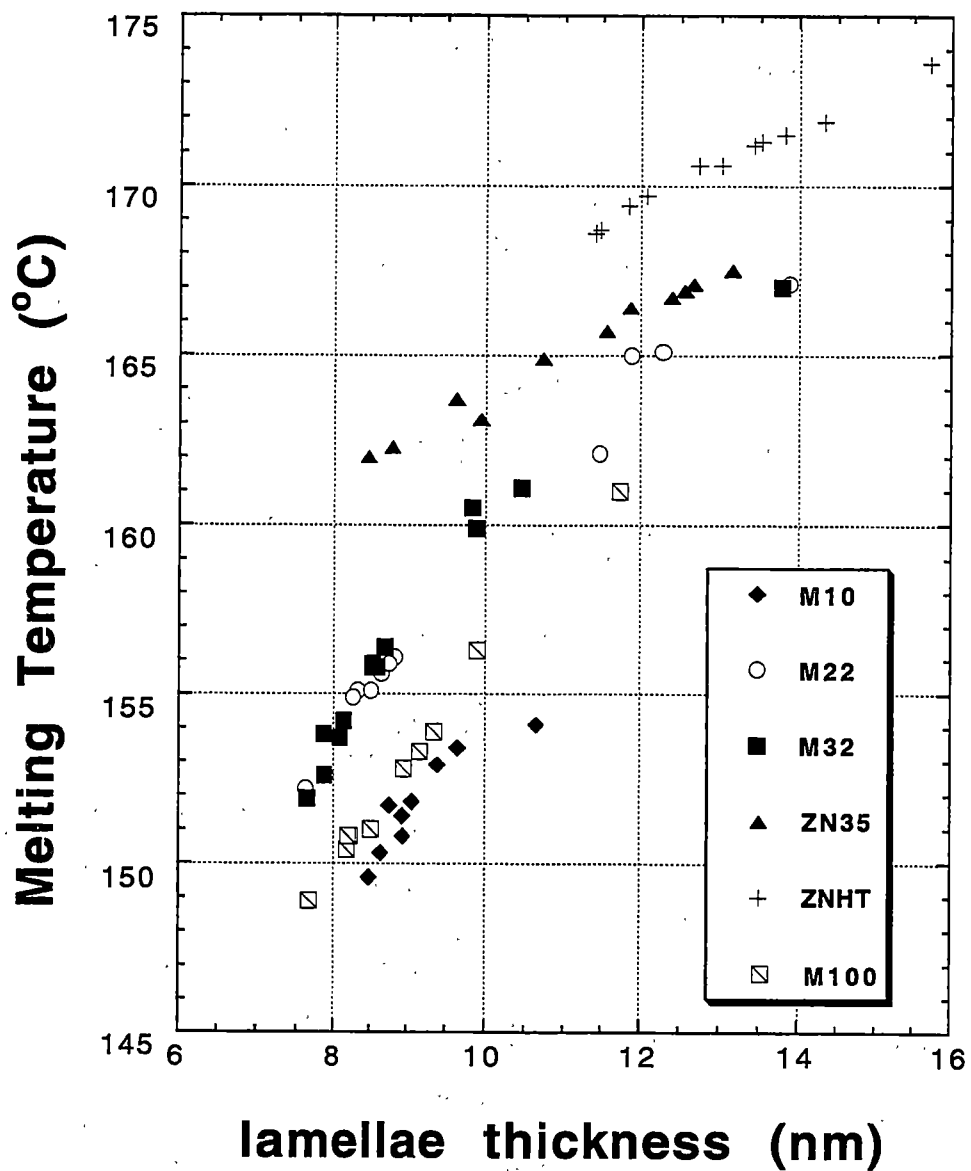
Figure 4.23 α-iPP T_m versus lamellae thickness.
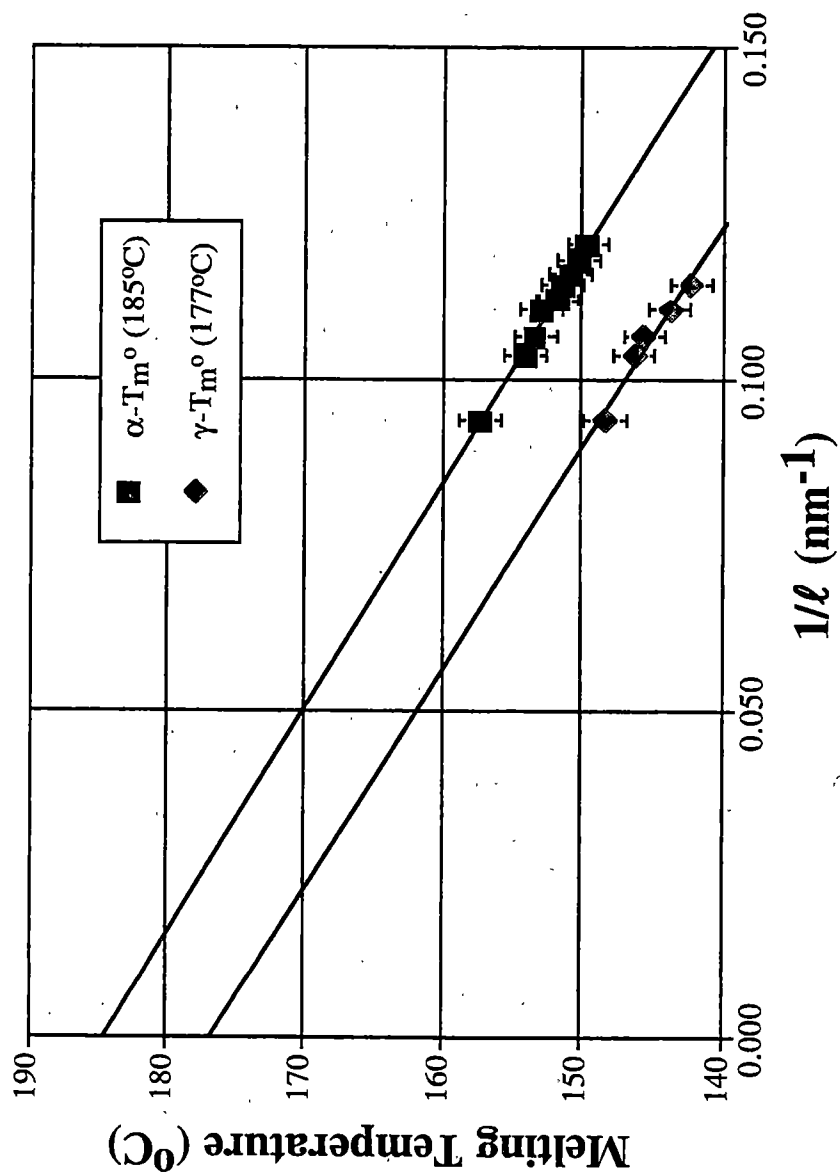
Figure 4.24 M10 α-iPP and γ-iPP T_m^0.
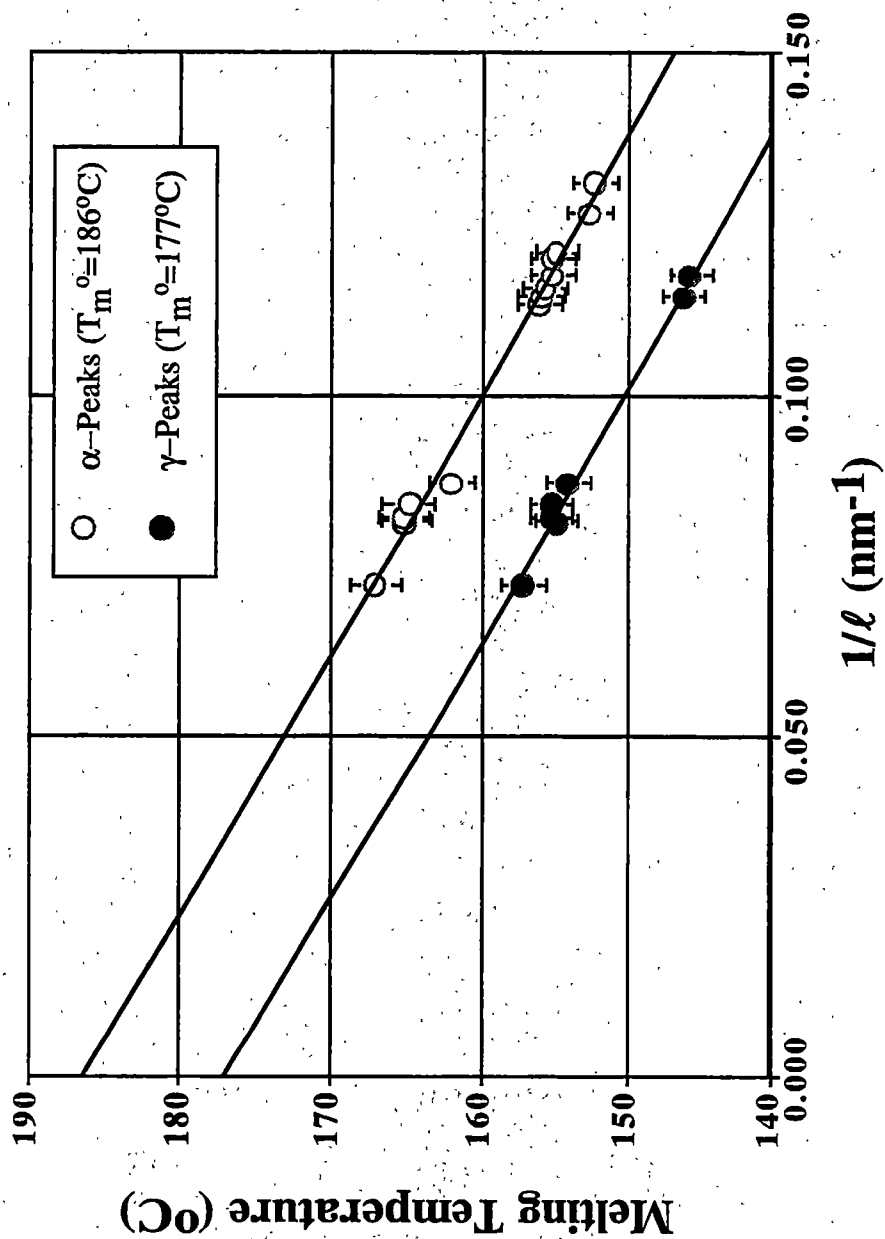
Figure 4.25   M22 α-iPP and γ-iPP $T_m^{\,0}$.
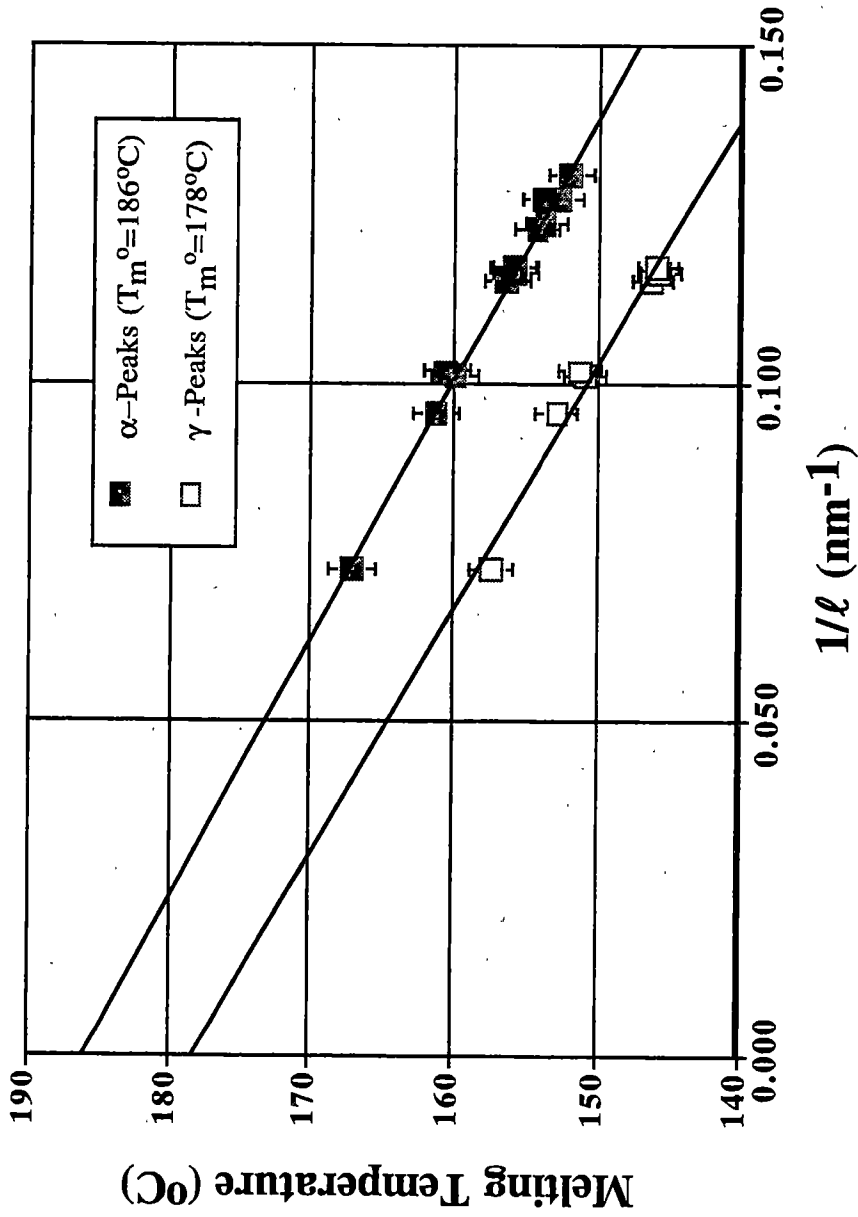
Figure 4.26 M32 α-iPP and γ-iPP T_m^0.
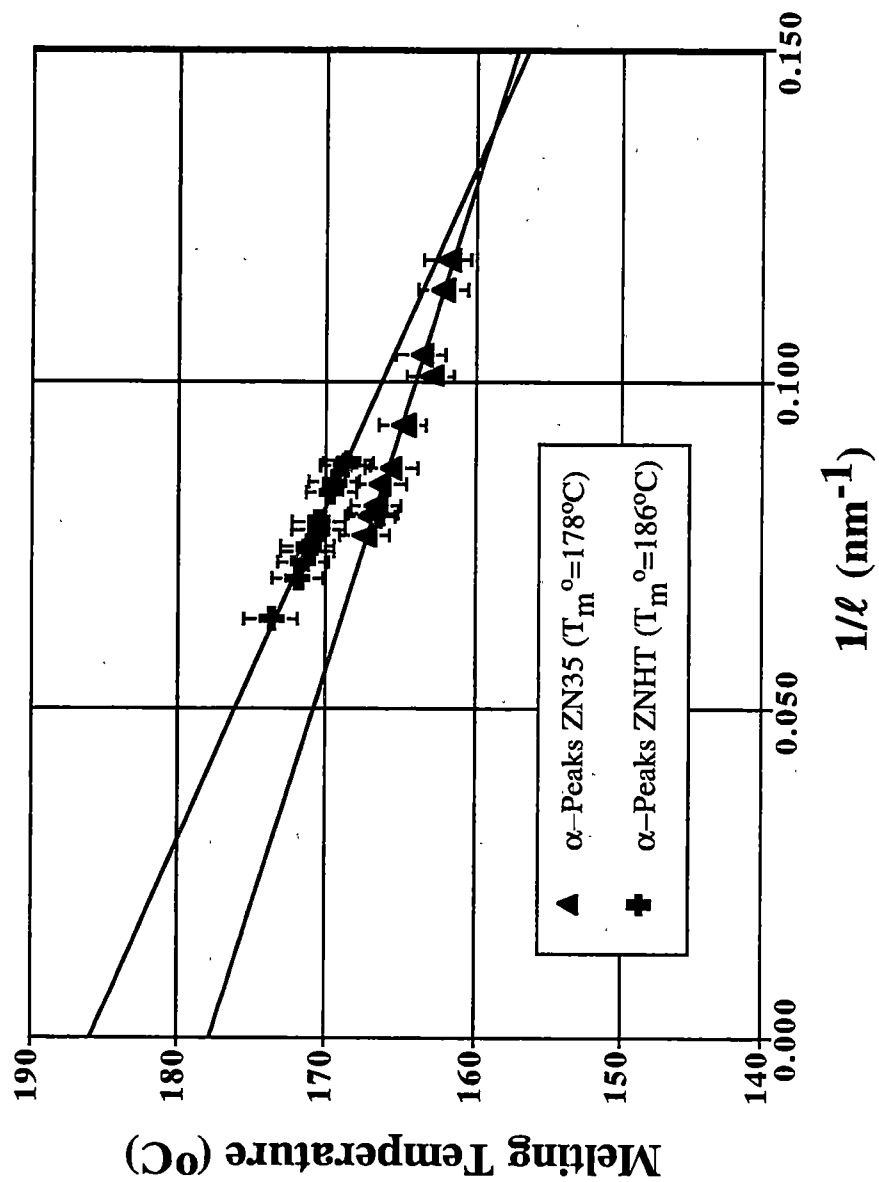
Figure 4.27 ZN35 and ZNHT α-iPP T_m^0.
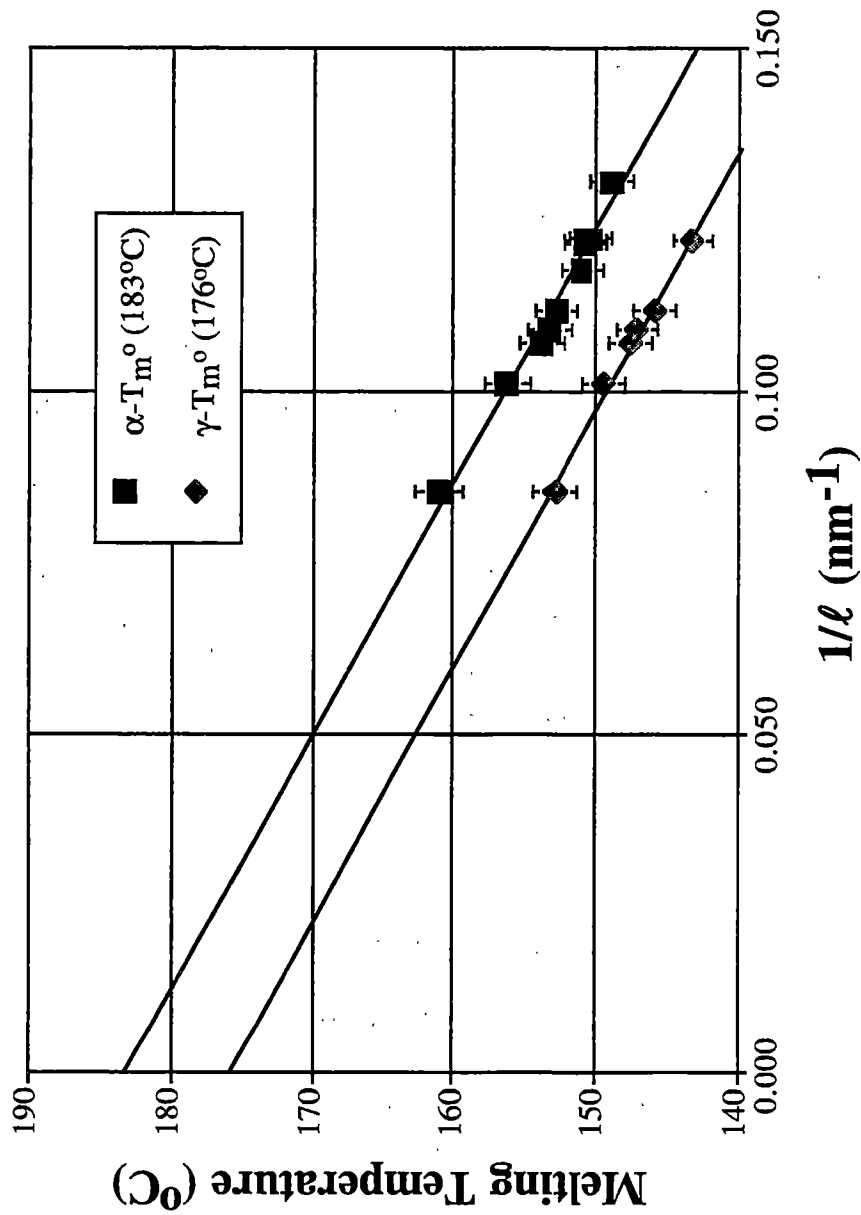
Figure 4.28 M100 α-iPP and γ-iPP T_m^0.

resin and 178±2°C for the ZN35 resin. The higher defect content resin M10 had a T_m^o of 185±2°C and M100 a T_m^o of 183±2°C. For resins M22, M32 and ZNHT, the α-phase T_m^o values are nearly identical and agree with recent literature values published for the α-phase T_m^o of highly isotactic zniPP. Mezghani et al. and others have found the T_m^o of various iPP resins to have a value near 186°C[91,209,218]. It also should be pointed out that the miPP resins have similar lamellae thicknesses as those found in the zniPP resins, as was shown in Figure 4.23. Since the lamellae thicknesses are similar and the miPP resins melt at lower temperatures than the Ziegler-Natta resins, the differences in melting temperatures must be a result of either differing fold surface free energy or differing heat of fusion (or both), according to the Gibbs-Thomson equation (see equation 2.1).

The results in Figures 4.29 and 4.30 show a plot of the measured heat of fusion of the iPP resins as a function of the crystallinity as measured by WAXD. By extrapolation to 100% crystallinity, the value of ΔH_f for α-iPP can be obtained. Figure 4.30 shows that the difference between the values of ΔH_f for the miPP resins is small and likely lies within our experimental error (±5J/g for each resin). Figure 4.29 shows that the difference between the values of ΔH_f for the zniPP resins is small and also lies within our experimental error (±5J/g for each resin) for all the resins considered. The values of ΔH_f for all of the resins represented in Figures 4.29 and 4.30, lie within the range 166-169 J/g, in good agreement with the literature value of 167 J/g[97,210,218]. Thus, it is unlikely that a difference in ΔH_f is responsible for the difference in actual measured melting temperature of the miPP and zniPP resins. The data also further suggest that there is little to no defect incorporation into the crystal matrix, since the heats of fusion are basically equivalent for all the materials.
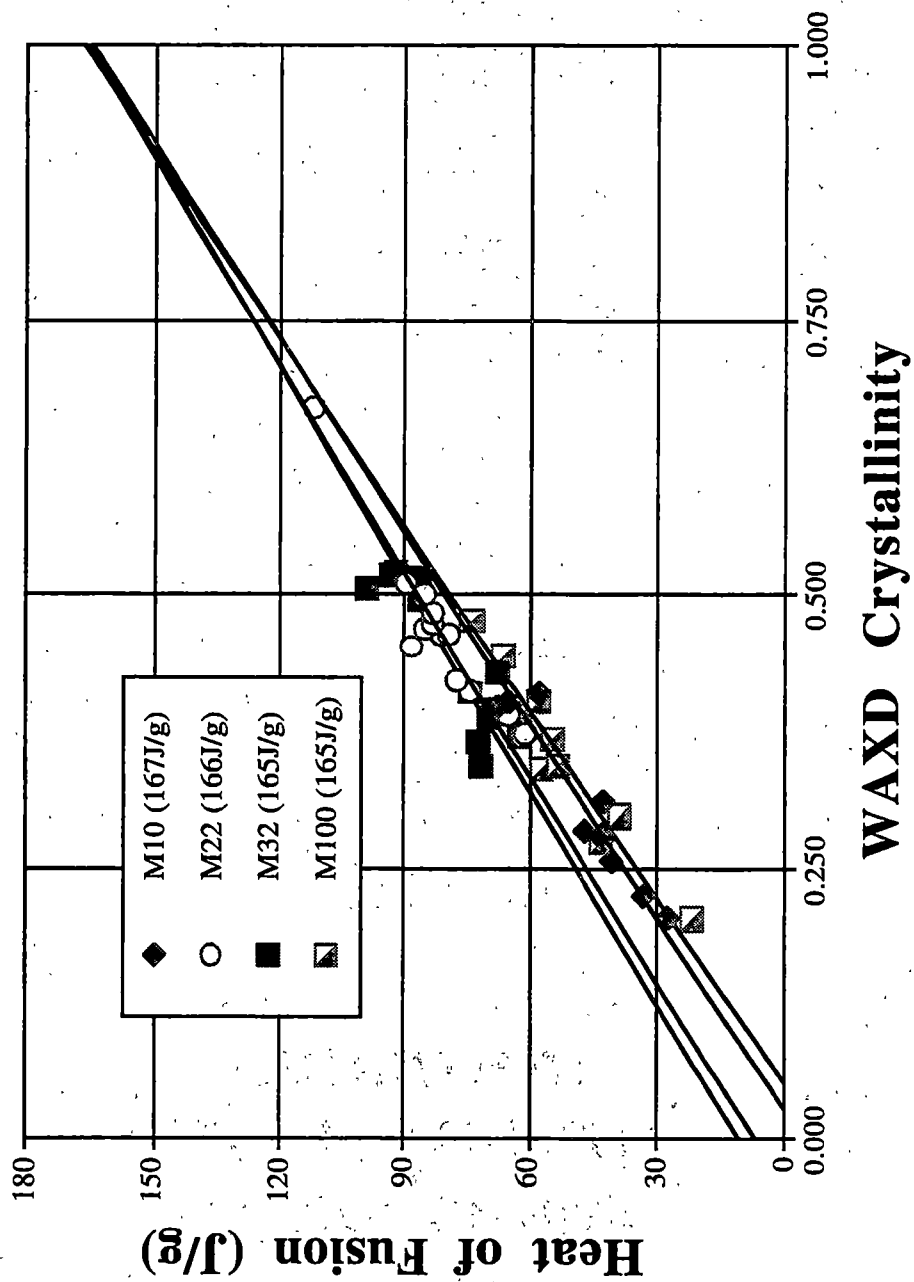
Figure 4.29 ΔH_f versus WAXD crystallinity for miPP resins.

202
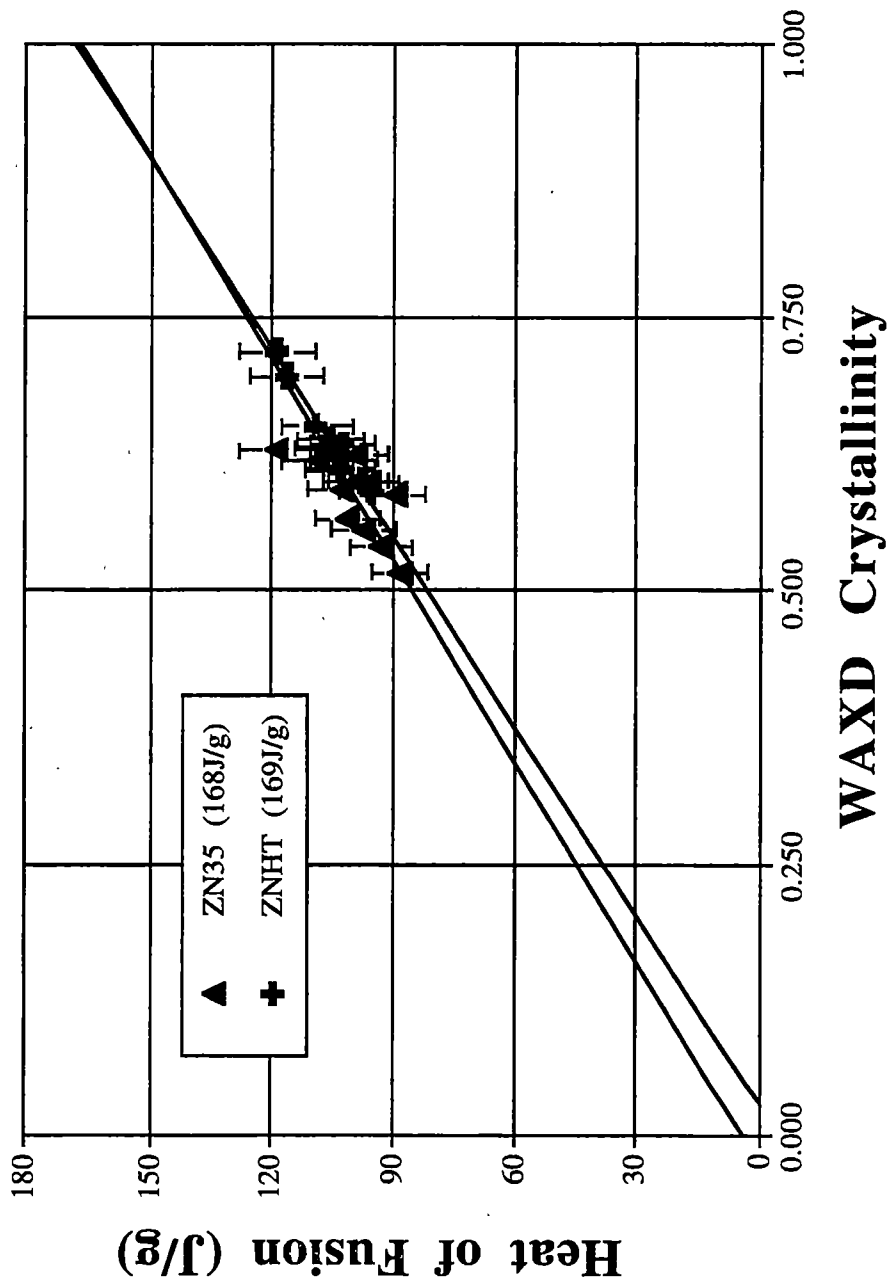
Figure 4.30 ΔH_f versus WAXD crystallinity for zniPP resins.

203

The decrease in T_m° for ZN35 can be explained by the presence of the atactic material in the xylene fractionation. The atactic material acts as a diluent for the polymer, lowering its T_m° according to Flory's model[219]. This observation and others on the T_m° of iPP will be the discussed shortly.

The extrapolated T_m° for the γ crystal structure is 177±2°C for M10 and M22, while M32 had a γ-T_m° of 178±2°C. M100 had a γ-T_m° of 176±2°C. Clearly, these variations are within experimental error, and they are significantly lower than the T_m° of the α-phase. There exists little literature[97,210] on the T_m° for the γ-crystal structure. Mezghani and Phillips[30,31] report a γ-T_m° of 187.2°C. However, this value is for samples crystallized at elevated pressures and melted at atmospheric pressure.

The x-ray and DSC results of this section on the isothermal crystallization of films indicate that iPP polymer chain defects are rejected from the crystal matrix when the crystallization is slow. This was shown by the extrapolation of the heats of fusion to 100% crystallinity. Under isothermal crystallization conditions, it would be reasonable for the defects to be rejected. In any system undergoing a phase change, there exists a Gibbs free energy difference (ΔG) associated with the change from solid to liquid. This is given by:

(4.1) $$\Delta G = \Delta H - T\Delta S$$

where ΔH is the heat of fusion associated with the phase change and ΔS is the entropy of fusion. At a particular temperature, the most stable phase for a particular substance is the one with the lowest value of G. At the melting temperature, T_m^0, $\Delta G=0$; i.e., $G_S = G_L$. Above T_m^0, $G_L < G_S$, below T_m^0, $G_S < G_L$. Therefore, at higher crystallization temperatures, ΔG begins to favor the melt more, which is the reason polymer crystals melt. The ΔG is a

function of both the change in enthalpy and change in entropy upon crystallization, meaning the stability of a particular phase is a function of both H and S. During the crystallization process, at a given crystal thickness, there is an amount of heat associated with a polymer stem attaching itself and snapping into crystallographic registry. There is also a loss of entropy associated with that particular length of molecule crystallizing. If a defect is incorporated into the crystal, the heat released will decrease, while the change in entropy of that length of molecule is very nearly the same. The net result of the defect being present in the crystal causes the solid phase to be less stable since the overall ΔG will not decrease to the level that it would had the defect not been present. At crystallization temperatures approaching T_m^0, the value of G of the melt and crystal are very similar. If a defect is present in a crystallizing chain, a reduction in the heat of fusion due to the presence of a defect could cause that chain to not crystallize, a result of the liquid phase being more stable than the crystal. This would, in turn, cause the growth front to sort through regions of molecules until a segment of a molecule is found, similar to the lamellae thickness, free of defects. This sorting process is sure to involve polymer chain deposition and removal. The removal process, essentially a back reaction, would cause the observed spherulitic growth rate to decrease.

4.1.4 Discussion of the T_m^0 of α-iPP

Polymer solution thermodynamics, to a very large extent, was first developed by Flory and coworkers[114-117,219-222]. The thermodynamic relationships of interest, those pertaining to atacticity, copolymerization and configurational defects have been developed from the theory of melting point depression. The change in melting point

occurs due to a difference in chemical potential of the various chemical species in the system under consideration.

In general, the chemical potential of a substance J in a given phase is defined as:

$$(4.3) \qquad \mu_J = \left(\frac{\partial G}{\partial n_J} \right)_{p,T,n'}$$

where G is the Gibbs free energy, p is pressure, T is temperature, n is the number of moles. The subscript n' signifies the amount of other components in the system. When equilibrium is present between the crystal and liquid phases of the polymer, the chemical potential of the polymer repeat unit in the two phases must be equal $\mu_u^l = \mu_u^c$. This thermodynamic relationship defines the melting temperature (T_m) of the mixture, which varies with the composition of the liquid phase. If a diluent is present in the liquid phase, T_m is the temperature at which the composition is a saturated solution. In a pure liquid polymer $\mu_u^l \equiv \mu_u^0$, where μ_u^0 is the chemical potential in the standard state of the pure liquid. At the equilibrium melting point (T_m^0) of the pure polymer, $\mu_u^0 = \mu_u^c$. In the presence of impurities, μ_u^l will be less than μ_u^0. After the addition of a diluent (impurities dilute the pure polymer), μ_u^l will be less than μ_u^0. At the previous value of T_m^0, $\mu_u^l < \mu_u^c$ which necessitates a decrease in temperature to reestablish equilibrium $\mu_u^l = \mu_u^c$, after addition of the diluent. Thus, the decrease in equilibrium melting temperature with addition of impurities results from a change in free energy associated with the dilution of the pure liquid polymer at the same temperature and pressure.

The impurity/melting temperature depression relationship has been applied to situations where there is a non-crystallizable diluent, which can be a small molecule

solvent, a polymer blend, polymer chain end groups and copolymerization. This discussion shall concern diluent and copolymerization effects. Configurational defects are treated in a similar manner as copolymerization, as explained below.

Diluent: For the case of a diluent at equilibrium with the crystalline polymer ($T = T_m^0$, $\mu_u^c - \mu_u^0 = \mu_u^l - \mu_u^0$), the Flory-Huggins expression is:

$$(4.4) \qquad \frac{1}{T_m} - \frac{1}{T_m^0} = \frac{R}{\Delta H_u} \frac{V_u}{V_1}\left[(1 - v_2) - \chi_1(1 - v_2)^2\right]$$

where V is the molar volumes of the chain repeat unit (subscript u) and diluent (subscript 1), χ is the Flory-Huggins interaction parameter and v_2 is the volume fraction of the crystallizable polymer in the mixture and $T_m°$ is the equilibrium melting temperature of the homopolymer. Using the solubility parameter concept, χ can be obtained using[223-225]:

$$(4.5) \qquad \chi = \frac{V_r}{RT}(\delta_1 - \delta_2)^2$$

where δ_1 and δ_2 are the solubility parameters (square of the cohesive energy density) of the two components, and V_r is the reference volume. The solubility parameter concept is based on a set of molar attraction constants that allow solubility to be approximated. If the two components form an ideal solution, or the diluent is present in small concentrations, equation 4.4 reduces to the copolymerization expression below.

Copolymerization: In a copolymer consisting of A units which crystallize and B units that do not crystallize, with the two units occurring in random sequence along the chain, the presence of B units depresses the melting point according to :

$$(4.6) \qquad \frac{1}{T_m} - \frac{1}{T_m^0} = \frac{R}{\Delta H_u}\ln X_A$$

where X_A is the mole fraction of A units in the random copolymer. Equation 4.6 holds only if the copolymer units are distributed at random along the polymer chains. If the A and B units of a copolymer occur in separate sequences, the melting point depression will be less than predicted by equation 4.6. If the B units tend to alternate with the A units along the chain, the melting depression will be greater.

According to Flory's original description[219] of what is classified as a copolymer, vinyl polymers that possess asymmetric carbon atoms consist of mixtures of d and l structural units. A rigorous application would include iPP as a copolymer.

Resin Defect Type and Content

The molecular weight distributions for the resins used in this study are narrow with all materials having a relatively high degree of polymerization, as shown in Table 3.1. Resin M100 has the lowest degree of polymerization (M_n), with an average of 1298 monomeric units. Therefore, the effects of chain ends can be neglected, as the maximum depression will be 0.4K when considering chain ends as defects[219].

The thermal properties for these materials were given in Table 3.2. The Ziegler-Natta catalyzed homopolymer resins have the highest observed peak melting temperatures, with the miPP homopolymers having significantly lower melting temperatures. The copolymer (ZN-5RCP) has an even lower peak melting temperature than the miPP resins, by roughly 10K. The melting enthalpy follows the same trend as melting temperature. The T_m^0 for each resin has already been determined, as was shown in Figures 4.24-4.28, with the exception of the copolymer. ZNHT, M22 and M32 all have extrapolated T_m^0 values of 186±2°C, while the other materials fall below 186°C. The

copolymer has the lowest T_m^0 at $151\pm2°C$, as determined by the Hoffman-Weeks method. One interesting finding is that ZN35 has the lowest homopolymer T_m^0, despite having the second highest peak melting temperature.

Stereoregularity and xylene solubles data are shown in Table 3.3. The copolymer contains 5.91 weight% ethylene, of which 79% can be found in -PPPEPPP- sequences. The mole fraction of meso diads is very similar for all materials. The difference between the highest and lowest mole fraction of meso diads is roughly 1%. The average meso run length is determined by the number of defects per 10,000 monomeric units. The zniPP homopolymer and copolymer resins had the fewest configurational defects, which we define as stereo and regio insertion errors during polymerization. It is also worth noting that the miPP resins have stereo and regio defects and that their total configurational defect level is twice that of the zniPP homopolymer resins.

Influence of Defect Type and Content

<u>Xylene Insolubles or Diluents</u>

Atactic polypropylene (aPP) and iPP are soluble in all proportions under most experimental conditions in the liquid melt. Recent work[226] has determined that aPP has a value of $\delta=15.14M\text{-}Pa^{0.5}$ and iPP has a value of $\delta=15.11M\text{-}Pa^{0.5}$. When $|\Delta\delta|<2$, solutions usually form. The solubility parameters for iPP and aPP are extremely close, which allows the use of an ideal solution for an aPP/iPP blend[218,226]. Therefore, we shall treat the xylene solubles fraction as a diluent and use equation 4.6 directly as the limiting form for the diluent relationship.

The mole fraction of diluent for each resin is calculated and tabulated in Table 4.7.

Table 4.7 Mole fraction of substituent defects of resins in T_m^0 study.

Sample Code	X_B (mole fraction defects)		
	diluent	copolymer	configurational
M10	0.0060	0	0.0219
M22	0.0036	0	0.0224
M32	0.0035	0	0.0248
ZN35	0.0362	0	0.0226
ZNHT	0.0030	0	0.0160
M100	0.0133	0	0.0262
ZN-5RCP	0.0672	0.073	0.0173

Copolymerization

For the case of iPP copolymerized with PE, the assumption is made that PE units are preferentially rejected from the growth front under most crystallization conditions. The samples in this study were crystallized slowly at high crystallization temperatures, an environment which should reduce or prevent any defect incorporation into the crystal. This is not without fault[227-231], experimental results have shown that at high cooling rates or under quench conditions some defect inclusion can occur due to kinetic reasons.

The mole percent ethylene content for the copolymer is calculated and given in Table 4.7.

Configurational Defects

Isotactic polypropylene can be treated as a copolymer consisting of meso and racemic diads[45,219]. Defects found (ignoring branching) in zniPP resins are stereo, while miPP resins have both regio and stereo defects. There has been no direct experimental evidence to show rejection of configurational defects during the crystallization process in iPP. However, it seems most probable based on the knowledge that configurational defects disrupt the helical structure of an iPP chain. Regio defects would seem to be even more disruptive to the helix, due to severe methyl group repulsion.

The mole percent configurational defects is given in Table 4.7.

Calculations

The mole fraction of crystallizable units is defined as X_A and non-crystallizable units X_B. X_B is the total mole fraction non-crystallizable units, combining diluent, copolymer and configurational defects for each resin:

$$(4.7) \qquad X_B = X_{diluent} + X_{copolymer} + X_{configurational}$$

211
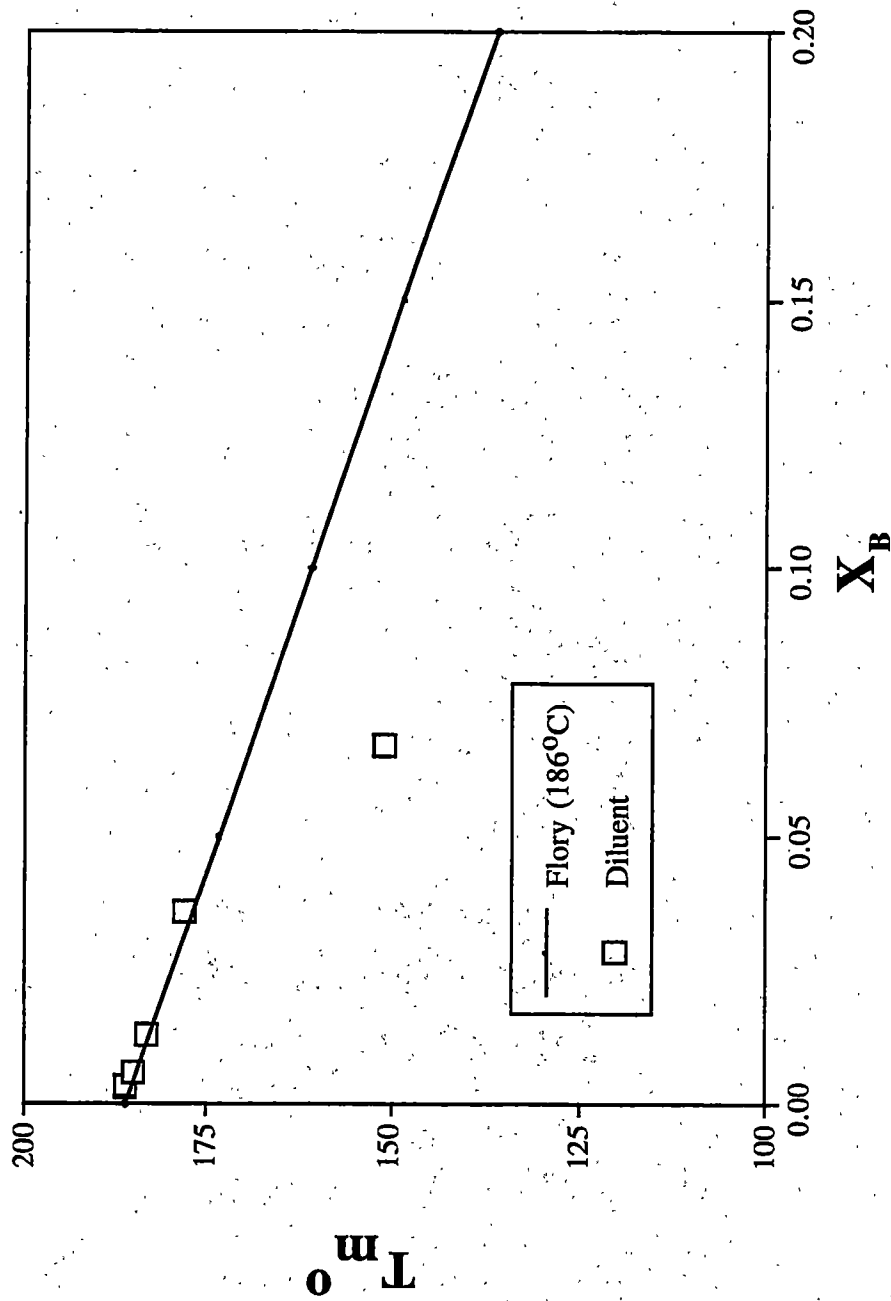
Figure 4.31 T_m^0 versus mole fraction diluent content.
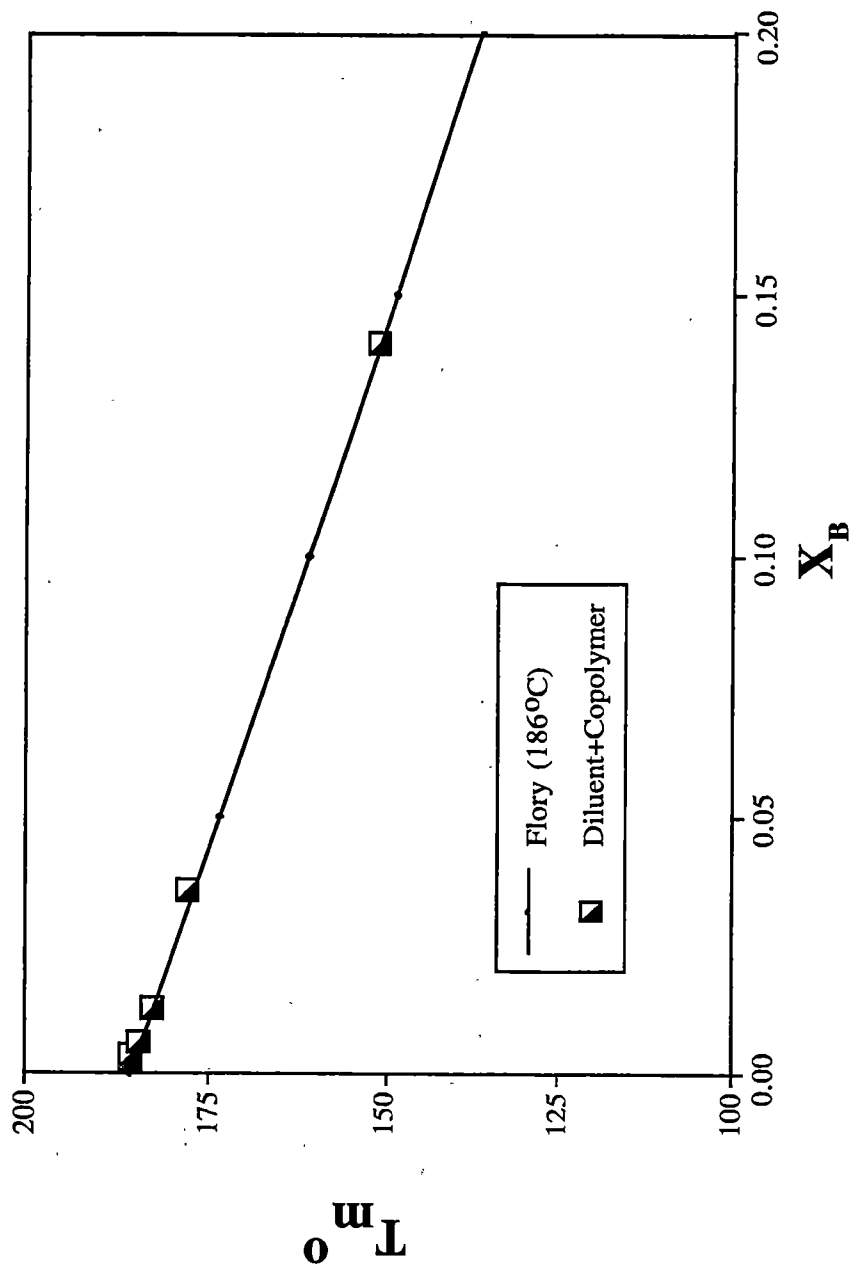
Figure 4.32 $T_m^{\,0}$ versus mole fraction diluent and comonomer content.
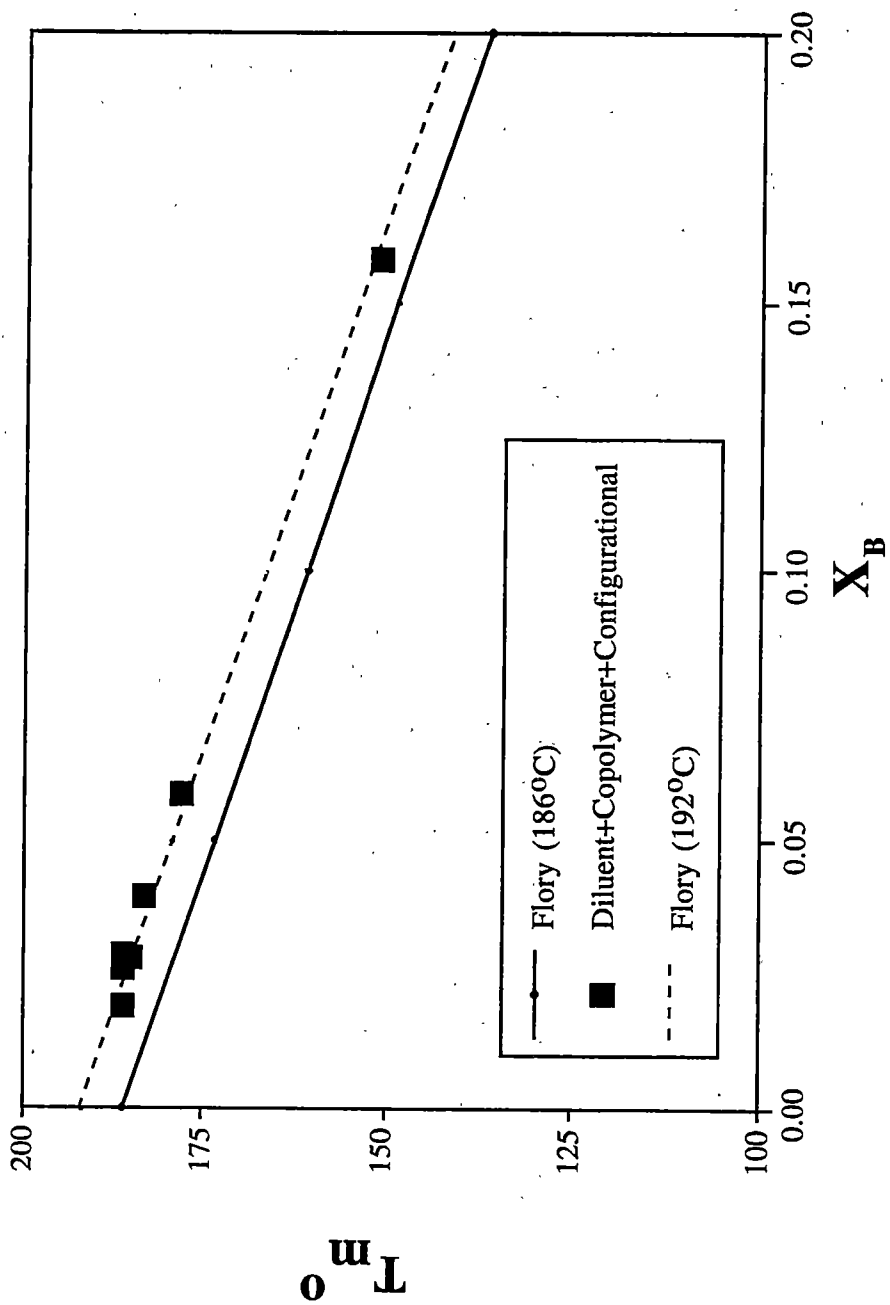
Figure 4.33 T_m^{o} versus mole fraction total defect content.

214

Using this approach, the calculations in Figures 4.31-4.33 show the relationship between Flory's melting depression relationship with experimental equilibrium melting temperatures as a function of molar defect content. The data are plotted as T_m^0 vs X_B, where X_B consists of just the diluent portion in Figure 4.31 for each material. The experimentally determined T_m^0 is plotted on the abscissa. In Figure 4.32, X_B includes both the diluent and copolymer content. Figure 4.33 includes diluent, copolymer content and configurational defects. In each case, the solid line is the theoretical prediction using Flory's method. For the calculation of Flory's prediction, a T_m^0 of 186°C was used. The heat of fusion (ΔH_f) was assumed to be 167J/g, based on experimental results on these same samples.

Flory noted that defect impurities less than 1 mole percent, will not likely effect T_m^0 appreciably, due to the low ΔH_f found in most polymers[219].

<u>Diluent</u>

When considering only the diluent effect for each resin, the comparison between theory and experiment are close for the homopolymers. However, the theory does not accurately predict the copolymer melting value.

<u>Copolymer</u>

The effects of diluent and copolymer together are predicted very accurately by the Flory theory, as shown in Figure 4.32. All data points fall on the theoretical prediction using the Flory treatment.

The mole percent ethylene has been modified from the original total of 5.91 weight percent. This was necessary due to only 79% of the ethylene units being isolated

among blocks of propylene units. The exact distribution is not known for all ethylene units, therefore, we split the difference and used an aggregate of 5.32% as the portion contributing to the *effective* random copolymer content.

Configurational

When all defects (i.e. diluent, copolymer and configurational) are included in the molar defect fraction calculation, none of the experimental points lie on the theoretical prediction line. Clearly, the theoretical prediction and experimental work disagree for these conditions. There are three possible reasons for the observed difference:

4. The ΔH_f used in the theoretical calculation is wrong.

5. The T_m^0 used in the calculation is wrong.

6. Another possible reason is that all previous researchers failed to account for configurational defects in their iPP resins.

We know that the ΔH_f is not the problem from experimental verification of ΔH_f on these resins, within experimental error, the ΔH_f is 167J/g. The equilibrium melting temperature of a highly isotactic α-iPP has been quoted in the literature as having two different values, 186°C and 210°C. Krigbaum[89], Miller[90], Campbell et. al.[91] report $T_m^{\,o}$ values of 186°C, while Fatou[92], Monnassee[93] and Fujiwara[94] report values near 210°C. Kamide and Yamaguchi[95-96] observed changes in melting temperature with crystallization time. The researchers observed that longer crystallization times lead to increased melting temperatures. This is now understood to be associated with lamellae thickening. Lamellae thickening increases as the crystallization temperature increases. Lamellae thickening is the most likely explanation for the two $T_m^{\,o}$ for α-iPP. Directly measuring

216

the lamellae thickness and making extrapolations to the T_m^o will decrease the error found in making extrapolations from the crystallization temperature alone[91], as we have done to obtain the T_m^o for our materials.

Only recently has stereoregularity information begun to appear with work associated with determining the T_m^o of iPP resins. It is quite possible that most highly isotactic iPP resins studied in the past have roughly the same amount of configurational defects, therefore all obtain similar T_m^o values.

A calculation using the mole percent configurational defects for each resin, with the corresponding melting temperature for each resin gives a defect free T_m^o for α-iPP of $192\pm2°C$, for each resin within experimental error. Using this new T_m^o for defect free α-iPP, Figures 4.33 shows the new theoretical prediction using Flory's model and the accuracy of the fit, indicated by the broken line.

The theoretical prediction for only diluent, as well as, diluent and copolymer defect content do not coincide with the experimental data, as it did using a T_m^o of 186°C for the diluent and copolymer defect plot. However, the new theoretical model does accurately fit the experimental data when all defect types are included. This would indicate that $192\pm2°C$ would be the experimentally determined T_m^o for defect free, high molecular weight α-iPP. This does imply that all previous experimental work is faulted, it means that previous investigators did not account for configurational defects that were present in all materials studied. These results would indicate that the T_m^o for all iPP determined thus far are for metastable crystals.

4.1.5 Fold Surface Free Energy

Using the value of 167 J/g for the value of ΔH_f for α-phase iPP, the fold surface free energy (σ_e) for the materials in this study can be evaluated. We have chosen to compute this for each crystallization condition, in order to show the variation in the result, rather than just from the slope of the T_m versus 1/ curve. The results are shown in Figure 4.34. The σ_e values for the γ-phase in the miPP resins are shown in Figure 4.35. In each case the appropriate T_m° and heat of fusion was used for the σ_e calculation.

The α- σ_e values for the miPP resins are similar to each other, but substantially higher than for the zniPP resins. The higher defect content M10 and M100 miPP resins have slightly higher α- σ_e values than M22 and M32. The data for all the miPP resins falls in the general order of increasing defects, increasing α- σ_e. However, on this basis, it would be expected that M100 should have the highest α- σ_e since it had the highest defect content of any of the homopolymers measured. The fact that it does not will be discussed below. The γ- σ_e values for the miPP resins were slightly lower than their α- σ_e values, though the differences are only slightly outside experimental error. The α- σ_e values for the ZNHT resin is also substantially higher than for the ZN35 resin.

The results from this work indicate γ-structure has a slightly lower σ_e value when compared to the α-structure for the miPP resins. A likely explanation is the partial relief of stress in the γ-structure arising from the angle of inclination of the stems relative to the basal plane[241,242]. It is also clear from these findings that the miPP defects clearly influence the fold surface structure and increase the fold surface free energy for all miPP resins.

Figure 4.34 α-iPP σ$_e$ versus lamellae thickness.

219
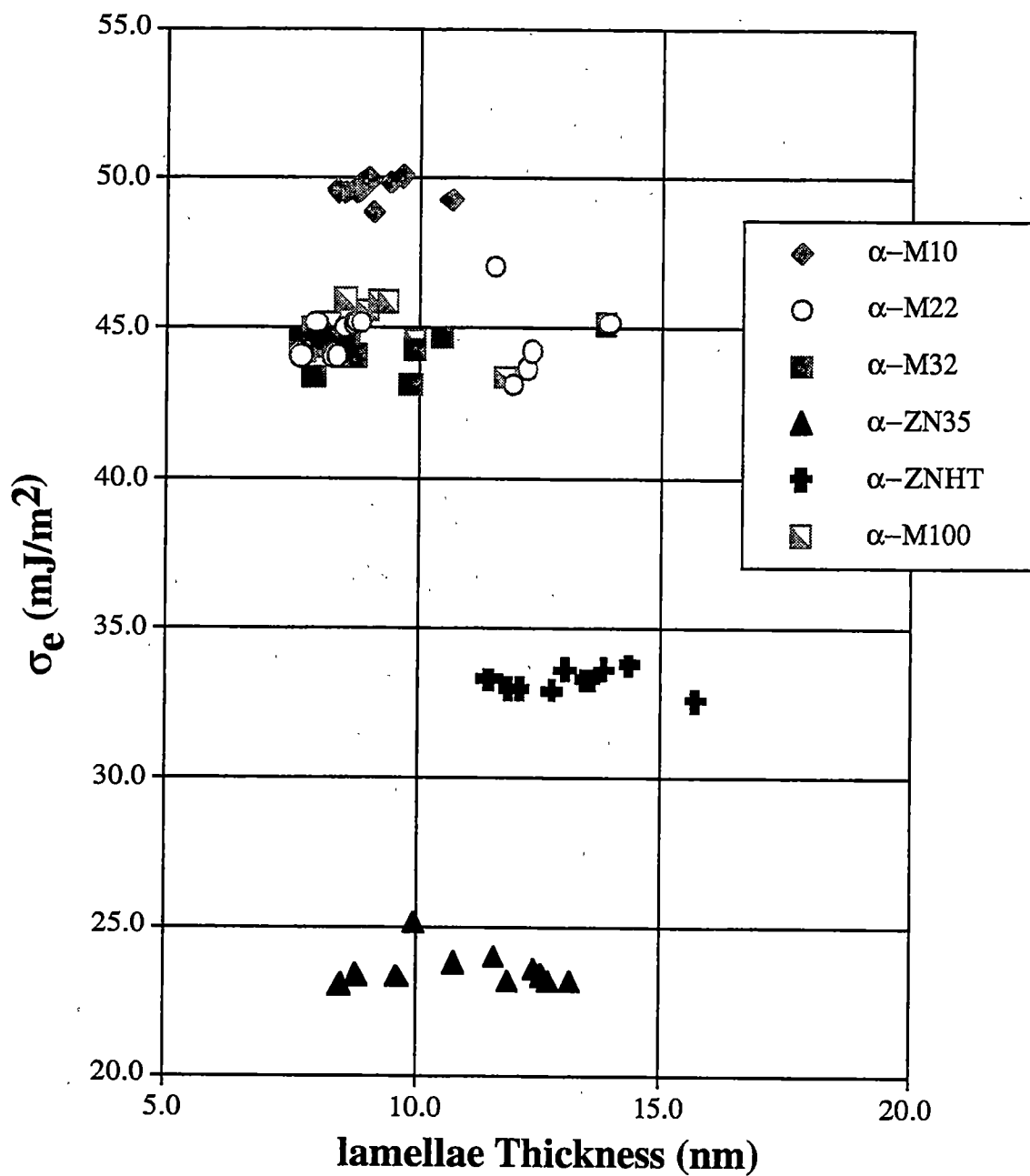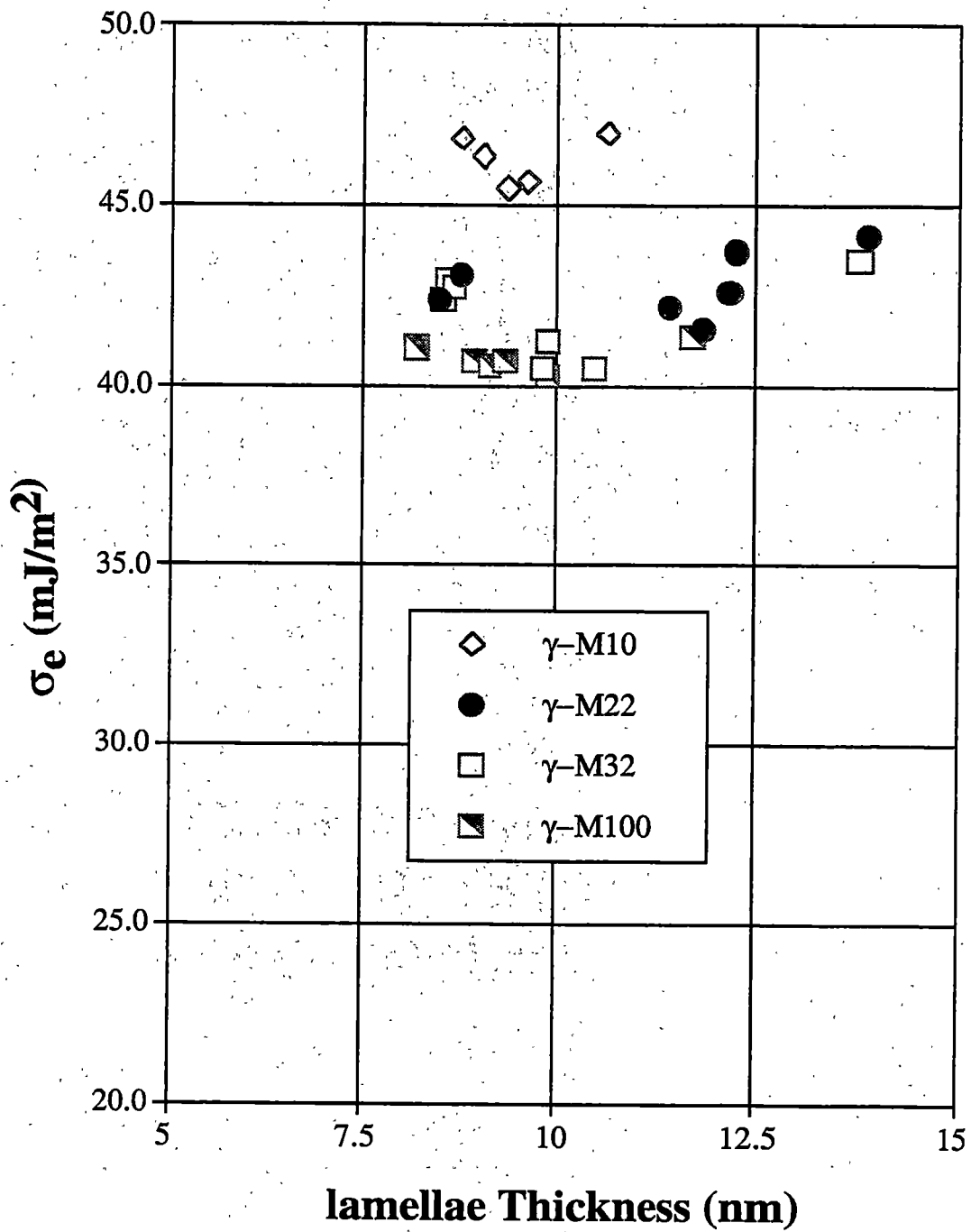
Figure 4.35 γ-iPP σ_e versus lamellae thickness.

The behavior of the Ziegler-Natta resins is also interesting. The behavior of ZNHT should be considered the standard against which the other iPP resins are compared since it has very few defects and a low xylene solubles content. The diluent present in ZN35 has clearly lowered the equilibrium melting temperature and σ_e value. M100 also has a significant portion of xylene solubles material, which may explain why its observed α- σ_e is lower than M10, even though it has more total defects. The nature of the fold surface/interfacial region and the influence of atactic material will be discussed further in section 4.5.

4.1.6 Nature of γ-Structure Formation

The γ-orthorhombic crystal structure of iPP is known to be formed in at least three different situations:

1) Low molecular weight material that has little or no chain folding[282].

2) iPP resins with defects in the chains, typically propylene ethylene copolymers and more recently in the present work and others with metallocene catalyzed iPP[13,24,27,31]. The mere presence of these defects may not be enough, as the samples must also be crystallized slowly, indicating lamellae thickness is important. These findings indicate there must not be only a thermodynamic driving force, but the crystallization kinetics must also be favorable.

3) The γ-structure is formed exclusively (as best can be determined) at high pressures in highly isotactic zniPP resins with little or no stereo defects or atactic material[233-234].

The proposal presented here is that these seemingly different situations where γ-iPP is formed have a common thermodynamic property, a higher fold surface free energy.

221

As will be discussed in section 4.5, the higher fold surface free energy likely results from a rough fold surface. Now we shall consider each situation using the concept of higher σ_e producing the γ-iPP crystal structure.

Case 1. Low molecular weight   Low molecular weight material that does not chain fold forms a high surface free energy system. Depending on where the cilia lie relative to the crystal surface, they may strongly influence the amount of interfacial or fold surface free energy. It is known that if the cilia protrude into the amorphous material the surface energy decreases. However, if the end is trapped near the surface in the interfacial region, it increases the surface free energy even higher than that found with tight chain folding[108,109].

As stated in the introduction, there are some differences between the α and γ-lamellae structures. In the α-lamellae, the crystallizing stems are nearly perpendicular to the basal planes of the crystal. In the γ-crystal, the chains are oriented at roughly a 40° angle to the basal plane (see Figure 2.7)[10,11,26]. The difference in stem to basal plane geometry means that a stem in a γ-crystal is approximately 1.3 times longer than the actual crystal thickness, dictating that more of the molecule is embedded in the crystal per unit crystal thickness for γ-iPP. Longer stem lengths embedded in the crystal would seem to counteract a higher fold surface free energy, since there is more enthalpy released in this γ-structure per unit crystal thickness than α-iPP, due to the longer γ stem length. It has also been shown in this work (see section 4.1.5) that γ- σ_e is slightly lower than α- σ_e.

The calculations shown in Figure 4.36 demonstrates the relationship in Gibbs free energy, the melting enthalpy and fold surface free energies between the α and γ crystal structures. The change in entropy from the melt for a α crystal is 0.364J/gK and 0.333J/gK for the γ crystal structure. These are determined from the equilibrium melting temperature and heat of fusion for each phase. The energies shown are for a single stem in each crystal structure, assuming the same crystal thickness for each crystal structure. The σ and σ_e values remain constant with a change in lamellae thickness (as was shown experimentally in Figures 4.34 and 4.35). The absolute value of the heat released increases as the crystal thickness increases. It is clear that the γ-crystal releases more heat than a comparable α-crystal of similar thickness (not stem length and not the same bulk volume), causing the Gibbs free energy to be slightly lower for the γ crystal structure, in agreement with theoretical packing energy calculations[243]. This is in spite of the α-enthalpy of fusion being approximately 10% higher (167J/g for the α-phase and 150J/g for the γ-phase). Therefore, from a thermodynamical standpoint, the γ crystal structure becomes the preferred structure thermodynamically, as crystal thickness increases.

Case 2. iPP with Chemical Defects The reason that zniPP resins have not previously produced amounts of γ-crystals in large amounts is likely due to the non-uniform distribution of these defects in bulk form. Recall in Figure 4.4, the WAXD patterns for the ZN35, that some γ-crystals are formed at relatively high crystallization temperatures. ZN35 has no regio defects, therefore, it is not a regio type defect that produces the γ-structure in this resin. In addition, there is also a small hump in the WAXD pattern of
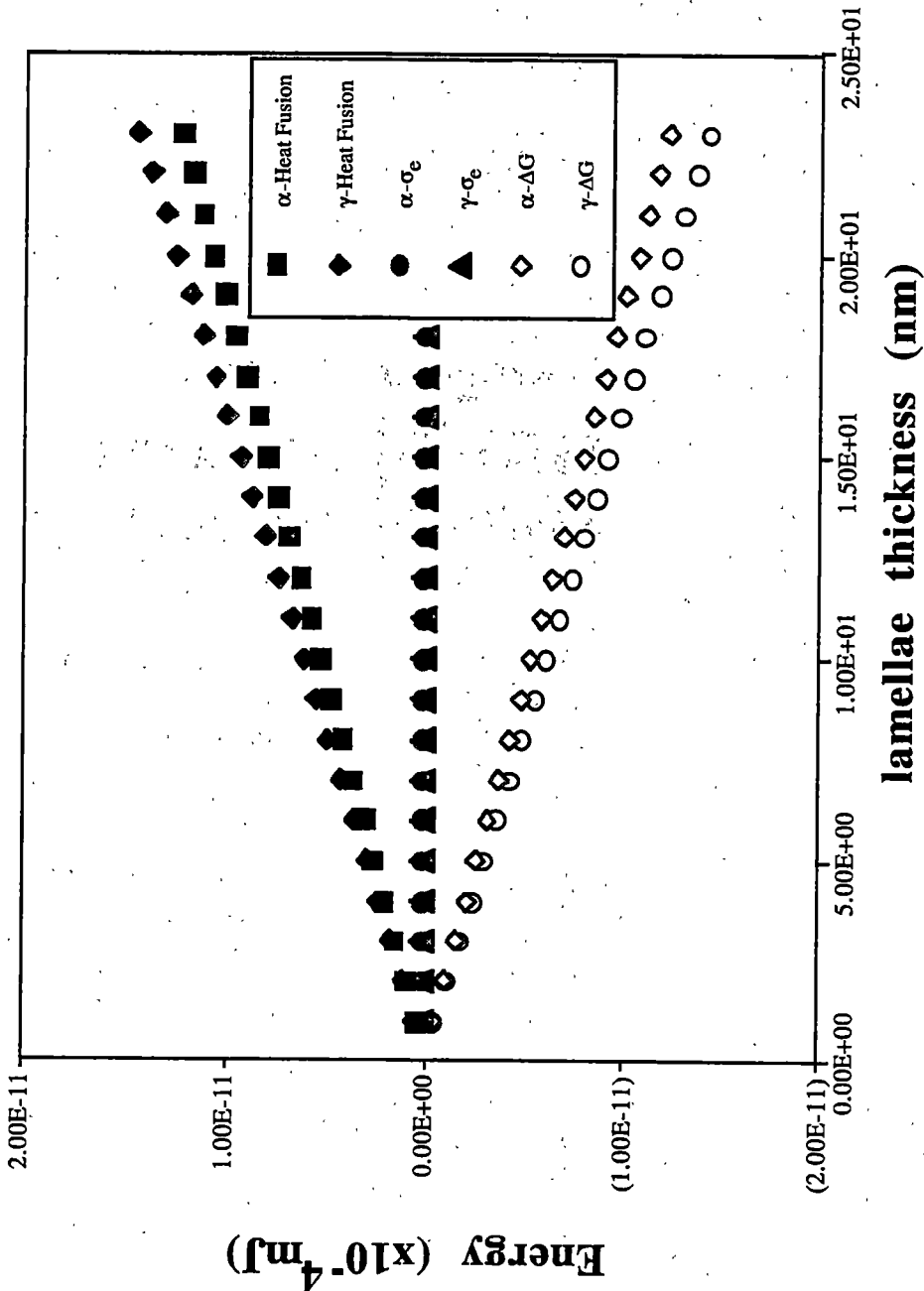
Figure 4.36 Single stem thermodynamic quantities versus lamellae thickness.

ZNHT (Figure 4.5) where the γ-crystal structure peak appears. The miPP resins clearly produce the γ-structure quite easily at moderate supercoolings. Other researchers[13,24,29,31] have also indicated it is not the nature of the defect in the chain, but the mere existence of the defects. Therefore, it is not the type of defect in the chain, but the number and distribution of defects within the polymer chains, along with any kinetic factors, that determine the formation of the γ-phase.

It has been clearly stated here and elsewhere that the distribution of defects is not uniform in zniPP resins. However, when copolymerized, the zniPP distribution of comonomer is much more uniform than the inherent tacticity defect distribution. Thus chains that are highly isotactic, except for comonomer defects occasionally can be synthesized. In a zniPP copolymer, the meso run length between comonomer defects is important in the formation of the γ-phase. Mezghani and others[13,24,29,31] have shown that zniPP propylene/ethylene copolymers easily produce γ-iPP at atmospheric pressure. The meso run length between defects also leads to an explanation of why the miPP resins produce the γ-structure.

The data in Tables 4.1 through 4.6 contain calculations for the α and γ stem length and requisite number of monomers to constitute a stem of that length. These values are calculated from the stem orientation to basal plane relationship and knowing that iPP is a 3/1 helix with repeat unit of 0.65nm. Recall the average meso run length for M22 is 68 monomers and 64 monomers for M32. The word "average" is used since the distribution of defects is not uniform, but is more uniform for miPP than zniPP, as discussed earlier. For M22, the shortest γ-stem length is 48 monomeric units and the longest is 84. The γ-stem lengths mean, statistically, that a defect will be located on at

225

least every molecule transverse through the crystal. If tight chain folding occurs, then a defect would be included in the crystal as that part of the molecule traverses the crystal due to the meso run length between defects. The samples in this study are not rapidly cooled, they are slowly crystallized isothermally and annealed at the crystallization temperature. Therefore, defect incorporation into the crystal matrix is not expected. In addition, the ΔH_f values do not suggest any defect incorporation. Studies and theory[79-83] have shown that as supercooling decreases, the amount of crystal defects also decreases. The meso run length between defects for the miPP resins is such that, if defect exclusion dominates, the basal plane folds would be necessarily loose. If the defects are trapped in the interfacial region, they can significantly raise the fold surface free energy[108,109]. As the crystal becomes thicker, the statistics are favorable for more and more defects to be trapped in the interfacial region.

Although not conclusive, the DSC crystallization of M22 at 140°C, as shown in Figure 4.9, may indicate the explanation of defect concentration in the fold surface produces the γ-phase. Crystallization at 140°C shows only one melting endotherm and would produce crystal thicknesses of approximately 15nm with γ-stem lengths of 19.58nm, a stem length that requires 90 monomers. Crystal thicknesses of this size would require that a defect be included in the crystal. Defect inclusion would be necessary to allow defects to be in the fold regions as the meso run lengths between defects is not long enough for a molecule segment to traverse the lamellae. There is also the possibility that all defects are included in the growing crystal structure and that internal crystalline defects generate the γ-structure. Based on the crystallization temperatures and ΔH_f results used in this study, crystal defect incorporation producing the

γ-crystal structure is not reasonable. The results may indicate that the chains with meso run lengths shorter than the crystal thickness do not crystallize, as the crystal thickness is too large. Therefore, the γ-crystal structure endotherm peak reduces in intensity in the melting endotherm after crystallization at 140°C.

Additionally, the mechanism presented here would explain why the γ-structure occurs at lower supercoolings. As the supercooling increases, the crystal thickness decreases, presenting statistically fewer opportunities for the defects to be in the critical fold surface region. The defects could be in the amorphous region or embedded in the crystal matrix.

<u>Case 3. High Pressure</u>   The application of a hydrostatic pressure to a polymer melt increases the density of the melt phase. The density of crystalline material also increases, but the change in relative density is higher for the amorphous state. The crystalline density does not change as much since the atoms are in crystallographic registry and compression of the crystalline matrix will meet with severe atomic repulsion. As the density in the melt increases, chain mobility decreases as the barriers to various thermal motions increase. Therefore, it may be expected that the crystal surface may become rough due to the limited mobility of the molecules as a result of the high pressure increasing the density of the noncrystalline material.

Another possible or additional increase in fold surface energy for this system may result from the application of the pressure on a growing crystal. The application of a pressure is felt throughout the body of the fluid that the pressure is acting on. Microscopically, the pressure exerted by a fluid on a surface in contact with it is caused by collisions of molecules of the fluid with the surface which imparts energy onto the

surface. The energy will manifest itself and effect the region where crystallization is occurring, as it is the one undergoing the phase transformation. The pressure increase will affect both chain folding and the energy of the fold surface. Recall in Case 1, the γ-structure has a longer crystalline stem length embedded in the crystal per unit crystal thickness than the stems found in α-iPP. Again in a similar manner, the surface free energy is higher, so in order to compensate, the stem length increases to regain more energy through crystallizing (enthalpy release). Crystallization studies at elevated pressures have shown that as pressure is increased, the percent γ-iPP increases at the same crystallization temperature.

From the rational presented above, it would seem that the fold surface free energy must be higher during the crystallization process (perhaps a result of a rough surface in each case). This explanation can then be used to induce the formation of γ-iPP in the low molecular weight, high defect content and high pressure situations.

4.2 Crystallization Kinetics of Isothermally Crystallized Resins

Crystallization kinetics are an important polymer property that is highly influenced by the various molecular variables a polymer chain may possess. In crystallization studies, it is often necessary to separate the effects of nucleation and growth rates of a polymer sample. These two factors are combined in bulk analysis. However, bulk crystallization behavior gives a good approximation of the behavior a particular resin will exhibit in various applications. In this work, both isothermal bulk and crystal growth kinetics were investigated.

The results in Figures 4.37 and 4.38 show the various resins overall bulk isothermal crystallization kinetics as determined by crystallization half-time versus crystallization temperature and degree of supercooling, respectively. At a given temperature, ZNHT has by far the fastest crystallization half-time ($t_{1/2}$) followed by M100, ZN35, M10, M22 and M32. This is a rather interesting finding since this is not the order in which the resins go from fewest to most defects.

Plotted in terms of supercooling, the $t_{1/2}$ data show that the bulk rate of ZNHT is the fastest followed by ZN35, M100, M10, M22 and M32. These results do not correspond to the order of defect content for each material, except for the zniPP resins. In order to understand this result, the effects of nucleation and growth rates must be separated.

The plot in Figure 4.39 shows the linear growth rate of spherulites as a function of crystallization temperature. This work indicates that ZNHT had the fastest linear growth rate at a given crystallization temperature, followed by ZN35, M22, M32, M10 and M100. M10 and M100 had very similar linear growth rates, with M10 having a slightly higher rate, within experimental error. These growth rates fall in the order of fewest defect content (ZNHT) resin having the fastest linear growth, to the slowest linear growth rate belonging to the resin with the highest amount of configurational defects, M100. This result would be expected for polymers with configurational defects at high crystallization temperatures. The slower growth rate is due to the back stem reaction, as explained in section 2.4.3 and shown in Figure 2.29. This term dominates due to the loss of enthalpy from the presence of the defect at the growth front interface which allows the stem to back off the substrate more readily. Defects present in the growth front should
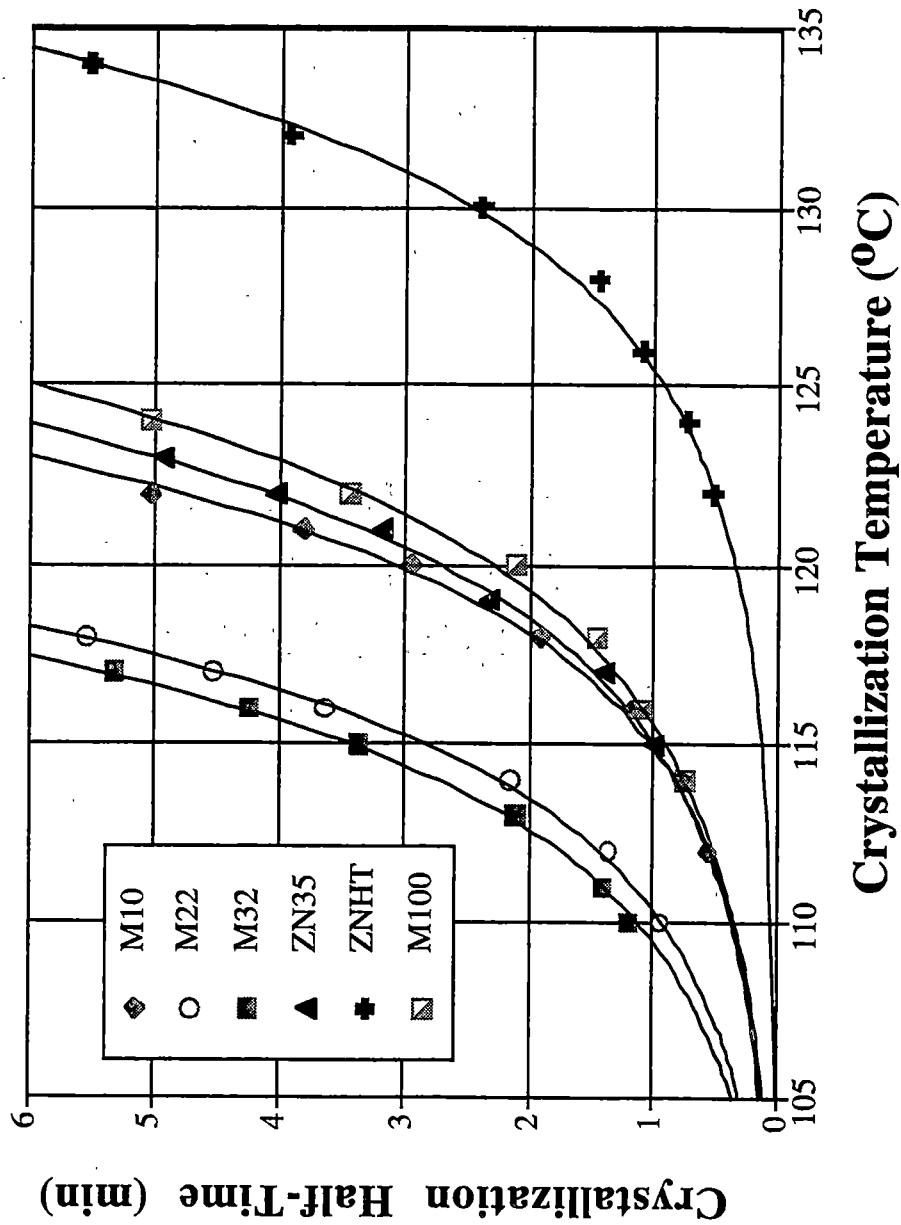
Figure 4.37 Isothermal crystallization half-time versus crystallization temperature.

230
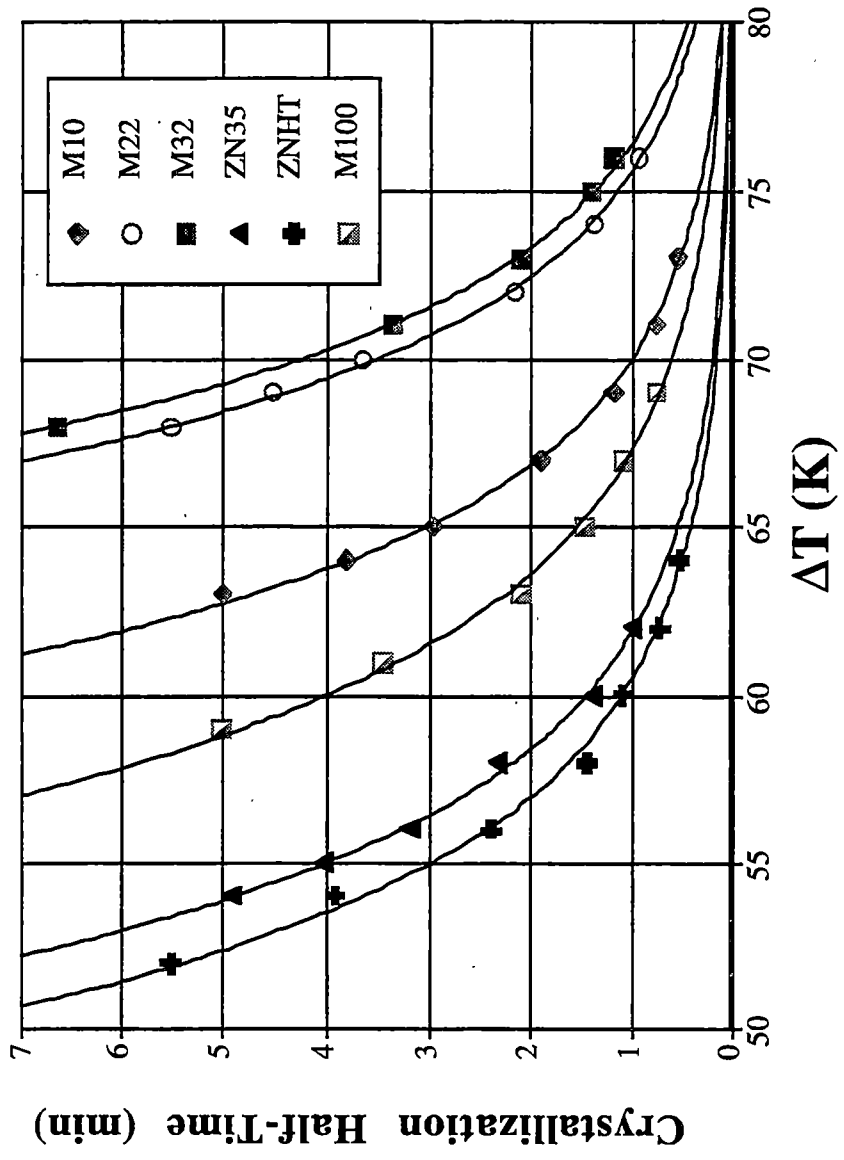
Figure 4.38 Isothermal crystallization half-time versus supercooling.
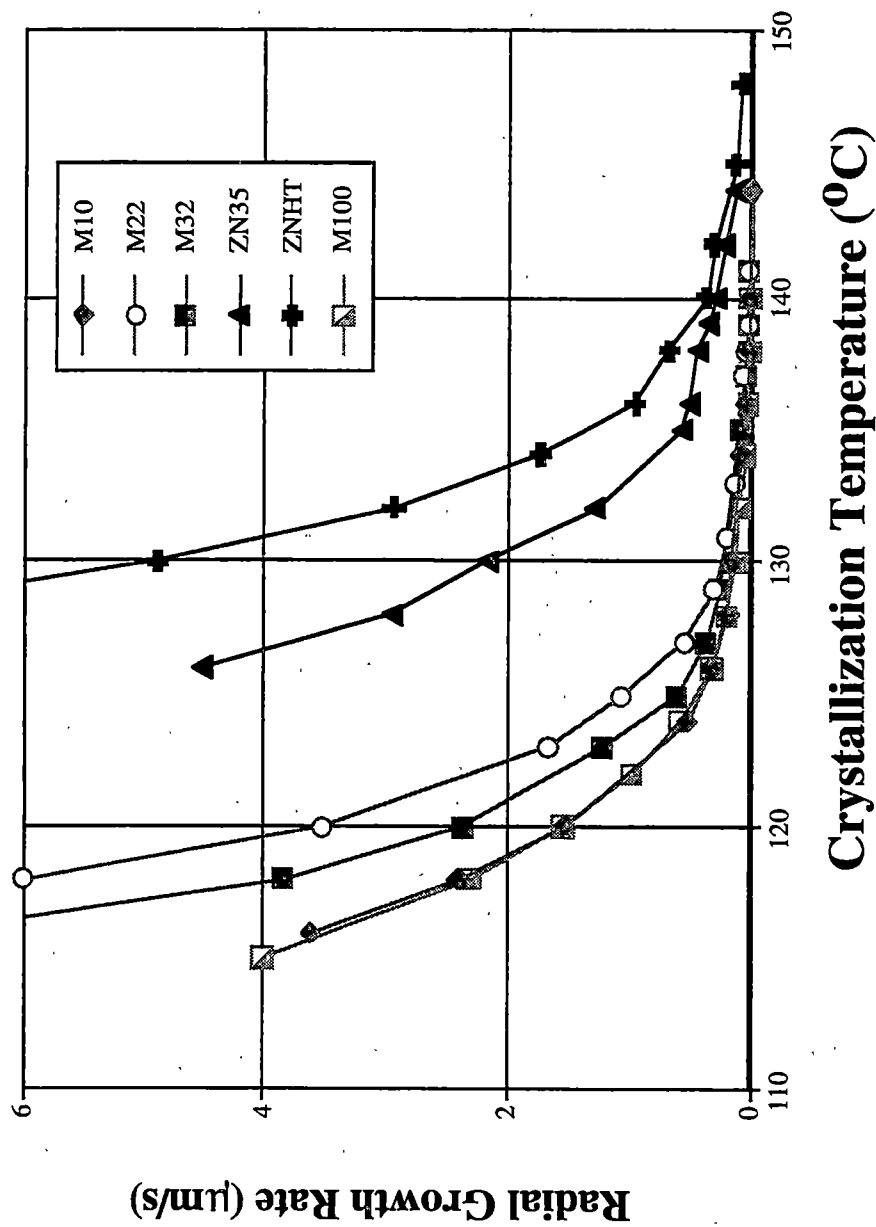
Figure 4.39 Isothermal spherulite growth rate versus crystallization temperature.

slow the macroscopically observed linear growth rate at higher crystallization temperatures, where the defects cause a lowering of the heat of fusion upon obtaining crystallographic registry. The lowering of the heat of fusion may be significant enough at higher crystallization temperatures that the just added stem becomes more stable in the melt than the crystal, due to the ΔG favoring the melt over the crystal. This will cause that stem to back off in part or total from the crystal. This was briefly discussed at the end of section 4.1.3.

When the linear growth rates are plotted against supercooling, ZN35 has the highest growth rate. This is shown in Figure 4.40. ZN35 is followed by ZNHT, with the group of miPP resins packed closely together. Within the miPP resins, M22 was the fastest with M32 and M100 virtually identical and slightly slower than M22, with M10 the slowest. These thermodynamically adjusted growth rates agree with those found in linear growth rates versus crystallization temperature except for the behavior of ZN35 and M100.

There is one common factor between ZN35 and M100 that may explain their thermodynamically adjusted linear growth rate behavior. Both of the resins contain a significant amount of xylene solubles material that was shown to lower the equilibrium melting temperature for each resin in an amount proportional to the xylene solubles material. It was stated that xylene solubles material acts as a diluent, thereby lowering the observed T_m°. Studies have shown that noncrystallizable material present in a crystallizable polymer (such as iPP) will slow the observed linear growth rates. However, most of these studies have used large fractions of noncrystallizable material and the amounts of non-crystallizable material present in this work is smaller. Therefore,

233
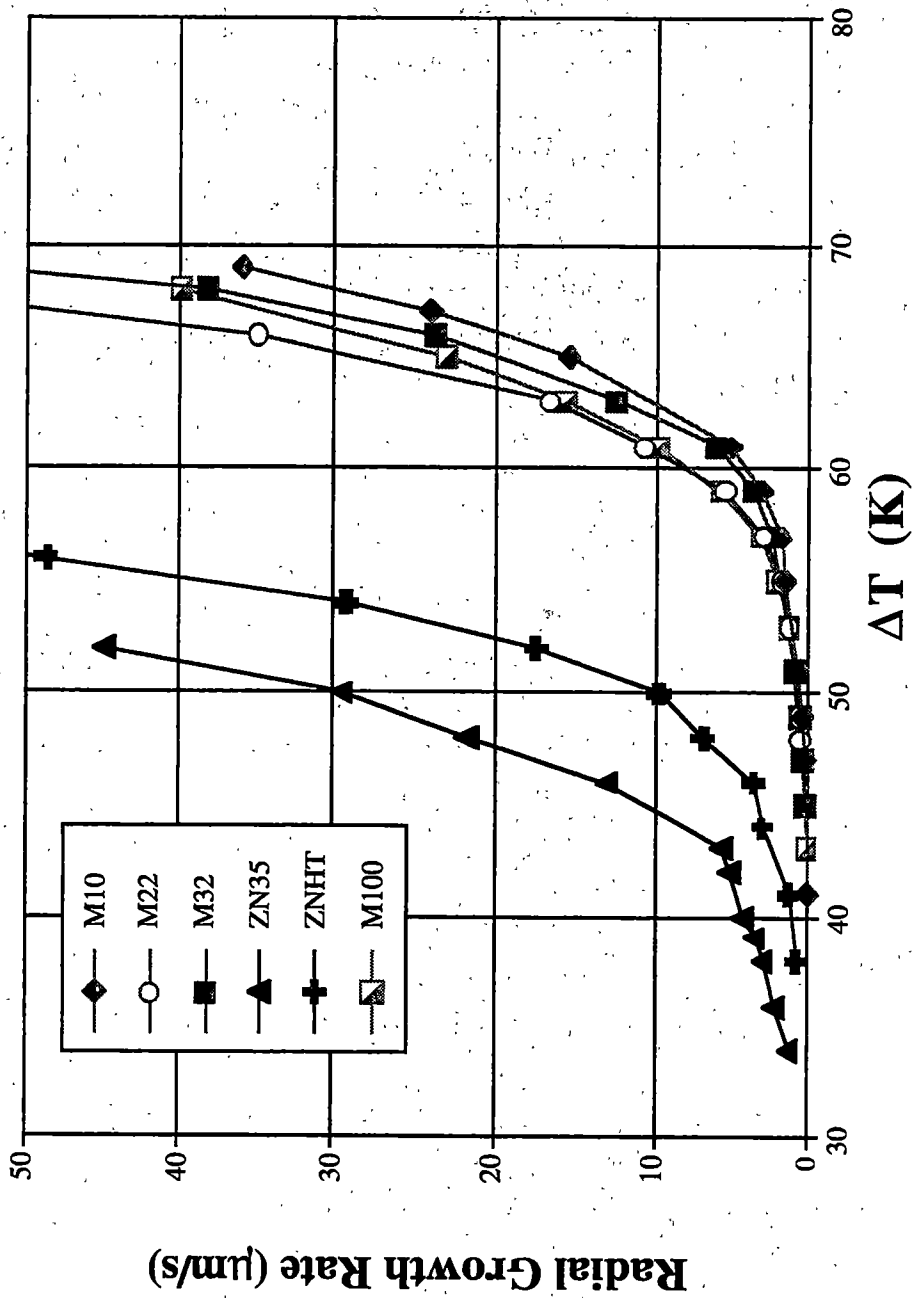
Figure 4.40   Isothermal spherulite growth rate versus supercooling.

the amount of xylene soluble material for ZN35 and M100 may not significantly decrease the linear growth rates in relation to its effect on the depression of the T_m° due to the diluent effect at the levels of xylene soluble material in this study. This then would explain why ZN35 and M100 have the observed linear growth rates when adjusted for supercooling, which raises the question concerning the validity of studying growth rates as a function of supercooling.

The experimentally determined nucleation density (N) for each material is shown in Figure 4.41. The nucleation density is the total number of primary nuclei of the sample, in an area over all time using a given sample thickness. In reality, unless the sample thickness is very thin, the observed nucleation density is only for the nuclei in the field of focus at the time of observation. If the sample thickness is quite large, the reported N will be much smaller than the actual N for that sample. In order to minimize this error, each sample used was made as thin as possible, typically 50-70μm. For the present purpose of comparing the nucleation process in these different resins, we believe that this approach is satisfactory, though the overall number densities of nuclei may be somewhat in error.

M100 has the highest nucleation density, followed by M10, ZN35, ZNHT, M22 and M32. It is difficult to make any conclusions about the polymer characteristics on the nucleation rate from these results since the nucleation mechanism for iPP is usually heterogeneous with all nuclei appearing at approximately the same time under isothermal conditions due to foreign matter present in the sample nucleating spherulites. Unless samples are highly purified, it is unreasonable to presume the origin of nuclei is anything other than foreign objects. The resins in this study are all production grade type materials
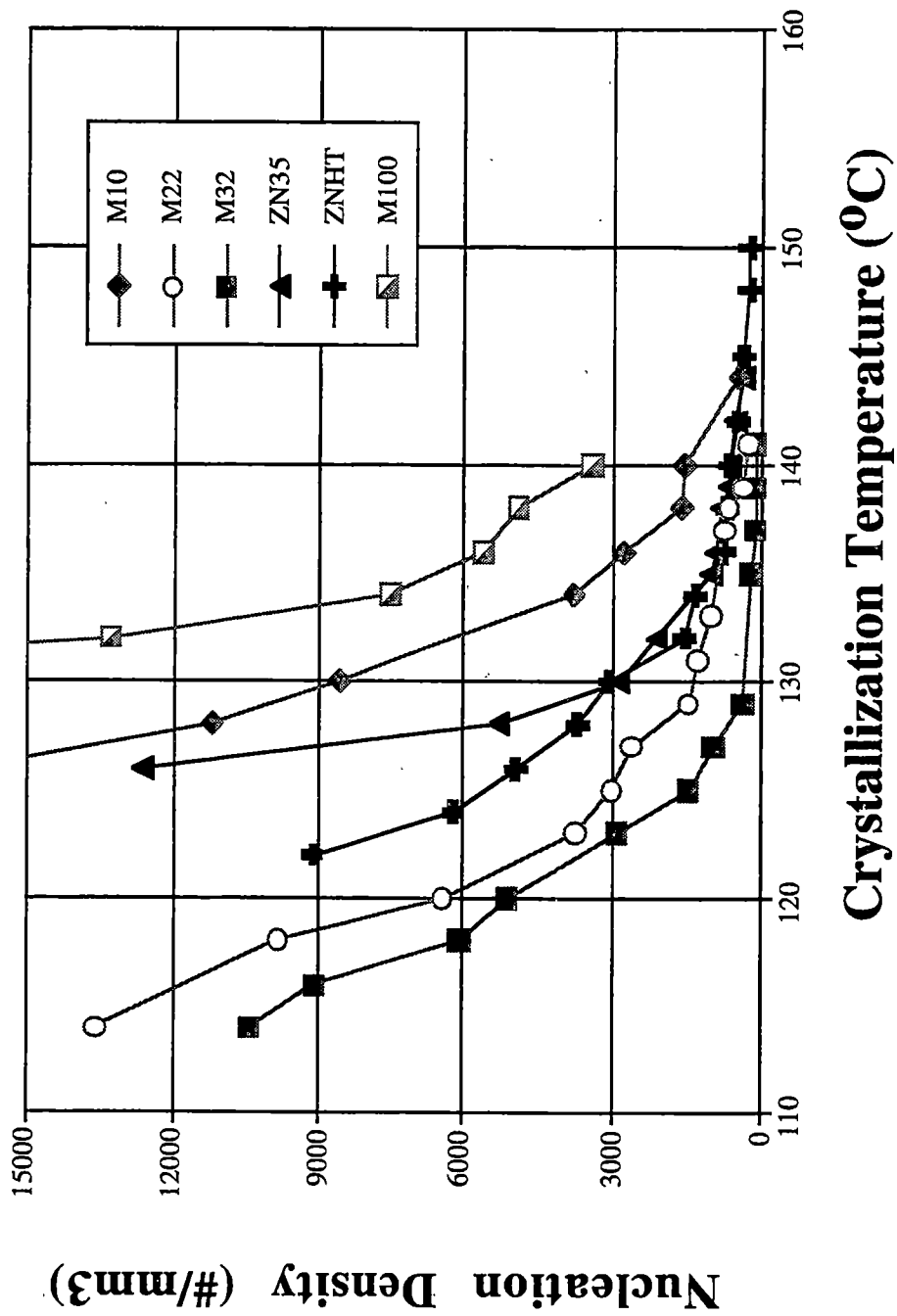
Figure 4.41 Isothermal nucleation density versus crystallization temperature.
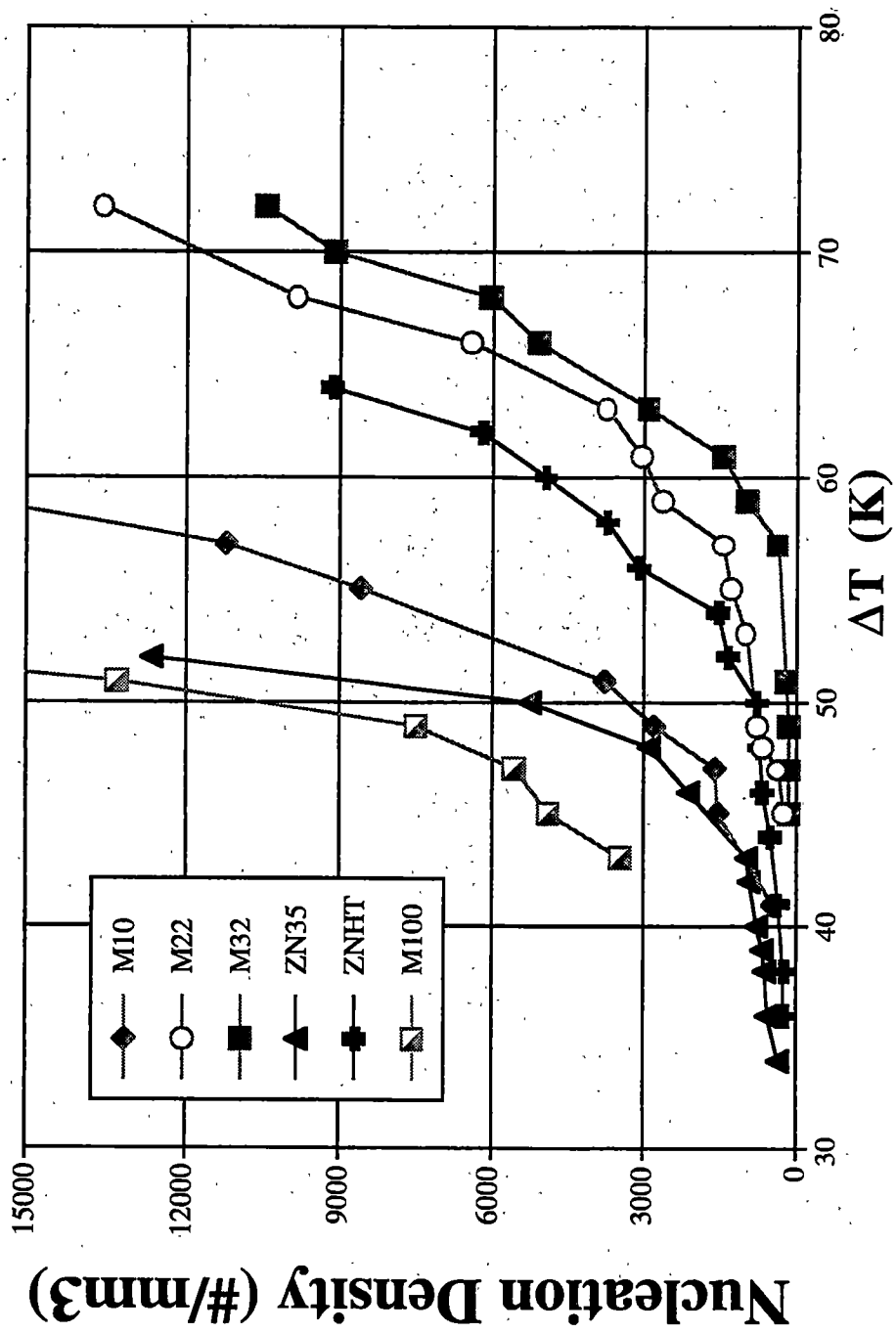
Figure 4.42 Isothermal nucleation density versus supercooling.

237

that surely contain a significant amount of additives, which may act as nucleating agents. However, to overlook the contribution of the nucleation density to bulk kinetics would be factually incorrect, as the data in Figure 4.37 show.

The results here show that the observed linear growth rates follow the order for each material of most defect free resin (ZNHT) having the highest linear growth rate to the resins containing the most defects (M100) having the lowest linear growth rates. Therefore the explanation for the bulk crystallization half-time behavior must be attributed to the differences in nucleation density for each material. If a resin has a higher nucleation density, it will form more nuclei per unit volume than another material. Producing more nuclei in the same volume as another resin will accelerate the bulk observed kinetics, with all other factors the same. So, if the resin with the lower linear growth rate has a higher nucleation density, the effect of more nuclei per unit volume can make it crystallize faster than the other resin with a lower nucleation density, but with a higher linear growth rate. This is the explanation for the observed trend in the crystallization half-time versus crystallization temperature plot (Figure 4.37).

The major point to be learned from this is that it is the combination of nucleation and linear growth rates together that dictate the overall bulk crystallization rate.

4.2.1 Regime Analysis for α-iPP

The use of the secondary nucleation rate analysis for understanding the microscopic activity of chain folding and observed linear growth rates has provided a technique for interpreting experimental findings for scientific and industrial use. Recently, Hoffman and Miller[108] updated their original theory and some of the changes

238

will be used in this work. The differences used in this work will be pointed out and discussed as needed.

The linear growth rate is now expressed as[108]:

$$(4.8) \qquad G = G_0 e^{\left(\frac{-Q_D}{RT}\right)} e^{\left(\frac{-K_g}{T\Delta Tf}\right)}$$

where the changes have occurred in the first exponential or the diffusion term. T is still the crystallization temperature and Q_D is the observed activation energy for centre-of-mass diffusion, which is 5736cal/mol for PE. We will use 5736cal/mol[108] for iPP also. The analysis is then carried out as outlined in section 2.4.2.2.

In order to identify a regime transition, it is best to plot ln G versus either the supercooling or crystallization temperature[108]. This is illustrated for ZN35 in Figure 4.43. The transition is clearly seen as occurring at 43.2K supercooling. A similar procedure was performed on all resins to ensure that the a true regime transition had occurred.

The results in Figure 4.44 show a regime plot for M10. The Roman numeral subscript indicates the regime operating in the crystallization process. Previous studies[111,114] for high molecular weight iPP have operated in Regime II and III under similar crystallization temperatures. Also the slope of the region indicated as regime III has nearly twice the slope of the other region indicated as regime II. These facts combined make the assertion of the operating regime for this resin as II and III highly certain. A similar procedure was performed on all resins and the results are shown in Table 4.8. Figure 4.45 shows all the resins on a single regime plot.

The regime transition temperature for ZNHT occurs at a ΔT of 48K, in agreement with earlier work for high molecular weight iPP[111]. As stated previously, the
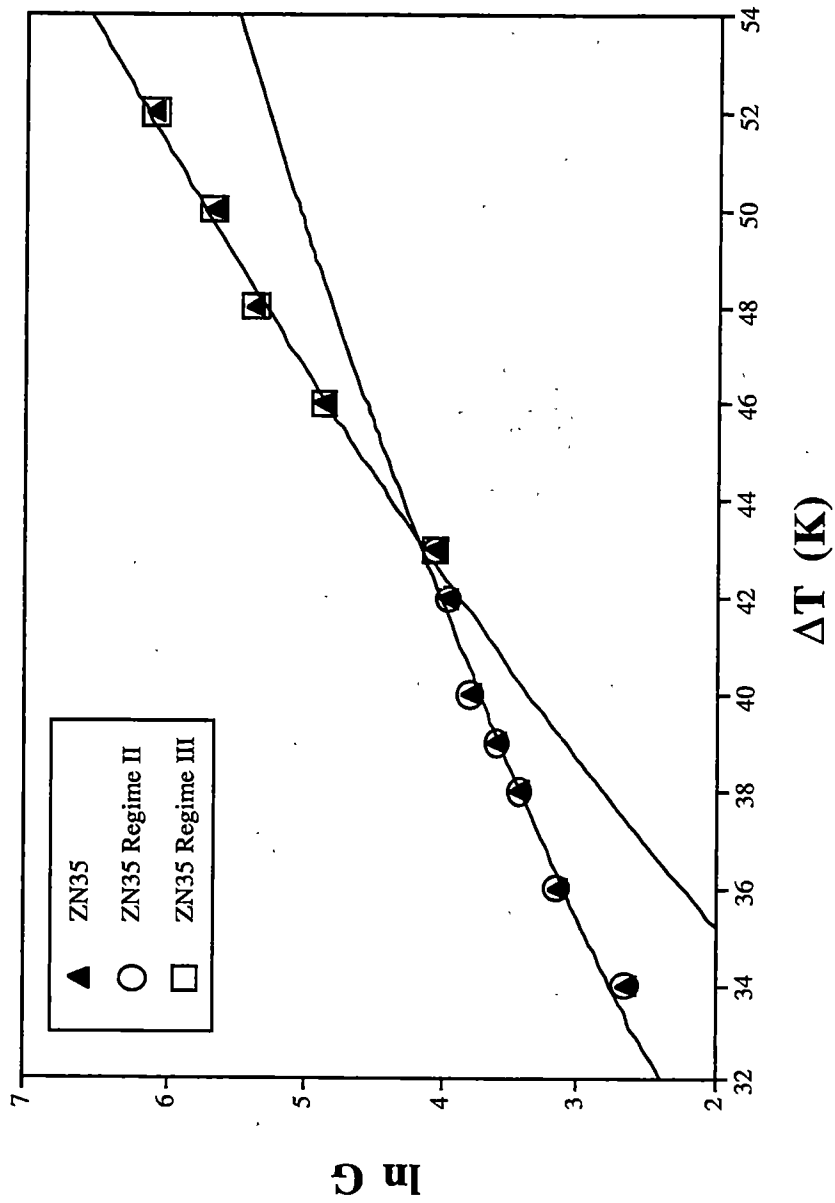
Figure 4.43 ZN35 regime II-III transition temperature at a supercooling of 43.2K.
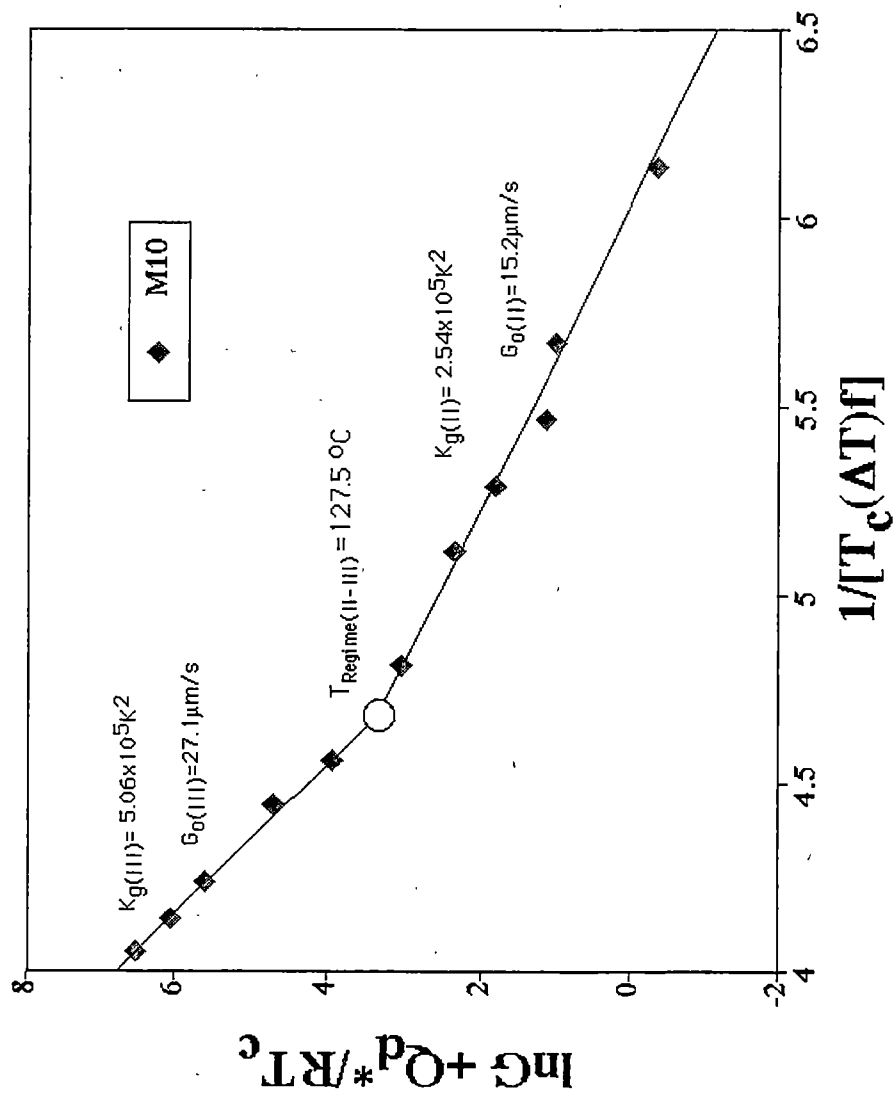
Figure 4.44 M10 Secondary nucleation analysis in regime II and III.

Table 4.8 K_g and G_o determined from regime analysis for α-iPP in regime II and III.

Resin	T_{II-III} (°C)	Regime II K_g (x10^{-5}K^2)	Regime II G_o (μm/s)	Regime III K_g (x10^{-5}K^2)	Regime III G_o (μm/s)	$K_g(III)/K_g(II)$
M10	127.5	2.54	15.2	5.06	27.1	1.99
M22	129.4	2.83	16.5	5.30	28.8	1.87
M32	128.0	2.55	16.0	5.29	27.9	2.08
ZN35	134.5	1.20	11.5	2.51	18.8	2.09
ZNHT	138.1	1.81	14.5	3.81	24.5	2.10
M100	127.3	2.53	15.5	4.96	27.2	1.96

242
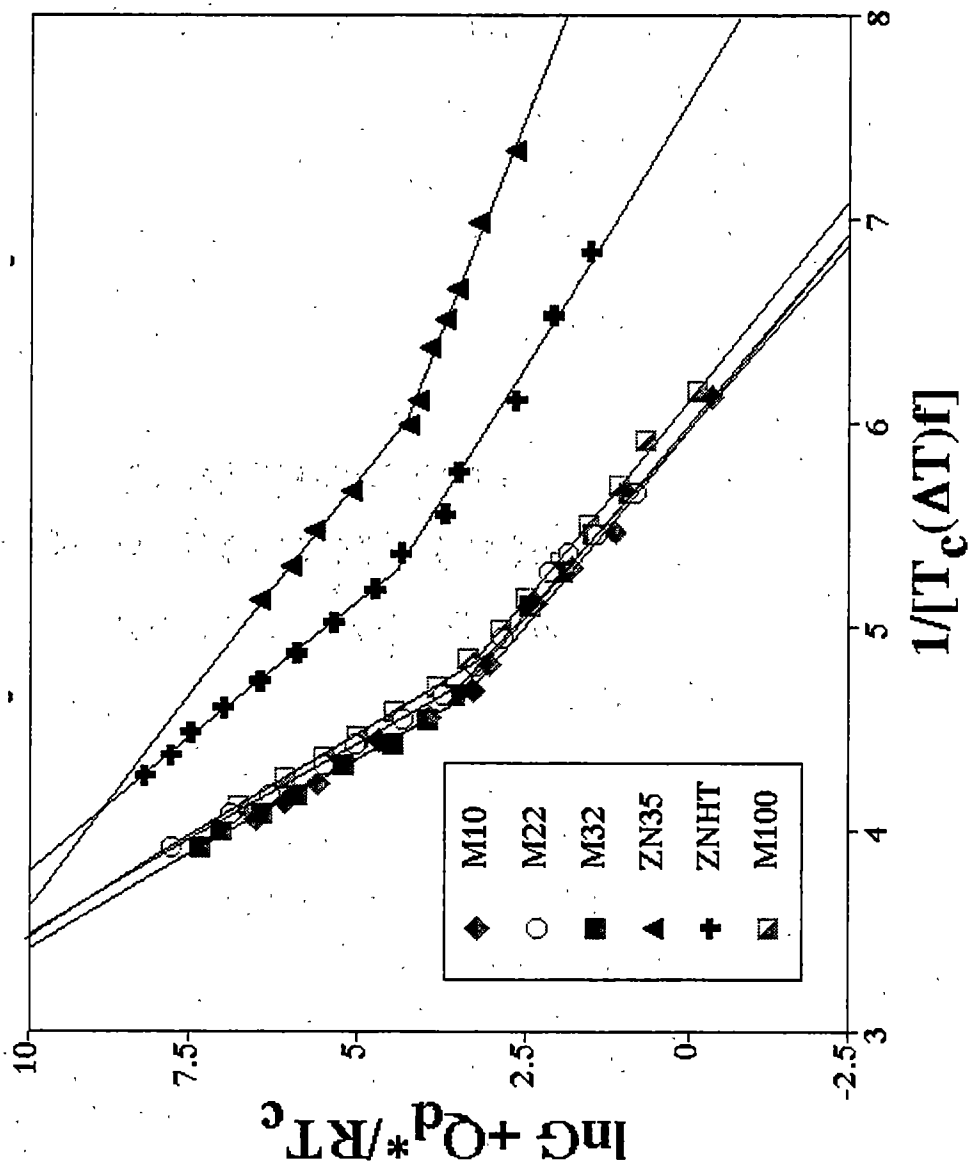
Figure 4.45 Secondary nucleation analysis in regime II and III for all resins.

crystallization behavior of ZNHT should be considered as the standard. The regime transition temperatures for each resin falls in order of decreasing regime transition temperatures with increasing defect content and decreasing meso run length. ZNHT has the highest meso run length and M100 the shortest meso run length. Since we have postulated and shown that defect incorporation at these crystallization temperatures is highly unlikely, rejection of defects pushes the regime transition temperature lower as the number of defects increases and the meso run length decreases. Decreasing the regime transition temperature means that the lamellae thickness also decreases since the crystal thickness is a function of crystallization temperature and time. Since defect exclusion dominates, the resin with more defects has to have a lower transition temperature to match its decreased meso run length. Therefore, increasing the number of configurational defects in iPP, in a random manner, decreases the regime transition temperature in a way similar to decreasing the average meso run length. The lowering of the regime transition temperature is also a further indication that defect exclusion is occurring.

The ratio of slopes for regime III and regime II show all resins have a value very nearly 2, as shown in the last column of Table 4.8. The theoretical value is two and the values in this work are very close to this ratio, in agreement with work from other researchers[110,111].

The slope of the line in a crystallization regime is the value for the formation of the critical nucleus (K_g). The nucleation equation for a given regime (see equation 2.14) allows the value of σ_e to be calculated. The value of σ used in the determination of σ_e in the regime analysis is 9.2mJ/m^2, since the average ΔH_f was taken as 167J/g (the

relationship between ΔH_f and σ can be found in equation 2.15). The values for σ_e calculated for each resin using regime analysis is listed in Table 4.9, along with the σ_e determined from SAXS measurements. The value of G_0 in each represents the pre-exponential growth factor that contains terms not strongly dependent upon temperature[108,109]. This expression contains terms that develop the factors controlling growth in a given regime.

As shown in Table 4.9, there is a substantial difference in between the σ_e values determined by SAXS and regime analysis for all the resins studied. The order of the σ_e values is consistent with those determined by SAXS (meaning as the number of defects increases, σ_e also increases), but the σ_e values using regime theory are nearly twice what is found using SAXS. This is not the first serious difference[210] found between the two methods using the primary method (SAXS) and secondary technique (regime analysis) for iPP. The authors of regime theory[79-88,107-111] clearly state that the theory, as they have developed it, works for polyethylene (PE). The σ_e values determined for PE using SAXS and regime theory agree quite well. Therefore, this suggests the problem must lie in using the surface nucleation equation for PE for iPP.

4.2.2 Regime Analysis for γ-iPP

A regime II-III analysis was also carried out for the γ-iPP crystal structure. Since γ-iPP was found in all the isothermally crystallized films (as determined by WAXD) for the miPP resins, it was assumed that the γ-iPP was present for all of the linear growth rate measurements made. The growth rate of γ-iPP was taken to be same as α-iPP since no

Table 4.9 Fold Surface Free Energies of α-iPP using SAXS data and polyethylene (PE) standard nucleation equationfor the regime III data. σ_e was calculated using a value of $0.92mJ/m^2$ as the lateral surface free energy.

Resin	α-iPP σ_e (mJ/m²)	
	SAXS	PE Nucleation Equation
M10	49.5	103
M22	44.0	83.5
M32	44.0	85.6
ZN35	23.3	38.8
ZNHT	33.5	60.4
M100	45.2	101

distinct morphological differences could be found to suggest otherwise. Also, it has been previously stated that both the α and γ crystal structure can occur within the same lamellae and spherulite. Where appropriate, each resins γ-T_m^0 was used and the ΔH_f was assumed to be 150J/g. For obvious reasons, the zniPP resins did not undergo the γ regime analysis.

The values for K_g and G_o determined from the slopes of the plot for each regime in the miPP resins is given in Table 4.10. The ratio of slopes in regime II and III is now slightly higher than two for each resin. The numerical values for K_g have also decreased for each resin in each regime. G_o has also decreased for each resin in each regime, but not as significantly as K_g.

The slopes (K_g) have decreased in each regime for γ-iPP from the changes in equilibrium melting temperature and heat of fusion, which are also smaller in γ-iPP when compared to α-iPP. σ_e was calculated for γ-iPP using the PE surface nucleation equation. These values are shown in Table 4.11 along with the SAXS σ_e values. The regime analysis σ_e values for γ-iPP are significantly higher than those determined by SAXS. Thus, it would appear, that the surface nucleation equation (K_g) derived for PE does not work for iPP.

4.2.3   Discussion of Regime Analysis and SAXS σ_e Values

An interesting question arises in the discussion of σ_e values determined by SAXS and regime analysis, should the surface nucleation σ_e have the same numerical value as the σ_e determined from the primary measurement method of SAXS? The answer is yes,

Table 4.10 K_g and G_o determined from regime analysis for γ-iPP in regime II and III.

Resin	T_{II-III} ($^\circ$C)	Regime II K_g ($\times 10^{-5}K^2$)	Regime II G_o ($\mu m/s$)	Regime III K_g ($\times 10^{-5}K^2$)	Regime III G_o ($\mu m/s$)	$K_g(III)/K_g(II)$
M10	127.5	1.71	12.6	3.69	23.1	2.16
M22	129.4	1.79	13.5	3.82	24.7	2.13
M32	128.0	1.73	13.1	3.73	23.8	2.16
M100	127.3	1.79	13.1	3.79	24.0	2.12

Table 4.11 Fold Surface Free Energies of γ-iPP from SAXS data and polyethylene (PE) standard nucleation equationfor the γ-iPP crystal structure.

Resin	γ-iPP σ_e (mJ/m^2)	γ-iPP σ_e (mJ/m^2)
	SAXS	PE Nucleation Equation
M10	46.2	77.0
M22	41.8	79.8
M32	42.7	77.7
M100	40.6	79.2

they should if in fact they represent the same thermodynamic quantity. The argument made here is that the σ_e determined from the kinetics is in fact the σ_e determined from SAXS measurements. Also, the importance of defects on growth rates can not be overlooked. The work here has shown without doubt the effect of σ_e on the observed melting temperature. The miPP resins have significantly lower melting temperatures with similar lamellae thicknesses (see Figure 4.23).

Another question that arises concerns whether or not the σ_e measured kinetically represents the fold energy of the critical nucleus and should it be compared to a post annealed mature crystal structure (i.e. the one determined from SAXS). If there *is* a difference between the kinetic and SAXS σ_e, then during the annealing process, the fold surface free energy decreases from the nearly twice the kinetic determined amount to the amount we measure using SAXS. The decrease in σ_e would presumably be a result of perfection and the relief of stress in the interfacial region. While this sounds good for an explanation, it is false.

Studies have shown that lamellae thickening becomes greater as the crystallization temperature increases. If we consider the data in Table 4.2, M22 crystallized at 135°C, we see that four different lamellae thicknesses are produced due to differences in crystallization time. However, all the samples crystallized at 135°C have virtually identical σ_e values with a spread of over 2nm in thickness. Also, over the entire range, σ_e, is relatively constant with crystallization temperature. Therefore, it is not reasonable to assume the σ_e value decreases any appreciable amount after initial stem deposition and the resulting fold of the stem. If annealing and lamellae thickening take place, the fold would have to be loose initially. It would necessarily tighten up producing

more stress in the interfacial region as the crystal thickens. This would, in turn, likely increase the fold surface free energy over the structure initially formed after stem deposition. So if anything, the post annealed lamellae structure measured by SAXS might be expected to have a higher fold surface free energy than the initial structure determined from linear growth rates and regime analysis. This is simply not found experimentally.

The alternative explanation for the difference in σ_e determined by nucleation analysis and SAXS is that the surface nucleation equation derived for PE is not adequate for iPP.

4.2.4 Calculated Growth Rates using Flux Based Nucleation Theory

The theory proposed by Hoffman et al. allows for the theoretical (as will be shown in the present case, pseudo theoretical) calculation of linear growth rates. Since most often iPP is crystallized in regime III with moderate to high supercoolings, the linear growth will be calculated and compared to the experimentally determined linear growth rate for the resins considered in this work.

In regime III, the linear growth rate (G) is defined as[108]:

$$(4.9) \qquad G_{III}(nm/s) \equiv b_0 i(n_{III} a_0)$$

where n_{III} is a number which depends on the spacing between adjacent stems and is taken to be 1.5 for PE at the onset of regime III behavior. The same value will be used here for α-iPP. Physically, n_{III} is the spacing between stems in a single layer of substrate. Recall in Figure 2.26 in regime III there are multiple stems depositing on the same layer

simultaneously. Equation 4.9 also dictates that the linear growth rate is only a function of i, the surface nucleation rate. Terms a_0 and b_0 are the same as before in section 2.4.2.2.

In the context of Hoffman et. al.[108-111], the surface nucleation rate (i) is defined exactly by the following equation[108]:

$$(4.10) \qquad i = \frac{C_0}{a_0}\beta\frac{1}{\ell_u}\left[\frac{kT}{2b_0\sigma} - \frac{kT}{2b_0\sigma + a_0b_0\Delta G}\right]e^{\frac{-4b_0\sigma\sigma_e}{(\Delta G)kT}}$$

where ΔG is defined as $\Delta H_f \Delta T / T_m^\circ$. C_0 is the configurational path degeneracy and is defined by[108]:

$$(4.11) \qquad N_0 = C_0 n_L$$

where N_0 is the number of reacting species and is proportional to the substrate length (L), which is $L = n_L a_0$. The substrate length is the same as W in Figure 2.25. n_L is the number of stems of width a_0 comprising the substrate of length L. ℓ_u in equation 4.10 is the monomer length, which for iPP is taken to be 0.650nm/3 or 0.2167nm. The factor β represents the retardation of the nucleation process associated with transport of chain segments through the subcooled melt to or from the growth front. The factor β has units of events per second. The factor β is defined as[108]:

$$(4.12) \qquad \beta = \frac{\kappa}{n}\left(\frac{kT}{h}\right)e^{\frac{-Q_d^*}{RT}}$$

where κ is a numerical constant evaluated from the monomeric friction coefficient. κ enters into the rate constant for a molecule that is reeled onto the surface as given by reptation theory. κ has been determined to be roughly 0.77 for PE and we shall use this value for iPP. The letter n is the degree of polymerization of a particular molecular

weight (i.e. the number of monomer units). For regime III, the calculation of n is determined by[108]:

$$(4.13) \qquad n = \frac{2}{42}\left(M_n M_w\right)^{0.5}$$

It is also worth while to calculate the rate constant for attainment of the first stem onto a substrate, which is the rate determining step (A_0) in secondary nucleation[108]:

$$(4.14) \qquad A_0 = \beta e^{\frac{-2b_0\sigma\ell}{kT}}$$

where ℓ is the substrate thickness at crystallization temperature T. The backward reaction or removal of the first stem rate constant is given by[108]:

$$(4.15) \qquad B_1 = \beta e^{\frac{-a_0 b_0 \ell(\Delta G)}{kT}}$$

The substrate thickness (same as lamellae thickness) as a function of crystallization temperature was determined by curve fitting the data shown in Figure 4.46. Notice that the zniPP resins form thicker crystals at similar crystallization temperatures. Also notice that there is scatter in the data, likely due to lamellae thickening that has occurred during the prolonged crystallization under isothermal conditions. Lamellae thickening is not taken into account in this plot since the independent variable in this figure is the crystallization temperature. Other variables not specified thus far are listed in Table 4.12 for the calculations to follow.

The calculated primary stem deposition rate constant (A_0) as a function of crystallization temperature is shown in Figure 4.47. A_0 is also shown as a function of supercooling in Figure 4.48. M100 has the highest primary stem deposition rate constant, followed by M22 and M32 which are nearly identical, then ZN35 and ZNHT. The
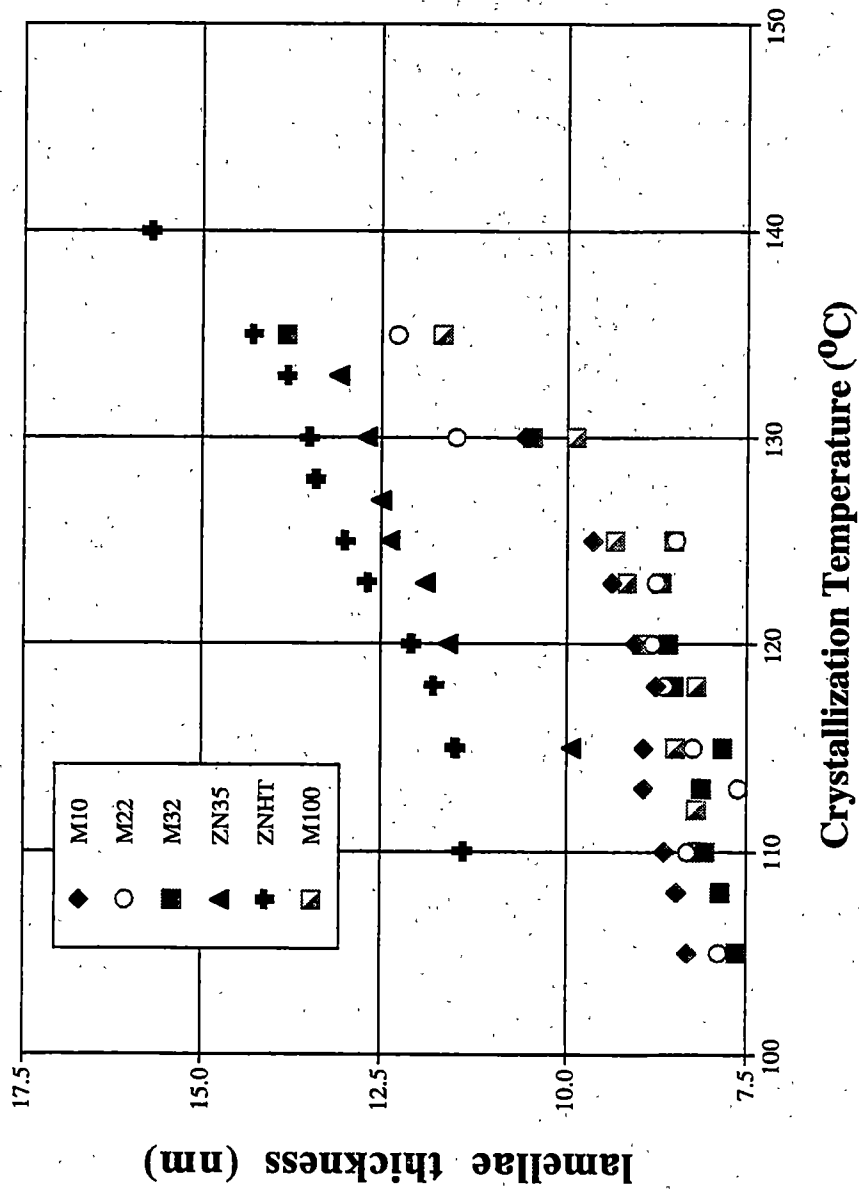
Figure 4.46 Lamellae thickness versus crystallization temperature.

Table 4.12 Values of variables used in calculating linear growth rates using Hoffman theory.

Resin	n (g/mol)	σ_e (mJ/m^2)	σ (mJ/m^2)	T_m^o (K)	L (nm)[*]
M10	6512	49	9.2	458	10.0
M22	6248	44	9.2	459	10.0
M32	5636	44	9.2	459	10.0
ZN35	5137	23	9.2	451	10.0
ZNHT	4189	33	9.2	459	10.0
M100	3995	45	9.2	456	10.0

*this value was chossen as a reasonable approxiamation since it could not be directly determined.
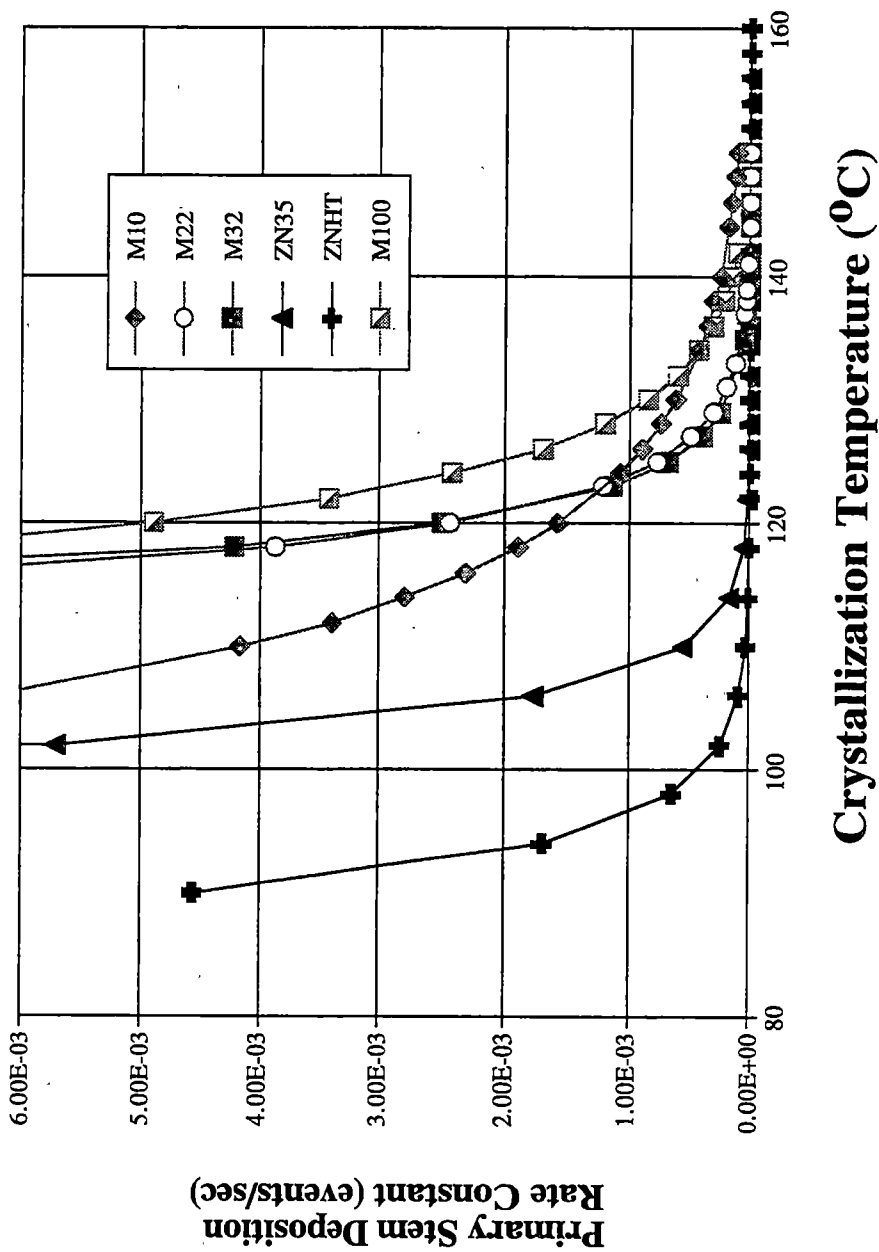
Figure 4.47 Primary stem depostion rate constant versus crystallization temperature.
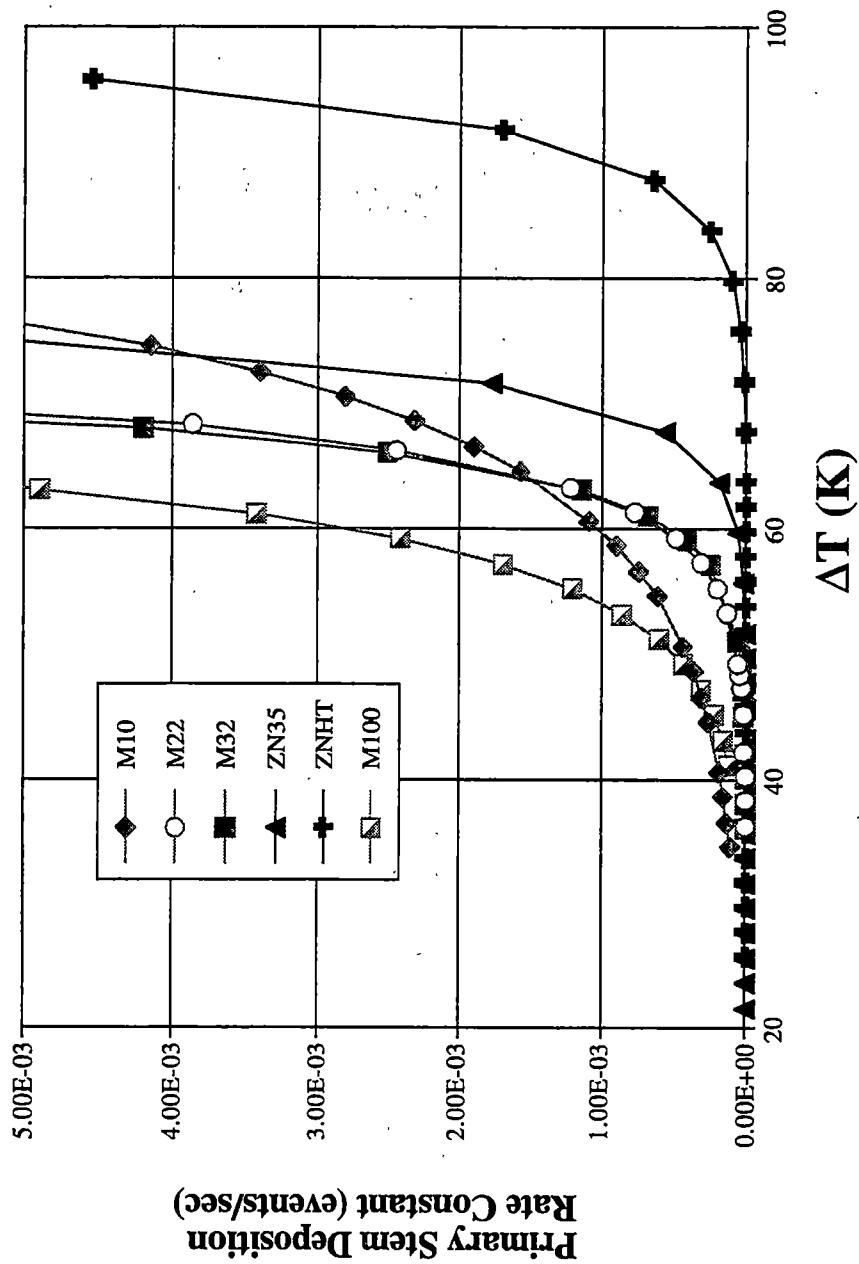
Figure 4.48 Primary stem depostion rate constant versus supercooling.

257

behavior of M10 seems quite peculiar. Ignoring M10, the primary stem deposition rate constant for each resin seems to fall in an interesting order. The resin with the most defects (M100) has the highest rate constant, and in order of decreasing defect content, the rate constants decrease. It would seem based on equation 4.14 and the observation of crystal thickness as a function of crystallization temperature in Figure 4.46, that the crystal thickness dominates the primary stem deposition rate constant for all the resins. If a careful observation of M10 is made in Figure 4.46 at lower crystallization temperatures (or higher supercoolings), M10 has a larger crystal thickness than the other miPP resins, but as the crystallization temperature increases further, the other miPP resins have similar thicknesses or larger in some cases. The behavior of M10 has elucidated the most prominent term for determining the primary stem deposition rate constant.

The primary stem deposition rate constant being a function of lamellae thickness at a given crystallization temperature indicates that the assumption of a polymer stem chain "snapping" into place after a pre-segmentalized alignment prior to obtaining crystallographic registry is likely[108]. We shall hereafter refer to this as quantized stem deposition. Based on the experimental factors built into these calculations, and the detailed understanding of polymer chain molecules, there appears to be no other reasonable explanation for describing the behavior exhibited in Figures 4.47 and 4.48. The primary deposition rate is clearly not directly dependent on defect content, fold surface energy or molecular weight within the range of materials and conditions in this work. Since the rate seems to depend mostly on crystal thickness, it would then be reasonable to presume that it takes longer for a stem of greater length to develop structure requisite for the substrate thickness at a given crystallization temperature. After all, the

258

longer the substrate the greater the loss of entropy needed before any enthalpy is released upon quantized stem deposition. However, since the defects do affect T_m^0 and σ_e, they are indirectly responsible for the lamellae thickness (see below).

While Figure 4.48 and the ones to follow are calculated values, they are not completely theoretical. As much as possible, values determined experimentally were used in the calculations.

The defects for each resin were not directly inserted into any expression to be accounted for explicitly. However, the effects of defects are indirectly accounted for by their influence on the fold surface free energies and equilibrium melting temperatures, which are used in the calculations. Thus, the calculated values in these figures do have some legitimate claim to reality and should be a good representation of the microscopic behavior, at least within the confines of secondary nucleation theory.

The calculations in Figure 4.49 and 4.50 show the stem removal rate constant as a function of crystallization temperature and supercooling, respectively. In Figure 4.50, M100 and M10 had the highest removal rate, followed by M22 and M32 and then ZN35 and ZNHT. It would appear on the surface that these rates are in direct agreement with the relative order of defect content for each material. Recall that defects were not directly considered in this theory. While defect content causing this behavior can not be ruled out, it is worth noting that the quantized stem length on the substrate may also influence the back reaction. As the substrate thickness increases, the amount of heat released upon crystallographic registry of a quantized chain attaching increases. Therefore, the probability of a back reaction once a quantized stem attaches should be expected to decrease. If in fact the defect distribution is considered in this process, the observed
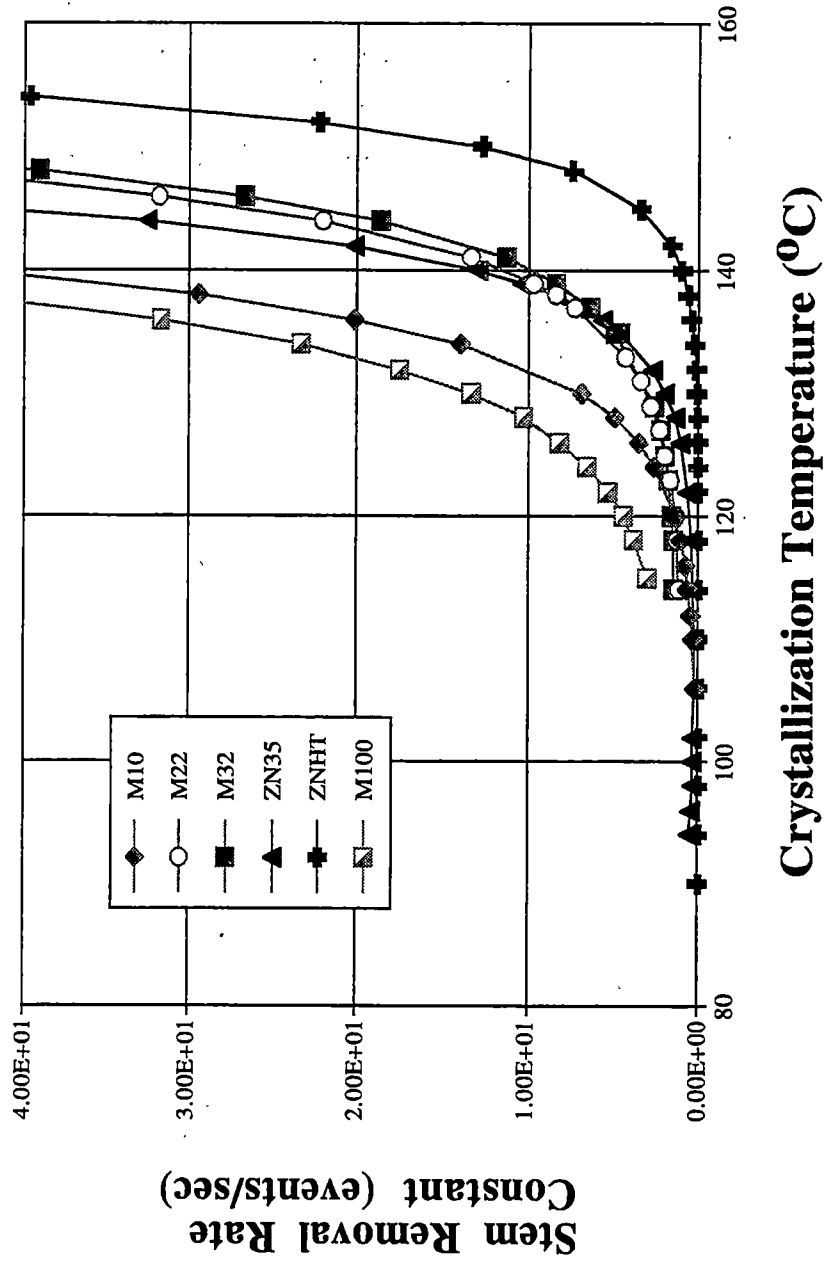
Figure 4.49 Stem removal rate constant versus crystallization temperature.

260
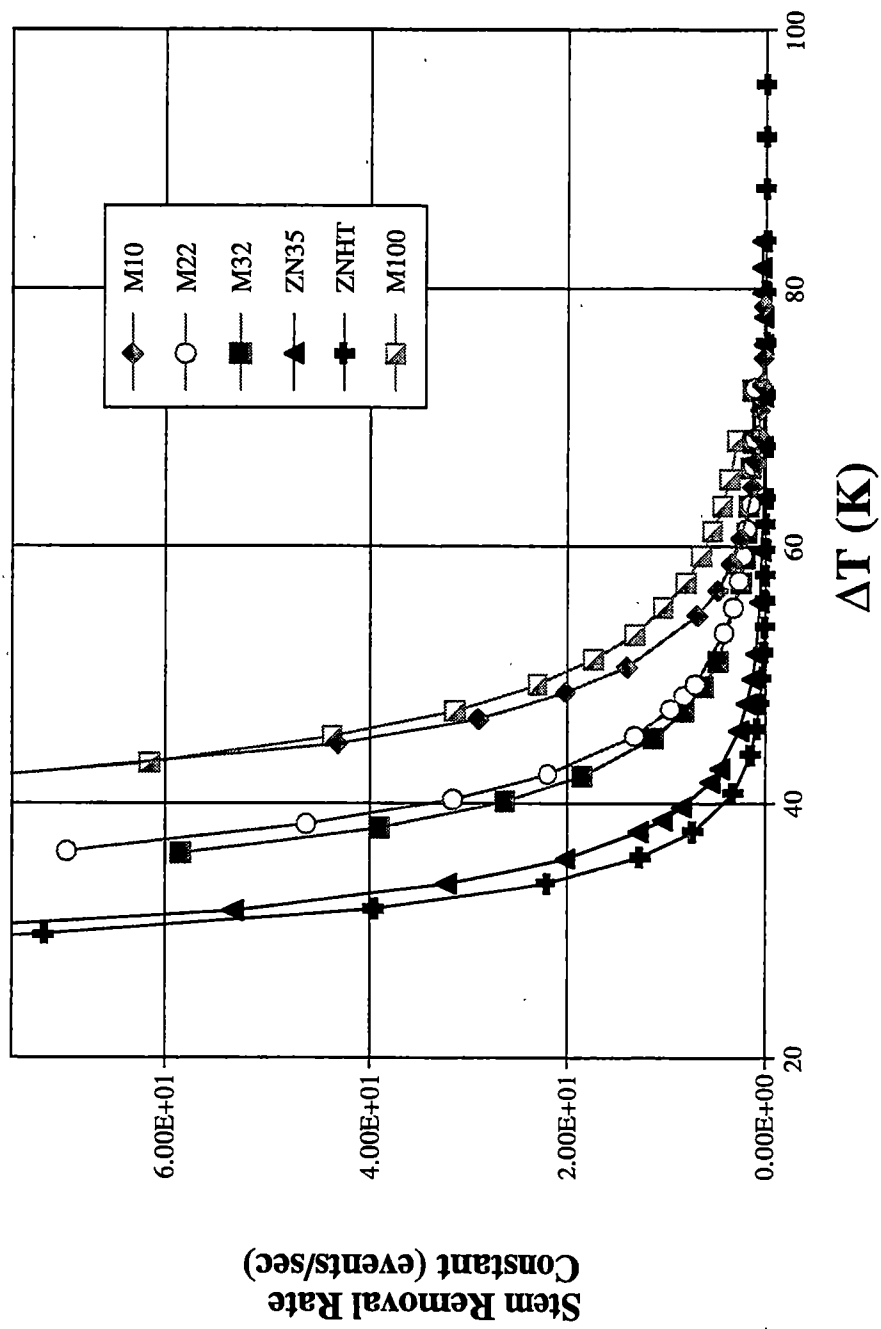
Figure 4.50 Stem removal rate constant versus supercooling.

order of back reaction as a function of resin and defect content is completely reasonable, especially when combined with the effect of enthalpy release upon crystallographic registry.

Based on equation 4.9 and 4.10, the linear growth rate for each resin was calculated as a function of crystallization temperature. The results of these calculations are shown in Figures 4.51 and 4.52. The calculated growth rates show that ZNHT has the highest linear growth rate, followed by ZN35, M22, M100, M32 and M10. Except for the behavior of M100, the calculated growth rate is in very good agreement with the values determined experimentally, when comparing Figure 4.39 and 4.51. When comparing the calculated and experimental growth rates as a function of supercooling (Figure 4.40 and 4.52 respectively), the order of predicted growth rates is also very good.

In order to test the accuracy of the calculated linear growth rates versus the experimental growth rates, the percent difference between the two was determined. The data shown are only for the miPP resins. The zniPP resins do not have a very uniform defect distribution and were not included in these calculations and results. The results in Figure 4.53 show that the percent difference between the calculated and experimentally observed growth rates increases as the number of configurational defects increases. This is an interesting observation in that it would appear that the calculated values do not fully account for the presence of configurational defects. This would be reasonable based on the fact that there existed no term or method of accounting for the average meso run length (or number of defects) directly into any of the nucleation based terms.

The inherent accuracy or absolute magnitude of the differences shown in Figure 4.53 is certainly questionable. There exist many possible points in which error can be
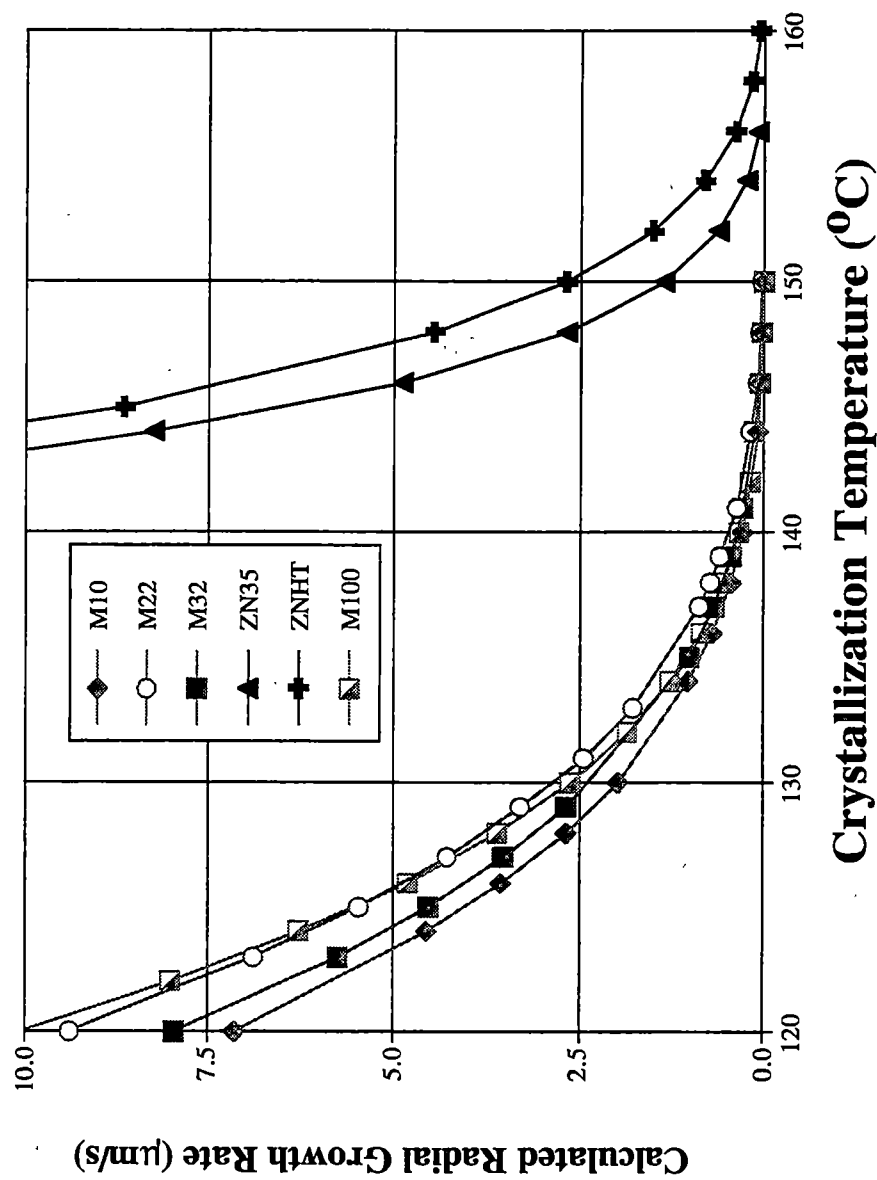
Figure 4.51 Calculated growth rate versus crystallization temperature.
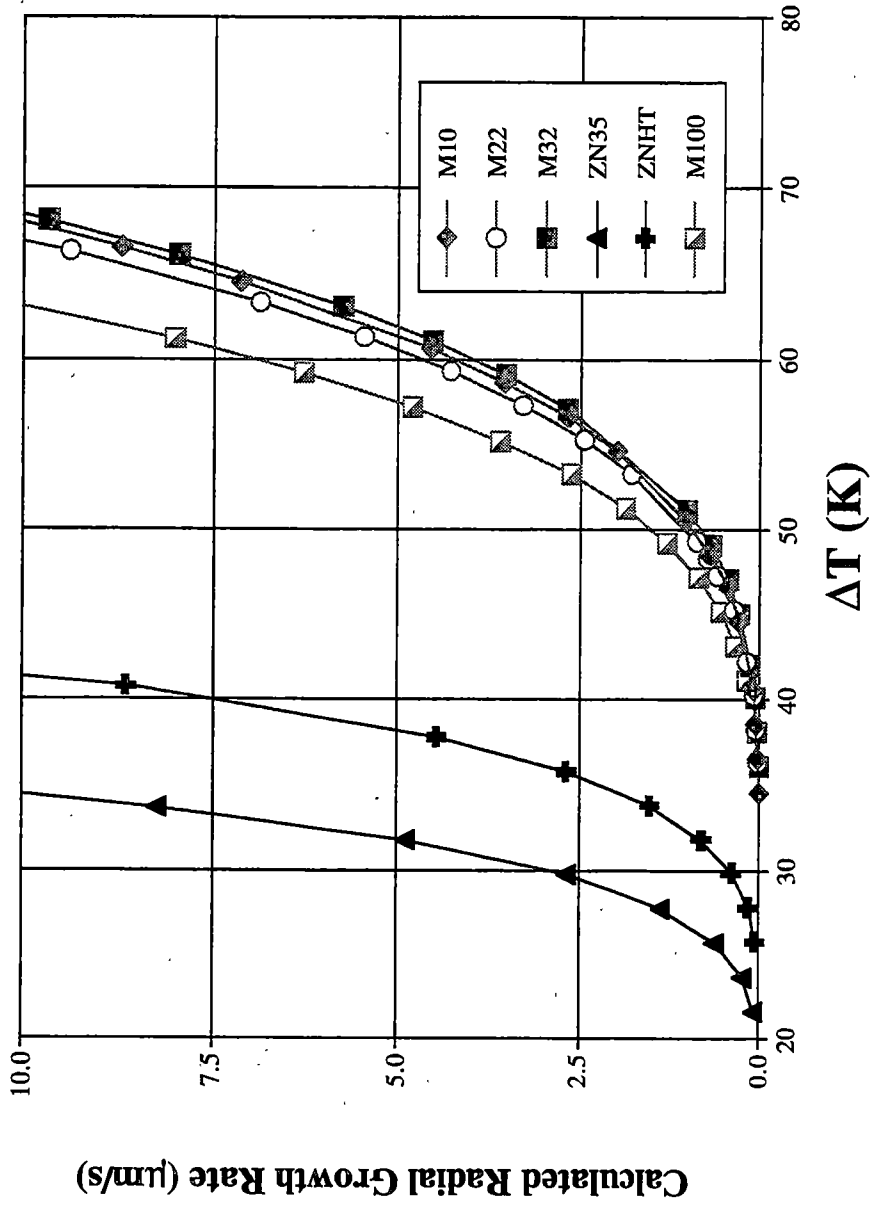
Figure 4.52 Calculated growth rate versus supercooling.
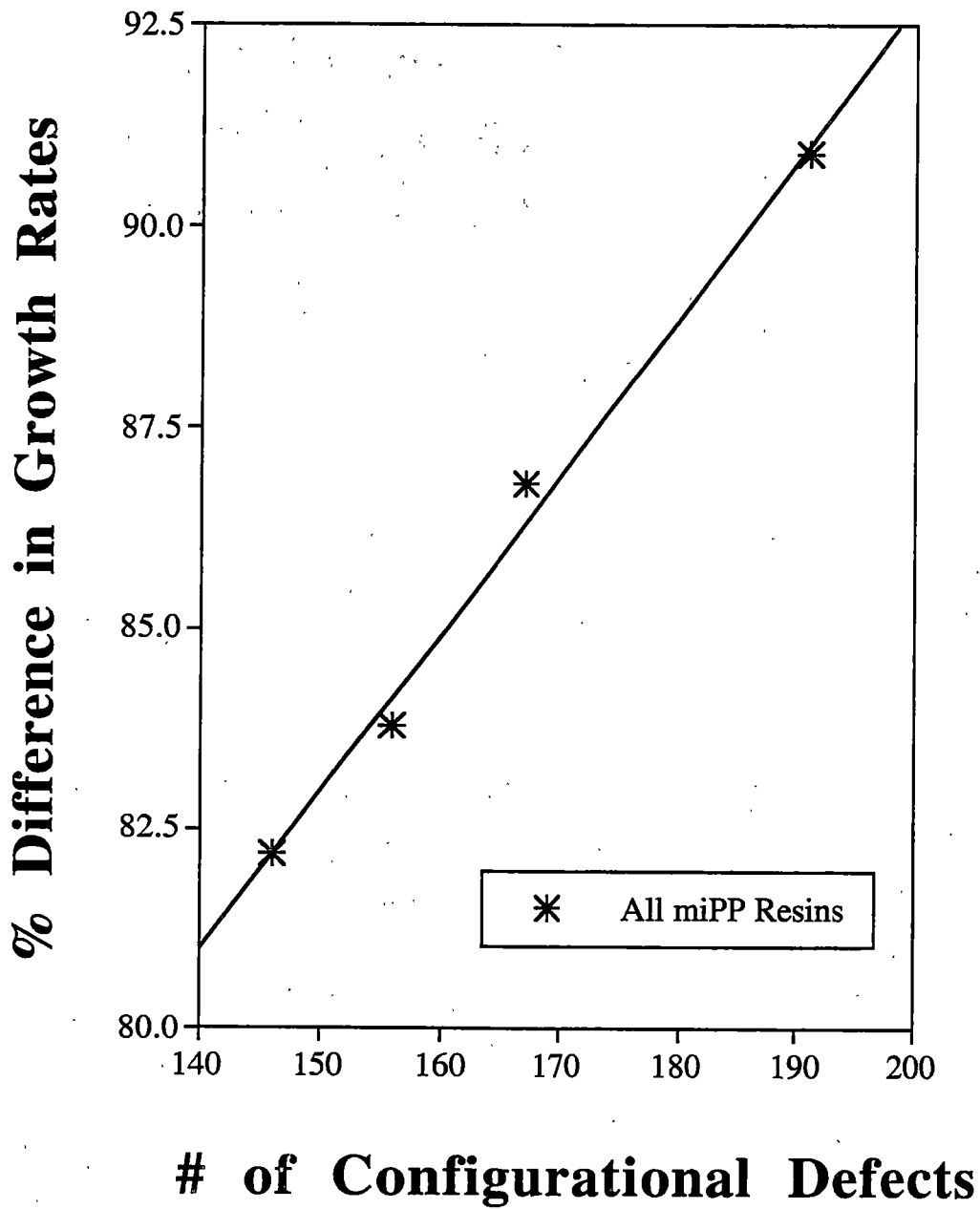
Figure 4.53 Growth rate difference versus number of configurational defects.

introduced in either the physically observed linear growth rates and the calculated growth rates, as many assumptions and approximations have been made. As such, only a qualitative point is made of the percent difference in growth rates versus number of configurational defects. It would appear that configurational defects do slow down the linear growth rate in a manner such that increasing the number of defects (decreasing the average meso run length) slows the linear growth rate observed experimentally.

The result of the calculated linear growth rates using the nucleation based equations show that the terms used in determining the growth rates do not directly take into account the effects of defects. As such, a comparison between the experimentally observed linear growth rates and the calculated growth rates can be made. The difference in growth rates obtained experimentally and calculated showed that the deviation increased as the number of defects increased.

4.3 Quiescent Nonisothermal Crystallization Studies

In most processing applications for iPP, crystallization occurs under temperature conditions that are not isothermal in nature. Therefore, it is of practical interest to study iPP under nonisothermal conditions that more closely simulate an actual processing type environment. For that reason, studies were conducted using the HCRLDM system.

Films nonisothermally crystallized in the high cooling rate light depolarizing microscopy system were also investigated using WAXD, SAXS and DSC. These results are combined in the present section to determine the equilibrium melting temperature and enthalpy of fusion for each resin under nonisothermal conditions, which will then be compared to the results determined under isothermal conditions. Crystallization kinetic

studies were also carried out on each resin using bulk and crystal growth analysis. A nonisothermal regime analysis will be performed on the growth rates observed under high cooling rate conditions.

4.3.1 WAXD of Nonisothermal iPP Films

WAXD patterns of some films nonisothermally crystallized in the HCRLDM system are shown in Figures 4.54-4.57. M10, M22, ZNHT and M100 have WAXD patterns shown at the average cooling rate (ACR) indicated in each figure.

The main point of interest in the WAXD patterns is the virtual lack of any γ-iPP crystal peaks for any films. For the films in this study, α-iPP was observed for all films crystallized under nonisothermal conditions. Isothermal studies show that M10 and M100 have up to 70% γ-iPP when crystallized at low supercoolings. Figure 4.54 and 4.57 do not indicate the presence of γ-iPP for any of the average cooling rates in this nonisothermal study. A slight inflection exists for the M10 sample crystallized using a ACR of 3000°C/min at a 2θ value 20°. This is the only sample that shows any inflection in the γ-iPP region. As such, the presence of γ-iPP to any large extent (as seen by WAXD reflections) for any films crystallized nonisothermally can be ruled out.

One additional point of interest is that all the films studied contain a large fraction of the α-monoclinic crystal structure, while the presence of any condis (smectic) crystal structure is limited or nonexistent in the WAXD patterns. This would indicate that the resins in this study are not capable of quenching to the level of producing the disordered structure in the HCRLDM system, within the cooling rates obtained within this work for

267
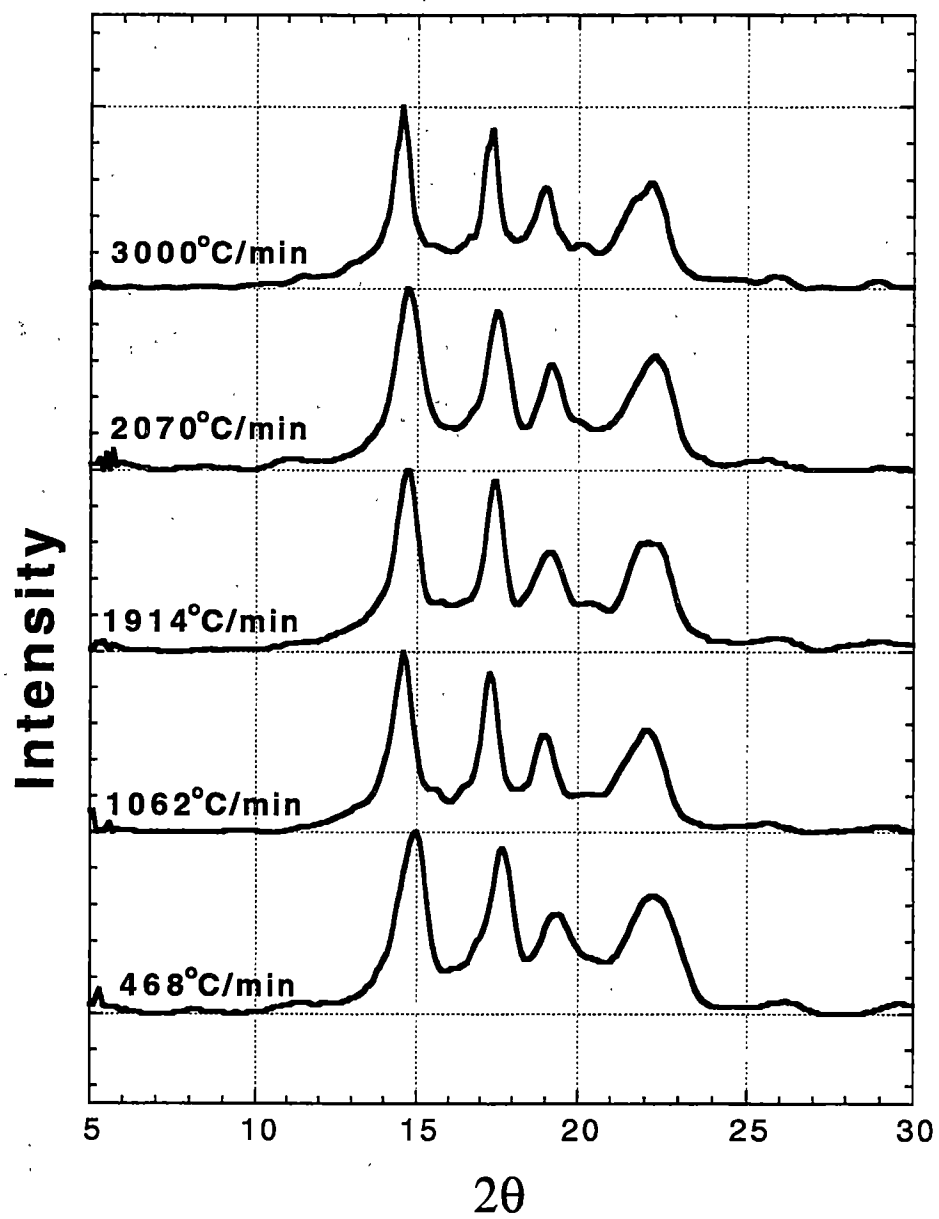
Figure 4.54 M10 Nonisothermal WAXD patterns.
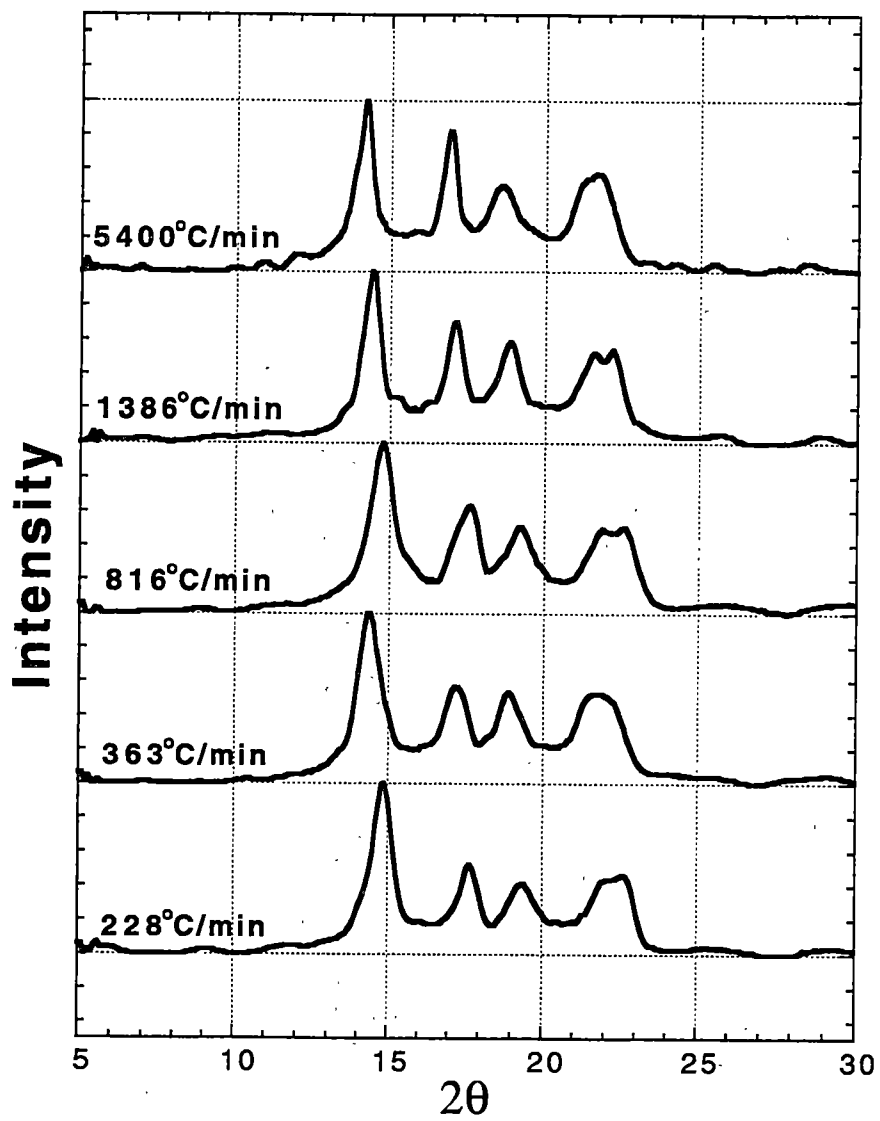
Figure 4.55 M22 Nonisothermal WAXD patterns.
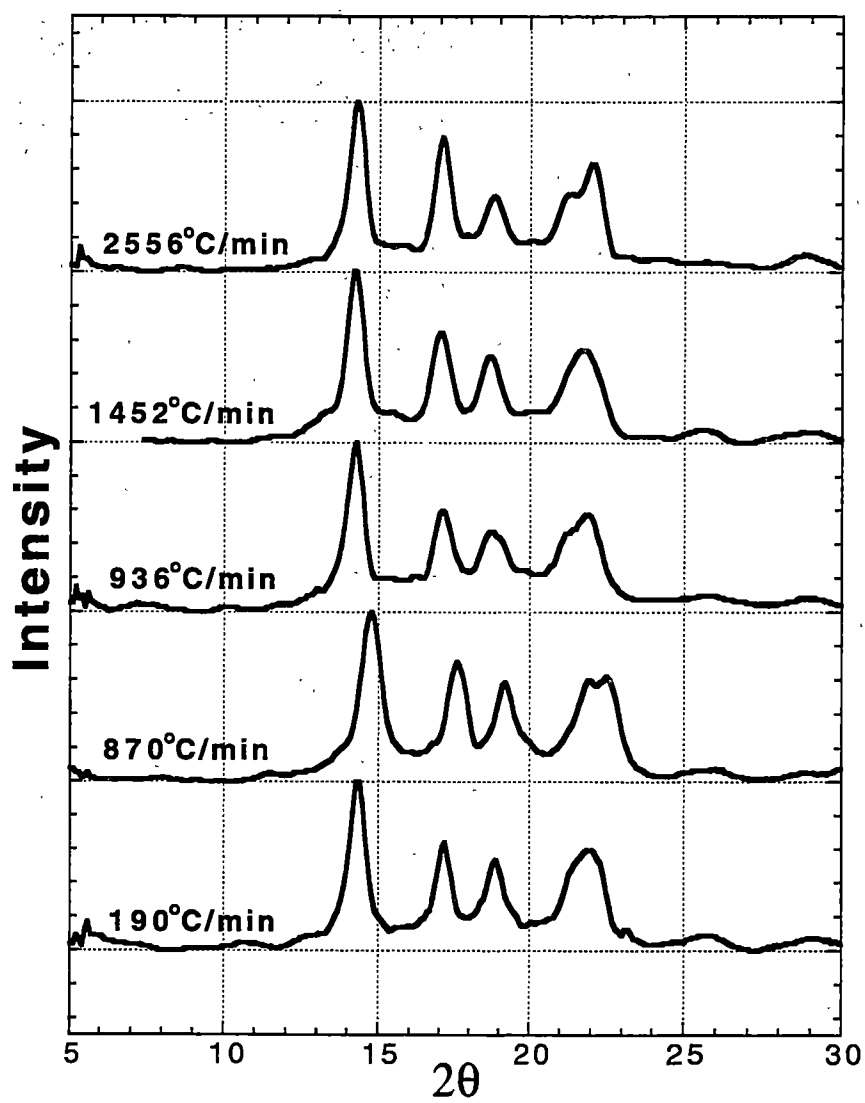
Figure 4.56 ZNHT Nonisothermal WAXD patterns.
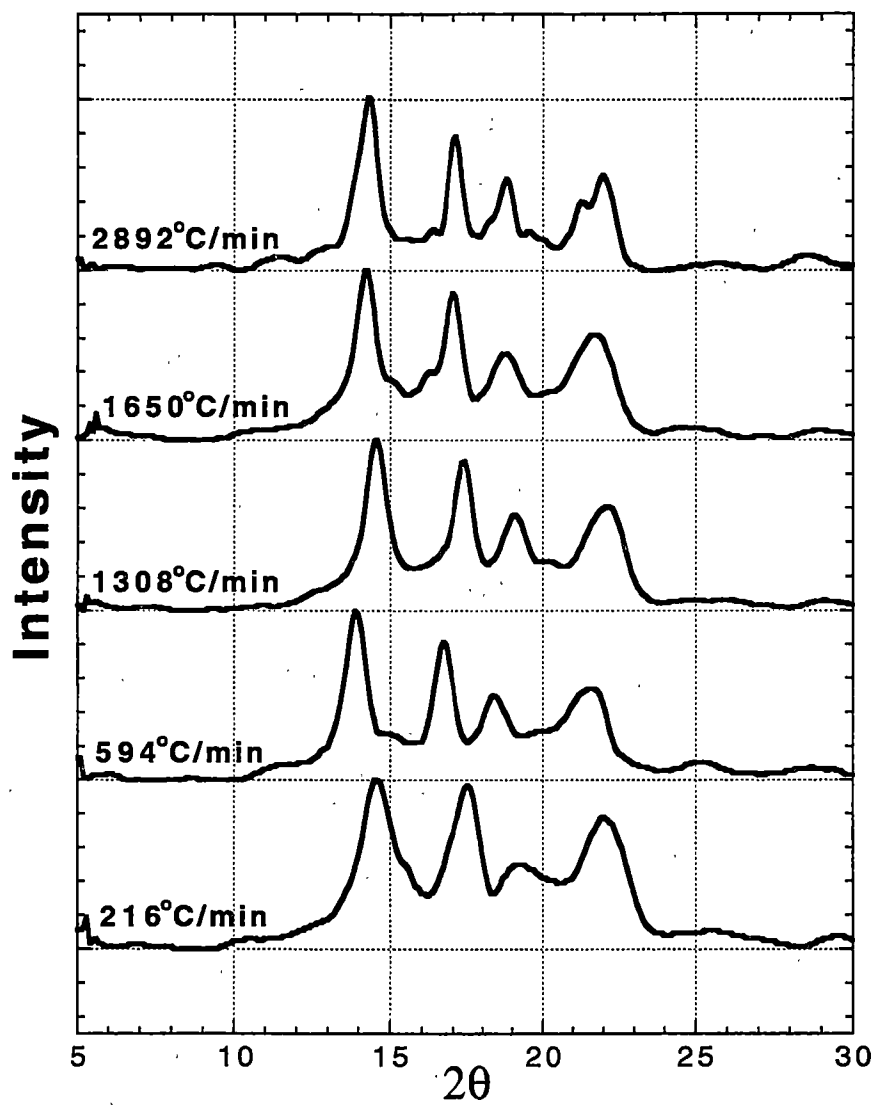
Figure 4.57 M100 Nonisothermal WAXD patterns.

these iPP resins. Previous work[244] indicated that cooling rates above 80K/s are needed to produce the mesomorphic phase in dominate amounts.

4.3.2 Differential Scanning Calorimetry

DSC was used to characterize the films shown in the WAXD section. The DSC was used to determine the T_m and ΔH_f of each resin crystallized under nonisothermal conditions.

4.3.3 Melting Temperature of Infinitely Thick Crystals from Nonisothermal Crystallization Studies

Films were used to determine the melting temperature of an infinitely thick crystal produced under nonisothermal (hence far away from equilibrium, i.e. nonequilibrium) conditions (T_m^{NE}). This term is in fact analogous to the equilibrium melting temperature measured under isothermal conditions and in some cases we shall discuss the two interchangeably, where appropriate. Determining the T_m^{NE} under nonisothermal conditions and comparing it to the isothermal T_m^0 is of interest to study the effect of the defects on an infinitely thick crystal under crystallization conditions far away from equilibrium. The T_m^{NE} for each material was determined in a similar manner to the procedure used for isothermally crystallized films. SAXS was used to determine the long period. WAXD was used to determine the crystallinity and DSC the melting temperature of each film.

The results in Figure 4.58 show the lamellae thickness versus cooling rate. The lamellae thickness is plotted versus plateau temperature in Figure 4.59.
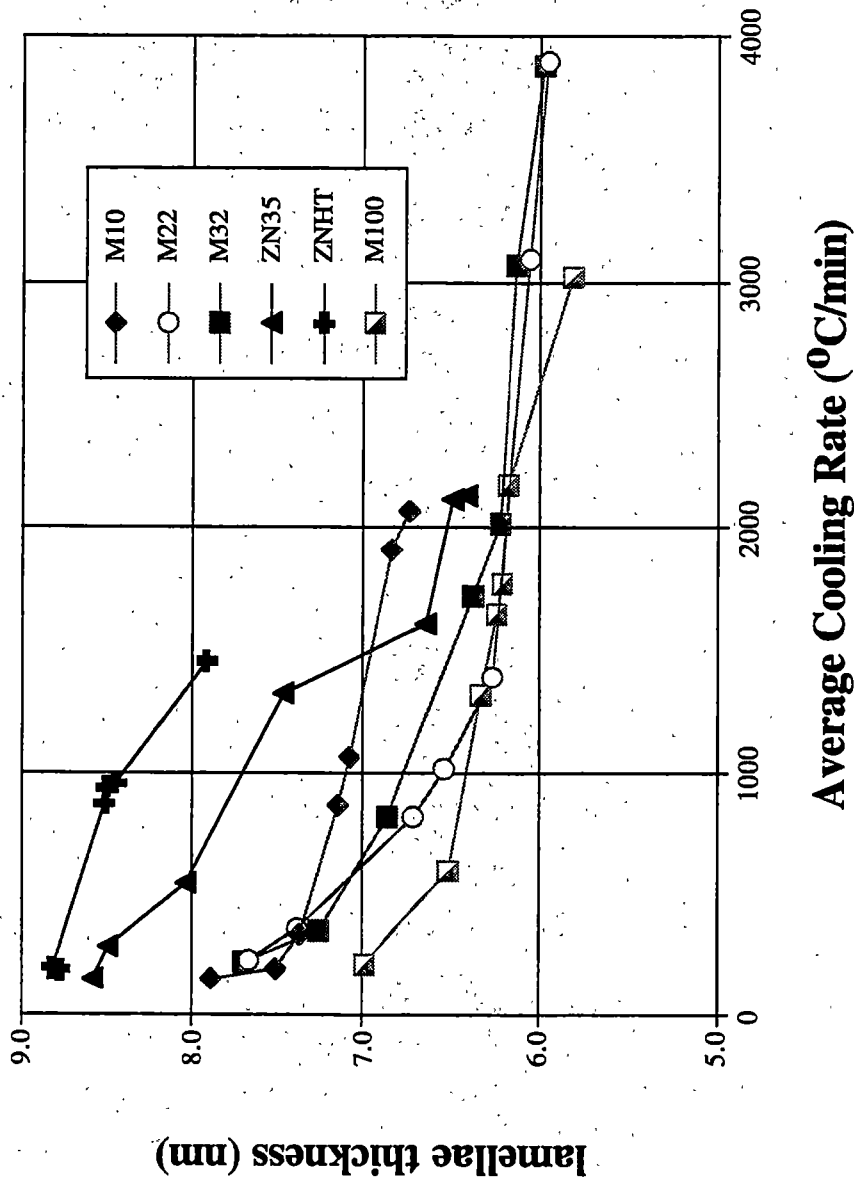
Figure 4.58 Lamellae thickness versus average cooling rate for nonisothermally crystallized films.
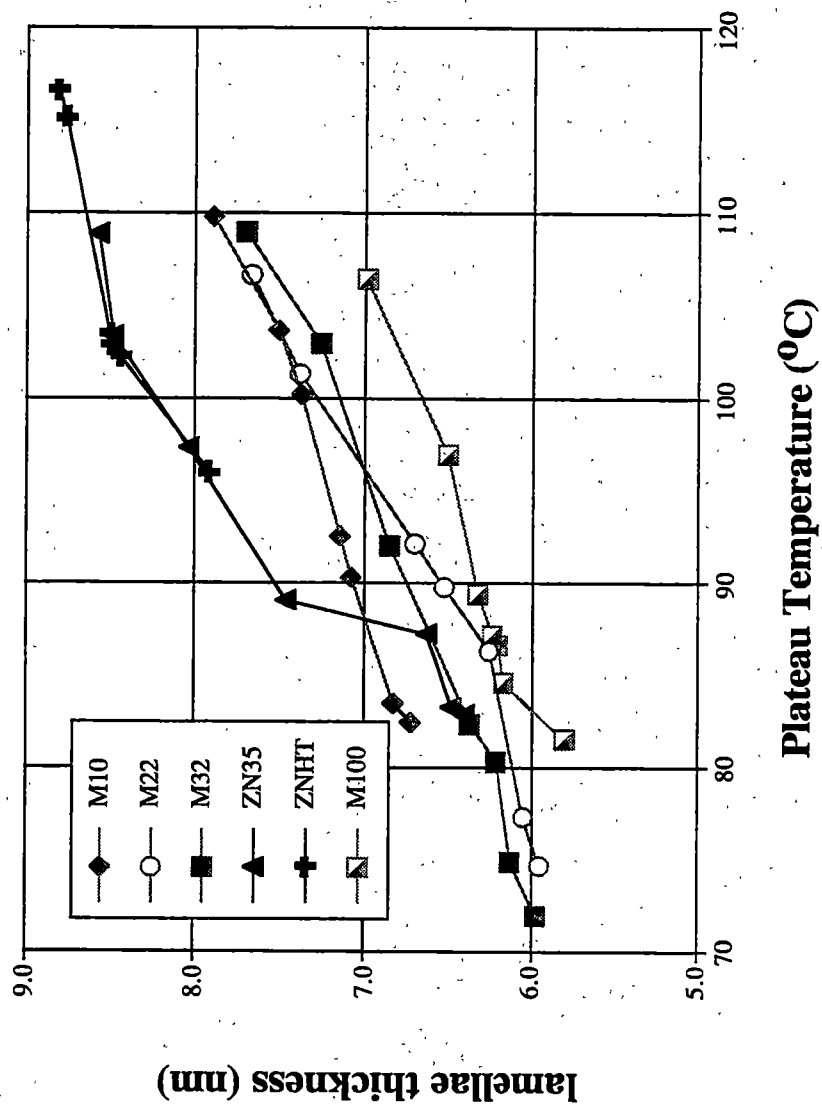
Figure 4.59 Lamellae thickness versus plateau temperature for nonisothermally crystallized films.

274

The determination of T_m^{NE} for each of the iPP resins is shown in Figures 4.60-4.62. M10 and M22 are shown in Figure 4.60. M32 and M100 are shown in Figure 4.61 and ZN35 and ZNHT are shown in Figure 4.62. The melting temperature at infinite thickness for M10 has decreased from 185°C in the isothermal case to 177°C for the nonisothermal data. M22 has shown a decrease from 186°C to 180°C, while M32 has decreased from 186°C to 179°C. M100 had the largest decrease from a T_m^0 of 183°C to a T_m^{NE} of 173°C. Within experimental error, the T_m^0 and T_m^{NE} are the same for ZN35 and ZNHT. The experimental error for the nonisothermal T_m^{NE} for each resin is ±3°C.

The explanation for the lower T_m^{NE} for the miPP resins under nonisothermal conditions can be explained by the decrease in the extrapolated heat of fusion for a 100% crystalline material. The extrapolation for the heat of fusion for a 100% crystalline sample for each material is shown in Figure 4.63 for the miPP resins and Figure 4.64 for the zniPP resins.

The results shown in Table 4.13 allow a direct comparison of the T_m^0 and ΔH_f obtained under isothermal (I) and nonisothermal (NI) conditions using the same experimental procedure. The decrease in T_m^{NE} follows the trend that increasing the number of configurational defects causes a larger change and decrease from the isothermal T_m^0. The explanation for the decrease in T_m^{NE} comes from the decrease in ΔH_f under isothermal conditions, with increasing configurational defects. The decrease in ΔH_f appears to be a result of defect incorporation into the crystal matrix. Defect incorporation into the crystal matrix causes the total amount of heat released for a given volume of α-iPP crystal to decrease over an otherwise defect free crystal. The more numerous the number of defects present in the crystal, the larger the decrease in the ΔH_f.
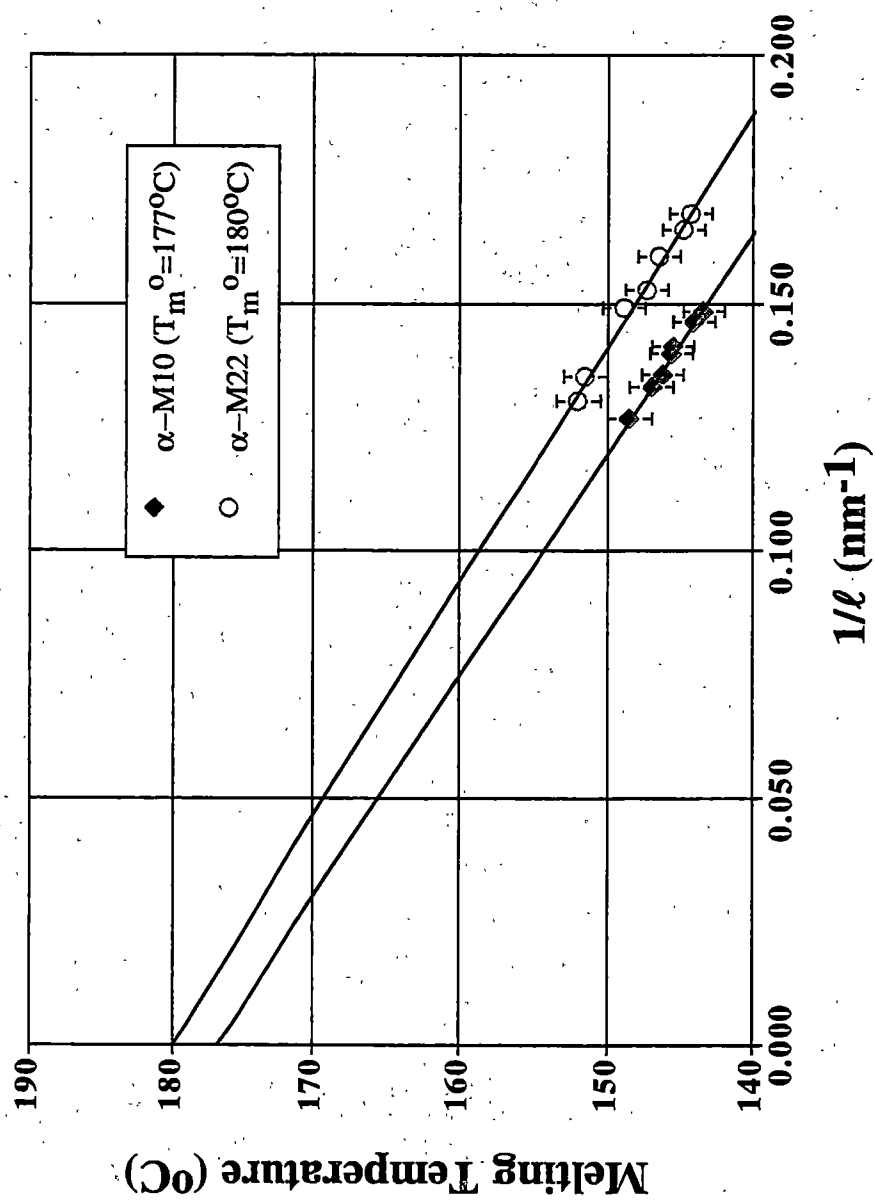
Figure 4.60 Nonisothermal T_m^{NE} of M10 and M22.
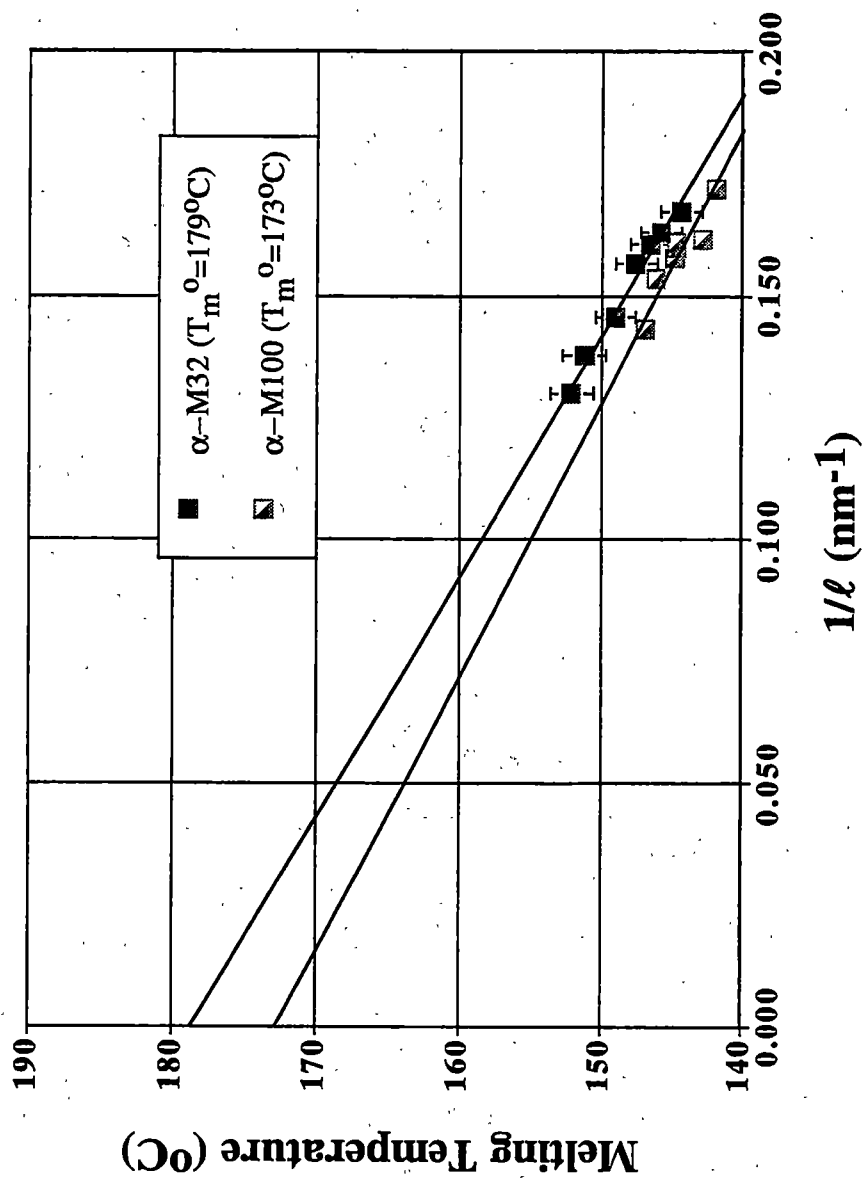
Figure 4.61 Nonisothermal T_m^{NE} of M32 and M100.

α–M32 (T_m^o=179°C)

α–M100 (T_m^o=173°C)

$1/\ell$ (nm^{-1})

Melting Temperature (°C)
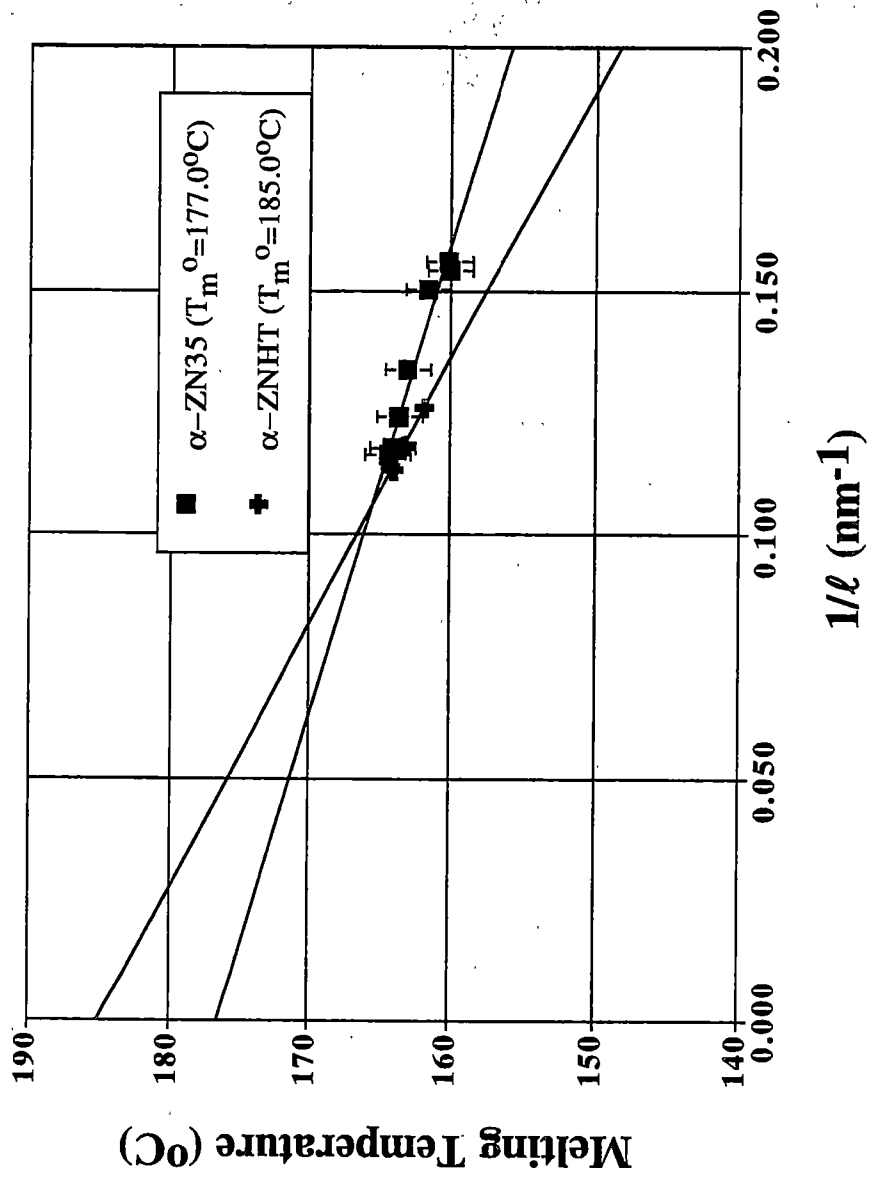
Figure 4.62 Nonisothermal T_m^{NE} of ZN35 and ZNHT.

WAXD Crystallinity

Heat of Fusion (J/g)

1.000 0.900 0.800 0.700 0.600 0.500

200 150 100 50

Legend:
- ◆ α–M10 (150J/g)
- ○ α–M22 (154J/g)
- ■ α–M32 (154J/g)
- ▨ α–M100 (148J/g)
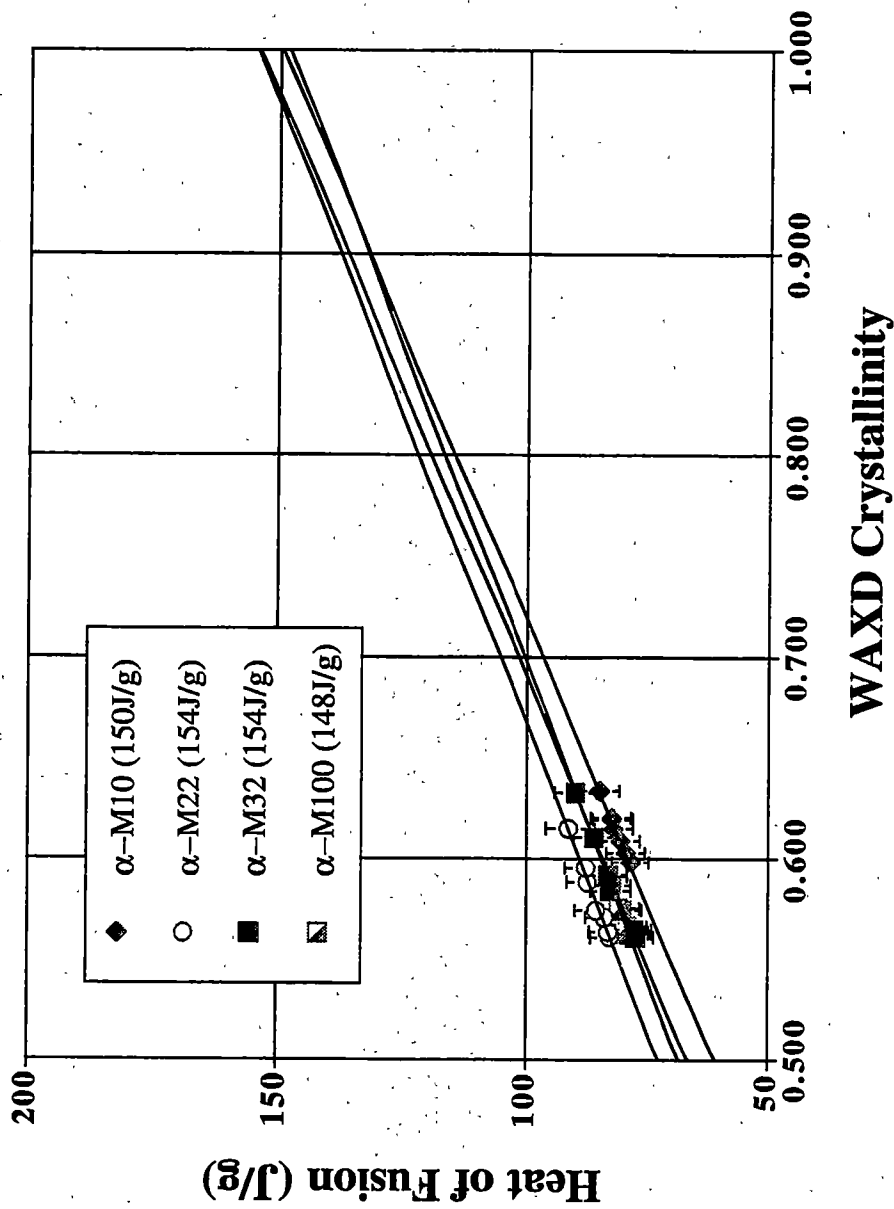
Figure 4.63 Nonisothermal ΔH_f of miPP resins.
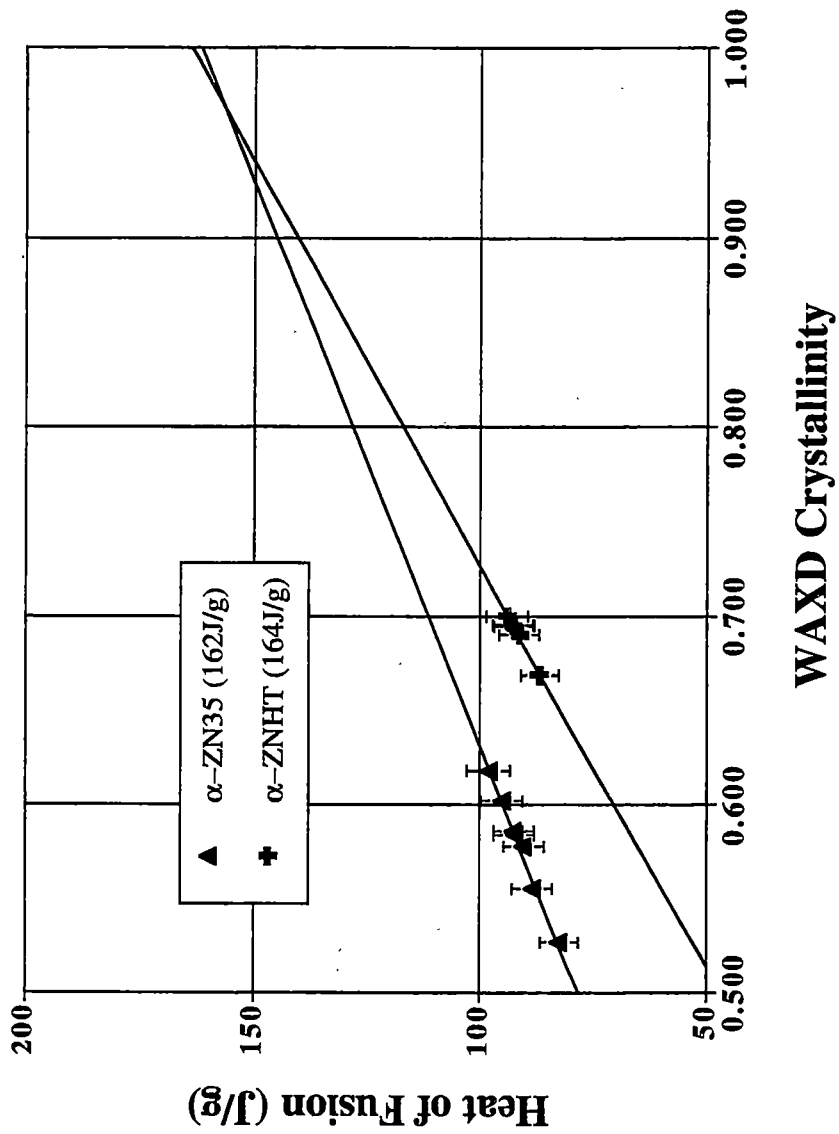
Figure 4.64 Nonisothermal ΔH_f of zniPP resins.

Table 4.13 Comparison of Isothermal and Nonisothermal T_m^0 and ΔH_f values.

Resin[a]	I-T_m^0 (°C)	NI-T_m^0 (°C)	ΔT_m^0 (°C)	I-ΔH_f (J/g)	NI-ΔH_f (J/g)	$\Delta \Delta H_f$ (J/g)
M10	185	177	8	167	150	17
M22	186	180	6	166	154	12
M32	186	179	7	165	154	11
ZN35	178	177	1	168	162	6
ZNHT	186	185	1	169	164	5
M100	183	173	10	165	148	17

a-Δ=I-NI (isothermal − nonisothermal)

This lowers the observed T_m of a sample by requiring less heat (i.e. a lower temperature) to melt a crystal of a given thickness versus a defect free crystal of the same thickness.

Defect incorporation becomes common at higher supercoolings (synonymous with higher cooling rates), as previous studies have shown[79-83]. This is due in large part to the speed at which a resin must crystallize at higher supercoolings. The thermodynamic driving force (Gibbs free energy) to crystallize becomes greater as the supercooling increases, the crystal becomes the thermodynamically more favorable phase. This in turn drives crystallization to occur at more rapid speeds. Higher crystallization speeds can be partially credited to lower crystallization temperatures producing thinner lamellae which require less time for a stem to deposit onto. The higher crystallization speeds mean that configurational defects present in stems depositing onto a substrate are not going to be rejected as frequently as in the isothermal case. The heat of fusion lost due to the disruption of the crystal matrix around the incorporated defect is offset by the Gibbs free energy favoring the phase change. The penalty for defect incorporation is paid when the sample is melted, the sample will melt at a lower temperature as outlined above. The data here suggests that the more numerous the defects in the resin, the larger the incorporation into the crystal matrix with the subsequent lowering of the nonisothermal ΔH_f and T_m^{NE}.

4.3.4   Fold Surface Free Energy

The fold surface free energies were determined for the nonisothermally crystallized films used in the SAXS and WAXD studies. The T_m^{NE} and ΔH_f determined

experimentally (Table 4.13) for each resin under nonisothermal conditions was used in the calculation of σ_e.

The results in Figure 4.65 show the σ_e values for each resin under nonisothermal conditions using SAXS, WAXD and DSC and the Gibbs-Thomson equation. M10 has the highest σ_e values followed by M22, M32, ZNHT, M100 and ZN35. Table 4.14 shows a direct comparison of σ_e determined under isothermal (I) and nonisothermal (NI) conditions using SAXS as the experimental method for each resin. In each case, the experimentally determined T_m^0 and ΔH_f are used (Table 4.13) in the calculation of σ_e.

All σ_e values determined from SAXS work crystallized under nonisothermal conditions showed a decrease in σ_e when compared to the σ_e for films crystallized using isothermal conditions. The change in σ_e (isothermal − nonisothermal) indicates that ZNHT decreased only slightly, from 33.5mJ/m² to 32.0mJ/m². ZN35 showed a decrease of 5.0mJ/m², while the miPP resins all showed a much greater decrease in σ_e. M22 and M32 had a decrease of 11.0mJ/m², while M10 decreased by 16.0mJ/m² and M100 decreased by 17.0mJ/m². The general order of decrease in σ_e follows the trend of increasing configurational defects. The more numerous the configurational defects, the larger the decrease in σ_e under nonisothermal crystallization conditions. A main point of interest is that the σ_e values are now quite similar for both the miPP resins and the ZNHT resin. The ZN35 resin is still lower, presumably as a result of the influence of the xylene solubles fraction.

A slight reduction in σ_e would be expected under nonisothermal conditions regardless of the presence of defects. Studies on PE have shown that rapid crystallization
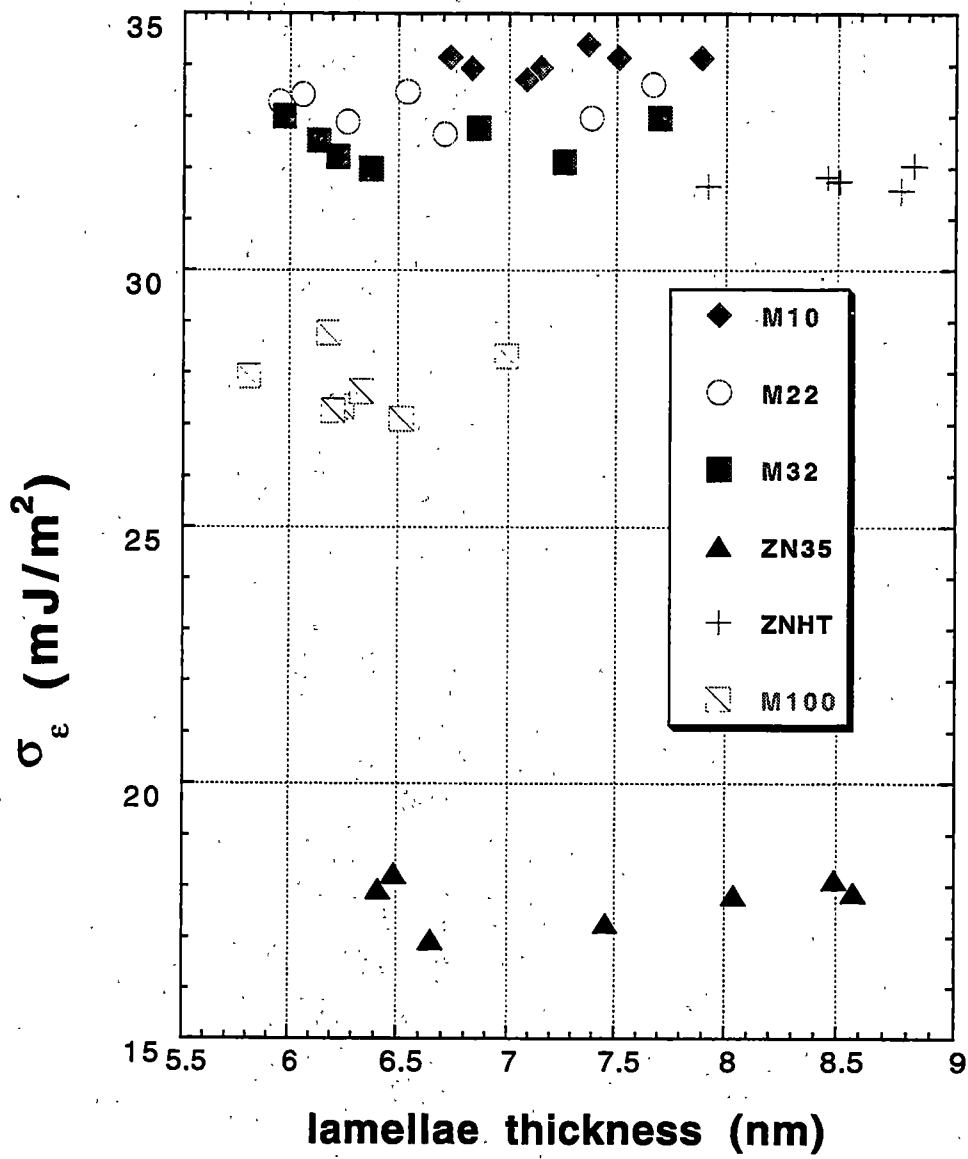
Figure 4.65 Nonisothermal σ_e determined using SAXS for all resins.

Table 4.14   Comparison of σ_e for α-iPP under isothermal and nonisothermal conditions determined from SAXS measurments.

Resin	σ_e (mJ/m^2)		
	Isothermal SAXS	Nonisothermal SAXS	ΔSAXS
M10	49.5	34.1	16
M22	44.0	33.2	11
M32	44.0	32.8	11
ZN35	23.3	18.0	5.3
ZNHT	33.5	32.0	1.5
M100	45.2	28.0	17

forms less adjacent reentry and tight chain folding. A similar finding would also be expected for iPP. ZNHT shows a slight decrease in σ_e. It has been stated that the crystallization behavior of ZNHT should be considered average or normal, in that ZNHT contains few defects and has a low percent of xylene solubles. Therefore, at least a $0.2 mJ/m^2$ decrease in σ_e should be expected for all resins.

The significance of the decrease in σ_e arises from an earlier point in the study of isothermally crystallized films. The explanation for the formation of γ-iPP was that configurational defects were preferentially rejected from crystal incorporation under isothermal conditions. The rejected segments that contain the defects were put into the fold surface region, more generally called the interfacial region. The defects in the interfacial region produced higher σ_e values that made the γ structure more thermodynamically favorable. It was also pointed out that the σ_e values for the miPP resins was significantly higher than for the zniPP materials.

Under nonisothermal crystallization conditions, preferential rejection of configurational defects does not occur as frequently due to kinetic and thermodynamic considerations, discussed previously. Therefore, if the defects are not present (or the concentration have decreased) in the fold surface region, a decrease in σ_e would be expected. Further, since defect numbers are reduced in the fold surface region, the presence of γ-iPP should be greatly reduced or eliminated. Both a reduction of σ_e and the absence of γ-iPP in the WAXD patterns is observed. These findings are also supported by the miPP resins with the most defects showing the largest decrease in σ_e in nonisothermal crystallization.

4.4 Nonisothermal Crystallization Kinetics

Nonisothermal crystallization kinetics were investigated using the HCRLDM system. Bulk and crystal growth kinetics were investigated. Bulk analysis was used to determine the crystallization half-time, plateau temperature, induction time and crystallization onset temperature. Direct crystal growth measurements were made to determine the linear growth rate and nucleation density for films crystallized under nonisothermal conditions. A regime analysis was applied to the linear growth rates under nonisothermal conditions.

4.4.1 Terminology used in Bulk Nonisothermal Crystallization Kinetics

Bulk kinetics were studied using the HCRLDM system previously described here and elsewhere[192-196]. The experimental variables of interest are the cooling rate, plateau temperature, crystallization half-time, crystallization onset temperature and induction time.

Important Bulk Variables

A brief discussion and definition for each important variable determined in nonisothermal kinetic analysis will be discussed and defined below.

Cooling Rate The cooling rate is determined from the slope of the plot, temperature versus time collected using a thermocouple embedded directly into the sample. While strictly speaking, the cooling rate factor (CRF) is more correct in describing the change in sample temperature versus time, the cooling rate is used here since it has a more useful physical meaning outside the confines of nonisothermal crystallization studies using the HCRLDM system. The cooling rate discussed here is actually a time averaged cooling

rate. Additionally, it has been shown[206,208] that the relationship between average cooling rate (ACR) and CRF is linear for iPP and PE over the range of crystallization rates used in this study.

Clearly there exists some error in using a linear expression to describe the curved experimental behavior of the temperature versus time profile in a HCR-LDM run. To minimize this error, the linear curve fit for the cooling rate was extended to the onset temperature of crystallization. At the onset of crystallization, heat is beginning to be released which influences the slope of the temperature profile, making the curve fit to points located after the onset of crystallization questionable.

Plateau Temperature   The plateau temperature (Tp) is the temperature at which the cooling rate of the sample is just matched and equaled by the heat released upon crystallization. As the ACR increases, the plateau region becomes smaller and all but disappears at extremely high cooling rates. In this situation, the point of inflection of the intercept of the line extending down from the liquid state polymer to the solid state semi-crystalline polymer is taken to be the plateau temperature. Although it is intuitive, crystallization begins before the plateau temperature and continues somewhat after reaching the plateau temperature. It is similar in many respects to the peak crystallization temperature in DSC type measurements.

Figure 4.66 shows the temperature versus time profile for ZNHT crystallized at 260°C/min (A) and 2000°C/min (B). The arrows point to the plateau region for each sample run. Notice that the A contains a much longer plateau temperature than B, a result of a much longer crystallization time at a lower cooling rate.
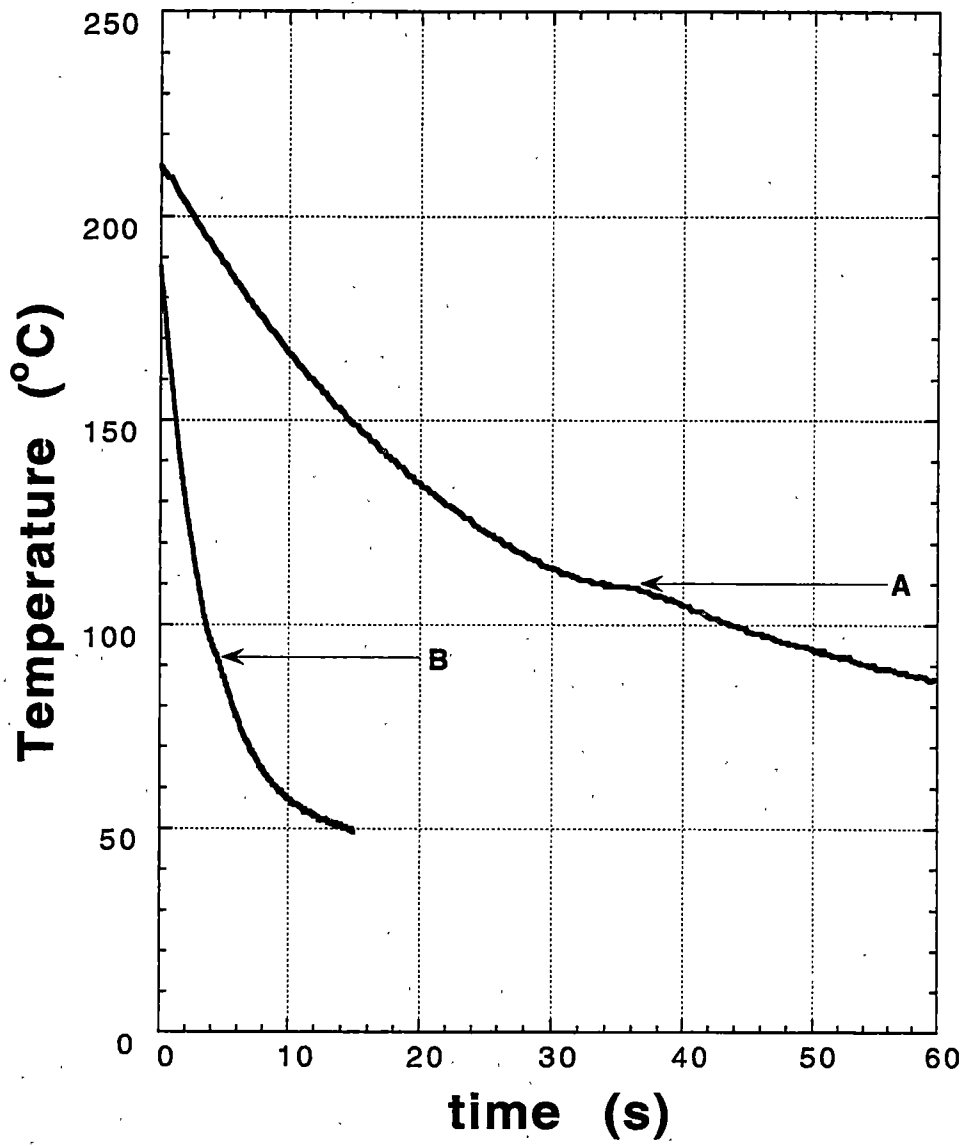
Figure 4.66 HCRLDM temperature versus time run.

<u>Crystallization Onset Temperature</u>   The crystallization onset time is determined from the plot of I_0 versus time (t), which is shown for run A of Figure 4.66 in Figure 4.67. The crystallization onset time is then used to determine the crystallization onset temperature (To). The crystallization onset time starts when the light intensity begins to decrease, indicated by the arrow in Figure 4.67, which corresponds to nuclei formation and absorption of light. The temperature versus time plot (or more accurately data) is used to determine the temperature at that time when light absorption begins. It is also closely related to the cooling rate of the sample.

<u>Induction Time</u>   The induction time is defined as the amount of time which the polymer takes as it passes below its T_m^0 until the crystallization onset temperature is reached. The induction time gives an indication of the nucleating ability of the resin, by either heterogeneous or homogenous mechanism.

<u>Crystallization Half-Time</u>   The nonisothermal crystallization half-time is determined from a plot of relative crystallinity versus time. The time at which 50% of the total relative crystallinity has been reached is determined. The crystallization half-time is the difference between this time and the induction time.

4.4.2   Bulk Kinetics Results and Discussion

The results in Figure 4.68 show that the relationship between plateau temperature and cooling rate is not linear. At lower cooling rates, the plateau temperature decreases more rapidly than at higher cooling rates. ZNHT has the highest Tp at all ACR. M100 and ZN35 have a similar Tp versus ACR profile, while M10 has a slightly higher Tp than M22 and M32 at most cooling rates. Figure 4.69, which shows To versus ACR, indicates
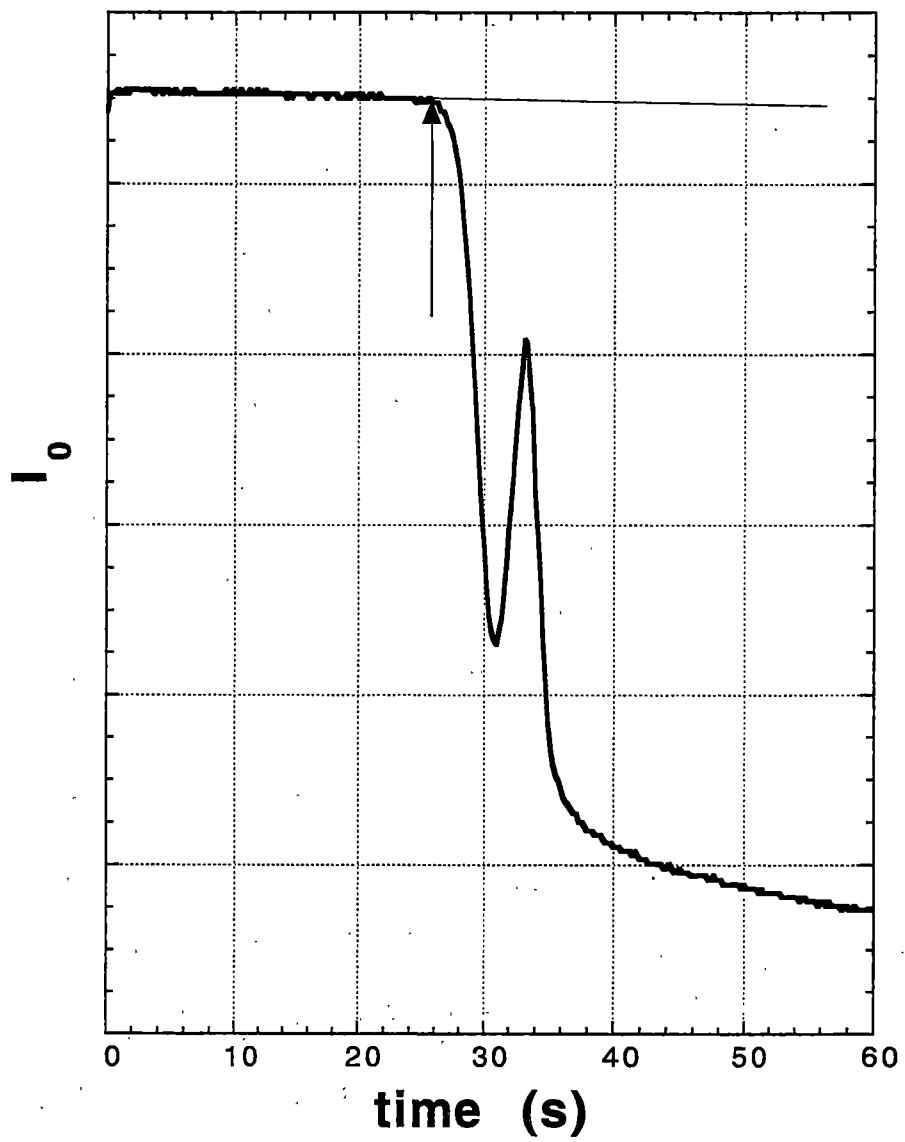
Figure 4.67 HCRLDM I_o versus time run for a typical sample.
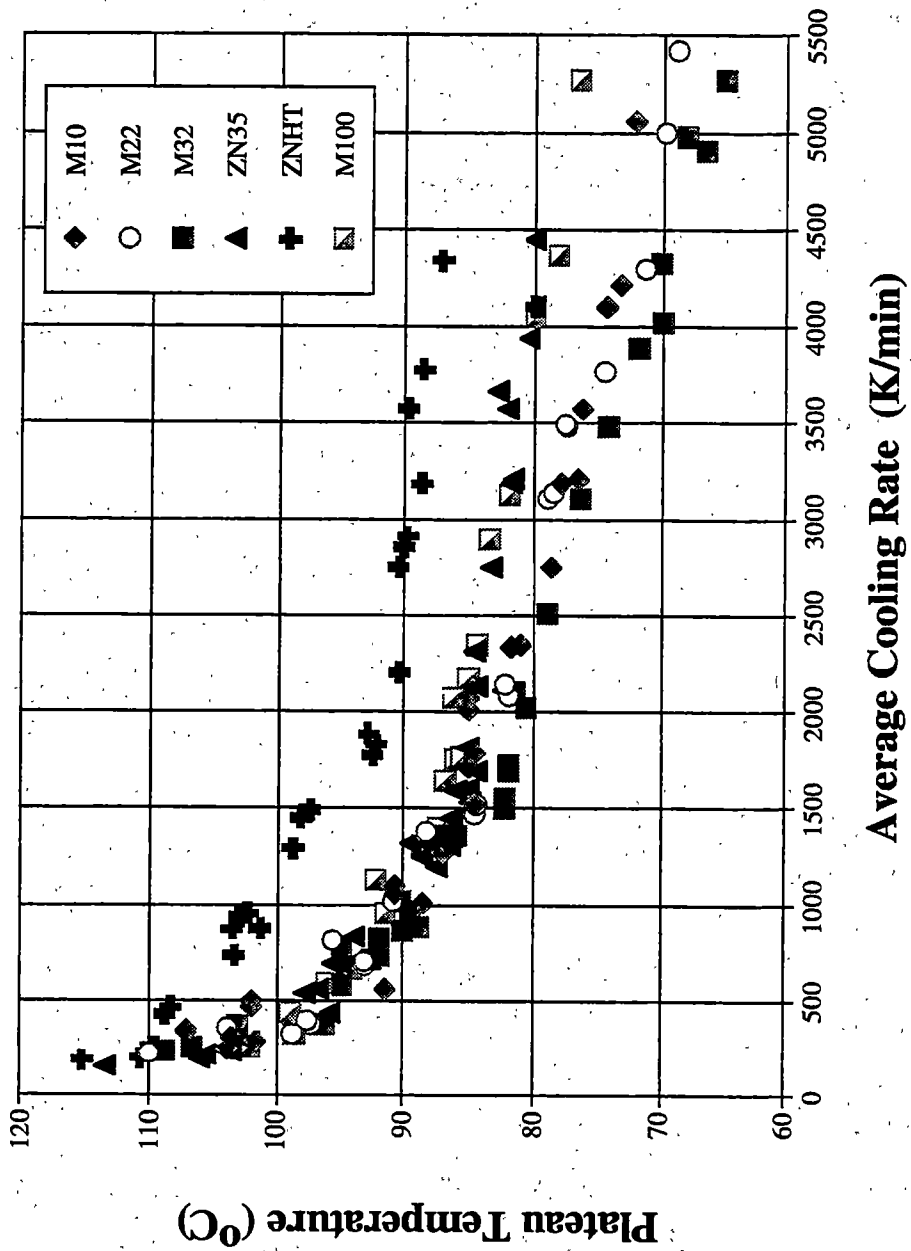
Figure 4.68 HCRLDM Plateau temperature versus average cooling rate for all resins.

that ZNHT also begins crystallization at much higher temperatures than any other resin in this study. The remaining resins are grouped together at lower temperatures with similar To values. More specifically, the miPP resins all have similar To values regardless of cooling rate. While the ZN35 resin has similar To values at most ACRs, but begins to level off at ACRs above 3500°C/min. ZNHT exhibits a similar leveling off at 2500°C/min. The miPP resins To values continue to decrease.

A further observation (from Figure 4.68) is that miPP resins with ACRs above 3500°C/min have a significantly lower Tp than ZN35 and ZNHT. The significance of this finding is very great, especially in a processing environment, which typically have very high ACRs. This result indicates that miPP resins having similar sample mass and thicknesses using high cooling rate conditions, have a delayed crystallization that starts at a lower temperature and occurs, in bulk, at a lower temperature (i.e. lower Tp) than do similar zniPP resins.

The reason for delayed crystallization can be determined from Figure 4.69. The crystallization onset temperature at high ACRs for the miPP resins is considerably lower than the zniPP resins at 4500°C/min. Beginning at 3500°C/min ACR, the miPP resins cool to a lower temperature before crystallization begins. At a ACR of 3000°C/min, the zniPP resins have leveled off and their To remains relatively constant, even as the ACR increases further. Therefore, at a given thickness and air flow rate, the zniPP resins cannot have the onset of crystallization delayed, which means the zniPP resins reach an upper limit critical supercooling value. The miPP resins do not appear to exhibit this behavior. The likely explanation is a result of the configurational defect distribution differences between the miPP and zniPP resins, as has been previously discussed. Nuclei

293
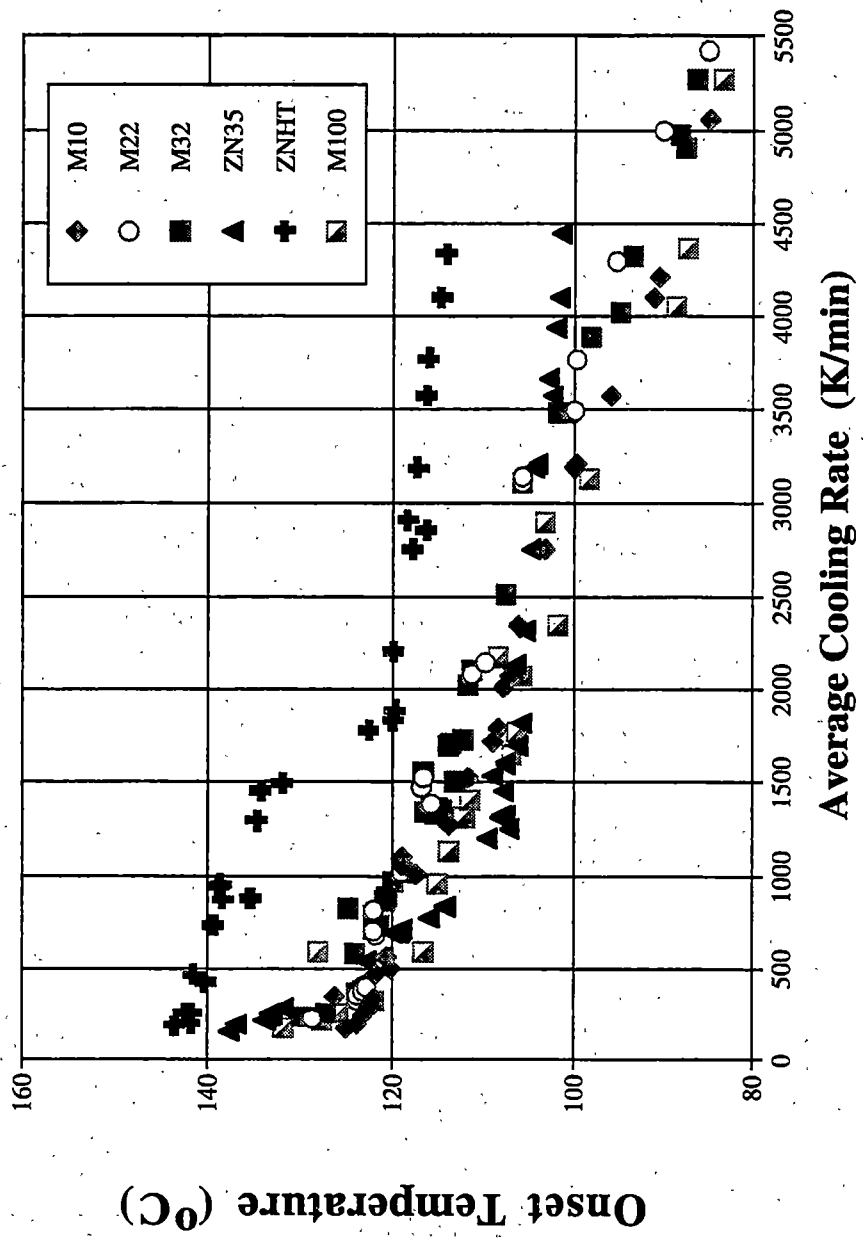
Figure 4.69 HCRLDM Onset temperature versus average cooling rate for all resins.

formation is inhibited in the miPP resins due to the presence and distribution of the configurational defects. In any case, these findings indicate there is good reason to proceed to measure growth and nucleation rates.

The results in Figure 4.70 show the nonisothermal crystallization half-time versus ACR. The data for all resins seems to be grouped together in a narrow band. However, when the nonisothermal crystallization half-time is plotted against the plateau temperature, as in Figure 4.71, some trends emerge. ZNHT and M100 have quite similar $t_{1/2}$, as do ZN35 and M10. M22 appears to crystallize slightly faster than M32 at higher plateau temperatures. Since bulk $t_{1/2}$ rates are a function of both the linear growth rate and nucleation density, it is difficult to make any kind of generalization about these results.

The results in Figures 4.72 and 4.73 show the nonisothermal induction time as a function of ACR and plateau temperature. The induction time should be largely dependent upon the nucleating ability of a particular resin, whether the origin is instantaneous or spontaneous. The results in Figure 4.72 show that the resins are grouped rather close together in a narrow band as a function of cooling rate. However, with careful observation, it can be noticed that generally, M100 and ZNHT have the smallest induction times, followed by ZN35, M22 and M32 with nearly identical values and M100, which appears to take the longest for nuclei to form. It is of interest to note that the order observed for the induction time as a function of cooling rate is similar to the order of each resin's number average molecular weight. The results in Figure 4.73, induction time versus plateau temperature, follow a trend close to the induction time versus ACR, although the data has more scatter. M10, M22 and M32 appear to be

295
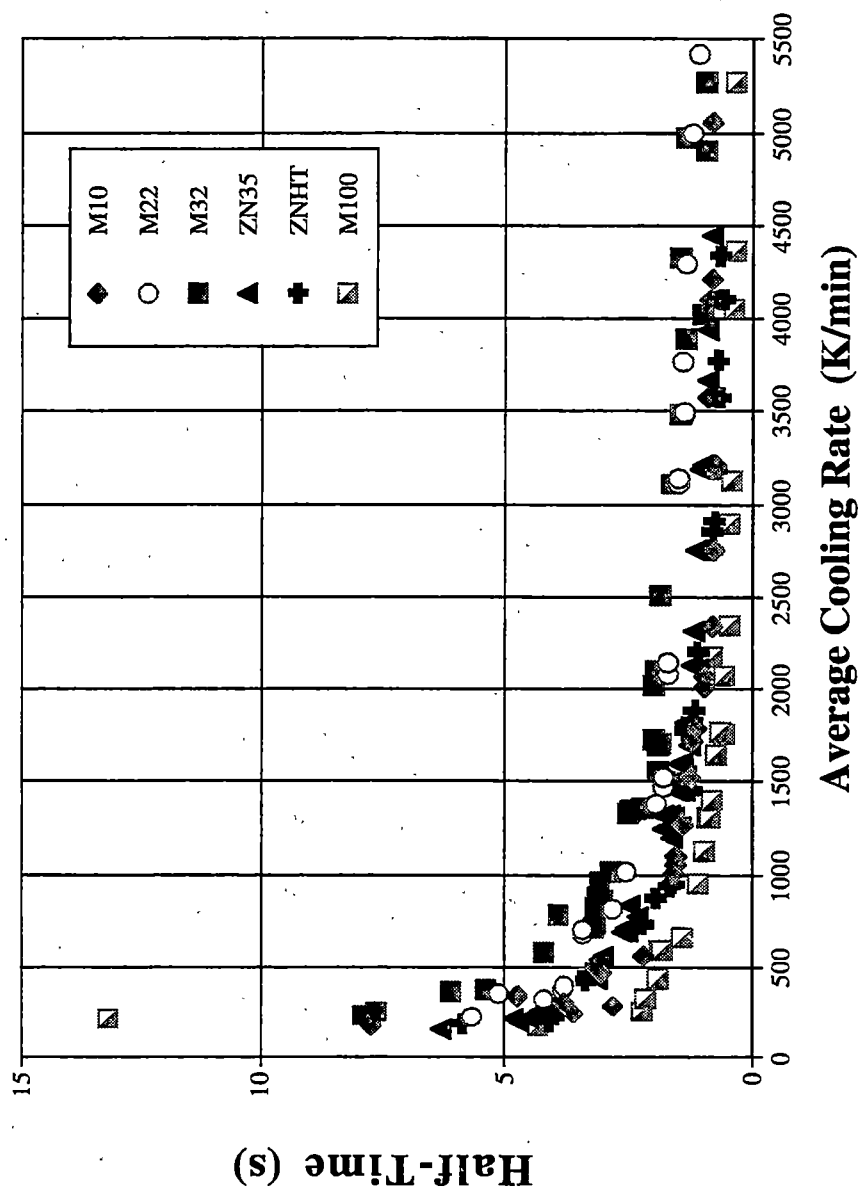
Figure 4.70 HCRLDM Crystallization half-time versus average cooling rate for all resins.
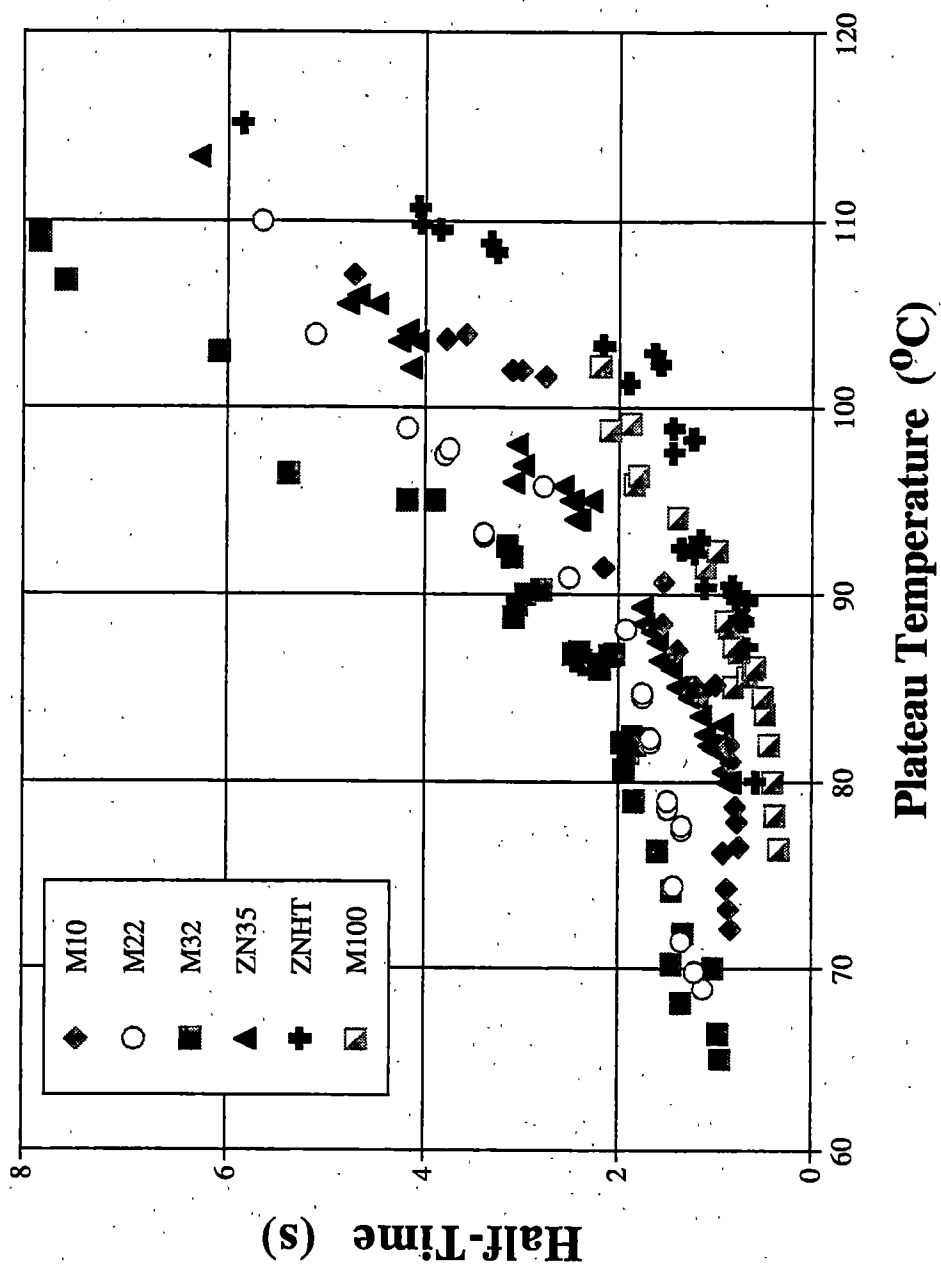
Figure 4.71 HCRLDM Crystallization half-time versus plateau temperature for all resins.
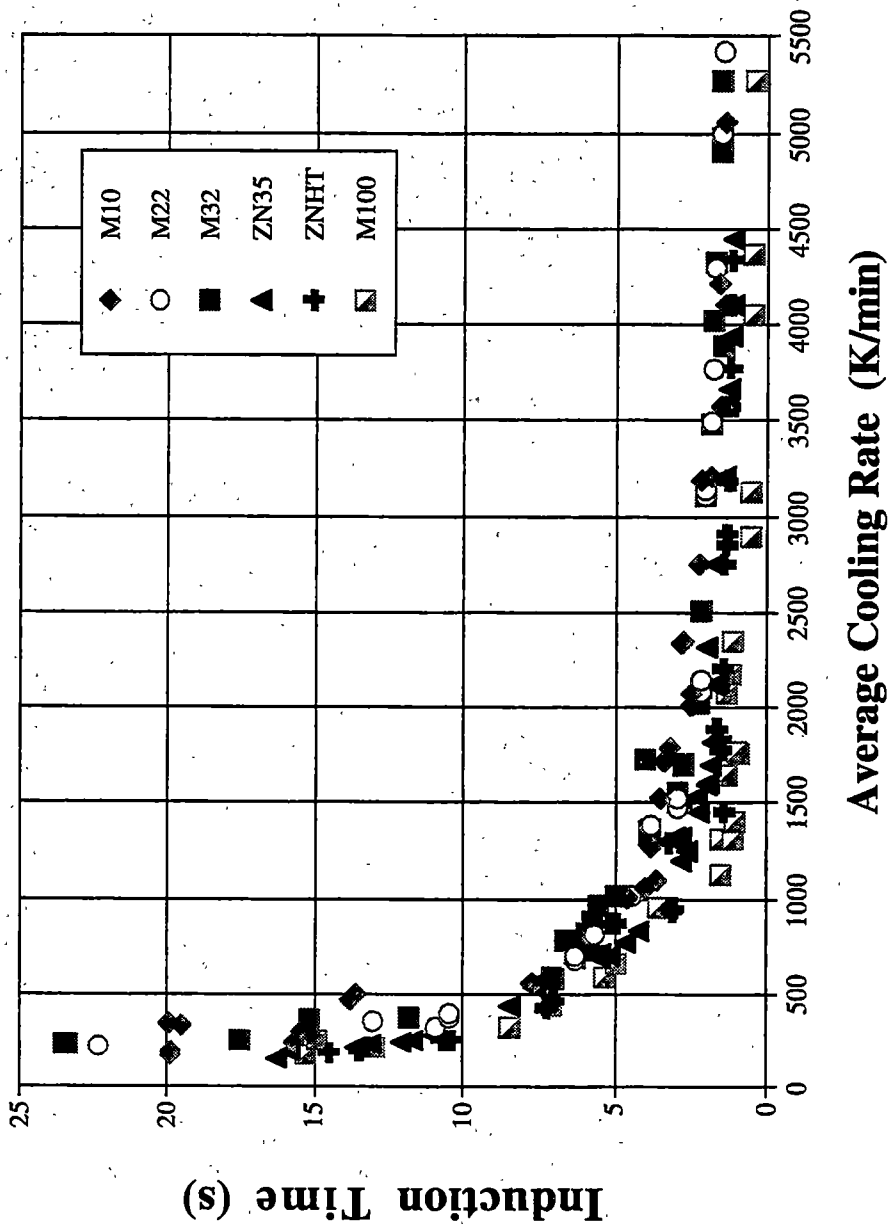
Figure 4.72 HCRLDM Crystallization induction time versus average cooling rate for all resins.
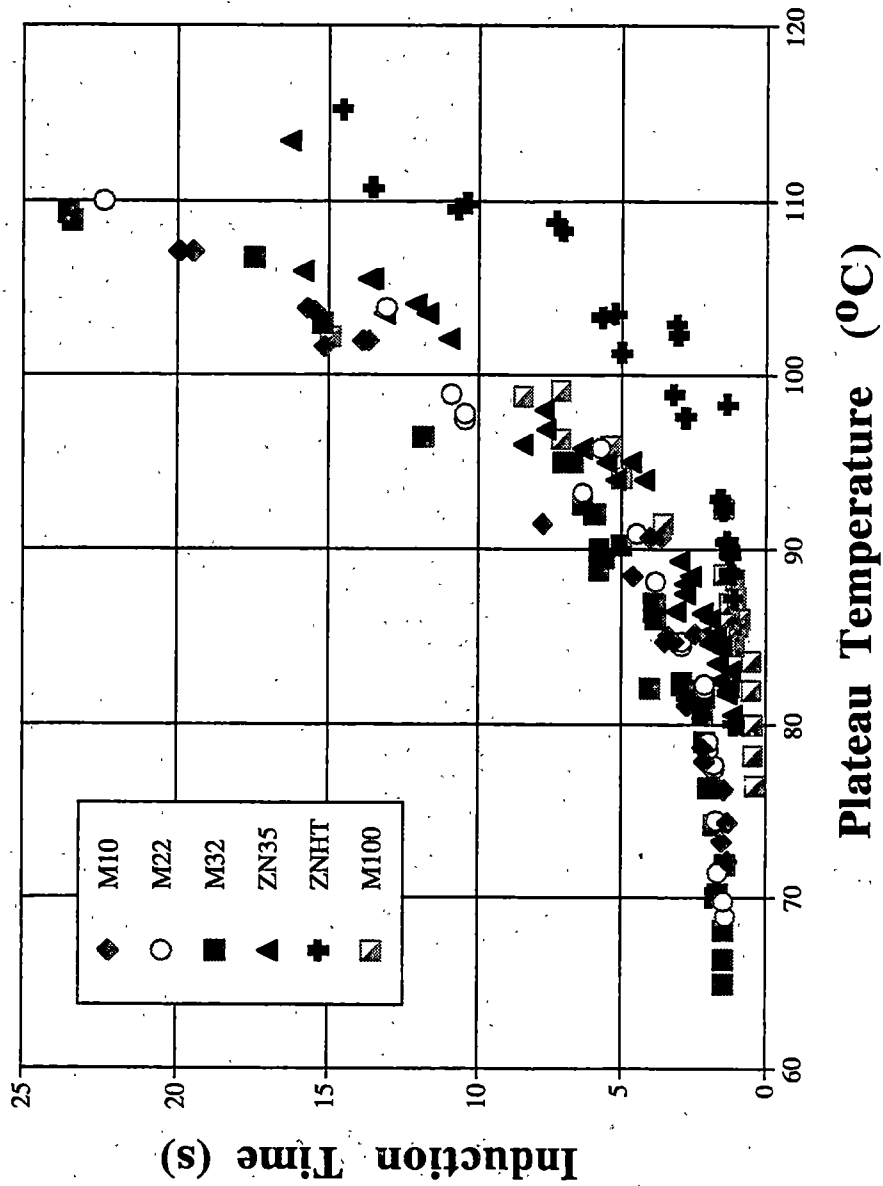
Figure 4.73 HCRLDM Crystallization-induction time versus plateau temperature for all resins.

grouped quite close together with the longest induction times. ZNHT has the fastest induction times, especially with Tp values greater than 90°C. M100 and ZN35 were grouped rather close together above 90°C also, with slightly shorter induction times than the M10, M22 and M32 group.

The results suggest that miPP and ZN35 have similar nonisothermal bulk crystallization kinetics, with M10 and M100 crystallizing slightly faster in some cases. The major difference is that the miPP resins and ZN35 have lower To and Tp values when compared to ZNHT. In the bulk kinetics, the influence of nucleation and growth rates can not be separated. It is, therefore, difficult to attribute a crystallization kinetic behavior to any one resin characteristic.

4.4.3 Nonisothermal Crystal Growth Nucleation Kinetics

The effects of nucleation and crystal growth rates were measured directly under nonisothermal crystallization conditions. The nonisothermal kinetics were performed using the HCRLDM system with a thermocouple directly embedded in the sample to enable accurate temperature profile to be obtained under each cooling condition. The growth and nucleation rates were recorded using a video camera and VCR.

4.4.3.1 Nonisothermal Growth Rates

The growth rates were assumed to be linear, although at high ACRs (above 2000°C/min) this is highly doubtful. This could not be accurately tested since the time scale for growth is so rapid that obtaining more than two frames in focus during nonisothermal growth is virtually impossible at the highest cooling rates with the present

video equipment. Due to the vibrations of the sample chamber, several attempts must be made at one set of mass flow settings to achieve, at best, one run in focus that allows for accurate analysis of growth rates and nucleation density. However, only the last couple of data points in each case are subject to this uncertainty.

The results in Figure 4.74 show the nonisothermal growth rate as a function of the ACR. Figure 4.75 shows the nonisothermal growth rate as a function of Tp. Figure 4.76 shows the isothermal and nonisothermal growth rates together. The data seem to form continuous curves for each resin. However, there is a break between the two sets of data (the left set of points is under isothermal conditions and right side data is nonisothermal), with the long break separating the two groups of data for each material. At a given Tp, ZNHT had the highest growth rate, followed by M100, ZN35, M32, M22 and M10. The observation is made that the trend in nonisothermal growth rate follows the same order as the number average molecular weight, except for M100 again. (Recall that under isothermal conditions the growth rate was determined by the number of configurational defects). ZNHT and M100 have very similar number and weight average molecular weights. With similar molecular weights, the deciding factor in determining which resin has the highest growth rate would go to ZNHT since it has far fewer configurational defects than M100. However, the data most closely reflect the order of number average molecular weight for each polymer.

The present data suggests that the limiting factor in determining the growth rate under nonisothermal conditions (for highly stereo regular iPP) is the molecular weight of a particular resin. Molecules with less repeat units will diffuse faster and have a higher mobility at similar Tps since these molecules have fewer entanglements. The viscosity of

301
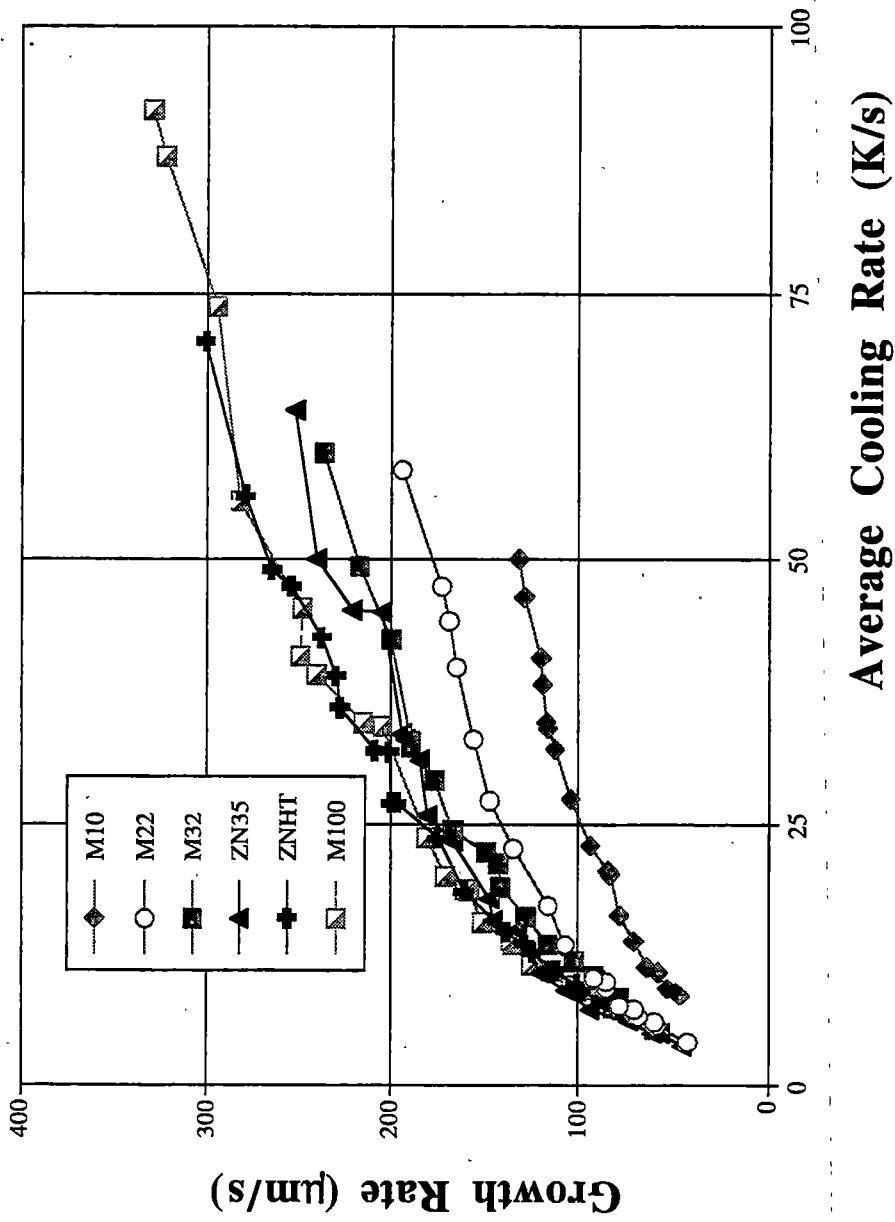
Figure 4.74 HCRLDM Spherulite growth rate versus average cooling rate.
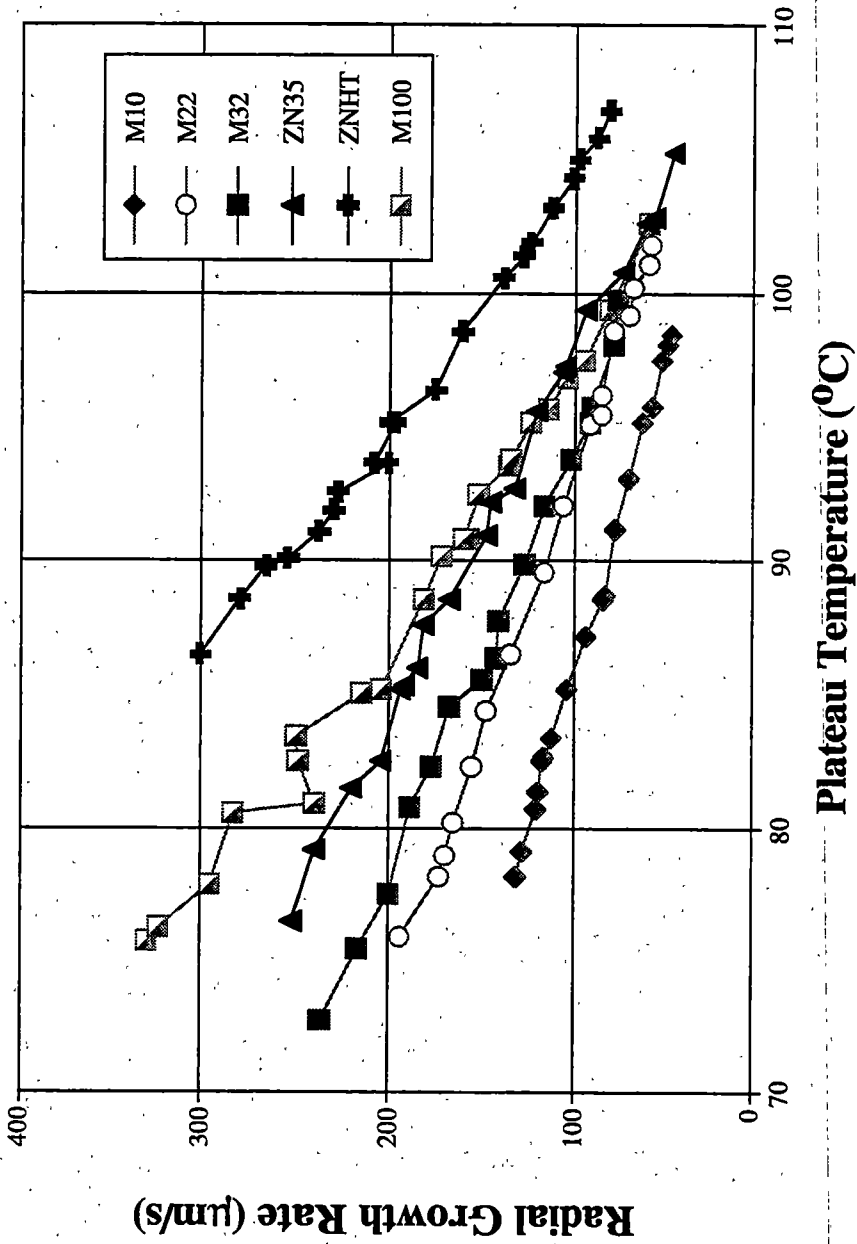
Figure 4.75 HCRLDM Spherulite growth rate versus plateau temperature.
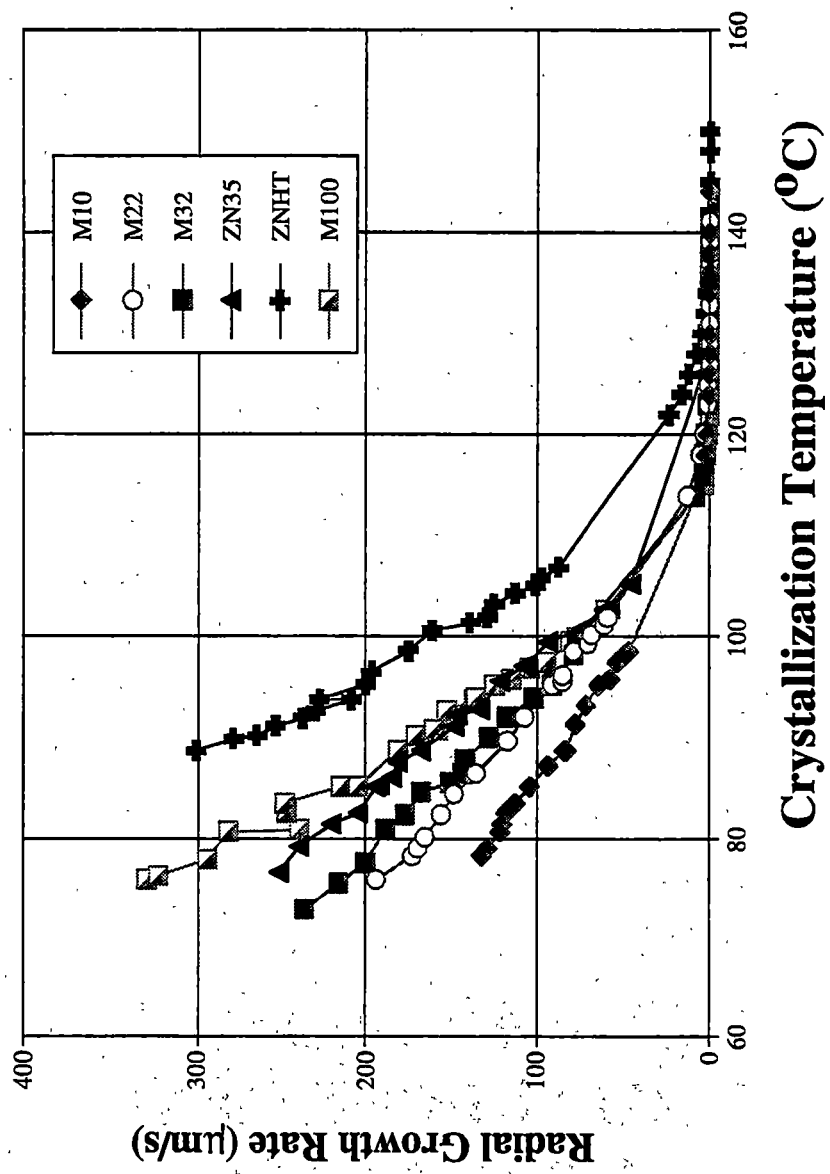
Figure 4.76 HCRLDM and isothermal spherulite growth rate versus crystallization temperature. The left set of data points are from nonisothermal growth rates and the right set of data points from isothermal growth rate studies.

a resin is strongly dependent upon temperature. Under nonisothermal conditions, the temperature at crystallization is approximately 90K or more below the equilibrium melting temperature. Therefore, the mobility of polymer chains under isothermal conditions is very different than polymer chains crystallized under nonisothermal conditions, when the temperature is substantially lower at crystallization onset. Based on viscosity as a function of temperature, the experimental growth rates under nonisothermal conditions do not seem unreasonable. However, molecular weight alone is not the only determining factor. The chemical homogeneity (tacticity or number of configurational defects) is also important and is a factor in determining the growth rate. For instance, as pointed out above for ZNHT and M100, when the molecular weights are similar, the highest growth rate will then go to the more stereoregular resin.

Section 4.3.3 discussed the reason for defect incorporation into the crystal. It was stated that the driving force to form the crystal increased as the crystallization temperature decreased. Under nonisothermal crystallization conditions, the loss in enthalpy due to defect incorporation is more than offset by the huge driving force to crystallize. The present growth rate data further suggest that when the driving force to crystallize is high, the molecular weight of a particular resin becomes the most important factor in controlling the linear growth rate under nonisothermal conditions. For both isothermal and nonisothermal linear growth rates, thermodynamics controls the linear growth rates of a resin at a particular crystallization temperature. However, the manner in which the thermodynamics influences the isothermal and nonisothermal process is quite different.

In isothermal crystallization, the crystallization temperatures are usually quite high and near the equilibrium melting temperature. Therefore, stem deposition occurs when the stability (ΔG) of the melt and crystal are quite similar (see section 4.1.3). When the enthalpy released upon crystallization is decreased, with the same loss in entropy, the driving force for that stem to back off is high since the full effect of the phase change is not realized. This factor then causes defects to be rejected for the most part from the crystal matrix, as was discussed in section 4.1.3.

For nonisothermal crystallization, the thermodynamic driving force for a stem to crystallize is much greater i.e. the stem depositing onto a crystal substrate with defects present is still more stable than the melt. The limiting factor in the rate of linear growth in this case will then be how fast the molecules can disentangle, align and snap into crystallographic registry. In this case, the thermodynamics cedes control of the crystallization process to the diffusion rate of the polymer molecules, which could be referred to as kinetic control. The kinetics in this case being temperature and molecular weight sensitive. However, the present data further suggest that the influence of stereoregularity is not completely lost, as ZNHT has a higher linear growth rate than similar molecular weight M100.

4.4.3.2 Nonisothermal Nucleation Density

The data in Figure 4.77 and 4.78 show the nucleation density as a function of both ACR and Tp (respectively). The data show that M100 has the highest nucleation density, followed by M10, M22, ZN35, M32 and ZNHT. Resin ZN35 shows a rather strange upturn at higher cooling rates. It is rather difficult to make any type of conclusions
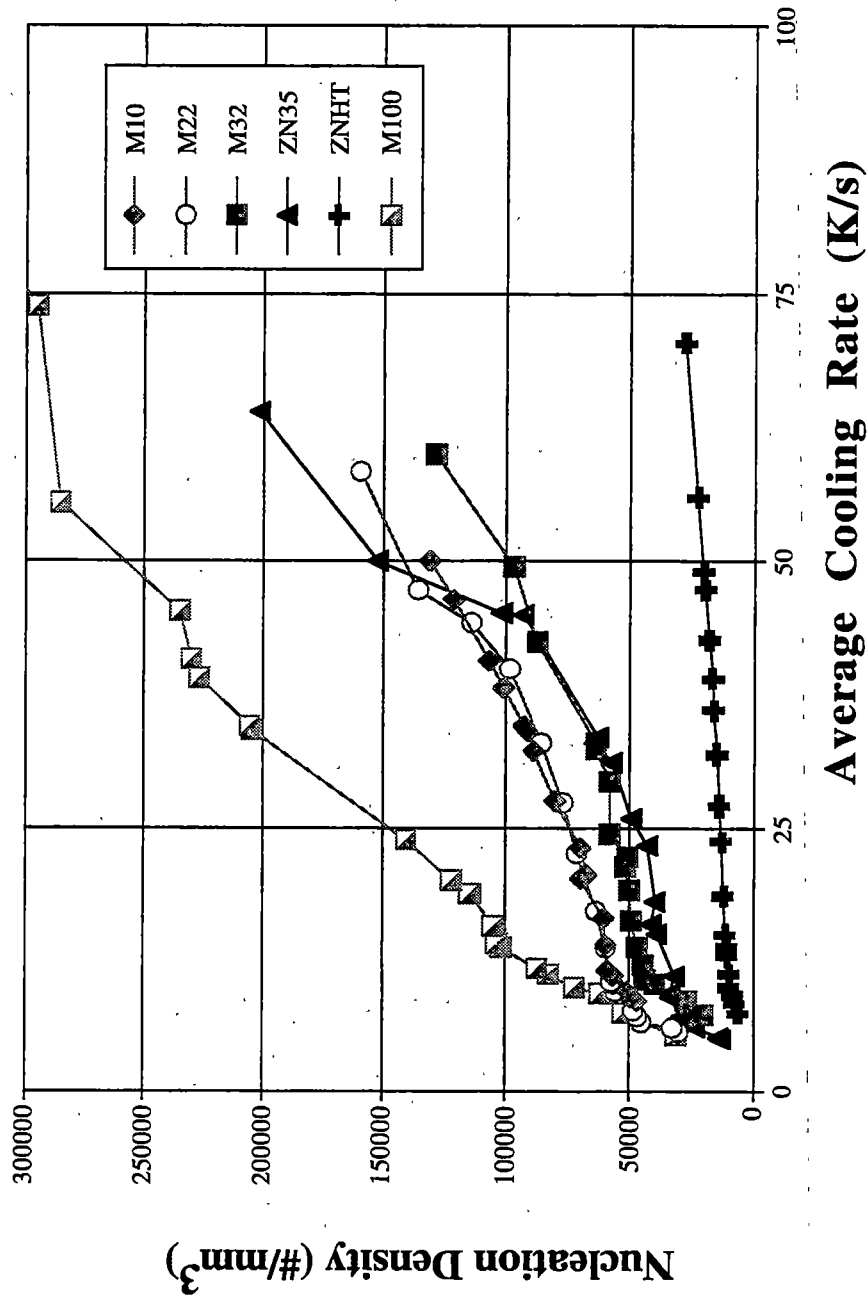
Figure 4.77 HCRLDM Nucleation density versus average cooling rate.
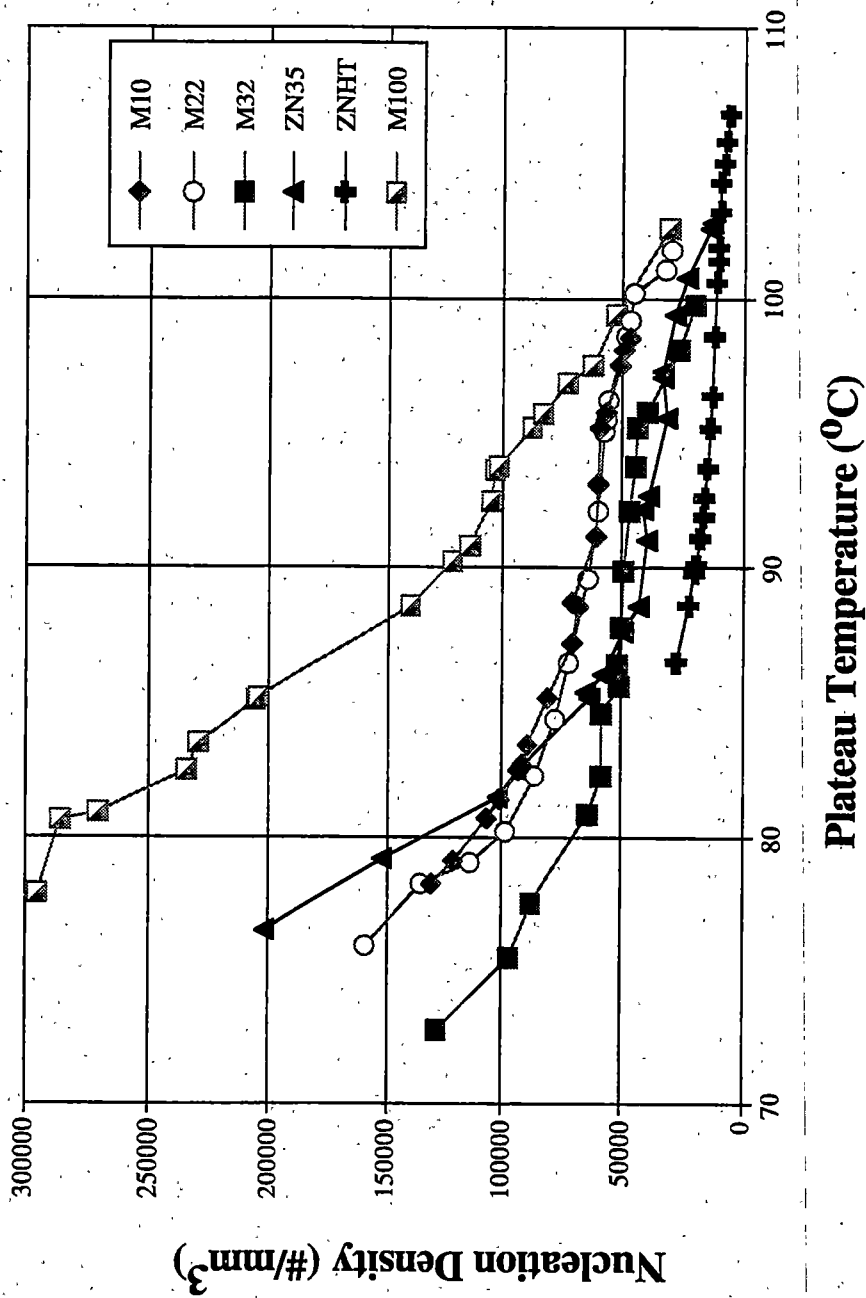
Figure 4.78 HCRLDM Nucleation density versus plateau temperature.

regarding molecular weight effects and tacticity effects on the nucleation density, a result of foreign debris being the most active form of nucleation in any particular resin. Without detailed information about the resin preparation procedure one can not know a priori whether a resin has more foreign nucleating material in it than any other resin. This is rather unfortunate since primary nucleation is the most important factor in crystallization in regime III and most definitely in any type of processing environment. However, the story of primary nucleation in this work does not end here.

It was observed during nonisothermal crystallization that a significant number of nuclei formed after the initial instantaneous burst of nuclei; the nuclei formed after the initial burst are termed athermal nuclei. Notice that the nucleation density increases as the ACR increases and Tp decreases, with the exception of ZNHT which is relatively constant. Athermal nuclei are homogenous in origin and are produced as initially transient metastable nuclei that become stable as the temperature continuously decreases during the rapid cooling of the sample. Therefore, more athermal nuclei are formed as the ACR increases. Recent theoretical and experimental work[204,205] on athermal nuclei has demonstrated that under nonisothermal conditions, conditions where a temperature gradient and/or molecular orientation are involved, athermal nucleation can become the dominate form of nucleation, in the absence of large scale addition of any type of nucleating agent.

In principle, the same molecular factors that influence growth rates are important in the nucleation process. In the production of athermal nuclei, both molecular weight and tacticity become important, with molecular weight likely the dominate term. The relaxation time for particular molecule depends on its number of repeat units or

molecular weight. The higher the molecular weight, the more entanglements the molecule will have with other molecules and the longer its relaxation time. A shorter relaxation time allows a low molecular weight molecule to relax before the athermal nucleation can be triggered at a given temperature. Tacticity becomes important because it will determine the local stability of a nucleus during nucleus formation, i.e. athermal nucleation occurs due to metastable nuclei becoming stable as a result of the temperature change. If the further complication of a defect is present it will further destabilize the metastable nucleus and cause a higher decay rate than otherwise would be found had the defects not been present at a given temperature. As noted earlier, defects present lower the enthalpy released upon crystallization. Therefore defects present in a forming critical nucleus will alter the stability of that nucleus under a given set of crystallization conditions (temperature and cooling rate most notably). However, the present nonisothermal nucleation density results do not seem to directly confirm or support the influence of molecular weight and defects on nuclei formation.

The nonisothermal nucleation density results generally agree in resin order with the isothermal nucleation density results (see Figure 4.41) for the miPP resins. M100 still has the highest nucleation density, with M10 and M22 having similar nucleation density values as a function of plateau crystallization temperature. M32 had the lowest nucleation density, although M32 was higher than ZNHT. ZNHT in the isothermal nucleation density case was intermediate between M10 and M22, so its relative behavior has changed. Again it is difficult to attribute any type of nucleation behavior to any particular resin characteristic since the factors affecting the nucleation process are not

completely known and these resins have not been purified to remove any atactic material or contaminants.

4.4.4 Nonisothermal Regime Analysis

A nonisothermal regime analysis was conducted on the resins in this study in a manner similar to the one carried out under isothermal conditions outlined in section 4.2.1. The plateau temperature was used as the crystallization temperature. With the present resins, all nonisothermal crystallization occurred in regime III. These details are known since the lowest regime II-III temperature was 127.3°C for M100. The highest Tp for any resin in this growth rate study was slightly under 110°C for ZNHT (see Figure 4.75). Where needed, the SAXS and DSC determined values for T_m^{NE} and ΔH_f under nonisothermal conditions are used from Table 4.13. The nonisothermal T_m^{NE} and ΔH_f were used since they more accurately reflect the thermodynamic state of polymer chains during the course of crystallization, under nonisothermal conditions.

The results in Figures 4.79 shows the regime plot for M10, M22, M32, ZN35, ZNHT and M100. Figure 4.80 shows the isothermal and nonisothermal regime data all on one plot. All resins exhibited a linear relationship within the temperature range investigated. The slope (K_g) and intercept (G_o) are tabulated in Table 4.15, along with the isothermal slopes and intercepts in regime III. The results are clearly divided into two groups. The zniPP resins have very similar K_g and G_o under isothermal and nonisothermal crystallization conditions. The K_g and G_o values have all decreased for the miPP resins.

311
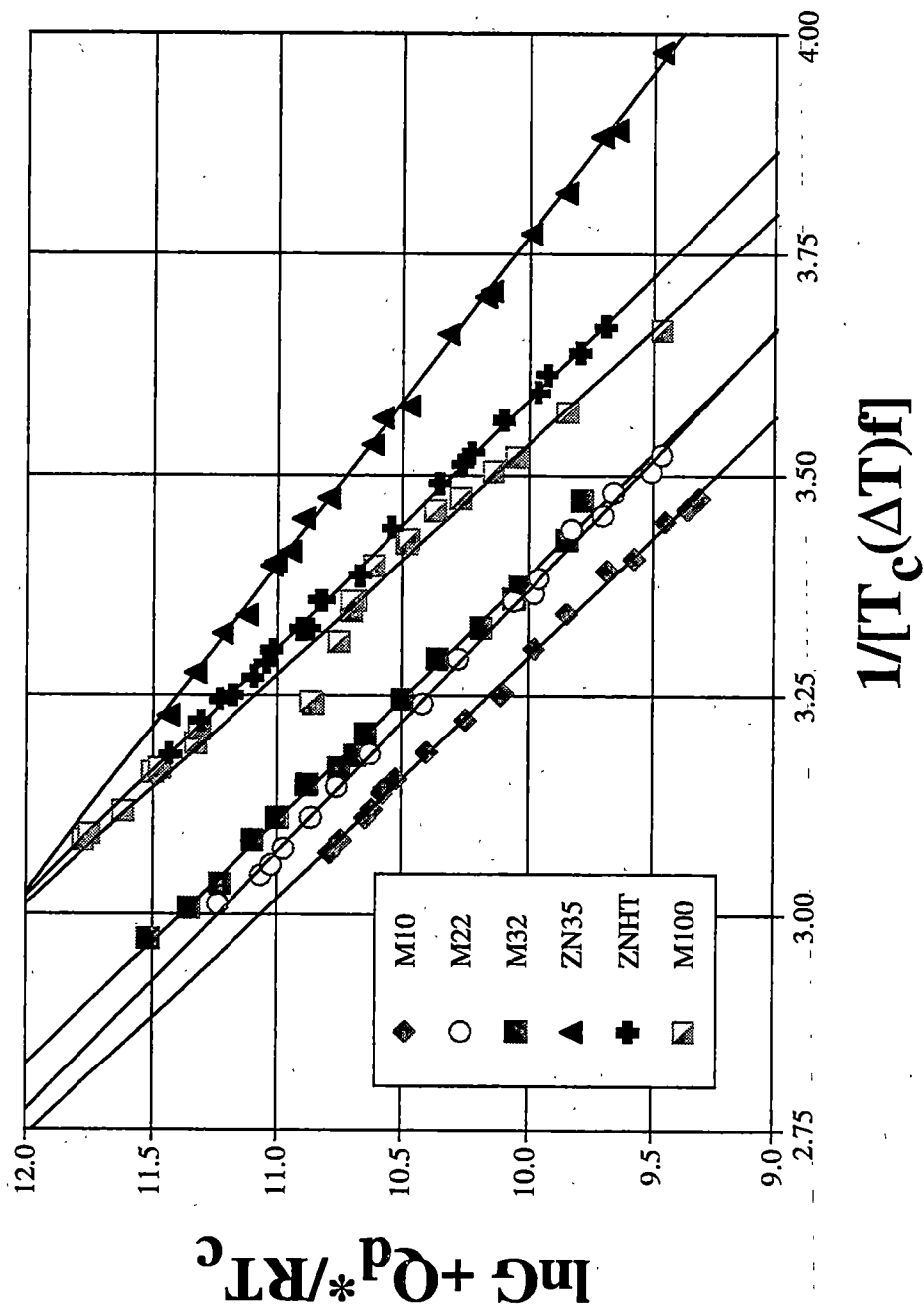
Figure 4.79 HCRLDM Regime analysis for all resins.
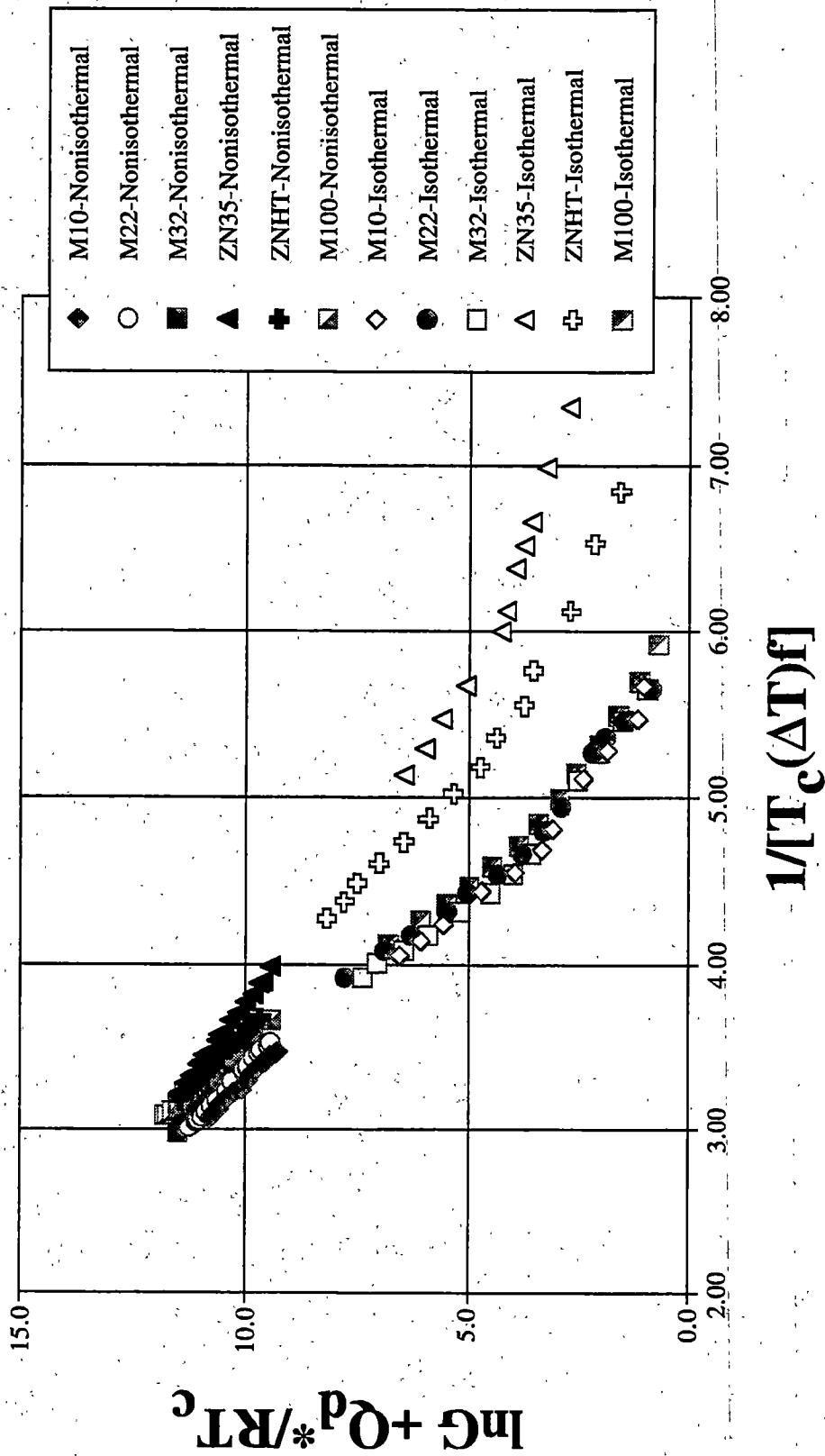
Figure 4.80 HCRLDM and Isothermal Regime analysis for all resins. The nonisothermal data points are in the upper left set of points while the isothermal data points are in the lower right side of the figure.

Table 4.15 Comparison of K_g and G_o determined using regime analysis in regime III under isothermal and nonisothermal conditions.

Resin	Isothermal		Nonisothermal	
	K_g (x10^{-5}K^2)	G_o (μm/s)	K_g (x10^{-5}K^2)	G_o (μm/s)
M10	5.06	27.1	3.65	22.0
M22	5.38	28.8	3.36	21.3
M32	5.25	27.9	3.58	22.1
ZN35	2.41	18.8	2.69	20.1
ZNHT	3.81	24.5	3.54	22.7
M100	4.96	27.2	3.81	23.5

314

The zniPP resins showed good agreement when comparing the regime analysis under isothermal and nonisothermal conditions. This confirms earlier work by Ding and Spruiell for the HCRLDM system using similar zniPP resins[196].

The changes in K_g and G_o for the miPP resins may be explained by understanding that the T_m^0, ΔH_f, σ and σ_e all changed for the miPP resins under nonisothermal conditions, due to configurational defect incorporation into the crystal matrix. Therefore, the value of the slope and intercept of the regime plot could also be expected to change in a manner consistent with the changes in thermodynamic properties since it is composed of these terms (recall equation 2.14).

In order to resolve the factors affecting the change in K_g (which is the nucleation term) for the miPP resins, the ratio of $\left(T_m^0 / \Delta H_f\right)^2$ was studied for any changes for each resin. The ratios are shown in Table 4.16. The change in the ratio from isothermal to nonisothermal crystallization does not change dramatically for any resin and can not be used to explain the differences in K_g from isothermal to nonisothermal regime analysis. In fact, with the exception of M10, the change in ratios for these two thermodynamic quantities would predict an increase in K_g. The supercooling term, ΔT, also decreases or remains constant for each resin as the T_m^0 for each resin has remained the same or decreased. Slight changes in σ are expected since it depends on ΔH_f, but not enough to explain the nearly 40% reduction in K_g. Therefore, the decrease in K_g is attributed to the change in σ_e. As was shown earlier in Table 4.14, the change in σ_e was very dramatic for the miPP resins when comparing the isothermal and nonisothermal σ_e determined by using SAXS, WAXD and DSC. The σ_e has been determined from nonisothermal regime

315

Table 4.16 Comparison of Isothermal and Nonisothermal $T_m^0/\Delta H_f$ values.

Resin	Isothermal $T_m^0/\Delta H_f$ (°Cg/J)	Nonisothermal $T_m^0/\Delta H_f$ (°Cg/J)
M10	11.2	9.01
M22	7.65	8.66
M32	7.74	8.62
ZN35	7.21	7.72
ZNHT	7.38	7.80
M100	7.64	9.09

analysis using the appropriate nonisothermal thermodynamic quantities and is shown in Table 4.17, along with the isothermal regime analysis calculated σ_e values.

The nonisothermal regime analysis σ_e values exhibit a decrease in σ_e when compared to the isothermal σ_e values. Clearly, the values of K_g for the miPP resins has decreased due to the decrease in σ_e values under nonisothermal conditions and these σ_e values are close to the σ_e values of the zniPP resins.

4.5 Crystallinity Measurements and Interfacial Thickness Values of Isothermally and Nonisothermally Crystallized Samples

The results of crystallinity measurements on the isothermally and nonisothermally crystallized films are discussed in this section. In addition, qualitative interfacial thickness measurements made on each set of films are presented. These data and calculations will be discussed in terms of σ_e and the nature of the fold surface region under isothermal and nonisothermal crystallization conditions.

Crystallinity for each film was determined using WAXD, DSC and density gradient column. DSC melting enthalpies were corrected for the amount of γ-content, if applicable, since the heat of fusion is lower for that crystal structure.

4.5.1 Isothermal Results

The crystallinity data for the isothermally crystallized films of the various resins is shown in Table 4.18, 4.19 and 4.20. The WAXD and DSC data for all resins agree quite well, with most of the crystallinities within ±2% of one another for each sample of a particular resin. (It should be noted that the DSC crystallinities are determined from ΔH

Table 4.17 Comparison of σ_e for α-iPP under isothermal and nonisothermal conditions using regime analysis.

Resin	σ_e (mJ/m²) Isothermal PE Nucleation Equation	σ_e (mJ/m²) Nonisothermal PE Nucleation Equation
M10	103	76.2
M22	83.5	69.8
M32	85.6	74.5
ZN35	38.8	56.2
ZNHT	60.4	72.7
M100	101	80.4

Table 4.18 M10 and M22 Crystallinity determinations by WAXD, DSC and density gradient column.

Sample M10	X-Ray	DSC[1]	Density	Sample M22	X-Ray	DSC[1]	Density
iso105	0.62	0.61	0.68	iso105	0.58	0.59	0.67
iso108	0.63	0.61	0.68	iso110	0.60	0.62	0.67
iso110	0.62	0.62	0.68	iso113	0.54	0.57	0.65
iso113	0.65	0.63	0.71	iso115	0.60	0.60	0.69
iso115	0.62	0.64	0.71	iso118	0.59	0.60	0.68
iso118	0.63	0.60	0.70	iso120	0.63	0.62	0.70
iso120	0.64	0.63	0.71	iso123	0.58	0.60	0.68
iso123	0.66	0.65	0.73	iso125	0.63	0.62	0.71
iso125	0.68	0.69	0.74	iso130	0.67	0.68	0.74
iso130	0.70	0.69	0.74	iso135	0.70	0.70	0.75

[1]DSC data has been corrected for the percent γ-content to accurately reflect the true crystallinity using DSC

Table 4.19 M32 and M100 Crystallinity determinations by WAXD, DSC and density gradient column.

Sample M32	X-Ray	DSC[1]	Density	Sample M100	X-Ray	DSC[1]	Density
iso105	0.56	0.58	0.67	iso105	0.58	0.59	0.68
iso110	0.59	0.61	0.67	iso110	0.61	0.61	0.72
iso113	0.57	0.58	0.66	iso113	0.60	0.61	0.71
iso115	0.56	0.58	0.67	iso115	0.62	0.61	0.73
iso118	0.58	0.59	0.69	iso118	0.59	0.62	0.72
iso120	0.60	0.61	0.70	iso120	0.63	0.63	0.74
iso123	0.58	0.62	0.68	iso123	0.63	0.64	0.74
iso125	0.57	0.59	0.69	iso125	0.64	0.66	0.74
iso130	0.62	0.61	0.69	iso130	0.66	0.66	0.74
iso135	0.67	0.67	-	iso135	0.71	0.73	-

[1]DSC data has been corrected for the percent γ-content to accurately reflect the true crystallinity using DSC

Table 4.20 ZN35 and ZNHT Crystallinity determinations by WAXD, DSC and density gradient column.

Sample ZN35	X-Ray	DSC	Density	Sample ZNHT	X-Ray	DSC¹	Density
iso115	0.61	0.62	0.65	iso115	0.69	0.67	0.73
iso120	0.62	0.65	0.64	iso120	0.70	0.67	0.74
iso123	0.65	0.66	0.68	iso123	0.70	0.70	0.74
iso125	0.68	0.69	0.70	iso125	0.70	0.70	0.74
iso128	0.63	0.62	0.67	iso128	0.73	0.71	0.74
iso130	0.66	0.63	0.68	iso130	0.72	0.69	0.74
iso133	0.64	0.66	0.68	iso133	0.71	0.69	0.74
iso135	0.72	0.70	-	iso135	0.72	0.70	0.74
iso140	0.66	0.65	0.68	iso140	0.71	0.70	0.74
iso145	0.67	0.68	0.70	iso145	0.71	0.71	0.74

and WAXD measurements extrapolated to 100% crystallinity under isothermal crystallization conditions. Therefore, they are not completely independent of one another) When the crystallinity by density data is compared to the DSC and WAXD crystallinities, two definite trends emerge. The zniPP resins, ZN35 and ZNHT, have crystallinity by density values that are typically 2-4% higher than either the WAXD or DSC values for each sample. The miPP resins all show a 6-10% higher crystallinity by density when compared to the WAXD and DSC crystallinities, which is significantly higher than that of the zniPP resins. As stated previously, the behavior of ZNHT should be considered the standard, since it has low xylene solubles and very few defects. Therefore, one might expect a 2-4% higher crystallinity by density for all iPP samples. This observation has been made previously by other researchers and has been attributed to the interfacial region surrounding lamellae having a higher packing density than the totally amorphous region[241,242,245-247]. With this in mind, the miPP resins exhibit increases in crystallinity by density of 1-6% higher than those found with zniPP.

The data in Figure 4.81 shows the interfacial thickness as a function of lamellae thickness, as determined from SAXS studies. The data show that the zniPP resins have a significantly thicker interfacial region than any of the miPP resins. The zniPP resin's interfacial thickness values remain constant or increase slightly with increasing lamellae thickness. The miPP resins are grouped fairly close together and tend to decrease in interfacial thickness as lamellae thickness increases. It is also worth noting that the general order of interfacial thickness, from thinnest to thickest, follows the order of highest to lowest fold surface free energy, i.e. M10 has the smallest interfacial thickness and the highest fold surface free energy.
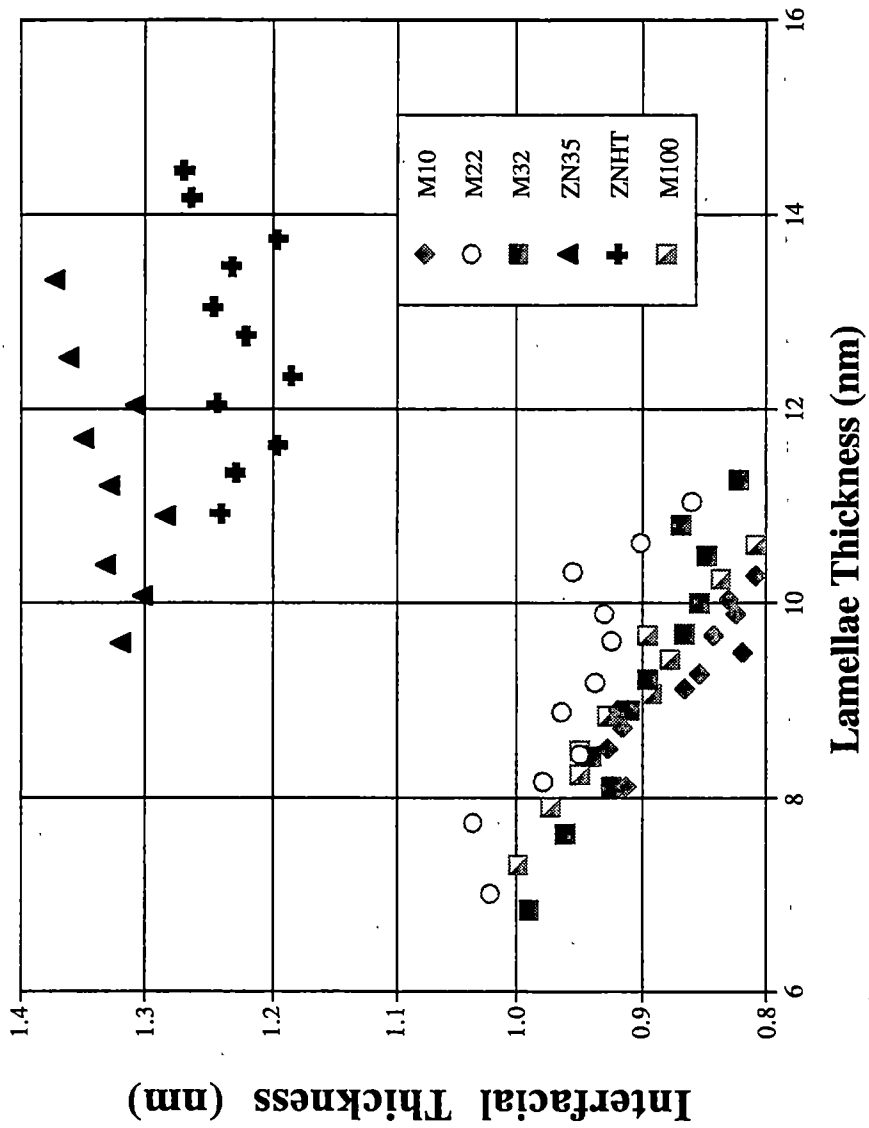
Figure 4.81 Interfacial thickness versus lamellae thickness determined by SAXS un der isothermal crystallization conditions.

4.5.2 Nonisothermal Results

The crystallinity data for the nonisothermally crystallized films is shown in Tables 4.21, 4.22 and 4.23. For all resins, the crystallinity by density data are higher than the WAXD values by roughly 5-7% for the same sample. The DSC crystallinity values are significantly lower, by roughly 10%, than the WAXD crystallinity for all samples of each resin except those of ZNHT. ZNHT had DSC crystallinity values roughly 15% lower than either the density or WAXD values.

The interfacial thickness of the nonisothermally crystallized films as a function of lamellae thickness is shown in Figure 4.82. The data indicates that the interfacial thickness decreases as the lamellae thickness decreases for each resin. Additionally, the interfacial thickness for these samples are generally thinner than for the isothermally crystallized films. The interfacial thickness of the miPP resins have not decreased as significantly as the zniPP resins. The data points in Figure 4.82 seem to fall on a rather broad common line for all materials as a function of lamellae thickness.

4.5.3 Discussion of Interfacial Thickness and Crystallinity Values

The results found in studying the crystallinities and interfacial thickness of the isothermally and nonisothermally crystallized films may further explain the reason why the miPP resins have lower overall melting temperatures for similar lamellae thickness.

In this chapter it has been stated that crystallization under isothermal conditions, i.e. relatively near equilibrium, causes configurational defects to be preferentially excluded from the crystal matrix. The excluded defects are thought to be present in the interfacial region, where the defects increase the fold surface free energy in a manner

Table 4.21 M10 and M22 Crystallinity determinations on nonisothermally crystallized films by WAXD, DSC and density gradient column.

Sample M10	X-Ray	DSC	Density	Sample M22	X-Ray	DSC	Density
1	0.60	0.47	0.67	1	0.62	0.54	0.68
2	0.62	0.49	0.69	2	0.60	0.52	0.67
3	0.61	0.48	0.67	3	0.57	0.50	0.63
4	0.62	0.49	0.68	4	0.57	0.51	0.64
5	0.62	0.49	0.68	5	0.59	0.52	0.65
6	0.60	0.48	0.67	6	0.56	0.49	0.63
7	0.63	0.50	0.69	7	0.56	0.50	0.63

Table 4.22   M32 and M100 Crystallinity determinations on nonisothermally crystallized films by WAXD, DSC and density gradient column.

Sample M32	X-Ray	DSC	Density	Sample M100	X-Ray	DSC	Density
1	0.63	0.54	0.70	1	0.59	0.50	0.67
2	0.61	0.51	0.68	2	0.59	0.49	0.65
3	0.59	0.50	0.66	3	0.57	0.47	0.64
4	0.58	0.48	0.65	4	0.56	0.47	0.63
5	0.56	0.46	0.65	5	0.58	0.48	0.63
6	0.57	0.47	0.63	6	0.57	0.48	0.63
7	0.56	0.47	0.62	7	0.56	0.47	0.62

Table 4.23 ZN35 and ZNHT Crystallinity determinations on nonisothermally crystallized films by WAXD, DSC and density gradient column.

Sample ZN35	X-Ray	DSC	Density	Sample ZNHT	X-Ray	DSC	Density
1	0.60	0.57	0.67	1	0.69	0.55	0.77
2	0.58	0.54	0.65	2	0.70	0.55	0.77
3	0.58	0.55	0.65	3	0.67	0.52	0.74
4	0.53	0.49	0.60	4	0.70	0.56	0.75
5	0.56	0.53	0.62	5	0.69	0.55	0.75
6	0.59	0.55	0.65	6	0.70	0.55	0.75
7	0.62	0.59	0.68	7	-	-	-
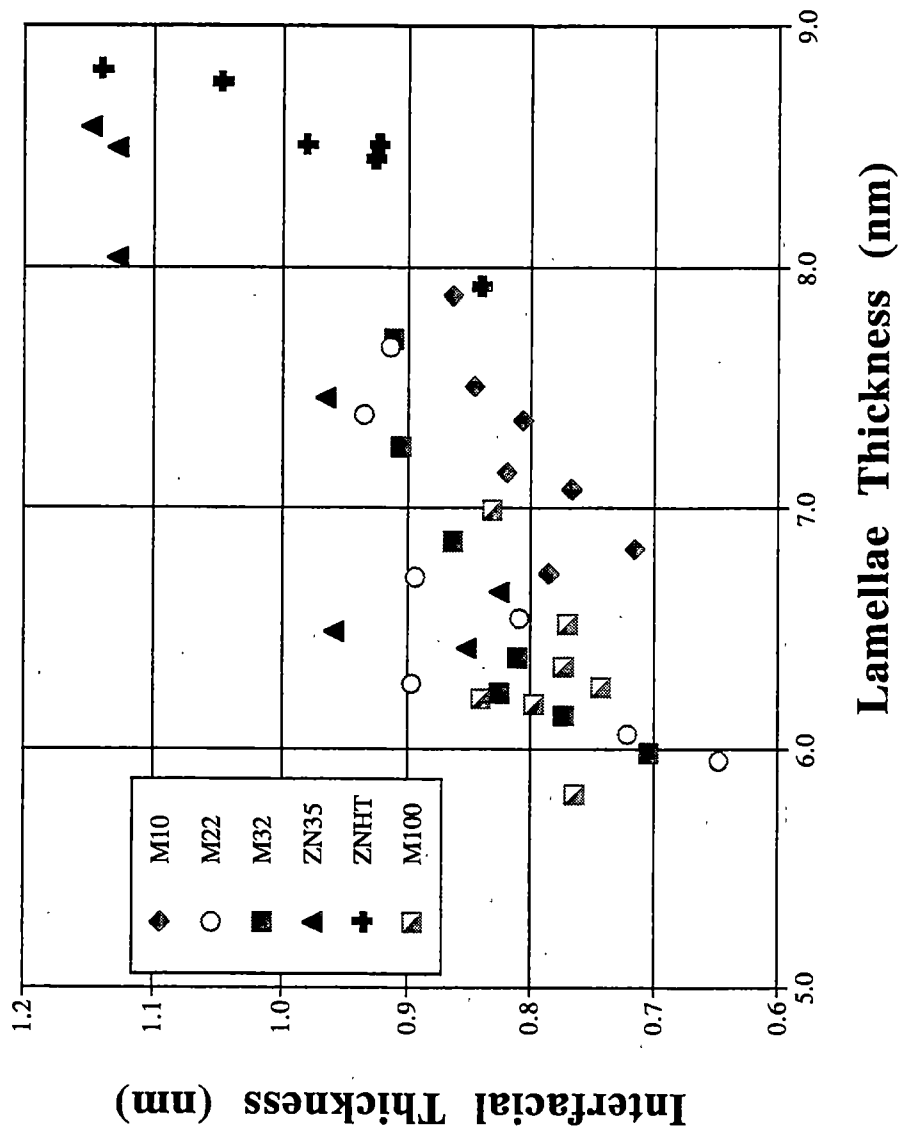
Figure 4.82 Interfacial thickness versus nonisothermal film lamellae thickness.

consistent with the number of defects in the resin. This was offered as the explanation for why the miPP resins could have much lower overall melting temperatures at the same lamellae thickness.

The nonisothermal crystallization results, which occur far away from equilibrium, indicated that defects were not as preferentially rejected. Defect incorporation and crystallization under nonisothermal conditions gave fold surface free energies for the miPP resins quite similar to those determined for the zniPP materials. Based on the isothermal and nonisothermal studies, combined with the crystallinity results and interfacial thickness findings in this section, a theory can be constructed to explain the melting behavior of the miPP resins. An explanation can also be presented to explain why ZN35 has such a low isothermal fold surface free energy.

The nonisothermal DSC crystallinity data indicate that all materials have a significant amount of interfacial material that relaxes before the peak melting temperature region is reached. This would explain the large discrepancy between the crystallinity by DSC and WAXD results. ZN35 did not exhibit such a large difference in crystallinity results determined by the various methods. This is of particular interest since it is the resin with the most xylene solubles. ZN35 also generally has the thickest interfacial region under both isothermal and nonisothermal conditions. It seems plausable that the atactic chains are rejected into the interfacial region, interfering with the folding process. In the interfacial region, the atactic chains are likely to cause the folds to be loose or produce considerable nonadjacent reentry folding due to the interference of these atactic chains during the crystallization process. Additionally, it is worth recalling that the atactic chains have a chemical potential difference with the crystal, therefore they would,

if anything, diffuse toward the interface regions of the crystal. Therefore, based on these arguments, it might be expected that these atactic chains are located at the crystal surface interface. At the interface, the atactic chains lower the interfacial tension since the chains in the interface are able to assume more total conformations. A similar argument can be made for M100, since it has a significant amount of atactic material and a lower than expected σ_e.

The structures in Figure 4.83 show two different depictions[248,249] of what a fold surface region may look like for a crystalline lamellae. The bottom part shows three figures, a, b, and c. The schematic in part a represents a lamellae growth surface before nucleation. The schematic in part c represents a lamellae with some surface roughness. The schematic in section b depicts a lamellae with a considerable amount of surface roughness. The top illustration in Figure 4.83 is the side view of what a rough surface would appear like. For whatever reason, the stems are not aligned from surface to surface of the lamellae in a smooth manner, which produces a rough lamellae surface. The uneven surface creates niches in the top and bottom basal planes of the lamellae crystal exposing more lateral surface of stems. Based on a rough crystal surface proposed above, it would seem reasonable that these niches would increase the total surface area (hence increase the total σ_e value, even though part of the energy is attributed to the lateral surface of the stems) of the lamellae over a relatively smooth two-dimensional lamellae type crystal surface.

The schematic in Figure 4.83(b) c, might represent the nature of the fold surface under isothermal conditions for a polymer that is relatively defect free and produces a rather smooth lamellae surface. The illustration of b in Figure 4.83(b) might be thought
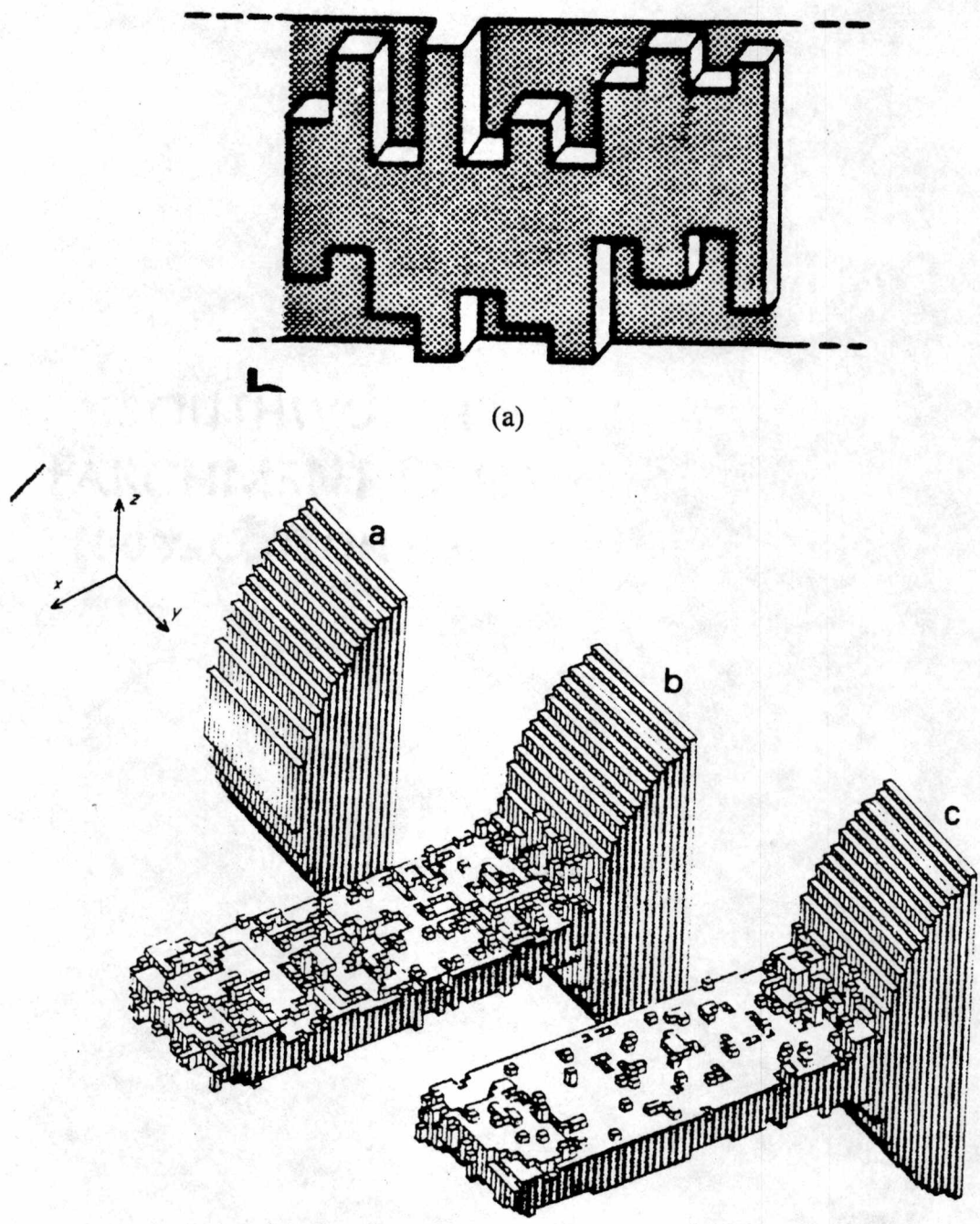
Figure 4.83 Surface roughness model. (a) side view of lamellae[248] (b) fold surface view of surface roughness[249].

of to represent crystallization under nonisothermal conditions, in which crystallization occurs very rapidly producing a rough crystal surface. However, it may also be reasonable to expect the miPP resins, with more total defects that are uniformly distributed, to have a lamellae surface that is rough when crystallized under isothermal conditions. The defects may be rejected to near/at/below/ or /and slightly above the crystal surface. Defects located in this region would seem to surely cause a rougher surface than in an otherwise defect free polymer, sic ZNHT. Therefore for a lamellae of the same dimensions, a miPP resin would have a rougher crystal surface with more effective surface area, than say ZNHT.

Obtaining the fold surface free energy from the Gibbs-Thomson plot assumes a flat crystal surface, where the dimensions are in energy per unit area. The total energy in the mathematical calculation using the Gibbs-Thomson equation is such that it normalizes to a 2-d surface. However, a rough surface with identical length (l) and width (w) will have more total surface area than lw (since it really is 3-d), while a 2-d surface area will be an area lw. This can be said succinctly by stating that a rough lamellae crystal surface has a larger crystal surface area for the interfacial free energy to act upon than a smooth 2-d surface. Since the Gibbs-Thompson equation normalizes to a 2-d flat surface, the total free energy per unit area is going to be indicated as greater in the 3-d rough surface in order to account for the total effect of the crystal surfaces on the melting temperature.

The rationale presented above would also explain why the surface energies for the miPP and zniPP change from very different values under isothermal crystallization to similar values using a nonisothermal crystallization environment. Under nonisothermal

crystallization conditions, there is less preferential rejection of defects and the surface regions of the crystal may actually become smoother than under isothermal conditions for the miPP resins. For the ZNHT resin, the nature of the fold surface under nonisothermal conditions is quite similar to the one formed under isothermal crystallization. In this case, the net result is that normalized lamellae surface areas are quite similar for the miPP resins and ZNHT under nonisothermal conditions (even though they are really 3-d structures), therefore they have similar fold surface free energies.

The crystallinity by density under isothermal condition differences can be explained by using the same rough crystal surface argument. The rough surface will have, in essence, a thicker interfacial region due to the unevenness of the surface. A thicker interfacial region would cause the density to increase, even though it would not be reflected in the DSC and WAXD data. The thicker interfacial region would be caused by the niches on either side of the basal plane. A molecule emerging from the crystal surface inside a niche would have to clear the top surface of the crystal and any other rigid molecules restricting its motion before it may assume its full range of conformations. The molecule would not be able to relax, and would in essence, be in a rigid amorphous structure with an orientation above that of a truly amorphous molecule and below that of a molecule in crystallographic registry. Therefore, the density of these molecules would be intermediate between amorphous and crystalline states. This would be reflected in any density measurements, which are higher than the WAXD for all nonisothermal films and for the miPP resins under isothermal crystallization conditions.

The interfacial data seem to contradict the miPP resins having a thicker interfacial region, as the data in Figure 4.78 clearly show they are thinner. The nonisothermal

interfacial thickness data tends to become thinner as the lamellae thickness decreases (or the plateau temperature decreases). It would be expected that as crystallization becomes more rapid the surface organization would become more nonuniform or rough. Therefore, it might be expected, intuitively, that the interfacial thickness would increase. However, the nonisothermal interfacial thickness values decrease as lamellae thickness decreases. In addition, the nonisothermal interfacial thickness values are becoming smaller. These results suggest that a rough interfacial surface has a thinner interfacial thickness, as determined by SAXS.

The interfacial thickness is determined from an electron density measurement using SAXS. For a rough crystal surface, the interfacial region/crystal surface boundary is somewhat diffuse or none distinct. Since this boundary is rough, it would stand to reason that the interfacial region/amorphous region boundary would be somewhat rough or nondistinct. The outer interfacial boundary being diffuse would affect the measured interfacial region thickness, since a rough boundary between an interfacial region that has many characteristics of a truly amorphous region would fall off in electron density much closer to the crystal surface (on the average) than a more uniform interfacial region/amorphous boundary. This would, in turn, explain the observed interfacial thickness values and why the miPP resins have a much lower experimentally determined interfacial thickness and that nonisothermally crystallized films thickness decrease as the crystallization temperature decreases.

The net result of crystallinity and interfacial work indicates that the differences in σ_e of the various resins can likely be attributed to differences in the lamellae fold surface

334

roughness. The amount of surface roughness depends on the number and distribution of defects, presence of atactic material and the crystallization temperature.

Chapter 5

Fiber Spinning Behavior of Metallocene Catalyzed

Isotactic Polypropylene

5.0 Introduction

The melt spinning of iPP into fibers has been studied since the early 1960s and continues today. Several important material characteristics have been identified in the melt spinning process of polymers, as was discussed in section 2.5.3. The present set of metallocene isotactic polypropylene (miPP) resins differs from previous investigations[154-158] of zniPP resins in that the molecular weight distribution (MWD) is quite narrow for the present set of miPP resins.

A preliminary study of two miPP resins and a third zniPP resin indicated that something very different was taking place with the miPP resins. The data in Figure 5.1 show some early results on the as-spun fiber tensile strength versus spinning speed. The resins in this figure are M22, M32 and ZN35. The results were surprising in that M32 produced stronger fibers than M22, which were stronger than ZN35. The M22 resin producing stronger fibers than ZN35 can be explained by M22 having a more narrow MWD, which previous studies[155-157] found produced stronger fibers with similar M_w. However, there is no explanation for M32 producing stronger as-spun filaments than M22. Both resins have similar polydispersity values, with M22 having a larger number and weight average molecular weights. According to previous research[155-157], M22 should
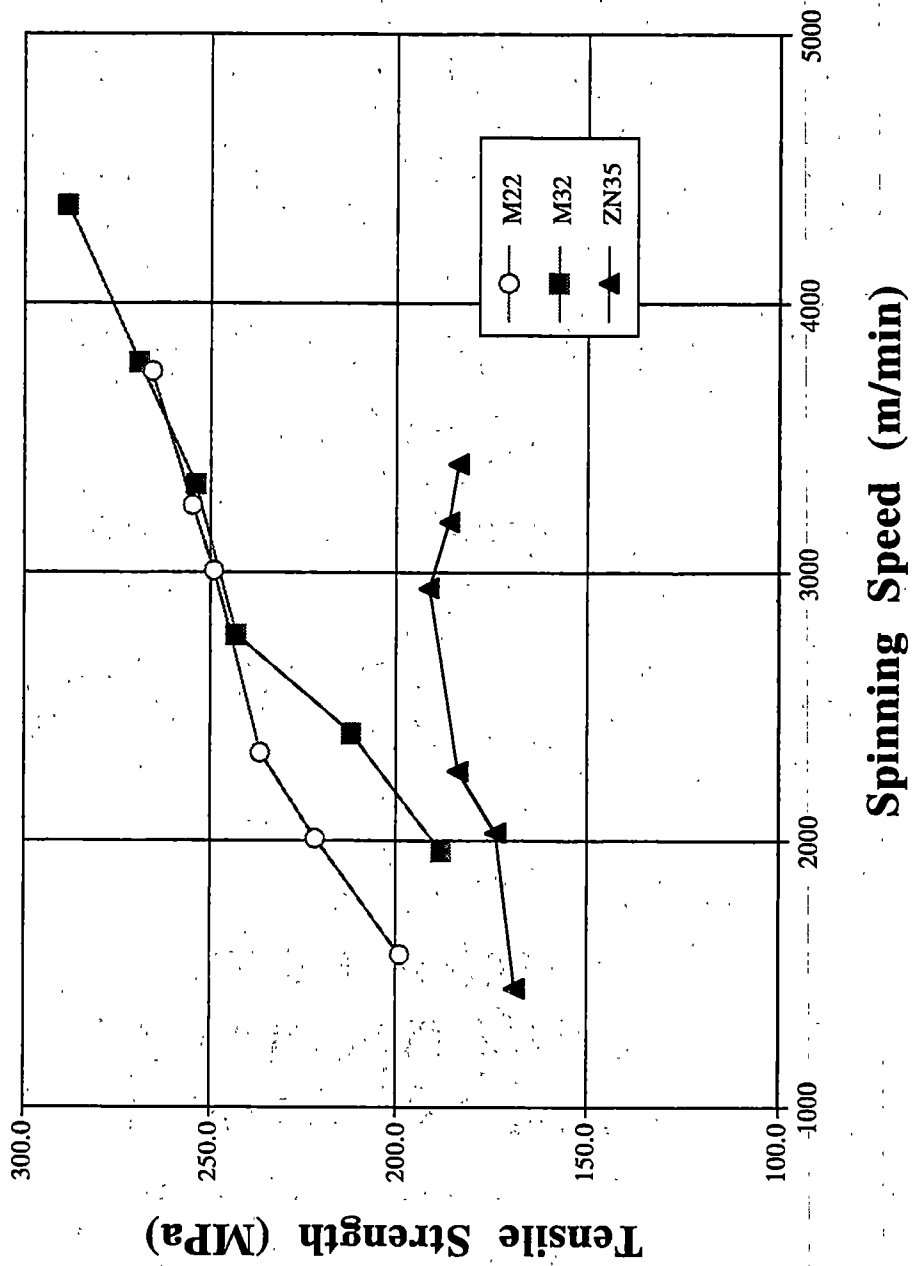
Figure 5.1 Preliminary results of tensile strength versus spinning speed for M22, M32 and ZN35.

form stronger filaments due to its higher weight average molecular weight. This chapter will explore the differences in structure and property development in a series of miPP resins. The miPP resin's fiber spinning behavior will be compared to a standard zniPP resin. On-line and off-line fiber structure and fiber property measurements will be made on each set of fibers to allow a comparison of each resin's fiber spinning properties.

The resins used in the fiber spinning study will be M10, M22, M32, ZN35, M45, M70 and M100. Each resin was melt spun and drawn down using a pneumatic suction device at a constant mass-throughput and extrusion temperature. Selected process conditions using M10, M22, M32, ZN35 and M100 were studied on-line. The on-line studies include determining the bulk crystallization kinetics, molecular orientation, on-line diameter profile, crystallization onset distance from spinneret and stress at crystallization onset. The as-spun fibers were characterized using WAXD, SAXS, birefringence and tensile mechanical properties.

Section 5.1 will present tabulated data on the processing conditions, as well as experimental results of most properties discussed throughout the chapter. The results of on-line fiber formation studies will be presented in section 5.2, followed by the structure of as-spun filaments in section 5.3. The tensile mechanical properties of the as-spun fibers will be presented in section 5.4. Section 5.5 will have a discussion and interpretation of the results found in the fiber study of the miPP resins. A summary of the results and conclusions will be presented in section 5.6.

5.1 Tabulated Results

The data in Tables 5.1-5.28 give the processing conditions for each resin and most of the other experimental results presented throughout this chapter.

Each fiber sample was drawn down by use of an air jet suction device. An air pressure (in psig) is applied to the device which results in high speed air surrounding the fiber. The high velocity air applies a drag force which draws the fiber down. The fiber is then blown into a container and collected for further use, if necessary. The applied pressure to the draw down device is varied to change the spinning speed. Higher applied air pressures produce higher spinning speeds. The spinning speed is calculated from the continuity equation (equation 2.26). The actual spinning speed is calculated from the density, mass-throughput and diameter of the filament. Figure 5.2 shows the spinning speed of each resin as a function of applied draw down pressure. It is important to note that the spinning speed is not the same for each resin at a given draw down pressure. The spinning speed for a particular resin at a given applied pressure depends on the rheology and crystallization kinetics of the resin.

The Tables 5.1-5.28 contain the extrusion temperature and mass-throughput for each sample. The extrusion temperature and mass-throughput were kept as constant and consistent as possible for all samples produced. The extrusion temperature was 210°C and the mass-throughput was 1.55±0.03g/min. The mass-throughput was measured before and after each set of fibers were spun. The diameter used in calculating the spinning speed came from the on-line, steady state diameter measured 2.20m from the spinneret. The off-line diameter is the final diameter of the filament after 30 days of annealing at room temperature. The fibers were annealed at room temperature to relax

Table 5.1 M10 fiber properties: Spinning speed, extrusion temperature, mass-through-putt, on-line fiber diameter, off-line fiber diameter and as-spun off-line final filament birefringence.

Pressure	Spinning Speed	Extrusion Temp	mtp	On-Line Diameter	Off-Line Diameter	Birefringence
(psig)	(m/min)	(°C)	(g/min)	(µm)	(µm)	(×10³)
5	1296	210	1.52	40.71	46.98	21.29
10	1572	210	1.52	36.95	40.76	21.34
15	1908	210	1.52	33.51	37.23	20.19
25	2169	210	1.52	31.43	35.61	20.19
40	2690	210	1.52	28.22	32.84	19.73
50	2800	210	1.52	27.66	32.12	19.48

Table 5.2 M10 fiber properties: Fiber density, crystallinity, tensile modulus, tensile strength and elongation-to-break.

Pressure	Spinning Speed	Density	Crystallinity	Tensile Modulus	Tensile Strength	Elongation-to-break
(psig)	(m/min)	(g/cm³)		(GPa)	(MPa)	(%)
5	1296	0.9009	0.5717	1.63	232	253
10	1572	0.9019	0.5840	2.15	265	250
15	1908	0.9032	0.6000	2.58	231	240
25	2169	0.9032	0.6010	2.82	232	192
40	2690	0.9034	0.6031	3.31	231	183
50	2800	0.9033	0.6024	3.40	204	177

340

Table 5.3 M10 Fiber properties: Noncrystalline birefringence, noncrystalline orientation function, crystalline orientation function, crystalline birefringence and drag tension.

Pressure (psig)	Spinning Speed (m/min)	Δn_{nc} ($\times 10^3$)	f_{nc}	f_c	Δn_c ($\times 10^3$)	Drag Tension (g)
5	1296	8.51	0.331	0.771	12.83	0.68
10	1572	7.22	0.289	0.834	14.17	0.85
15	1908	5.17	0.215	0.863	15.07	1.09
25	2169	5.08	0.212	0.867	15.16	1.16
40	2690	4.30	0.180	0.882	15.48	1.36
50	2800	3.43	0.144	0.919	16.11	1.57

Table 5.4 M10 Fiber properties: Long period, lamellae thickness, fiber plateau temperature and onset of crystallization stress.

Pressure (psig)	Spinning Speed (m/min)	Long Period ($\times 10^{-8}$cm)	($\times 10^{-8}$cm)	Plateau Temperature (°C)	Melting Temperature (°C)	Onset Stress (MPa)
5	1296	113.4	64.8	75.5	147.8	2.04
10	1572	116.1	67.8	83.2	149.3	3.30
15	1908	118.5	71.1	91.8	149.9	4.76
25	2169	119.5	71.8	93.6	150.5	5.06
40	2690	119.5	72.1	94.2	150.6	7.13
50	2800	120.0	72.3	94.8	150.8	8.23

Table 5.5 M22 fiber properties: Spinning speed, extrusion temperature, mass-through-putt, on-line fiber diameter, off-line fiber diameter and as-spun off-line final filament birefringence.

Pressure	Spinning Speed	Extrusion Temp	mtp	On-Line Diameter	Off-Line Diameter	Birefringence
(psig)	(m/min)	(°C)	(g/min)	(μm)	(μm)	(x10³)
5	1578	210	1.55	37.25	41.00	18.84
10	2008	210	1.55	33.01	38.20	20.97
15	2333	210	1.55	30.62	35.45	22.24
25	3005	210	1.55	26.97	33.72	23.18
40	3248	210	1.55	25.93	29.49	23.10
55	3748	210	1.55	24.13	28.31	23.58

Table 5.6 M22 fiber properties: Fiber density, crystallinity, tensile modulus, tensile strength and elongation-to-break.

Pressure	Spinning Speed	Density	Crystallinity	Tensile Modulus	Tensile Strength	Elongation-to-break
(psig)	(m/min)	(g/cm³)		(GPa)	(MPa)	(%)
5	1578	0.9013	0.5765	2.13	199	305
10	2008	0.9018	0.5828	2.45	222	257
15	2333	0.9022	0.5879	2.85	245	255
25	3005	0.9030	0.5980	3.16	249	245
40	3248	0.9038	0.6081	4.14	255	227
55	3748	0.9043	0.6144	4.46	266	224

Table 5.7 M22 Fiber properties: Noncrystalline birefringence, noncrystalline orientation function, crystalline orientation function, crystalline birefringence and drag tension.

Pressure (psig)	Spinning Speed (m/min)	Δn_{nc} (x10³)	f_{nc}	f_c	Δn_c (x10³)	Drag Tension (g)
5	1578	6.86	0.269	0.717	12.03	0.64
10	2008	7.71	0.307	0.785	13.31	0.80
15	2333	7.91	0.319	0.841	14.39	1.05
25	3005	8.29	0.343	0.859	14.95	1.12
40	3248	7.58	0.322	0.880	15.57	1.25
55	3748	7.56	0.326	0.899	16.07	1.52

Table 5.8 M22 Fiber properties: Long period, lamellae thickness, fiber plateau temperature and onset of crystallization stress.

Pressure (psig)	Spinning Speed (m/min)	Long Period (x10⁻⁸cm)	(x10⁻⁸cm)	Plateau Temperature (°C)	Melting Temperature (°C)	Onset Stress (MPa)
5	1578	106.9	61.6	80.7	146.8	2.81
10	2008	108.8	63.4	84.0	148.2	3.92
15	2333	109.8	64.6	86.2	148.7	5.51
25	3005	115.0	68.8	93.8	150.4	7.19
40	3248	116.3	70.7	97.2	151.3	8.66
55	3748	117.2	72.0	99.6	151.5	12.20

Table 5.9 M32 fiber properties: Spinning speed, extrusion temperature, mass-through-putt, on-line fiber diameter, off-line fiber diameter and as-spun off-line final filament birefringence.

Pressure (psig)	Spinning Speed (m/min)	Extrusion Temp (°C)	mtp (g/min)	On-Line Diameter (μm)	Off-Line Diameter (μm)	Birefringence (x10³)
5	1961	210	1.57	33.83	39.58	18.82
10	2405	210	1.57	30.53	36.00	21.83
15	2768	210	1.57	28.43	34.04	23.30
25	3324	210	1.57	25.89	30.63	24.85
45	3786	210	1.57	24.22	28.17	25.17
65	4363	210	1.57	22.55	25.19	25.29

Table 5.10 M32 fiber properties: Fiber density, crystallinity, tensile modulus, tensile strength and elongation-to-break.

Pressure (psig)	Spinning Speed (m/min)	Density (g/cm³)	Crystallinity	Tensile Modulus (GPa)	Tensile Strength (MPa)	Elongation-to-break (%)
5	1961	0.8909	0.4434	2.29	188	287
10	2405	0.8918	0.4548	2.77	213	216
15	2768	0.8936	0.4781	2.95	243	212
25	3324	0.8973	0.5252	3.81	254	191
45	3786	0.9001	0.5617	4.53	269	189
65	4363	0.9011	0.5740	5.67	289	186

344

Table 5.11 M32 Fiber properties: Noncrystalline birefringence, noncrystalline orientation function, crystalline orientation function, crystalline birefringence and drag tension.

Pressure (psig)	Spinning Speed (m/min)	Δn_{nc} (x10³)	f_{nc}	f_c	Δn_c (x10³)	Drag Tension (g)
5	1961	9.27	0.277	0.743	9.59	0.64
10	2405	11.82	0.361	0.759	10.05	0.77
15	2768	12.19	0.389	0.801	11.14	0.99
25	3324	11.82	0.414	0.856	13.08	1.00
45	3786	10.86	0.412	0.878	14.35	1.33
65	4363	10.16	0.397	0.909	15.18	1.56

Table 5.12 M32 Fiber properties: Long period, lamellae thickness, fiber plateau temperature and onset of crystallization stress.

Pressure (psig)	Spinning Speed (m/min)	Long Period (x10⁻⁸cm)	(x10⁻⁸cm)	Plateau Temperature (°C)	Melting Temperature (°C)	Onset Stress (MPa)
5	1961	100.2	44.4	38.7	142.5	3.33
10	2405	106.5	48.5	47.8	146.2	4.91
15	2768	108.1	51.7	54.9	149.3	7.40
25	3324	112.0	58.8	70.6	152.4	9.56
45	3786	114.5	64.3	82.8	154.4	13.40
65	4363	113.8	65.3	85.0	154.9	17.80

Table 5.13 ZN35 fiber properties: Spinning speed, extrusion temperature, mass-through-putt, on-line fiber diameter, off-line fiber diameter and as-spun off-line final filament birefringence.

Pressure (psig)	Spinning Speed (m/min)	Extrusion Temp (°C)	mtp (g/min)	On-Line Diameter (μm)	Off-Line Diameter (μm)	Birefringence (x10³)
5	1446	210	1.56	39.21	41.17	17.33
10	2030	210	1.56	33.04	37.87	19.51
15	2264	210	1.56	31.26	36.07	19.71
25	2940	210	1.56	27.39	32.90	19.90
35	3187	210	1.56	26.29	31.02	19.36
48	3401	210	1.56	25.44	29.40	18.79

Table 5.14 ZN35 fiber properties: Fiber density, crystallinity, tensile modulus, tensile strength and elongation-to-break.

Pressure (psig)	Spinning Speed (m/min)	Density (g/cm³)	Crystallinity	Tensile Modulus (GPa)	Tensile Strength (MPa)	Elongation-to-break (%)
5	1446	0.8935	0.4772	2.01	169	330
10	2030	0.8964	0.5138	2.40	174	322
15	2264	0.8980	0.5339	2.65	184	308
25	2940	0.9004	0.5655	2.90	191	297
35	3187	0.9018	0.5828	3.20	186	298
48	3401	0.9023	0.5894	3.80	184	302

Table 5.15 ZN35 Fiber properties: Noncrystalline birefringence, noncrystalline orientation function, crystalline orientation function, crystalline birefringence and drag tension.

Pressure (psig)	Spinning Speed (m/min)	Δn_{nc} (x10³)	f_{nc}	f_c	Δn_c (x10³)	Drag Tension (g)
5	1446	7.22	0.230	0.730	10.14	0.64
10	2030	7.65	0.262	0.796	11.90	0.80
15	2264	6.87	0.245	0.829	12.88	1.06
25	2940	5.29	0.203	0.891	14.66	1.07
35	3187	3.98	0.159	0.910	15.43	1.20
48	3401	3.94	0.160	0.869	14.90	1.46

Table 5.16 ZN35 Fiber properties: Long period, lamellae thickness, fiber plateau temperature and onset of crystallization stress.

Pressure (psig)	Spinning Speed (m/min)	Long Period (x10⁻⁸cm)	(x10⁻⁸cm)	Plateau Temperature (°C)	Melting Temperature (°C)	Onset Stress (MPa)
5	1446	113.7	54.3	70.6	160.4	2.63
10	2030	120.0	61.7	78.9	161.9	3.43
15	2264	121.9	65.1	82.7	163.1	4.61
25	2940	132.5	74.9	93.7	164.5	4.96
35	3187	136.0	79.3	98.7	165.1	5.92
48	3401	125.9	74.2	92.9	165.7	7.64

Table 5.17 M45 fiber properties: Spinning speed, extrusion temperature, mass-through-putt, on-line fiber diameter, off-line fiber diameter and as-spun off-line final filament birefringence.

Pressure (psig)	Spinning Speed (m/min)	Extrusion Temp (°C)	mtp (g/min)	On-Line Diameter (μm)	Off-Line Diameter (μm)	Birefringence (x10³)
5	1965	210	1.55	33.59	37.57	20.34
10	2531	210	1.55	29.57	34.80	23.37
15	2766	210	1.55	28.26	32.45	26.24
25	3438	210	1.55	25.28	29.27	26.43
50	3893	210	1.55	23.71	26.45	26.70
70	4702	210	1.55	21.55	22.13	27.25

Table 5.18 M45 fiber properties: Fiber density, crystallinity, tensile modulus, tensile strength and elongation-to-break.

Pressure (psig)	Spinning Speed (m/min)	Density (g/cm³)	Crystallinity	Tensile Modulus (GPa)	Tensile Strength (MPa)	Elongation-to-break (%)
5	1965	0.8902	0.4341	2.54	192	269
10	2531	0.8917	0.4538	2.96	229	229
15	2766	0.8934	0.4758	3.40	259	192
25	3438	0.8983	0.5381	4.18	274	172
50	3893	0.9018	0.5828	5.12	279	158
70	4702	0.9037	0.6071	7.71	287	143

348

Table 5.19 M45 Fiber properties: Noncrystalline birefringence, noncrystalline orientation function, crystalline orientation function, crystalline birefringence and drag tension.

Pressure	Spinning Speed	Δn_{nc}	f_{nc}	f_c	Δn_c	Drag Tension
(psig)	(m/min)	$(\times 10^3)$			$(\times 10^3)$	(g)
5	1965	10.97	0.323	0.744	9.40	0.62
10	2531	13.42	0.409	0.756	9.98	0.73
15	2766	14.94	0.474	0.819	11.34	0.95
25	3438	13.15	0.474	0.851	13.33	0.96
50	3893	11.76	0.469	0.884	14.99	1.33
70	4702	11.92	0.505	0.871	15.39	1.53

Table 5.20 M45 Fiber properties: Long period, lamellae thickness, fiber plateau temperature and onset of crystallization stress.

Pressure	Spinning Speed	Long Period		Plateau Temperature	Melting Temperature	Onset Stress
(psig)	(m/min)	$(\times 10^{-8} cm)$	$(\times 10^{-8} cm)$	(°C)	(°C)	(MPa)
5	1965	-	-	-	-	3.72
10	2531	-	-	-	-	5.48
15	2766	-	-	-	-	7.12
25	3438	-	-	-	-	7.69
50	3893	-	-	-	-	11.60
70	4702	-	-	-	-	16.00

Table 5.21 M70 fiber properties: Spinning speed, extrusion temperature, mass-through-putt, on-line fiber diameter, off-line fiber diameter and as-spun off-line final filament birefringence.

Pressure (psig)	Spinning Speed (m/min)	Extrusion Temp (°C)	mtp (g/min)	On-Line Diameter (µm)	Off-Line Diameter (µm)	Birefringence (x10³)
5	2075	210	1.56	32.84	36.54	21.93
10	2675	210	1.56	28.87	32.53	23.23
15	2798	210	1.56	28.18	30.78	25.24
25	3303	210	1.56	25.90	26.61	26.99
50	3975	210	1.56	23.58	25.85	27.55
70	4468	210	1.56	22.2	24.44	27.75

Table 5.22 M70 fiber properties: Fiber density, crystallinity, tensile modulus, tensile strength and elongation-to-break.

Pressure (psig)	Spinning Speed (m/min)	Density (g/cm³)	Crystallinity	Tensile Modulus (GPa)	Tensile Strength (MPa)	Elongation-to-break (%)
5	2075	0.8876	0.4000	2.69	192	247
10	2675	0.8910	0.4444	3.4	226	216
15	2798	0.8938	0.4810	3.8	246	212
25	3303	0.8965	0.5153	5.08	253	187
50	3975	0.8987	0.5432	5.38	263	175
70	4468	0.9021	0.5866	6.02	250	175

Table 5.23 M70 Fiber properties: Noncrystalline birefringence, noncrystalline orientation function, crystalline orientation function, crystalline birefringence and drag tension.

Pressure (psig)	Spinning Speed (m/min)	Δn_{nc} (x10³)	f_{nc}	f_c	Δn_c (x10³)	Drag Tension (g)
5	2075	13.50	0.375	0.726	8.45	0.61
10	2675	13.72	0.411	0.738	9.54	0.70
15	2798	13.89	0.445	0.814	11.39	0.90
25	3303	14.41	0.495	0.842	12.62	0.91
50	3975	14.16	0.516	0.850	13.44	1.34
70	4468	12.80	0.515	0.879	15.01	1.57

Table 5.24 M70 Fiber properties: Long period, lamellae thickness, fiber plateau temperature and onset of crystallization stress.

Pressure (psig)	Spinning Speed (m/min)	Long Period (x10⁻⁸cm)	(x10⁻⁸cm)	Plateau Temperature (°C)	Melting Temperature (°C)	Onset Stress (MPa)
5	2075	-	-	-	-	4.23
10	2675	-	-	-	-	5.60
15	2798	-	-	-	-	7.23
25	3303	-	-	-	-	7.91
50	3975	-	-	-	-	14.00
70	4468	-	-	-	-	17.90

351

Table 5.25 M100 fiber properties: Spinning speed, extrusion temperature, mass-through-putt, on-line fiber diameter, off-line fiber diameter and as-spun off-line final filament birefringence.

Pressure	Spinning Speed	Extrusion Temp	mtp	On-Line Diameter	Off-Line Diameter	Birefringence
(psig)	(m/min)	(°C)	(g/min)	(µm)	(µm)	(x10³)
5	2149	210	1.57	32.31	34.35	15.69
10	3040	210	1.57	27.15	30.74	20.97
15	3374	210	1.57	25.75	28.87	24.88
25	4108	210	1.57	23.31	25.60	29.54
50	4858	210	1.57	21.41	25.55	28.20
60	5261	210	1.57	20.57	23.91	28.09

Table 5.26 M100 fiber properties: Fiber density, crystallinity, tensile modulus, tensile strength and elongation-to-break.

Pressure	Spinning Speed	Density	Crystallinity	Tensile Modulus	Tensile Strength	Elongation-to-break
(psig)	(m/min)	(g/cm³)		(GPa)	(MPa)	(%)
5	2149	0.8913	0.4479	3.03	155	339
10	3040	0.8922	0.4596	3.79	196	258
15	3374	0.8937	0.4789	4.29	230	200
25	4108	0.8955	0.5029	5.46	278	150
50	4858	0.8976	0.5299	5.48	261	163
60	5261	0.8980	0.5350	5.67	242	160

Table 5.27 M100 Fiber properties: Noncrystalline birefringence, noncrystalline orientation function, crystalline orientation function, crystalline birefringence and drag tension.

Pressure (psig)	Spinning Speed (m/min)	Δn_{nc} (x10³)	f_{nc}	f_c	Δn_c (x10³)	Drag Tension (g)
5	2149	7.61	0.229	0.622	8.11	0.59
10	3040	11.27	0.347	0.728	9.74	0.69
15	3374	14.01	0.447	0.783	10.91	0.85
25	4108	17.91	0.599	0.798	11.68	0.90
50	4858	15.35	0.543	0.836	12.89	1.25
60	5261	14.67	0.525	0.865	13.47	1.50

Table 5.28 M100 Fiber properties: Long period, lamellae thickness, fiber plateau temperature and onset of crystallization stress.

Pressure (psig)	Spinning Speed (m/min)	Long Period (x10⁻⁸cm)	(x10⁻⁸cm)	Plateau Temperature (°C)	Melting Temperature (°C)	Onset Stress (MPa)
5	2075	96.4	43.2	41.6	140.8	4.72
10	2675	103.6	47.6	52.3	143.5	6.57
15	2798	103.3	49.5	56.9	146.2	8.90
25	3303	105.1	52.8	64.9	149.1	11.20
50	3975	106.5	56.5	73.9	150.6	15.70
70	4468	108.8	58.2	78.0	151.3	21.00

353
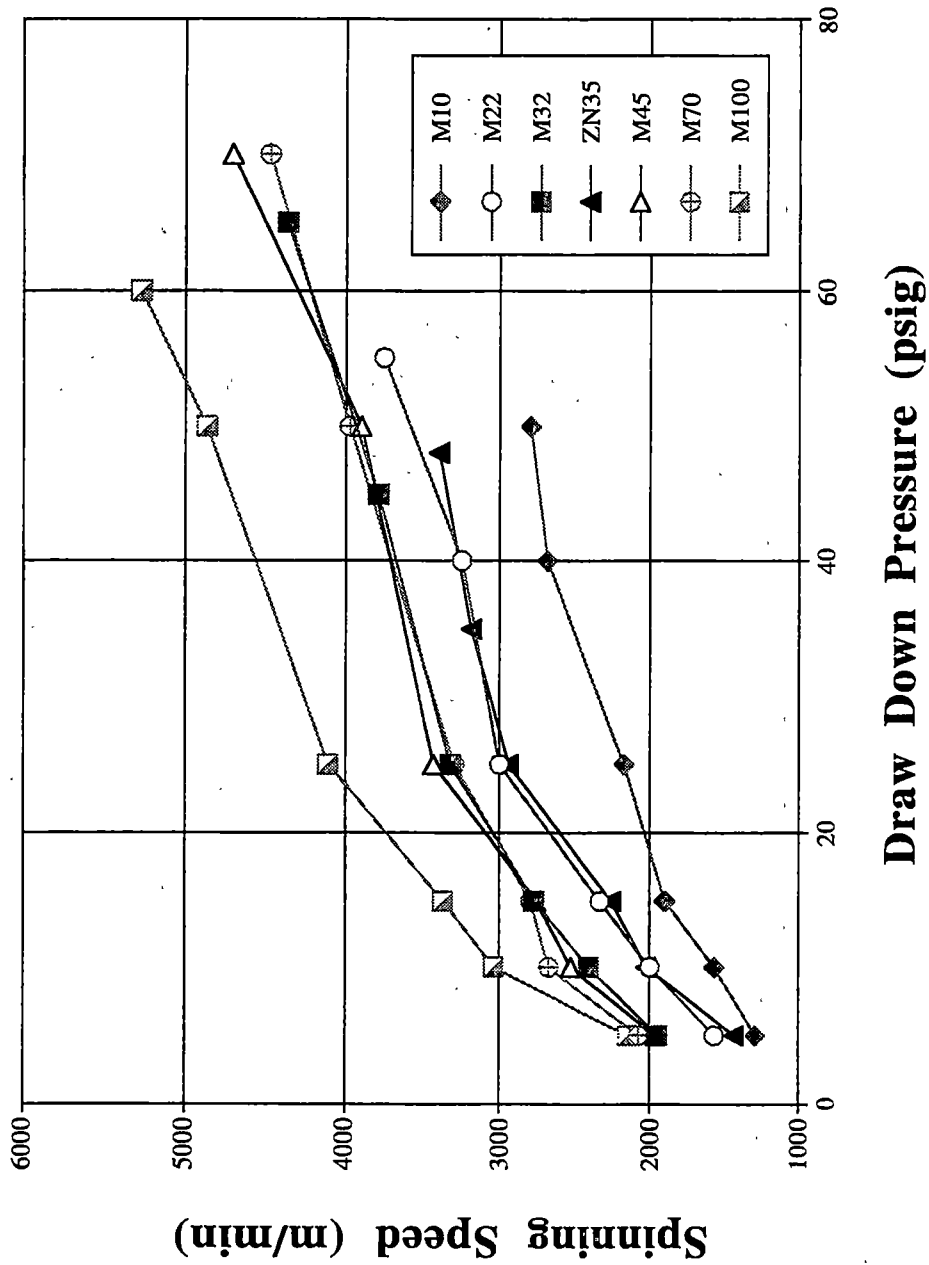
Figure 5.2 Spinning speed versus draw down pressure.

354

any residual stresses after the initial spinning process. Initial studies indicated that the fiber properties were not constant with time after the initial spinning process and that the fiber properties became relatively constant after 30 days. The birefringence indicated in the tables is measured at the same time as the off-line diameter. As-spun filament density, mechanical properties, long period, melting temperature and orientation functions were also measured after the annealing period.

The tables contain part of the on-line data collected in the fiber spinning experiments. The drag tension and onset stress were determined from on-line data. On-line diameter and birefringence profiles were obtained under different applied stresses, though the data at each position is not included in the tables.

5.2   Results and Discussion of the On-line Fiber Spinning Studies

Previous research[145-158] has indicated that the plateau and leveling out in the diameter versus distance from the spinneret profile is a strong indication of crystallization occurring in the spinline. Figure 5.3 shows the diameter in the spinline as a function of distance from the spinneret for applied air pressures of 5, 15 and 25psig of resin M32. The data in Figure 5.3 indicates the fiber diameter attenuates at distances roughly 90 to 110cm from the spinneret, depending on the applied air pressure. As the draw down force is increased, or the spinning speed increases, the fiber draw down moves closer to the spinneret and the final filament diameter decreases. The fiber draw down process stops and the filament diameter becomes constant as a result of crystallization.

A considerable amount of information can be learned from an on-line study of a running filament using birefringence measurements. Birefringence is itself a measure of
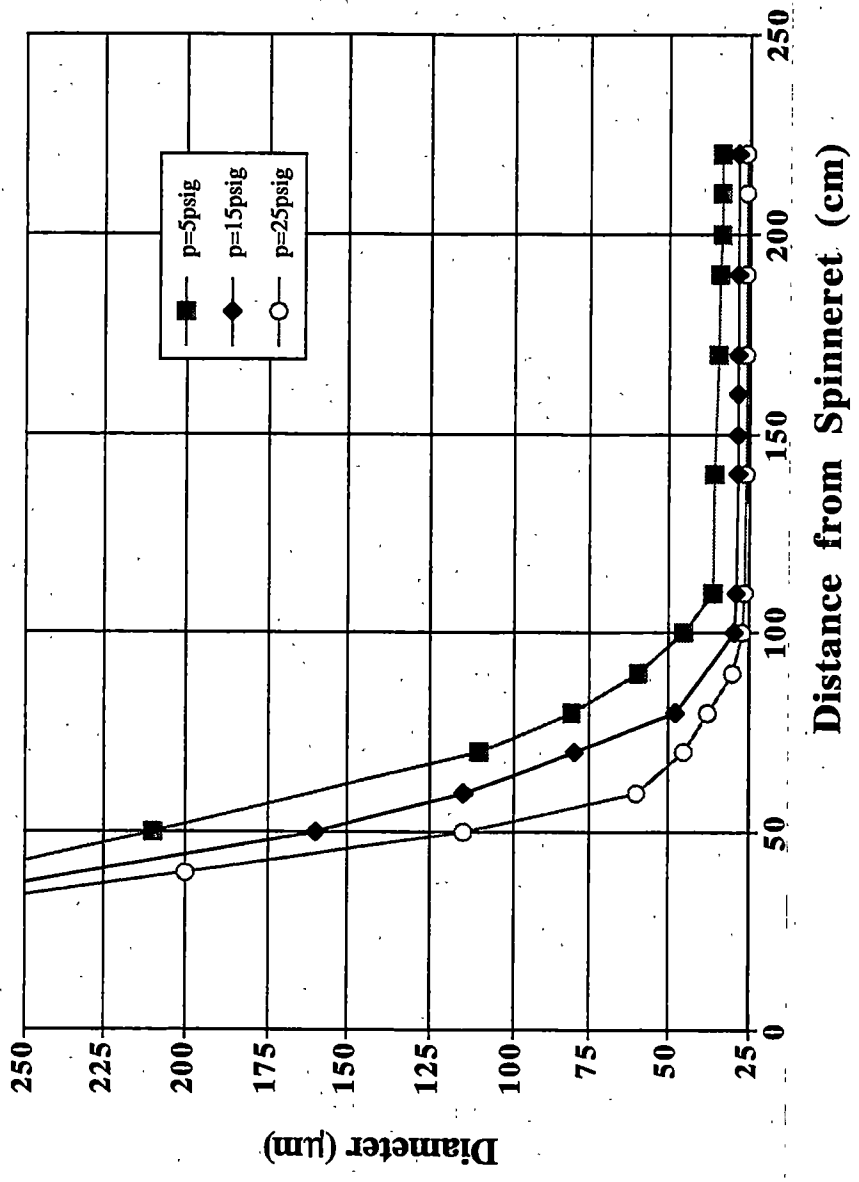
Figure 5.3 On-line diameter profile versus distance from spinneret for M32.

orientation. The growth of crystals from oriented nuclei during stress enhanced crystallization causes a rapid increase in orientation and birefringence[154,155]. Therefore, with these facts in mind, the birefringence can be measured on-line to estimate where crystallization has started and when crystallization has been completed. Crystallization onset occurs near the position in the spinline where the birefringence increases rapidly from a small value near zero. Crystallization is essentially complete when the birefringence plateaus to a relatively constant final value. The results in Figure 5.4-5.6 show the on-line birefringence profile as a function of distance from the spinneret, at air pressure settings of 5, 15 and 25psig, respectively.

The on-line birefringence study at 5psig in Figure 5.4 shows that crystallization begins at a distance from the spinneret of approximately 70cm for M10, followed by M22, ZN35, M32, M45, M70 and finally M100 at a distance of 140cm away from the spinneret. A draw down pressure of 15psig in Figure 5.5 shows that ZN35 now begins crystallization closest to the spinneret at 50cm, followed by M10, M22, M45, M32, M70 and M100 at 110cm. Increasing the draw down pressure to 25psig, as indicated in Figure 5.6 induces crystallization closer to the spinneret for all resins. M10 and ZN35 both begin crystallizing at 40cm, followed by M22, M45, M32, M70 and M100 at 100cm. As discussed above, the birefringence changes from a very small value rapidly in the spinline as a result of the oriented crystallization that is occurring in the spinline. The initial nuclei formed in the spinline are highly oriented, with subsequent growth of other oriented crystals. The plateau in the on-line birefringence profile indicates that crystallization is complete. The differences in the final birefringence profile after the

357
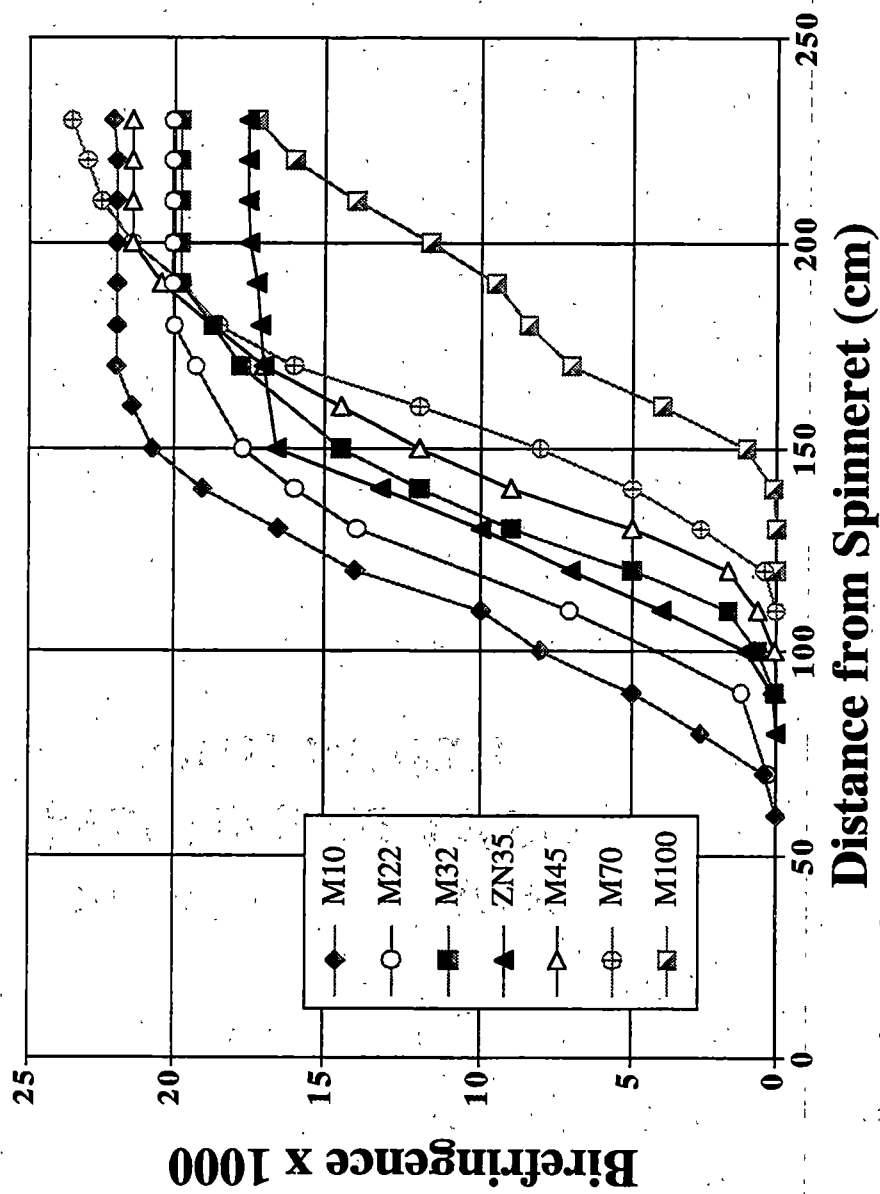
Figure 5.4 On-line birefringence versus distance from spinneret using draw down pressure 5psig.
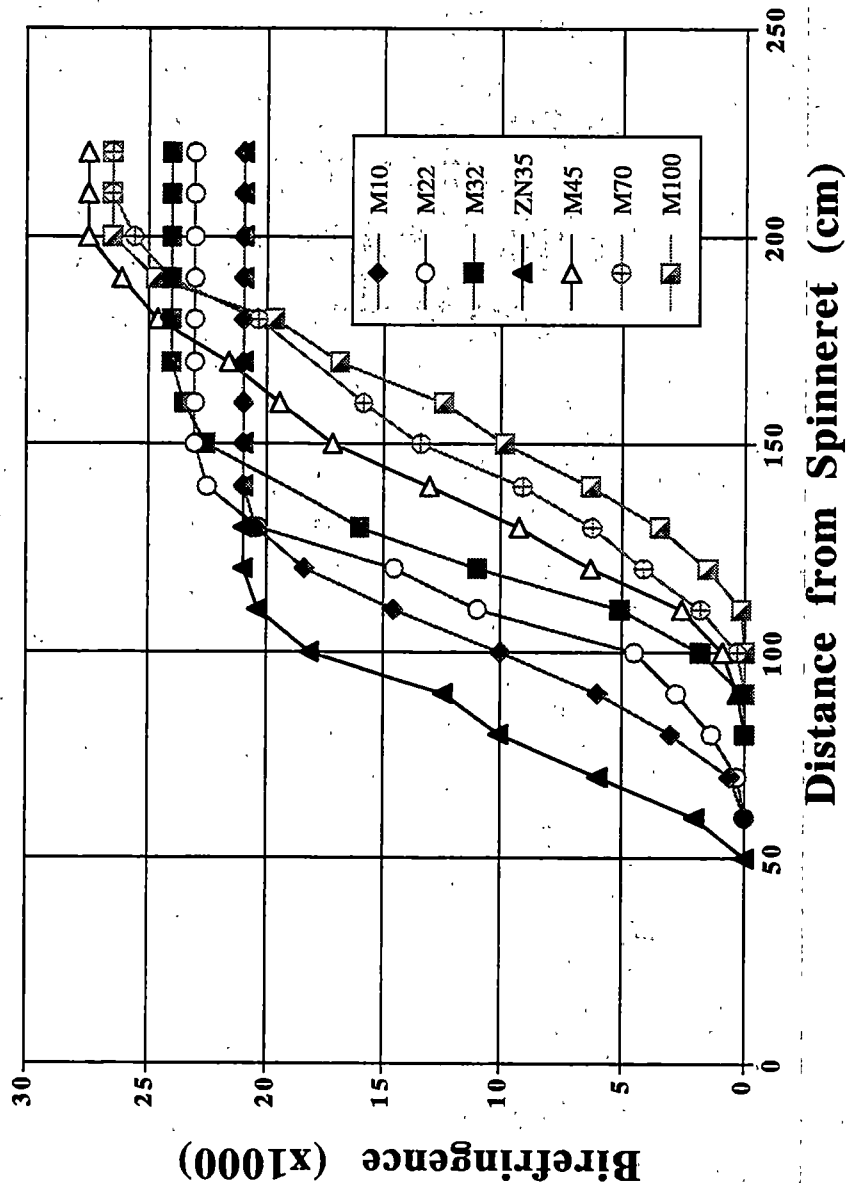
Figure 5.5 On-line birefringence versus distance from spinneret using draw down pressure 15psig.
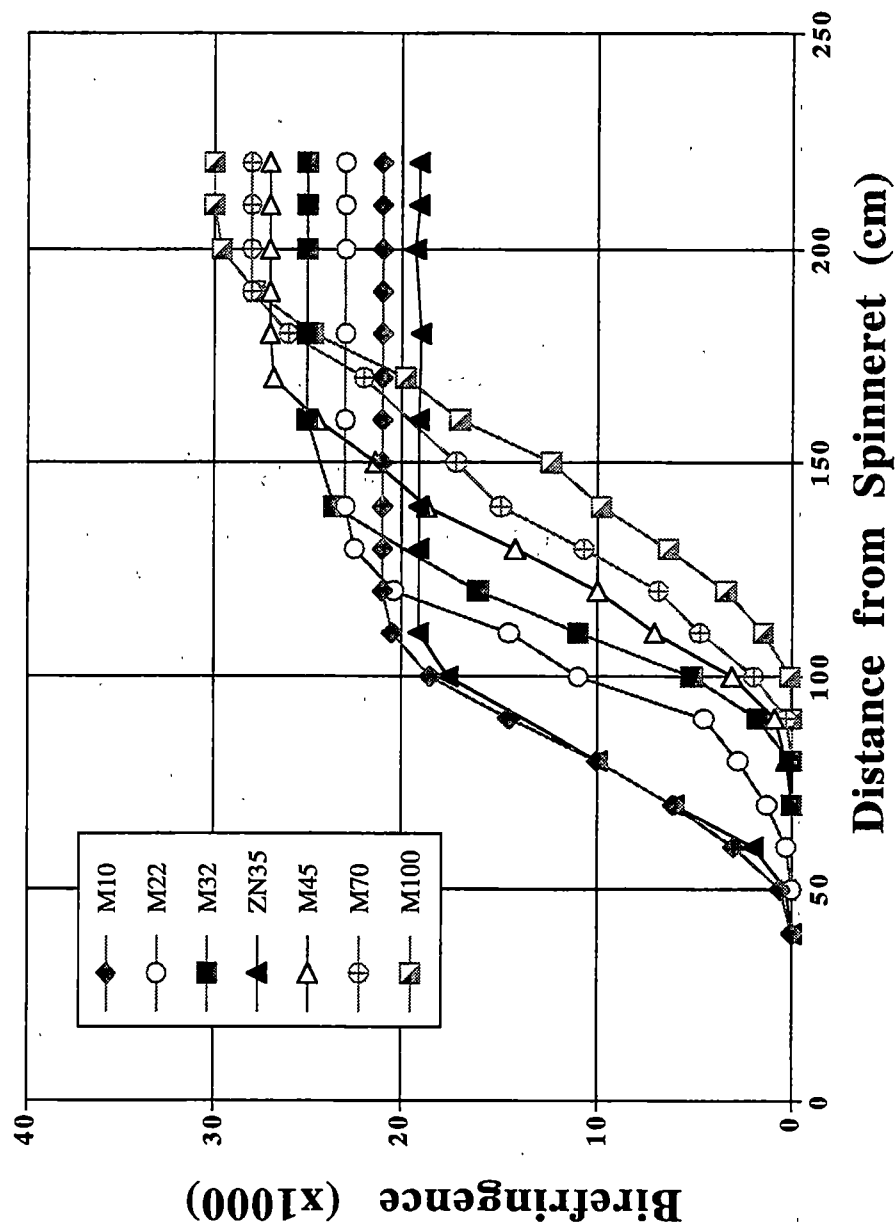
Figure 5.6 On-line birefringence versus distance from spinneret using draw down pressure 25psig.

completion of crystallization is a result of differences in final overall molecular orientation.

As stated previously, the onset of crystallization was taken to corresponded to the point on the spinline at which the birefringence increases rapidly from a small value near zero. Figure 5.7 shows the crystallization onset distance from the spinneret as a function of spinning speed. With the exception of ZN35 and M45, the crystallization onset distance gets closer to the spinneret as the resin molecular weight increases and the spinning speed increases.

The onset distance of crystallization for M45 and ZN35 shows the effects of their broader MWD. For a broad MWD resin, as the spinning speed increases, the larger molecular weight chains become oriented faster due to the larger relative number of entanglements. A broader MWD resin has a (relative to another resin with a more narrow MWD and same weight average molecular weight) more numerous population of higher molecular weight chains, referred to as the higher molecular weight tail. For a broader MWD resin, the high molecular weight chains align with one another and with the draw down direction early in the spinline. The oriented high molecular weight chains then initiate the growth of row nuclei. A more uniform molecular weight distribution would produce a more uniform alignment of the melt in the spinline, and at the same average molecular weight, results in a smaller amount of preferential early alignment since the population of chains in a nMWD resins is more uniform. Therefore, with a broader MWD, M45 and ZN35 initiate crystallization closer to the spinneret, even though they have lower weight average molecular weights when compared with M32 and M10, respectively. The effects of MWD have been reported elsewhere, with a similar result[157]
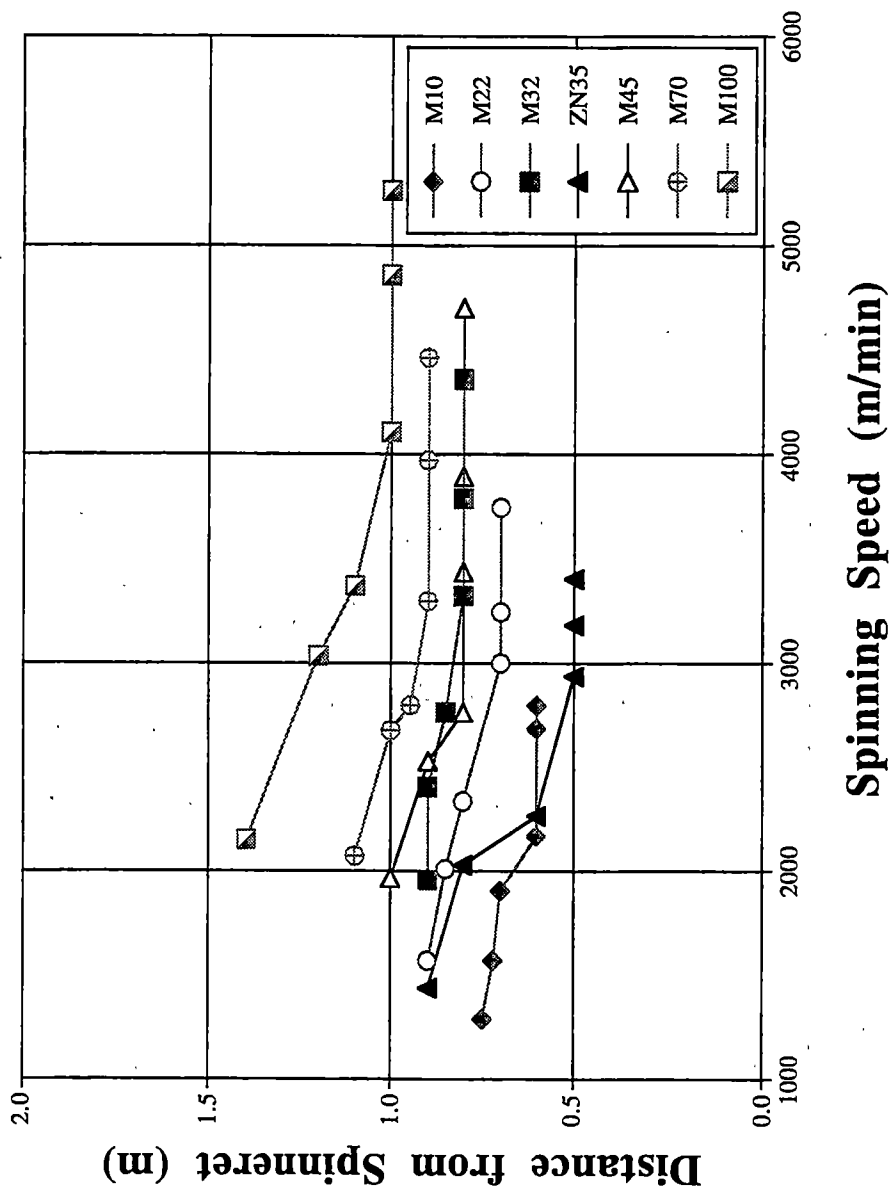
Figure 5.7 Distance of crystallization onset versus spinning speed.

using similar reasoning. The authors in the previous study[157] suggested that crystallization occurs closer to the spinneret and at higher temperatures in broad MWD resins (this is of course relative to a more narrow MWD similar mfr resin) because they are more susceptible to stress enhanced crystallization.

The data in Figure 5.8 shows, the final filament diameters are very nearly a function of spinning speed only, all results lying in a narrow band of final filament diameters as a function of spinning speed. This band is determined by the continuity equation and the fact that the mtp and density of as-spun fibers are relatively constant from sample to sample.

The diameter at crystallization onset as a function of spinning speed is shown in Figure 5.9. The trend generally follows from lowest to highest molecular weight resins having the smallest to largest diameters at the onset of crystallization. The low molecular weight M100 draws down to the smallest diameter fibers at crystallization onset, while M10 and ZN35 have the largest fiber diameters. M45 and ZN35 exhibit slightly different behavior, due to their broader molecular weight distributions. M45 and ZN35 crystallize closer to the spinneret, where the filament diameter is larger. Therefore, the explanation for the low molecular weight resins having smaller diameter at each spinning speed is that the lower MW resins have a delayed crystallization, which allows the fiber to draw down into a much finer filament before the onset of crystallization. This is most easily seen when M10 and M22 are compared, as well as M45 and M100 in Figure 5.9. It is also quite clear that the onset diameter for all resins do not fit a uniform master curve as a function of spinning speed. Therefore, each fiber's draw down behavior in the spinline is

363
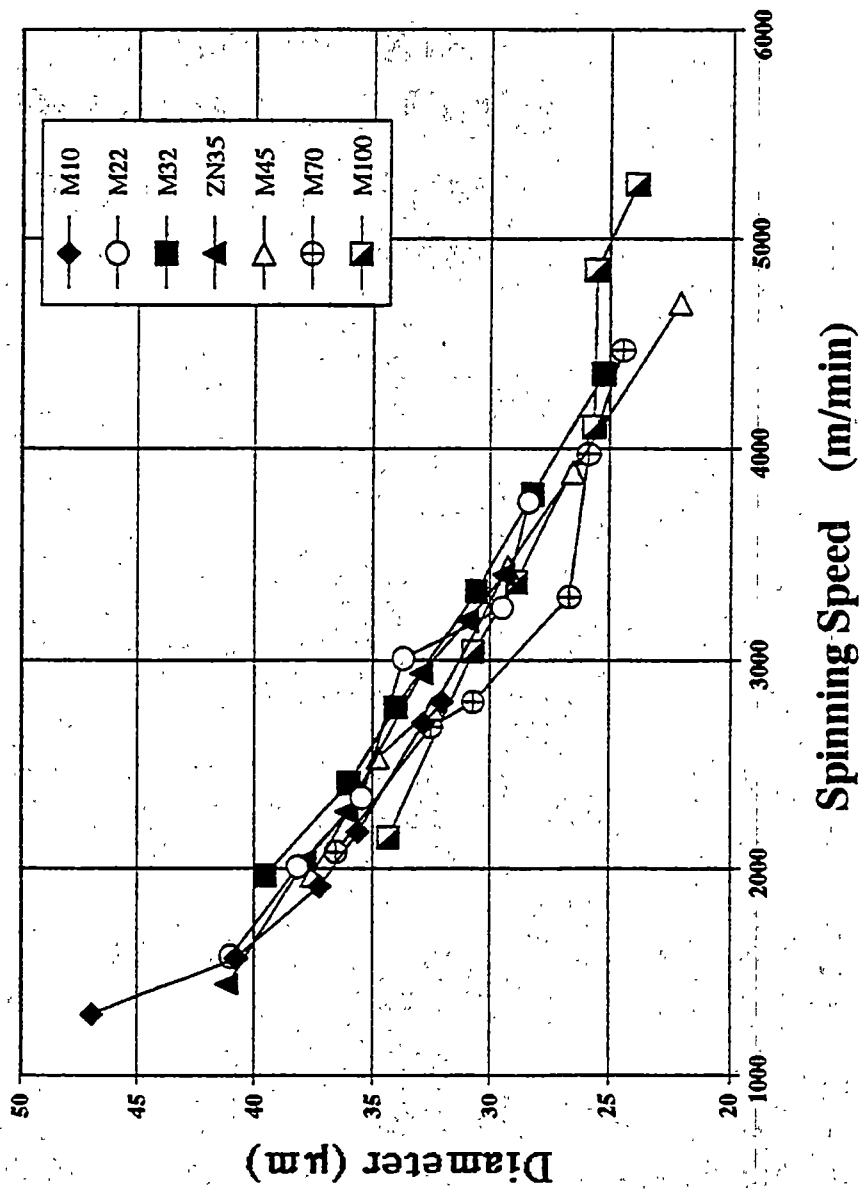
Figure 5.8 Final diameter of fibers versus spinning speed.
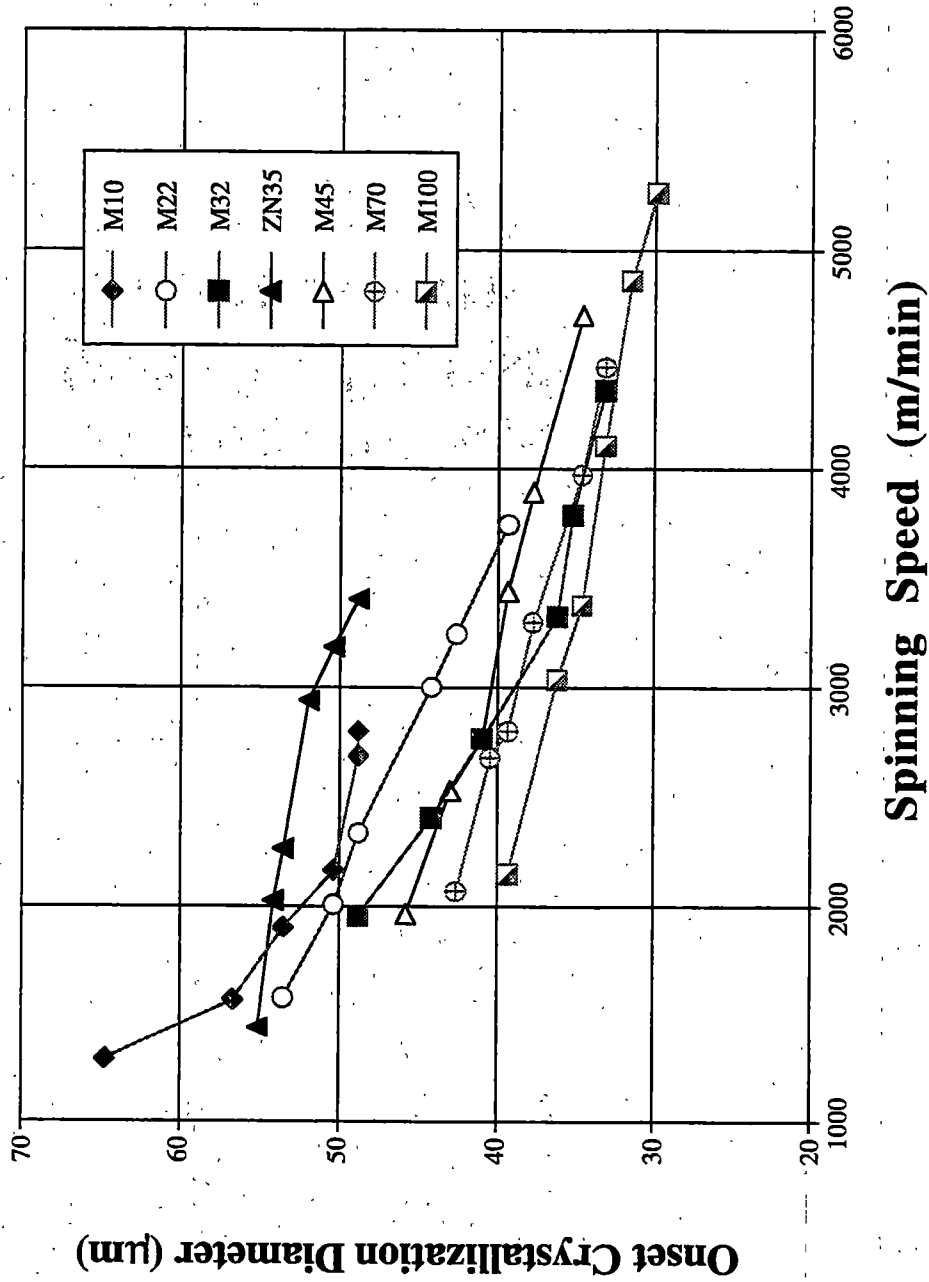
Figure 5.9 Filament diameter at the onset of crystallization versus spinning speed.

determined by the rheology of the resin, which is molecular weight and MWD dependent, and to a lesser extent, by variations in the crystallization kinetics of different resins.

The rheology of a particular resin is very important in the fiber spinning process. The viscosity of a resin is determined by the material properties and processing conditions. For iPP, the material properties are the molecular weight distribution (M_n, M_w and M_z). The most important processing factors are temperature and shear rate. The complex viscosity data for M22, M32 and ZN35 are shown in Figure 5.10. Although these three resins are not the complete set of resins, they do illustrate the substantial differences in viscosity in the low shear rate region. M22 has the highest complex viscosity followed by ZN35 and M32. ZN35 shows a slightly greater shear thinning behavior at high shear rates than either M22 or M32. This behavior would seem to correlate with its broader MWD. In fiber spinning, shear deformation occurs within the spinneret capillaries, followed by elongation of the molten filament after extrusion. The elongational viscosity of a material can be roughly approximated as three time the shear viscosity. This is important in that polymers with low shear viscosities also have lower elongational viscosities, with a low elongational viscosity being generally desirable as it produces finer filaments in the spinline. Thus, within the three resins in the complex viscosity figure, it would be expected that M32 would form finer filaments at a given draw down stress than either M22 or ZN35, which it does. Therefore, if finer filaments are desired, resins with low elongational viscosities should be used. Another important point to note is the different shear viscosity behavior of similar mfr resins M32 and ZN35.
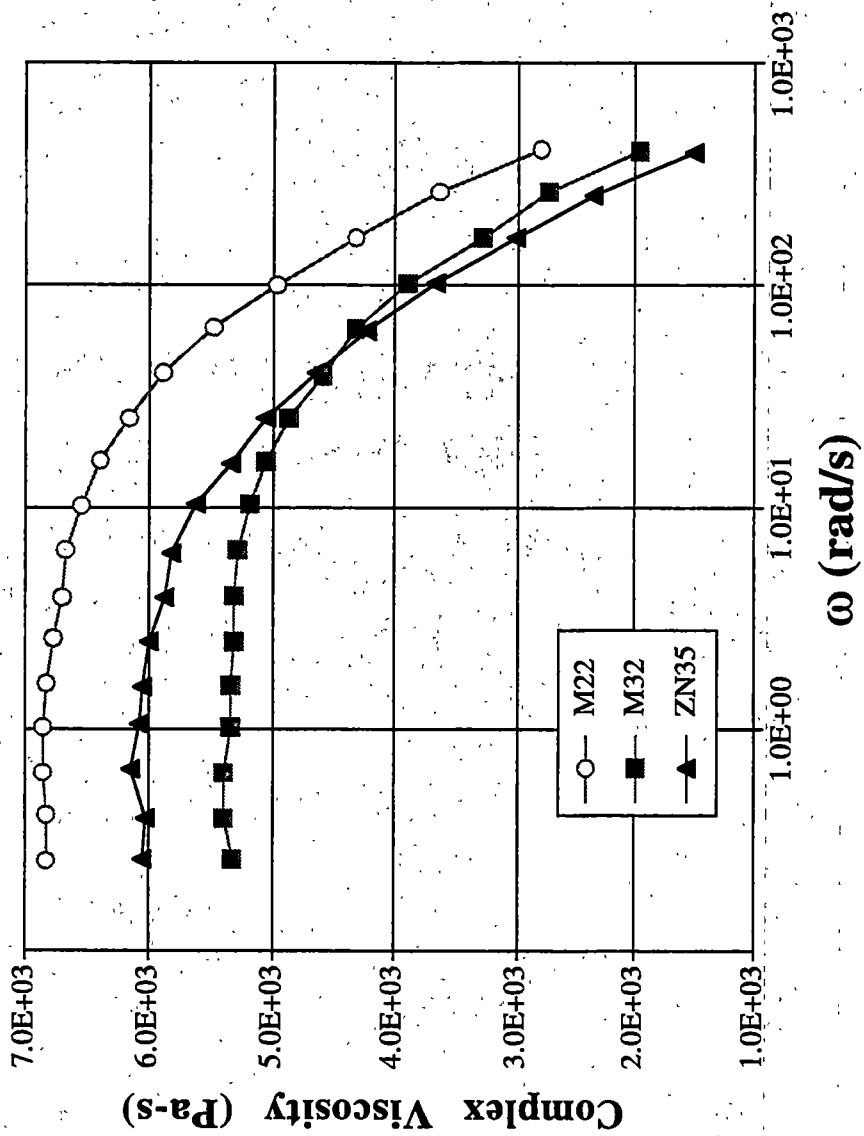
Figure 5.10 Complex viscosity versus shear rate for M22, M32 and ZN35 using a cone and plate rheometer.

The drag load or tension on each fiber as a function of spinning speed is shown in Figure 5.11. The trend indicates that as the spinning speeds increase, the drag tension increases for all resins. The drag load also increases as a function of increasing molecular weight. The drag load is related to fiber diameter. The higher molecular weight resins have larger diameters, initially during crystallization onset and as final filament diameter. The force the air suction device provides on the fiber during deformation becomes greater at larger diameters, as the surface area increases as a function of filament radius. It is worth noting that M22 and ZN35 carry a similar load as a function of spinning speed, as shown in Figure 5.11.

The load on the filament is maintained throughout the length of the spinline. Therefore, the stress at crystallization onset can be calculated since the diameter at crystallization onset is also known. The stress at crystallization onset is shown in Figure 5.12 as a function of spinning speed. The stress at crystallization onset for each resin appears to be a function of spinning speed, with the spinning speed a function of molecular weight and molecular weight distribution. The lower molecular weight and more narrow MWD resins crystallize under a higher stress since their spinning speeds are higher at the same applied air pressure.

Figure 5.13 shows the stress at crystallization onset as a function of distance from the spinneret. The data appears to fall in bands according to the resin molecular weight and MWD, with higher molecular weight and broader MWD resins crystallizing closer to the spinneret. The order is ZN35 followed by M10, M22, M45, M32, M70 and M100. It would seem that each resin has a characteristic stress that must be produced at a given distance from the spinneret for crystallization to occur. The characteristic stress depends
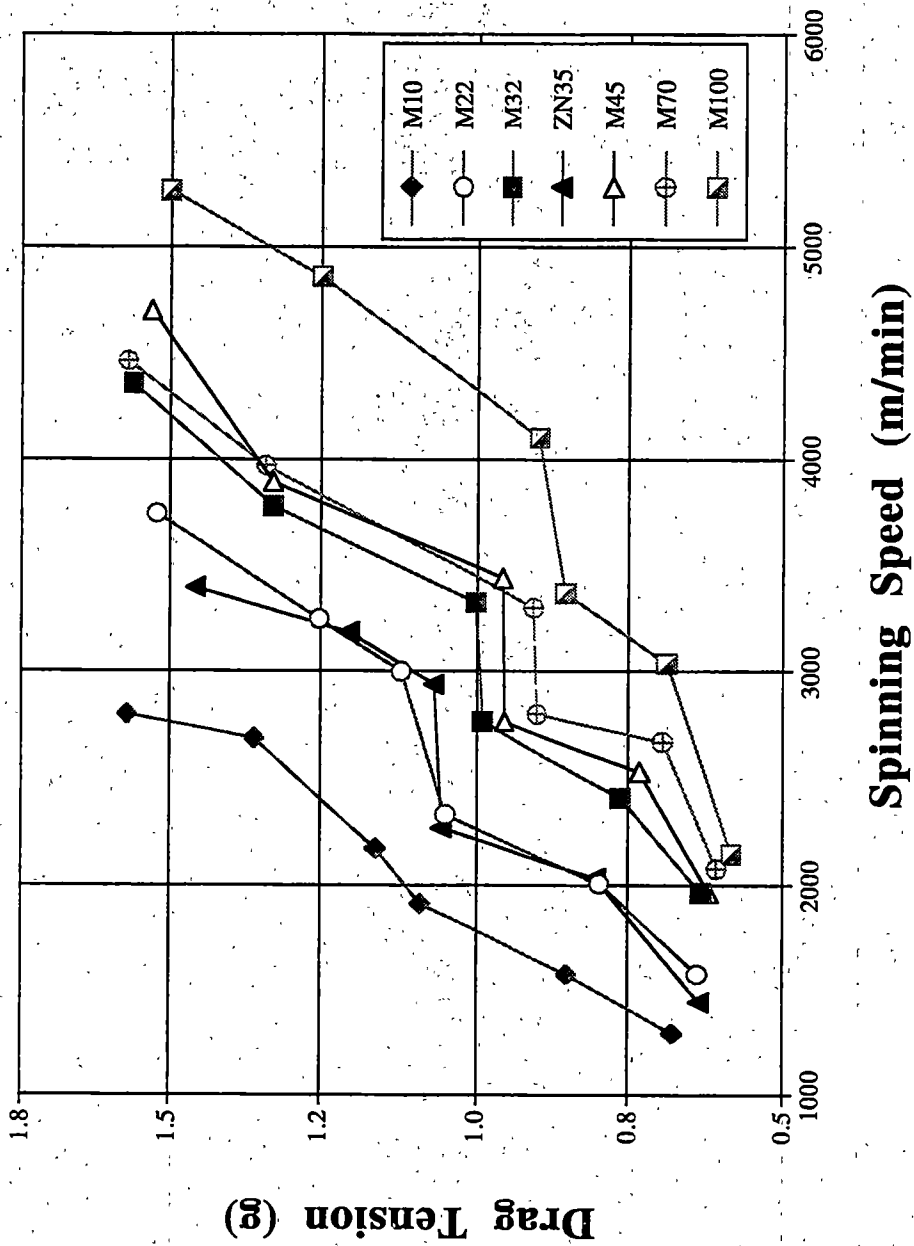
Figure 5.11 Drag tension versus spinning speed.

369
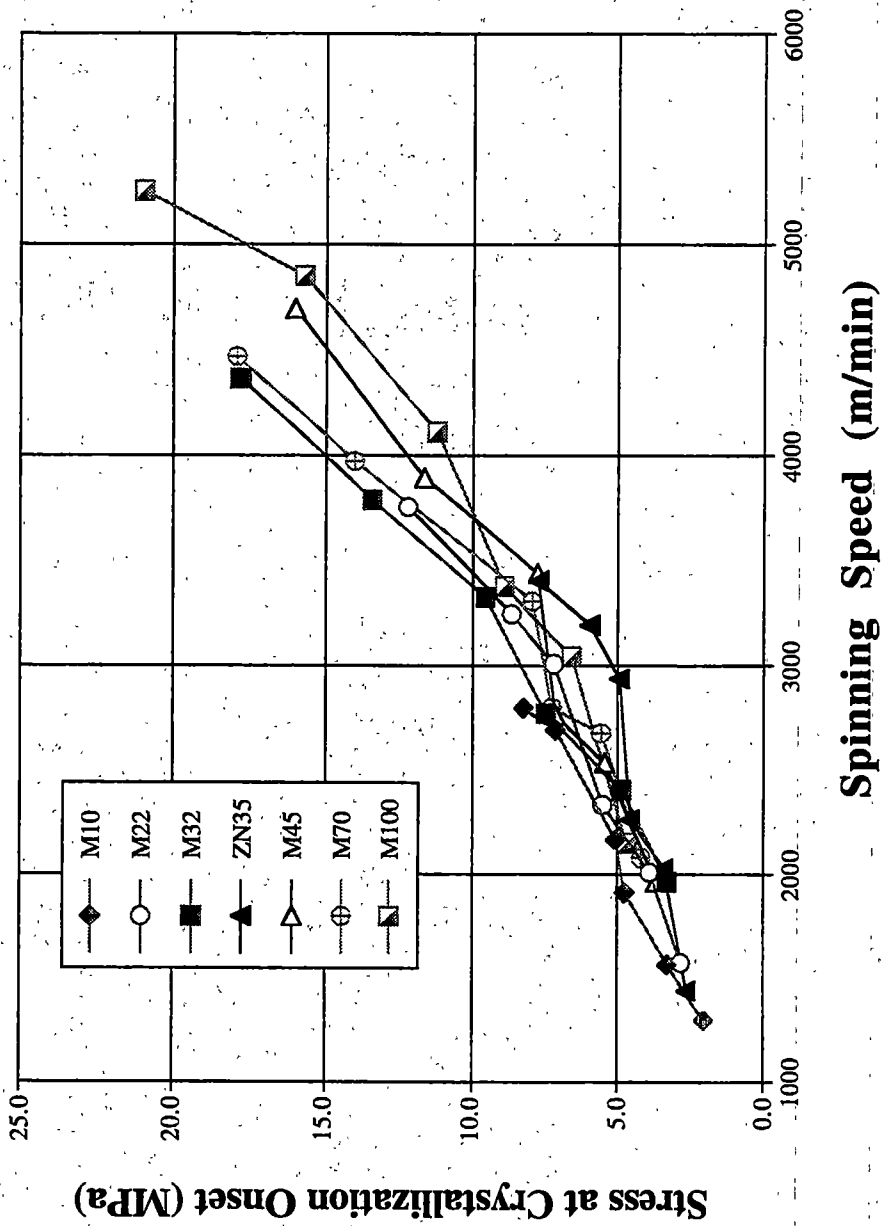
Figure 5.12 Stress at crystallization onset versus spinning speed.
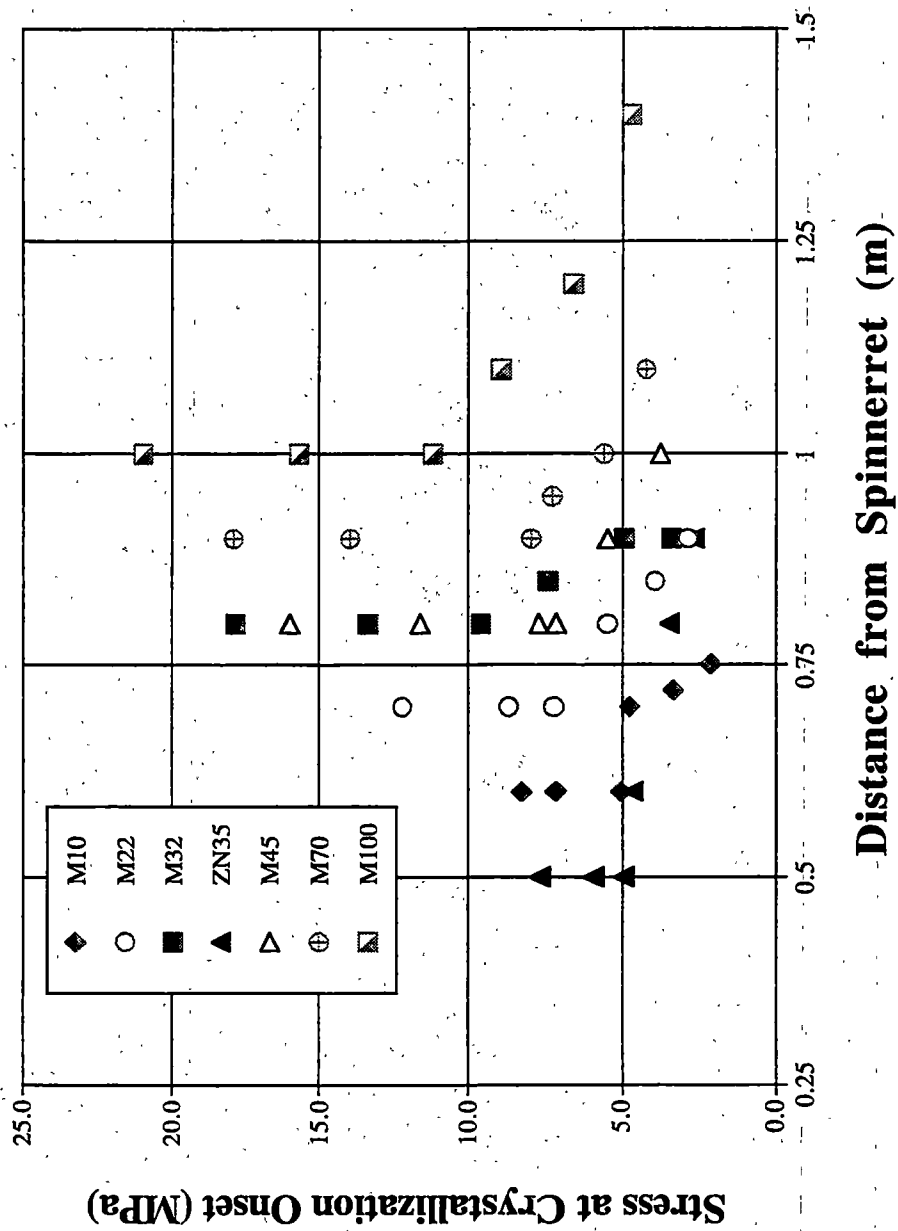
Figure 5.13 Stress at crystallization onset versus distance from spinneret.

upon the molecular weight characteristics (number and weight average molecular weights and their distribution), as indicated by the finding in Figure 5.13.

The results thus far are reasonable when the rheology of the resins is considered. As the molecular weight increases, the relaxation time and number of chain entanglements increases. Studies have indicated[204,205] that full relaxation does not occur in polypropylene melts (entanglement density is too high for the process time) during a high speed cooling process, as the crystallization times are to short. The larger molecular weight resins have many more entanglements and will take longer to relax. However, partial relaxation might be expected for some of the lower molecular weight chains. Therefore, higher MW chains would seem statistically more probable to produce a nucleus at any given temperature. Broader MWD resins with the same mfr initiate nucleation even closer due to the formation of row nuclei, as discussed earlier. Research has indicated that higher molecular weight chains are more likely to produce a critical nucleus even under quiescent conditions due to athermal nucleation[204,205]. This was discussed in Chapter 4 section 4.4.

In order to further understand the properties of the as-spun fibers, the fibers were studied to determine their crystallization temperature as a function of spinning speed in the spinline. Since it was not possible to obtain the on-line temperature profiles directly, the approximate on-line crystallization temperature was determined by using the long period of the as-spun fibers determined using SAXS. The lamellae thickness was obtained by multiplying the long period by the percent crystallinity, as determined by density. Additionally, in order to convert the lamellae thickness into an actual crystallization temperature, a plot of lamellae thickness versus plateau crystallization

temperature was constructed for M10, M22, M32, ZN35 and M100, using the nonisothermal films studied previously in Chapter 4. A curve fit of these data (where the original data is shown in Figure 4.59) will allow the crystallization temperature of the as-spun fibers to be estimated. It is assumed implicitly that the lamellae thickness is determined only by the crystallization temperature, whether under quiescent crystallization conditions or otherwise. M45 and M70 could not be studied using this method since they were not studied under quiescent nonisothermal conditions. While this method is not perfect, it should provide a reasonably valid and useful method for approximating the crystallization temperature of the fibers.

The long period of each fiber as a function of spinning speed is shown in Figure 5.14. After multiplying the long period by the crystallinity (which is given in Tables 5.1-5.28), the lamellae thickness for each fiber sample is shown as a function of spinning speed in Figure 5.15. Figure 5.16 shows the estimated crystallization temperature as a function of spinning speed. The data are clearly grouped by M_w. The high MW resins, have significantly higher T_c value compared to M32 and M100 at similar spinning speeds. The high molecular weight resins have similar T_c to the values obtained under quiescent nonisothermal studies (see Figure 4.68), which range from 80°C to 100°C. At the medium to high spinning speeds M32 and M100 have similar T_c to the quiescent nonisothermal conditions. At low spinning speeds, M32 and M100 have very low crystallization temperatures, in the 40-60°C range well below any crystallization temperatures observed using the HCRLDM system. It should be pointed out here that the cooling rates involved in this type of fiber spinning are well in excess of 150,000K/min. Therefore, it is quite remarkable that the crystallization temperatures of the fibers in the
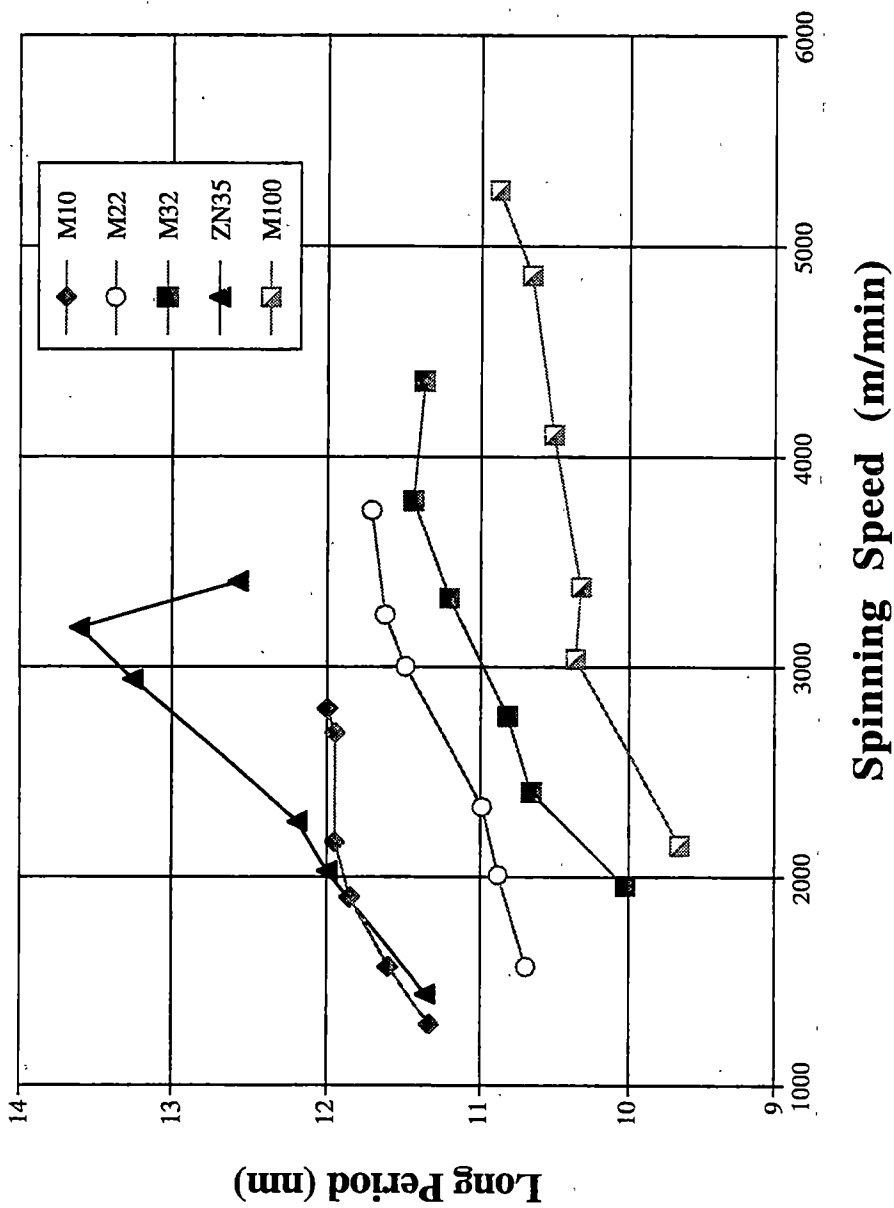
Figure 5.14 Long period of fibers versus spinning speed for all as-spun fibers determined by SAXS.

374
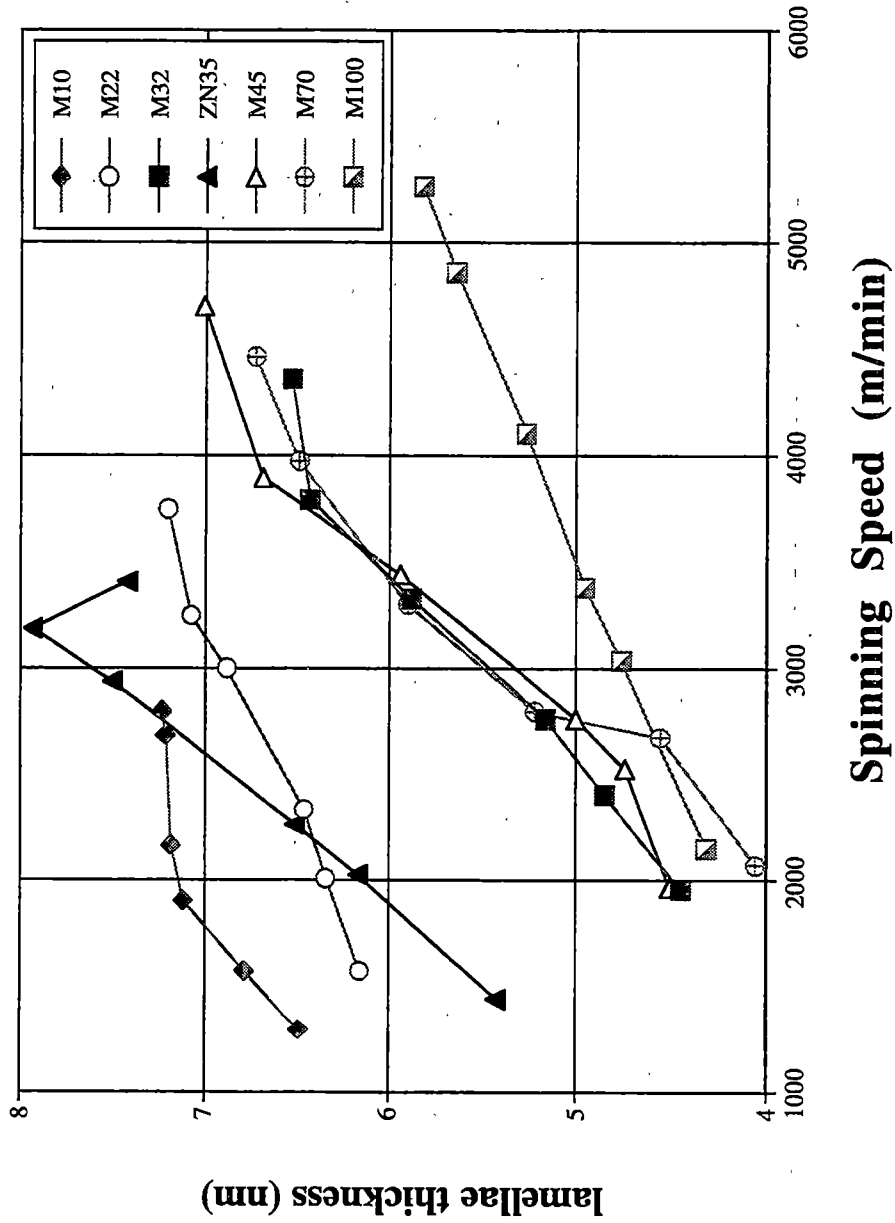
Figure 5.15 Lamellae thickness versus spinning speed for as-spun filaments.

375
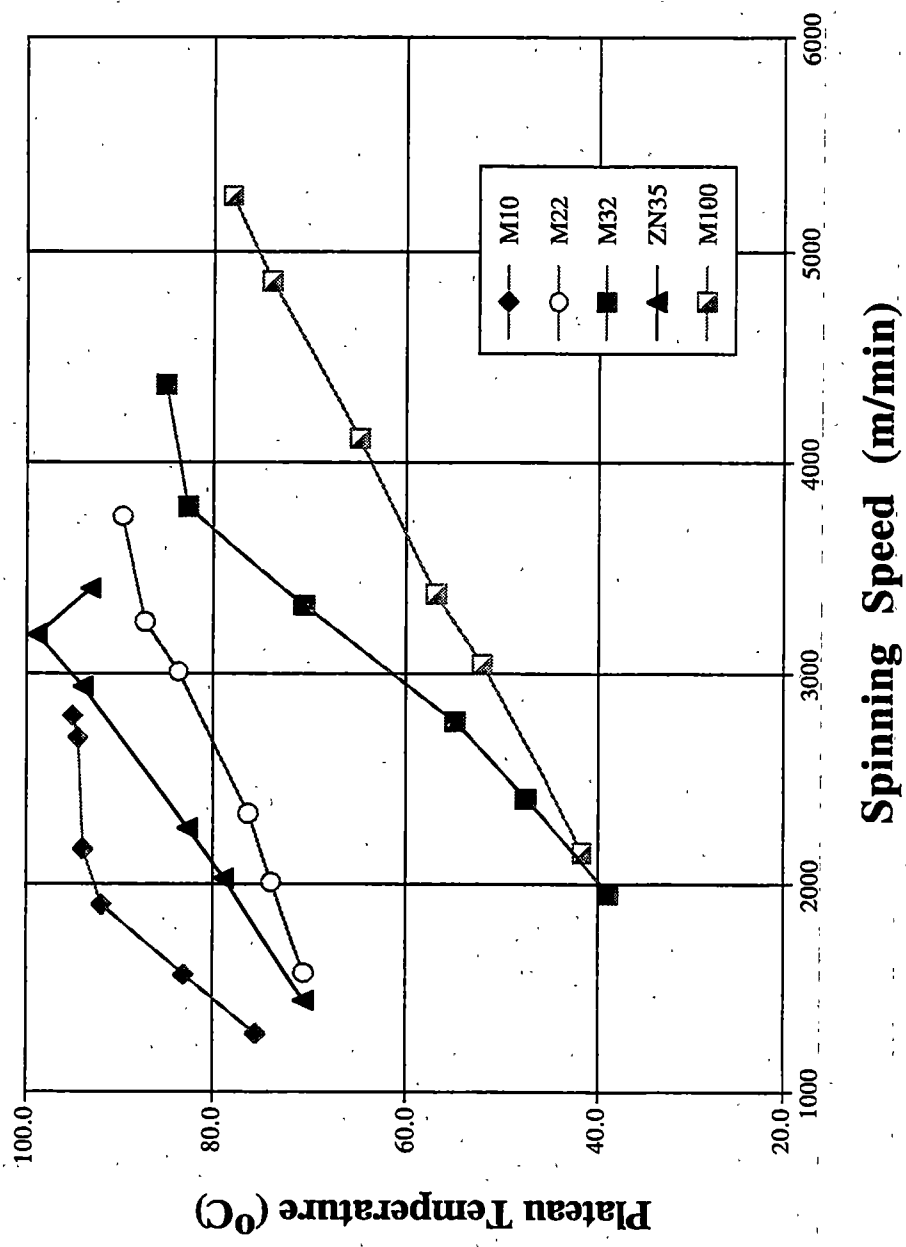
Figure 5.16 Plateau temperature of fibers versus spinning speed.

spinline are comparable with those obtained quiescently at much lower cooling rates. The effect of stress enhanced crystallization is clearly evident and will be discussed further in section 5.5.

The results of on-line fiber spinning studies have shown that each resin has a different spinning speed at the same applied draw down pressure. The differences in spinning speed are a result of differences in rheology, which is primarily determined by M_w and MWD. On-line birefringence studies show that decreasing the molecular weight for a series of narrow MWD resins, delays crystallization in the spinline to distances further away from the spinneret. Increasing the molecular weight initiated crystallization closer to the spinneret, at higher crystallization temperatures and at larger filament diameters in the running spinline. Stress at crystallization onset and final filament diameter results indicated that each parameter was a function of spinning speed only, with the series of resins at each spinning condition forming a broad band of values.

5.3 Structure of As-spun Filaments

In this section it will be of use to compare some of the properties of as-spun fibers with results of previous investigations[146-158] on the fiber spinning properties of iPP with broader MWD values. This is useful since the present set of resins all have very narrow MWD, which as will be shown, have different filament properties.

The density of as-spun filaments is presented in Figures 5.17. The results in Figure 5.17 show that M10 and M22 have very similar densities (i.e. crystallinities), which are clearly higher than the others, followed by ZN35, M45, M32, M70 and M100 at higher spinning speeds. At spinning speeds below 2500m/min, M32, M45, M70 and
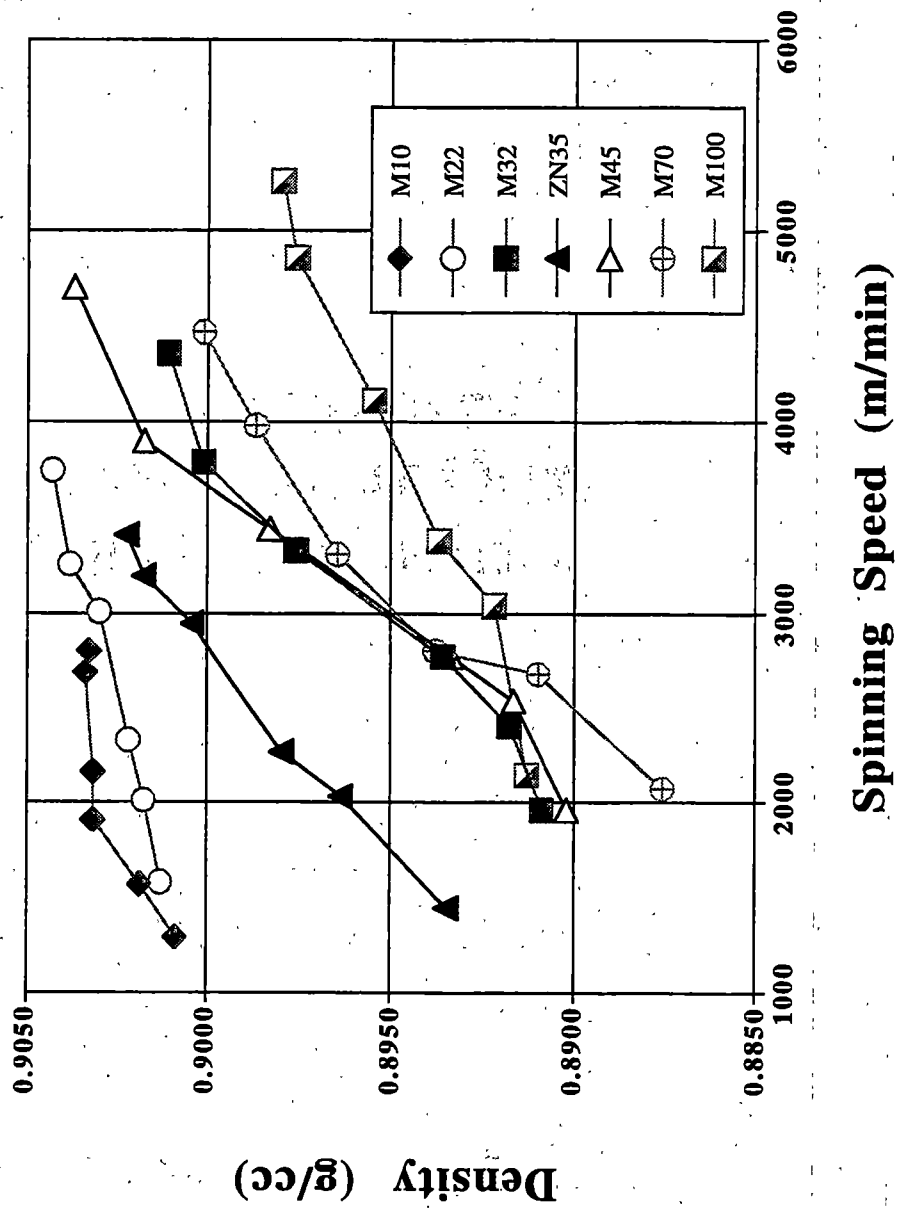
Figure 5.17 Density of filaments versus spinning speed.

M100 have similar crystallinities, with M70 slightly below the others. The resins follow the weight average molecular weight trend for increasing density with increasing molecular weight. The density of these films span a range of 0.8900g/cm^3 to 0.9050g/cm^3, similar to previous studies of iPP fibers[155-158] However, two interesting observations are made, the behavior of ZN35 and M45.

Typically, the melt flow rate (MFR) of a resin would be compared to a similar MFR resin in fiber spinning behavior. In the present case M32 and ZN35 have similar MFR values, but as has already been shown in this work, ZN35 and M32 behave very differently in their spinning behavior due to their differences in MWD. (This was also pointed out in the discussion of the shear rate behavior in Figure 5.10) Therefore, making MFR comparisons, at least within the present work, may lead to difficulty in explaining a resin's fiber spinning behavior. For this reason we shall use molecular weight and MWD values in understanding and explaining the fiber spinning behavior of these materials.

ZN35 and M22 have very similar M_w. However, their polydispersity values are different. Studies have shown that increasing polydispersity produces a more crystalline filament, with all other conditions identical[154-158]. Clearly, this is not true for the present situation. The likely explanation is the method of determining the density/crystallinity of the fibers. It is well known that oriented amorphous polymers have higher densities than their unoriented isotropic states. This is also true for semicrystalline polymers. As the final filament birefringence data in Figure 5.18 shows, ZN35 has a significantly lower overall molecular orientation when compared to M22. M45 also has a higher density and birefringence than M32, even though M32 has a higher weight average molecular weight.
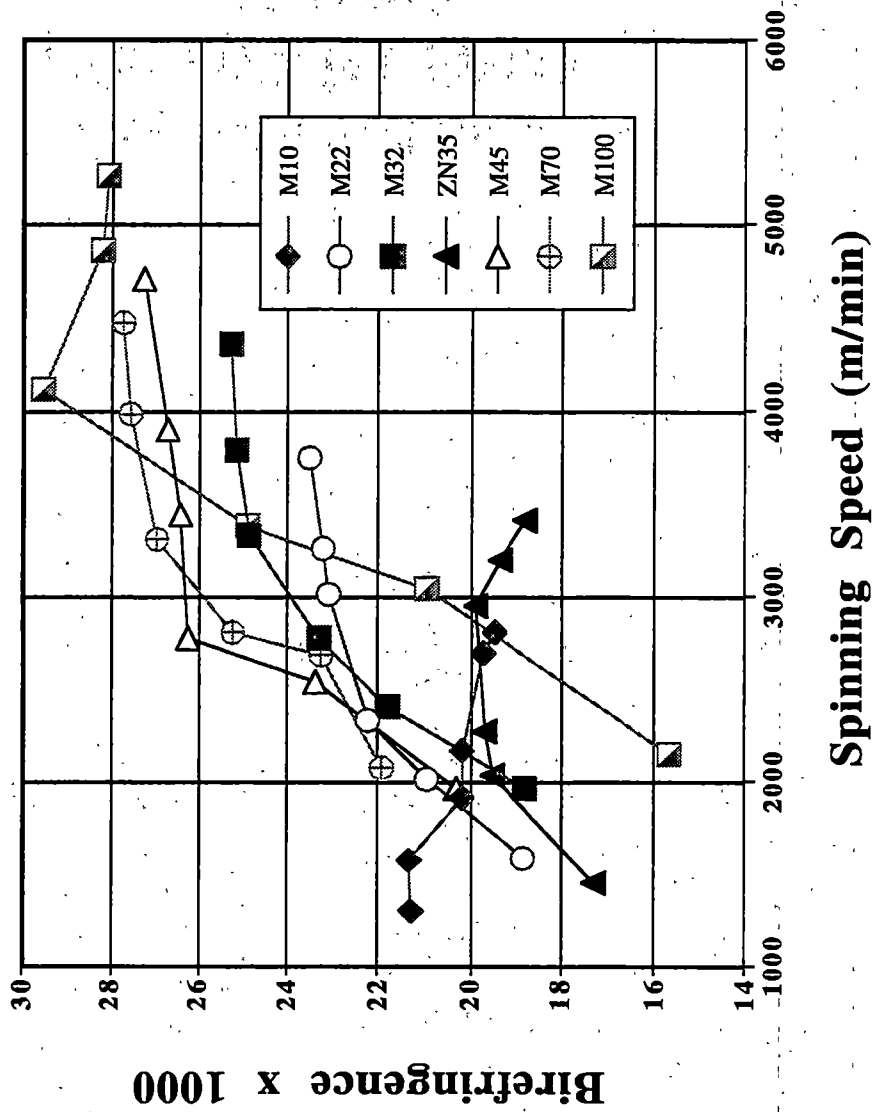
Figure 5.18 Birefringence of filaments versus spinning speed.

M45 also has a slightly broader MWD than M32. The density of a semicrystalline polymer is determined by the crystallinity and overall molecular orientation. Therefore, the combination of a fiber's crystallinity and overall molecular orientation must be taken into consideration when comparing the densities of various fibers and can explain the densities observed in the present set of fibers.

The birefringence results in Figure 5.18 show that as the spinning speed increases the final birefringence increases for all resins, except for M10 and ZN35. Figure 5.18 also indicates that as the molecular weight decreases the final birefringence generally increases for all resins. M10 and ZN35 birefringence values decrease with increasing spinning speed in the range of spinning speeds investigated in this study. This result contradicts previous experimental work[154-158]. Previous studies have stated that increasing molecular weight produces a higher birefringence, a result of more stress in the spinline when compared at the same spinning speed. The present data suggest the stress at crystallization onset is quite similar for all the resins as a function of spinning speed as was shown in Figure 5.12. Additionally, the present data (see M10, M22 and ZN35 in Figure 5.16) further indicates that the higher molecular weight resins crystallize closer to the spinneret at higher temperatures at the same spinning speed. However, in the present case, we observe that the order of birefringence of the resins is a strong function of spinning speed as well as their molecular weight. In the lower spinning range, the higher molecular weight resins tend to lead to higher birefringence values, as previously reported. But at higher spinning speeds this trend is reversed according to Figure 5.18. At higher spinning speeds the lower molecular weight samples crystallize further from the spinneret and at lower temperatures. Crystallizing further away from the spinneret

allows the molecules to become more highly oriented before the onset of crystallization since the melt is being continuously elongated until crystallization is complete. In addition, crystallizing at a lower temperature means crystallization is more rapid. Rapid crystallization would tend to produce more tie molecules that are frozen in more effectively due to the lower crystallization temperature.

Preceding studies[148-158] on zniPP resin with different MWD values indicated that broad MWD samples develop a higher crystallinity and lower final birefringence than do samples spun with narrow MWD resins with similar mfr. In this case the authors took the density measurement and directly used its value as the crystallinity, with no qualification that noncrystalline orientation can effect the observed density, hence the crystallinity. Filament birefringence values tended to decrease as the molecular weight decreased or the MWD broadened. Typical birefringence values ranged between 0.013 and 0.022, while the present studies birefringence values range from 0.016 and 0.030. Clearly there are substantial differences in the birefringence values in the two sets of work. However, it must be noted that the present set of miPP resins have a very narrow range of polydispersity values. It must also be stated that any work done using a series of resins with these MWD values has not been published in the literature, i.e. there is no basis for comparison with this series of resins for iPP.

Previous researchers[154-158] indicated that higher molecular weight resins, or broader MWD resins compared to similar molecular weights had a more pronounced bimodal orientation of crystals, indicated by the a' axis reflection in Figure 5.19. The crystals responsible for these reflections are approximately perpendicular to the primary row nucleated discs. The bimodal orientation causes a reduction in the measured

a'-Axis Oriented Reflections

110
130

111

130
040
110
c-Axis Oriented Reflections

ANNEALED OR SPUN POLYPROPYLENE FIBER

No a'-Axis Oriented Reflections

111

130
040
110
c-Axis Oriented Reflections
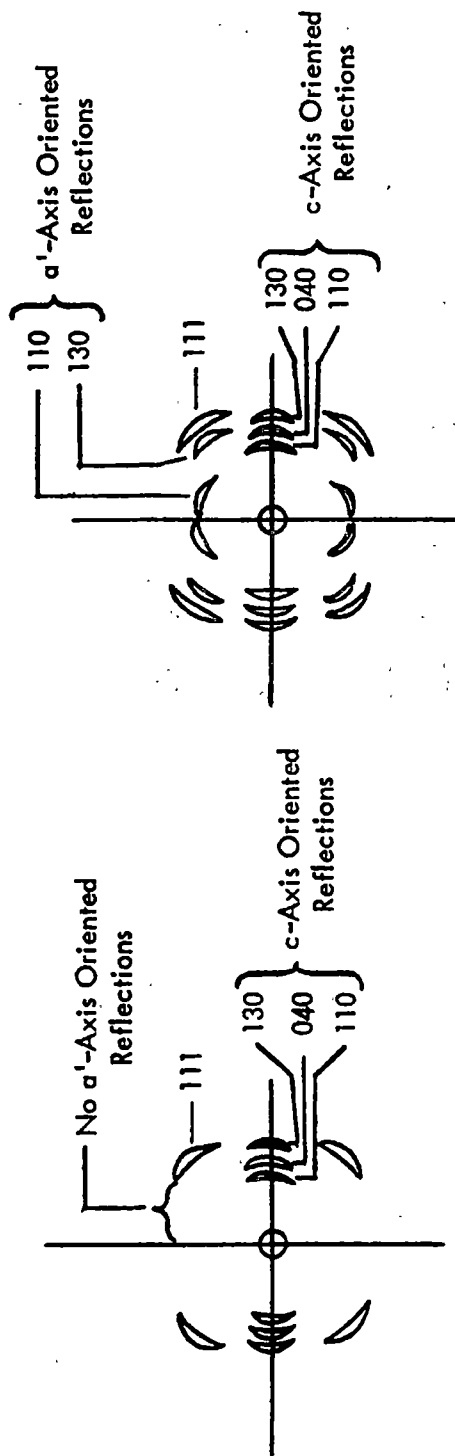
COLD DRAWN POLYPROPYLENE FIBER

Figure 5.19 Flat plate patterns of draw and as-spun iPP fibers.

383

birefringence in iPP. The flat plate x-ray patterns for the as-spun filaments in this study are shown in Figures 5.20-5.26 for the indicated resin. As can be clearly seen in all the figures, crystalline orientation increases as the spinning speed increases. Also, most if not all the films exhibit an a' 110 reflection, indicating that all the fiber samples have some bimodal orientation. The only samples that exhibited any significant a' 130 reflection were M10 and ZN35, although M22 did also at the higher spinning speeds. The a' 130 reflection has a weak intensity for the bimodal population of crystals, its presence indicates a significant amount of bimodal orientation in a fiber sample. M10 and ZN35 crystallize closest to the spinneret at the highest crystallization temperatures. These resins are also the ones with the lowest observed filament birefringence. The flat plate patterns also show that there is a significant amount of smectic structure in the miPP resins at lower spinning speeds. As the molecular weight decreases, the presence of the smectic structure is present even at spinning speeds approaching 4000m/min for M70 and M100.

In order to determine the origin of the higher birefringence in the miPP resins, the crystalline and noncrystalline orientation functions were determined for each fiber. Separating the birefringence for each phase then allows the contribution of each phase to the total birefringence to be calculated. The basic method for determining the orientation functions is described in section 2.5.1.4 and section 3.6.3.2. For iPP, the 110 and 040 reflections are used for determination of the crystalline orientation function.

The crystalline orientation function (f_c) for the as-spun filaments is shown in Figures 5.27. The data show that for each resin, as the spinning speed increases, the crystal orientation function generally increases, most dramatically for all resins at lower
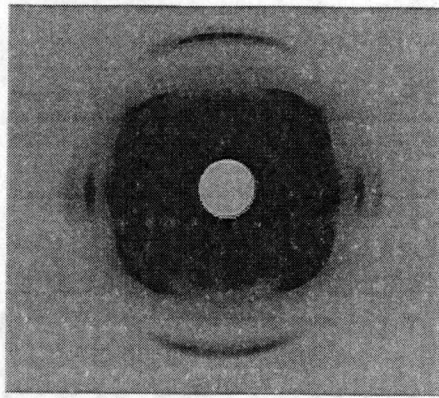
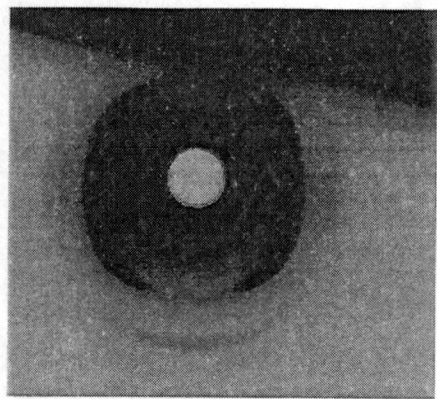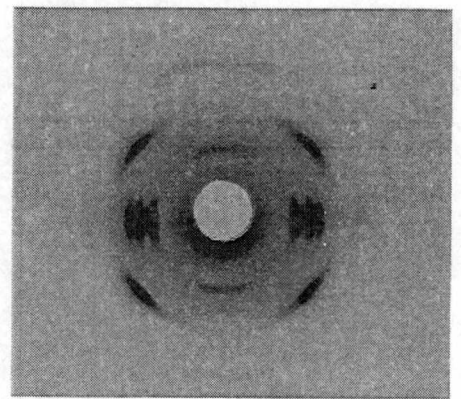1296m/min
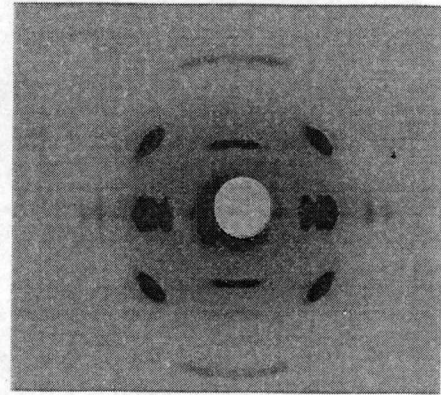
1572m/min
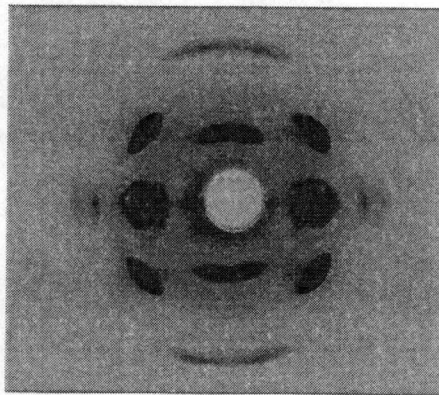
1908m/min
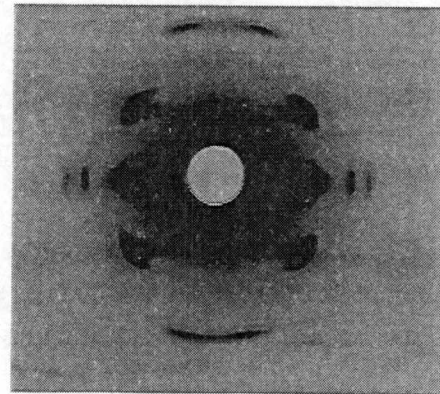
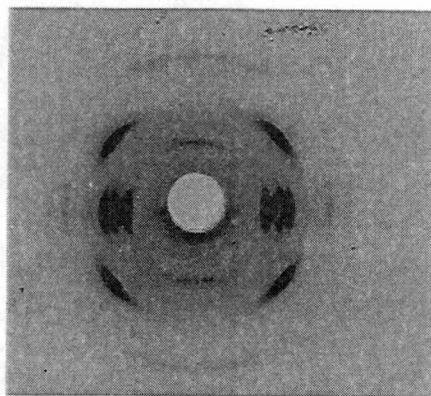2169m/min
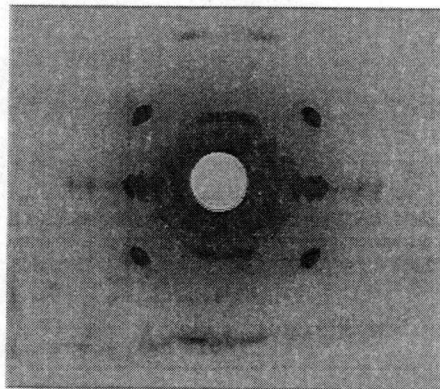
2690m/min
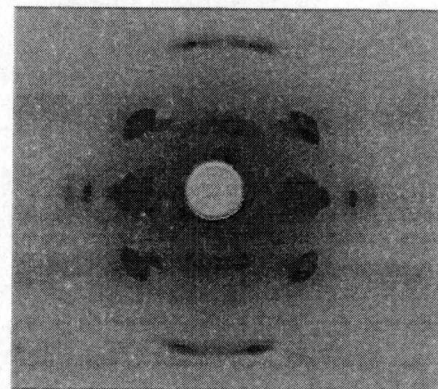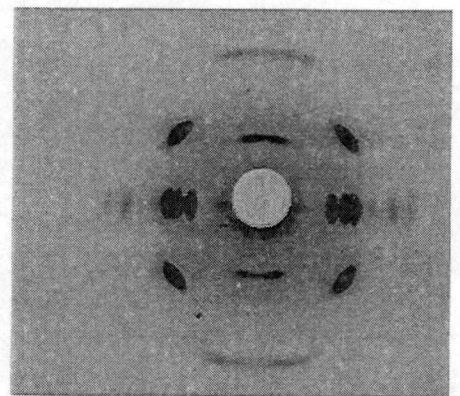
2800m/min
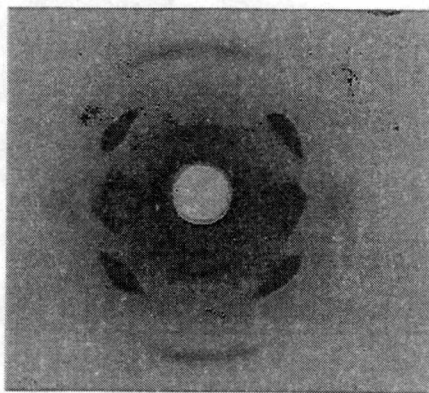
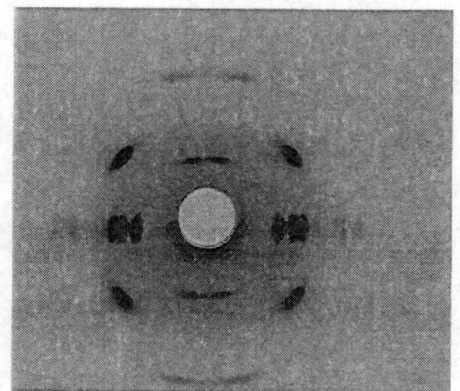Figure 5.20 Flat plate WAXD pattern of M10 as-spun fibers.
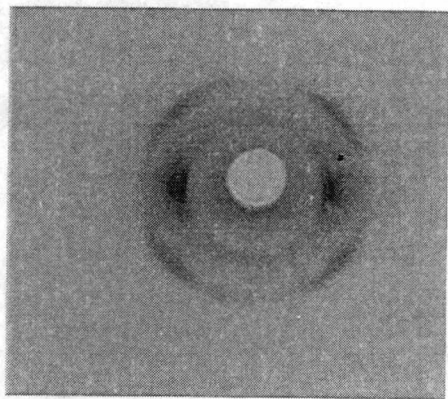
385

1578m/min

2008m/min

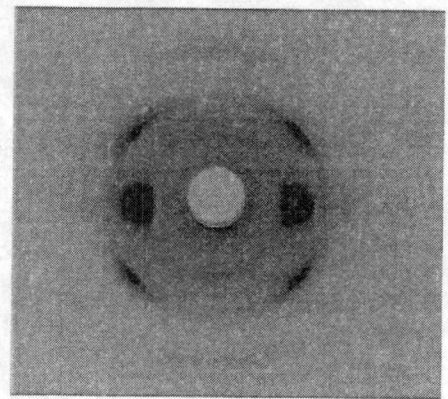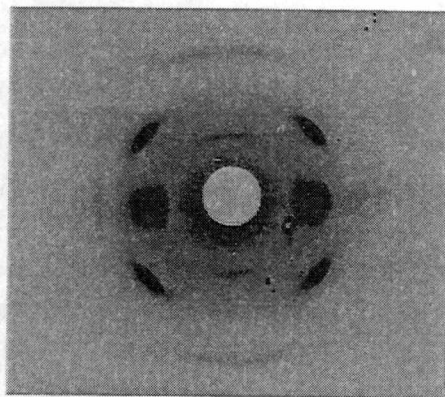2333m/min

3005m/min

3248m/min
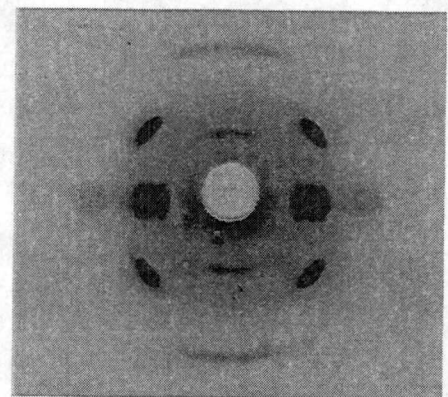
3748m/min

Figure 5.21 Flat plate WAXD pattern of M22 as-spun fibers.

386

1961m/min
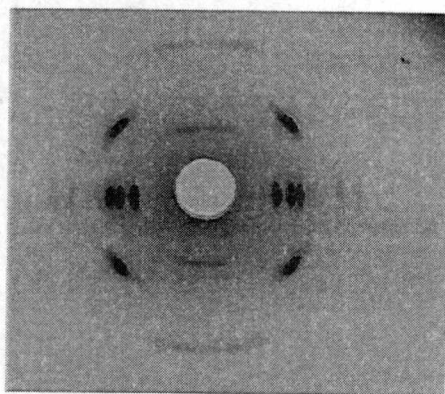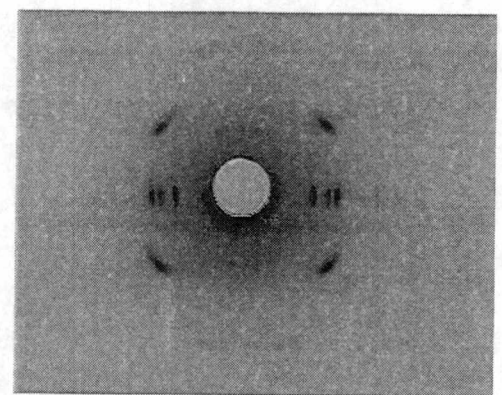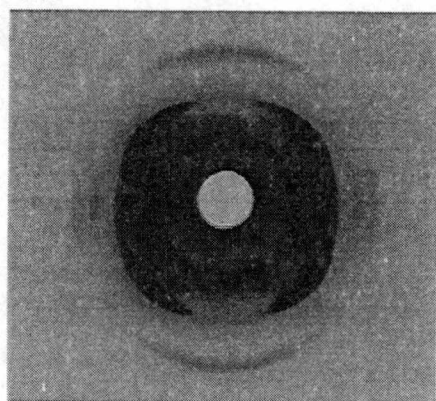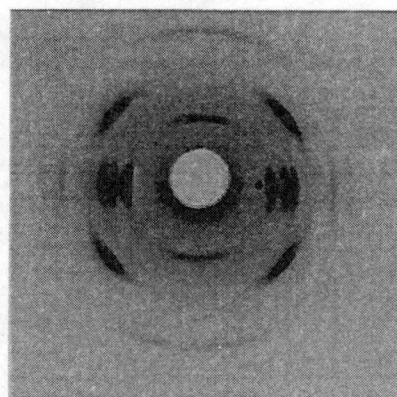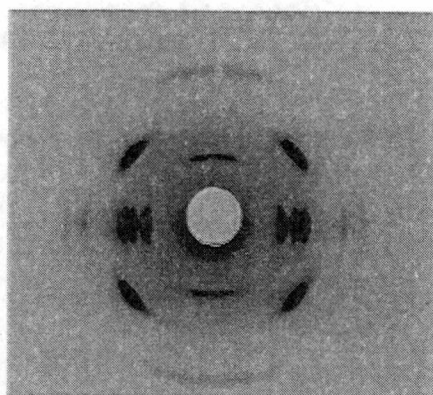
2405m/min

2768m/min

3324m/min

3786m/min

4363m/min

Figure 5.22 Flat plate WAXD pattern of M32 as-spun fibers.

387
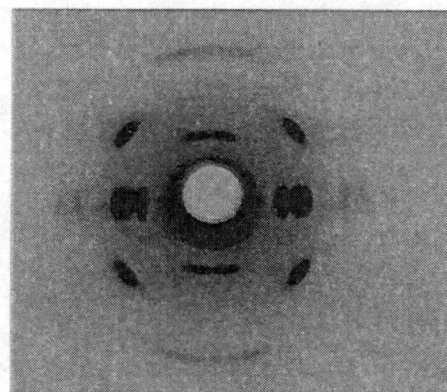
1446m/min

2030m/min

2264m/min

2940m/min
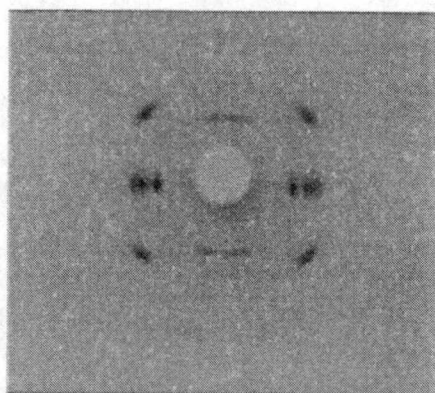
3187m/min
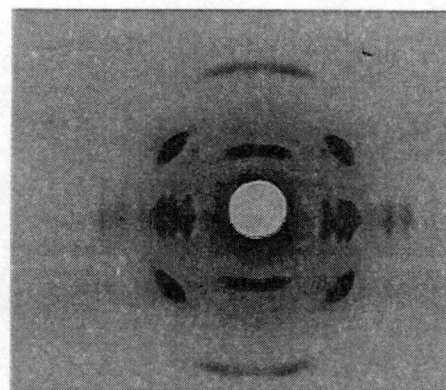
3401m/min

Figure 5.23 Flat plate WAXD pattern of ZN35 as-spun fibers.

388

1965m/min

2531m/min

2766m/min
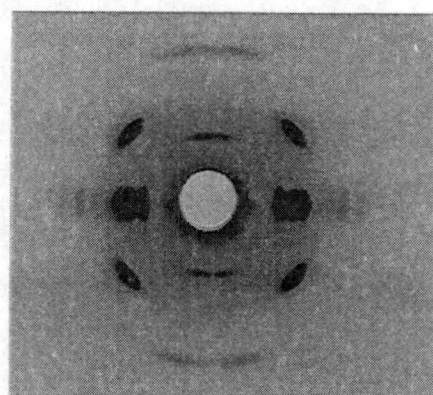
3438m/min
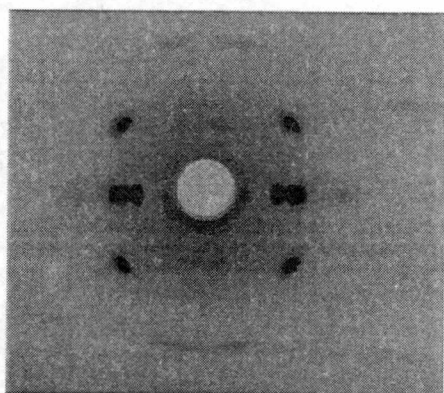
3893m/min
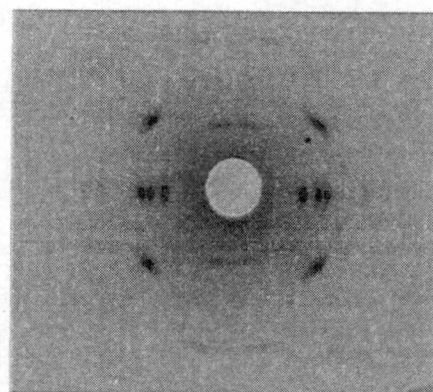
4702m/min

Figure 5.24 Flat plate WAXD pattern of M45 as-spun fibers.

389

2075m/min

2675m/min

2798m/min

3303m/min
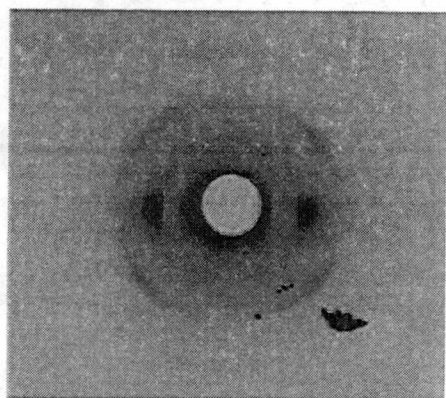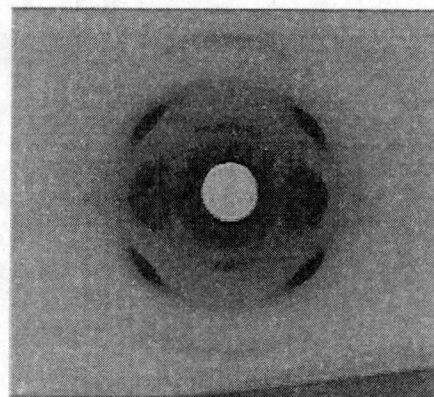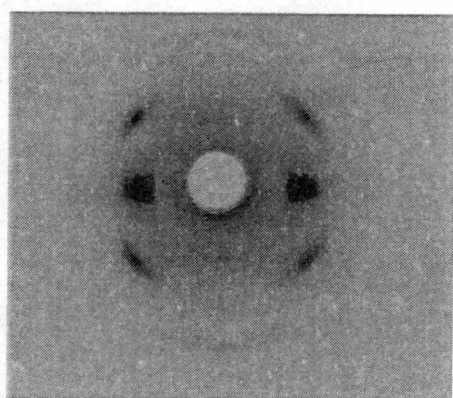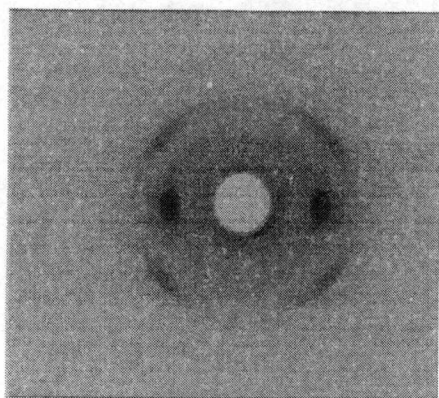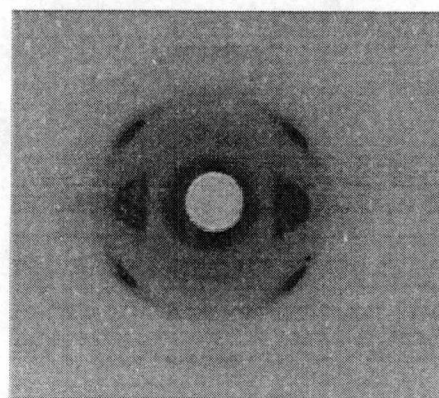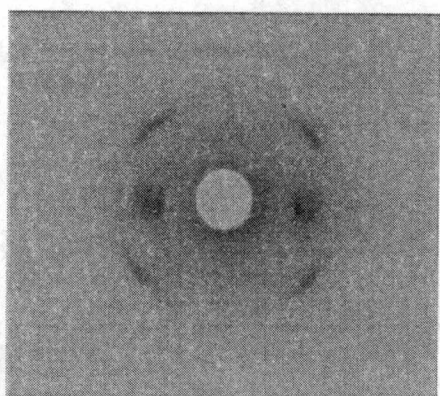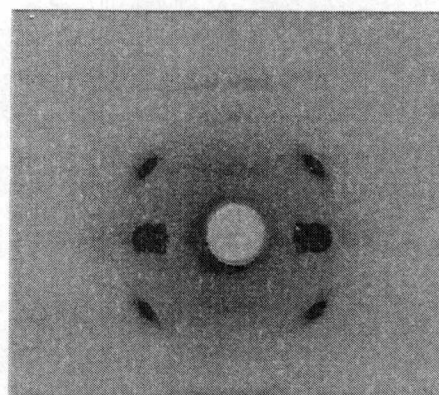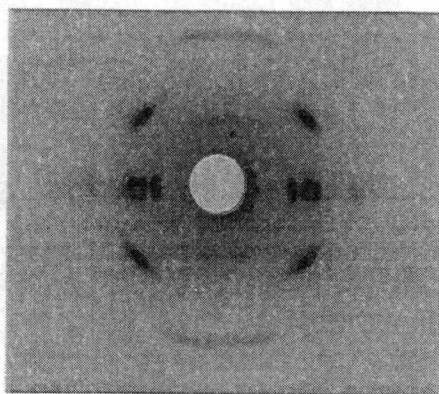
3975m/min
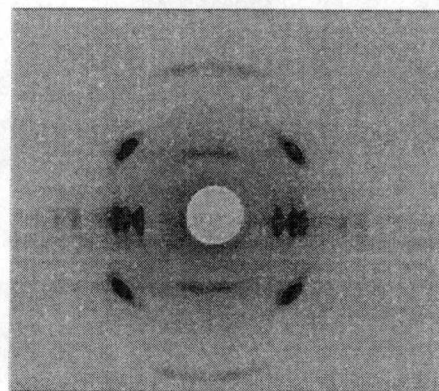
4468m/min

Figure 5.25 Flat plate WAXD pattern of M70 as-spun fibers.
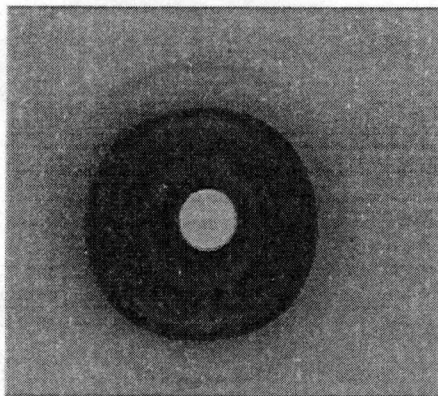
2149m/min
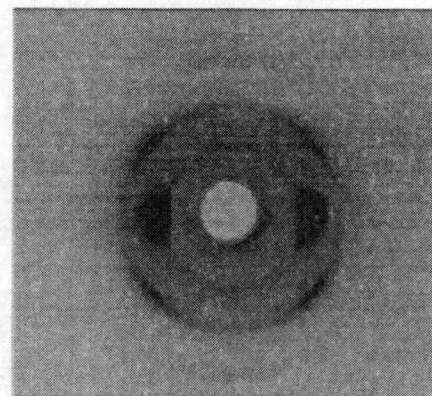
3040m/min
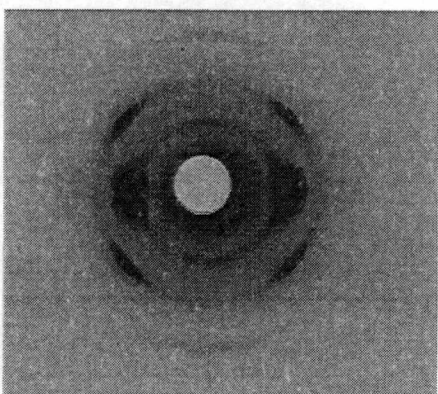
3374m/min
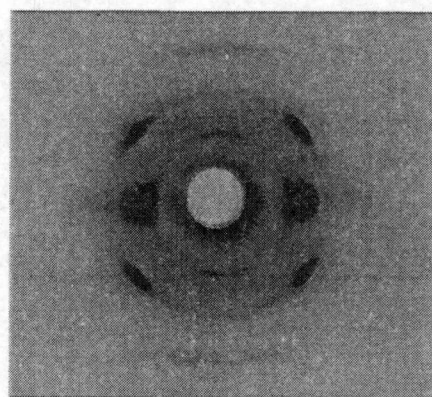
4108m/min
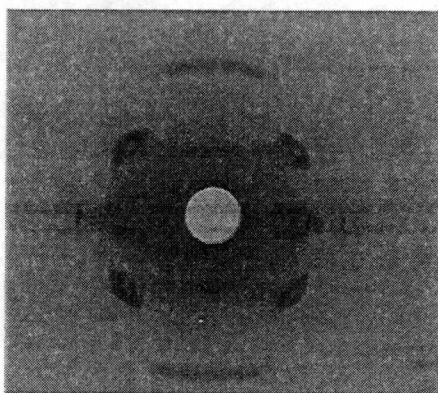
4858m/min
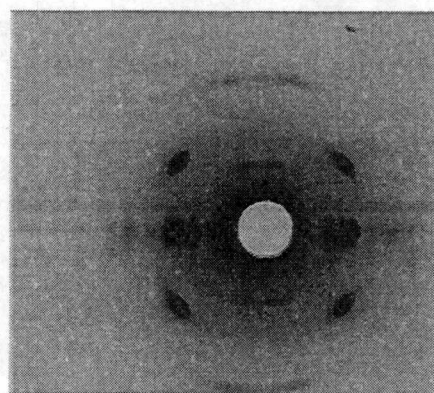
5261m/min

Figure 5.26 Flat plate WAXD pattern of M100 as-spun fibers.
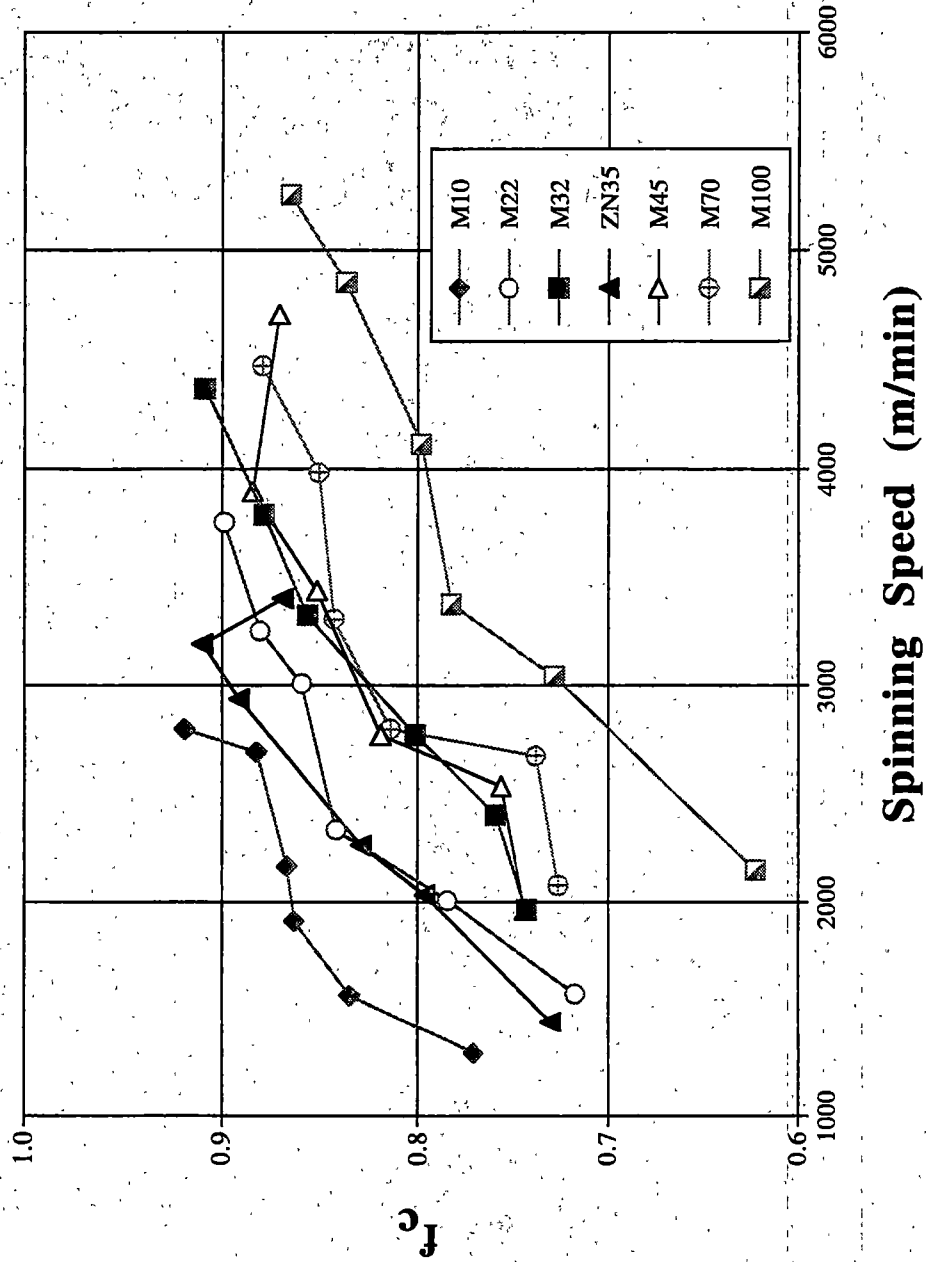
Figure 5.27 Crystalline orientation function versus spinning speed.

spinning speeds. Most of the resins had a gradual increase in f_c even at the highest spinning speeds. Moreover, as the molecular weight increases, the crystalline orientation function also increases, i.e. the crystalline orientation function for M10>M22> etc. at the same spinning speed. The on-line birefringence studies showed that the higher MW resins crystallized closer to the spinneret, which seem to produce more highly oriented row nuclei. Another result of crystallization at higher temperatures and closer to the spinneret is more time for the noncrystalline regions to relax.

The noncrystalline orientation function (f_{nc}) for each resin is shown in Figure 5.28. The value of f_{nc} for the miPP resins increases with spinning speed, except for the behavior of M10, which decreases as spinning speed increases. M10 and ZN35 show a decrease in f_{nc} as a function of increasing spinning speed. Some of the resins exhibited a maximum in f_{nc}, then either a plateau or slight decrease in f_{nc} as the spinning speed is increased further. M22 increased slightly, but not as dramatically as the low MW resins. It is worth recalling that as the spinning speed increases for a given resin, the crystallization temperature increases. As the crystallization temperature increases, it becomes possible for oriented noncrystalline chains to relax, due to increased thermal energy. The data suggest that there is a critical crystallization temperature, above which for a given resin, noncrystalline regions will relax. The temperature at which the noncrystalline regions relax would seem to depend on the molecular weight, most likely in some rough correspondence with the WLF equation.

Figures 5.29 and 5.30 show the crystalline and noncrystalline birefringence contributions for each resin as a function of spinning speed, respectively. The total observed birefringence of the as-spun fibers has been broken down by phase for each
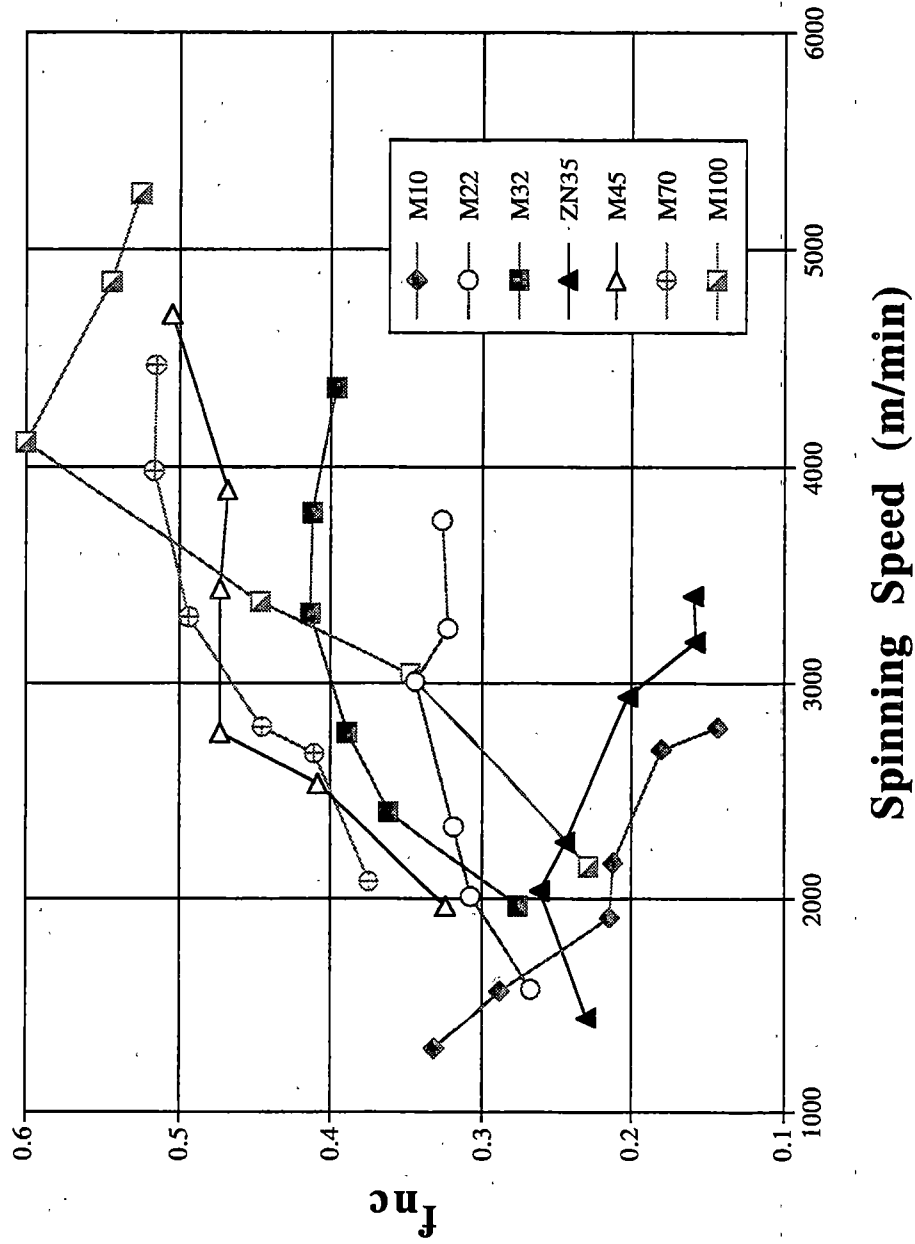
Figure 5.28 Noncrystalline orientation function versus spinning speed.

394
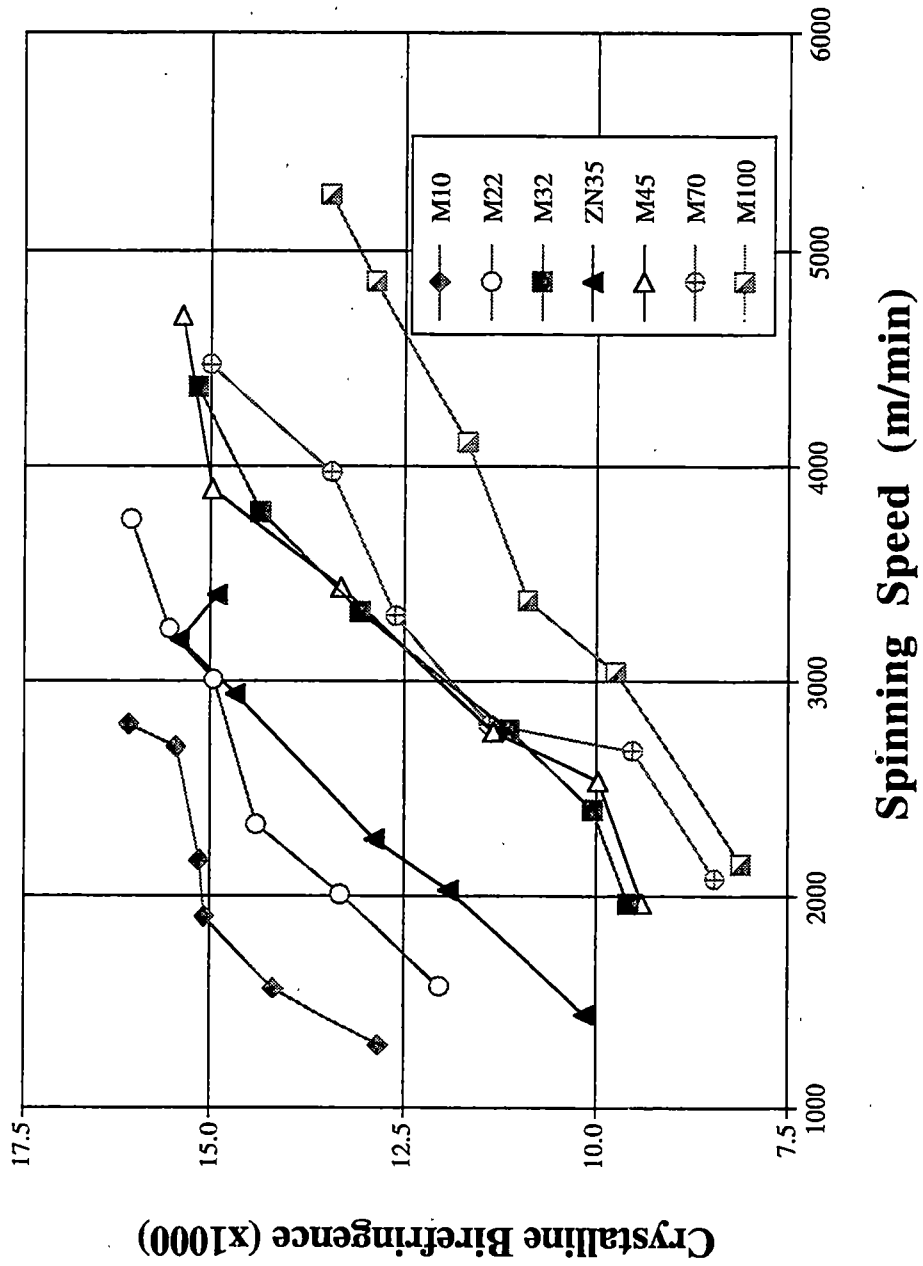
Figure 5.29 Crystalline birefringence versus spinning speed.
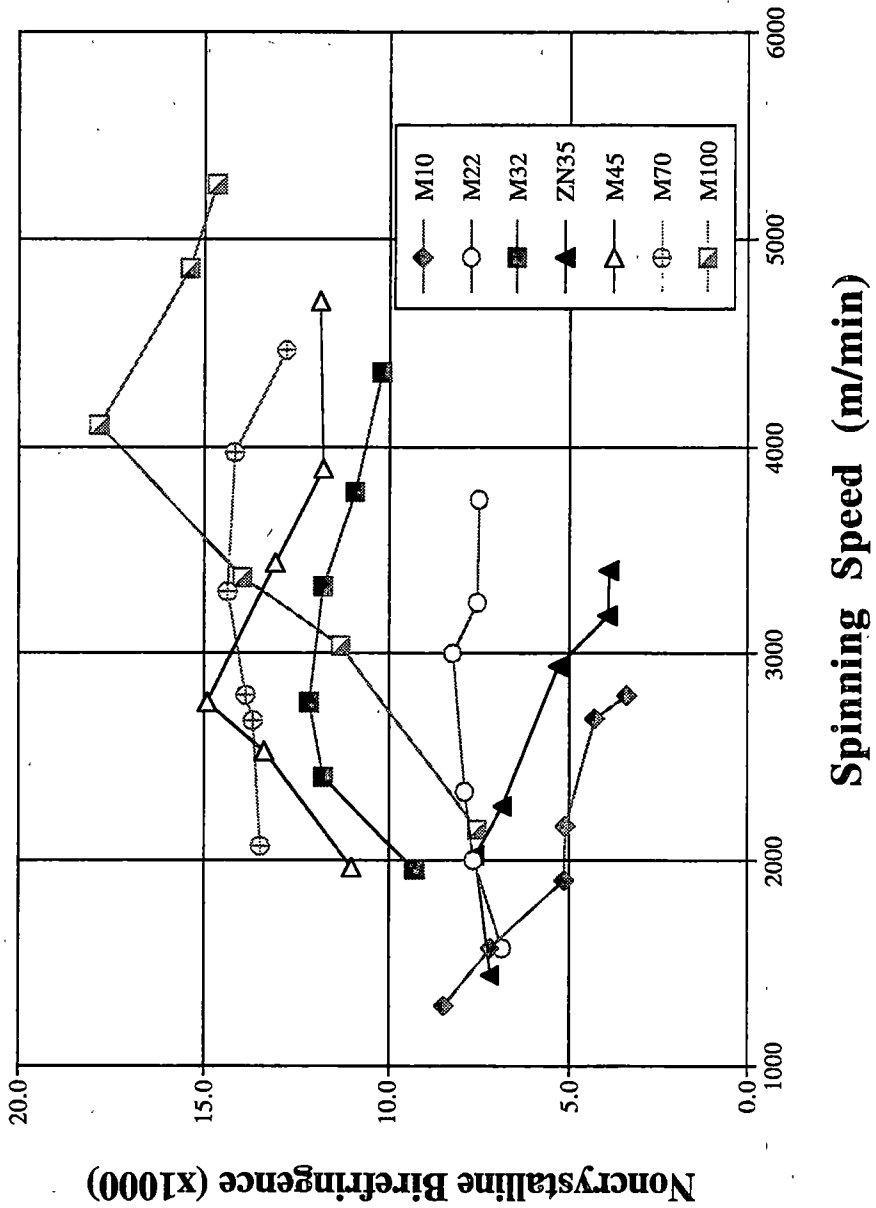
Figure 5.30 Noncrystalline birefringence versus spinning speed.

396

fiber. The relative contribution of each phase has been calculated according to equation 2.44. The crystalline birefringence contribution is much higher than the noncrystalline birefringence for the higher MW resins; M10, M22 and ZN35 at all spinning speeds. The crystalline birefringence values are still increasing for the miPP resins at the highest spinning speed, while ZN35 has leveled off. The noncrystalline birefringence contribution is very much the reverse of the crystalline birefringence, with regard to the effects of MW. The noncrystalline birefringence is virtually identical to the f_{nc} figure (Figures 5.28) with regard to general shape. Decreasing MW for the miPP resins tended to increase the f_{nc} contribution to the total birefringence. Also noteworthy is the fact that at lower spinning speeds, the noncrystalline birefringence is higher than the crystalline birefringence for the miPP resins, except for M10 and M22.

The structure developed in as-spun filaments in the present study was found to be strongly dependent on the molecular weight and its distribution. For the miPP resins at a given spinning speed, increasing the molecular weight generally increased the density, crystalline orientation function, crystalline contribution to the total birefringence and decreased the birefringence, noncrystalline orientation function, and noncrystalline contribution to the total birefringence. The properties above are largely determined by the spinning speed, which for a given resin, determines the crystallization temperature and stress at crystallization onset, as discussed in the on-line fiber spinning section 5.2. Therefore, the differences in fiber structure can be traced to the differences found in the on-line fiber spinning studies for all the resins in this study, including ZN35.

5.4   Tensile Mechanical Properties of the Melt Spun Fibers

The tensile modulus for each resin as a function of spinning speed is shown in Figure 5.31. For all resins, the tensile modulus increases as the spinning speed increases. The results in Figure 5.31 indicate that the tensile modulus values for all resins in this study seem to cluster near a common line as a function of spinning speed. Tensile modulus is a function of both crystallinity and overall molecular orientation. As the spinning speed increases, both the crystallinity (i.e. density) and birefringence increase for most of the resins. The tensile modulus increases in a manner consistent with the combination of these factors, even though the crystallinities and birefringence values are not independently identical for the resins under any given spinning speed.

Previous work[155-157] on iPP fibers found that the tensile modulus increases as the molecular weight, MWD and spinning speed increases. The present data does not exhibit this trend, save for the effect of spinning speed which seems to be the only important parameter. However, the present resins have a much more narrow MWD than any previously published studies which produce orientation levels (as measured by birefringence) that are also contrary to other investigations. It would, in light of the present work, stand to reason that a more highly oriented sample would have a higher tensile modulus as the present data suggest.

The tensile strength for the fibers in this study are shown in Figure 5.32, as a function of spinning speed. Except for M100 at the lowest spinning speed, all miPP resins have significantly higher tensile strength than ZN35. In general, the tensile strength increases as the spinning speed increases, with the exception of M10 and ZN35. The tensile strength of M10 decreases slightly as the spinning speed increases, while the
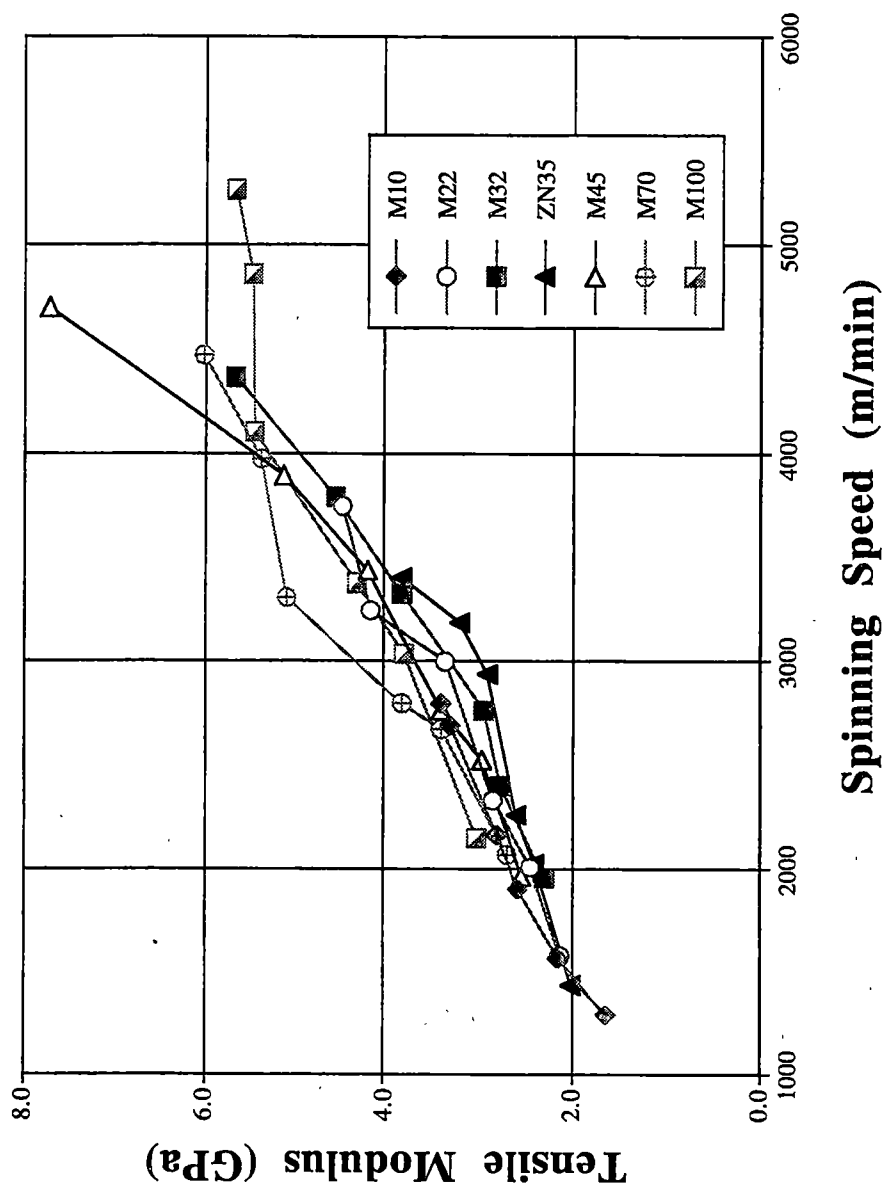
Figure 5.31 Tensile modulus versus spinning speed.

399
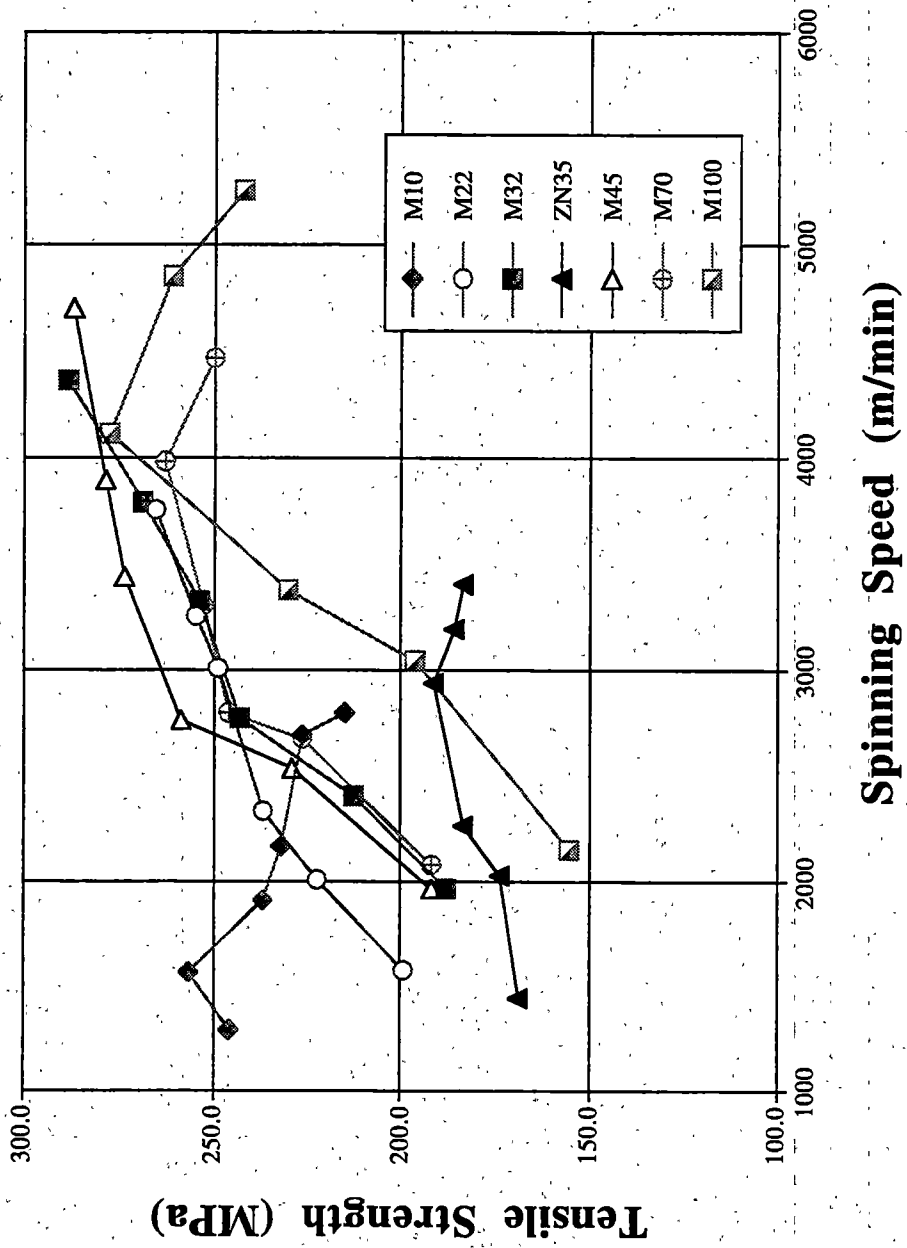
Figure 5.32 Tensile strength versus spinning speed.

400

tensile strength of ZN35 is relatively constant with spinning speed. Tensile strength depends strongly on the number of tie molecules connecting the various crystallites together. Tensile strength is also dependent upon the crystallinity to a small extent. The crystallites act as an anchor for the tie molecules, which allows the stress to be transferred throughout the material during deformation. Also, an experimental relationship has been found between the observed birefringence and tensile strength for iPP resins[157]. As the total birefringence increases, the tensile strength has been observed to increase. The noncrystalline portion of the birefringence is likely the key component in this relationship. The tie molecules are in the noncrystalline regions and become oriented during the fiber spinning process.

The results in Figure 5.33 show the tensile strength of the fibers versus the fiber's overall molecular orientation (birefringence). The results indicate there exists a strong correlation between the birefringence and strength of a fiber, as the fiber birefringence increases the tensile strength increases. This type of observation has been made previously[157] with iPP. It is also noteworthy that the data in Figure 5.33 fits in a narrow band regardless of molecular weight or MWD. The present results further validate the relationship between overall molecular orientation and fiber strength.

The results in Figure 5.34 show the fiber tensile strength plotted against the noncrystalline orientation function for each fiber sample. Figure 5.34 indicates there exists a strong relationship between the orientation of the noncrystalline chains and the strength of the fiber, as f_{nc} increases the tensile strength increases. The orientation of the noncrystalline chains strongly influences the observed birefringence, according to equation 2.44. The results in Figure 5.34 do not form a band quite as narrow as the data
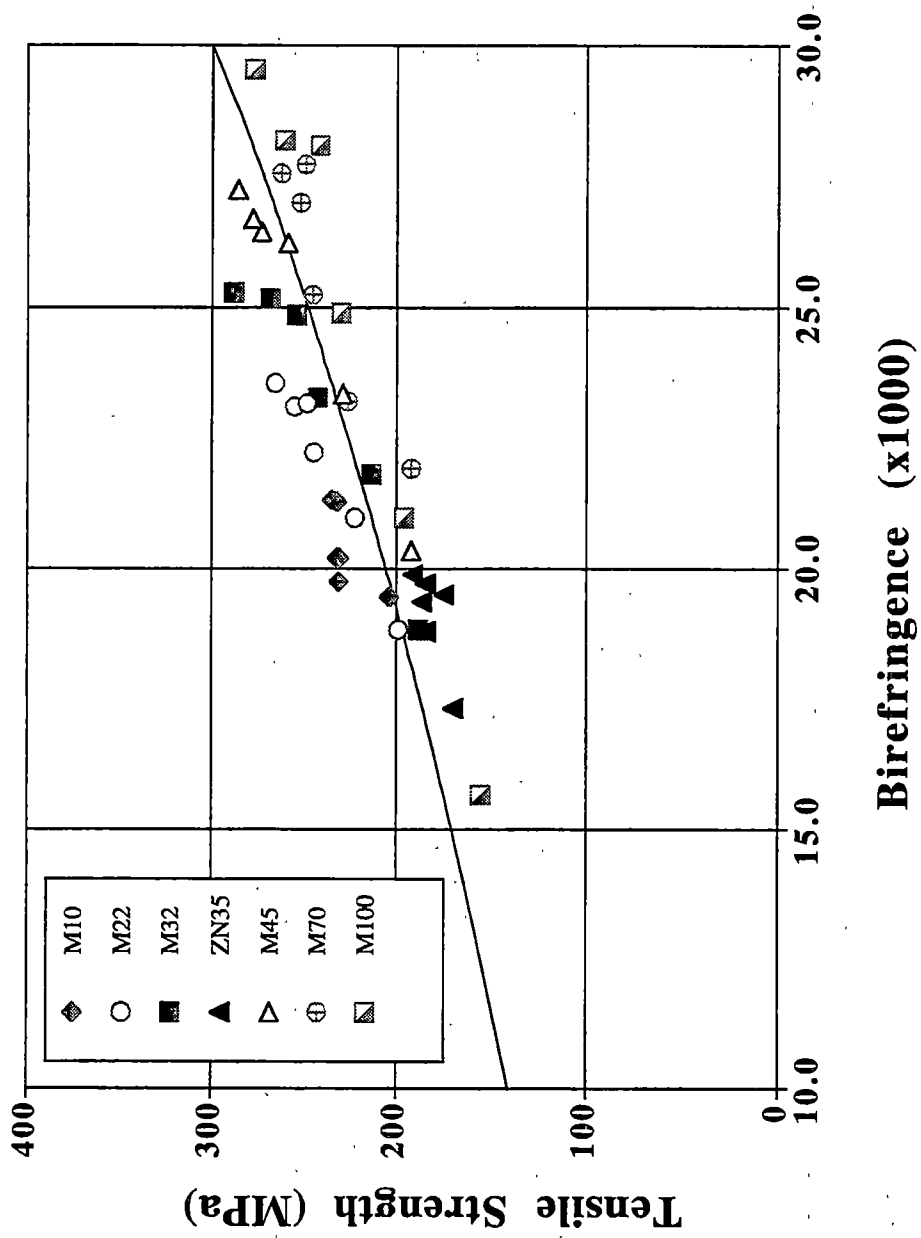
Figure 5.33 Fiber tensile strength versus total fiber birefringence.
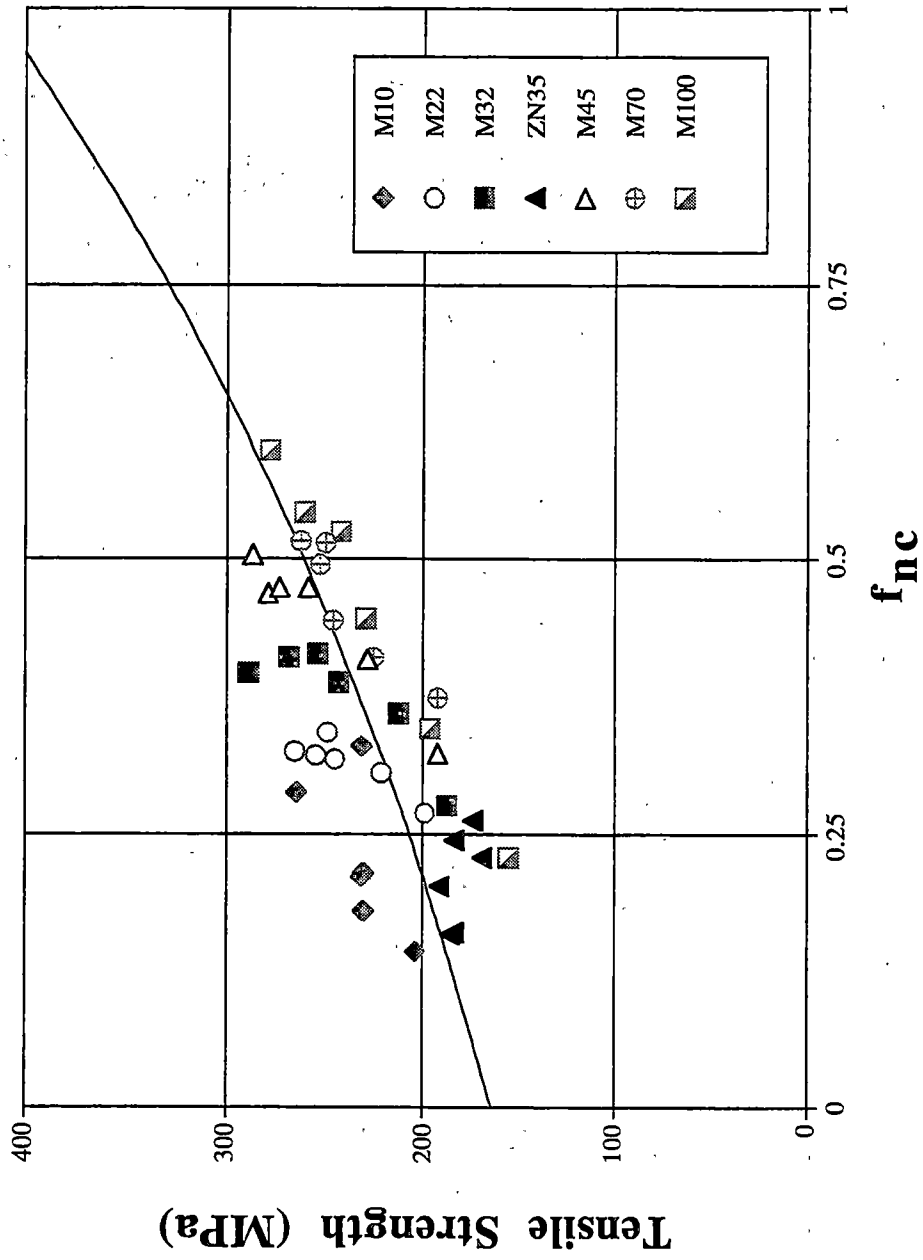
Figure 5.34 Fiber tensile strength versus fiber non-crystalline orientation function.

in Figure 5.33, perhaps due to experimental error. Birefringence can be directly measured using a compensator. The noncrystalline orientation function (which is a more fundamental property than birefringence) is determined from measuring the f_c using WAXD, density and birefringence measurements. Therefore, there are several possible experimental errors involved in the measurement of each data point in Figure 5.34. However, the possible error in calculating f_{nc} does not seem to have altered the correlation between the tensile strength and f_{nc}.

Elongation-to-break (ETB) data is typically the inverse of tensile strength since the added strength produced by more tie molecules that are highly oriented is offset by the fact the taunt tie molecules don't draw as far before fracture upon uniaxial extension. The data in Figures 5.35 shows the ETB versus spinning speed. The data indicate that as the spinning speed is increased, the ETB decreases, a result of higher overall molecular order for the same material as the spinning speed increases. The only seemingly odd behavior in this graph is the position of M10. M10 would be expected to have a slightly higher ETB based on its relative position in the tensile strength data. However, M10 had a very high density, which could have influenced the drawability of the fibers under uniaxial extension. At relatively low draw temperatures, a highly crystalline material would be expected to fracture much sooner than a material with a lower portion of crystalline material at the uniaxial extension rates (200%/min) used in this work.

5.5   Discussion of Results for Fiber Formation and Crystallization

Stress-enhanced crystallization is the concept in fiber spinning responsible for the massive acceleration of crystallization kinetics in the spinline. Stress-enhanced
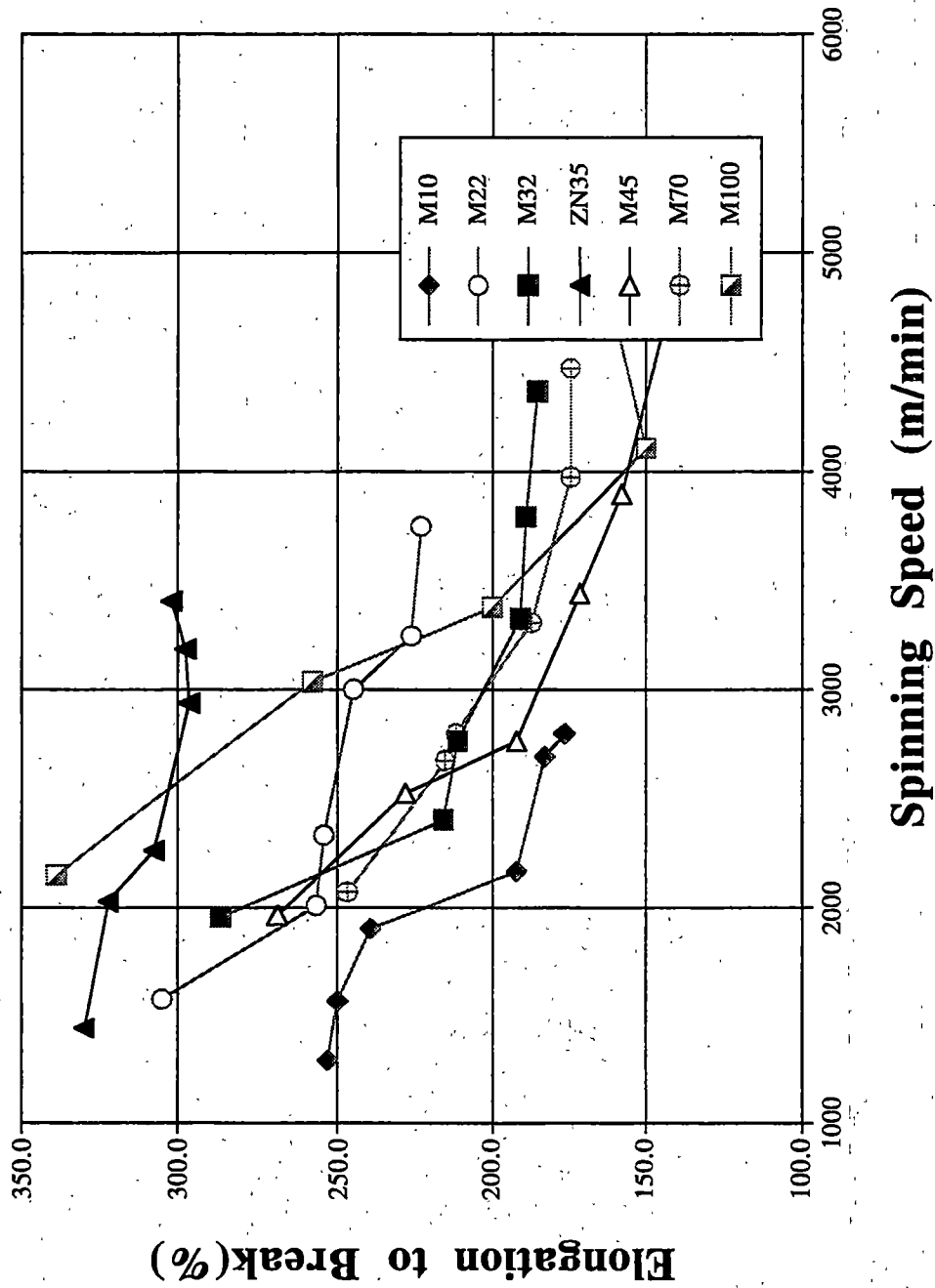
Figure 5.35 Elongation-to-break versus spinning speed.

crystallization results from molecular orientation of the melt in the spinline. Previous research[146-158] has found that the effects of stress-enhanced crystallization increase as the molecular weight and MWD increase. Since the data for the present set of resins under quiescent isothermal crystallization conditions is available, it would be insightful to calculate the effects of molecular orientation on the crystallization process in the spinline for the current set of resins. Since nucleation is the major component of crystallization that changes with molecular orientation in the spinline, calculating the effects of orientation on the effective nucleation density was done. The ratio of nucleation density of an oriented sample to unoriented sample at the same cooling rate was calculated using an Avrami type relationship.

The results in Figure 5.36 show the ratio of the total nucleation density of the oriented sample divided by the nucleation density of an unoriented sample, as a function of spinning speed. The Avrami equations in Table 2.2 were used to compute the nucleation density from crystallization half-time data. The crystallization kinetics in the on-line fiber spinning studies were used to calculate the oriented nucleation rate density of the fibers, while the unoriented nucleation density was computed using the quiescent nonisothermal half-time data obtained using the HCRLDM system. The specific manner in which each nucleation density was determined is:

Fiber Spinning

The on-line birefringence measurements were used to determine the crystallization half-time (see Figures 5.4-5.6). The onset of crystallization was determined to be the point at which the birefringence increased from values near zero. Crystallization was assumed to be complete when the birefringence leveled off. The total
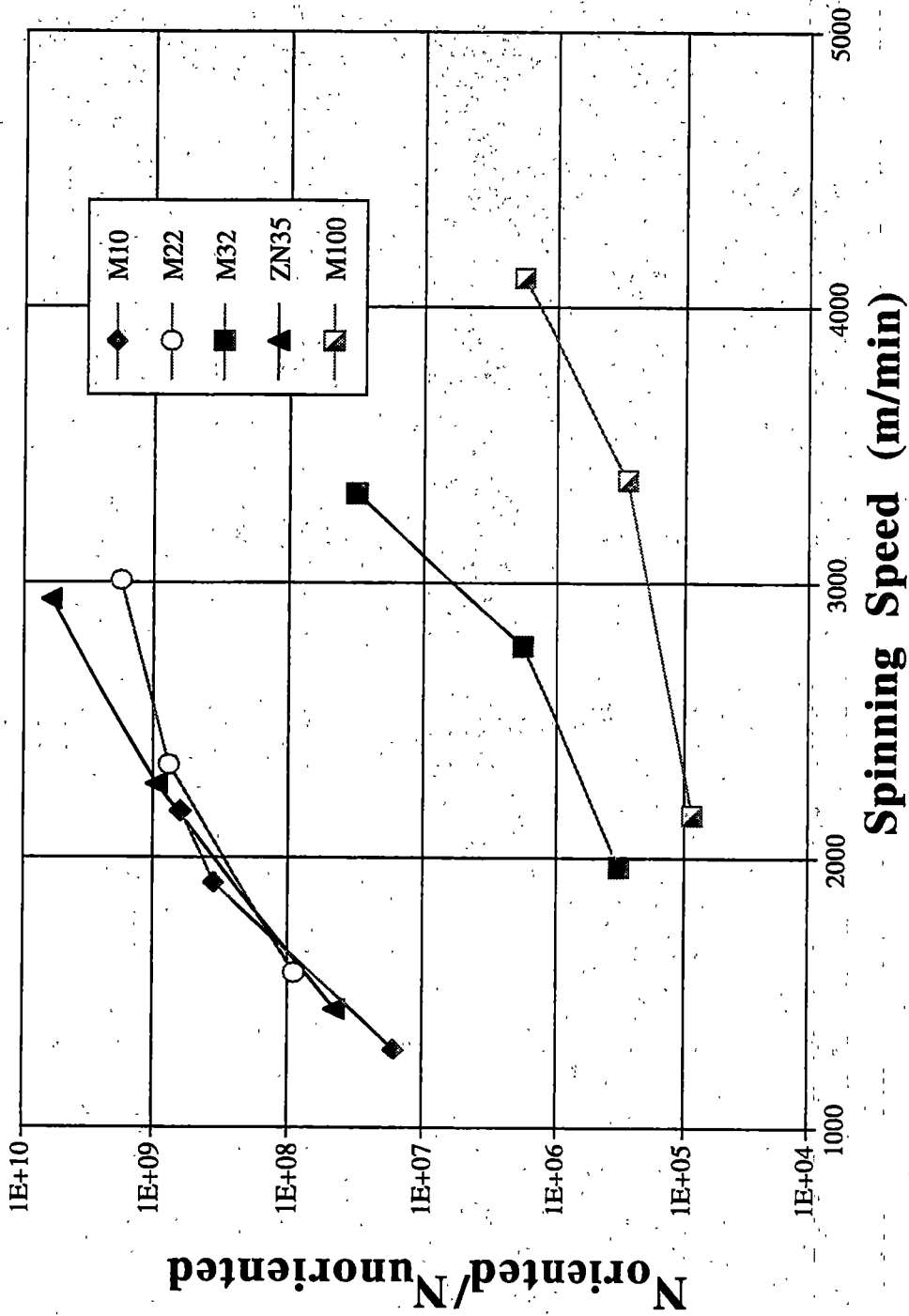
Figure 5.36 Ratio of oriented nucleation density to unoriented nucleation density versus spinning speed.

407

crystallization time was calculated by dividing the spinning speed into the total distance in the spinline between the onset and completion of crystallization. This is the total crystallization time.

Sporadic nucleation was chosen as the nucleation mechanism using a disc growth geometry. Sporadic nucleation was chosen because the nucleation is assumed to be homogenous, a result of an oriented melt accelerating the nucleation process. Studies also have shown that the crystal morphlogy is disc shaped at high spinning speeds[148-154]. The Avrami expression for calculating the fiber crystallization kinetics has the form:

$$(5.1) \qquad K = \frac{\pi}{3} \dot{N} G^2 D$$

rearranged to obtain the nucleation rate gives:

$$(5.2) \qquad \dot{N} = \frac{3K}{G^2 D \pi}$$

The definition of the terms was given in Table 2.2. The disc thickness (D) was taken to be the same as the lamellae thickness for the calculation of the crystallization temperature of the fiber samples. The lamellae thickness was determined from the fiber samples using SAXS. The growth rate was obtained from a curve fit of the growth rate versus plateau temperature data shown in Figure 4.75. The plateau temperature for each fiber sample was determined earlier in this chapter and was given in Figure 5.16. The on-line fiber spinning crystallization rate constant was calculated using the crystallization half-time of each fiber sample. Since the spinning speed for each sample is known, the point at which crystallization begins and ends (from the on-line birefringence profiles), the crystallization half-time can be determined. The half-time data was used along with

equation 2.4, using an ideal Avrami constant of 3, to determine the crystallization rate constant.

The nucleation rate was converted into nucleation density by multiplying the nucleation rate by the total crystallization time.

The results of the nucleation density in the running spinline are similar if instantaneous nucleation is assumed. The mathematical number is not identical, but the order of magnitude is similar and would not affect the oriented to nonoriented nucleation density ratio calculations and conclusions.

Quiescent Nonisothermal

The quiescent nonisothermal nucleation density was calculated to simulate the behavior of the same material under quiescent conditions and at similar crystallization temperatures of the fibers in the spinline. In order to do this, the plateau crystallization temperature of the fiber was used as the crystallization temperature. The crystallization half-time was determined from the plateau temperature by applying a curve fitting equation to the data shown in Figure 4.71.

The growth mechanism was assumed to be sporadic in nature and to have the growth geometry of a sphere. The Avrami equation for this is:

$$5.4 \quad K = \frac{\pi}{3} \dot{N} G^3$$

which gives the following when solved for the nucleation rate:

$$5.5 \quad \dot{N} = \frac{3K}{G^3 \pi}$$

The growth rates used in the fiber spinning calculation as a function of plateau crystallization temperature are used in these nucleation density calculations. An Avrami

exponent of 4 was used in the calculation of the crystallization rate constant for sporadic spherulitic growth.

The results in Figures 5.36 and 5.37 clearly show that the higher MW resins have a significantly higher oriented to unoriented nucleation density ratio than M32 and M100. M32 also has a higher ratio than does M100, further indicating that MW significantly enhances the nucleation density ratio. This data is very similar to the crystallization temperature versus spinning speed data in Figure 5.12. All resins had at least a 10^5 increase in nucleation density when placed in an oriented melt, which shows the effects of molecular orientation on accelerating the crystallization rate. The results in Figure 5.37 show the application of stress on a higher molecular weight polymer has a more pronounced effect on accelerating the nucleation rate for higher molecular weight resins than narrow or lower molecular weight resins. It was concluded in the crystallization chapter that higher MW resins have a slightly higher nucleation rate under quiescent conditions. It would appear that they have a much higher nucleation rate (density) in fiber spinning. It is quite remarkable that the higher MW resins have similar plateau crystallization temperatures to those obtained under quiescent nonisothermal conditions, despite the fact that the cooling rates in fiber spinning are from 100,000 to 500,000°C/min. For most of these resins the total crystallization time in melt spinning was on the order of 10ms.

As has been pointed out in this work, ZN35 has a mfr approximately equal to M32. When comparing M32 and ZN35 molecular weight characteristics, the weight average molecular weights differ only by 7% and the number average by 25%. Comparing the fiber spinning properties of these two resins illustrates the powerful
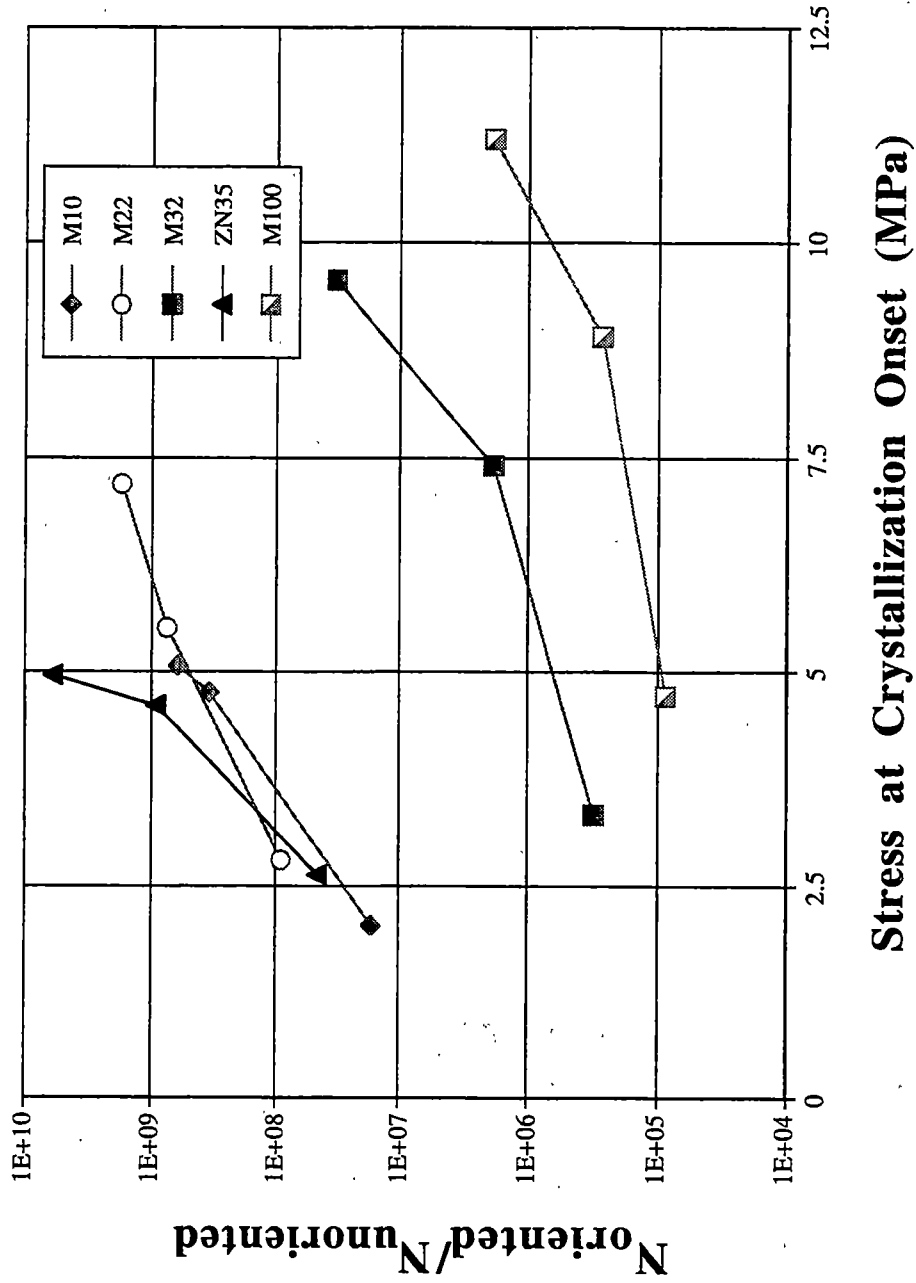
Figure 5.37 Ratio of oriented nucleation density to unoriented nucleation density versus stress at crystallization onset.

411

effects of MWD on the various fiber properties, as these resins produced fibers with very different properties.

One factor that affects fiber formation not explicitly addressed thus far in this study is the effect of crystallization kinetics. Crystallization kinetics can be separated into nucleation and growth rate effects. There is no reason *a priory* to think the lamellae growth rate changes in fiber formation, after all, the growth rate is determined by the crystallization temperature. The crystallization temperature of the fibers were quite similar to the nonisothermally crystallized films for most of the fiber samples. Within the range of temperatures in the nonisothermal film studies, the linear growth rates were determined by molecular weight. Nucleation effects in the spinline have already been discussed above. As the data showed in Figure 5.36, the nucleation density has changed by at least five orders of magnitude in the spinline over the quiescent values. The changes in nucleation density are consistent with increasing molecular weight increasing the nucleation density. The present results of on-line and quiescent crystallization kinetics suggest the influence, at least with the present set of homopolymers, of the quiescent crystallization kinetics is not significant. Meaning the effects of defect type and distribution do not appear to appreciably influence these resins in the fiber spinning process. However, this is not to say they are never important in fiber spinning. At very low spinning speeds, where the stress levels are very low in the spinline, the effects of quiescent kinetics are likely more significant. Additionally, if iPP were copolymerized, as was done in an earlier study[158] (with ethylene), the effects of the quiescent kinetics may also influence structure development in the spinline. A careful review of the iPP fiber spinning paper with some PP-PE copolymers by the present author indicates the

412

differences found between the homopolymer and copolymer can be explained by differences in molecular weight and MWD, as easily as the differences in copolymer content as the paper's authors explained for the observed fiber property differences. Clearly, this topic needs to be studied further to fully understand the effects of quiescent crystallization kinetics in the running spinline.

The data shown in Figure 5.38 shows the melting temperature of each fiber as a function of spinning speed. As the spinning speed is increased, the melting temperature increases. M32 and M100 show a much higher sensitivity to melting temperature as a function of spinning speed in the range of spinning speeds investigated. When the data in Figure 5.36 is compared with the lamellae thickness data for each resin in Figure 5.15, the observation is made that M32 and M100 at higher spinning speeds have similar melting temperatures to M10 and M22. This is spite of the fact that M10 and M22 have thicker lamellae. This indicates that the level of molecular orientation has an effect on the observed melting temperature of these fibers.

The effect of molecular orientation of fibers on a thermal spunbonding process will be investigated in Chapter 6. The results in Figure 5.38 suggest that molecular orientation can effect the thermal behavior of the present set of fibers, which is itself important.

5.6 Summary of Results and Conclusions

The results of the fiber spinning study show that the molecular weight and molecular weight distribution of iPP resins have a significant influence on the fiber spinning properties of the resins considered in this work.
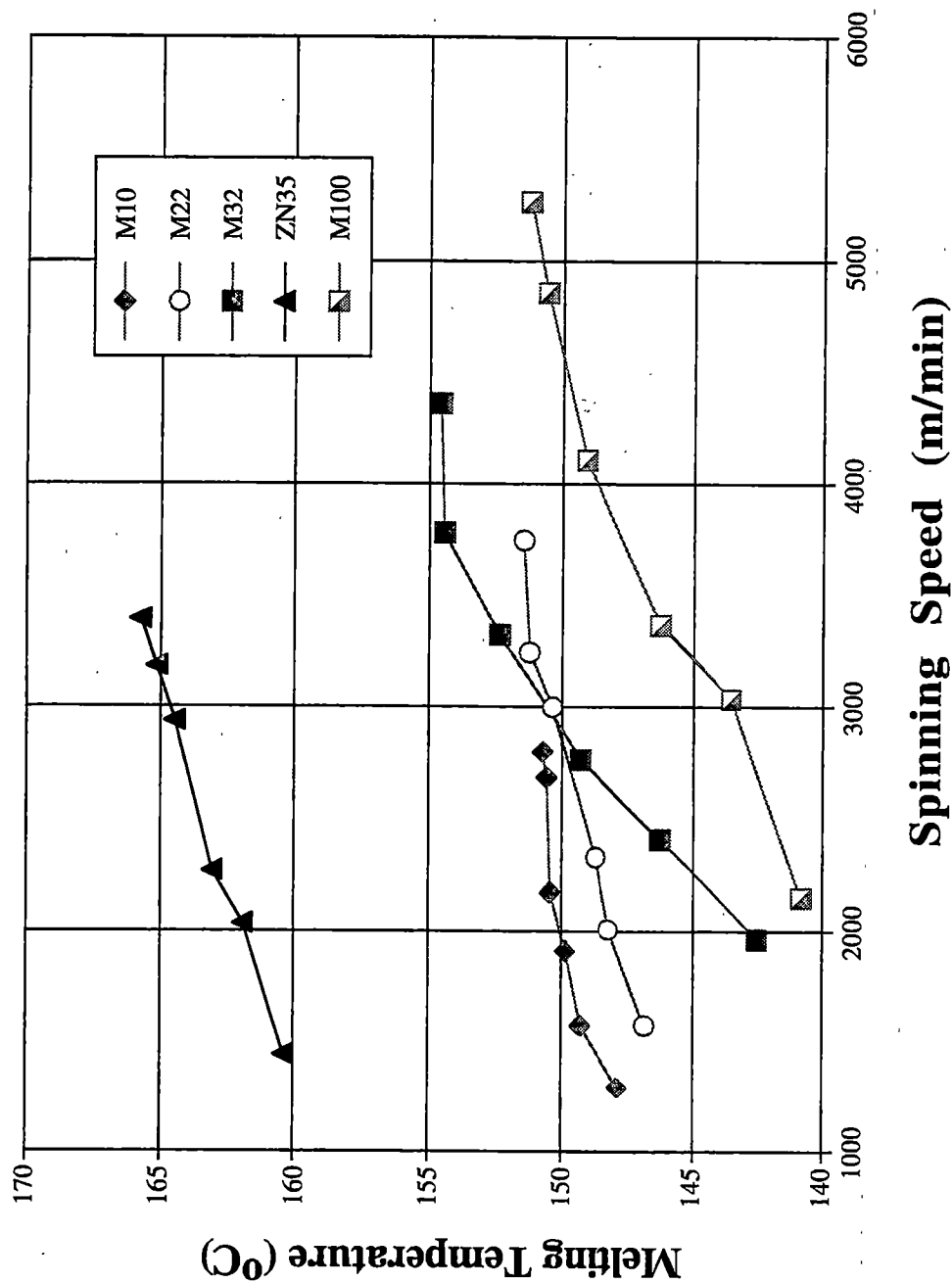
Figure 5.38 Fiber melting temperature versus spinning speed.

On-line studies using diameter and birefringence measurements showed that as the molecular weight increases, crystallization occurs closer to the spinneret at higher crystallization temperatures; the fibers have a larger diameter and crystallize under a lower stress at the point of crystallization onset. As the draw down pressure is increased, or as the spinning speed increases, crystallization occurs closer to the spinneret, the onset diameter decreases and the stress at crystallization onset increases.

Density measurements showed that as the spinning speed and molecular weight increased, the as-spun filament density increased. Slight variations in this trend were observed for ZN35 and M45. These variations were explained by the higher MWD found for these resins. Fiber density increases as a function of spinning speed and molecular weight due to crystallization occurring at higher temperatures, which allows more time for the fiber to crystallize before the molecular mobility becomes too low.

The as-spun filament birefringence values show that as spinning speed increases, the birefringence increases. Further, as the molecular weight decreases, the final filament birefringence increases. The contributions of birefringence from the crystalline and noncrystalline domains were separated by determining the crystalline orientation function using WAXD and using the total observed birefringence. The results showed that as the MW decreased, the noncrystalline orientation function increased and crystalline orientation function decreased at a given spinning speed. The orientation functions both generally increased as the spinning speed increased, with the exception of M10 and ZN35. The tensile strength showed a similar trend; as MW decreases, the tensile strength increased. A very strong correlation was found between the noncrystalline orientation function, birefringence and the tensile strength. Tensile strength is strongly dependent on

415

the number of tie molecules connecting the various crystallites together. The tensile strength is also somewhat dependent on the crystallinity, in that the number and size of the crystals will also influence the tensile strength since the crystallites act as an anchoring point for the tie molecules. If the population of crystallites is small or they are very thin, the tie molecules may easily pull out of the crystal.

The tensile modulus is a function of both crystallinity and molecular orientation. The tensile modulus was observed to be determined primarily by the spinning speed at which the fibers were spun. It was observed that as MW decreased, the tensile moduli of the filaments were generally higher than for the higher MW, more crystalline resins, a result of higher overall molecular orientation. This illustrates the importance of both crystallinity and overall molecular orientation on tensile modulus.

Elongation-to-break data was shown to be the inverse of the tensile strength data. This again is attributed to the number of tie molecules. As the number and orientation of the tie molecules increases, the elongation-to-break decreases since less extension and drawing is allowed before rupture of the molecules and specimen failure.

Estimates of the bulk nucleation densities were carried out using the on-line birefringence profiles. The results showed that the nucleation density ratio under oriented and quiescent conditions increased more significantly as the molecular weight increased, where the stress was lower at crystallization onset. The higher MW resins apparently need a smaller level of stress to initiate crystallization in the running spinline. Lower MW resins require a higher onset stress to compensate for the lower entanglement density to initiate crystallization, i.e. more work must be done to orient the melt to initiate

crystallization as the MW decreases. Therefore, the stress needed to initiate crystallization varies from resin to resin and depends on the MW and MWD.

Chapter 6

Results and Discussion

on the Influence of Fiber Properties

on the Thermal Spunbonding Process

6.0 Introduction

The results of thermal spunbonding work using M22, M32 and ZN35 will be presented and discussed in this chapter. Each material was used to melt spin fibers that were then thermally bonded together using a point bonding calender. The extrusion temperature was kept constant for all studies. The mass-throughput, basis weight, primary and cooling air speeds were all changed to produce fibers with differing properties. Additionally, a given set of fibers were bonded over a range of bonding temperatures to optimize the fabric/fiber strength relationship.

This work is separated into two sections due to the manner in which the research was conducted. The first part will present initial studies conducted using M32 and ZN35 in which the bonding temperature was kept constant. The primary and cooling air speed were changed to produce fibers with different diameters and birefringence values. Two basis weight fabrics were produced, 25 and $40g/m^2$. The mass-through-putt was also changed from 0.2 to 0.3 and 0.4g/hole-min. The fiber properties (diameter and birefringence) are then compared as a function of primary and cooling air speeds, as well as basis weight and mass-through-putt. The fiber diameter and birefringence were then plotted with fabric strength to determine if a correlation exists. This section concludes

418

with scanning electron micrographs detailing the structure of thermal bond points before and after deformation.

The second part of the thermal spunbonding studies was more focused on producing fabrics with the best mechanical properties. This study was carried out using M22, M32 and ZN35 spun under very high and low primary and cooling air speeds to produce fibers with the highest and lowest mechanical properties. The fibers were thoroughly characterized to determine their density, birefringence, crystalline and noncrystalline orientation functions, diameters and uniaxial mechanical properties. These fibers were thermally bonded together over a range of bonding temperatures to produce bonding curves. The optimum bonding temperature was taken to be the point in which the fabric strength was greatest. The fiber properties were then plotted with fabric mechanical properties to determine if any correlation exists.

6.1   Results and Discussion of Initial Studies

The initial studies were carried out to learn about the importance of fiber properties on the thermal point bonding process, without optimizing he bonding temperature. The effective spinning speed for each polymer was changed by adjusting the mass-throughput, primary air suction fan speed (PAS) and cooling air fan speed (CAS). The bonding temperature was kept constant at 140°C.

The data in Figure 6.1 show the average fiber diameter of fibers spun at the indicated mtp using a constant CAS of 2000rpm. Resin M32 and ZN35 were used in this part of the research. The nomenclature in the box indicates the resin identification, the mtp and the basis weight. For instance, M32q2bw25, means the resin is M32 at a mass

Figure 6.1 Off-line fiber diameter versus primary air speed for a 25g/m² basis weight fabric using a cooling air speed of 2000rpm and bonding temperature of 140°C.
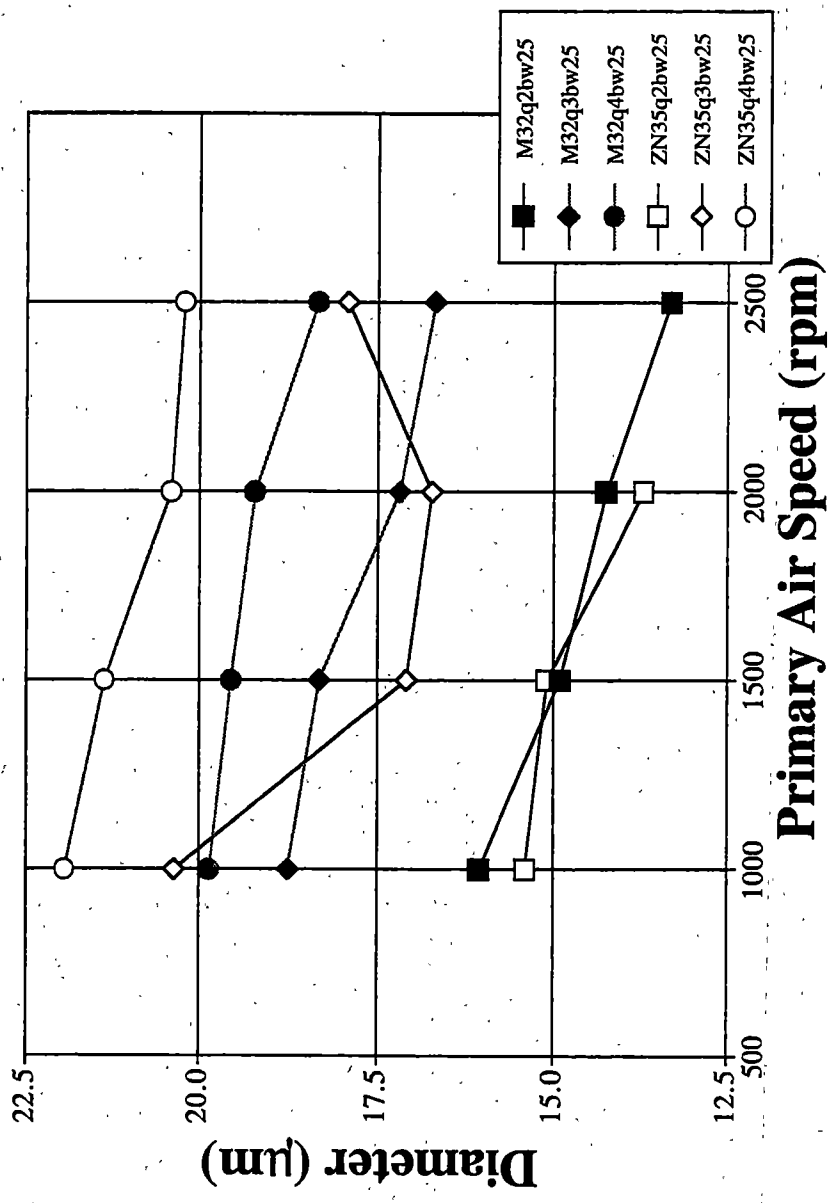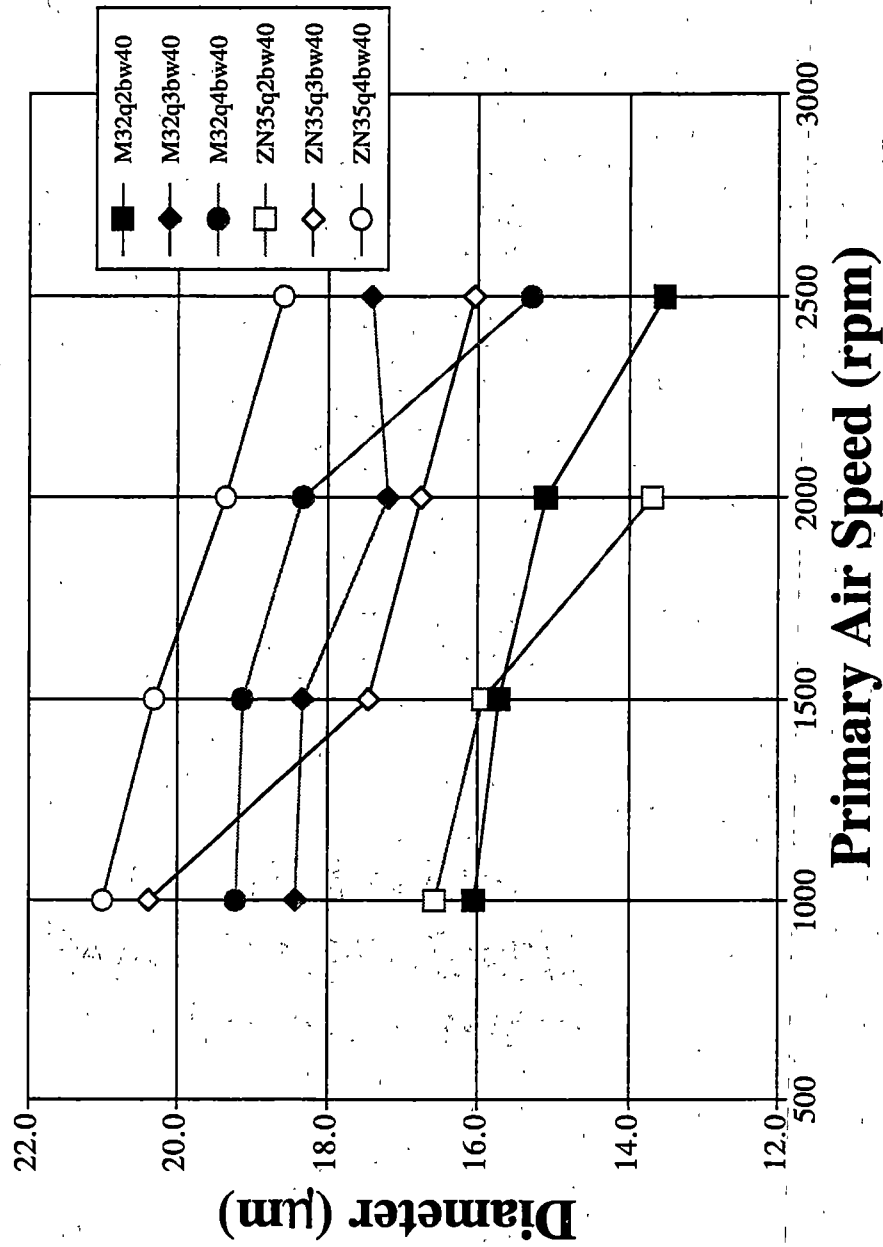
Figure 6.2 Off-line fiber diameter versus primary air speed for a 40g/m² basis weight fabric using a cooling air speed of 2000rpm and bonding temperature of 140°C.

through-put of 0.2g/min-hole (the mtps are 0.2, 0.3 and 0.4g/min-hole) and the basis weight is 25g/m^2. The only other basis weight tested was 40g/m^2. The data show that as the PAS is increased, the fiber diameter decreases for each resin at all mtp. The fiber diameters are similar for each material at 0.2 and 0.3g/min-hole mtps. At the highest mtp, 0.4g/min-hole, M32 produced finer filaments under all spinning conditions. These results were explained in Chapter 5 and results from the more narrow MWD of M32. The more narrow MWD delays crystallization in the spinline which allows the fiber to draw down to a smaller filament before crystallizing. Figure 6.2 shows the same materials processed under the same conditions except the basis weight of the fabric has been increased to 40g/m^2. This means that the belt speed has decreased in order to produce a higher weight fabric using the same mtp. The fiber diameters are very similar to the 25g/m^2 fabrics.

Figure 6.3 and 6.4 show the birefringence values of the fibers before bonding under the various processing conditions. The birefringence values are for the same fibers used in diameter measurements. The data show that the birefringence values for M32 are at least equal to or higher than the ZN35 resin under similar processing conditions. These differences also appeared in the small scale spinning behavior (see Chapter 5) and were attributed to the more narrow MWD of the M32 resin delaying crystallization which produces a more oriented noncrystalline region. Notice that the heavier basis weight fabric had similar birefringence values (Figure 6.4). The combination of the diameter and birefringence values for fibers differing only in basis weight, allows for fibers to be collected only once for each processing condition, i.e. fibers will not have to be collected for a basis weight change from 25 to 40g/m^2.

Figure 6.3 Off-line fiber birefringence versus primary air speed for a 25g/m² basis weight fabric using a cooling air speed of 2000rpm and bonding temperature of 140°C.

423

Figure 6.4 Off-line fiber birefringence versus primary air speed for a 40g/m² basis weight fabric using a cooling air speed of 2000rpm and bonding temperature of 140°C.

The data in Figure 6.5 and 6.6 show the maximum tensile load of nonwoven fabrics of basis weight $25g/m^2$ in the machine and transverse directions, respectively. The maximum load for each fabric generally increases as the PAS is increased. As the PAS is increased, the fibers are generally becoming more oriented, hence the birefringence increasing. As the birefringence increases, the tensile strength generally increases as was shown in Chapter 5 and other previous works. It is difficult to determine if any comparisons can be made between M32 and ZN35. Each fabric has not been bonded under optimum conditions. However, two trends exist. The first, as has already been pointed out, as the PAS increases the fabric maximum load increases. The second, the machine direction maximum load is higher than the transverse direction load. Figure 6.7 and 6.8 illustrate the maximum load in the machine and transverse direction for the heavier basis weight fabric. The same trends emerge for the heavier fabrics as for the lighter ones. A notable difference is that the maximum load for the heavier fabrics is higher than the lighter fabrics, a result of more total fibers present.

Figure 6.9 shows the machine direction (MD) divided by transverse direction (TD) maximum load ratio as a function of belt speed. The belt speed is determined from the mtp and basis weight of the fabric and comes on the run data collected for each fabric. There are two points of interest in this figure. The first is that the MD/TD ratio for most all points falls in between 1.25 and 2.00. The second is that there seems to be no increase in MD/TD ratio as the belt speed increases. One might expect the fibers to become more aligned in the MD due to mechanical alignment by the belt as belt speed increases. This does not seem to occur under these processing conditions.
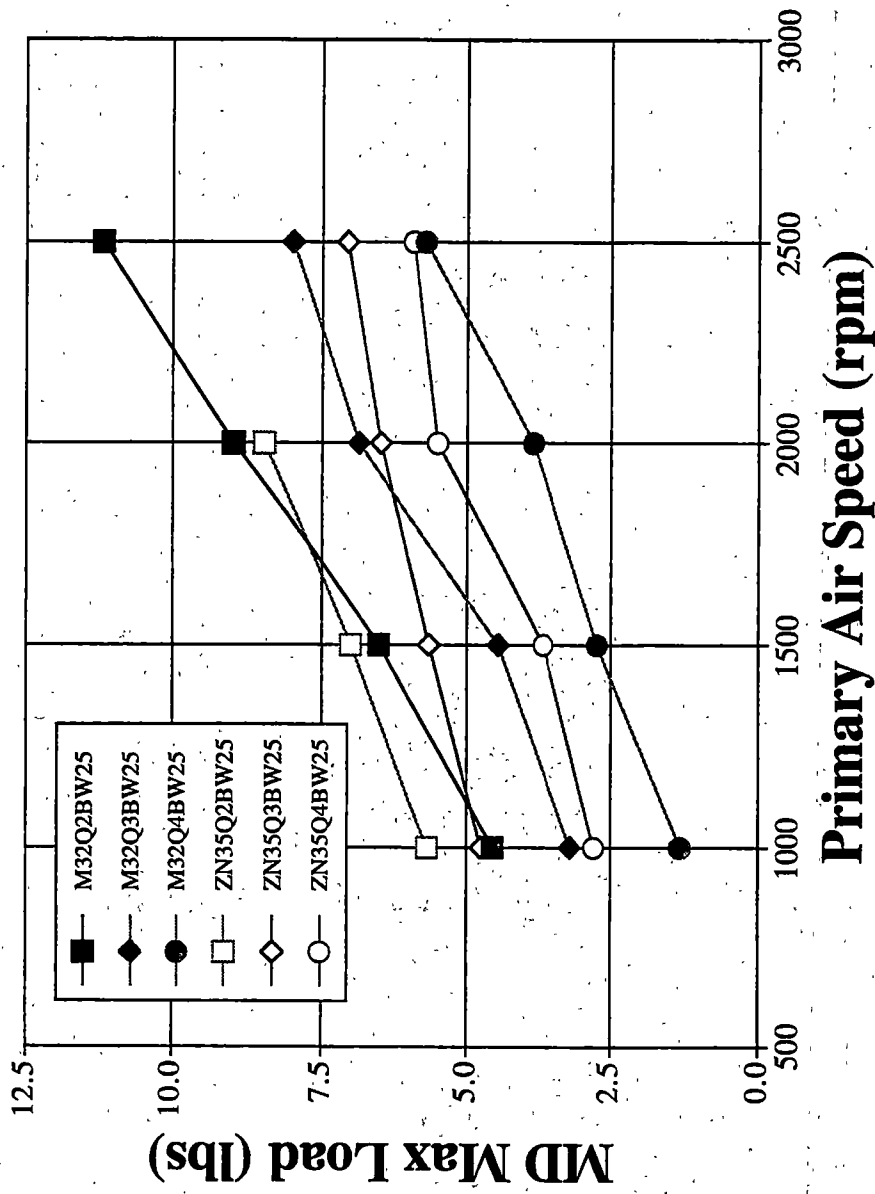
Figure 6.5 Machine direction maximum tensile load versus primary air speed for a 25g/m² basis weight fabric using a cooling air speed of 2000rpm and bonding temperature of 140°C.
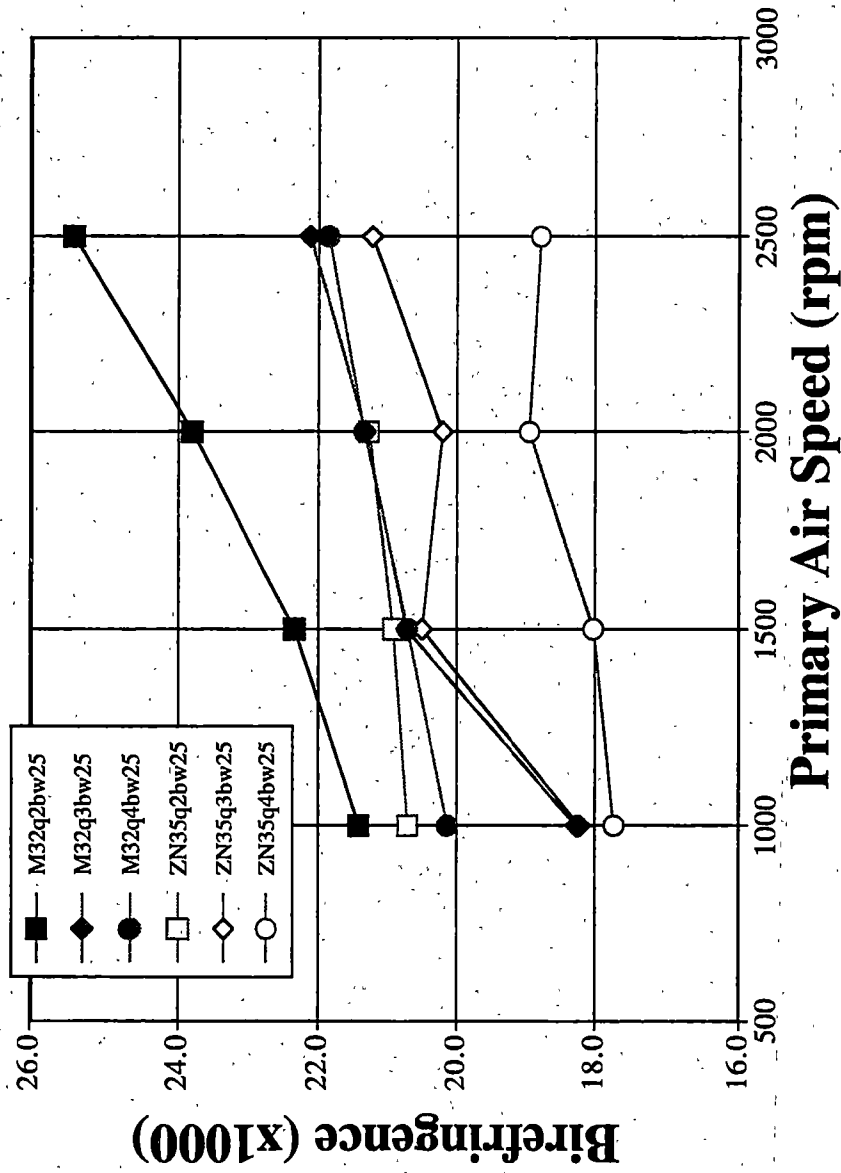
Figure 6.6 Transverse direction maximum tensile load versus primary air speed for a 25g/m² basis weight fabric using a cooling air speed of 2000rpm and bonding temperature of 140°C.

427
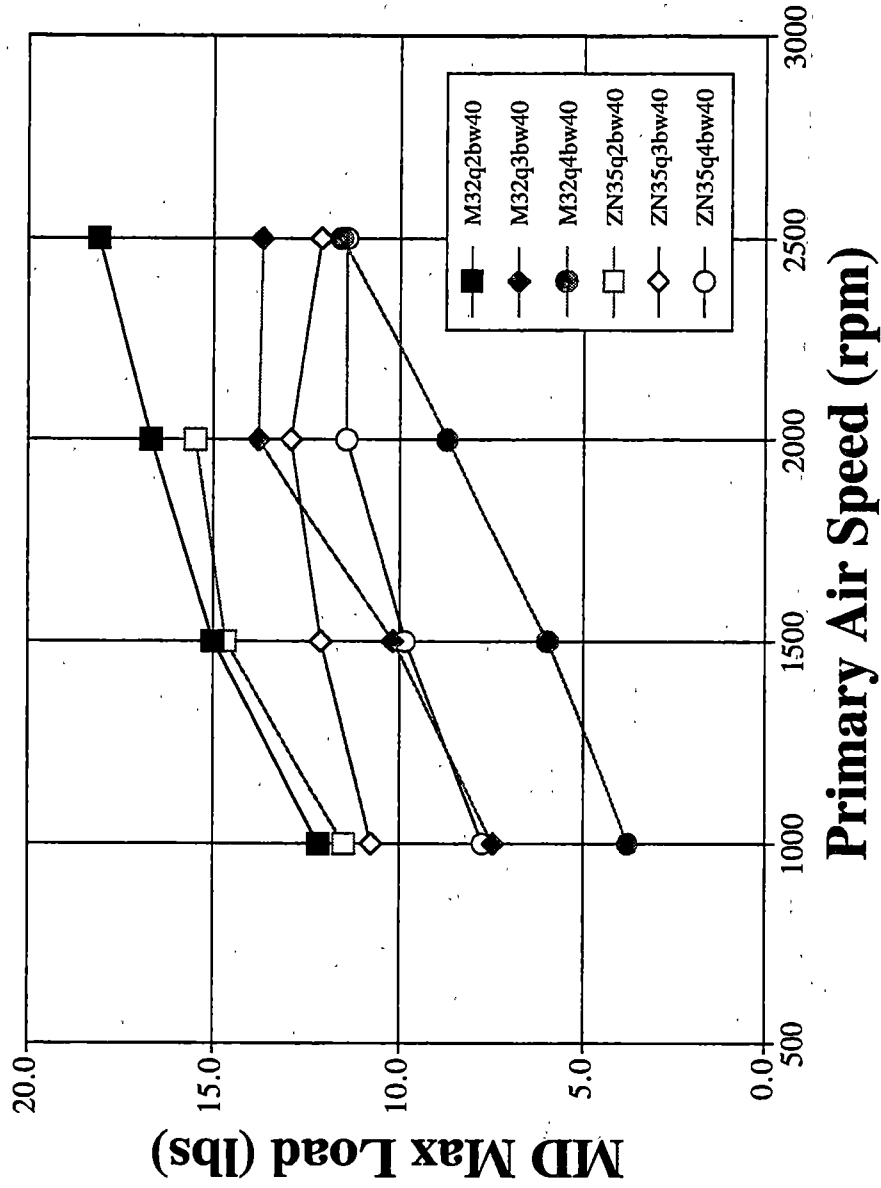
Figure 6.7 Machine direction maximum tensile load versus primary air speed for a 40g/m² basis weight fabric using a cooling air speed of 2000rpm and bonding temperature of 140°C.
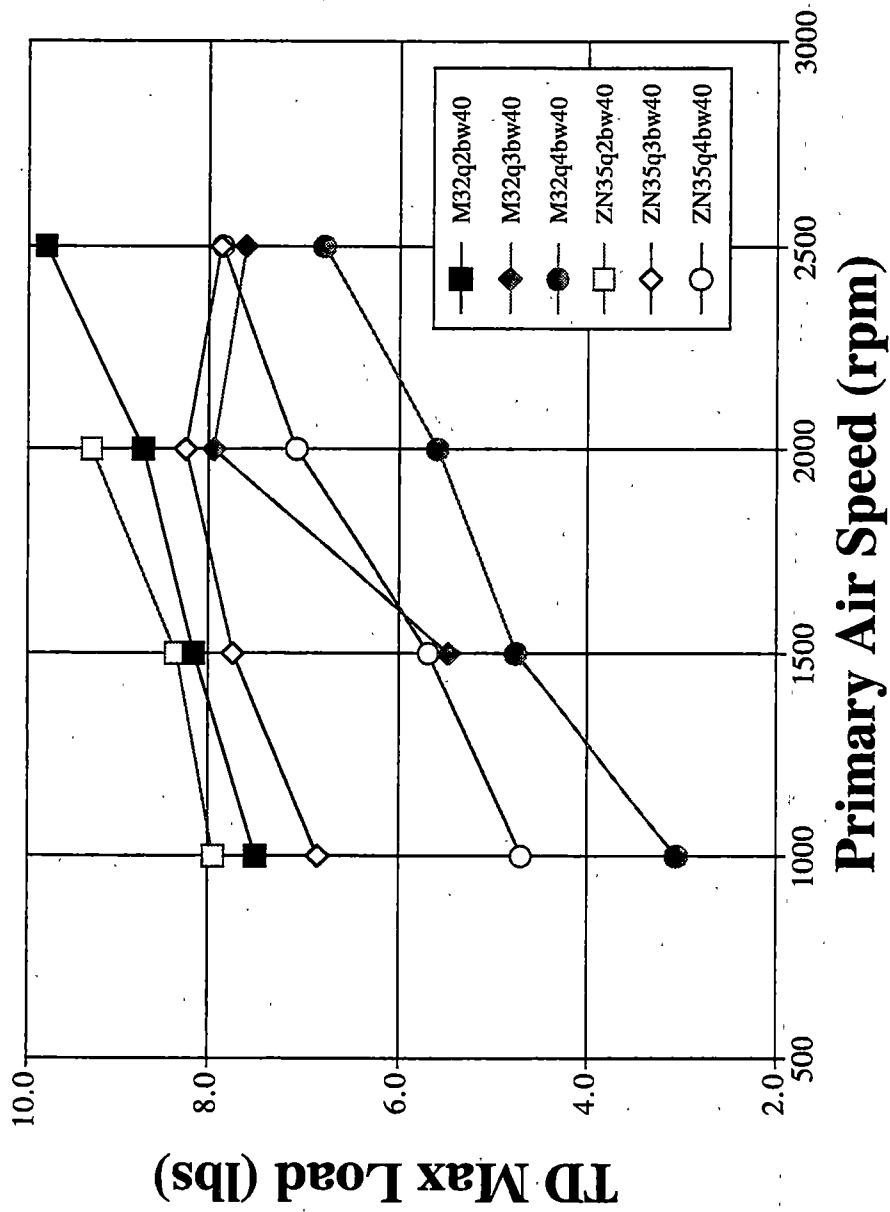
Figure 6.8 Transverse direction maximum tensile load versus primary air speed for a 40g/m² basis weight fabric using a cooling air speed of 2000rpm and bonding temperature of 140°C.
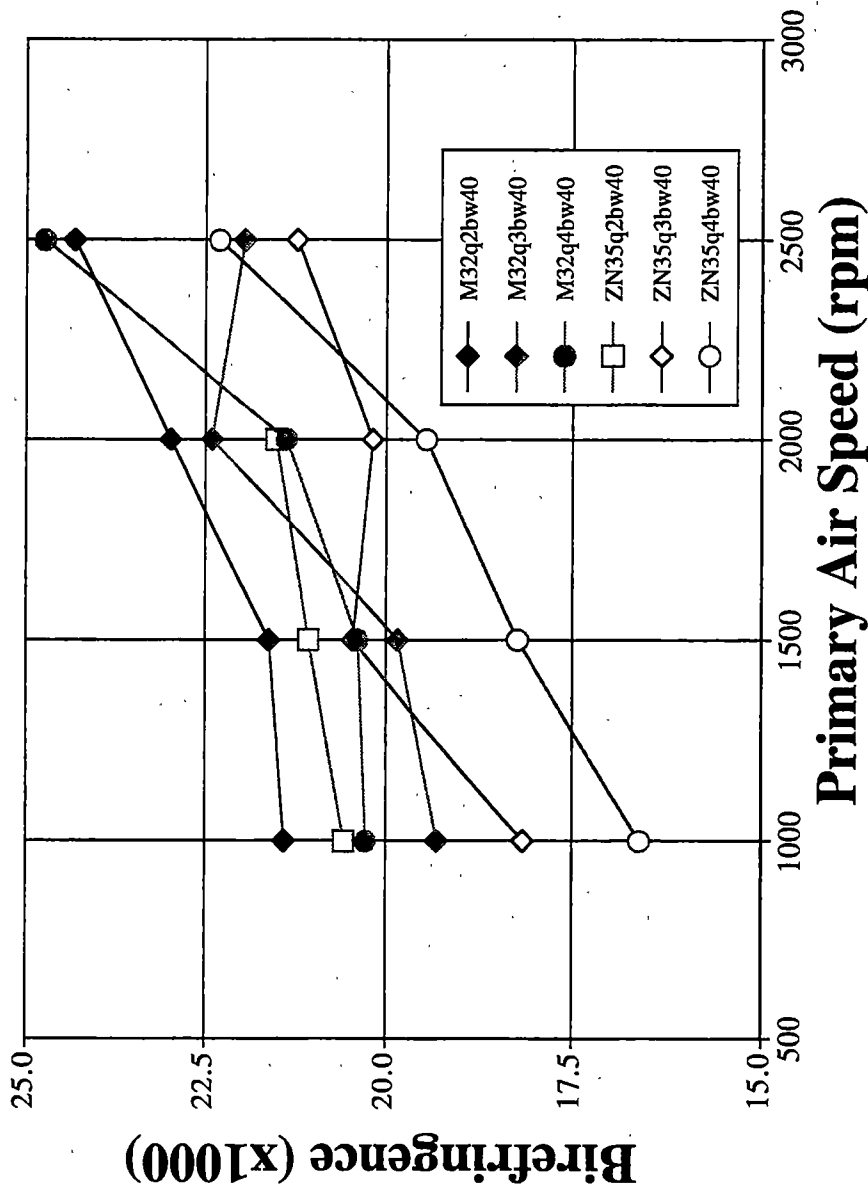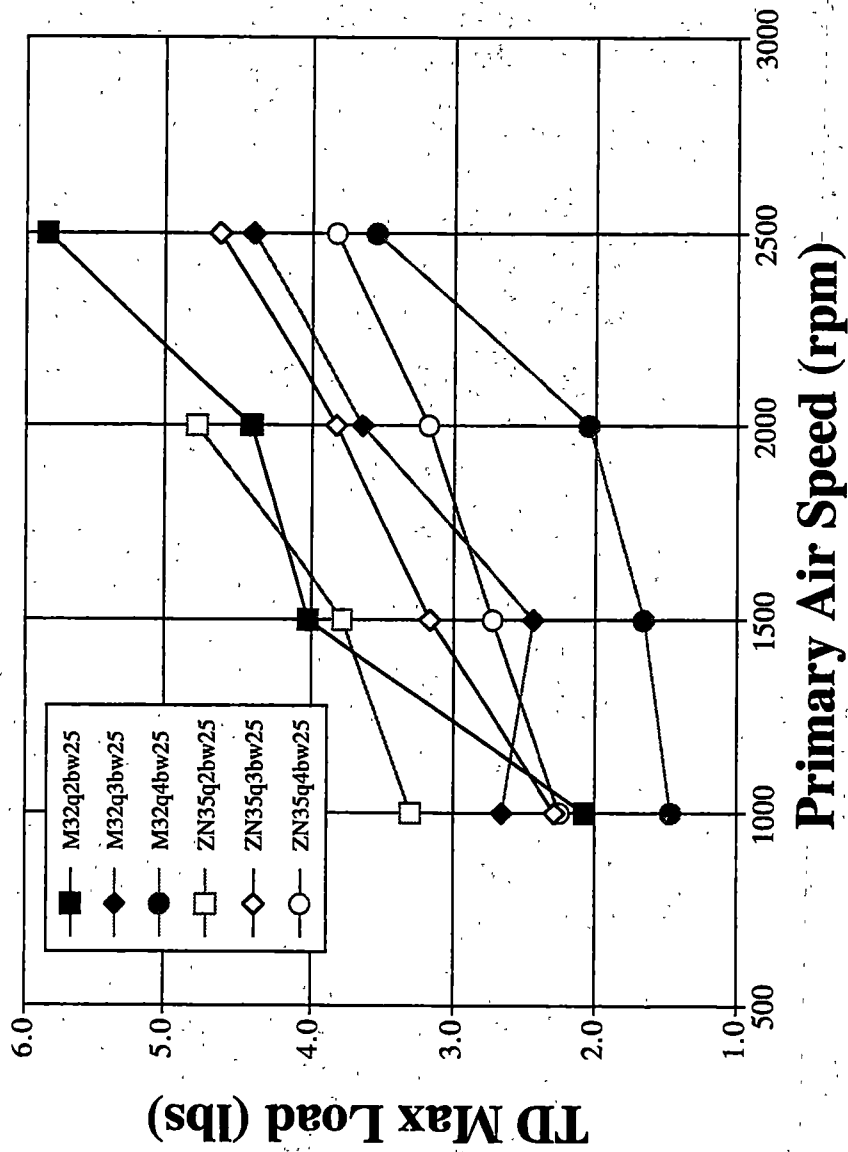
429
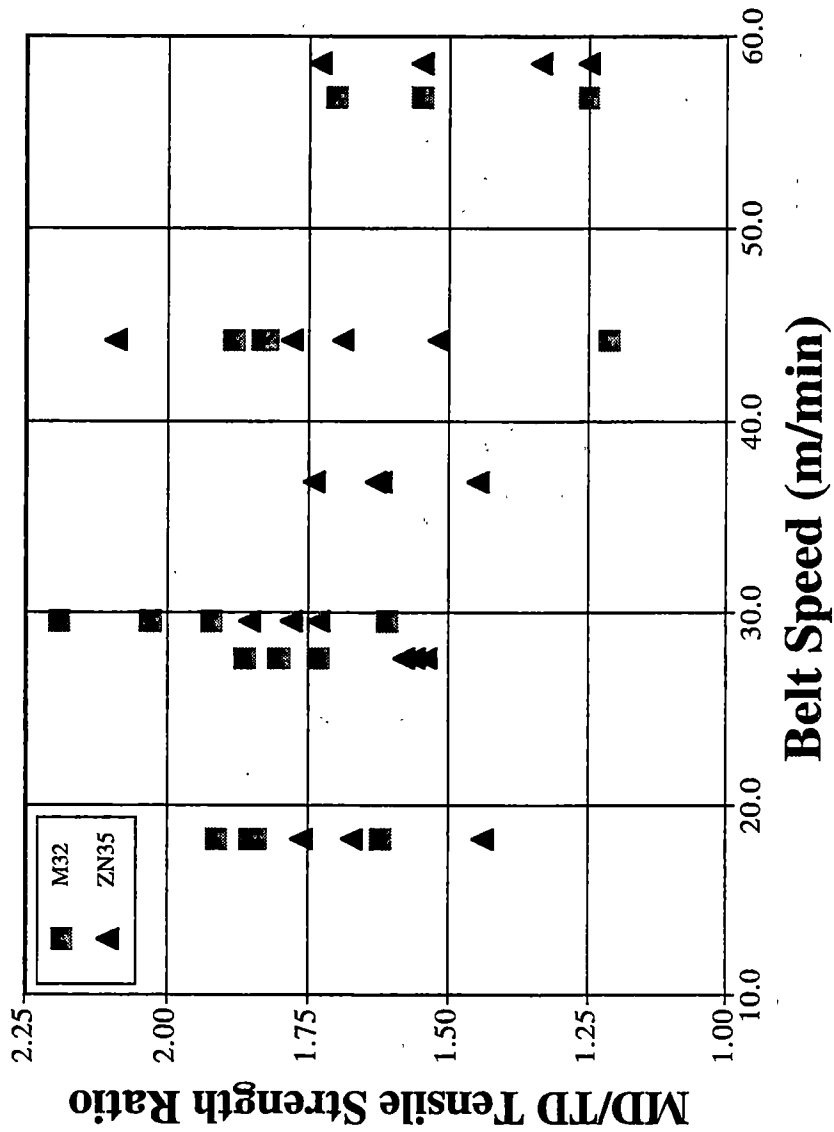
Figure 6.9 Machine direction/transverse maximum tensile load ratio versus belt speed for all fabrics using a cooling air speed of 2000rpm and bonding temperature of 140°C.

The data in Figure 6.10 and 6.11 show the maximum load of the fabrics as a function of diameter and birefringence, respectively. Figure 6.10 indicates that as the diameter decreases, the maximum load increases. There are two lines present, one for each basis weight, with the upper line for the $40g/m^2$ fabric. It might be expected that the load of the fabric would increase as the diameter decreases, since there will be more total fibers per unit area to carry the load. Figure 6.11 indicates that as the birefringence increases, the maximum load increases for each basis weight fabric. As the birefringence increases, overall molecular orientation increases and the tensile strength of the individual fibers increases. Therefore, the increase in fiber tensile strength seems to be increasing the fabric tensile strength.

The pictures in Figures 6.12, 6.13, 6.14 and 6.15 are bond points of the fabrics in this study photographed using SEM. In Figure 6.12, weak fabric bond points are shown. The weak bond point exhibits some melting outside the calender contact area. The weak bond also has a film-like appearance with very little of the underlying fiber morphlogy visible. Figure 6.13 shows the strong bond point has a well defined bond pattern with the underlying fiber structure still clearly visible. Figure 6.14 shows a bond point in a fabric that has fractured under uniaxial extension. The bond point remains intact while the fibers connected to it have fractured. This failure mechanism is typically observed in the fabrics with better mechanical properties. Figure 6.15 shows a fabric in which the bond point has failed. This sample is overbonded, which results in the bond becoming weakened. The film-like bond point begins to pull apart, resulting in fabric failure.
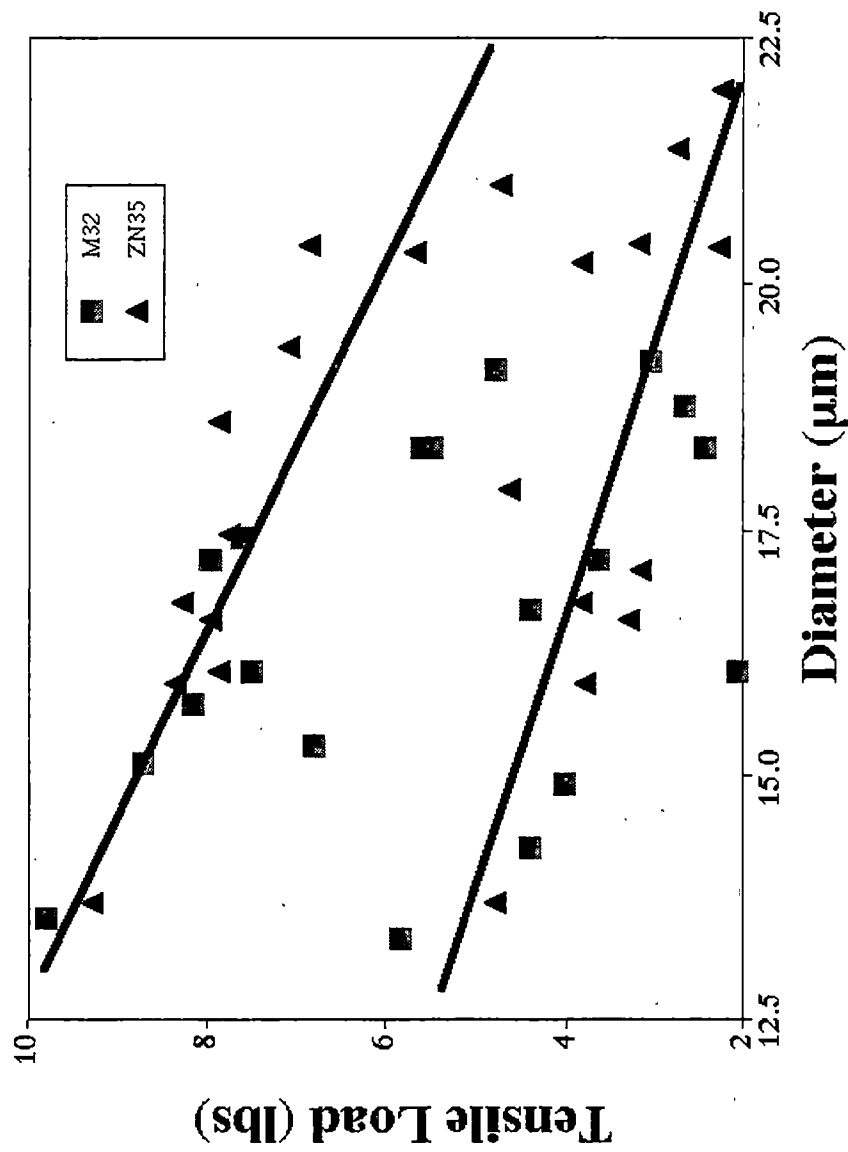
Figure 6.10 Fabric tensile load versus unbonded fiber diameter for all fabrics using a cooling air speed of 2000rpm and bonding temperature of 140°C. The upper solid line represents the 40g/m² samples for both resins, while the lower line represents the 25g/m² samples for both resins.
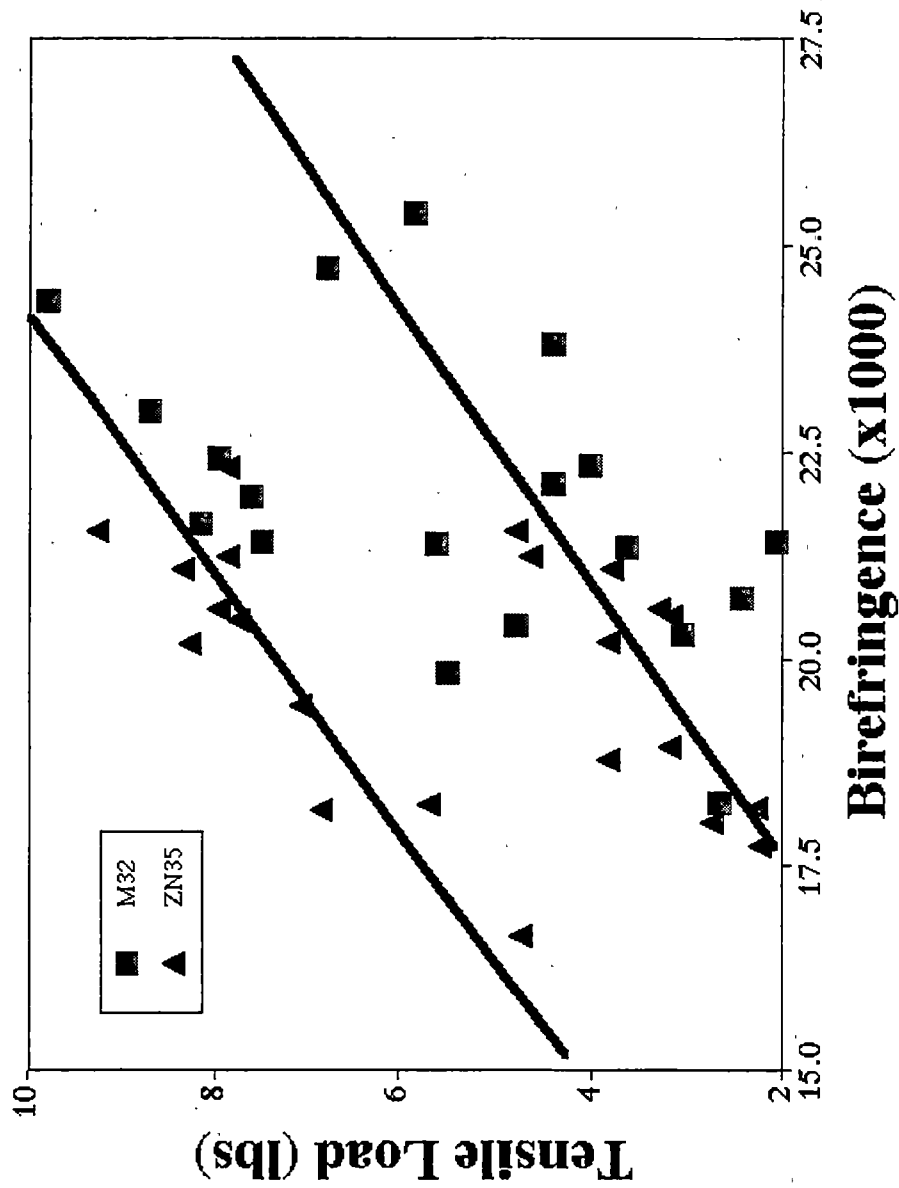
Figure 6.11 Fabric tensile load versus unbonded fiber birefringence for all fabrics using a cooling air speed of 2000rpm and bonding temperature of 140°C. The upper solid line represents the 40g/m² samples for both resins, while the lower line represents the 25g/m² samples for both resins.
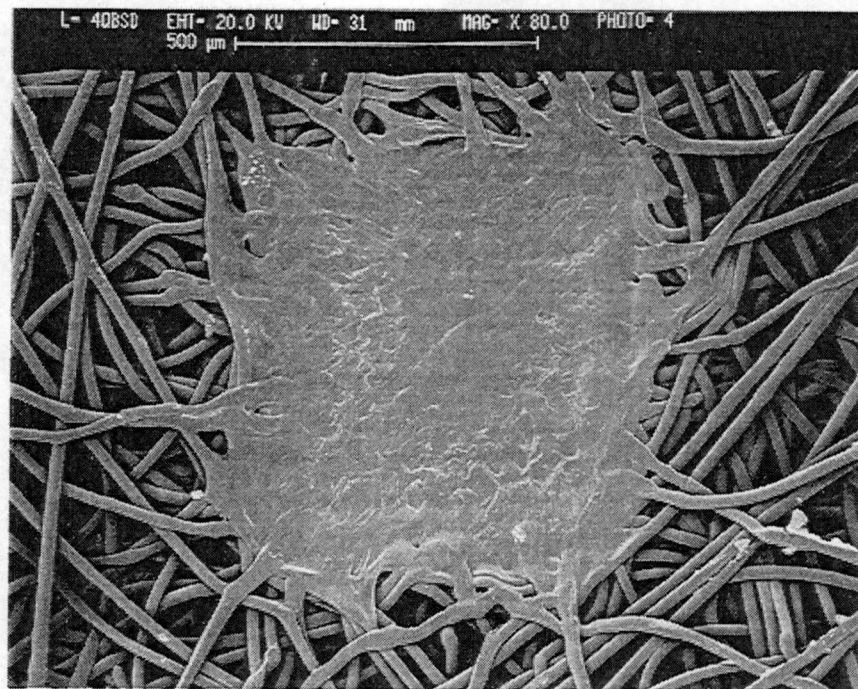
M32q4bw25   PAS=1000rpm   CAS=2000rpm
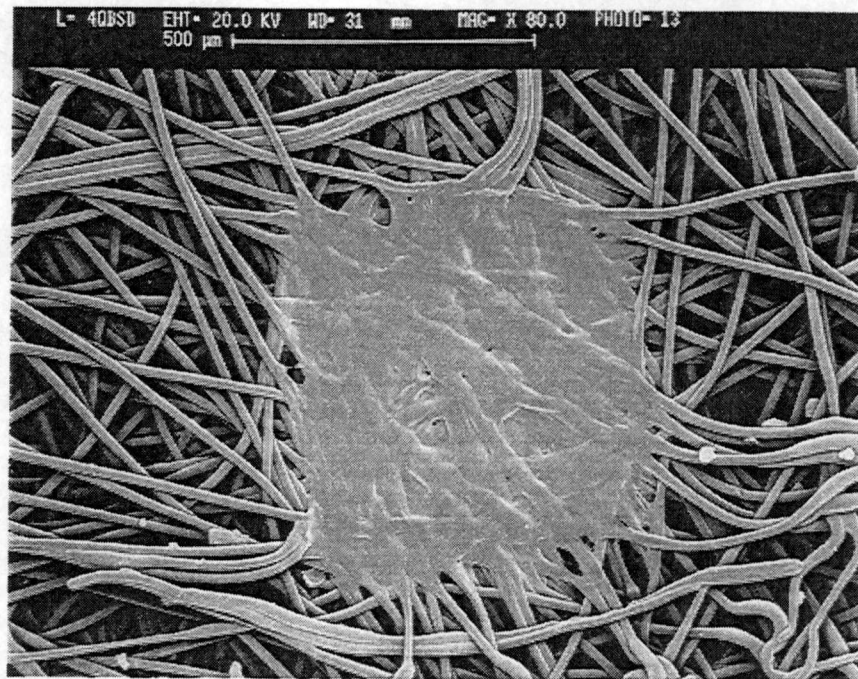
M32q2bw25 PAS=1000rpm   CAS=2000rpm

Figure 6.12 SEM photomicrographs of bond points before deformation of fabrics with poor mechanical properties. The processing conditions and resin type are indicated under each image.

434
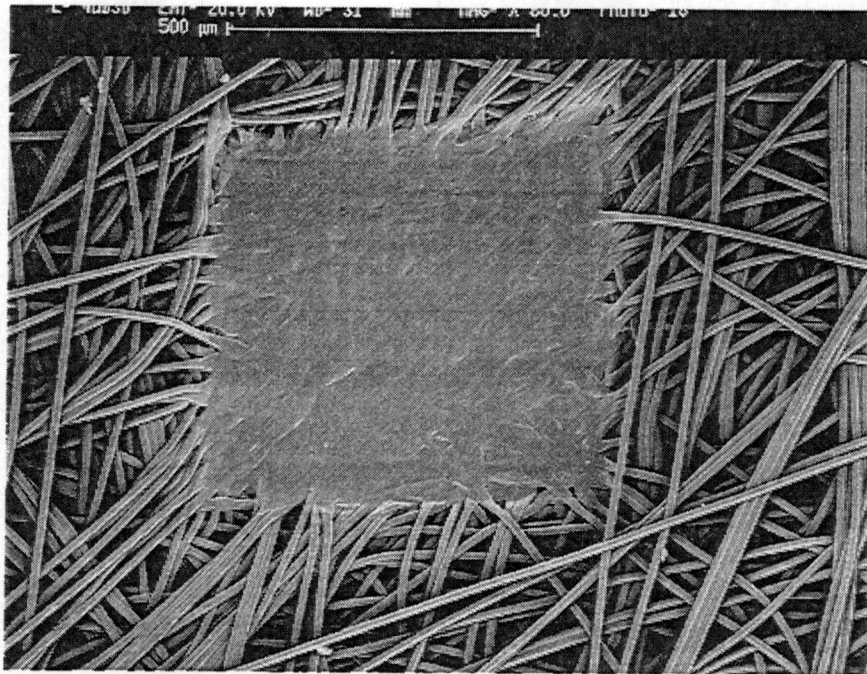
M32q2bw40 PAS=2500rpm   CAS=2000rpm
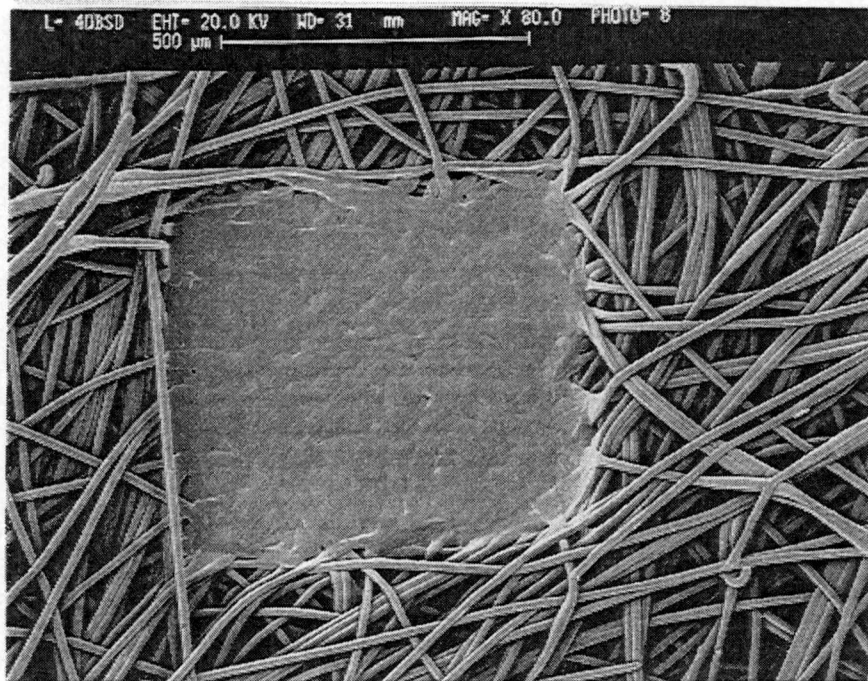
ZN35q2bw40 PAS=2000rpm   CAS=2000 rpm

Figure 6.13 SEM photomicrographs of bond points before deformation of fabrics with good mechanical properties. The processing conditions and resin type are indicated under each image.

435
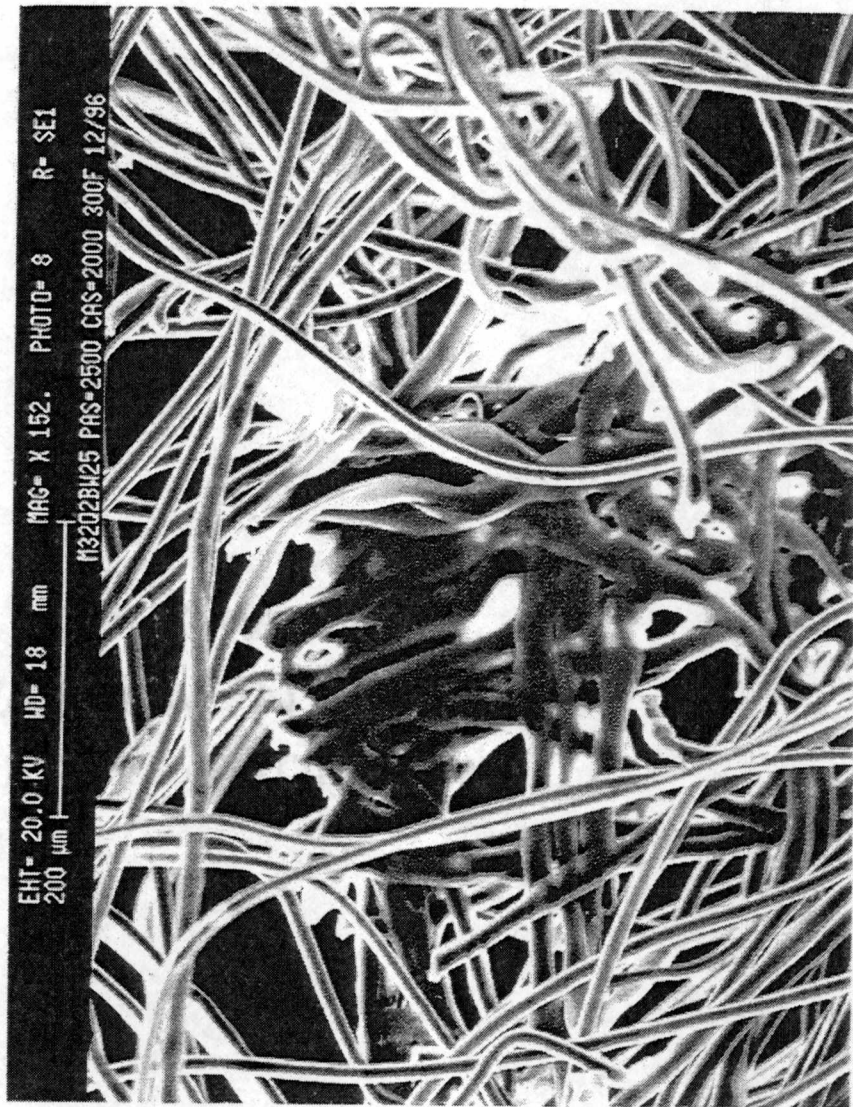
Figure 6.14 SEM photomicrograph of a strong bond point after uniaxial elongational failure for M32 spun using a mtp of 0.2g/min-hole, 25g/m² basis weight, PAS=2500 and CAS=2000.

Figure 6.15 SEM photomicrograph of a weak bond point after uniaxial elongational failure for M32 spun using a mtp of 0.2g/min-hole, 25g/m^2 basis weight, PAS=1000 and CAS=2000.

Conclusions from Initial Studies

1. Each set of fibers spun using a specific set of processing variables has a set of corresponding bonding conditions that need to be used in order to maximize the fiber property/fabric strength relationship.

2. Within the range studied, line speed (belt speed) has a very small effect on the MD/TD ratio.

3. Three types of failure were observed in the thermally bonded non-woven fabrics in this study:

   a. Underbonded-the bond points pull apart with the substituent fibers maintaining their integrity. The fabric fails in a ductile manner.

   b. Overbonded-the bond point is weakened due to the melting of the fibers into a film-like state. The fabric fails abruptly.

   c. Ideally bonded-the bond point maintains its integrity while the fibers entering the bond draw down and then fail by a cohesive mechanism. The fabric fails abruptly after appreciable initial elongation.

6.2 Results and Discussion of Ideally Bonded Fabrics

In this section, M22, M32 and ZN35 were melt spun into fibers to produce nonwoven fabrics. The resins were spun at very high and low CAS and PAS values using a mtp of 0.2 and 0.4g/min-hole. Fibers were collected before bonding and characterized. The as-spun fibers were characterized in the same manner as those in Chapter 5, for the small scale monofilament conditions. The as-spun fiber properties are given in Tables 6.1 and 6.2. The fibers were then thermally bonded over a range of

Table 6.1 Conditions and properties of as-spun nonwoven fibers spun under high fan speeds.

Resin	Conditions	Spinning Speed (m/min)	Diameter (µm)	Δn (x10³)	Density (g/cm³)	fc	fnc	Elongation-to-Break (%)	Tensile Strength (MPa)	Modulus (GPa)
M22	Q=0.4g/min-hole Pas=2500rpm Cas=3000rpm	2828	14.1	28.8	0.902	0.730	0.658	247	218	2.56
M22	Q=0.4g/min-hole Pas=2500rpm Cas=2000rpm	2450	15.3	26.8	0.888	0.669	0.530	260	196	2.48
M22	Q=0.2g/min-hole Pas=2500rpm Cas=2000rpm	2344	11.0	33.2	0.898	0.761	0.765	242	168	3.66
M32	Q=0.4g/min-hole Pas=2500rpm Cas=3000rpm	2883	14.1	29.4	0.891	0.683	0.617	220	238	2.20
M32	Q=0.4g/min-hole Pas=2500rpm Cas=2000rpm	1780	17.9	19.7	0.893	0.614	0.356	316	174	1.94
M32	Q=0.2g/min-hole Pas=2500rpm Cas=2000rpm	2741	10.2	29.6	0.893	0.745	0.611	222	230	2.82
ZN35	Q=0.4g/min-hole Pas=2500rpm Cas=3000rpm	2698	14.5	22.9	0.898	0.772	0.391	312	181	2.48
ZN35	Q=0.4g/min-hole Pas=2500rpm Cas=2000rpm	2030	16.8	21.2	0.889	0.729	0.353	323	172	3.03
ZN35	Q=0.2g/min-hole Pas=1700rpm Cas=1900rpm	2995	9.7	26.8	0.898	0.757	0.539	283	193	3.13

Table 6.2 Conditions and properties of as-spun nonwoven fibers spun under low fan speeds.

Resin	Conditions	Spinning Speed (m/min)	Diameter (μm)	Δn (x10³)	Density (g/cm³)	fc	fnc	Elongation-to-Break (%)	Tensile Strength (MPa)	Modulus (GPa)
M22	Q=0.4g/min-hole Pas=1000rpm Cas=1500rpm	979	24.3	16.3	0.881	0.409	0.330	387	120	2.48
M22	Q=0.2g/min-hole Pas=1000rpm Cas=1500rpm	1256	15.1	25.0	0.889	0.579	0.514	347	141	3.00
M32	Q=0.4g/min-hole Pas=1000rpm Cas=1500rpm	1066	23.2	16.8	0.889	0.384	0.344	403	101	2.54
M32	Q=0.2g/min-hole Pas=1000rpm Cas=1500rpm	1723	12.9	27.3	0.888	0.610	0.593	314	158	2.84
ZN35	Q=0.4g/min-hole Pas=1000rpm Cas=1500rpm	1309	20.9	17.3	0.891	0.631	0.259	328	158	2.62
ZN35	Q=0.2g/min-hole Pas=1000rpm Cas=1500rpm	1691	13.0	23.5	0.893	0.705	0.428	281	171	3.08

temperatures to optimize the fabric properties. The fabric properties were characterized for maximum tensile load and elongation-to-break in both the machine and transverse directions. Only the fabric properties in the TD direction are presented from here forward.

In order to understand the effects of overall molecular orientation on the bonding temperature and fabric properties, bonding curves were obtained using M22, M32 and ZN35 spun under different conditions. The resins were spun using two mass-throughputs (mtp) and three different applied fan speeds. The goal was to produce highly oriented fibers at the lowest and highest mtp. The highest mtp was also spun at a reduced cooling air speed (the speed indicated is the number of r.p.m. the fan is turning) to study this effect on fiber properties. A total of nine different fibers were made to produce a total of eighteen different non-woven fabrics. Each set of fibers were used to produce a 25 and $40g/m^2$ basis weight fabrics. The conditions under which fibers were produced, as well as the mechanical properties for each set of fibers are shown in Tables 6.1 and 6.2.

The results in Table 6.1 and 6.2 indicate that as the noncrystalline orientation function (f_{nc}) increases, birefringence (Δn) increases and the tensile strength increases. The results and findings for the nonwoven fibers are similar to the behavior observed for these resins in the small scale spinning line, as was discussed in Chapter 5. The densities of the various fibers are grouped together and have similar values. The elongation-to-break (ETB) generally decreases as the tensile strength increases. The spinning speed was calculated using the diameter, density and mtp using the continuity equation.

The results in Figure 6.16 show the fabric peak load in the transverse direction as a function of bonding temperature for a $25g/m^2$ basis weight fabric made using M22, in

Figure 6.16 Fabric tensile load versus calender surface bonding temperature for 25g/m² fabrics using resin M22.

the transverse direction (all directions hereafter are transverse). The data indicated that the lower mtp highest fan speed fibers produce the strongest web. The data also shows that reducing the cooling air speed (CAS) for the higher mtp as-spun fibers lowered the ideal bonding temperature by 5°C to 140°C, which was the ideal bonding temperature for the lower mtp fibers. The low fan speed (or low spinning speed) fibers have significantly lower fabric strengths and ideal bonding temperatures. The decrease in bonding temperature is attributed to the decrease in the noncrystalline orientation function and birefringence (these two properties are related). A more highly oriented noncrystalline phase will need a higher temperature to relax these regions and allow diffusion to occur during the bonding process, compared to a region with lower orientation in the noncrystalline phase. It is most likely that the molecules in this region must relax, then diffuse and entangle with other molecules of other fibers during bonding to allow a load to be shared by multiple fibers.

The data in Figure 6.17 show the same fibers spun using M22 into a 40g/m^2 basis weight fabric. The data indicate the same trend in strength as the 25g/m^2 basis weight samples. However, two differences are observed. The first; the strength of the fabric has increased significantly, an expected result since there are more fibers per unit area. Hence, there are more fibers in each bond point. The second; each set of fibers now has a different ideal bonding temperature. The lower mtp fibers are still bonded the best at 140°C. The high mtp, low CAS fibers are bonded best at 145°C and the highest mtp, highest CAS fibers are bonded best at 150°C. The added mass of fibers in a heavier basis weight fabric has increased the bonding temperature for the higher mtp fibers.
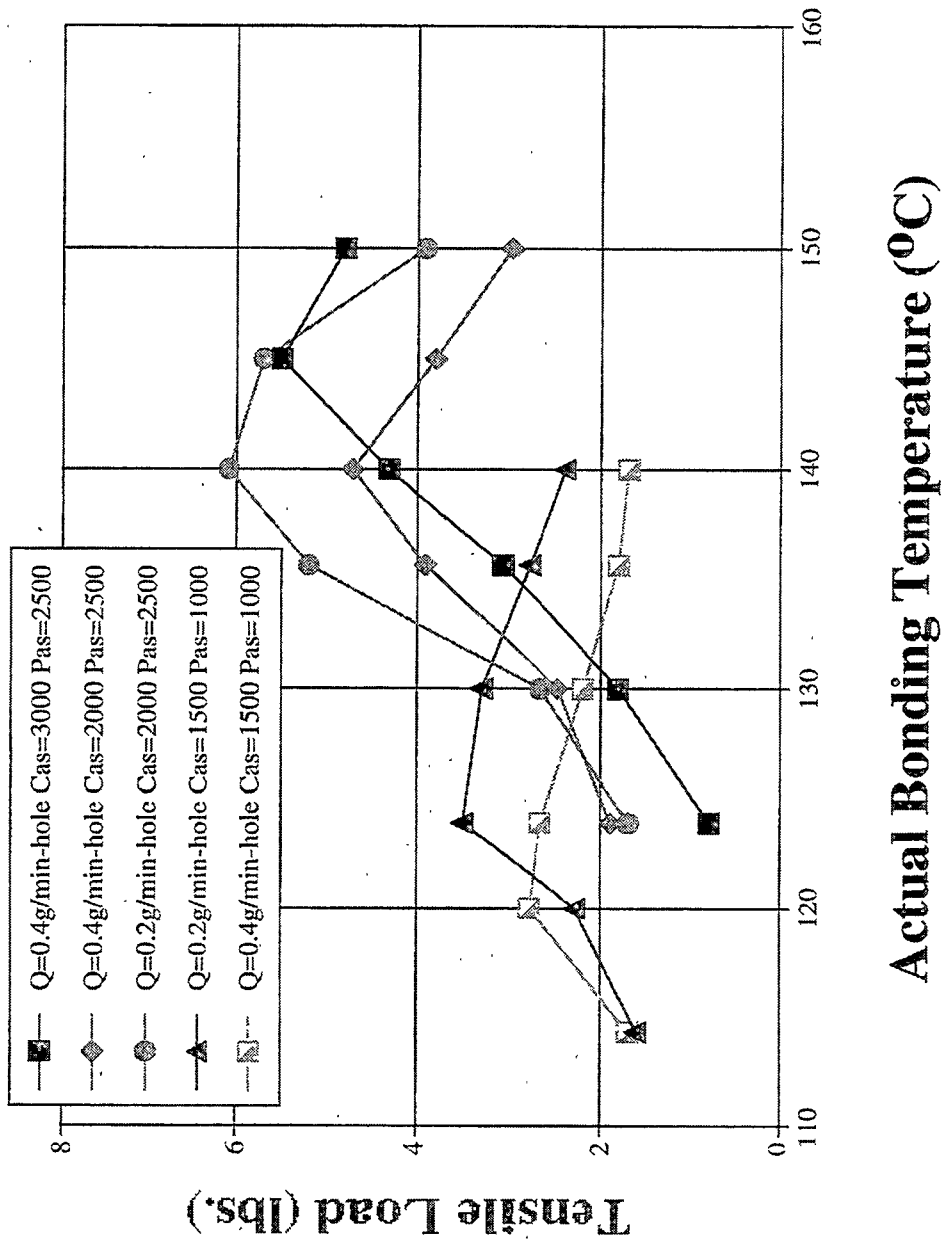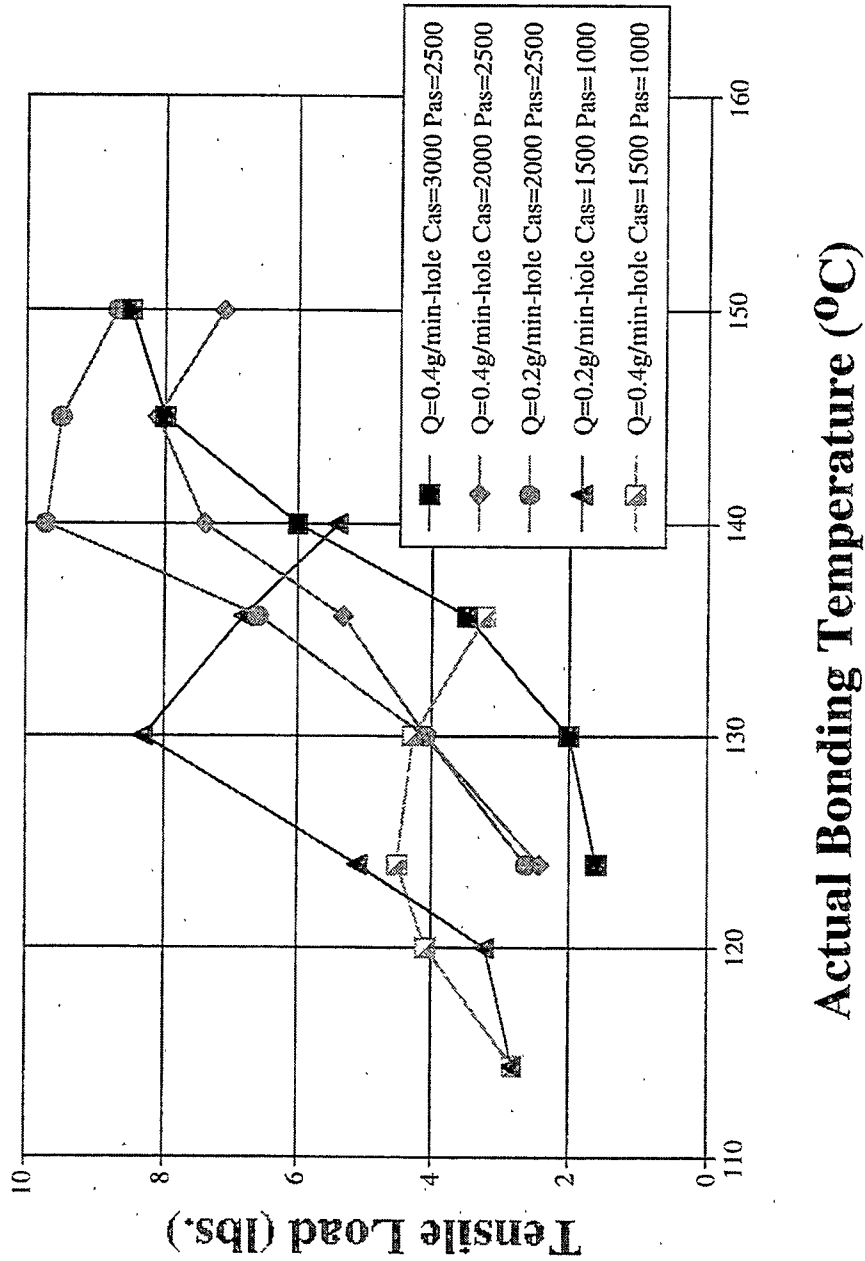
Figure 6.17 Fabric tensile load versus calender surface bonding temperature for 40g/m² fabrics using resin M22.

444

The reason for this increase in bonding temperature is likely due to the differences in line speed or time in the bonding zone and sample basis weight. When the basis weight is increased, the line speed decreases, which means one might expect the bonding temperature to either decrease or stay the same. However, there is a larger sample mass which requires more heat to bond the fibers together. At the higher mtp, the line speeds are much higher. When the fabric basis weight is increased at higher mtp, the line speed decreases, but is still much higher than a similar basis weight fabric at the lower mtp. In other words, there is a heat transfer problem at higher mtp, heavier basis weight fabrics. In order to ideally bond the fabrics, the temperature must be increased to ensure the proper amount of heat is present to bond the heavier basis weight fabrics. Therefore, when total contact time is changed, the amount of heat transferred. Depending on the direction of the change, the temperature of the calender must also be changed for that set of fibers to reestablish optimum bonding conditions.

The results in Figure 6.18 show the elongation-to-break of lower basis weight (BW) fabrics as a function of bonding temperature (T_b) for M22. The data is the peak ETB, meaning the elongation at the point of highest strength in the fabrics. When a fabric is ideally bonded (and overbonded) the peak ETB and failure ETB are the same. When the fabric is underbonded, there can exist large differences in peak and failure ETB. This is illustrated in Figure 6.19. These are simulated patterns of what actual load versus displacement plots would look like. Notice that the peak load and final ETB are the same for each curve. Using the final ETB for the two underbonded curves would give a misleading value of what the ETB would be for a sample. An overbonded fabric has a load versus displacement curve similar to the ideally bonded curve, with the
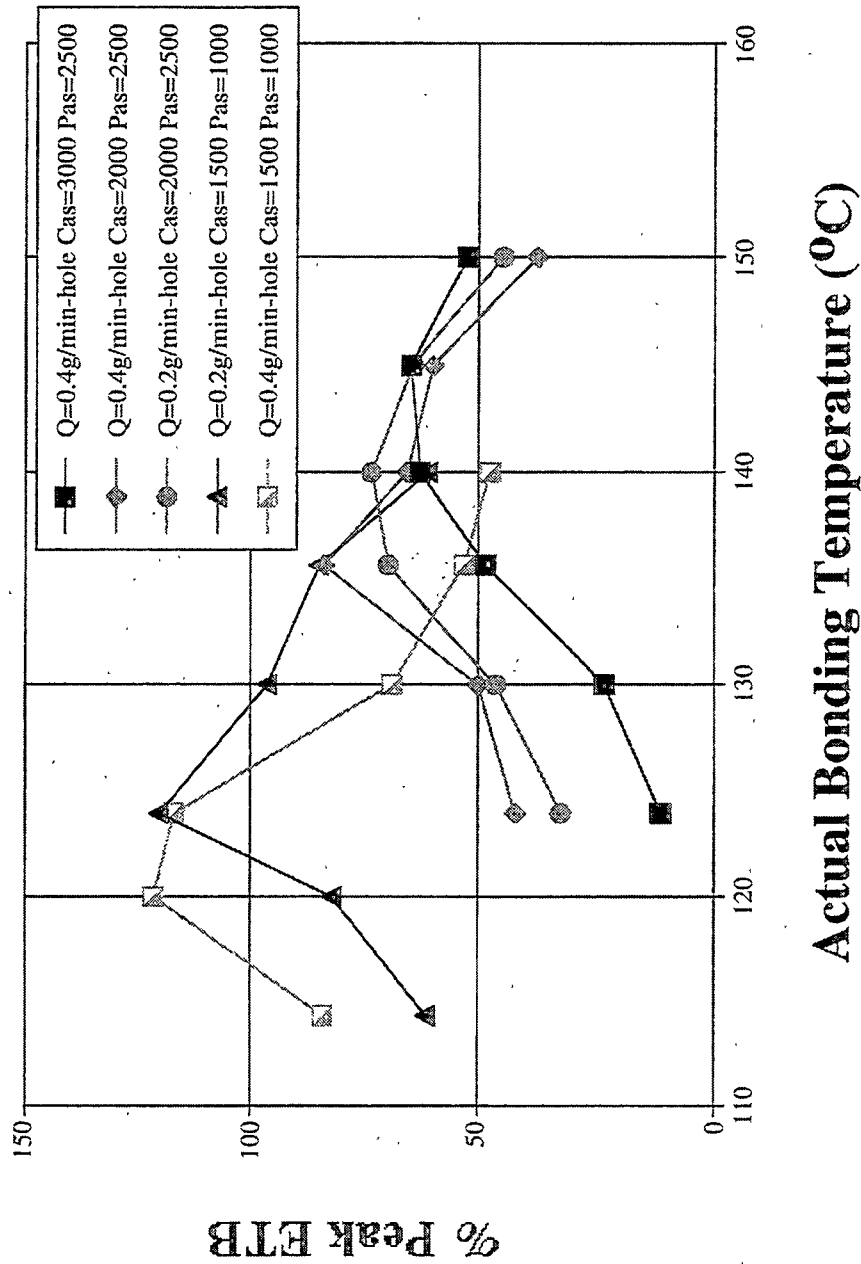
Figure 6.18 Fabric peak elongation-to-break versus calender surface bonding temperature for $25g/m^2$ fabrics using resin M22.

Figure 6.19 Simulated fabric elongation-to-break at different levels of bonding versus displacement.

Figure 6.20 Fabric peak elongation-to-break versus calender surface bonding temperature for 40g/m² fabrics using resin M22.

difference being the overbonded sample has a decreased ETB. The results indicate that each set of fibers has an ideal T_b to maximize the ETB. The higher mtp, lower CAS sample's ideal T_b has decreased by 4°C. These results indicated that the ideal strength T_b and ideal ETB T_b may not be at exactly the same temperature for all fiber/fabric/BW combinations. Additionally, the low spinning speed fibers produced higher ETB fabrics, a characteristic of their prebonded structure and properties, i.e. the higher ETB of the fibers. The higher mtp, lower CAS fibers have a lower f_{nc} and birefringence, compared to the higher mtp, higher CAS as-spun fibers, which appear to determine the fabric properties.

The results in Figures 6.21-6.28 are similar plots of data obtained using M32 and ZN35, as indicated in the figure. The results can be interpreted and explained using the explanations found for M22 above. The lone exception to the behavior occurs in Figure 6.25, ZN35 load versus bonding temperature for the low CAS and PAS high mtp fibers. This sample had a much higher maximum load than the other $25g/m^2$ fabrics. The heavier basis weight fabrics in Figure 6.26 did not exhibit a pronounced higher load capacity. The explanation for this behavior is not understood.

The data in Figure 6.29 shows the ideal bonding temperature as a function of prebonded fiber as-spun birefringence for all fabrics and resins. The ideal bonding temperature is where the maximum load is carried for each fabric, thus there exists one ideal bonding temperature for each mtp and basis weight combination. The groups are broken down into four categories, grouping the mtp and basis weights together. This grouping allows the line speed to be kept constant for each processing condition of the fibers/fabrics. While there exists some scatter in the data, there is a general increase in

449
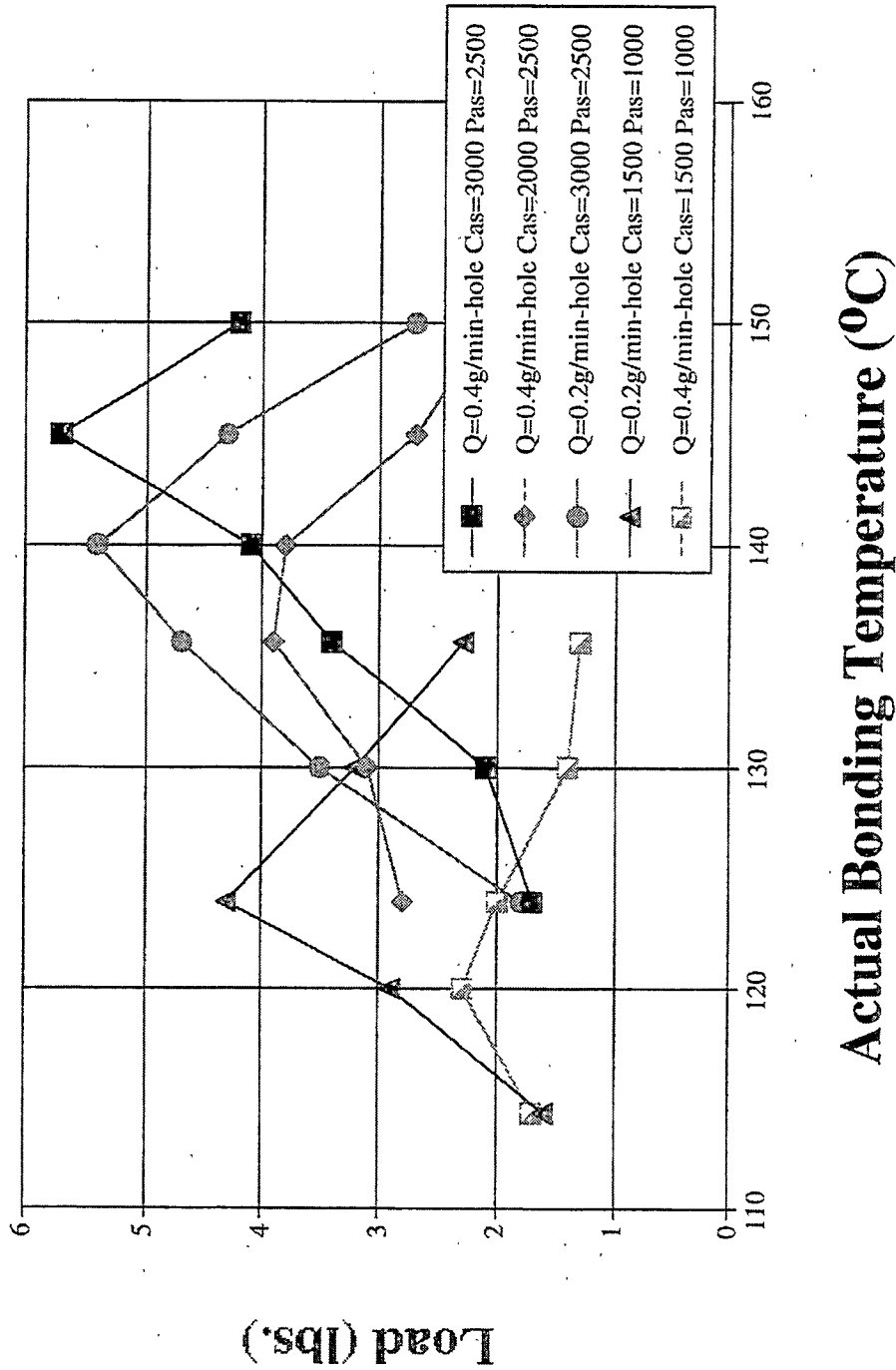
Figure 6.21 Fabric tensile load versus calender surface bonding temperature for 25g/m² fabrics using resin M32.

450

Actual Bonding Temperature (^{o}C)

Legend:
- Q=0.4g/min-hole Cas=3000 Pas=2500
- Q=0.4g/min-hole Cas=2000 Pas=2500
- Q=0.2g/min-hole Cas=2000 Pas=2500
- Q=0.2g/min-hole Cas=1500 Pas=1000
- Q=0.4g/min-hole Cas=1500 Pas=1000
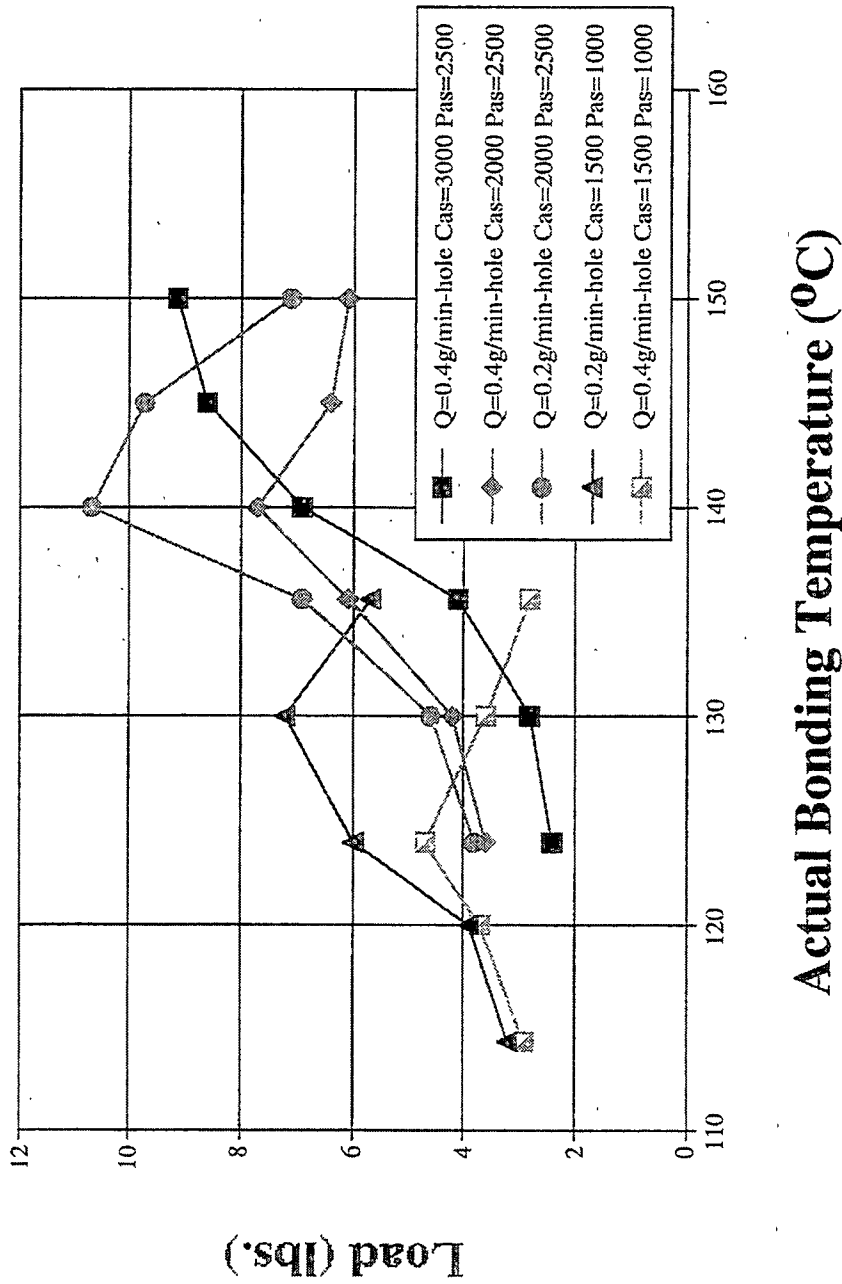
Figure 6.22 Fabric tensile load versus calender surface bonding temperature for 40g/m^{2} fabrics using resin M32.

Figure 6.23 Fabric peak elongation-to-break versus calender surface bonding temperature for 25g/m^2 fabrics using resin M32.
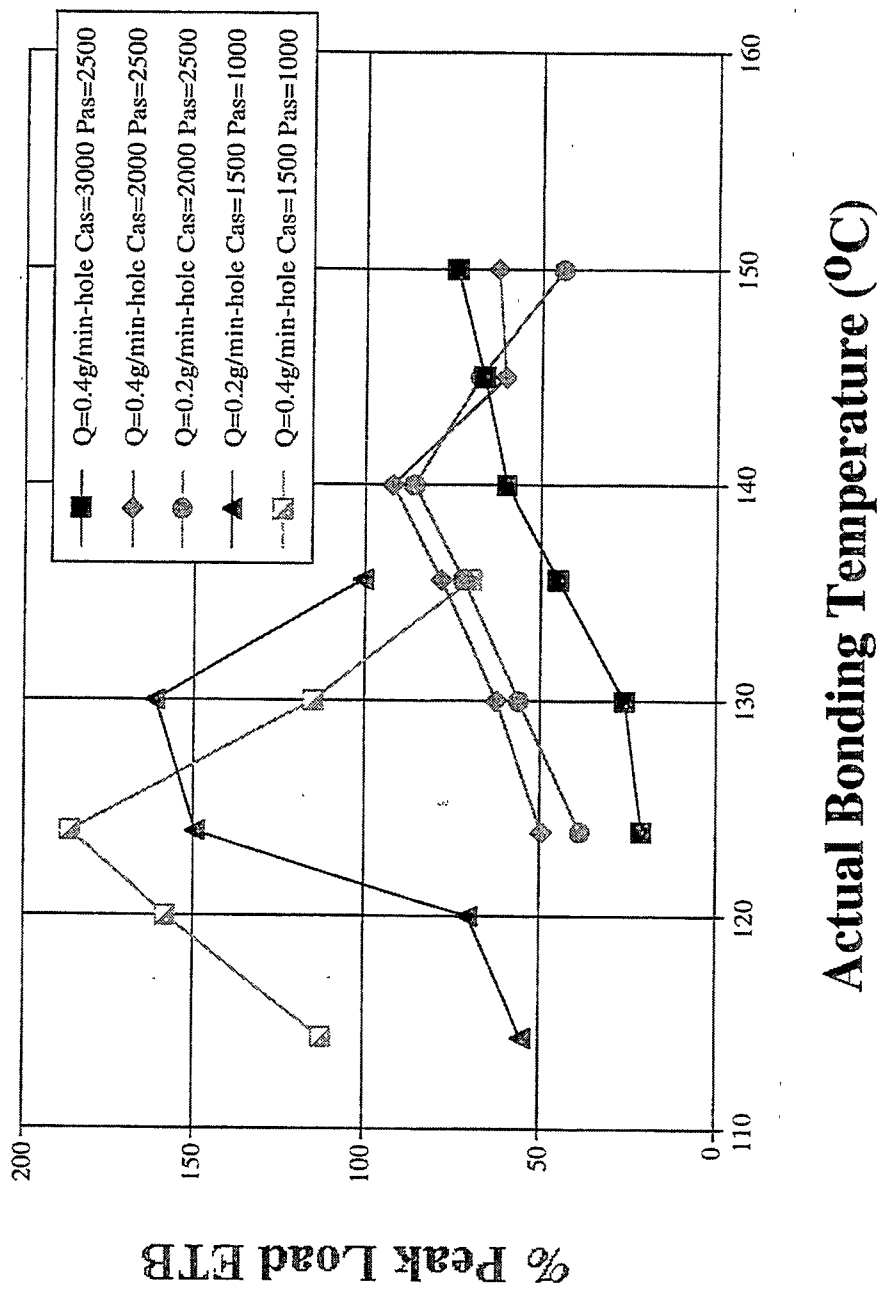
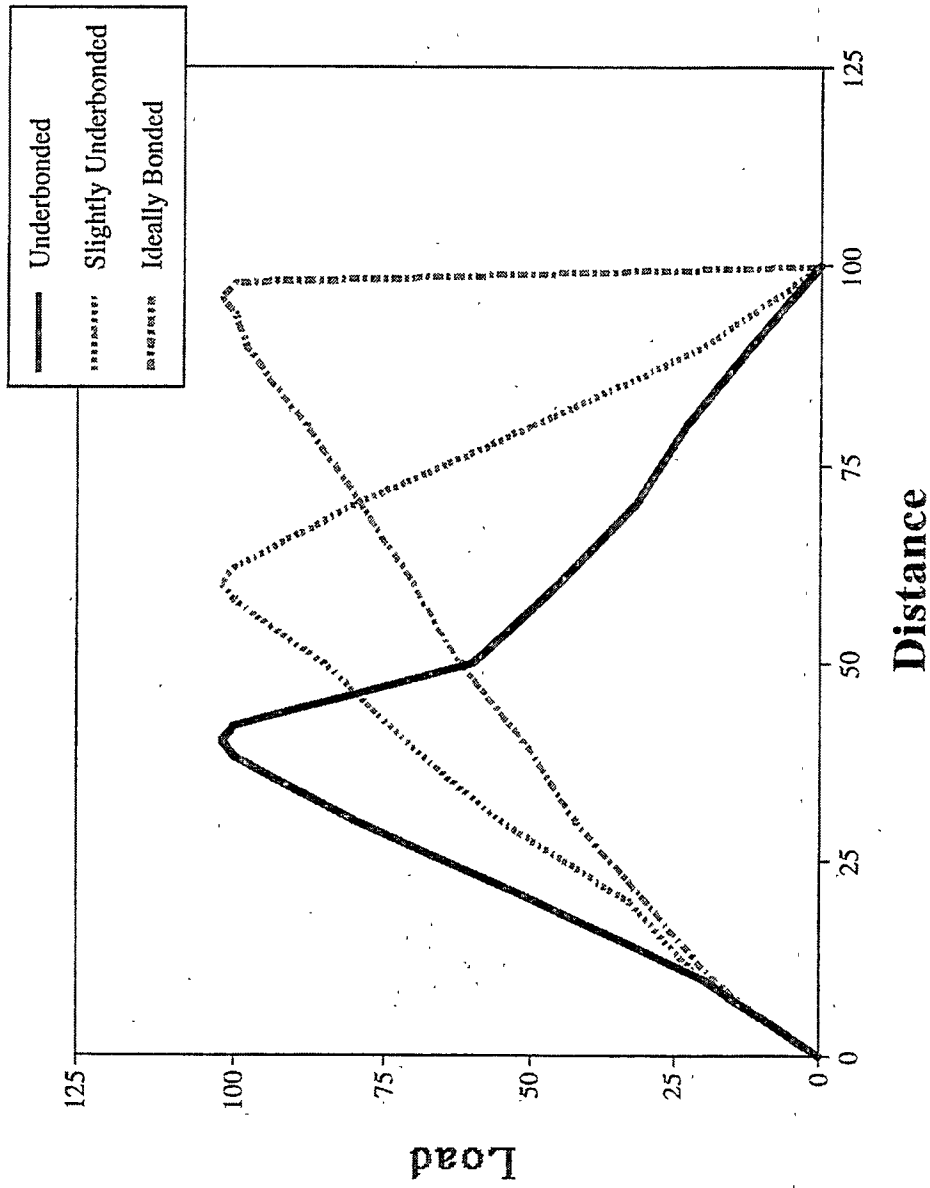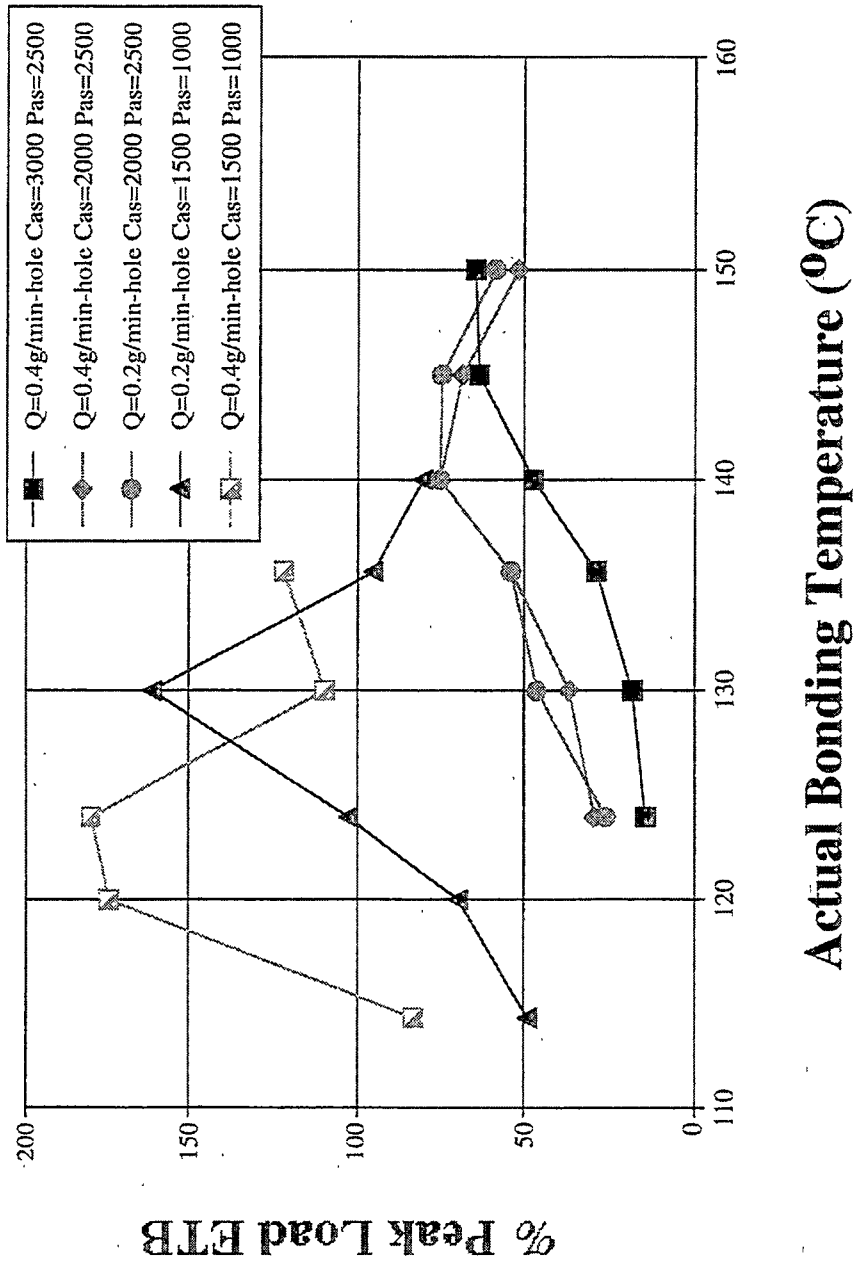**Figure 6.24** Fabric peak elongation-to-break versus calender surface bonding temperature for 40g/m² fabrics using resin M32.
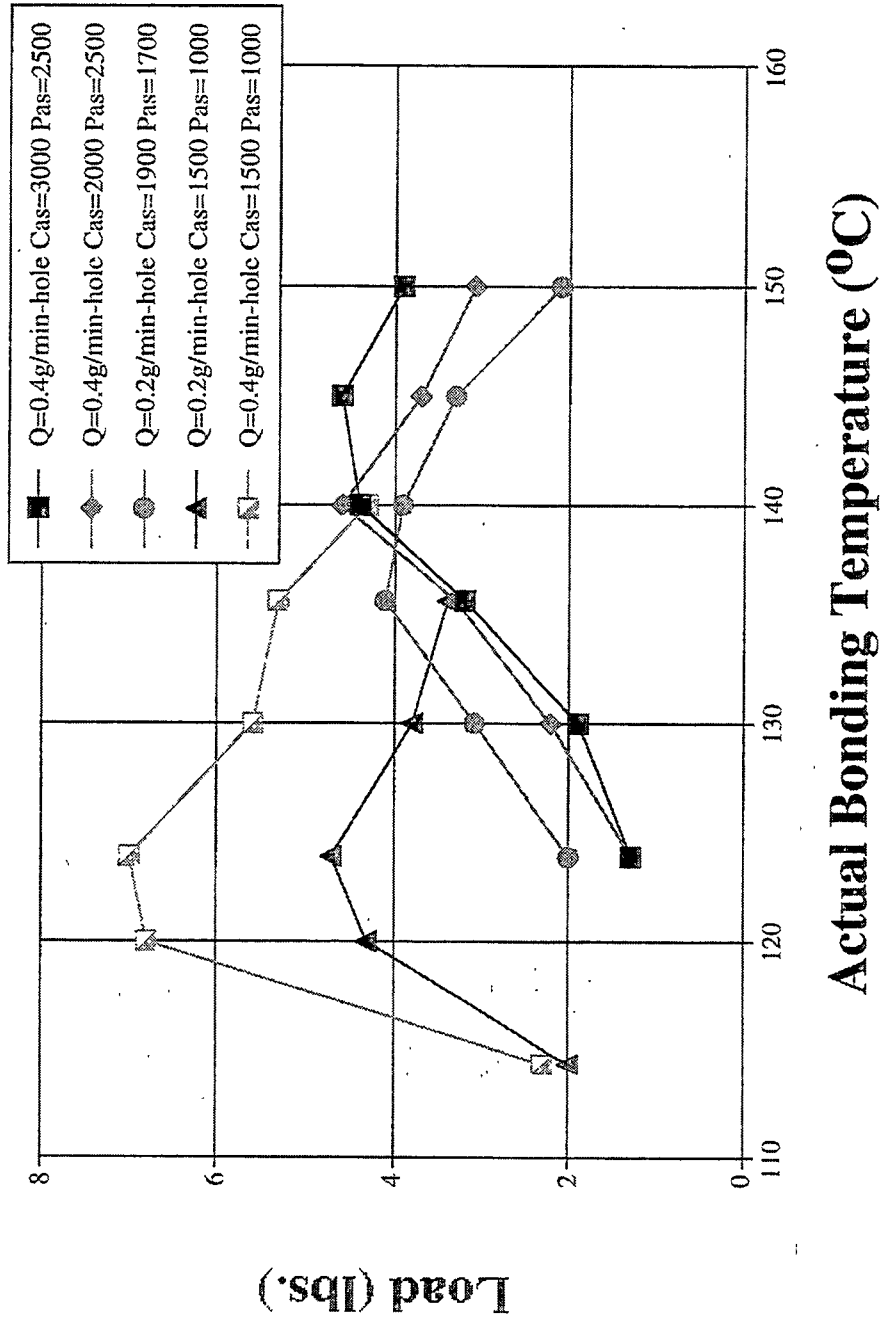
Figure 6.25 Fabric tensile load versus calender surface bonding temperature for 25g/m² fabrics using resin ZN35.

The chart legend reads:

- Q=0.4g/min-hole Cas=3000 Pas=2500
- Q=0.4g/min-hole Cas=2000 Pas=2500
- Q=0.2g/min-hole Cas=1900 Pas=1700
- Q=0.2g/min-hole Cas=1500 Pas=1000
- Q=0.4g/min-hole Cas=1500 Pas=1000

X-axis: **Actual Bonding Temperature (°C)**

Y-axis: **Load (lbs.)**

454
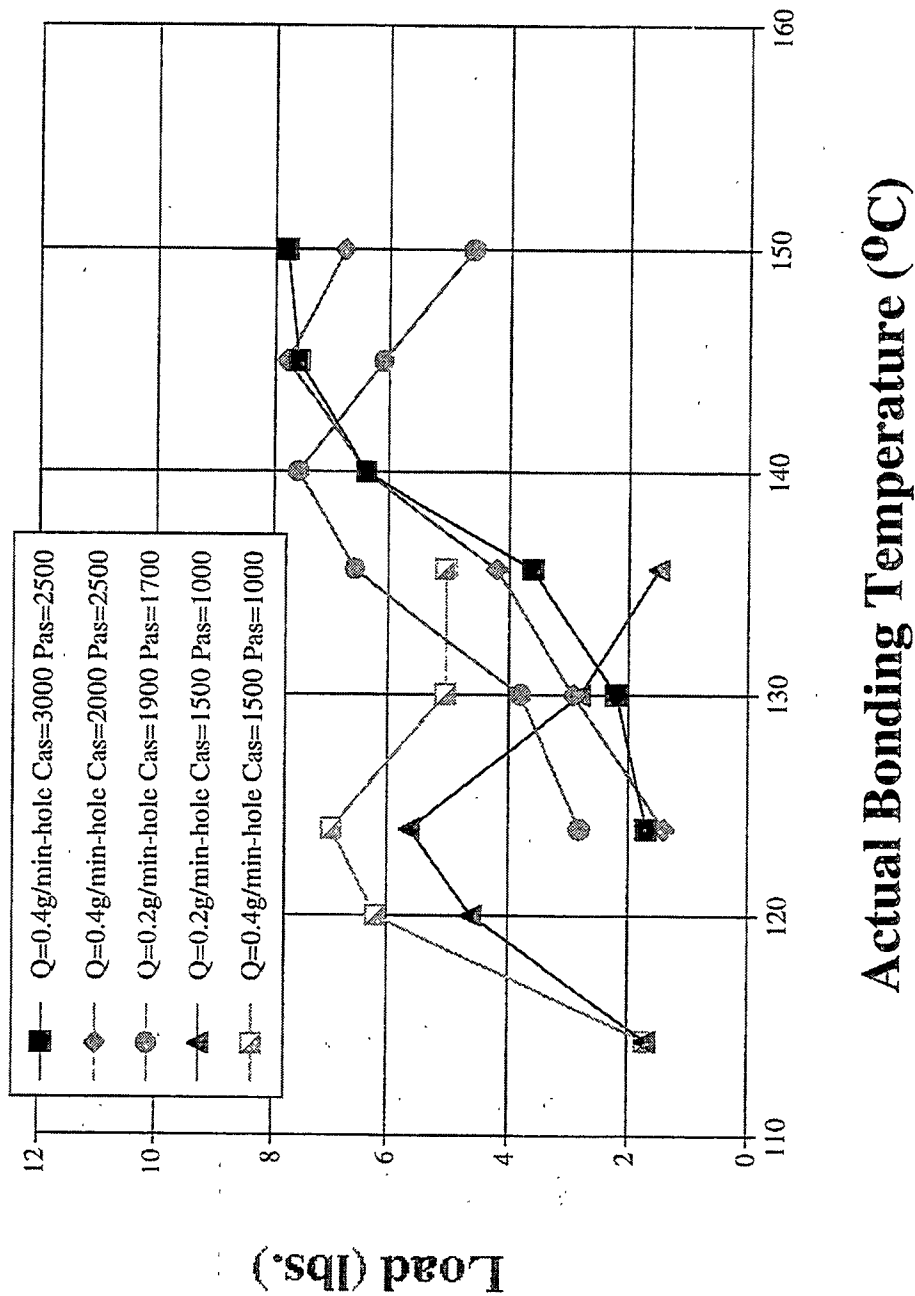
Figure 6.26 Fabric tensile load versus calender surface bonding temperature for 40g/m² fabrics using resin ZN35.
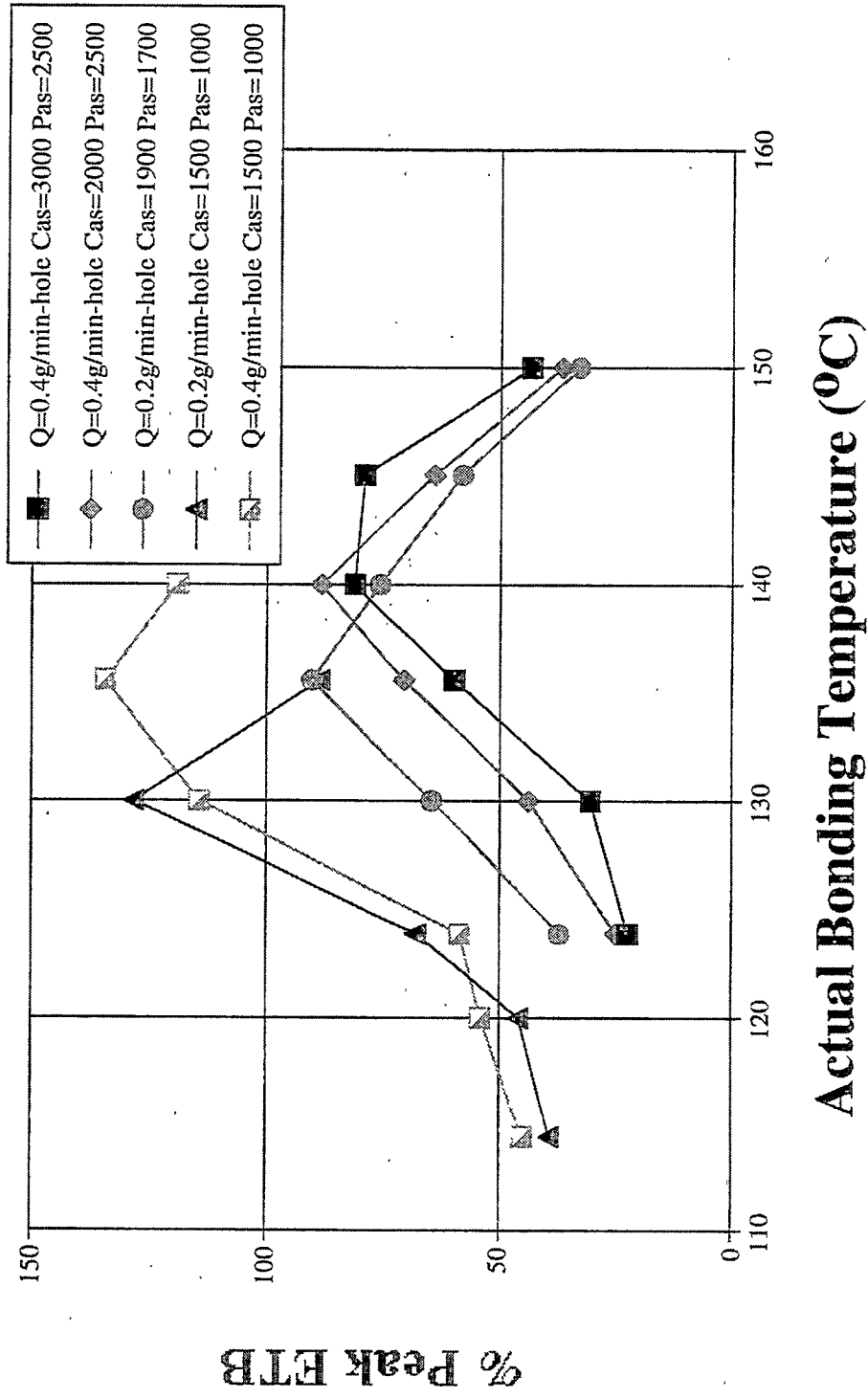
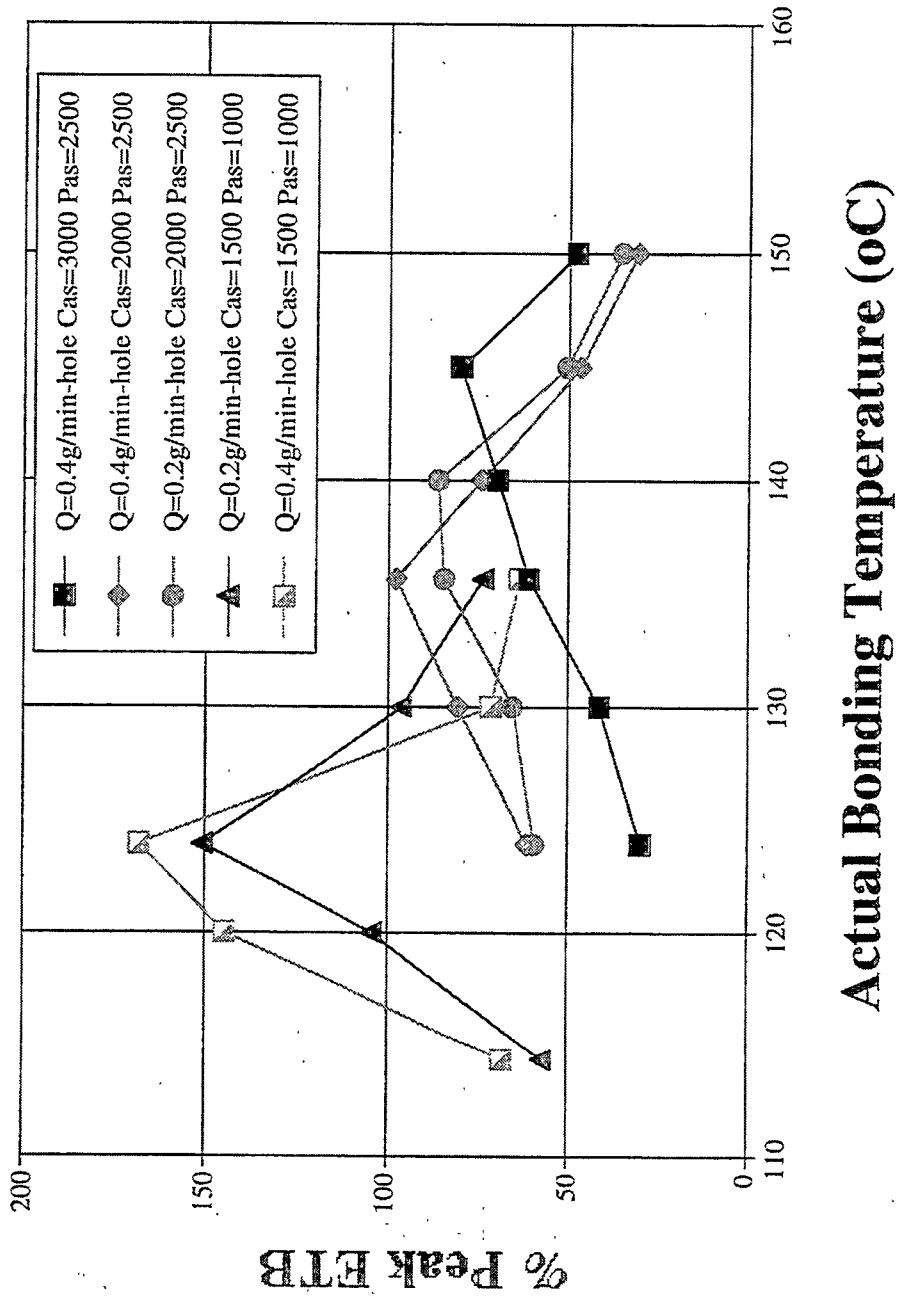**Figure 6.27** Fabric peak elongation-to-break versus calender surface bonding temperature for 25g/m² fabrics using resin ZN35.

456
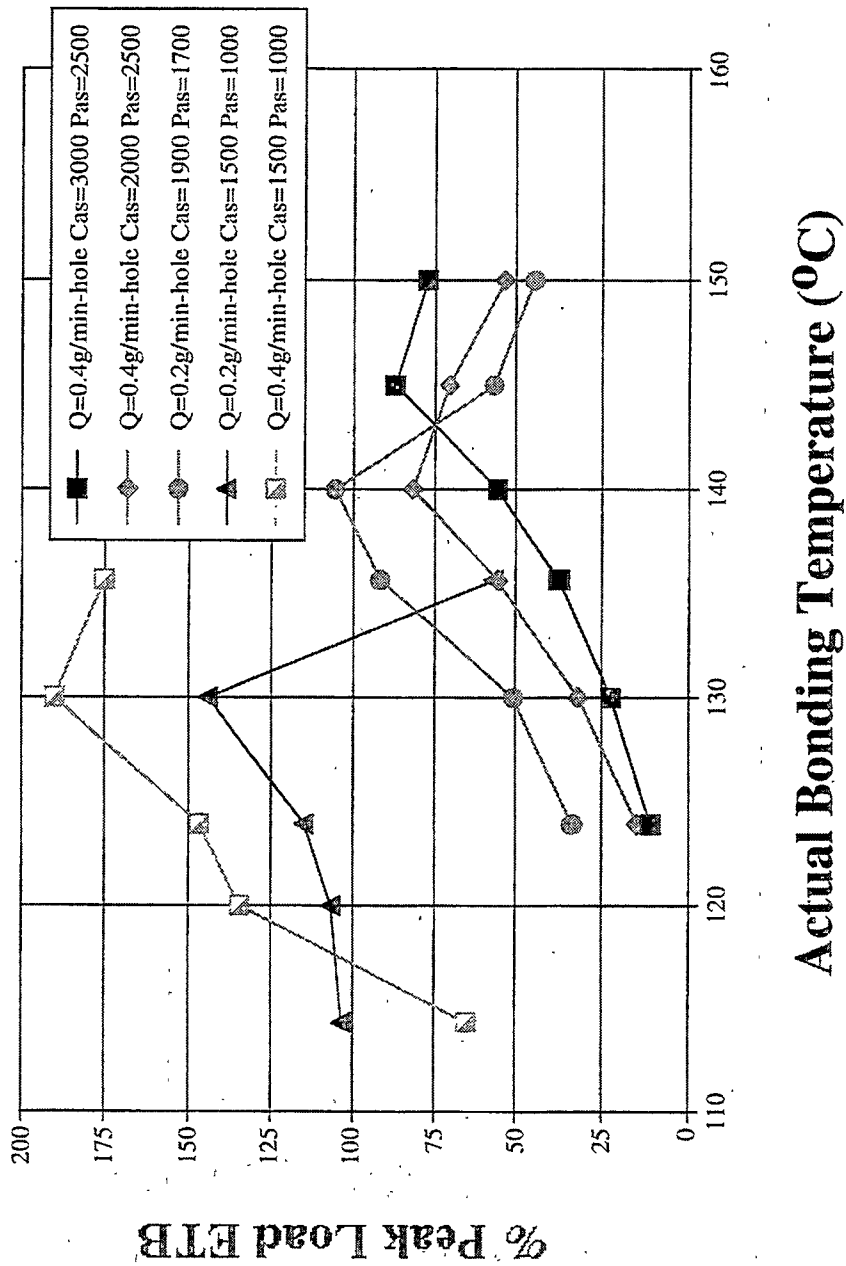
Figure 6.28 Fabric peak elongation-to-break versus calender surface bonding temperature for 40g/m² fabrics using resin ZN35.

457
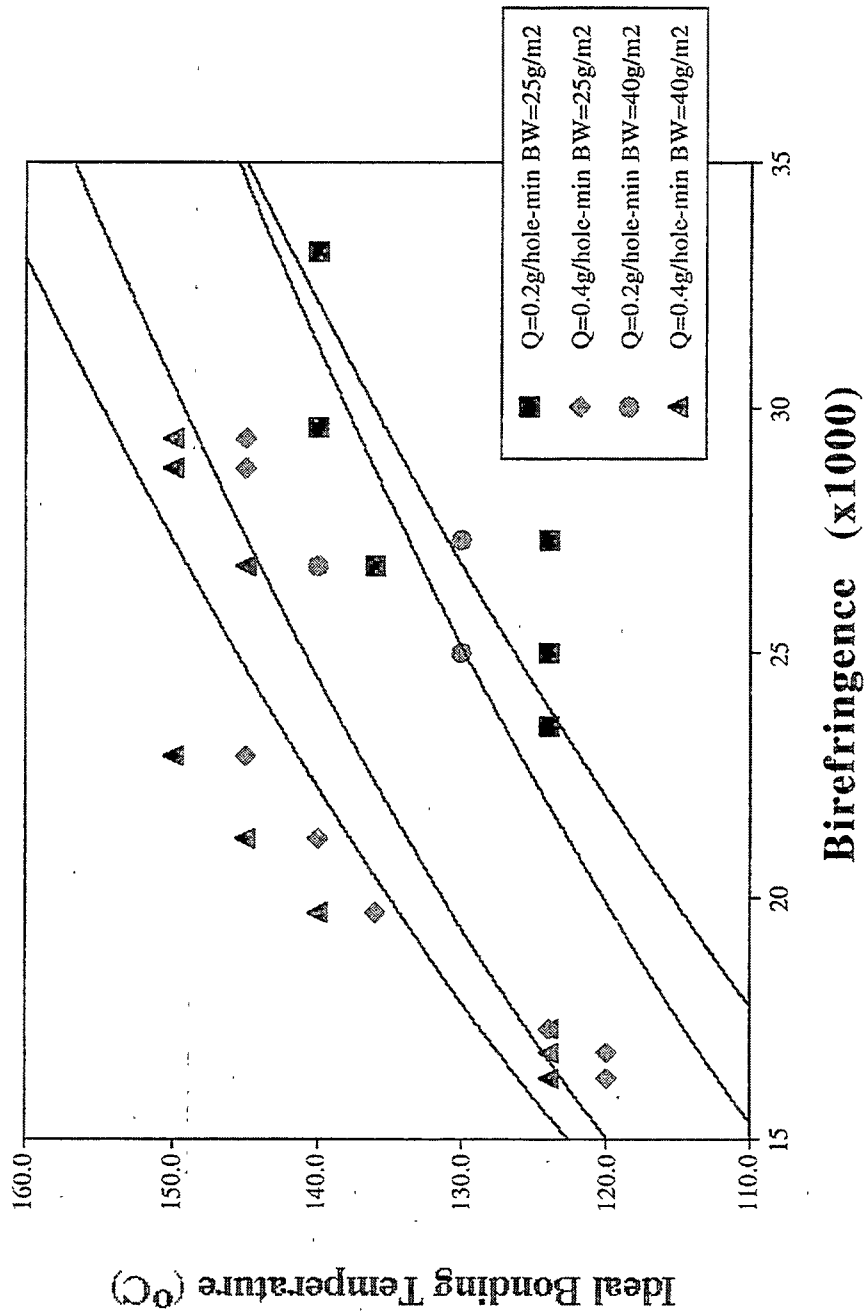
Figure 6.29 Fabric ideal bonding temperature versus unbonded fiber birefringence for all fabric basis weights using all resins.

the ideal bonding temperature as the as-spun fiber birefringence increases. When the ideal bonding temperature is plotted against the noncrystalline orientation function for the as-spun fibers, as shown in Figure 6.30, a general increase in bonding temperature is also found. It should be noted again that the belt speed and time in the bonder are the same for each of the four groupings. Therefore, the difference in bonding temperature and fabric properties is directly related and attributed to the prebonded fibers structure and properties. Again, there exists some scatter in this data. However, all three resins are combined together in this figures and the data all seem to fit together quite nicely. Also, there was a 5°C increase in the bonding temperature between points. Realistically, the ideal bond temperature for many samples is likely between these temperature increments for some samples. Additionally, the fiber properties were not checked for every sample produced. Therefore, there is likely some variation in fiber properties from sample to sample, further complicating the precision. However, the data clearly indicate for the same line speed, increasing fiber birefringence and noncrystalline orientation function dictates a higher bonding temperature to produce fabrics with ideal tensile properties.

Figures 6.31 and 6.32 show the fabric maximum load as a function of as-spun nonbonded fiber birefringence and noncrystalline orientation function, respectively. Figure 6.31 clearly shows that as fiber birefringence increases, the maximum load increases. The data in this figure also does not contain the scatter that was observed in Figures 6.29 and 6.30. The data in Figure 6.32 contain even less scatter and show that as the fiber noncrystalline orientation function increases, the fabric load increases. Figure 6.33 shows that as the fiber strength increases, the fabric load increases. This is not a
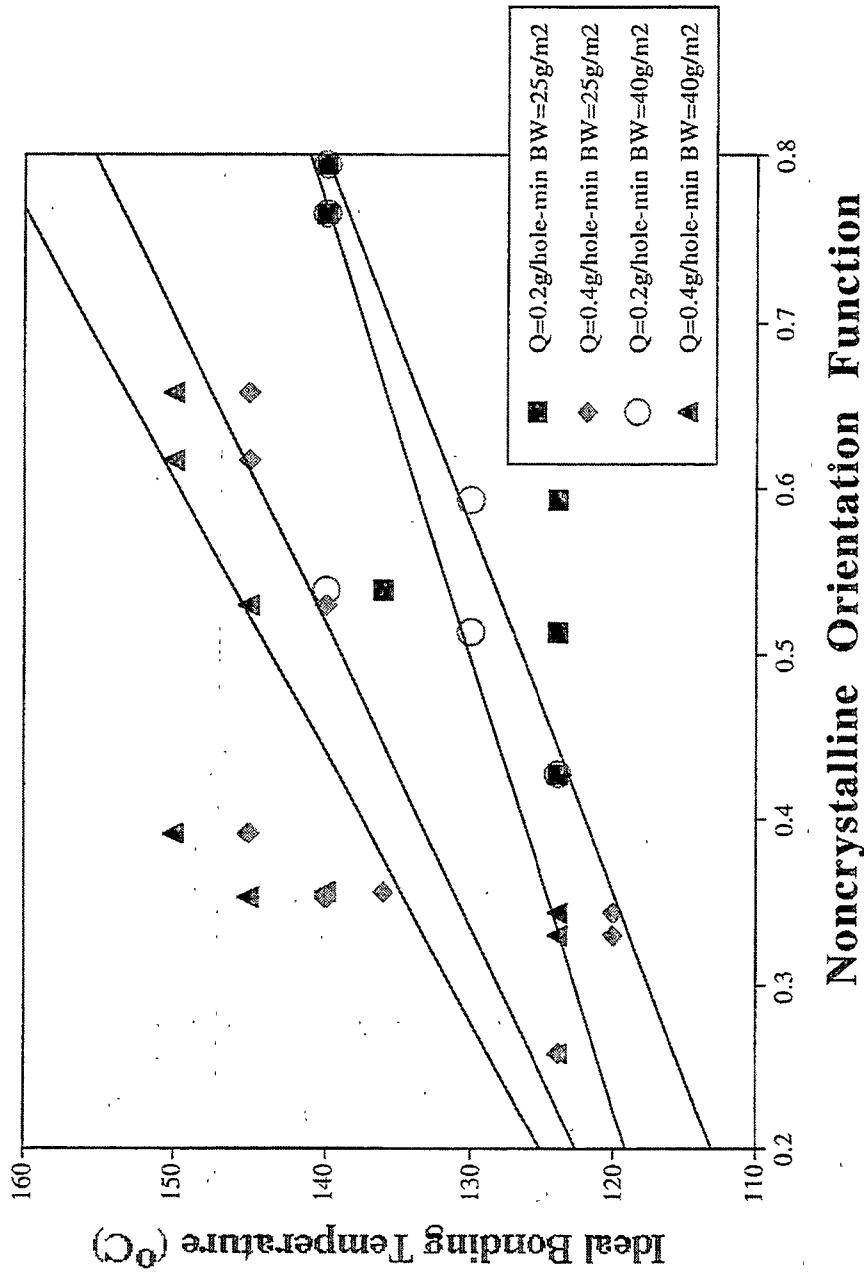
Figure 6.30 Fabric ideal bonding temperature versus unbonded fiber noncrystalline orientation function for all fabric basis weights using all resins.

460
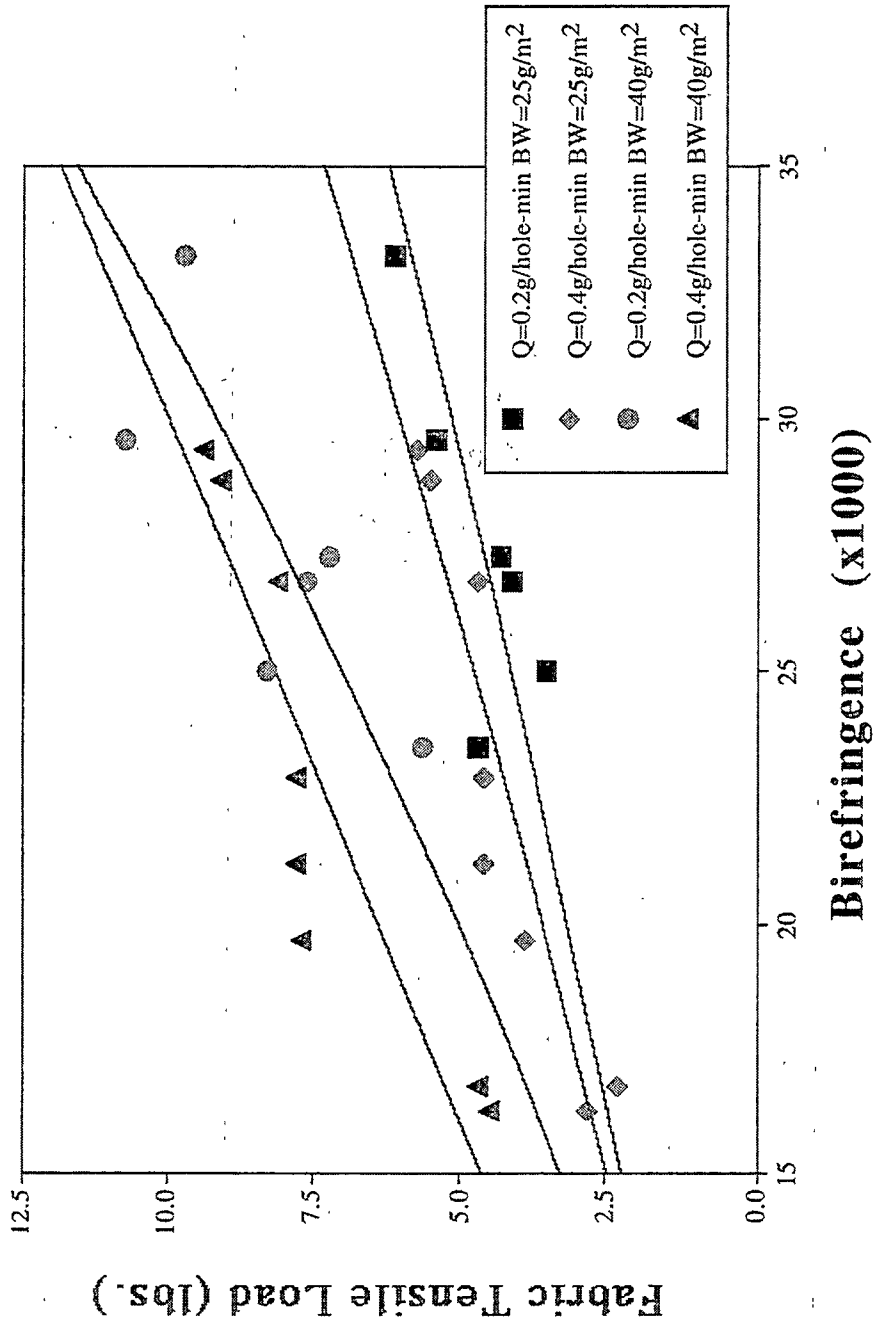
Figure 6.31 Fabric tensile load at the ideal bonding temperature versus unbonded fiber birefringence for all fabric basis weights using all resins.

461
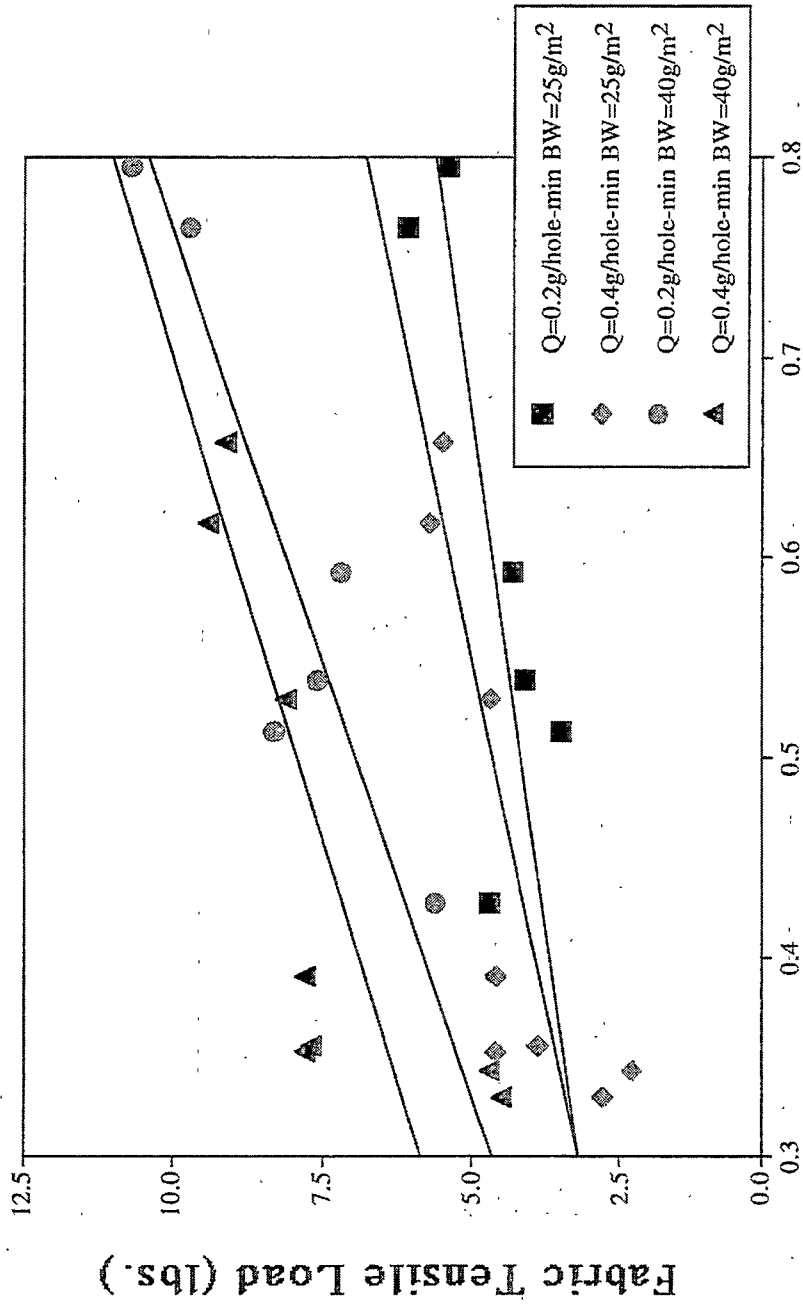
Figure 6.32 Fabric tensile load at the ideal bonding temperature versus unbonded fiber noncrystalline orientation function for all fabric basis weights using all resins.
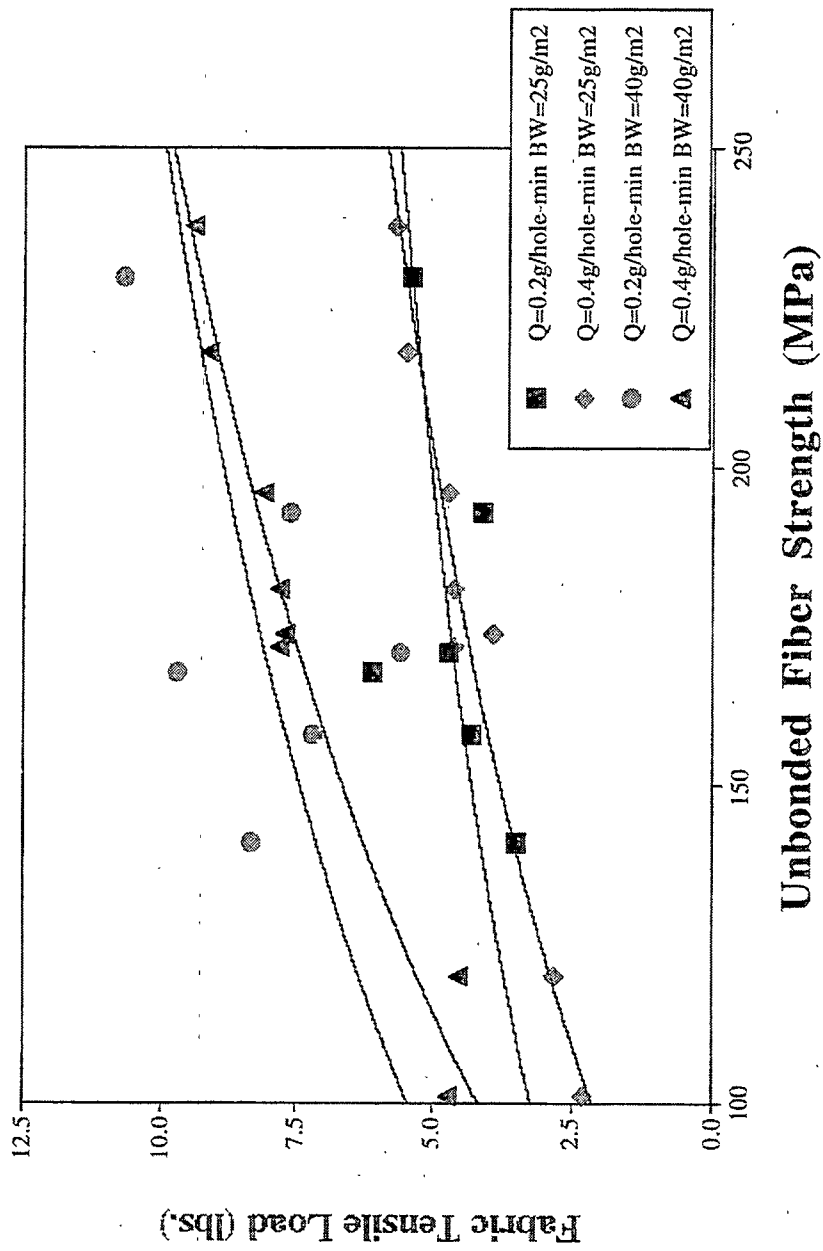
Figure 6.33 Fabric tensile load at the ideal bonding temperature versus unbonded fiber tensile strength for all fabric basis weights using all resins.

surprise based on finding that the fabric load increased with increasing fiber birefringence and noncrystalline orientation function.

The data in Figure 6.34 show the fabric ETB versus as-spun fiber ETB. The data indicates a very strong correlation between the two since as fiber ETB increases, fabric ETB increases.

The results found in this study indicate that as the as-spun fiber properties increase in birefringence, noncrystalline orientation function and tensile strength (these properties are related) the ideal bonding temperature increases and fabric mechanical properties increase. Further, there seemed to be no segregation of a particular resin into its own fabric/fiber behavior. Once the fiber properties are determined, the bonding temperature and fabric properties are then set. These results make scientific sense. One would not expect fibers with similar properties made from slightly different resins to have widely differing bonding temperatures and fabric strengths. These results also strongly suggest that the mechanical properties of the fabrics are determined by the mechanical properties of the as-spun fibers, provided optimum bonding conditions are used.

The onset of melting and peak melting temperature are illustrated in Figure 6.35. The onset of melting is when the melting endotherm breaks from the baseline, it is not the same as the melting onset temperature a typical DSC would give. The onset of melting and peak melting temperature for each set of as-spun nonbonded fibers are shown in Table 6.3. The data clearly shows that M22 and M32 have significantly lower peak melting temperatures, as has been shown throughout this work. The onset of melting
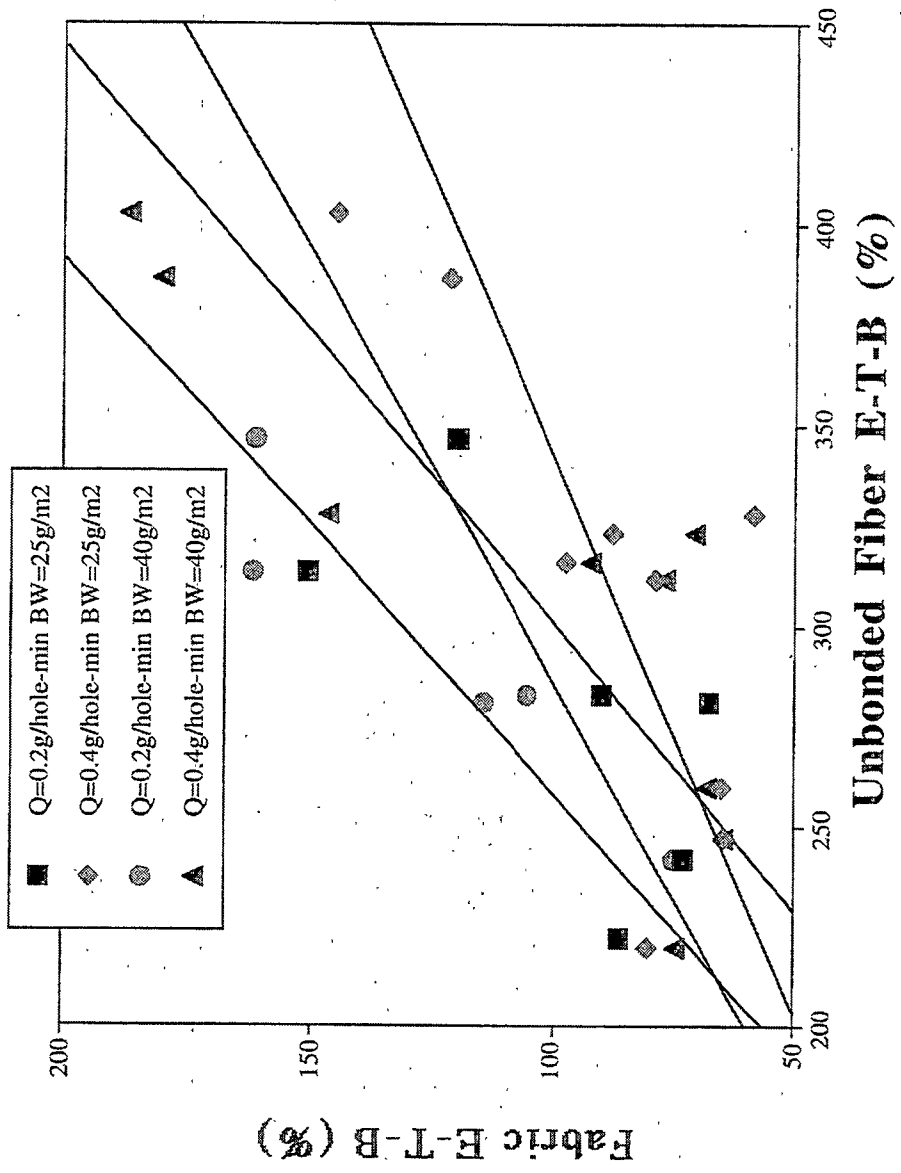
Figure 6.34 Fabric elongation-to-break at the ideal bonding temperature versus unbonded fiber elongation-to-break for all fabric basis weights using all resins.

465
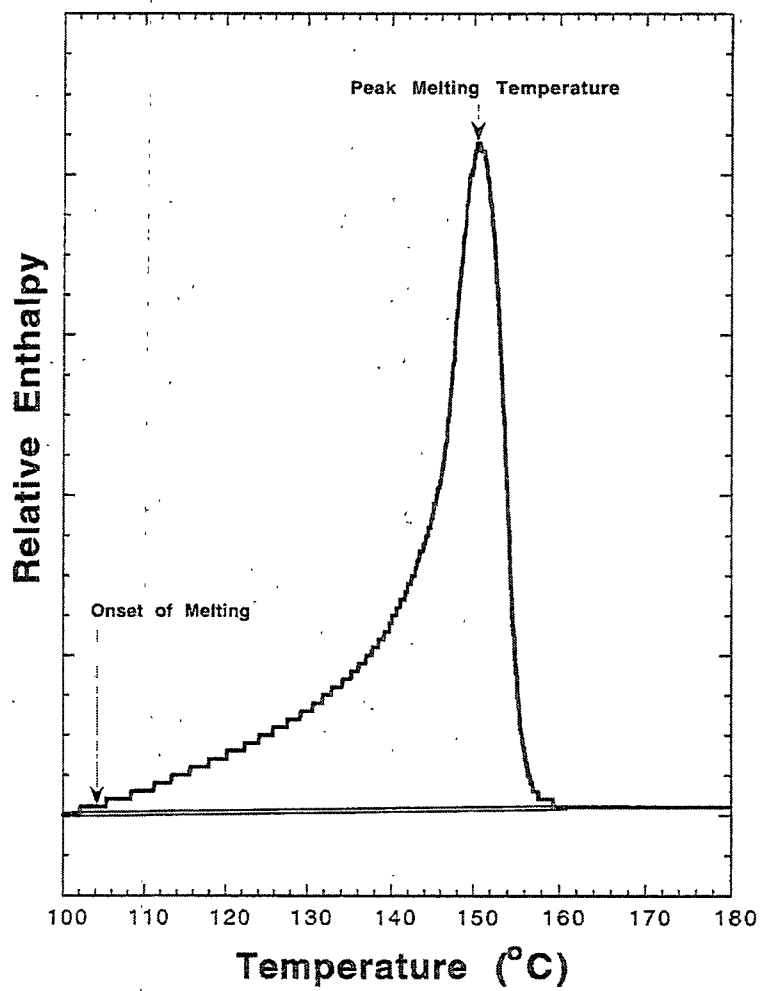
Figure 6.35 DSC endotherm of M22 indicating the point of onset of melting and the peak melting temperature.

Table 6.3 Onset and peak melting temperature of as-spun nonwoven fibers spun under high and low fan speeds.

Resin	Conditions	Melting Onset Temperature (°C)	Melting Peak Temperature (°C)
M22	Q=0.4g/min-hole Pas=2500rpm Cas=3000rpm	133.2	148.3
M22	Q=0.4g/min-hole Pas=2500rpm Cas=2000rpm	133.2	145.5
M22	Q=0.2g/min-hole Pas=2500rpm Cas=2000rpm	132.5	148.6
M22	Q=0.4g/min-hole Pas=1000rpm Cas=1500rpm	135.2	146.9
M22	Q=0.2g/min-hole Pas=1000rpm Cas=1500rpm	131.3	145.9
M32	Q=0.4g/min-hole Pas=2500rpm Cas=3000rpm	135.2	148.7
M32	Q=0.4g/min-hole Pas=2500rpm Cas=2000rpm	128.7	145.7
M32	Q=0.2g/min-hole Pas=2500rpm Cas=2000rpm	132.3	145.6
M32	Q=0.4g/min-hole Pas=1000rpm Cas=1500rpm	128.0	145.9
M32	Q=0.2g/min-hole Pas=1000rpm Cas=1500rpm	134.3	147.5
ZN35	Q=0.4g/min-hole Pas=2500rpm Cas=3000rpm	136.5	158.3
ZN35	Q=0.4g/min-hole Pas=2500rpm Cas=2000rpm	138.2	157.1
ZN35	Q=0.2g/min-hole Pas=1700rpm Cas=1900rpm	136.5	159.1
ZN35	Q=0.4g/min-hole Pas=1000rpm Cas=1500rpm	135.2	163.6
ZN35	Q=0.2g/min-hole Pas=1000rpm Cas=1500rpm	138.3	159.0

467

temperatures are quite similar for the various resins, with the range from 129 to 138°C. In most cases, the ZN35 fibers are at the highest end of that melting range.

The melting data indicates that the melting window is much narrower for the miPP resins since the peak melting temperature of these resins is roughly 12°C lower than the ZN35 resin. However, this does not seem to be important is this work as the bonding conditions for both materials are approximately the same. This indicates that the molecules involved in the bonding process must posses a similar morphlogy. Most likely these molecules are at the surface of the fiber, where the highest level of orientation exists and has been quenched with most rapidly. Therefore, in bonding, this molecules must melt and diffuse together during the heat and deformation in the calender. The ideal bonding temperature did not appear to be resin dependent. The ideal bonding temperature data indicates that it depends mostly on fiber molecular orientation, more specifically the noncrystalline orientation function. This result shows that in fact it is the fiber structure that determined the ideal bonding temperature and that the properties of the fibers do determine the properties of the webs when the bonding temperature has been optimized.

Chapter 7

Conclusions and Recommendations for Future Work

7.0 Conclusions

A brief summary of the results and conclusions from quiescent isothermal and nonisothermal crystallization studies, fiber spinning and thermal spunbonding studies will be presented in this chapter. Recommendations for future research will also be presented based on the findings in this investigation.

7.1 Quiescent Isothermal and Nonisothermal Crystallization Studies

Isothermally crystallized films studied by WAXD indicate that miPP resins produce α and γ-crystal structure under high crystallization temperatures. SAXS, WAXD and DSC studies were combined to determine the T_m^0 of the miPP and zniPP resins. Only one maximum could be found in the miPP raw and Lorentz corrected SAXS intensity data, which indicates that the α and γ crystal structure lamellae thicknesses are quite close or identical. The lamellae thickness and melting temperature data was combined to determine that the equilibrium melting temperature of the α-crystal structure of the resins in this study was 186±2°C, unless a diluent (atactic material) was present. The presence of atactic material lowered the T_m^0, as was the case with ZN35 and M100. The γ-crystal structure was found to have a T_m^0 of 178±2°C for the miPP resins, when crystallized at atmospheric pressure.

Defects excluded during isothermal crystallization are thought to be present in the crystal fold surface region when crystallization occurs at low supercoolings. The appearance of the γ-crystal structure also occurred in the miPP resins, which had significantly higher fold surface free energies. The higher fold surface free energy is attributed to a roughing of the crystal fold surface due to defect exclusion. As the crystallization temperature decreases, defect incorporation increases, and the occurrence of γ-crystal structure decreased and the fold surface free energy for the miPP resins decreases to a value near that of ZNHT. The zniPP resins formed very little of the γ-crystal structure and had significantly lower fold surface free energies. It was found that the presence of atactic material in the iPP resins in this study had a lower fold surface free energy, notably for ZN35 and M100. The difference in the observed melting temperature of the miPP and zniPP resins at similar lamellae thicknesses is attributed to the higher fold surface free energy of the miPP resins causing the lamellae crystals to melt at lower temperatures, according to the Gibbs-Thomson equation.

A theory was proposed to explain the formation of the γ-crystal structure. The theory asserts the formation of the γ-crystal structure becomes more favorable as the crystal thickness increases and the fold surface free energies increase. Higher fold surface free energies are present when iPP resins with stereochemical defects are crystallized at elevated temperatures, with low molecular weight iPP or when iPP is crystallized at elevated pressures. The higher fold surface free energies are a result of a rough crystal fold surface that is not two dimensional, but has a three dimensional contour and much higher total basal plane surface area.

The linear growth rates at high to moderate crystallization temperatures was found to be determined by the number and distribution of defects for a given iPP sample. Increasing the number of defects for the miPP resins decreased the observed linear growth rates, which had slower linear growth rates than either zniPP resin. Under nonisothermal crystallization conditions, where defects are included into the crystal, the linear growth rate was found to be determined most strongly by the molecular weight of the resin, with the influence of defects becoming less important. The bulk crystallization kinetics under isothermal and nonisothermal conditions showed the importance of both the linear growth rates and nucleation density in determining the overall crystallization kinetics.

7.2 Fiber Spinning Studies

The results of the fiber spinning study show that the molecular weight and molecular weight distribution of the iPP resin have a significant influence on the fiber spinning properties of the resins considered in this work.

On-line studies using diameter and birefringence measurements showed that as the molecular weight increases; crystallization occurs closer to the spinneret, at higher crystallization temperatures, the fibers have a larger diameter and crystallize at a lower stress at the point of crystallization onset. As the draw-down pressure is increased, or as the spinning speed increases, crystallization occurs closer to the spinneret, the onset diameter decreases and the stress at crystallization onset increases.

Estimates of the bulk nucleation densities were carried out using the on-line birefringence profiles. The results showed that the nucleation density ratio under

oriented and quiescent conditions increased more significantly as the molecular weight increases, despite the lower stress at crystallization onset. It would be expected that the higher MW resins have a higher entanglement density, therefore a lower stress is required to form a critical size nuclei. The same approach also explains the behavior of the lower MW resins. They require a higher onset stress to compensate for the lower entanglement density to initiate crystallization, i.e. more work most be done to orient the melt to initiate crystallization as the MW decreases. Therefore, the stress needed to initiate crystallization varies from resin to resin and depends on the MW and MWD.

Density measurements on the as-spun filaments indicated that as the spinning speed and molecular weight increased, the as-spun filament density increased due to crystallization occurring at higher temperatures, which allows more time for the fiber to crystallize in a given environment. Slight variations in this trend were observed for ZN35 and M45. These variations were explained by the higher MWD found for these resins.

The as-spun filament birefringence values showed that as spinning speed increases, the birefringence increases. As the molecular weight decreases, the as-spun filament birefringence increases. The contributions of birefringence from the crystalline and noncrystalline domains were separated by determining the crystalline and noncrystalline orientation functions. The orientation results showed that as the MW decreased, the noncrystalline orientation function increased and crystalline orientation function decreased. The orientation functions both generally increased as the spinning speed increased, with the exception of M10 and ZN35. The tensile strength of the as-spun filaments showed a similar trend as the birefringence, as MW decreases, the tensile

strength increased. Additionally, a strong positive correlation was found between the noncrystalline orientation function and the tensile strength. The tensile strength of the fibers is strongly dependent on the number of tie molecules which connect the various crystallites together, and to some extent dependent on the crystallinity of the sample. The crystallinity is important in that the number and size of the crystals will influence the tensile strength, since the crystallites act as an anchoring point for the tie molecules. If the population of crystallites is small (or perhaps they are very thin) the tie molecules may easily pull out of the crystal.

The tensile modulus was observed to be very much dependent on the spinning speed at which the resin was capable of being spun. It was observed that as MW decreased, the tensile modulus of the filaments were generally higher than the higher MW, more crystalline resins, a result of higher overall molecular orientation. This illustrates the importance of both crystallinity and overall molecular orientation on tensile modulus.

Elongation-to-break data was shown to be the inverse of the tensile strength data. This again is attributed to the number of tie molecules. As the number and orientation of the tie molecules increases, the elongation-to-break decreases since less extension and drawing is allowed before specimen failure.

7.3 Thermal Bonding

The thermal spunbonding results showed that when the bonding conditions for the fibers are optimized, the relative order of the as-spun fiber properties tend to be a good indication of the relative order of fabric properties, when processed under similar

473

processing conditions. The fabric properties are said to be optimized when the fabric strength and elongation-to-break are the highest in a bonding curve(a bonding curve is a graph of fabric strength versus bonding temperature).

The results indicated that increasing the birefringence or noncrystalline orientation function increased the ideal bonding temperature with constant mass-throughput and basis weight. This is due in part to a higher temperature required to relax the more highly oriented molecular chains in the fibers and to allow time for diffusion of chains at the fiber/fiber interface during bonding.

Studies on the as-spun fibers in the thermal spunbonding line had similar properties as those spun on the monofilament line under similar spinning speeds.

No significant differences were found between the bonding behavior of the zniPP and miPP resins that could not be explained by their differences in fiber properties, which are a result of the differences in molecular weight, molecular weight distribution and tacticity.

7.4 Recommendation for Future Research

Although this work was comprehensive in its study of iPP behavior, several points of speculation need to be investigated further. In addition, it would be of use to study other types of iPP resins with different properties. Future studies should involve:

1) Studies of miPP resins at elevated pressures. The equilibrium melting temperature and growth rates need to be determined at elevated pressures and compared to atmospheric studies. The fold surface free energies need to be determined under these conditions. Additionally, determining the melting temperature of samples

produced at elevated pressure in these studies should also be have the melting temperature determined at elevated pressures.

2) The interfacial region of polymers needs to be investigated thoroughly. The crystal surfaces (both lateral and fold) need to be studied to ascertain the crystal surface morphlogy of various iPP resins under isothermal and nonisothermal conditions, with and without defects present. These same samples then need to be studied using SAXS to correlate and understand the electron density measurements observed for the crystal core, interfacial region and pure amorphous domain.

3) The fiber spinning behavior of miPP resins needs to be studied further, using broader molecular weight distribution resins. These studies would complement the present work and allow the true effects of chemical homogeneity to be resolved in the fiber spinning process. It would also be of interest to study the effects spinning fibers into an oxygenated, heated spinning chamber. The on-line crystallization kinetics and as-spun filament properties could then be compared to conventionally spun fibers of the same resins to further resolve the influence of the quiescent crystallization kinetics in the running spinline.

4) Modifications to the high cooling rate light depolarizing microscopy equipment should be made in order to study the effects of shear and shear rate on the overall bulk crystallization kinetics. Primary nucleation seems to be the most important factor in bulk kinetic studies. Most processing methods have moderate to high levels of molecular orientation during the cooling and solidification process. It would be highly useful to not only qualitatively understand the importance of molecular orientation on accelerating the nucleation rate, but quantitatively. For instance, it

would be very useful to be able to predict the effect a given shear rate has on the nucleation rate as a function of molecular weight, molecular weight distribution and chemical homogeneity.

5) A model of the thermal bonding process needs to be formulated. The model needs to contain the important as-spun fiber properties and processing conditions, namely belt speed, bonding temperature and calender diameter. This model should also include the heat transfer equations and be able to predict the optimum conditions under which a given set of fibers need to be bonded to determine the best fabric properties.

References

References

(1) Wunderlich, B. Thermal Analysis Academic Press, Boston (1990).

(2) Pino, P., Mulhaupt, R. Agnew. Chem. Int. Ed. Eng. **19** 857 (1980).

(3) Natta, G. J. Polym. Sci. **16** 143 (1955).

(4) Natta, G., Corradini, P. Suppl. Nuovo Cimento **15** 3 (1960).

(5) Natta, G., Corradini, P. Suppl. Nuovo Cimento **15** 9 (1960).

(6) Natta, G., Corradini, P. Suppl. Nuovo Cimento **15** 40 (1960).

(7) Corradini, P. Structural Order in Polymers Pergani, NY (1981).

(8) Wright, N., Taylor, P. Polymer **28** 2004 (1987).

(9) Snetivy, D., Vansco, G. Polymer **35** 461 (1994).

(10) Meille, S., Bruckner, S., Porzio, F. Macromolecules **23** 4114 (1990).

(11) Lotz, B., Wittman, J., Lovinger, A. Polymer **37** 4979 (1996).

(12) Addink, E., Berentena, T. Polymer **2** 185 (1961).

(13) Turner-Jones, A., Aizlewood, J., Beckett, D. Makromol. Chem. **75** 134 (1964).

(14) Binsberger, F., Lange, B. Polymer **9** 23 (1968).

(15) Norton, D., Keller, A. Polymer **26** 704 (1985).

(16) Awaya, H. Polymer **29** 59 (1988).

(17) Bruckner, S., Meille, S., Petraccone, V., Pirozzi, B. Prog. Polym. Sci. **16** 361 (1990).

(18) Varga, J. J. Materials Sci. **27** 2557 (1992).

(19) Meille, S., Ferro, D., Bruckner, S., Lovinger, A., Padden, F. Macromolecules **27** 2615 (1994).

(20) Crissman, J. J. Polym. Sci. **A2** 398 (1969).

(21) Fijiwara, Y. Coll. Polym. Sci **253** 273 (1975).

(22) Lovinger, A., Chua, J., Bryte, C. J. Polym. Sci. Phys. **15** 641 (1977).

References con't

(23) Keith, H., Padden, F., Walter, N., Wychoff, H. J. Appl. Phys. **20** 1485 (1959).

(24) Turner-Jones, A., Cobbold, A. J. Polym. Sci. **6** 539 (1968).

(25) Samuels, R., Yee, R. J. Polym. Sci. Phys. **10** 385 (1972).

(26) Bruckner, S., Meille, S. Nature **340** 455 (1989).

(27) Thomann, R., Wang, C., Kressler, J., Mulhaupt, R. Macromolecules **29** 8425 (1996).

(28) Lotz, B., Graff, S. Wittmann, J. J. Polym. Sci. Phys. **24** 2017 (1986).

(29) Turner-Jones, A. Polymer **12** 487 (1971).

(30) Mezghani, K., Phillips, P. Polymer **38** 5725 (1997).

(31) Mezghani, K., Phillips, P. Polymer **36** 2407 (1995).

(32) Campbell, R., Phillips, P., Lin, JS. Polymer **34** 4809 (1993).

(33) Morrow, D., Newmann, B. J. Appl. Phys. **39** 4944 (1968).

(34) Miller, R. Polymer **1** 135 (1960).

(35) Hoseman, R. Acta Crystall. **4** 520 (1951).

(36) Zanneti, R., Celotti, G., Armigliato, F. Eur. Polymer. J. **6** 879 (1970).

(37) Wunderlich, B., Grebowicz, J. J. Adv. Polym. Sci. **60** 1 (1984).

(38) Bodor, G., Grell, M., Kallo, A. Faserforsch Textil-Tech **15** 527 (1964).

(39) Gomez, M., Tanaka, H., Tonelli, A. Polymer **28** 2227 (1987).

(40) Osawa, S., Porter, R. Polymer **35** 545 (1994).

(41) Osawa, S., Porter, R., Ito, M. Polymer **35** 551 (1994).

(42) Saraf, R. Polymer **35** 1359 (1994).

(43) Saraf, R., Porter, R. Polym. Eng. Sci. **28** 842 (1988).

(44) Grubb, D., Yoon, D. Polymer Comm. **27** 84 (1986).

(45) Randall, J. Macromolecules **30** 803 (1997).

(46) Kaminsky, W., Arndt, M. Adv. Polym. Sci. **127** 143 (1997).

References con't

(47) Paukkeri, R., Vaananen, T., Lehtinen, A. Polymer 34 2488 (1993).

(48) Inoue, Y., Itabashi, Y., Lehtinen, Y., Chujo, R., Doi, Y. Polymer 25 1640 (1984).

(49) Busico, V., Corradini, P., DeMartino, L., Giaziario, F., Iadiccio, A. Makromol. Chem. 192 49 (1991).

(50) Kakugo, M., Miyatake, T., Naito, Y., Mizununa, K. Macromolecules 21 314 (1988).

(51) Hayashi, Y., Inoue, Y., Chujo, R., Doi, Y. Polymer 30 1714 (1989).

(52) Albizzati, E., Gianni, U., Morris, G., Smith, C., Ziegler, R. Ziegler-Catalysts Springer-Verlag (1995).

(53) Sacchi, M., Tritto, I., Shan, C., Mendichi, R., Noust, L. Macromolecules 24 6823 (1991).

(54) Martuscelli, E., Avella, M., Segre, A., Rossi, E., Drusco, G., Galli, P., Simonazzi, T. Polymer 26 259 (1985).

(55) Martuscelli, E., Pracella, M., Crispino, G. Polymer 26 693 (1983).

(56) Burfield, D., Loi, P. J. Appl. Polym. Sci. 41 1095 (1990).

(57) Janimak, J., Cheng, S., Zhang, A., Hsieh, E. Polymer 33 729 (1992).

(58) Paukkeri, R., Lehtinen, A. Polymer 34 4081 (1993).

(59) Ewen, J. J. Am. Chem. Soc. 106 6355 (1984).

(60) U.S. Patent 4,522,982 Exxon (1985).

(61) Cardin, D., Lappert, M., Rastar, C. Chemistry of Organo Zirconium and Hafnium Conmpounds J. Wiley and Sons NY (1986).

(62) Coates, G., Waymouth, R. Science 267 217 (1995).

(63) Schmutenhaue, H., Brintzinger, H. Angew. Chem. Int. Ed. Eng. 18 777 (1979).

(64) Wild, F., Zsolnai, L., Hutter, G., Brintzinger, H. J. Organomet. Chem. 232 233 (1982).

References con't

(65) Tritto, I., Li, S., Sacchi, M. Macromolecules **26** 7112 (1993).

(66) Zambelli, A., Luango, P., Grassi, A. Macromolecules **22** 2186 (1989).

(67) Yang, X., Stein, C., Marks, T. J. Am. Chem. Soc. **113** 3623 (1991).

(68) Jordan, R., Bajgur, C., Willet, R., Scott, B. J. Am. Chem. Soc. **108** 7410 (1986).

(69) Hatky, G., Eckman, R., Turner, H. Organometallics **11** 1413 (1992).

(70) Wunderlich, B. Macromolecular Physics Vol. 1. Crystal Structure, Morphlogy and Defects Acedemic Press NY (1973).

(71) Geil, P. Polymer Single Crystals J. Wiley and Sons NY (1973).

(72) Fava, R. J. Polym. Sci. **5** 1 (1971).

(73) Phillips, P. Rep. Prog. Phys. **53** 549 (1990).

(74) Hoffman, J., Lauritzen, J. J. Res. Natl. Bur. Stds. **65A** 297 (1961).

(75) Bunn, C. Trans. Faraday Soc. **35** 482 (1939).

(76) Keller, A. Phil. Mag. **2** 1171 (1957).

(77) Stork, K. J. Am. Chem. Soc. **60** 1753 (1938).

(78) Flory, P. Trans. Faraday. Soc. **51** 848 (1955).

(79) Sanchez, I., Eby, R. J. Res. Natl. Bur. Stds. **77A** 353 (1973).

(80) Sachez, I., Eby, R. Macromolecules **8** 688 (1975).

(81) Colson, J., Eby, R. J. Appl. Phys. **37** 3511 (1966).

(82) Lauritzen, J., DiMarzio, E., Passaglia, E. J. Chem. Phys. **45** 444 (1966).

(83) Helfand, E., Lauritzen, J. Macromolecules **6** 631 (1973).

(84) DiMarzio, E., Guttmann, C., Hoffman, J. Macromolecules **13** 1194 (1980).

(85) DiMarzio, E., Guttmann, C., Hoffman, J. J. Bull. Am. Phys. Soc. **24** 382 (1979).

(86) Gibbs, J. The Scientific Works of J. Williard Gibbs Green NY 1906.

(87) Hoffman, J., Weeks, J. J. Res. Natl. Bur. Stds. **A66** 13 (1962).

(88) Hoffman, J., Weeks, J. J. Chem. Phys. **37** 1723 (1962).

References con't

(89) Krigbaum, W., Vermatsu, I. J. Polym. Sci. Phys. **3** 767 (1965).

(90) Miller, R., Sidney, E. J. Polym. Sci. Phys. **20** 2297 (1982).

(91) Mezghani, K., Campbell, R., Phillips, P. Macromolecules **27** 997 (1994).

(92) Fatou, J. Eur. Polymer J. **7** 1057 (1971).

(93) Monnasse, B., Handin, J. Colloid Polym. Sci. **263** 822 (1985).

(94) Fujiwara, Y. Colloid Polym. Sci. **265** 1027 (1987).

(95) Kanide, K., Yamaguchi, K. Makromol. Chem. **162** 219 (1972).

(96) Kanide, K., Yamaguchi, K. Makromol. Chem. **162** 205 (1972).

(97) Mezghani, K., Phillips, P. Polymer *in Press*.

(98) Avrami, M. J. Chem. Phys. **7** 1103 (1939).

(99) Avrami, M. J.Chem. Phys. **8** 212 (1940).

(100) Avrami, M. J. Chem. Phys. **9** 177 (1941).

(101) Nakamura, K., Watanabe, T., Katayana, K., Amano, T. J. Appl. Polym. Sci. **16** 1077 (1972).

(102) Nakamura, K., Katayana, K., Amano, T. J. Appl. Polym. Sci **17** 1031 (1973).

(103) Ozawa, T. Polymer **12** 150 (1971).

(104) Ziabicki, A. Appl. Polym. Symp. **18** 142 (1967).

(105) Patel, R., Spruiell, J. Polym. Eng. Sci. **31** 730 (1991).

(106) Dietz, W. Colloid Polym. Sci. **259** 413 (1981).

(107) Lauritzen, J., Hoffman, J. J. Appl. Phys. **44** 4340 (1973).

(108) Hoffman, J., Miller, R. Polymer **38** 3151 (1997).

(109) Hoffman, J., Davis, G., Lauritzen, J. Treatise on Solid State Chemistry Plenum Press Vol. 3 (1976).

(110) Clark, E., Hoffman, J. Macromolecules **17** 878 (1984).

(111) Cheng, S., Janimak, J., Zhang, A. Macromolecules **23** 298 (1990).

References con't

(112) Phillips, P., Vatansever, N. Macromolecules **20** 2138 (1987).

(113) Point, J., Dosiere, M. Polymer **30** 2292 (1989).

(114) Flory, P. J. Chem. Phys. **15** 684 (1947).

(115) Flory, P. J. Chem. Phys. **15** 685 (1947).

(116) Flory, P. J. Chem. Phys. **17** 223 (1949).

(117) Flory, P. Trans. Faraday Soc. **57** 848 (1955).

(118) Flory, P. J. Am. Chem. Soc. **84** 2857 (1962).

(119) Eby, R. J. Res. Natl. Bur. Stds. **68a** 269 (1964).

(120) Eppe, E., Fischer, W., Stuart, M. J. Polym. Sci. **34** 721 (1959).

(121) Price, F. J. Chem. Phys. **35** 1884 (1961).

(122) Vilgis, T., Halperin, A. Macromolecules **24** 2090 (1991).

(123) Carothers, W. and Hill, J. J. Am. Chem. Soc. **54** 1579 (1932).

(124) Mark, H. and Whitby, G. Collected Papers of W. H. Carothers on High Polymeric Substances Interscience, NY 1940.

(125) Ziabicki, A. Fundamentals of Fiber Formation Wiley, London 1976.

(126) Sano, Y and Orii, K. Sen-i Gakkaishi **24** 212 (1968).

(127) Cross, M. Polymer Systems: Deformation and Flow McMillian, London 1968.

(128) Carreau, P. Ph.D. Dissertation, University of Wisconsin 1979.

(129) Shimizu, J., Okui, N. and Kikutani, T. High Speed Fiber Spinning--Science and Engineering Aspects ed. Ziabicki, A. and Kawai, H. Wiley, NY 1985.

(130) Zeminski, K. and Spruiell, J. J. Appli. Polym. Sci. **35** 2223 (1988).

(131) Patel, R., Bheda, J. and Spruiell, J. J. Appl. Polym. Sci. **42** 1671 (1991).

(132) Kase, S. and Matsuo, T. J. Polym. Sci. **A3** 2541 (1965).

(133) Kase, S. and Matsuo, T. J. Appl. Polym. Sci. **11** 251 (1967).

(134) Oda, K., White, J. and Clark, E. Polym. Eng. Sci. **18** 53 (1978).

References con't

(135) Janeschitz-Kriegl, H. Polymer Melt Rheology and Flow Birefrigence Springer-Verlag, NY 1983.

(136) Van Krevelen, D. "Properties of Polymers" Elsevier, NY 1976.

(137) Hermans, P. and Platzek, P. Kolloid-Z. **88** 68 (1939).

(138) Hermans. P., Hermans, J., Vermaas, D. and Weidinger, A. J. Polym. Sci. **3** 1 (1947).

(139) Stein. R. and Norris, F. J. Polym. Sci. **21** 381 (1956).

(140) Stein, R. J. Polym. Sci. **31** 327 (1958).

(141) Bunn, C. and Daubeny, R. Trans. Faraday Soc. **50** 1173 (1954).

(142) Denbigh. K. Trans. Faraday Soc. **36** 936 (1940).

(143) Stein, R. J. Polym. Sci. A2 **7** 1021 (1969).

(144) Vuks, M. Opt.-i-Spektroskopiya **2** 494 (1957).

(145) Katayama, K. and Yoon, M. High Speed Fiber Spinning--Science and Engineering Aspects ed. Ziabicki, A. and Kawai, H. Wiley, NY 1985.

(146) White, J. and Spruiell, J. Polym. Eng. Sci. **21** 859 (1981).

(147) Patel, R. and Spruiell, J. Polym. Eng. Sci. **31** 730 (1991).

(148) Ziabicki, A. and Kedzierska, K. J. Appl. Polym. Sci. **2** 14 (1959).

(149) Ziabicki, A. and Kedzierska, K. Kolloid-Z. **171** 51 (1960).

(150) Ziabicki, A. Kolloid-Z. **175** 134 (1975).

(151) Ziabicki, A. and Kedzierska, K. J. Appl. Polym. Sci. **6** 111 (1962).

(152) Ziabicki, A. and Kedzierska, K. J. Appl. Polym. Sci. **6** 361 (1962).

(153) Ziabicki, A. Fundamentals of Fiber Formation Wiley, London 1976.

(154) Nadella, H., Henson, H., Spruiell, J., White, J. J. Appl. Polym. Sci. **21** 3003 (1977).

References con't

(155) Lu, FM., Spruiell, J. J. Appl. Polym. Sci. **34** 1521 (1987).

(156) Lu, FM., Spruiell, J. J. Appl. Polym. Sci. **34** 1541 (1987).

(157) Misra, S., Lu, FM., Spruiell, J., Richeson, G. J. Appl. Polym. Sci. **56** 1761 (1995).

(158) Spruiell, J., Lu, FM., Ding, Z., Richeson, G. J Appl.Polym. Sci. **62** 1965 (1996).

(159) Reed, R. U.S. Patent 2,277,049.

(160) Kumin, V. U.S. Patent 3,438,844.

(161) Schwartz, P. U.S. Patent 3,912,567.

(162) Schwartz, P. U.S. Patent 4,100,319.

(163) Gibson, P., McGill, R. Tappi J. **10** 82 (1987).

(164) Shimalla, C., Whitwell, J. Text. Res. J. **46** 405 (1976).

(165) DeAngelis, V., DiGioacchirio, T., Olivieri, E. 2nd Conference on Propylene Fibers and Textiles **52** 1 (1979).

(166) Bechtner, D., Kurz, G., Maag, E., Schutz, W. Textil-Praxis **46** 1236 (1991).

(167) Muller, D. INDA J. Nonwoven Res. **1** 35 (1989).

(168) Warner, S. Text. Res. J. **59** 151 (1989).

(169) Deakyne, C., Rebenfeld, D., Whitwell, J. Text. Res. J. **47** 491 (1977).

(170) Rolando, R., Krieger, D., Morric, H. Plast. & Rubber Process & Appl. **10** 245 (1988).

(171) Cappuccio, V., Coen, A., Bertinotti, S., Conti, W. Chim. Industr. **44** 463 (1962).

(172) Andreasson, E., Myhre, O., Hinrichsen, E., Braathen, M., Grostad, K. J. Appl. Polym. Sci. **58** 1633 (1998).

(173) Galanti, A., Mantell, C. Polypropylene Fabrics and Fibers Plenum Press, NY (1965).

References con't

(174) Morrison, R., Boyd, R. Organic Chemistry Prentice Hall, NJ (1992).

(175) Randall, J. Carbon-13 NMR in Polymer Science ed Pasika, W. ACS, NY (1979).

(176) Busico, V., Cipullo, R., Corradini, P., Landriani, L., Vacatello, M. Macromolecules 28 1887 (1995).

(177) Inoue, Y., Nishioka, A., Chujo, R. Die Makromol. Chem. 152 15 (1972).

(178) Tonnelli, A., Schilling, F. Acc. Chem. Res. 14 233 (1981).

(179) Randall, J. J. Polym. Sci. Phys. 14 2083 (1976).

(180) Hummonil, D. Infrared Spectra of Polymers Inter-Science, NY 1966).

(181) Schroder, E., Muller, G., Arndt, K. Polymer Characterization Hanser, Munich (1989).

(182) Kampf, G. Characterization of Plastics by Physical Methods, Experimental Techniques and Practical Application Hanser, Munich (1986).

(183) Rabek, J. Experimental Methods in Polymer Chemistry J. Wiley and Sons, NY (1980).

(184) Hermans, P., Weidinger, A. Makromol. Chem. 44-46 24 (1961).

(185) Hermans, P., Weidinger, A. Makromol. Chem. 50 98 (1961).

(186) Ruland, W. Acta. Crystallogr. 14 1180 (1961).

(187) Ruland, W. Polymer 5 89 (1964).

(188) Alexander, L. X-Ray Diffraction Methods in Polymer Science Inter-Science, NY (1969).

(189) Crist, B., Moroscoff, N. J. Polym. Sci. Phys. 11 1023 (1973).

(190) Kifle, Z., Harrison, I., Herman, R. J. Polym. Sci. Phys. 24 633 (1986).

(191) Higgins, J., Stein, R. J. Appl. Crystallogr. 11 346 (1978).

(192) Ding, Z., Spruiell, J. J. Polym. Sci. Phys. 34 2783 (1996).

(193) Ding, Z., Spruiell, J. ANTEC 1994 40 1485 (1994).

References con't

(194) Ding, Z. Ph. D. Dissertation, Univ. of Tennessee (1996).

(195) Supaphol, P., Spruiell, J. J. Polym. Sci. Phys. **36** 681 (1998).

(196) Ding, Z., Spruiell, J. J. Polym. Sci. Phys. **35** 1077 (1997).

(197) Hannoi, C., Koch, J., Whitney, J. J. Appl. Polym. Sci. **1** 170 (1959).

(198) Ward, I. Proc. Phys. Soc. London **80** 1176 (1962).

(199) Ward, I. Text. Res. J. **34** 806 (1964).

(200) Mosely, W. J. Appl. Polym. Sci. **3** 266 (1960).

(201) Samuels, R. J. Polym. Sci. **A3** 1741 (1965).

(202) Ballou, J., Silverman, S. Text. Res. J. **14** 282 (1944).

(203) Samuels, R. J. Polym. Sci. **6** 1101 (1968).

(204) Ziabicki, A. Colloid Poyl. Sci. **274** 209 (1996).

(205) Ziabicki, A. Colloid Poyl. Sci. **274** 705 (1996).

(206) Ding, Z., Spruiell, J. J. Polym. Sci. Phys. **35** 1077 (1997).

(207) Doi, M., Edwards, S. The Theory of Polymer Dynamics Oxford Science, U.S.A. (1995).

(208) Supaphol, P., Spruiell, J. J. Poylm. Sci. Polym. Phys. **36** 681 (1997).

(209) Moore, E. Polypropylene Handbook Hanser, NY (1996).

(210) Mezghani, K. Ph.D. Dissertation, Univ. of Tennessee (1996).

(211) Khoury, F., Passaglia, E. Treatise on Solid State Chemistry Plenum Press Vol. 3 (1976).

(212) Mark, J. Physical Properties of Polymers Handbook AIP Press, NY (1996).

(213) Samuels, R. Structured Polymer Properties Wiley and Sons, NY (1974).

(214) Pae, K. J. Polym. Sci. **6** 657 (1968).

(215) Samuels, R. J. Polym. Sci. Phys. **13** 1417 (1975).

(216) Petraccone, V., Guerra, G., DeRosa, C., Tuzi, A. Macromolecules **18** 813 (1985).

References con't

(217) Yadav, Y., Jain, P. Polymer **27** 721 (1986).

(218) Wunderlich, B. Macromolecular Physics Academic Press, New York Vol. 3 (1980).

(219) Flory, P. Principles of Polymer Chemisty Cornell Press, NY (1953).

(220) Evans, R., Mighton, H., Flory, P. J. Chem. Phys. **15** 685 (1947).

(221) Flory, P., Vrij, A. J. Am. Chem. Soc. **85** 3548 (1963).

(222) Evans, R., Mighton, H., Flory, P. J. Am. Chem. Soc. **72** 2018 (1950).

(223) Hildebrand, J., Scott, R. The Solubility of Nonelectrolytes Nostrand-Reinhold, NY (1950).

(224) Hildebrand, J., Scott, R. Regular Solutions Prentice-Hall, NJ (1971).

(225) Biros, J., Zeman, L., Patterson, D. Macromolecules **4** 30 (1971).

(226) Maier, R., Thomann, R., Kressler, J., Mulhaupt, R., Rudolf, B. J. Polym. Sci. Polm Phys. **35** 1135 (1997).

(227) Cole, E., Holmes, D. J. Polym. Sci. **4** 245 (1960).

(228) Walter, E., Reding, F. J. Polym. Sci. **21** 561 (1956).

(229) Eichon, R. J. Polym. Sci. **31** 197 (1958).

(230) Swan, P. J. Polym. Sci. **56** 409 (1962).

(231) Helfand, E., Lauritzen, J. Macromolecules **6** 631 (1973).

(232) Morrow, D., Newman, B. J. Appl. Phys. **39** 4944 (1968).

(233) Sauer, J., Pae, K. J. Appl. Phys. **39** 4959 (1968).

(234) Campbell, R., Phillips, P., Lin, J.S. Polymer **34** 4809 (1993).

(235) Mo, Z., Zhang, H. J. Macromolecular Sci. Rev. C35(4) 555 (1995).

(236) Koberstein, J., Morra, B., Stein, R. J. Appl. Cryt. **13** 34 (1980).

(237) Ruland, W. J. Appl. Cryst. **4** 70 (1971).

(238) Vonk, C., Pijpers, J. J. Polym. Sci. Phys. **23** 2517 (1985).

References con't

(239) Vonk, C. J. Appl. Cryst. **6** 81 (1973).

(240) Strobl, G., Schneider, M. J. Polym. Sci. Phys. **18** 1343 (1980).

(241) Flory, P., Yoon, D., Dill, K. Macromolecules **17** 862 (1984).

(242) Yoon, D., Flory, P. Macromolecules **17** 2260 (1984).

(243) Ferro, D., Bruckner, S., Meille, S., Ragazzi, M. Macromolecules **25** 5231 (1992).

(244) Piccarolo, S. J. Macromol. Sci. Phys. **B31**(4) 501 (1992).

(245) Mandelkern, L. J. Polym. Sci. C **50** 457 (1975).

(246) Mandelkern, L. Characterization of Materials in Research: Ceramics and Polymers University Press, NY 1975.

(247) Manderkern, L. J. Appl. Cryst. **11** 548 (1975).

(248) Sadler, D., Gilmer, G. Polymer **25** 1446 (1984).

(249) Sadler, D. Polymer **24** 1401 (1983).

VITA

Eric Bryan Bond was born on August 15, 1969 in Beaufort, South Carolina. He graduated from Alleghany High School in June of 1987. Upon graduation of high school he enlisted in the United States Navy. He was trained as an electronic technician, boxsian mate, advanced fire fighting and physical security. After the Navy, he attended college at Clinch Valley College of the University of Virginia, receiving a Bachelor of Science degree in both Chemistry and Mathematics in May 1995. The degree in Chemistry had a concentration in biochemistry and biology related studies.

In December of 1999, he will graduate from the University of Tennessee-Knoxville with a Ph.D. in Polymer Engineering under major advisor Dr. Joseph E. Spruiell. Isotactic polypropylene catalyzed using metallocene and Ziegler-Natta catalysts were studied using crystallization kinetics, fiber spinning and thermal spunbonding studies. The requirements for the degree were completed in September of 1998.

Ziegler-Natta and Metallocene Catalyzed

Isotactic Polypropylene:

A Comprehensive Investigation and Comparison

using

Crystallization Kinetics, Fiber Spinning

and

Thermal Spunbonding.

A Dissertation Presented for the Doctor of Philosophy Degree

The University of Tennessee, Knoxville

Eric Bryan Bond

December 1999